

On Biomass Milling for Power Generation

by

Orla Williams MEng CEng MCIBSE MIMechE

Thesis submitted to the University of Nottingham for the degree of Engineering Doctorate

April 2016

Abstract

Biomass combustion has increasingly been used in pulverised fuel coal fired power stations as a way of addressing a wide range of emissions reduction targets. The reuse of existing equipment such as coal mills is essential to minimise the costs of conversion. However the fundamental fracture mechanics involved in biomass comminution are completely different to coal. Thus a thorough knowledge of the comminution properties of all biomass types in coal and biomass mills is necessary in order to minimise operational issues and to optimise milling and combustion.

This thesis provides extensive novel characterisation on densified biomass before and after milling. The study analysed 9 densified biomasses, 2 non-densified biomasses, and a sample coal in five different mills; planetary ball mill, Hardgrove Grindability Index testing mill, Bond Work Index ball mill, cutting mill, and a ring-roller mill.

Milling was found to have little impact on particle shape, even when an order of magnitude change in particle size was observed. Particle shape is inherent to the particles which comprise a pellet, and is determined by the pre-densified comminution processes. Milling had little impact on compositional particles of herbaceous or wood pellets. Olive cake had the most spherical of all the materials. Thermal pre-treatments of woody biomass not only saw a significant improvement in grindability in all mills, but also enhanced shape factors.

The Hardgrove Grindability Index is a poor indicator of the grindability of biomass. The Bond Work Index can be used to analyse the choking potential of biomass pellets prior to full scale mill trials. To optimise milling in coal mills, biomass pellets should be composed of particles close to the required size so that only the pellet comminution stage occurs. The milling behaviour of densified biomass in a laboratory scale ring-roller mill with dynamic classification was investigated for the first time. The milling studies showed that knowledge of a materials critical particle size for comminution through compression is essential to understand its milling behaviour in different mills.

The results presented in this thesis not only provide new insight and addresses significant gaps in knowledge, they also provide useful and practical guidance for addressing operational issues such as mill choking, as well as ways to optimise biomass comminution in laboratory and full scale mills, such as mill classifier optimisation based on real particle characteristics.

Acknowledgements

I'd like to give special thanks my academic supervisors Dr Carol Eastwick and Dr Donald Giddings for their support and guidance throughout the doctorate, as well as Prof. Ed Lester and Prof. Sam Kingman for additional supervision. I'd like to thank Prof. Colin Snape and the EFET EngD centre for providing support and facilities to allow me to conduct my research, and to the technical staff for general support and the refurbishment of the ring-roller mill. I'd like to thank Dr Shalini Graham, Dr Lee Stevens, and Dr Andrew Rawlinson for all giving me the opportunity to collaborate with them on their research, which has greatly enhanced the quality of my own.

I'd like to thank my industrial supervisors at EDF Energy plc; Norman Byrne and Stephen Lormor, who provided fantastic resources and unprecedented access to all areas of EDF Cottam and West Burton coal fired power stations, as well as providing copious amounts of samples for testing. I'd also like to thank Dr Will Quick at E.On, Dr Bill Livingston at Doosan, and Rod Taylor at Microwave Ltd for providing additional samples and industrial insight into biomass and coal comminution in the power generating sector. I'd also like to thank BF2RA and the EPSRC for their financial support during the project.

Finally, I'd like to thank my friends and family for their support during the doctorate, especially my friends and colleagues in the EFET and Thermofluids Research Groups. In addition, I'd like to thank Julian Parsley, Alper Erten, and Moana Reynau on the West Coast of the USA for their help and support in my decision to return to academia, and to Laura Smith, Rory Condon, Callum Hall, and Nikki Goddard for their support and keeping me sane through the course of the EngD.

Table of Contents

Abstract ..... **i**

Acknowledgements ..... **ii**

List of Figures ..... **ix**

List of Tables ..... **xiv**

Nomenclature ..... **xvi**

List of Publications ..... **xx**

Chapter 1 - Thesis Introduction **1**

1.1. Project Rationale 2

1.2. Aims, Scope & Significance 3

1.3. The Engineering Doctorate Scheme 4

1.4. Thesis Overview 4

Chapter 2 - Literature Review **7**

2.1. Project Context 7

2.2. Biomass Combustion Options 9

2.3. Biomass Structure and Properties 10

2.4. Woody Biomass 12

2.5. Herbaceous Biomass 14

2.6. Fruit Biomass 14

2.7. Biomass Thermal Pre-Treatments 15

2.8. Biomass Densification 16

2.9. Coal Structure and Properties 19

2.10. Impact of Biomass and Coal Compositional Differences on Combustion 20

2.11. Pulverised Fuel Milling and Classification Systems 20

2.12. Milling theory 26

2.13. Mill Breakage Modes and Particle Breakage Mechanisms 27

2.14. Hardgrove Grindability Index 30

2.15. Bond Work Index 31

2.16. Tube and Ball Mills 32

2.17. Vertical Spindle Mill 34
2.18. Hammer Mills 36
2.19. Beater Mills 38
2.20. Planetary Ball Mills 39
2.21. Mill Comparison Studies 41
2.22. Co-milling 41
2.23. Conclusions 42
Chapter 3 - Experimental 43
3.1. Characterisation of Samples 45
3.1.1. Moisture Content 45
3.1.2. Pellet Disintegration Test 46
3.1.3. Pellet Diameter and Length 46
3.1.4. Particle Size Distribution by Sieving 46
3.1.5. Digital Image Processing 47
3.1.6. Particle Distribution Analysis 47
3.1.6.1. Rosin-Rammler 47
3.1.6.2. Distribution Analysis 48
3.1.6.3. Size Parameters 48
3.1.6.4. Dispersion Parameters 49
3.1.7. Distribution Shape Parameters 50
3.1.8. Digital Imaging Shape Analysis 51
3.1.9. Moisture Re-Adsorption Test 53
3.1.10. Mechanical Strength of Pellets 53
3.1.11. Split Hopkinson Pressure Bar Test 55
3.1.12. Differential Scanning Calorimetry 60
3.1.13. Thermogravimetric Analysis 60
3.1.13.1. Slow Heating Pyrolysis Test 61
3.1.13.2. Reactivity Test 61

3.1.14. Bomb Calorimeter 61
3.1.15. Ultimate Analysis 62
3.1.16. Pellet and Particle Density 62
3.1.17. Pellet Durability 63
3.1.18. Abrasion Index 63
3.2. Milling of Samples 64
3.2.1. Energy Data Logging 65
3.2.2. Regression Analysis 66
3.2.3. Planetary Ball Milling 67
3.2.3.1. Optimisation 69
3.2.3.2. Impact of Drying on Different Biomass Materials 70
3.2.4. Cutting Milling 70
3.2.4.1. Cutting Mill Optimisation Experiments 70
3.2.4.2. Material Comparison & Impact of Drying Experiments 72
3.2.5. Ring-Roller Milling 72
3.2.6. Bond Work Index Test 76
3.2.7. Hardgrove Grindability Index 77
Chapter 4 - Biomass Characterisation 79
4.1. Materials and Methods 79
4.2. Biomass Pellet Dimensions 79
4.3. Particle Size Distributions of Pre-milled Samples 81
4.4. Sieved and Camsizer Pre-Milled Particle Size Distributions 84
4.5. Comparison of Pre-Milled Particle Size Distributions 88
4.6. Cumulative Shape Distributions of Pre-Milled Samples 89
4.7. Moisture Content and Moisture Re-adsorption 93
4.8. Pellet Durability 96
4.9. Quasi Static Mechanical Strength of Pellets 97
4.10. Split Hopkinson Pressure Bar Data 101
4.11. Abrasion Index 105

4.12. Thermal Characterisation 106
4.13. Conclusions 109
Chapter 5 - Application of Standard Coal Grindability Tests on Biomass 110
5.1. Materials and Methods 110
5.2. HGI Test 111
5.3. BWI Test Overall Results 112
5.4. BWI Mill Behaviour 113
5.5. Bond Index Test Particle Size Distributions 118
5.6. Impact of Pre-densified Pellet Particle Size on Bond Work Index 119
5.7. Thermal Composition of the Samples 120
5.8. Suitability of HGI test for Biomass 121
5.9. Comparison of HGI and BWI Methods 122
5.10. HGI and BWI Correlations for Biomass 123
5.11. Conclusions 124
Chapter 6 - Planetary Ball Mill 126
6.1. Materials and Methods 126
6.2. Planetary Ball Mill Optimisation Study 126
6.2.1. Milling Specific Effective Energy Consumption Rate Optimisation 128
6.2.2. Optimisation of Rosin-Rammler Size Parameter 130
6.3. Heat Generation and Caking within a Planetary Ball Mill 131
6.4. Impact of Drying on Milling Behaviour of Different Biomass Materials 145
6.4.1. Energy Consumption and Particle Size 146
6.4.2. Particle Shape 150
6.4.3. Heat Transfer with Materials 154
6.5. Conclusions 157
Chapter 7 - Cutting Mill 159
7.1. Materials and Methods 160
7.2. Cutting Mill Optimisation Study 160
7.2.1. Specific Effective Energy Optimisation 161
7.2.2. Optimisation of Mass Holdup 164

7.2.3. Optimisation of Rosin-Rammler Distribution Parameter 167
7.3. Optimal Conditions for Impact of Drying Tests 169
7.4. Impact of Drying on Material Comminution in a Cutting Mill 170
7.5. Impact of Drying on Milling Behaviour of Shredded Bagasse 171
7.6. Selected Cutting Milling Conditions 173
7.7. Impact of Drying on Biomasses Comminution in a Cutting Mill 173
7.7.1. Energy Consumption 174
7.7.2. Particle Size 177
7.8. Particle Shape 181
7.9. Conclusions 185
Chapter 8 - Ring and Roller Mill 186
8.1. Materials and Methods 186
8.2. Idle Conditions 187
8.3. Material Runs 190
8.4. Mill Pressures, Temperatures and Mass Output 192
8.5. Von Rittinger and HGI Relationships 197
8.6. Particle Size and Shape Characteristics 199
8.7. Conclusions 203
Chapter 9 - Practical Implications of the Study for Industry and Academia 204
9.1. Energy Consumption, Pellet Durability and Von Rittinger Relationships 204
9.2. Von Rittinger Constant and Particle Size Relationships 209
9.3. Mechanical Response and Milling Energy Relationships 210
9.4. Particle Size and Particle Shape Relationships 213
9.4.1. Woody Biomass 214
9.4.2. Herbaceous Biomass 217
9.4.3. Fruit Biomass 220
9.4.4. Thermally Treated Biomass 222
9.4.5. Coal 225
9.5. Particle Size-Shape Correlation 227
9.6. Use of the Planetary Ball Mill for Critical Particle Size Determination 228

9.7. Conclusions 229

Chapter 10 - Conclusions 231

10.1. Biomass Characterisation 231

10.2. Applicability of Standard Coal Grindability Tests for Biomass 231

10.3. Olive Caking 231

10.4. Mill Optimisation 231

10.5. Ring-Roller Mill 232

10.6. Overall Results 232

10.7. Directions for Future Research 233

References 235

Appendix A – Quasi-Static Mechanical Response Data 250

Appendix B – Mill Optimisation Regression Data 259

Appendix C – Ring-Roller Mill Pressure & Temperature Data 268

List of Figures

Figure 2.1: Co-firing Injection Options (Cremers, 2009) 9
Figure 2.2: Mean Structural Composition of the Biomass Groups and Sub-Groups Based on 93 Biomass Varieties, wt. % (Vassilev et al., 2012) 11
Figure 2.3: Macrostructure of Wood (Ashby et al., 1998) 12
Figure 2.4: Dynamic Classification of Coal from a Coal Mill Using a Separator (EDF Energy plc, 1981b) 22
Figure 2.5: Static Classification of Coal from a Coal Mill Using Buoyancy Classifier (EDF Energy plc, 1981a) 23
Figure 2.6: Relationship between the diameter of a Circumscribed Sphere (a) and the Nominal Diameter of a Sphere with the same Volume as the Particle (d) (Zavala, 2012) 24
Figure 2.7: Breakage Modes in Industrial Mills (Perry et al., 2008) 28
Figure 2.8: Compressive forces (a) are best for comminuting hard, brittle feedstocks, while shear forces (b) are best for soft feedstocks (Blair, 2014) 28
Figure 2.9: Pulverised Fuel Tube-Ball Mill (EDF Energy plc, 1981a) 33
Figure 2.10: Pulverised Fuel Ring-Roller Mill (EDF Energy plc, 1981b) 35
Figure 2.11: Cutting Mill (a) and Swinging Hammer Mill (b) (Blair, 2014) 37
Figure 2.12: Types of Beater Wheel Mills (Zhu, 2012) 39
Figure 2.13: Scheme of planetary disks with movement in a normal and counter direction (Burmeister et al., 2013) 40
Figure 3.1: (From top left to right) Spanish Olive Cake, La Loma Coal, Mixed Wood Pellets, Microwave Pellets, White Wood Pellets, South African Eucalyptus Pellets, Miscanthus Pellets, Steam Exploded Pellets, Olive Pellets, Torrefied Pellets, Sunflower Husk Pellets, Shredded Bagasse. Scale is in cm grid. 44
Figure 3.2: Definition of Feret Diameter (d_{Fe_max}), Shortest Chord/Sieving Diameter (d_{c_min}), Martin Diameter (d_{ma}), and Area Diameter (d_{area}) (Retsch Gmbh, 2009) 51
Figure 3.3: Mechanical testing of Pellets in a) Axial, b) Diametric, c) Flexure Modes 53
Figure 3.4: SHPB Schematic Arrangement (W. W. Chen et al., 2010) 55
Figure 3.5: SHPB Arrangement at the University of Nottingham 56
Figure 3.6: Incident and Transmitted Pulse for No Sample Condition 57
Figure 3.7: Incident, Reflected and Transmitted Pulse for Eucalyptus Pellets in Diametric Orientation 57
Figure 3.8: Positioning of Test Pellet in SHPB Rig 58
Figure 3.9: Langrangian Wave Propagation Diagram showing Stress Wave Propagation through space and time in SHPB (W. W. Chen et al., 2010) 59
Figure 3.10: Planetary Ball Milling Pot containing Milling Balls and Olive Cake (left) and Milling Pot Secured in Retsch PM100 Planetary Ball Mill (right) 68
Figure 3.11: Point Temperature Measurements of Comminuted Biomass (left) and Milling Balls (right) immediately after Planetary Ball Milling Test 68
Figure 3.12: Mill Rotor and Screen of Retsch SM300 Cutting Mill 71
Figure 3.13: Retsch SM300 Cutting Mill with Vibrating Bed Feeder (left) and Fritsch Vibrating Bed Feeder with Biomass Pellets Being Fed into Mill Hopped (right) 71
Figure 3.14: Lopulco LM 1.6 Flat Bed Ring-Roller Mill 73
Figure 3.15: Lopulco LM 1.6 Flat Table Ring-Roller Mill Schematic 74
Figure 3.16: Bico-Braun Bond Work Index Test Mill (left) and Milling Balls within (right) 76

Figure 3.17: Environmental Scientifics Group HGI Test Machine (left) and Biomass Sample Post HGI Test in Milling Pot with Balls (right) 78
Figure 4.1: Range of Pellet Diameters of Biomass Pellets 80
Figure 4.2: Range of Aspect Ratios for Biomass Pellets (Aspect Ratio Tolerance Line of 5 Indicated) 81
Figure 4.3: Cumulative Distribution of Particle Size for Disintegrated Pellets, La Loma coal and Olive Cake by Sieving 83
Figure 4.4: Comparison of Camsizer and Sieving Cumulative Distributions of Particle Size for La Loma Coal and Disintegrated Sunflower Pellets 84
Figure 4.5: Cumulative Distribution of Particle Sphericity 90
Figure 4.6: Cumulative Distribution of Particle Circularity 91
Figure 4.7: Cumulative Distribution of Particle Aspect Ratio 92
Figure 4.8: Cumulative Distribution of Particle Symmetry 92
Figure 4.9: Moisture Reabsorption over 24 hours for Various Biomass 94
Figure 4.10: Trend of Moisture Reabsorption for Varying Temperature and Relative Humidity for Eucalyptus Pellets over 6 Day Period 95
Figure 4.11: Pellet Durability of Samples Tested in Accordance with BS EN ISO 17831-1 (The British Standards Institution, 2013b) 96
Figure 4.12: Quasi-static Compressive Axial, Diametric, and Flexure Stress for Raw and Dry Steam Exploded Pellets 97
Figure 4.13: Quasi-Static Mean Compressive Axial, Diametric, and Flexure Stress for Raw and Dry Biomass Pellets 98
Figure 4.14: a) Axial Failure by Shear (Sunflower Pellets) b) Axial Failure by Delamination (Mixed Wood Pellets), c) Diametric Failure by Shear (Sunflower Pellets), d) Diametric Failure by Delamination (Mixed Wood Pellets) 99
Figure 4.15: Quasi-Static Compressive Axial, Diametric, and Flexure Young's Modulus for Raw and Dry Steam Exploded Pellets 100
Figure 4.16: Quasi-Static Mean Compressive Axial, Diametric, and Flexure Young's Modulus for Raw and Dry Biomass Pellets 101
Figure 4.17: Slow Motion Video Stills of SHPB Test on Mixed Wood Pellet in Diametric Orientation 102
Figure 4.18: Axial and Diametric Maximum Compressive Stress in Quasi-Static and Dynamic Mechanical Tests 104
Figure 4.19: Axial and Diametric Young's Modulus in Quasi-Static and Dynamic Mechanical Tests 105
Figure 4.20: Abrasion Index for Biomass & Coal 106
Figure 5.1: Mass per Size Fraction & Revolution Count against Run Count for BWI Test: a) Wood Pellets, b) Miscanthus Pellets, and c) Sunflower Pellets 114
Figure 5.2: Mass per Size Fraction & Revolution Count against Run Count for BWI Test: d) Eucalyptus Pellets, e) Olive Cake, and f) La Loma Coal 115
Figure 5.3: Mass per Size Fraction & Revolution Count against Run Count for BWI Test: g) Steam Exploded Pellets, h) Torrefied Pellets and, i) Microwave Pellets 116
Figure 5.4: Cumulative Distributions for the Final 3 runs for Biomass Sample 118
Figure 5.5: Bond Work Index (BWI) versus Hardgrove Grindability Index (HGI) 124
Figure 6.1: Tri-modal Structure of as Received Olive Cake 2013 Obtained by Sieving 127
Figure 6.2: Interaction Plots of the Variables in the Specific Effective Energy Consumption Rate Regression Analysis for the Planetary Ball Mill 128
Figure 6.3: Specific Effective Energy Consumption Rate against Time for 100ml of Sample 129

Figure 6.4: Interaction between Speed and Energy Input for Rosin-Rammler Size Parameter Regression Analysis 131
Figure 6.5: Caking of Olive Cake within the Planetary Ball Mill at 600 RPM, 200 ml and 8 kJ mill settings (a) and dusting at 200 RPM, 200 ml and 8 kJ mill settings (b) 131
Figure 6.6: Thermal Imaging of Heat Generation in Olive Cake Milled in a Planetary Ball Milling at 200 RPM for 10-50 Minutes 133
Figure 6.7: Thermal Imaging of Heat Generation in Olive Cake Milled in a Planetary Ball Milling for 60 Seconds at 100-600 RPM 134
Figure 6.8: Impact of Varying Speed and Volume on Specific Effective Energy Consumption and Percentage Loose Mass of Olive Cake Milled in a Planetary Ball Mill for 60 Seconds 135
Figure 6.9: Specific Effective Energy Consumption for As Received and Dried Olive Cake in Un-sieved, Pulp, Pip, and Lump Sections 136
Figure 6.10: Cumulative Particle Size Distribution for Pre-Milled and Milled As Received and Dried Olive Cake 137
Figure 6.11: Cumulative Particle Size Distribution for Milled as Received and Dried Olive Cake Pulp (0-850 µm), Pips (850-350 µm), and Lumps (3350+ µm) 138
Figure 6.12: Caking and Heat Generation for Milled As Received and Dried Olive Cake in Un-sieved and Pulp Sections 139
Figure 6.13: Caking and Heat Generation for Milled As Received and Dried Olive Cake in Pip and Lump Sections 140
Figure 6.14: Specific Effective Energy Consumption against Particle Size Reduction Ratio for Milled and Dried Olive Cake 141
Figure 6.15: First (top) and Second (bottom) Heating Scan in DSC for As Received and Dried Olive Cake 144
Figure 6.16: Specific Effective Energy Consumption for Densified Biomasses and Olive Cake in As Received and Dried States in a Planetary Ball Mill 146
Figure 6.17: Specific Effective Energy Consumption against Particle Size Reduction for As Received and Dried Densified Biomasses and Olive Cake in a Planetary Ball Mill 149
Figure 6.18: Cumulative Particle Size Distributions for Disintegrated, Planetary Ball Mill Comminuted Miscanthus in As Received and Dried States 150
Figure 6.19: Planetary Ball Mill Comminuted Biomass Particle as Received (a) and Dried (b) Sphericity and Circularity (c and d) Cumulative Particle Shape Distributions 152
Figure 6.20: Planetary Ball Mill Comminuted Biomass Particle as Received (e) and Dried (f) Symmetry and Aspect Ratio (g and h) Cumulative Particle Shape Distributions 153
Figure 6.21: Thermal Imaging of Heat Generation in As Received (above) and Dried (below) Olive Pellets, Olive Cake 2013 and 2014 (left to right) Milled in a Planetary Ball Mill 154
Figure 6.22: Thermal Imaging of Heat Generation in As Received (Above) and Dried (Below) Eucalyptus, Mixed Wood, and Miscanthus Pellets (Top 2 Rows left to right) and Sunflower, Steam Exploded and Microwave Pellets (Bottom 2 Rows left to right) Milled in a Planetary Ball Mill 155
Figure 6.23: Biomass and Ball Temperatures for Biomass Milled in a Planetary Ball Mill 156
Figure 6.24: First Heating Scan in DSC for As Received Biomass Samples 157
Figure 7.1: Cutting Mill Idle Average Energy Consumption versus Mill Speed 161
Figure 7.2: Interaction plots for Speed and Feed Rate for the Cutting Mill Optimisation Experiments 162

Figure 7.3: Predicted and Measured Specific Energy Consumption for the Cutting Mill..... 163
Figure 7.4: Interaction Plots of the Variables in the Mass Holdup Regression Analysis for the Cutting Mill 165
Figure 7.5: Pre-milled and Milled Particle Size Distribution at a Speed of 2200 RPM for low (0.006 kg/s), Medium (0.01 kg/s) and High (0.06 kg/s) Feed Rates and 1.5 mm and 4 mm Screens 166
Figure 7.6: Predicted & Measured Percentage Mass Holdup 167
Figure 7.7: Interaction Plots of the Variables in the Distribution Parameter Regression Analysis for the Cutting Mill 168
Figure 7.8: Predicted & Measured Rosin-Rammler Distribution Parameter 169
Figure 7.9: Specific Effective Energy Consumption against Screen Size for Bagasse 172
Figure 7.10: Specific Effective Energy Consumption for As Received and Dried Samples for the Cutting Mill 174
Figure 7.11: As Received Cutting Mill Specific Effective Energy Consumption against Pellet Durability 176
Figure 7.12: Specific Effective Energy Consumption E_e against Particle Size Reduction Ratio for the Cutting Mill 177
Figure 7.13: Cumulative Particle Size Distributions for Disintegrated, Cutting Mill Comminuted As Received and Dried Olive Cake 178
Figure 7.14: Cumulative Particle Size Distributions for Disintegrated, Cutting Mill Comminuted As Received and Dried Miscanthus 179
Figure 7.15: Cutting Mill Comminuted Biomass Particle as Received (a) and Dried (b) Sphericity, and As Received (c) and Dried (d) Circularity 183
Figure 7.16: Cutting Mill Comminuted Biomass Particle as Received (e) and Dried (f) Symmetry, and As Received (g) and Dried (h) Aspect Ratio 184
Figure 8.1: Observed Speed (RPM) against Speed Setting (Hz) for Screw Feeder 187
Figure 8.2: Observed Speed against Speed Setting for the Mill Bed 188
Figure 8.3: Fan, Rotary Air Valve, Mill Bed and Screw Feeder Idle Energy Consumption Profile 189
Figure 8.4: Idle Pressures for Ring-Roller Mill: Vent Pressure Tap (P1), Mill Inlet Pressure Tap (P2), Mill Outlet Pressure Tap (P3), Venturi Upstream Pressure Tap (P4), Venturi Inlet Pressure Tap (P5), Venturi Central Pressure Tap (P6), Venturi Downstream Pressure Tap (P7) 190
Figure 8.5: Specific Effective Energy Consumption for Densified Biomass & La Loma Coal in the Ring-Roller Mill 191
Figure 8.6: Ring-Roller Mill Specific Effective Energy Consumption against Pellet Durability for Biomass Pellets 192
Figure 8.7: Microwave Mill Inlet, Chamber, and Outlet Temperatures and Inlet (P2) and Outlet (P3) Differential Pressures 193
Figure 8.8: Microwave Mass Output from the Ring-Roller Mill and Associated Output Mass Flow Rate 194
Figure 8.9: Mixed Wood Mill Inlet, Chamber, and Outlet Temperatures and Inlet (P2) and Outlet (P3) Differential Pressures 195
Figure 8.10: Mixed Wood Mass Output from the Ring-Roller Mill and Associated Output Mass Flow Rate 196
Figure 8.11: Specific Effective Energy Consumption E_e versus Difference in Feed and Product Particle Size for the Ring-Roller Mill 198
Figure 8.12: Ring Roller Mill Von Rittinger's Constant against HGI Values for Biomass and La Loma Coal 198

Figure 8.13: Ring-Roller Mill Comminuted Biomass and Coal Cumulative Particle Shape Distributions for Sphericity (a), Circularity (b), Symmetry (c), and Aspect Ratio (d) 201
Figure 8.14: Relationship between Particle Sphericity and Particle Shape of Milled Biomass and Coal 202
Figure 9.1: Specific Effective Energy Consumption for Different Mills by Biomass and Coal Type 205
Figure 9.2: Relationship between Specific Effective Energy Consumption and Pellet Durability for a Planetary Ball Mill, Cutting Mill, and Ring-Roller Mill for Different Densified Biomasses. Biomass Samples have same Pellet Durability for Each Mill Type. 208
Figure 9.3: Von Rittinger Constant against Rosin-Rammler Characteristic Particle Size for Biomass Milled in Different Mills 209
Figure 9.4: Von Rittinger & HGI Relationships for a Planetary Ball Mill, Cutting Mill, and Ring-Roller Mill for Different Densified Biomass 210
Figure 9.5: Specific Effective Energy Consumption against Flexure Stress for Planetary Ball Mill, Cutting Mill and Ring-Roller Mill. 211
Figure 9.6: Specific Effective Energy Consumption against Maximum Axial Stress for Planetary Ball Mill, Cutting Mill and Ring-Roller Mill. 212
Figure 9.7: Specific Effective Energy Consumption against Maximum Diametric Stress for Planetary Ball Mill, Cutting Mill and Ring-Roller Mill. 213
Figure 9.8: Pre-milled and Milled Eucalyptus Particle Size Distributions (top) and Particle Size (based on d_{c_min}) and Shape Images (bottom) 215
Figure 9.9: Pre-milled and Milled Mixed Wood Particle Size Distributions (top) and Particle Size (based on d_{c_min}) and Shape Images (bottom) 216
Figure 9.10: Pre-milled and Milled Sunflower Particle Size Distributions (top) and Particle Size (based on d_{c_min}) and Shape Images (bottom) 218
Figure 9.11: Pre-milled and Milled Miscanthus Particle Size Distributions (top) and Particle Size (based on d_{c_min}) and Shape Images (bottom) 219
Figure 9.12: Pre-milled and Milled Olive Cake Particle Size Distributions (top) and Particle Size and (based on d_{c_min}) Shape Images (bottom) 221
Figure 9.13: Pre-milled and Milled Microwave Particle Size Distributions (top) and Particle Size (based on d_{c_min}) and Shape Images (bottom) 223
Figure 9.14: Pre-milled and Milled Steam exploded Particle Size Distributions (top) and Particle Size (based on d_{c_min}) and Shape Images (bottom) 224
Figure 9.15: Pre-milled and Milled La Loma Coal Particle Size Distributions (top) and Particle Size (based on d_{c_min}) and Shape Images (bottom) 226
Figure 9.16: Mean Sphericity and Particle Size (d_{80}) for Different Biomasses and Coals Comminuted in Different Mills 227

List of Tables

Table 3.1: Matrix of Milling Experiments Conducted for Each Sample 64
Table 4.1: Shape, Dispersion, and Distribution Shape Parameters of the Cumulative Size Distributions Disintegrated & Powdered Biomass & Coal by Sieving Notably Results Discussed in the Text are in Bold 85
Table 4.2: Shape, Dispersion, and Distribution Shape Parameters of the Cumulative Size Distributions Disintegrated & Powdered Biomass & Coal by Digital Image Analysis (Camsizer) Notably Results Discussed in the Text are in Bold 86
Table 4.3: Percentage Difference between Sieved and Camsizer Rosin-Rammler, Size, Shape and Distribution Shape Parameters 87
Table 4.4: Mean Sphericity, Circularity, Aspect Ratio, and Symmetry for Disintegrated and Powdered Samples 90
Table 4.5: Moisture Content and Moisture Reabsorption for Exposed Biomass and Biomass Stored in Sealed Bags 93
Table 4.6: Mean Diametric and Axial Young's Modulus, Maximum Stress and Strain Rates 103
Table 4.7: Reactivity Analysis of Pre-Milled Biomass & Coal 107
Table 4.8: Slow Pyrolysis Results for Pre-Milled Biomass and Coal 108
Table 4.9: Dry Higher Heating Value, Particle and Pellet Density and Ultimate Analysis for Pre-milled Biomass and Coal 108
Table 5.1: Summary of HGI and BWI Data for all Samples; Hardgrove Grindability Index HGI, 80% Passing Feed Size F_{80}, 80% Passing Product Size P_{80} , Grindability per Revolution G, Final Revolution Count RF, Bond Work Index W_i, Work Input W, Dry Higher Heating Value HHV_d, Work Input- Dry Higher Heating Value Ratio W/HHV_d 111
Table 5.2: Rosin-Rammler and Geometric Mean Diameter Analysis of Cumulative Distributions of Product from Final 3 Runs; 80% Passing Product Size P_{80} , Rosin-Rammler Characteristic Particle Size d', Rosin-Rammler Size Distribution Parameter n, Rosin-Rammler Coefficient of Determination R^2, Geometric Mean Diameter d_{gw}, Geometric Standard Deviation s 119
Table 5.3: Pellet Particle Size FPP_{80}, and Revised Bond Work Index WPP_i, Work Input WPP for Pellet Particle Size FPP_{80} 120
Table 5.4: Thermal Composition Data for the Samples from TGA on wt.% of Dry Fuel (Standard Deviation Across all Runs are shown in Brackets) 121
Table 5.5: Comparison of HGI & BWI Test Conditions 123
Table 6.1: Mill Settings used for Mill Optimisation Tests in Planetary Ball Mill 127
Table 6.2: Von Rittinger's Constant for As Received and Dried Milled Olive Cake Sections 142
Table 6.3: Shape, Dispersion and Distribution Shape Parameters of the Cumulative Particle Size Distributions for As Received (blue) and Dried (red) Biomass Milled in the Planetary Ball Mill. Sunflower Particle Sizes are for Sub 4750 µm, Olive Cake 2013 and Pellets sub 3350 µm, and Miscanthus sub 2360 µm. Notable Results are in Bold 148

Table 6.4: Von Rittinger's Constant for As Received and Dried Milled Densified Biomass and Olive Cake 149
Table 6.5: Impact of Drying on Average Particle Sphericity, Circularity, Symmetry and Aspect Ratio for Biomass Milled in Planetary Ball Mill (As Received in Blue, Dried in Red). Notably Results in Bold 151
Table 7.1: Comparison of Evaporation Energy for Wet Bagasse and the Difference in Milling Energies of Wet and Dried Bagasse..... 173
Table 7.2: Comparison of Evaporation Energy for Wet Biomass and the Difference in Milling Energies of Wet and Dried Biomass 176
Table 7.3: Shape, Dispersion and Distribution Shape Parameters of the Cumulative Particle Size Distributions for As Received and Dried Biomass Milled in the Cutting Mil. Notable results in Bold 180
Table 7.4: Impact of Drying on Average Particle Sphericity, Circularity, Symmetry and Aspect Ratio for Biomass Milled in Cutting Mill 182
Table 8.1: Average Idle Pressure Readings for Ring-Roller Mill: Vent Pressure Tap (P1), Mill Inlet Pressure Tap (P2), Mill Outlet Pressure Tap (P3), Venturi Upstream Pressure Tap (P4), Venturi Inlet Pressure Tap (P5), Venturi Central Pressure Tap (P6), Venturi Downstream Pressure Tap (P7)..... 190
Table 8.2: Percentage Mass Output at End of Feed, Percentage Mass Loss, Feed Rate, Mass Output Rate, and Mass Stabilisation Time Post Feed for Densified Biomass and La Loma Coal Comminuted in the Ring-Roller Mill..... 197
Table 8.3: Shape, Dispersion and Distribution Shape Parameters of the Cumulative Particle Size Distributions for Biomass and Coal Milled in the Ring-Roller Mill 199
Table 8.4: Impact of Drying on Average Particle Sphericity, Circularity, Symmetry and Aspect Ratio for Biomass Milled in Ring-Roller Mill 200
Table 9.1: Pre-milled and Milled Specific Effective Energy Consumption E_E, Ratio of E_E to Dry Higher Heating Value (HHV_d), Rosin-Rammler Analysis and Von Rittinger (VR) Constants..... 206

Nomenclature

Notation	Description
a	Maximum intercept through a particle (μm)
A	Area (m^2)
A_B	Cross-sectional area of Split Hopkinson Pressure Bar (mm^2)
A_S	Cross-sectional area of specimen (mm^2)
AF	Amplification factor (dimensionless)
AI	Abrasion Index (dimensionless)
AR	Particle Aspect Ratio (dimensionless)
APR	Pellet Aspect Ratio (dimensionless)
b	Exponent of energy comminution equation (dimensionless)
B	Characteristic system dimension (μm)
C	Circularity of a particle (dimensionless)
C_b	Elastic wave bar speed (ms^{-1})
C_c	Coefficient of Curvature (dimensionless)
C_u	Uniformity Coefficient (dimensionless)
d	Nominal diameter of a particle (μm)
d'	Rosin-Rammler characteristic particle size (μm)
d_5	Particle size at 5th percentile of cumulative distribution (μm)
d_{10}	Particle size at 10th percentile of cumulative distribution or effective size (μm)
d_{16}	Particle size at 16th percentile of cumulative distribution (μm)
d_{25}	Particle size at 25th percentile of cumulative distribution (μm)
d_{30}	Particle size at 30th percentile of cumulative distribution (μm)
d_{50}	Particle size at 50th percentile of cumulative distribution (μm)
d_{60}	Particle size at 60th percentile of cumulative distribution (μm)
d_{63}	Particle size at 63.2 percentile of cumulative distribution (μm)
d_{75}	Particle size at 75th percentile of cumulative distribution (μm)
d_{84}	Particle size at 84th percentile of cumulative distribution (μm)
d_{90}	Particle size at 90th percentile of cumulative distribution (μm)
d_{95}	Particle size at 95th percentile of cumulative distribution (μm)
d_a	Area equivalent diameter of a particle (μm)
d_{area}	Area diameter (μm)
d_{c_min}	Shortest chord diameter (μm)
d_{Fe_max}	Maximum Feret diameter (μm)
d_{gw}	Geometric mean diameter by mass (mm)
d_i	Nominal sieve aperture size of the ith sieve (mm)
$\bar{d}_i$	Mean geometric diameter of the nominal sieve aperture size of the ith sieve, mm
d_{ma}	Martin diameter (μm)
d_p	Perimeter equivalent diameter of a particle (μm)
d_P	Particle size (μm)
d_s	Diameter of spherical particle (μm)
D_U	Pellet Durability Rating (%)
d_v	Diameter of a sphere having the same volume of a non-spherical particle (μm)

Notation	Description
e_s	Engineering strain (dimensionless)
$\dot{e}_s$	Engineering strain rate (s^{-1})
E_a	Compressive axial Young's Modulus (MPa)
E_B	Young's Modulus of the Split Hopkinson Pressure Bar (MPa)
E_d	Compressive diametric Young's Modulus (MPa)
E	Net specific energy (kWh/t)
E_e	Total effective specific energy (kWh/ton)
E_{flex}	Flexure Young's Modulus (MPa)
E_I	Total Input Energy (kJ)
$\dot{E}_i$	Specific Effective Energy Consumption Rate (kW/t)
E_s	Total specific energy (kWh/ton)
F	Applied force (kN)
F_{80}	80% passing size of the feed (µm)
FPP_{80}	Pre-milled pellet particle 80th passing size (µm)
g	Gravitational acceleration (m/s^2)
G	Gram per revolution (g/rev)
GF	Gauge factor (dimensionless)
GS_i	Inclusive graphic skewness (dimensionless)
HGI	Hardgrove Grindability Index (dimensionless)
HHV	Higher Heating Value (J/g)
HHV_d	Dry Higher Heating Value (J/g)
hs	Distribution geometric standard deviation of high region (dimensionless)
I	Second moment of area (mm^4)
k	Gradient of force-displacement curve (kN/mm)
K	Material constant in general comminution energy equation (dimensionless)
K_B	Bond constant
K_g	Geometric kurtosis (dimensionless)
K_K	Kick constant
k_v	Stokes number shape factor (dimensionless)
K_{VR}	Von Rittinger constant
L	Span length between 3-point bend test supports (mm)
L_s	Split Hopkinson Pressure Bar specimen length (mm)
l	Length of a pellet (mm)
l_i	Compressed length of pellet (mm)
ls	Distribution geometric standard deviation of low region (dimensionless)
M	Moisture content (%)
m	Mass of sample in milling tests (g)
m_1	Total initial mass of the four abrasion index blades (g)
m_2	Total final mass of the four abrasion index blades (g)
m_3	Mass of the Abrasion Index test portion (kg).
m_a	Mass of pellet in air (g)
m_A	Mass of sieved pellets after the tumbling treatment (g)
m_E	Mass of pre-sieved pellets before the tumbling treatment (g)

Notation	Description
m_f	Mass retained on the 75µm sieve (g)
m_i	Mass of pellet in water (g)
M_i	Mass on ith sieve (g)
MRS	Mass Relative Span (dimensionless)
n	Rosin-Rammler size distribution parameter (dimensionless)
p	Measured circumference of a particle projection (µm)
P	Instantaneous power consumption (kW)
P_1	Target equilibrium sieve size (µm)
P_{80}	80% passing size of the product (µm)
P_A	Normal force on incident bar (kN)
P_B	Normal force on transmitted bar (kN)
P_i	Average idle power consumption (kW)
Q_{50}	50th Percentile of a cumulative distribution
r	Radius of a pellet (mm)
r_1 *and* r_2	Distance from the centre of area of the borders in measuring direction (µm)
R(d)	Rosin-Rammler cumulative percentage undersize mass (%)
RF	Final revolution count (dimensionless)
s	Geometric standard deviation of log-normal distribution by mass in ten-based logarithm (dimensionless)
s_s	Engineering stress (MPa)
S_t	Stokes Number (dimensionless)
Symm	Symmetry of a particle (dimensionless)
t	Time (seconds)
T_g	Glass transition temperature (°C)
$u_{P,0}$	**Velocity of particle (m/s)**
V_{ex}	Excitation Voltage (volts)
V_{out}	Strain gauge measured voltage (volts)
W	Work input (kWh/t)
W_i	Bond Work Index (kWh/t)
WPP	Work input for FPP_{80} (kWh/t)
WPP_i	Bond Work Index for FPP_{80} (kWh/t)
x	Characteristic dimension of product (µm)
x_1	F particle size (d_{50} or d_{80}) (µm)
x_2	Product particle size (d_{50} or d_{80}) (µm)
ε	Compressive strain (dimensionless)
ε_I	Incident strain (dimensionless)
ε_R	Reflected strain (dimensionless)
ε_s	True strain (dimensionless)
ε_T	Transmitted strain (dimensionless)
$\dot{\varepsilon}_s$	True strain rate (s^{-1})
Θ	Burning enhancement factor (dimensionless)
μ	Dynamic viscosity of settling medium (Pa.s)
ρ_b	Density of Split Hopkinson Pressure Bar (kg/m^3)

Notation	Description
ρ_f	Density of settling medium (kg/m^3)
ρ_i	Density of deionised water (kg/m^3)
ρ_m	Density of a pellet (kg/m^3)
ρ_P	Density of particles (kg/m^3)
σ_a	Compressive axial stress (MPa)
σ_d	Compressive diametric stress (MPa)
σ_f	Compressive flexure stress or Modulus of Rupture (MPa)
σ_s	True stress (MPa)
φ	Sphericity of a particle (dimensionless)

List of Publications

Journal Publications:

Williams, O., Eastwick, C., Kingman, S., Giddings, D., Lormor, S., & Lester, E. *Investigation into the applicability of Bond Work Index (BWI) and Hardgrove Grindability Index (HGI) tests for several biomasses compared to Colombian La Loma coal*. Fuel. 158. (2015): 379-387

Dawson, R., Stevens, L. A., Williams, O. S., Wang, W., Carter, B. O., Sutton, S., Drage, T. C., Blanc, F., Adams, D. J., & Cooper, A. I. *'Dry bases': carbon dioxide capture using alkaline dry water*. Energy & Environmental Science 7.5 (2014): 1786-1791.

Rollinson, A.N. & Williams, O. *Experiments on torrefied wood pellet – Study by gasification and characterisation for waste biomass to energy applications*. (Accepted for publication in Royal Society Open Source)

Williams, O., Newbolt, G., Eastwick, C., Kingman, S., Giddings, D., Lormor, S., & Lester, E. *Influence of Mill Type on Densified Biomass Comminution.* (Submitted for publication in Applied Energy)

Conference Proceedings:

Williams, O., Eastwick, C., Lester, E., Giddings, D., & Lormor, S. (2015). *The Mechanical Response of Biomass Pellets in Standard Coal Grindability Tests*. In: ICCS&T/ACSE 2015

Williams, O., Eastwick, C., Lester, E., Giddings, D., & Lormor, S. (2015). *Paper Number 152180910: Impact of Mill Type on Biomass Mill Behavior*. In: 2015 ASABE Annual International Meeting.

Williams O, Eastwick C, Lester E, Giddings D, Byrne N. 2014 *Bond Index & Hardgrove Grindability Index Tests For Biomass & Coal* In: 10th ECCRIA (European Conference on Coal Research and its Applications) 49

Williams O, Eastwick C, Lester E, Giddings D, Byrne N. 2014 *The impact of moisture on the milling behaviour of different biomasses*. In: 22nd European Biomass Conference and Exhibition. 467–71. (Winner of the student award for excellent research work in the field of biomass)

Williams, O., Eastwick, C., Graham, S., Cooper, A., 2013. *The Impact of Storage on the Optimisation of Milling of Biomasses used in Power Generation*. In: 3rd IEA CCC Workshop on Co-firing Biomass with Coal

Williams, O., Eastwick, C., Lester, E., Giddings, D., Byrne, N., 2013. *Optimisation of Biomass Milling for Conveyance and Combustion*. In: 21st European Biomass Conference and Exhibition. 1164 – 1166

Chapter 1 - Thesis Introduction

Over the past decade, biomass combustion has increasingly been utilised in pulverised fuel coal fired power stations across Europe as a way of addressing a wide range of emission reductions targets (Climate Change Act, 2008; European Parliament and Council, 2001). The reuse of existing equipment is essential to minimise costs in plants which are often towards the end of their useful life. However one of the main limiters in increasing biomass combustion is in the comminution section of the plant. The fundamental fracture mechanics involved in biomass comminution are completely different to coal; coal has a brittle micro-structure with pre-existing macro and micro flaws which coal mills are designed to exploit, while biomass is a ductile orthotropic material and struggles to be comminuted in coal mills, resulting in reduced thermal boiler output, mill choking, and mill explosions (Loo et al., 2008). In order to optimise biomass combustion, biomass milling either needs to be optimised over the range of coal mills available or replacement mills need to be identified. Current research has focuses on the agricultural sector and energy crops, but little work has been published on biomass milling for the power sector, particularly in respect to biomass pellets. The field of biomass milling is rapidly changing as new feed stocks are sought to supply the increasing demand for bioenergy, and research is required to understand their milling behaviour compared to traditional feedstocks. Beyond the operational demands for this research, the data on particle size and shape characteristics is urgently required in the field of combustion and particle flow Computational Fluid Dynamics (CFD) to give more accurate mill classification, pneumatic conveying, and combustion models for biomass conversions and new builds.

This thesis examines the milling characteristics of a wide range of densified biomasses for several mill types. The research focuses on the comminution properties of wood, herbaceous, fruit, and thermally treated biomass in five different mills; planetary ball mill, Hardgrove Grindability Index (HGI) testing mill, Bond Work Index (BWI) ball mill, cutting mill, and a ring-roller mill. This chapter will introduce the engineering doctorate scheme, the industrial partner, and project rationale for the research undertaken during this study. The aims and objectives of the study, along with the significance of the work will be set out, and finally the thesis overview, novelty and significance of the work will be outlined.

1.1. Project Rationale

In spite of concerns and legislation to combat increasing carbon emissions, global coal consumption by power generators is growing annually (BP plc, 2014). Coal remains the second largest energy source worldwide and consumption is expected to rise annually by 1.3% until 2020, and is still expected to provide as much as 37% of the worlds fuel for electricity generation in 2040 (US EIA, 2013). However in the UK, the Large Combustion Plant Directive (European Parliament and Council, 2001) will result in the closure of 6 coal fire power plants in the UK by the end of 2015 (Department of Energy & Climate Change, 2007). The Industrial Emissions Directive (IED) could lead to further coal plant closures by 2023 (Department of Energy & Climate Change, 2015e). The UK government, through the Climate Change Act 2008, has legally committed to cut carbon emissions by 80% by 2050 compared to 1990 levels (Climate Change Act, 2008). To achieve this, it is estimated that an economy wide emissions cut of around 6% is needed by 2030, which would require a complete decarbonisation of the electricity sector by 2030 (Committee on Climate Change, 2011). Large investments have been made in coal power plants to reduce emissions in the last decade, but further investments will be required due to the LCPD and IED regulations to reduce particulate, nitrogen oxides (NO_X) and sulphur oxide (SO_X) emissions. Biomass Co-firing offers a near-term low cost solution for reducing carbon and NO_X emissions from conventional fossil fuel power plants.

In 2014, renewable energy accounted for 7% of the all UK energy consumption (64.7 TWh generation, and 24.6 GW capacity) (Department of Energy & Climate Change, 2015b). Of this, bioenergy sources contributed 13.1 TWh, mainly due to the conversion of a second unit at Drax power station to dedicated biomass. Co-firing of biomass with coal has decreased due to changes in the subsidies available for biomass combustion in the UK. However after a spate of fires at biomass power plants across Europe (Argus Media Ltd, 2012; BBC, 2012, 2014; ClickGreen, 2012; D. Williams, 2012), some of which related to the conveying and milling portions of the plant, there is an urgent need to gain a greater understanding of biomass milling behaviour. Milling studies tend to be aimed at one group of biomasses or mill types. This study aims to provide a comprehensive study of commercially available biomass from all biomass groups in a diverse range of comminution systems. Currently there are no standard grindability tests for biomass. The standard grindability test for coal for vertical spindle mills (HGI) has been tested with little success for biomass (Bridgeman et al., 2010; Ohliger et al., 2013), and the BWI test has not been tested on biomass until this study. There has been little research on the impact of biomass milling on particle shape

characteristics, which are essential for CFD conveying and combustion models. Different biomasses exhibit different milling behaviours, and the emergence of thermally treated biomasses means that milling behaviour data is needed beyond the traditional sources of wood and grass. While significant research been conducted on the comminution of non-densified biomasses, there have only been a few studies for densified biomass feedstocks. This study is the first to look at the comminution behaviour of densified biomasses from all biomass groups. It is also the first to compare the milling behaviour in five distinct types of mills, and the first to analyse the impact of milling on the particle shape and size of densified biomass.

1.2. Aims, Scope & Significance

The aim of this thesis is to analyse and characterise the milling behaviour of a wide range of biomasses in several different types of laboratory scale coal and biomass mills, providing data which will enable power generators to make more informed decisions about the likely mill performance for a given type of biomass in a given type of mill. In this thesis, detailed experimental and analytical data will be presented to characterise the biomass physical and thermo-chemical characteristics before and after milling. Extensive mechanical and physical characterisation using novel techniques will provide a previously unseen insight into the impact of milling on the physical parameters and mechanical properties of biomass before, during and after milling. The research objectives of the thesis are:

i. Review the state of the art in biomass milling and ascertain the suitable testing methodologies for the study
ii. Characterise the mechanical and thermo-chemical biomass properties prior to and after milling
iii. Understand how variable mill settings impact the milling behaviour of biomass in a planetary ball mill and cutting mill
iv. Understand the impact of drying on biomass milling behaviour for a wide range of biomasses in a planetary ball mill and cutting mill
v. Investigate the applicability of standard coal grindability tests for biomass
vi. Investigate the milling behaviour of a laboratory scale ring-roller mill with dynamic classification for densified biomass
vii. To replicate known milling comminution issues such as mill choking and material caking on a laboratory scale

viii. To compare biomass milling performance across the range of mills and provide the industrial sponsor with a summary of milling performance by biomass and mill type

The significance of this study is that it brings new knowledge and insight into how the physical properties of biomass are impacted by different mill types. From an academic perspective, the study will present novel methods of characterising mill behaviour, such as 3D particle shape characterisation, which bring an increased understanding of the fracture mechanics of biomass within mills, and the impact of milling on the physical and mechanical characteristics of biomass. The study will highlight the opportunities and limitations of laboratory scale milling trials for informing full scale milling optimisation. From an industrial perspective, the study will provide applicable and current milling performance data on a wide range of commercially sourced biomasses, as well as providing data to improve biomass milling, conveying, and combustion modelling. The novel use of existing standard coal tests, such as the BWI test, provides industry and academia with a method of replicating operational issues such as mill choking on a lab scale, in addition to providing fundamental insights into the opportunities and limitations of biomass milling.

1.3. The Engineering Doctorate Scheme

This research project forms part of a collaboration between the University of Nottingham Centre in Efficient Fossil Energy Technologies (EFET) Engineering Doctorate (EngD) programme and the Biomass and Fossil Fuel Research Alliance (BF2RA). The project is co-funded between the Engineering and Physical Sciences Research Council (EPSRC) and BF2RA as the industrial partner. BF2RA is formed of several power generators including Alstom, British Sugar, Doosan Power Systems, Electric Power Research Institute (EPRI), Électricité de France (EDF) Energy plc, and E.ON New Build & Technology Ltd. Principal industrial supervision was provided by EDF Energy plc at Cottam coal fired power station in the UK, with additional support and materials from British Sugar, E.On and Doosan Power Systems. The materials and output from this project will feed into several related EngD and PhD projects being run between BF2RA, EFET EngD Centre, and the Carbon Capture and Storage and Cleaner Fossil Energy (CCS CFE) EngD Centre at the University of Nottingham.

1.4. Thesis Overview

The thesis consists of a further 9 chapters within three main parts. In Part I (Chapters 2 & 3), the current literature related to the field is situated, and the research methodology is established. Part II (Chapter 4 –8) presents the results from the experimental studies, and

Part III (Chapter 9 & 10) presents the discussion, conclusions, and recommendations for future work. The chapters can be summarised as follows:

Chapter 2 details the literature review and background study of the fundamental aspects of biomass comminution. A review of the commonalities and variations in biomass physical and chemical structures is provided by biomass group (woody, herbaceous, fruit, and thermally treated) in comparison to coal. An overview of comminution systems and the varying fracture mechanics is included, along with the drivers and requirements of classification for pulverised fuel combustion. The current status of biomass milling is provided, as well as the use of standard coal tests for biomass in the absence of specific biomass standards.

Chapter 3 details the experimental methodology used to address the aims and objectives of this thesis. Firstly a detailed overview of the samples used in the study is provided. Following this the chapter is divided into two sections. Section one details the characterisation techniques used to analyse the biomass and coal samples before and after milling. These methods include standard biomass and coal tests such as moisture content and pellet durability. Data analysis techniques for particle size distribution evaluation are also provided. The second part of the chapter outlines the methodology of the five milling studies along with mill specific analysis such as thermal imaging and energy consumption metering.

Chapter 4 investigates the pre-comminuted properties of biomass. The physical characteristics of biomass pellets were investigated in terms of pellet dimensions and particle size distributions of disintegrated pellets. The cumulative distributions of the disintegrated pellets and powdered samples were characterised by size parameters, dispersion parameters, and distribution shape parameters. The impact of drying and moisture reabsorption is investigated to understand the hydroscopic properties of different biomasses. Quasi-static and dynamic mechanical testing of biomass pellets provides an insight into the mechanical response of pellets in low and high strain rate applications. Finally thermo-chemical characterisation of the samples shows their suitability and potential for combustion beyond the comminution process.

Chapter 5 investigates the applicability of the two main standard coal grindability tests; the HGI and the BWI tests. The impact of particle composition is analysed and a correlation between HGI and BWI is ascertained. Mill choking, which is an operational issue on full scale tube and ball mills, is replicated and explored at a laboratory scale through the BWI test.

Chapter 6 focuses on the comminution of biomass in a planetary ball mill. The chapter looks at the optimal mill settings for comminution in terms of energy consumption and particle size. The study also looks into understanding the olive caking phenomenon which is encountered with olive cake in industry. The second part of the chapter analyses the impact of drying on biomass comminution. The energy consumption, heat generated during milling in the biomass, milled particle size and shape are found for a wide range of as received and dried densified biomasses and olive cake.

Chapter 7 investigates the optimal milling conditions for densified white wood biomass in a cutting mill in terms of specific effective energy consumption and Rosin-Rammler distribution parameter, in addition to the novel analysis of mass holdup during milling. The impact of mill settings on energy consumption was analysed for wet and dried bagasse, and the impact of drying on the milling of densified biomasses and olive cake was analysed in a cutting mill in terms of energy consumption, particle size, and particle shape.

Chapter 8 provides the first study of densified biomass in a ring-roller mill with dynamic classification. The idle milling run conditions and milling behaviour of densified biomass and coal were analysed in terms of energy consumption, pressure, temperature, mass flow rate and mass output. The data gives a detailed insight into the varying milling behaviours of the tested samples. The particle size and shape of the milled product gives new insight into the workings of the aerodynamic classification system on the mill.

Chapter 9 draws on the results of chapters 4 to 8 to provide a comprehensive overview of the practical implications of this study for industry and academia, with future work being identified from the results.

Chapter 10 summarises the observations and conclusions from the chapters 4 to 8, along with general conclusions with regard to the EngD. In addition, recommendations for future work and links to other ongoing EngD projects are provided.

Chapter 2 - Literature Review

2.1. Project Context

The drive to use biomass in coal fired power stations originates with the European policy to increase the use of renewable energy. In March 2007, the European Council agreed to a common strategy for energy security and tackling climate change (Department of Energy & Climate Change, 2015b). This common strategy included establishing a target of 20% of EU's energy to come from renewable sources. In 2009, the Renewable Energy Directive ('RED') was implemented on this basis, which resulted in a 15% target of final energy consumption (calculated on a net calorific value basis) should be from renewable energy sources by 2020 in the UK (European Parliament and Council, 2009). In order to achieve this, the UK has implemented several renewable energy policies, with the latest being the UK Renewable Energy Roadmap. This roadmap focused around key policies and measures which aimed to encourage increased renewable energy deployment (Department of Energy & Climate Change, 2013):

- Putting in place appropriate financial incentives to bring forward and support the uptake of renewable energy, including the "banded" Renewables Obligation, Feed-in Tariffs (FiTs) for small scale (<5 MW) electricity generation, the Renewable Transport Fuel Obligation, the Renewable Heat Incentive tariff scheme, and the Renewable Heat Premium Payment Scheme; and, Contracts for Differences under Electricity Market Reform.
- Identifying and removing the most significant non-financial barriers to renewables deployment
- Overcoming supply chain blockages and promoting business opportunities in the renewables sector in the UK.

In April 2002 the Renewables Obligation (RO) came into effect and it obliged electricity suppliers to source a specific and annually increasing proportion of electricity from eligible renewable sources or pay a penalty. The RO was a successful mechanism in enabling power generators to uptake biomass power in the UK, particularly for low levels of biomass co-firing in coal fired power stations. However due to financial constraints within the UK government budget, the available subsidies for biomass power was reduced to 0.3 ROCs/MWh at the end of 2014, even at facilities burning more than 50% biomass. In August 2015, the climate change levy exemption for renewables was discontinued (Ofgem,

2015), further reducing the attractiveness of biomass power. In July 2015, the UK government started to further roll back support for renewable energy through the Levy Control Framework (LCF) due to subsidy overspends (Evans, 2016). This included the removal of the "grandfathering" policy, which stated that once a generating station is accredited and receiving support under the RO, the level of support that it receives would not change for the lifetime of its support under that scheme (Department of Energy & Climate Change, 2015c). In December 2015, further revisions to renewable energy subsidies were announced, including revised tariffs for FiTs and changes to the requirements of ROCs with the aim of saving £500-600 million from the LCF overspend (Department of Energy & Climate Change, 2015d). UK government analysis suggests that if of all the pipeline biomass projects come forward under the RO, about 4.6GW would be deployed, which would exceed the upper limit of the Electricity Market Reform delivery range (Department of Energy & Climate Change, 2015a). With Drax providing the majority of the allowed capacity, there is little subsidy left for other power generators to convert their facilities under the current schemes.

Electricity Market Reform will replace the RO for new schemes from April 2017 (Department of Energy & Climate Change, 2015b). The reforms tackle the risks and uncertainties of the underlying economics of different forms of electricity generation by offering long term contracts for low carbon energy called Contracts for Differences (CfD). Future subsidies for biomass conversions will be provided through the CfD scheme, with the European Commission recently approving the subsidised conversion of RWE's Lynemouth coal-fired power plant in northern England to burning biomass (Chee, 2015).

In 2016, the benchmark thermal coal prices have fallen to or below $50 per tonne for the first time since before the global financial crisis of 2008-2009, as reduced industrial demand and a mild winter in the northern hemisphere has dented demand (Basu, 2016). However, in one of its steepest falls on record, oil prices have fallen by over 75% in 18 months, as producers around the world pump 1-2 million barrels of crude every day in excess of demand. By December 2015, the price of gas had plummeted to its lowest level since 1998, which has resulted in US power companies burning more natural gas than coal for the first time in its history to generate electricity (Disavino, 2016).

However in the UK, it was the doubling of the carbon floor price (CFP) which has led to early closures of coal fire power plants during 2015. The CFP went up from £9.54 to £18.08 per tonne of CO_2 in April 2015, raising the cost of a tonne of carbon for British power plants to

£23, when allowances on the EU's emissions trading system (ETS) are factored in (Neslen, 2015). This has led to the early closure of Ferrybridge in West Yorkshire and Longannet in Fife, reducing Britain's peak load electricity generating capacity by 6% (Lodge, 2015). The CFP taxes emissions from coal-burning power stations at a rate nearly five times higher than the equivalent taxes in the rest of Europe, as the price for power stations across the EU is just £5.30 per tonne of CO_2 emitted, but British coal-power plants pay £23.38 per tonne emitted. When combined with falling commodity prices, it is likely that coal fired power stations will not be sustainable in the future without conversion to biomass.

2.2. Biomass Combustion Options

From March 2016 there will be 8 coal fired power stations over 200 MW operating in the UK, with a generating capacity ranging from 420 MW (Lynemouth) to 3870 MW (Drax). Coal fired power stations generally either co-fire biomass up to 20% or are fully converted to combust only biomass. Figure 2.1 shows the three main forms of co-firing biomass with coal; direct injection, parallel and indirect injection co-firing (Loo et al., 2008). Direct injection co-combustion (route 1, 2, or 3) involves simultaneous biomass-coal combustion in the original or modified coal burners with either separate or common biomass-coal milling and mixing. Parallel co-firing entails separate biomass combustion to produce steam, which is used with steam from the main fuel for electricity production. Indirect injection (route 4) requires initial biomass gasification followed by combustion of the product gas in the main coal-fired boiler or as a re-burn fuel to reduce NO_X emissions.

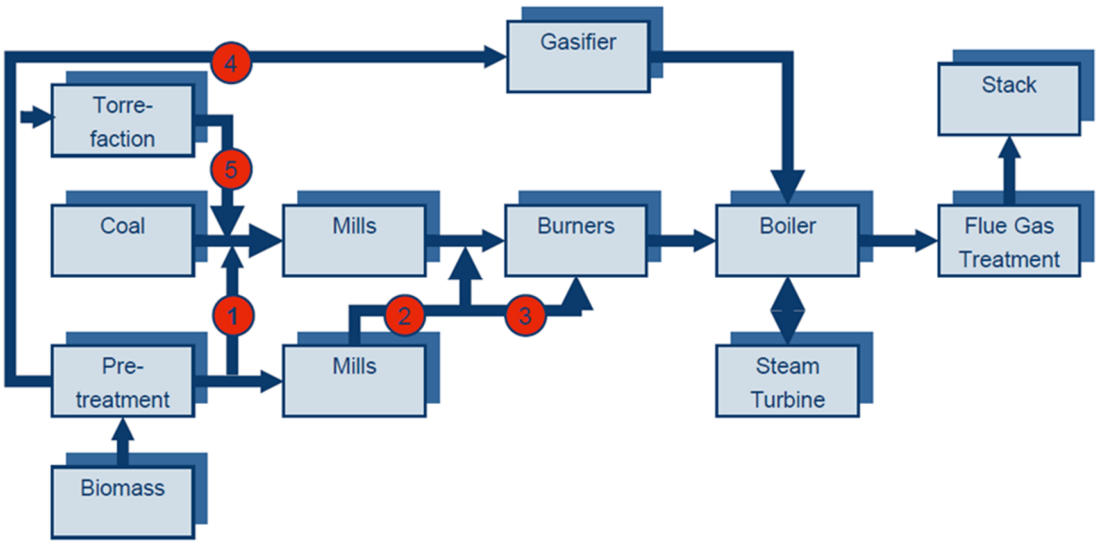


Figure 2.1: Co-firing Injection Options (Cremers, 2009)

Given that many of the plants are near the end of their useful lives, existing mills and burners are used and only economically modified for biomass conversion. Thus a thorough knowledge of the comminution properties of all biomass types in coal and biomass mills is essential.

Future developments in pulverised fuel generation are focusing on smaller scale units (<400 MW) with integrated gasification combined cycle (IGCC). This promising technology offers eco-friendly and high performance pulverised fuel combustion. The pulverized coal is converted into syngas (H_2/CO) via a gasification process, and the ash contents and acid gas are removed from syngas (Park et al., 2015). Overall, net power and efficiency of the IGCC power plant is higher than a traditional pulverized coal fired power plant due to the incorporation of a gas or steam turbine combined cycle into the IGCC plant. It has been conceptually shown that biomass, lignite, and coal mixtures can produce hydrogen at a cost ranges from $1.42/kg to $2.77/kg depending on feedstock, which is lower than the US Department of Energy announced hydrogen cost goal of $3.00/kg (Q. Chen et al., 2014). Thus while large scale traditional pulverised fuel power stations are being shut down in the UK, developments in technologies such as IGCC mean that optimising biomass and coal milling will have benefits and applications beyond current pulverised fuel applications.

2.3. Biomass Structure and Properties

Biomass is defined as the *non-fossilised and biodegradable organic material originating from plants, animals and micro-organisms, including products, by-products, residues and waste from agriculture, forestry and related industries as well as the non-fossilised and biodegradable organic fractions of industrial and municipal wastes, including gases and liquids recovered from the decomposition of non-fossilised and biodegradable organic material* (European Commission, 2007).

There are three main groups of biomass which are used in the power sector; woody, herbaceous, and fruit (The British Standards Institution, 2014b). Biomasses are composed of three main structural components; cellulose, hemicellulose and lignin, and the amount of each vary by type (Vassilev et al., 2015), as shown in figure 2.2. Biomass structural components, extractives, and inorganic constituents vary considerably across the spectrum of biomasses, and these characteristics differ significantly to those of coal. Figure 2.2 shows how biomass types can be placed in one of six sectors based on their Cellulose (C), Hemicellulose (H), and Lignin (L) components, with each sector characterised by decreasing

quantities of the components. The six structural orders for biomass groups, subgroups and varieties are:

i. CHL order for groups and sub-groups of wood stems, herbaceous and agricultural biomass (grasses, straws, stalks, fibres, shells– husks, residues) and contaminated biomass (semi-biomass);
ii. CLH order for sub-groups of wood stems and agricultural shells–husks;
iii. HLC order for sub-groups of wood barks, twigs and leaves;
iv. HCL order for sub-groups of tree leaves and grasses;
v. LCH order groups and sub-groups of some herbaceous and agricultural biomass (shells–husks, pits, residues) and animal biomass (cattle manure only);
vi. LHC order for wood bark and hazelnut shell

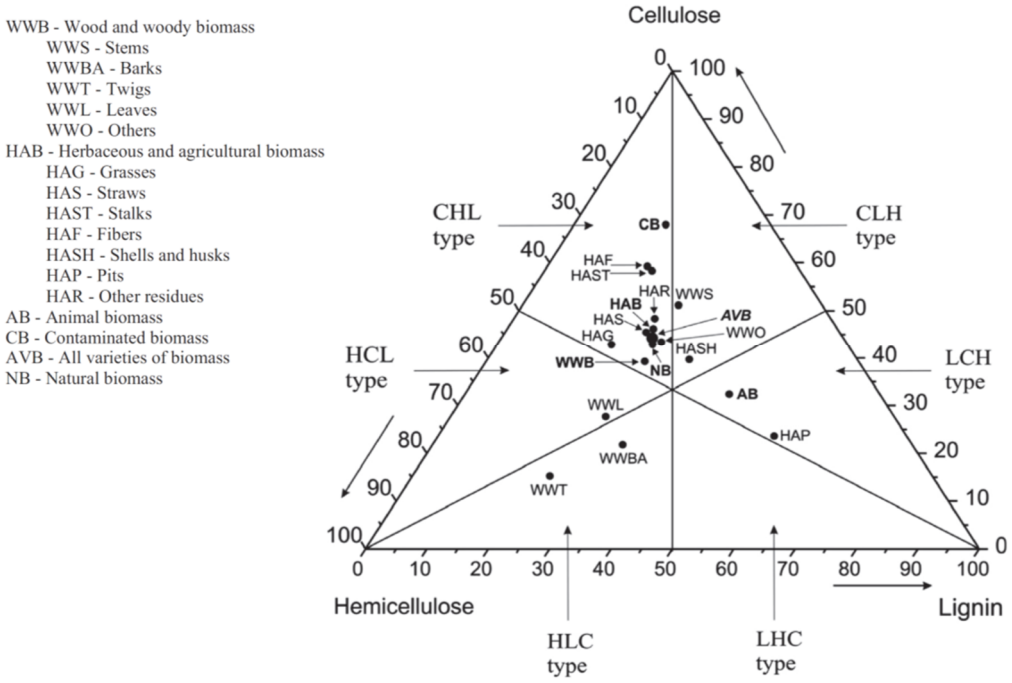


Figure 2.2: Mean Structural Composition of the Biomass Groups and Sub-Groups Based on 93 Biomass Varieties, wt. % (Vassilev et al., 2012)

Cellulose $(C_6H_{10}O_5)_n$ is a linear polymer which crystallises easily into micro-fibrils of great strength with a degree of polymerisation of around 10^4, accounts for 45% of wood cell walls, and is formed from tree glucose ($C_6H_{12}O_6$) by a condensation reaction (Ashby et al., 1998). The individual cellulose molecules are arrayed in bundles known as micro-fibrils each of which contain approximately 40 individual cellulose molecules, and within these bundles the cellulose is highly ordered and appears crystalline in diffraction measurements (Kirk et al., 1998).

Hemicellulose is a complex carbohydrate and partly crystalline polymer of glucose with a lower degree of polymerisation than cellulose, and makes up 25-30% of total wood dry weight (Ashby et al., 1998; Pérez et al., 2002). Hemicelluloses are generally found in association with cellulose in the secondary walls of plants, but they are also present in the primary walls (Jeffries, 1993). Glucuronoxylan or Xylan is the main component of hemicellulose in deciduous wood and is also the most reactive component in thermal decomposition (Prins et al., 2006), while in soft woods the principal component is glucomannan.

Lignin is an aromatic polymer with the substituents connected by both ether and carbon-carbon linkages (Jeffries, 1993). This cross linking makes lignin more thermally stable than hemicellulose (Biswas, Umeki, et al., 2011). Lignin accounts for 23-33% of the mass of softwoods and 16-25% of the mass of hardwoods and is more difficult to dehydrate than cellulose or hemicelluloses (Mohan et al., 2006). Most cellulosic plants, such as algae, contain low levels or no lignin (Dinwoodie, 2000; C. S. Jones et al., 2012).

2.4. Woody Biomass

Woody biomass is biomass from trees, bushes and shrubs (The British Standards Institution, 2014a). Trees belong to the spermatophyte species (seed bearing plants), and can be subdivided into two classes – hard wood (angiosperm) and soft wood (gymnosperms) (Sjostrom, 1993). The trunk of a tree has 3 distinct functions (Dinwoodie, 2000); support the crown of the tree, allow the transport of mineral solutions absorbed at the roots to the crown, and store manufactured foods (carbohydrates). Timber can be considered to be a low density, cellular, polymeric composite. The macroscopic structure of wood is shown in the isometric cross section of a typical tree trunk in figure 2.3. The main cells of the wood, known as fibres or tracheids, run axially up and down the tree, and strength is greatest in this direction (Ashby et al., 1998).

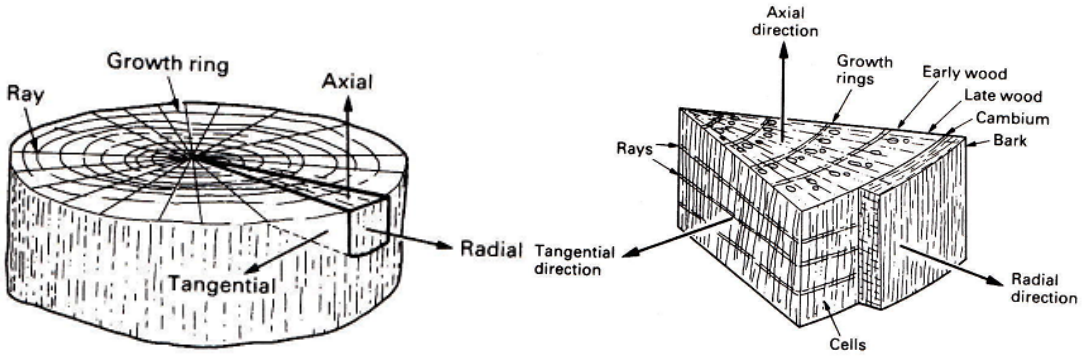


Figure 2.3: Macrostructure of Wood (Ashby et al., 1998)

Conduction and storage is restricted to the outer zone of the trunk called sapwood, and the heartwood is the region in which cells no longer perform this function. Sapwood typically represents 20-50% of the trunk. As the Sapwood transforms into heartwood, substances, collectively known as extractives, form in the heartwood in small quantities and give the heartwoods colour and resistance to fungal and insect attack. The formation of extractives varies in quantities between different species of wood, with some being devoid of extractives all together. Wet wood areas can occur in the heartwood in cases of high moisture content, which are frequently darker in colour. Wood is divided radially by growth rings, which grow rapidly in spring and summer, then slower in the autumn and winter, resulting in differences in density and cell size. Most of the growth occurs in the cambium, which is a thin layer just below the bark of the tree. With increasing radial growth of the trunk, existing branches are integrated into the trunk to form knots. Grain directions in the vicinity of knots are often distorted and result in a loss of strength in the timber.

The macrostructure of wood has an axial, tangential and radial co-ordinate system (Fig. 2.3). The Young's Modulus in axial loading (along the grain) varies linearly with density, while the radial and tangential loading (across the grain) vary as a square of the density, resulting in an increase in anisotropy (ratio of the Young's Modulus along the grain to that across the grain) with decreasing density (Ashby et al., 1998). Increasing growth rates in softwood leads to reduced density and strength, while in diffuse porous hardwoods increasing the growth rates has little effect on density and mechanical properties, and in ring-porous hardwoods, increasing growth rates actually increases density and strength.

The strength, stiffness and toughness of wood is defined by its fibres or tracheids (Dinwoodie, 2000; Sjostrom, 1993). Ashby and Jones (1998) compare the structure of the tracheid cells to that of a composite material such as fibreglass, with the role of the strong glass fibres being performed by crystalline cellulose. The cellulose micro-fibrils in wood can be considered as fibres, and the lignin and hemicellulose the matrix within which the fibre resides. The high tensile strength of wood is due to the covalent bonds within and between the anhydroglucose units in the cellulose fibres. The hemicellulose matrix binds the micro-fibrils together in bundles of cellulose chains along with a polycrystalline sheath of hemicellulose material. The prime function of lignin is to protect the hydrophilic non-crystalline cellulose and hemicellulose, which are mechanically weak when wet. The lignin is regarded as lying outside the micro fibril forming a protective sheath around it (Dinwoodie, 2000).

2.5. Herbaceous Biomass

Herbaceous biomasses are from plants that have a non-woody stem and which die back at the end of the growing season, and includes grains and their by-products such as cereals (The British Standards Institution, 2014a). Herbaceous biomasses are also ligno-cellulosic materials (Sun et al., 2002). While woody biomasses are characterised by slow growth and composed of tightly bound fibres, which gives its hard external surface; herbaceous biomasses are perennial, with more loosely bound fibres, indicating a lower proportion of lignin (McKendry, 2002).

2.6. Fruit Biomass

Fruit biomass is the biomass from the parts of a plant which are from or hold seeds (The British Standards Institution, 2014a). Olive cake is a waste product from olive oil production and is commonly used as a co-firing material in UK power stations. Olives contain soluble sugars (simple sugars) and sugar polymers (complex sugars) such as cellulose, hemicellulose, and lignin (Kailis et al., 2007). For green olives, cellulose accounts for over 50% of total fibre, with the Gordal variety containing 53-60%, and the Manzanilla variety containing 63-90% (Fernandez et al., 1997). Percentages of lignin are inversely proportional to those of cellulose in olive fruit, and lignin is concentrated in the stone section of the olive. Hemicellulose and cellulose (3-6% w/w) are structural components in the cell walls of the olive flesh which link adjacent cells, and give olives their fleshy texture. The maturity of the olive will impact the amount of cellulose and hemicellulose within the olive, as cellulose drops with maturity, leading to an increase in hemicellulose. Lignin content remains stable during growth.

The main soluble sugars in olive flesh are glucose, fructose, sucrose, and mannitol. The level of soluble sugars in raw olive flesh ranges from 0.5% w/w to over 5% w/w depending on olive variety and growing conditions, with glucose predominating. Soluble sugars decrease as the olive fruit develops and oil synthesis begins, with soluble sugars in green-ripe olives being twice the level of black-ripe olives. Soluble sugar levels are inversely related to the oil content, and concentrations are also dependent on the moisture content of the olive flesh. Spanish green-ripe olives have around 4% fermentable substrates (sugars), while untreated black-ripe olives 2-2.5% fermentable substrates.

2.7. Biomass Thermal Pre-Treatments

Due to the low bulk density, high moisture content, hydrophilic nature, and low calorific value of non-densified biomass, its large scale use has proven to be problematic in pulverised fuel power stations (Arias et al., 2008). One way of addressing these issues is to use thermal pre-treatments which alter the biomass physical and chemical properties (Sierra et al., 2008). There are currently three forms of thermal pre-treatments which are used on commercially available biomass pellets; torrefaction (Swaan, 2012), steam explosion (Zilkha Biomass Energy, 2011), and microwave (Rotawave Ltd, 2010).

Torrefaction is defined as isothermal pyrolysis of biomass in an inert environment and at a temperature of between 200-300 °C (Jaya Shankar Tumuluru et al., 2011). Torrefaction results in devolatilisation and the carbonisation of hemicelluloses, as well as depolymerisation and devolatilisation of lignin and cellulose. It has been shown to increase carbon content and higher heating values, with additional improvements to energy density, grindability, and densification of biomass (Arias et al., 2008; Bridgeman et al., 2010; Ohliger et al., 2013; Phanphanich et al., 2011; Repellin et al., 2010; Shang et al., 2012; Van Essendelft et al., 2013). Commercial scale torrefaction systems are still not fully developed (Mafakheri et al., 2014; Uslu et al., 2008), but the system usually involves a drying process followed by the torrefaction process, after which the material is densified into pellets (Chiueh et al., 2012). The thermal energy demand for torrefaction including grinding is 2.88 MJ_{el} per kg of processed biomass (Chiaramonti et al., 2011). While torrefaction has been shown to improve particle circularity (Phanphanich et al., 2011) it's impact on operational sphericity has not been quantified.

Steam explosion is the most commonly used pre-treatment of lignocellulosic materials for the production of ethanol (Sun et al., 2002), but is increasingly being used as a thermal treatment to improve the properties of wood pellets (Biswas, Umeki, et al., 2011). The steam explosion process involves separating the main components of woody biomass (lignin, cellulose and hemicelluloses) by both chemical degradation and mechanical deformation. The process involves adiabatic expansion of water inside the wood tissue pores and auto hydrolysis of cell components (Biswas, Yang, et al., 2011). Steam exploded Black™ Pellets (Zilkha Biomass Energy, 2011) are a commercially available steam exploded pellet made from American white wood. Steam explosion has seen improvements in the pellet density, and enhanced carbon content (Biswas, Yang, et al., 2011), as well as improved grindability in

several studies (Adapa et al., 2010, 2011). The thermal energy demand of steam explosion is between 0.9 and 2.7 MJth per kg of processed biomass (Chiaramonti et al., 2011).

Microwave heat treatment is an emerging biomass thermal treatment. Microwave biocoal produces commercial scale thermally treated pellets by using microwaves to directly and volumetrically heat biomass. This induces pyrolysis at temperatures below 350 °C in shorter production times than torrefaction (Rotawave Ltd, 2010). Microwave processing of biomass has been shown to increase energy density and improve grindability, as well as creating a more hydrophobic material (Lanigan, 2010; Robinson et al., 2010; Satpathy et al., 2014). Microwave treatments have also been shown to significantly improve the grindability of coal (Lester et al., 2004). For straw, the electrical demand of microwaves is between 1.3 MJ per kg, with the heat and conversion loss of electricity to thermal energy at around 42% (Luque et al., 2012).

Studies on the biomass thermal treatments usually focus on non-densified biomasses and do not compare how different thermal treatments impact the physical and mechanical properties of densified biomasses. While it is known that grindability and some 2D shape factors are improved through thermal treatment, the impact on the operational sphericity of biomass particles has not been measured, data which is crucial for optimising mill classifier, pneumatic conveying and combustion in pulverised fuel power stations. Real data on the operational sphericity for all biomass types is not present in literature and represents a significant gap in knowledge in the field.

2.8. Biomass Densification

The aim of biomass densification is to increase the bulk density of the biomass to reduce transportation costs (Gilbert et al., 2009). Pellets generally cost around 136.6 €/t, and pellet production costs are dominated by raw material and drying costs, which amount to almost 80% of the total pellet production costs (Obernberger et al., 2010a). The total specific energy consumption of pellet production is 1.315 kWh/t, and 93% of this energy is associated with the thermal energy used during drying. It is important to note that long haul transport can represent a significant energy penalty. The transport energy penalty of imported biomass pellets from the USA to Italy has been shown to be equivalent to 7-11% of the total energy of wood pellets (Paolotti et al., 2015).

Biomass pellets for bioenergy application can be produced in several ways, and the system used will impact the chemical and physical properties of the final product. Densification is a

process applied to biomass materials to increase the bulk density from 40 Kgm^{-3} to 200 Kgm^{-3} up to 600 kgm^{-3} through tumble or pressure agglomeration methods, with the resulting material being extruded, pelletized or briquetted (Axelsson et al., 2012; Kaliyan et al., 2009). International standards exist for the quality of the densified biomass which provide specifications on pellet parameters such as pellet dimensions, moisture content and mechanical durability (The British Standards Institution, 2014d), as well as particle size distribution for wood pellets (The British Standards Institution, 2014c).

The raw material for wood pellets is usually wood shavings, saw dust, and wood dust (Obernberger et al., 2010a), agricultural by-products such as straw and pruning residues (Carone et al., 2011), or food production residues such as coffee husks, grape wastes, or rice husks (Gil et al., 2010; Kaliyan et al., 2009). Some materials such as sawdust will require drying before processing. Pellet production usually consists of 4 to 5 stages after initial drying; particle size reduction, drying, conditioning, densification, and cooling. Usually particle size reduction is conducted on a hammer mill with a screen size of 3.2 mm to 6 mm (Mani, Sokhansanj, et al., 2006). The recommended particle size for good pellet quality is 0.6 mm to 0.8 mm (Turner, 1995), with Franke and Ray recommending a particle size of 0.5 mm to 0.7 mm for more durable pellets (Franke et al., 2006). Particles greater than 1 mm will act as predetermined breaking points in pellets but the increased cost of production of fine pellets results in pellets with particle sizes in excess of 1mm.

After milling, the material is typically dried in a rotary kiln to reduce the moisture content for optimal palletisation. The densification process depends on the friction between the compression channel and the materials and this process is moisture content dependent. Prior to pelleting, the biomass is conditioned with steam to provide even surface and ensure the binding mechanisms take place. Large scale pelletisation is usually done in a ring die pellet mill, which consist of a die ring around fixed rollers. The material is fed into the rollers sideways and pressed through the die bore holes to form the pellets. The important parameters in pelletising are the press ratio, quality of bore holes and the resulting open area of the holes. After pelletising the pellets are cooled to enhance their mechanical durability and reduce moisture content.

It has been shown that increasing temperature rather than pressure results in improved mechanical properties in biomass pellets. Gilbert et al. (2009) found that for switch grass pellets, the maximum potential softening of lignin occurred at 70 ^{O}C, which then acts as a binding agent in its softened state, followed by an increase of pellet hardening due to

moisture evaporation. A pellet produced at 166 bar and 75 ^{O}C was more durable than a pellet formed at 522 bar at room temperature. Carone et al. (2011) also found that compression force had virtually no effect in influencing the mechanical properties of pellet formed from olive tree pruning residue, as temperature, moisture, and raw material particle size were the main influencers on pellet mechanical properties.

There are several ways of testing the durability of pellets and briquettes. Temmerman et al. (2006) looked at three methods for measuring the durability of briquettes and pellets and found that the results were heavily influenced by the fuel type and properties. Mechanical durability of wood pellets is defined by British Standard BS EN ISO 17831-1 (The British Standards Institution, 2013b) as the ability of densified briquettes or pellets to remain intact during handling and transport. Low mechanical resistance leads to higher dust emissions, which increases the health, fire and explosion risks during pellet handling, storage and transport. Samuelsson et al. (2009) found that moisture content and long storage periods for conifers sawdust pellets lead to increased bulk densities and energy consumption during palletisation. However long storage and intermediate moisture levels gave favourable mechanical durability, as water plays a central role in the binding mechanisms in the pellets. Fasina (2008) found that moisture content attainment in low and high humidity environments significantly influenced the bulk density, particle density and durability of the peanut hull pellets, and that while relative humidity significantly influenced the rate at which the pellets exchange moisture with the environment, air temperature did not. Theerarattananoon et al. (2011) found that increased moisture content resulted in decreased durability, bulk and true density of pelletized corn stover, sorghum stalk, wheat straw, and big bluestem. There is little information in literature on the abrasion indexes of biomass. The impact of the high hardness of biomass particles coupled with their low density on mill and conveyancing pipe work materials has not been widely researched, with significant implications for reducing wear and increasing the life of these systems. Gil et al. (2010) used a modified version of the mechanical strength of coke for a range of biomass pellets to test the mechanical durability of pellets based on how they broke up in rotary drum. It was found that the pellets formed from chestnut sawdust showed the highest mechanical durability, followed by pine sawdust pellets. Cellulose residue and eucalyptus sawdust showed lower mechanical durability, with coffee husks and grape waste pellets showed very poor mechanical durability.

2.9. Coal Structure and Properties

Coal is a biogenic sedimentary rock, derived from lithified plant debris. Exposure of plant debris to high temperatures for long periods of time promotes a series of changes, known as rank advance, that transform it into coals of varying rank; from lignite, bituminous to anthracite. The rank of a coal describes the extent to which these post-depositional changes have taken place and determine the properties of the coal. The coal type within each rank identifies the nature of the original plant debris and the degree of degradation prior to burial. The grade of a coal describes the non-organic material within it and determines the grinding behaviour of a coal (Ward et al., 1987).

Coal can be chemically analysed to determine its composition, namely carbon, hydrogen, oxygen, nitrogen, sulphur and inorganic material matter (Gibson, 1979). Chemical analysis provides the basis for classifying coal as coals tend to fall into a well-defined bands when their hydrogen and carbon composition is plotted against each other (Rimmer et al., 2009). As oxygen content decreases, hydrogen content remains stable, leading to an increase in carbon content, and in latter stages hydrogen content decreases. Coals can be classified from low to high rank based on their properties:

- *Low rank* coal has randomly orientated small layers connected by cross links, resulting in a highly porous structure
- *Medium rank* or coking coals show a greater degree of orientation and thus are more likely to parallel stack. There are fewer cross links and pores, with its structures having similarities to that of a liquid
- *High rank* coals and anthracites exhibit individual growth layers with a marked increase in the degree of orientation, as well as evidence of elongated pores parallel to the layer stacks.

Combustible matter in coal can also be characterised by the microscopic identification of its specific petrographic constituents called lithotypes (Klimpel, 1987). Petrographic analysis is used to obtain the key macerals of vitrinite, liptinite and inertinite to give a petrographic index of coal rank (Gibson, 1979). The Stopes-Heerlen System recognises four distinct constituents:

- *Vitrain*: bands of black glassy material with a low specific gravity and carbon content
- *Clarain*: laminated coal with a fine, vitrain like bands and an overall silky lustre with a low specific gravity and carbon content and is fairly friable

- *Durain*: homogeneous, tough organic material with dull lustre, is hard and difficult to crush, and has a higher specific gravity and carbon content
- *Fusain:* thin bands of granular carbonaceous material with a fibrous structure, usually soft and powdery but sometimes harder due to mineral matter, has a high specific gravity and is very soft and friable

2.10. Impact of Biomass and Coal Compositional Differences on Combustion

Biomasses have higher percentage of combustible volatile matter content and lower initial ignition and combustion temperatures compared to coal (Vassilev et al., 2015). Biomass has a volatile matter to Fixed Carbon ratio above 4, while coals are always below 1. This higher volatile matter content results in the lower ignition temperatures, easier and rapid ignition, devolatilisation and burnout, and production of combustible gas and inorganic vapours, improved combustion with less unburnt carbon in ash, and the formation of biochars with high specific surface areas. Co-combustion of biomass coal will result in a more stable flame but combustion of high volatile matter biomass is rapid and difficult to control, and requires more system optimisation to achieve complete combustion.

2.11. Pulverised Fuel Milling and Classification Systems

Legislation to reduce NO_x emissions in coal fired power stations has led to improvements in combustion efficiency through the introduction of low NO_x burners since the mid 1990's. As NO_x emission reduction targets grow ever stringent, enhanced combustion efficiency can be achieved through improved fineness of coal particles (Larsen, 2012). Volatile matter decreases with decreasing particle size, and the impact of particle size on coal combustion has been shown in several studies (Barranco et al., 2006; R. B. Jones et al., 1985; Mathews et al., 1997; Yu et al., 2005). Low NO_x burners have lower coal particle residence times due to reduced mixing intensities and the formation of fuel rich zones (Van Der Lans et al., 1998), which means optimized coal particle size is essential to ensure complete burnout of the coal particles. The size of particles reaching the burner is dictated by the comminution equipment in the power station. Coal mills use static classifiers or dynamic classifiers to select the correct size and consistency of particle for combustion. In the separator the heavier particles of coal are separated from the entrained pulverised fuel-air mixture and are returned by gravity to the mill for further grinding. Pulverized fuel of the correct fineness leaving the separator is transported by the high velocity hot air through piping to the burners (Fig. 2.4).

In a static classifier, pulverised fuel is drawn from the mill by an exhauster fan and enters the classifier via the mill outlet damper (Fig. 2.5). This damper is mechanically linked to the purge damper so that when it is closed the purge damper is open. This enables the classifier and exhauster pipework to be purged before shut-down. From the mill outlet damper the pulverised fuel flows up the gap between the outer casing and the outer cone of the reject hopper. It then enters the guide blades where it is swirled into the exit volute. The smaller particles are carried up and discharged to the burners while the larger particles tend to flow radially outwards and then drop into the rejects slot. The rejects fall through the rejects outlet pipe onto the weighted flap of the reject valve. The weight of rejects on the flap causes it to open and allow the coarse material into the mill outlet scroll where it is returned to the mill for further grinding.

For sub-bituminous coal used in UK coal PF power stations, the industry standard for a classifier is that 75% of coal delivered to the burner must pass a 200 mesh screen (75 µm) and < 0.3%, a 50 mesh screen (300 µm) (Afolabi, 2012), although the performance of classifiers in general is measured by a cut size of the mean diameter of the sample (d_{50}) (Fuerstenau et al., 2003). Mill classifiers separate particles of 0.1-1000 µm in air through a combination of physical forces. These forces include gravity, aerodynamic drag, centrifugal force, and collision forces, and classifiers use a mixture of these for sizing. The capture efficiency is defined as the ratio of the cross sectional area of the fluid stream from which all particles are removed to the cross sectional area, projected in the direction of the flow, of the rotor pin, and is a function of the Stokes number. The dimensionless Stokes number (S_t) which is a measure of the ability of particles to follow the surrounding flow (Toneva et al., 2011), is defined as:

$$S_t = \frac{\rho_P d_P^2 u_{P,0}}{18\mu B} \qquad \text{(eq. 2.1)}$$

where ρ_P is the particle density (kgm^{-3}), d_P is the particle size (m), $u_{P,0}$ is the velocity of the incoming particle far away from the pin (ms^{-1}), μ is the dynamic viscosity of the settling medium (Pa.s), and B is a characteristic system dimension, in this case the diameter of the pin. However this equation assumes spherical particles and therefore shape factors need to be introduced for non-spherical particles.

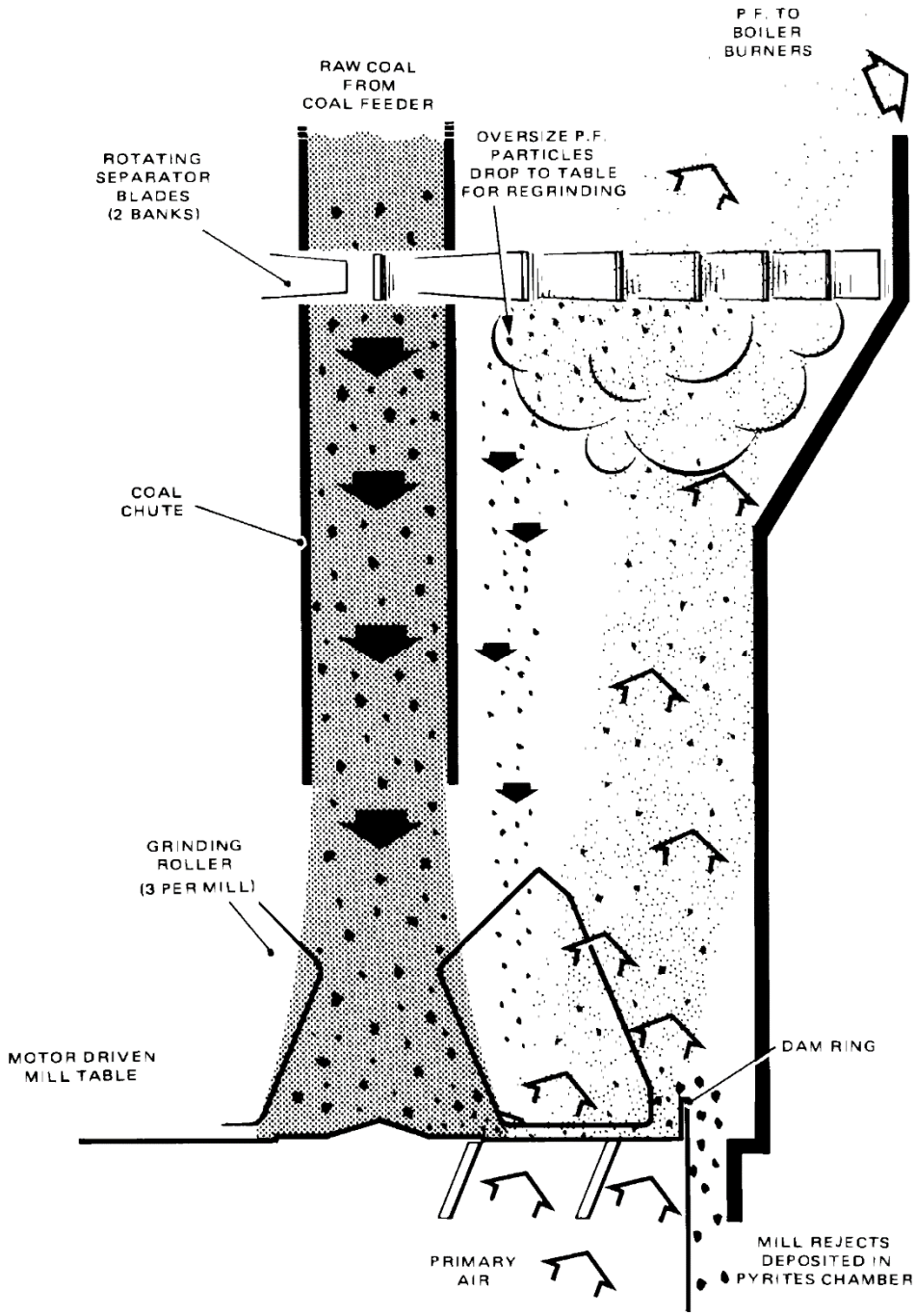


Figure 2.4: Dynamic Classification of Coal from a Coal Mill Using a Separator (EDF Energy plc, 1981b)

In the Stokes regime, the terminal settling velocity, u_t, of a spherical particle can be written as:

$$u_t = \frac{(\rho_P - \rho_f) g {d_s}^2}{18\mu} \qquad \text{(eq. 2.2)}$$

Where ρ_f is the density of the settling medium (kgm^{-3}), g is the gravitational acceleration (ms^{-2}), d_s is the diameter of the spherical particle (m). The Stokes shape factor of a non-spherical particle, k_v, is defined as:

$$k_v = \frac{u_t}{(u_t)_v} = \frac{18\mu u_t}{(\rho_P - \rho_f) g d_v^2} \qquad \text{(eq. 2.3)}$$

Where d_v is the diameter of a sphere having the same volume of the particle of a non-spherical particle (m). Thus, by knowing the viscosity and density of the settling medium, the particle density and volume size of a non-spherical particle, the Stokes shape factor can be obtained by the measurement of the particle terminal velocity in Stokes regime.

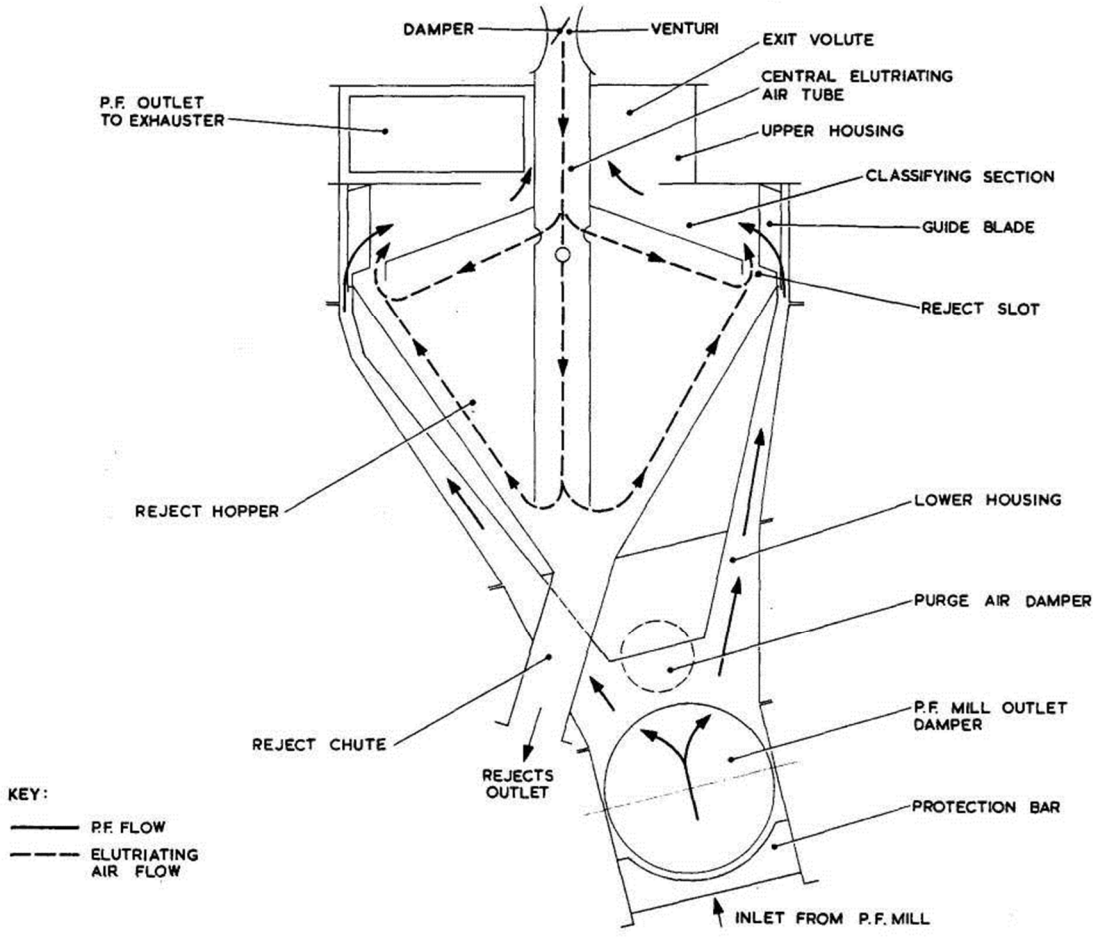


Figure 2.5: Static Classification of Coal from a Coal Mill Using Buoyancy Classifier (EDF Energy plc, 1981a)

Xie and Zhang (2001) found a correlation between the Stokes shape factor for a range of specific shapes and the data from Pettyjohn and Christiansen (1948) for isometric particles which showed that the Stokes shape factor k_v can be correlated with particle sphericity φ to:

$$k_v = \varphi^{0.83} \quad \text{(eq. 2.4)}$$

For particles which differ significantly in shapes. True sphericity φ was defined by Wadell (1932) as:

$$True\ Sphericity, \varphi = \frac{Surface\ area\ of\ a\ Sphere\ with\ the\ Same\ Volume}{Surface\ Area\ of\ the\ Particle}$$

However, as noted by Krumbein and Sloss (1963), the measurement of true sphericity of an irregular particle is not feasible, and Wadell (1935) proposed a practical operational definition of sphericity called Operational Sphericity:

$$Operational\ Sphericity, \varphi = \sqrt[3]{\frac{Volume\ of\ the\ Particle}{Volume\ of\ Circumscribing\ Sphere}}$$

Krumbein and Sloss (1963) showed that operational sphericity as denoted by Wadell (1935) can be reduced to:

$$\varphi = \frac{d}{a} \quad \text{(eq. 2.5)}$$

Where *d* is the nominal diameter of the sphere (based on particle volume) and *a* is the maximum intercept through the particle, as illustrated in figure 2.6. Operational sphericity is used along with Krumbein Roundness for the "Krumbein Scale" charts for evaluating particle shape.

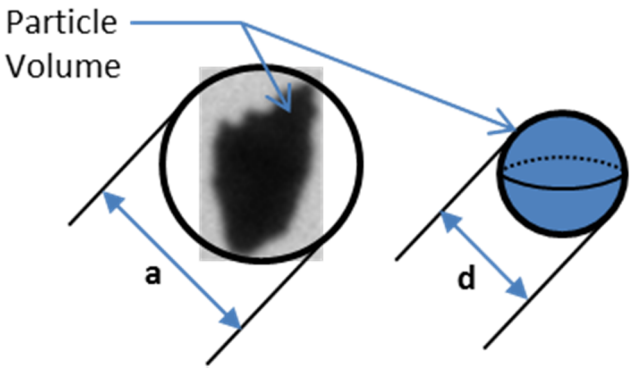


Figure 2.6: Relationship between the diameter of a Circumscribed Sphere (a) and the Nominal Diameter of a Sphere with the same Volume as the Particle (d) (Zavala, 2012)

Biomass conversion and co-firing use the existing coal pulverized fuel (PF) burners, and it has been postulated that the Stokes number of a biomass particle should match that of an equivalent coal particle in order to pass the aerodynamic filter used to classify particles in traditional coal mills. As the Stokes number is dependent not only on the sphericity of the

particle but also its Reynolds number, it's possible for large biomass particles to have similar aerodynamic properties to that of a much smaller coal particle provided it has a sufficiently low sphericity (Mandø et al., 2010). Currently in CFD models of biomass PF combustion, the sphericity of biomass is either a calculated value or obtained experimentally from microscopy. Particle size and shape distribution are the most influential factors in the correct prediction of straw combustion in a commercial multi-fuel pulverized fuel burner. This increase in size has been noted experimentally for swirl burners. For or a 150 kW pilot burner, the optimal burn conditions for wood feed stocks was 95% of particles (by weight) were smaller than 1000 µm with a moisture content lower than 15% (Esteban et al., 2006), and good flame stability has been obtained in a swirl burner with coarse pulverized wood, particularly with lower moisture contents (Adams et al., 1988). In numerical models of co-firing biomass in wall fired burners, a burning enhancement factor based on a sphericity factor compared to a sphere with the same diameter (Θ) has been developed to calculate the surface reaction rate (Yin et al., 2004):

$$\Theta = \frac{0.3\varphi + 0.7}{\varphi} \qquad \text{(eq. 2.6)}$$

The burning enhancement factor was developed by Gera et al. (2002) who found that the increase in surface area of a cylindrical switchgrass particle was larger than the increase in the overall burning rate. Thus the burning enhancement factor can be seen as an estimate on the efficiency of the increase in surface area to promote combustion for an arbitrary shaped particle. There is relatively little data available on the shape factors for biomass, and that which is available is based on microscopy. Guo et al. (2012) showed through microscopy that ground pine, beanstalk, rice straw and reed particles have needle like shapes and variable aspect ratios, but microscopy is limited by a small sample size and is based on a 2D measurement, which brings in inherent risks for inaccuracy for non-spherical heterogeneous samples. Thus in order to improve the accuracy of CFD models its necessary to obtain more accurate experimental shape factor data for biomass and coal. Gil et al. (2014) showed that particle shape of paramount importance in the sieving classifying process, as two kinds of particle patterns were identified as incorrectly classified: particles with a wider or narrower width than expected which were retained in upper or lower sieves than they should have been. Most wrongly classified particles showed a high aspect ratio, a hook shape, or silhouette irregularities at fracture section.

2.12. Milling theory

All work indices are derived from the general comminution energy equation proposed by Walker et al. (1937) which relates the net specific energy *E*, the characteristic dimension of the product *x*, the exponent *m*, and a constant *K* related to the material:

$$dE = -K\frac{dx}{x^b} \quad \text{(eq. 2.7)}$$

The value of *b* provides the three "laws of comminution" which describe empirical size reductions; these being Rittinger's (1867), Kick's (1885) and Bond's (1952). When *b* = 2, integration of equation 2.7 gives Rittinger's first theory of comminution, which states that "*The energy required for size reduction is proportional to the new surface area generated*" (von Rittinger, 1867), and is expressed as:

$$dE = K_{VR}\left(\frac{1}{x_2} - \frac{1}{x_1}\right) \quad \text{(eq. 2.8)}$$

Where K_{VR} is the constant characteristic for the material, x_1 is the 50th or 80th feed passing size (µm), and x_2 is the 50th or 80th product passing size (µm). When *b* = 1, integration of equation 2.7 gives Kick's second theory of comminution, which is that "*the work required is proportional to the volume reduction of the particles concerned*", and is expressed as:

$$dE = K_K\, ln\left(\frac{x_1}{x_2}\right) \quad \text{(eq. 2.9)}$$

Where K_K is the constant characteristic for the material. When *b* = 1.5, integration of equation 2.7 gives Bond's third theory of comminution (Bond, 1952), assumes that the energy transmitted to a body by a compressive force is initially distributed in the mass and is proportional to x_1^3, but as soon as surface cracking starts, that energy is concentrated in the cracks and is then proportional to x_1^2. Consequently, it is assumed that grinding proper is halfway between x_1^2 and x_1^3. According to this theory, "*the work input is proportional to the new crack tip length produced in particle breakage*", and is expressed as:

$$dE = K_B\left(\frac{1}{\sqrt{x_2}} - \frac{1}{\sqrt{x_1}}\right) \quad \text{(eq. 2.10)}$$

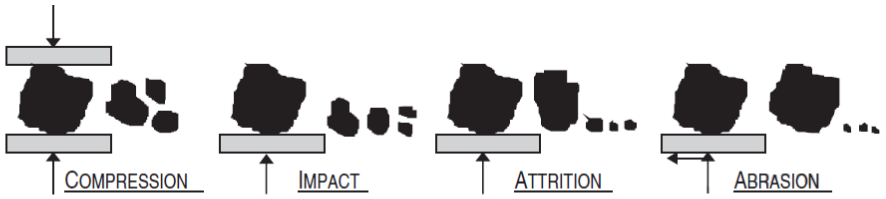
Where K_B is the constant characteristic for the material. The application of milling theory has identified some of the key variables in biomass milling. Temmerman et al. (2013) milled wood chip and wood pellet, in a flailing hammer mill, and developed von Rittinger's theory

for this mill. Energy consumption was found to depend on 3 main factors: material moisture content, particle size difference and material itself. Ghorbani et al. (2010) measured the energy requirement for alfalfa chops in a swinging hammer mill, and found exponential relationships between specific energy and screen sizes. They also found that von Rittinger's model fitted best to the results from the three milling theories, but also that a simple linear model worked best in relating energy to ratio of initial to final screen sizes used. Van Essendelft et al. (2013) have also used a planetary ball mill to find a hybrid work index for torrefied materials.

2.13. Mill Breakage Modes and Particle Breakage Mechanisms

In order to ensure that biomass comminution can be optimised for different mills, knowledge of the fracture mechanism experienced within a mill is essential. Before coal or biomass can be combusted, it needs to be reduced to the appropriate size. Recent studies have used a particle size criteria of 1000 µm and below for biomass dust burners, with optimal burn conditions for wood feed stocks in a 150 kW pilot burner being 95% by weight of particles smaller than 1000 µm and moisture content lower than 15% (Esteban et al., 2006). PF coal burners require below 100µm (Freeman et al., 2000). Industrial mills can be classified by the four ways they apply fundament stresses on a material: impact, attrition, shear/abrasion, and compression (Perry et al., 2008). Figure 2.7 summarises the breakage modes used in industrial mills. The stress state and breakage reaction of any material are affected by many parameters which can be grouped into particle properties and loading conditions. The material properties, the current state of stress and the presence of micro-cracks and flaws influence the reaction of the particle to the state of stress, and size reduction will start and continue so long as there is sufficient energy for the creation of new surfaces (Perry et al., 2008). A large portion of the energy supplied during grinding is lost to sound, heat and plastic deformation of the material.

Less than 5% of the energy input into a typical grinding device actually goes into the breaking of the material, and mill efficiency can be judged in terms of energy input into the device as compared to the particle size for a given material. Coal mills are designed so that under normal running conditions there is a definite relationship between the quantity of coal and air passing through it, known as the air/fuel ratio. The ratio is determined by the coal drying requirements, mill design, and fuel pipe velocities to ensure that coal particles remain in suspension, and coal burner design.



COARSE				
crushers	XX			
hammer crusher		XX		
MEDIUM				
roller mills	XX			X
high pressure	XX			X
rolls	XX	XX	XX	X
tumbling mills				
FINE				
vibrating mills	X	XX	XX	
planetary mills	X	XX	X	
hammer mills		XX		
cutter mills		XX	X	
SUPER FINE				
pin mills		XX	XX	
micro impact mills		XX	XX	X
opposed jet mills		XX	XX	X
spiral jet mills		X	XX	X
stirred ball mills			XX	XX

Figure 2.7: Breakage Modes in Industrial Mills (Perry et al., 2008)

Compressive and shear forces dominate mechanical processing (Blair, 2014), as illustrated in figure 2.8. Brittle materials are easily fragmented under the application of compressive force, while soft materials are more easily processed by the application of shear force. Comminution devices are typically optimized for one type of force, and coal and biomass have fundamentally different fracture mechanisms. Coal mills use are optimised for brittle fracture mechanisms, as the formation of coal through the subjection of forces results in a highly flawed structure with an inherent crack system. These pre-existing macro-flaws strongly influence the brittle breakage mechanisms and subsequent size distributions produced by grinding. The micro-porous structure of coal can lead to a plastic type of breakage behaviour (Klimpel, 1987).

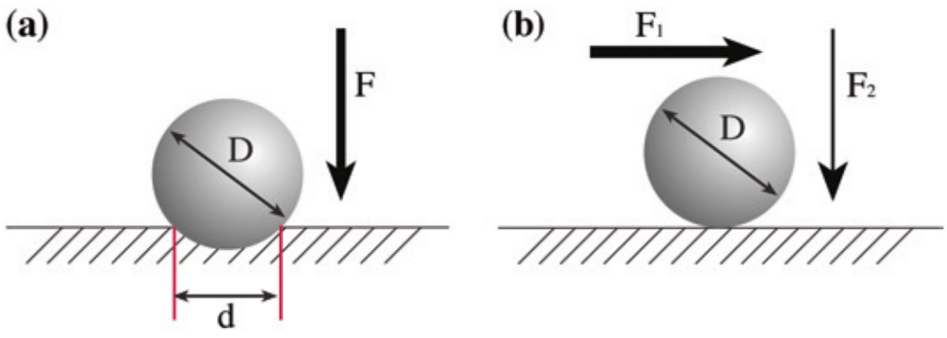


Figure 2.8: Compressive forces (a) are best for comminuting hard, brittle feedstocks, while shear forces (b) are best for soft feedstocks (Blair, 2014)

The grinding of coal involves the complex and highly variable application of a mixture of tensile, compressive and shear forces. For short periods of tensile stress application, coal behaves as an elastic material, and therefore Hooke's law of elasticity applies. Thus if the coal is not stretched too far it will return to its original shape when the stress is removed. As the force is increased, catastrophic brittle failure will occur at the tensile strength of the coal. However due to the flawed and microscopic nature of coal, the fracture mechanism is not ideal and is directly related to these flaws. Fractures originate from these stress-activated flaws, and in practice different particle sizes break at different rates. Smaller coal particles require higher energy inputs to break, as there is a less chance of finding a large flaw in a smaller volume of a small particle. Thus the repeated use of size reduction will eliminate weak or large flaws and the remaining solid particles will be stronger. When the size particles are too large, breakage may not occur as the stresses required to initiate fracture in larger particles may never be reached.

For the grinding of biomass, shear forces are more appropriate due to the structure of biomass. Wood is an orthotropic material and therefore has two or three mutually orthogonal two-fold axes of rotational symmetry, resulting in anisotropic mechanical properties, and hence the properties are dependent on the direction in which they are measured. Wood can fail through maximum load failure or by excessive deformation (5% strain) (Bodig et al., 1993). Unlike coal, biomass does not have an inherent crack system. Van der Put (2007) showed that the singularity approach of fracture mechanics, applied to all materials, is not able to give the right fracture criterion for orthotropic materials. Based on the failure criterion of a flat elliptical crack, the mixed I-II mode fracture criterion can be derived as a consequence of the ultimate tensile strength condition for the uniaxial stress along the micro-crack boundary. In wood cracks will generally grow along the wood fibres, irrespective of both the original notch orientation and the mode of fracture (Jernkvist, 2001). Cracks oriented parallel to the wood fibres grow self-similarly, and the fracture criterion contains the mode I fracture toughness as the only material dependent fracture parameter. Cracks originally oriented across the wood fibres hardly ever grow in their own plane, and instead make a perpendicular kink and extend along the fibres immediately after onset of fracture. Mode I and II fracture toughness for cracks oriented across the fibres in wood can be related to the mode I fracture toughness measured along the fibres through the elastic properties of the orthotropic material.

The fracture mechanics and mode of failure of the biomass will depend on the proportions of HCL and extractives within the material. Stelte et al. (2011) found that beech pellets fracture surfaces showed areas of cohesive failure, which indicated that high energy fracture mechanisms due to lignin flow and inter-diffusion between the adjacent wood particles which were absent in spruce and straw pellets. It was also observed that both temperature and chemical composition had a significant influence on the bonding quality between biomass particles during the pelletizing process. Bergander and Salmen (2002) found that for three wood polymers cellulose were found to dominate the elastic properties in the longitudinal direction of cell walls, and in the transverse direction the properties of hemicellulose were more pronounced.

While coal comminution invokes brittle fracture mechanisms, densified biomass involves two stages of comminution. The first is the breaking down of the weak bonds holding together the pellet and the second is the breaking down of the particles to the desired size. The milling energy involved in each stage of pellet comminution is unknown. In addition, the impact on particle shape of milling densified biomasses in different mills has not been explored.

2.14. Hardgrove Grindability Index

Most mill manufacturers use the Hardgrove Grindability Index (HGI) test to analyse a coals grindability (Scott, 1995). It is based on Rittinger's first theory of comminution (Unsworth et al., 1991), and the index varies from 20 to 110. A lower HGI indicates that a coal is harder to grind and will require more energy to reach the required degree of fineness. The test is conducted on a standardised laboratory scale ball-and-race mill and is covered by BS 1016-112:1995 (The British Standards Institution, 1995). A strong, hard coal will often have a high rank and be difficult to reduce in size; a weak, soft coal of lower rank will be easier to grind; but very low rank coals can also be difficult to reduce in size. For coal, HGI correlates to compressive and tensile strength measurements which roughly correlate with coal rank, and increasing bulk modulus (Klimpel, 1987).

However, Kendall (1978) showed that crack propagation becomes impossible via compression once a critical particle size is reached, the length of which is material dependant, and particles below this size are ductile in compression. Zuo et al. (2012) showed that the relationship between coal size reduction and energy input is a nonlinear curve, thus it is difficult to represent coal grindability with a single numerical value. Rubiera et al. (1999)

showed that the HGI of binary coal blends cannot be predicted from the weighted average of the individual coals in the blend, which has important implications in the co-milling and combustion performance of biomass and coal blends, as the actual performance may be quite different to the predicted behaviour for a blend due to the interactions between the blends. The observation by Agus and Waters (1971) that mills are volumetric devices, and that the traditional HGI method favours denser coals with small volumes has led to the HGI test to be modified to use volume rather than mass, and this method is commonly used to analyse biomass and coal HGI values experimentally (Bridgeman et al., 2010; Edwards et al., 1980; Ohliger et al., 2013), although industry uses the standardised mass based method (ASTM D409 / D409M-12, 2012; The British Standards Institution, 1995).

HGI has been used on biomass as a method of indicating the grindability of biomass in comparison to coal. For biomass and coal blends, Mroczek (2009) stipulated that HGI is not a proper indicator for co-milling of coal and biomass. Bridgeman et al. (2010) showed that for torrefied fuels that particle size distribution is a more reliable method of analysing grindability of biomass than HGI due to different temperature and residence times for different biomasses to obtain similar grinding behaviour to coal.

2.15. Bond Work Index

The Bond Work Index (BWI or W_i) is defined as the calculated specific energy (kWh/t) applied in reducing material of infinite particle size to 80 per cent passing 100 microns (Warren Spring Laboratory, 1962). The higher the value for W_i, the more energy is required to grind a material in a ball mill (Bond, 1952, 1961). The BWI test is used extensively in the mining industry to analyse the absolute resistance of different materials to ball milling, the energy consumption for ball milling, and scale up (Man, 2002). While the BWI has been used extensively on brittle materials (Ahmadi et al., 2009; Bond, 1952; Deniz, 2004; Gent et al., 2012; Ipek et al., 2005; Jankovic et al., 2010; McIntyre et al., 1980; Sütçü et al., 2003), limited testing (using modified forms of the theory) of biomass has been conducted in planetary ball mills (Van Essendelft et al., 2013) and hammer mills (Temmerman et al., 2013). As the BWI and the HGI are both measures of the grindability of a material, it might be expected that results from the two tests could be correlated. Studies have shown an approximate correlation of HGI and BWI based on the findings of several studies for a wide range of materials, but biomass was not amongst the materials tested (Directorate-General for Energy, 1990; Scott, 1995). Bond proposed the following equation for finding the equivalent wet grinding work index (W_i) from the Hardgrove grindability Index (Bond, 1961):

$$W_i = \frac{435}{HGI^{0.91}} \quad \text{(eq. 2.11)}$$

As McIntyre and Plitt noted (1980), no data was provided to support this correlation. They modified the correlation based on the testing of a wide range of brittle materials, including limestone, subbituminous, and bituminous coal, and for materials with a BWI value above 8.5 kWh/ton, the correlation between HGI and BWI was found to be:

$$W_i = \frac{1622}{HGI^{1.08}} \quad \text{(eq. 2.12)}$$

However, these correlations have not been tested on biomass samples commonly used in the power sector.

2.16. Tube and Ball Mills

A ball mill is a retention mill in which a reservoir of particles are acted upon repeatedly (Austin et al., 1984). The energy used in a ball mill is created by lifting the balls and then allowing them to fall by gravity over the material. A full scale coal tube-ball mill is shown in figure 2.9. Coal stored in the bunker is delivered to a coal feeder via a chute incorporating a bunker discharge valve to control the flow. The horizontal valve incorporates two gates, each hydraulically and independently operated. The controlled quantity of coal is discharged into the feed hopper via the drag link feeder. Coal is drawn from the hopper by a series of chain driven drag links moving across the mouth of the hopper and on the return lower path of the drag links, moving around the chain sprockets, the coal is discharged into the mill inlet chute. There are two feeders for each mill and four mills for each boiler.

The pulverised fuel produced in the mill, by tumbling the coal with a charge of steel balls, is carried by a warm air flow, tapped off the combustion air system, to the classifier. The static classifier (Fig. 2.5) extracts the heavier pulverised fuel particles and returns them to the mill, passing through a rotary rejects valve. Two classifiers are fitted for each mill, supplied from a splitter box attached to the mill discharge.

The pulverised fuel is drawn from the classifier by a variable speed fan and delivered through ducting to the burners. After leaving the exhauster fan, each duct is divided into four lines to supply the pulverised fuel to a group of four burners. At the division point in the ducting a riffle box is fitted to ensure an equal delivery to each burner.

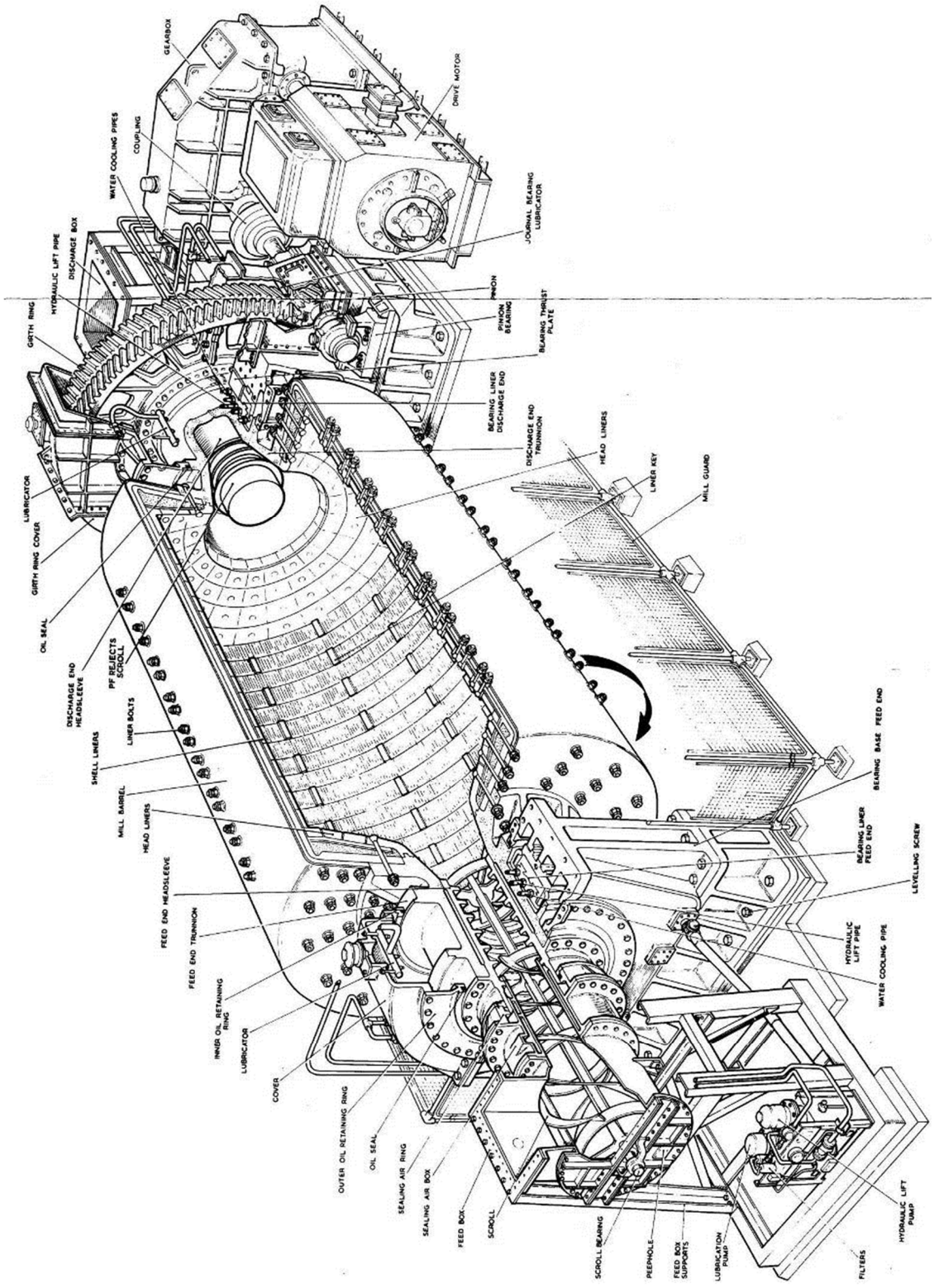


Figure 2.9: Pulverised Fuel Tube-Ball Mill (EDF Energy plc, 1981a)

The BWI test (section 2.15) is widely used for the design and analysis of ball mill circuits, even those that treat Autogenous or Semi-Autogenous (AG/SAG) mill or high-pressure grinding roll (HPGR) and ball mill circuit products, which have a non-standard particle size distribution (Mcken et al., 2005). Despite biomass milling trials in full scale tube and ball mills, and up to 5% olive cake being co-milled with coal at EDF Cottam, the BWI test has not been conducted on non-densified or densified biomass materials.

2.17. Vertical Spindle Mill

Vertical spindle mills refer to a family of mills in which the milled material is caught and ground between a grinding roller and grinding surface of a ring or casing, and are often referred to as ring-roller mills (Fig. 2.10). The most common are bowl mills, Babcock and Wilcox mills, and Raymond ring-roller mills, the former two being most common in coal pulverised fuel boilers (Zulfiquar et al., 2006). Ring-Roller mills are fed with coal via a bunker onto a chain feeder, which delivers an even depth of coal via a chute into the mill. The chute deposits the raw coal onto the mill grinding table. The coal is ground between the driven table and free rotating rollers. The resultant fine ground coal is fluidised by the passage of primary air through the mill. Coal in suspension is conveyed through the separator (Fig.2.4) where particles larger than the separator screen are returned to the mill for further grinding. Un-grindable solids are ejected from the mill by a plough into a chamber below the mill. Pulverized fuel of the correct consistency and moisture content is conveyed in the primary airstream through pipes, riffle boxes and flap valves to the boiler burners where the pulverized fuel and primary air is mixed with a secondary air supply provided by the force draught fans.

The HGI test is usually used to assess the grindability of coals within a vertical spindle mill, and UK coals generally have a HGI value between 40 and 100. Zulfiquar et al. (2006) looked into co-milling of biomass with coal in a pilot scale vertical spindle mill and found biomass could be co-milled up to 5%. Tamura et al. (2014) analysed waste cedar wood chip, pinus bark and wood pellet in co-firing experiments and simulations. They milled woody biomass in a ball mill, vertical roller mill and a vibration mill, and used an industrial scale ring-roller mill to test wood chip and pellet grindability compared to coal. For a target size of particles below 1 mm it was found that a ring-roller mill is suitable for woody biomass comminution. Livingston et al. (1998) use a mini-ring-ball mill with static classification to analyse the comminution of biomass and coal and found a relationship between the new surface area created and the energy consumption per unit new surface area.

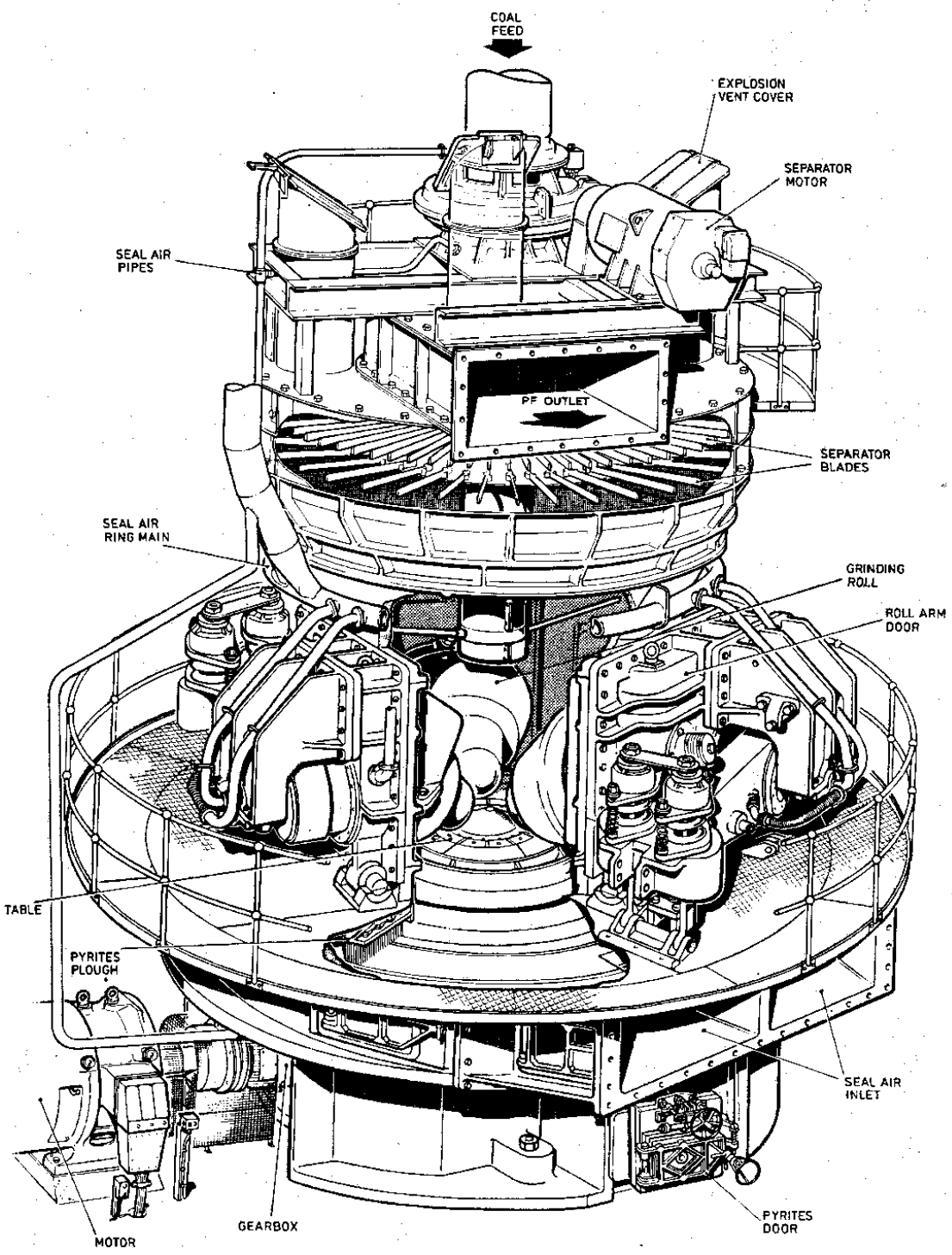


Figure 2.10: Pulverised Fuel Ring-Roller Mill (EDF Energy plc, 1981b)

However there are no studies available in literature on the comminution behaviour of densified biomass pellets from all major biomass groups in a Ring-Roller mill, and no literature available on how the use of a classifier impacts biomass particle size and shape in a laboratory scale ring-roller mill, or any other laboratory scale mill.

2.18. Hammer Mills

Biomass mills originate from the agricultural sector and these mills are now being adapted for power generating situations. However, the variable feed stocks and high through put of biomass mills in power stations has led to several issues relating to the quality of product, wear rates on the mill and in the subsequent conveyancing system. Conversion of lignocellulosic biomass to sugars in a processing plant presents a materials handling problem (Blair, 2014). The raw forms of woody and herbaceous biomass do not lend themselves to conveyance. Although there are many milling technologies available, two technologies have come to the forefront for size reduction: cutting mills and hammer mills. Fundamentally, these mills differ in the type of mechanical force that is applied.

Cutting mills use blades to produce high shear forces that slice the material into smaller pieces (Fig. 2.11). Cutting mills optimize the process that generates sawdust when producing lumber. They are essentially saws whose purpose is to produce fine particles. Cutting mills do not work efficiently when dry hard feedstocks are used (such as grains). Processing of these feedstocks is typically performed using mills that use swinging arms (hammers) that produce large compressive forces upon impact that shatter the material into small pieces. The material is reduced in size by rubbing the space between the hammer and the screen, and once the material is small enough it will fall through the screen and out of the mill. Both of these technologies are optimized for attrition alone (Perry et al., 2008). Chemical processes are suppressed through short dwell times and rigorous control of the temperature during comminution. Comminution processes can be energy intensive and extensive work has gone into characterizing the optimal configuration for size reduction and energy consumption. Hoque (2007) reviewed the performance of productivity of hammer mills for fibrous material particle size reduction. Hammer mills are widely used due to their high size reduction ratio, good control of particle size range with relatively good cubic shape of particles.

In terms of mill operating variables, there are extensive studies on the comminution of unprocessed biomass materials for agricultural and biofuel pellet applications in hammer mills. First real study in biomass hammer milling optimisation was by Himmel (1985), who identified that grinding biomass to smaller particle size requires more energy. Bochat (2015) compared the designs of new and traditional hammer mills for cereal grain grinding. The greatest influence on the amount of powdery fraction was the diameter of holes in the

screen, followed by the hammer angle, the hammer end peripheral speed, and the hammer gap.

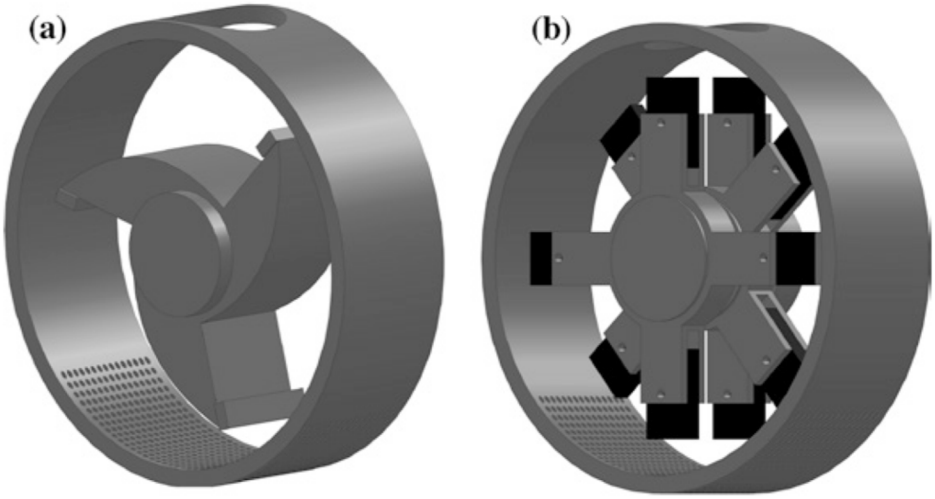


Figure 2.11: Cutting Mill (a) and Swinging Hammer Mill (b) (Blair, 2014)

Gil (2014) milled poplar and corn stover to analyse operating and physical conditions effect on particle size distribution in a hammer mill with 3 fixed blades in a side disc and 6 flailing hammers. Gil et al. (2013) also investigated varying speeds, screen size and found moisture content and screen size were the main variables in the process. The geometric mean diameter of the product was mainly influenced by the classification on the screen and the angular velocity of the hammer governs the variability and dispersion in sizes, with higher angular speed resulting in lower dispersion in particle size. Gil et al. (2012) also used the pilot hammer mill plant to analyse the milling of Cardoon (Cynara Cardunculus) in whole, stem and densified form. They found that pellets were the easiest to mill while the whole and stem forms milled equivalently. Bitra et al. (2008; 2009) looked at swtichgrass, wheat straw, and corn stover in a flailing hammer mill and investigated the impact of hammer angle. They found strong correlation between hammer mill speed and specific effective energy. Rosin-Rammler size parameter, median diameter, and effective size had strong negative correlation with speed.

Esteban (2006) reviewed different strategies for the pulverisation of forest biomass. They specified the product size for biomass in a pulverised fuel boiler as 95% by weight passing a 1000 µm mesh and 12% weight passing a 125 µm mesh. The milled poplar chips, pine chips and crushed pine bark in biomass pilot plant with two hammer mills in series, and found that screen sizes of 4 mm gave the best results for the targets output product size. Laskowski (1997) analysed barley kernels grinding in a hammer mill. The also analysed horse bean, pea, lupine and vetch (all leguminous seeds) in a hammer mill (Laskowski et al., 1999). They

found a significant relationship between the characteristic of compression curves in an Instrom mechanical compression test and the grinding energy requirement. Tumuluru (2014) comminuted wheat, canola, oat and barley straw in hammer mill with swinging hammers, which built on their previous work (Adapa et al., 2011). They found that the bulk and tapped densities are inversely proportional to particle size of the grinds.

Similar controllable mill variables are exhibited in knife and cutting mills. Bitra et al. (2009) investigated the particle size distributions of corn stover in a knife mill operation at varying screens, speeds and flow rates. Screen size and feed rate directly influenced particle size, whereas speed had a weak indirect relation to particle size. Bitra et al. (2009) also looked at the impact of milling conditions on switch grass particle size distributions. The knife mill screen largely determined the particle size of the switch grass chop, with feed rate having a lower impact on the particle size. Both studies showed that the milled product had a good fit with Rosin-Rammler function. Zhang (2012) looked at the size reduction of poplar chips in a cutting mill for 3 sieve sizes, and noted that as screen sizes increased, the energy consumption in knife milling decreased.

2.19. Beater Mills

The milling plant for lignites is fundamentally different to that used for bituminous coals (Zhu, 2012). The key issue for pulverising lignites is achieving adequate drying and avoiding mill fires. This is achieved by using flue gas in addition to air to dry the lignite, as it gives the heat required for drying and reduces the oxygen concentration in the mills to a level where explosions cannot occur. Due to the soft nature of lignite coal, beater wheel mills are normally used to pulverise the lignite to achieve defined fineness and to lower its moisture content to the desired level to ensure efficient combustion of the fuel. A beater wheel mill works by crushing, shattering, or pulverising lignite upon impact, and come in three configurations; mill with classifier, mill with vapour classification, and mill with staged grinding (Fig. 2.12). The fineness of pulverised coal is usually assessed on the basis of the residues on the 1 mm sieve (usually between 3-6%). Beater mills are equipped with static classifiers, with a 70-90% of the product within the classification size fraction of <63 µm. The power consumption for grinding is typically 15–20 kWh/t for hard coal and 4–14 kWh/t for lignite (Nikolopoulos et al., 2015). The metal consumption is 60–160 g/t for hard coal, 20–80 g/t for lignite, and 2000 g/t for quick coke. For coals at moisture levels of 10–14%, air at 300–400 °C may be used as the heating medium. When the moisture content is above 15-25%, combustion gases at temperature of 700–1000 °C are used. Coals with high

moisture content (25–35%) are partially pre-dried at the chute to the mill by means of hot combustion gases.

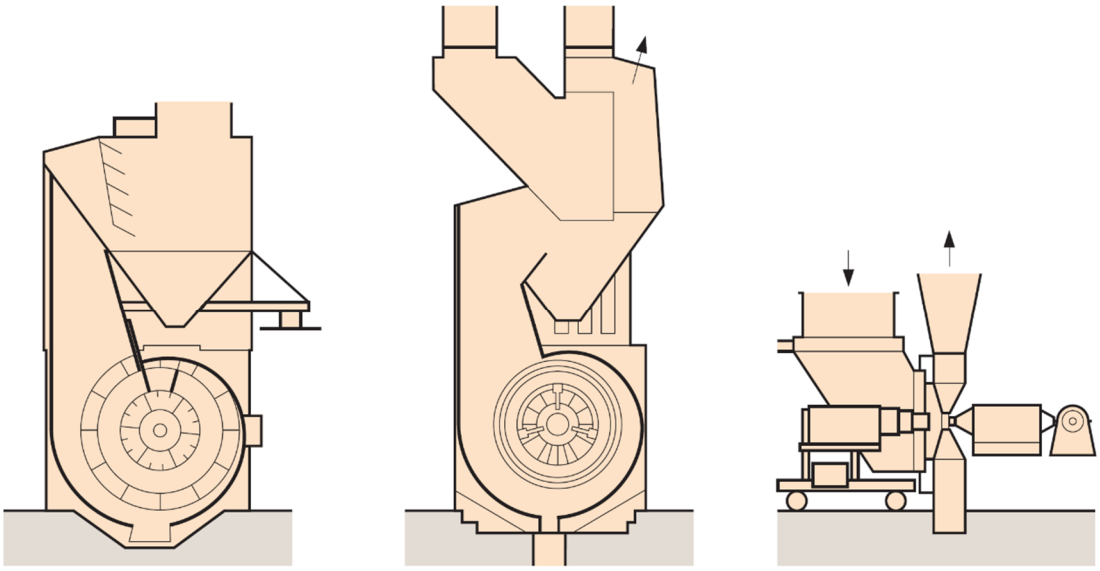


Figure 2.12: Types of Beater Wheel Mills (Zhu, 2012)

Forest biomass has been comminuted in modified beater wheel mills in a power station in Hungary, with moisture content significantly effecting the comminution energy consumption (Csőke et al., 2009). Indeed, the study recommended a pre-comminution stage for the biomass using hammer mills, and major modifications were required to be made to the classification system. Due to their different milling principle, HGI is a poor predictor of the grindability of lignite in beater mills. Alstom and RWE developed a procedure and a test impact mill to determine an impact grindability index (PMI) for lignite, which is a good indicator for grindability in large scale beater wheel mills (Ohliger et al., 2013).

2.20. Planetary Ball Mills

Planetary ball mills are used for sample processing, colloidal grinding and material development due to their good reproducibility, safe handling and short processing times (Burmeister et al., 2013). Planetary ball mills normally have 1 (with counter balance), 2 or 4 pots (Fig. 2.13). The pots are attached to a disk that rotates around a common central axis while the pots are simultaneously rotating around their own axis. The high rotational speed of both, the pots and the disk, leads to large impact energies of milling balls inside the pots to achieve an effective grinding performance. The materials under comminution are located between surfaces and crushed due to the impact and/or frictional forces that are caused by collisions. As well as the rotation of the pot, the powder charge influences the ball motion

inside. The powder particles are trapped between the colliding balls and make the collision less elastic so that the ball motion is slowed down and the energy dissipation is reduced.

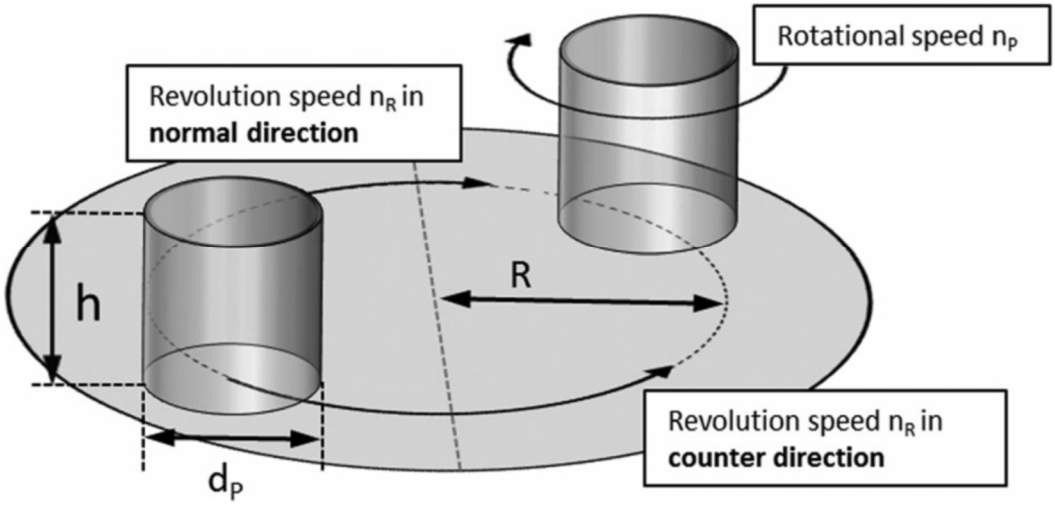


Figure 2.13: Scheme of planetary disks with movement in a normal and counter direction (Burmeister et al., 2013)

The motion of the balls influences the number of collisions, the ball velocity and therefore the impact intensity of the balls which contributes to the energy input to the powder charge. The balls show complex behaviour in the grinding chamber during processing and the motion pattern varies depending on the operation parameters. It changes from cascading to cataracting up to centrifugation or rolling with increasing filling ratio and/or increasing revolution speed. In the cascading regime the milling balls are taken along by the pot wall and unroll upon each other from the bulk top to its base while in the cataracting regime the balls detach from the wall and impact with high intensity the bulk or the opposite wall. Rolling or centrifuging balls align to the wall rotation with almost no relative velocity.

Planetary ball mills are usually used in biomass applications for reducing the crystallinity of the biomass to realise improved acid and enzymatic hydrolysis rates while at the same time limiting the amount of undesirable by-product for the biological conversion of cellulosic biomass to fuels and chemicals (Blair, 2014). Avolio et al. (2012) looked at the impact of dry ball milling on cellulose structure, morphology and properties, and found the crystallinity reduced as milling time increased. Planetary ball mills have also been used to investigate the increase in surface area of biochars through process optimisation (Peterson et al., 2012). A modified HGI test method was developed by Bridgeman et al. (2010) in a Retsch PM100 planetary ball mill and used by Ibrahim et al. (2013) to look at the improvement in

grindability through the torrefaction of biomass materials. Van Essendelft et al. (2013) used a planetary ball mill to find a hybrid work index for torrefied materials.

2.21. Mill Comparison Studies

Comparison studies of biomass milling in different mills are limited in literature. The generally focus on comparison of similar mills and fracture mechanisms for similar feed stocks (usually wood or agricultural crops). Miao et al. (2011) investigated miscanthus, switch grass, willow and energy cane in a cutting mill and a cross beater mill. They found that specific energy consumption of biomass comminution and screen sizes are related in power law forms. Biomass moisture significantly impacted comminution energy requirements. The cross beater mill was more energy efficient than cutting mill due to higher speeds and axial feeding mechanism. For the samples analysed, the particle size was found to be inversely proportional to bulk density, and the comminution ratio (ratio of final mean diameter to original mean diameter) was proportional to energy consumption. Paulrud (2002) used mixed pine and spruce stemwood in 5 different industry mills; four different hammer mills and one knife mill, and one laboratory knife mill. The hammer mills produced finer particles than knife mills. Bridging tendency was higher for hammer mills than knife mills, which is related to particle size and shape. Tamura et al. (2014) analysed waste cedar wood chip, pinus bark and wood pellet in co-firing experiments and simulations. They milled woody biomass in a ball mill, vertical roller mill and a vibration mill, and used a ring-roller mill in industry to test with wood chip and pellet compared to coal. It was found that a ring-roller mill is suitable for woody biomass comminution.

2.22. Co-milling

Over the past 15 years, co-milling of biomass and coal is routinely practiced in coal fired power stations across the globe. In the Wallenberg Power Station in Australia, co-milling at 3 wt. % to 7 wt. % biomass with coal was trailed at the plant. At 3% there were minimal impact on system; 5% saw decreased mill outlet temperature with increased differential pressure and power consumption; and 7% showed a drop in mill temperature with unacceptably high differential pressure and power consumption which was resolved by lowering the feeder speed to 75% (Loo et al., 2008). Mroczek (2009) showed that a decrease in the grindability and density of a fuel blend, as well as higher moisture content can cause a drop in mill capacity, increased mill power consumption, increased energy demand for drying and transporting the fuel, and an increase particle size to the milled product. Whilst

there are several studies on biomass co-milling with coal (Mroczek, 2009; Zilkha Biomass Energy, 2011; Zulfiquar et al., 2006), there is little ranking of biomass types to coal mill types in the literature, or which types coals mill best with different types of biomasses in different mills, which would aid users to identify the most suitable biomass to mill in existing coal mills.

2.23. Conclusions

A thorough knowledge of the comminution properties of all biomass types in coal and biomass mills is essential for minimising operational issues and optimising milling and combustion. Biomass structural components, extractives and inorganic constituents vary considerably across the spectrum of biomass type and differ significantly to those of coal. Biomass conversions and co-firing use the existing coal pulverized fuel burners, and for co-combustion of biomass and coal, the Stokes number of a biomass particle should match that of an equivalent coal particle in order to pass the aerodynamic filter used to classify particles in traditional coal mills. While it is known that grindability and 2D shape factors are improved through thermal treatment, the impact on the operational sphericity of biomass particles has not been measured. Real data on the operational sphericity and shape factor data for all biomass types is not present in literature and represents a significant gap in knowledge in the field.

Two types of force; compressive and shear, dominate mechanical processing. Brittle materials such as coal are easily fragmented under the application of compressive force, while soft materials such as biomass are more easily processed by the application of shear force. Densified biomass involves two stages of comminution. The first is the breaking down of the weak bonds holding together the pellet and the second is the breaking down of the particles to the desired size. The impact on particle shape of milling densified biomasses in different mills has not been explored.

The use of traditional coal grindability tests such as HGI and BWI have been met with little success for non-densified biomass, however there is no literature on their applicability for densified biomasses. While extensive work has been conducted on the milling of non-densified biomasses in hammer and cutting mills, there is very little work on densified biomasses, mill choking, or the impact on particle shape. There is little ranking of biomass types to coal mill types in the literature. The aim of this thesis is to address these identified gaps in knowledge, and provide useful and applicable data and recommendations for addressing these issues.

Chapter 3 - Experimental

This chapter details the experimental methods used during the doctorate. The chapter is broken into two sections. The first (section 3.1) details the characterisation techniques and data analysis methods used to evaluate the samples before and after milling. The second (section 3.2) provides an outline of the experimental methodology of the milling trials. A total of 12 different samples have been chosen for this study (11 biomasses and 1 coal), although not every sample was used in each test. The samples used are pictured in figure 3.1. These samples have been sourced via Biomass & Fossil Fuel Research Alliance (BF2RA) members, or from commercial suppliers. The biomasses used in this project were: Spanish olive cake (2013 & 2014), Columbian La Loma coal, olive pellets, mixed wood pellets, white wood pellets, miscanthus pellets, sunflower husk pellets, South African eucalyptus pellets, torrefied pellets, microwaved pellets, shredded bagasse, and steam exploded white wood pellets. The samples have been classed into four groups according to BS EN 14961-1:2010 (The British Standards Institution, 2010a); woody, herbaceous, fruit, and treated biomass.

Woody Biomass: Three types of woody biomass were used; mixed wood pellets, eucalyptus pellets and white wood pellets. All samples pellets are chemically untreated wood residues (class 1.2.1) according to BS EN 17225-1:2014 (The British Standards Institution, 2014b). The mixed wood pellets were supplied by EDF Energy plc, and originate from Portugal. They consist mainly of softwood pine (*pinus*) with a small amount of Eucalyptus (*eucalyptus*). Hardwood eucalyptus (*eucalyptus*) pellets were provided by E.ON UK plc, and are South African in origin. White wood pellets were commercially from a local supplier, and are white softwood of unknown origin.

Herbaceous Biomass: The miscanthus (*miscanthus × giganteus)* or elephant grass pellets were sourced from E.ON UK plc. Miscanthus is a tall, woody, perennial, rhizomathous grass commonly used as an energy crop in the UK, and is classed as herbaceous biomass from agriculture and horticulture, grasses (class 2.1.2) according to BS EN 17225-1:2014 (The British Standards Institution, 2014b). Shredded bagasse (*gramineae saccharum officinarum L.*) was sourced from AB Sugar. Bagasse is a fibrous residue remaining after the extraction of juice from the crushed stalks of sugar cane, and is classed as herbaceous biomass from agriculture and horticulture, grasses (class 2.1.2) according to BS EN 17225-1:2014 (The British Standards Institution, 2014b).



Figure 3.1: (From top left to right) Spanish Olive Cake, La Loma Coal, Mixed Wood Pellets, Microwave Pellets, White Wood Pellets, South African Eucalyptus Pellets, Miscanthus Pellets, Steam Exploded Pellets, Olive Pellets, Torrefied Pellets, Sunflower Husk Pellets, Shredded Bagasse. Scale is in cm grid.

The bagasse originated from Zambia in Africa and due to the high moisture content was stored in cold storage until use to avoid decomposition and fugal growth. Sunflower husk (*helianthus annus L.*) pellets were provided by EDF Energy plc. The sunflower husk pellets are chemically untreated herbaceous residues, oil seed crops, husks or shells (class 2.1.3.4) according to BS EN 17225-1:2014 (The British Standards Institution, 2014b). The sunflower husk pellets originate from Russia and the Ukraine, and are a by-product of the sunflower oil pressing process.

Fruit Biomass (By products and Residues): Spanish olive cake (*olea Europaea*) was provided by EDF Energy plc from 2013 and 2014 supplies. The olive cake is very variable in quality and

is affected by seasonal changes. The olive cake is stored externally in Spain and the moisture content can be up to 8% higher in winter compared to the summer. The olive pellets were sourced via E.ON UK plc. The olive cake and olive pellets are chemically untreated fruit residues, crude olive cake (class 3.2.1.4) according to BS EN 17225-1:2014 (The British Standards Institution, 2014b).

Treated Biomass: The steam exploded pellets were provided by E.ON UK plc. The pellets were used as part of a biomass storage Engineering Doctorate project conducted by Shalini Graham at the University of Nottingham in conjunction with E.ON UK plc (Graham et al., 2012). The steam exploded pellets were stored for 35 months in 2.4 m x 2.4 m x 1.5 m stockpiles internally and externally to analyse the impact of storage on biomass properties. At the end of the project samples were taken from the indoor pile for use in this project. Due to commercial sensitivity, limited information is known about the source and origin of the materials used. The virgin wood is known to be chemically untreated softwood residues (class 1.2.1) according to BS EN 17225-1:2014 (The British Standards Institution, 2014b) of a white softwood variety prior to the steam explosion process which originate from Northern America. Torrefied pellets were provided by E.ON UK plc. Softwood chips of an undisclosed origin were torrefied in a commercial plant at 270-300 °C with an input moisture of 8-10% and output moisture of 0-1%, and then densified into pellets with a net calorific value of 21 wt. % to 23 GJ/ton, moisture range of 2-6%, ash content of 1-4%, and bulk density of 650 kgm^{-3} to 800 kgm^{-3} (Swaan, 2012). The microwaved bio-coal pellets were provided directly via Energy Environmental Group. The microwave pellets uses a patented an innovative microwave assisted torrefaction process to convert biomass (generally softwood sawdust) into biocoal.

Coal: Columbian La Loma coal was provided by EDF Energy plc. La Loma is a bituminous low Nitrous Oxide (NO_x) coal and is used at EDF Cottam to reduce NO_x levels.

3.1. Characterisation of Samples

In order to understand the impact of milling on the samples, extensive characterisation has been conducted on the samples prior to and after milling. The testing uses a combination of standard biomass and coal tests and novel experimental methods.

3.1.1. Moisture Content

Moisture content was measured in accordance with BS EN 14774-1:2009 (The British Standards Institution, 2009a). 300 g ± 1 g of each sample was dried in a Thermo Scientific

Heraeus UT 6 (Waltham, MA, USA) forced-air oven at 105 °C ± 2 °C for 24 hours. The moisture content was ascertained by periodically weighing the samples during the drying process. After drying the weight of the sample was recorded and used to calculate the moisture content of the biomass, with each sample being tested in triplicate. The dried samples used in the milling tests were dried under the same conditions, and then placed in zip-lock sealed bags until use.

3.1.2. Pellet Disintegration Test

The pellet disintegration test followed BS EN 16126:2012 (The British Standards Institution, 2012). 2 litres of boiling deionised water was poured over 300 g ± 1 g of each pellet sample and then soaked for 24 hours. The samples were then dried at 35 °C to 60 °C until they reached 5-15% moisture content. The moisture content was ascertained by periodically weighing the samples during the drying process. The samples were then split into two portions; 150 g was used to obtain the moisture content via BS EN 14774-1:2009 (The British Standards Institution, 2009a) as per section 3.1.1, while the other 150 g portion was split and sieved to obtain a particle size distribution according to BS EN 15149-2:2010 (The British Standards Institution, 2010b), as per section 3.1.4.

3.1.3. Pellet Diameter and Length

Pellet diameter and length was found in accordance with BS EN ISO 17829 (Draft) (The British Standards Institution, 2014f). 100 pellets were measured using a Clarke CM145 Digital Vernier Calliper (Epping UK) for diameter (mm) and length (mm). The pellet aspect ratio *ARP* is found in accordance with ÖNORM M 7135 (ÖNORM, 2000) and should be below 5 to avoid blockages in the comminution system:

$$ARP = \frac{length}{diameter} \quad \text{(Eq. 3.1)}$$

3.1.4. Particle Size Distribution by Sieving

Particle size distributions were determined by sieving the milled product in accordance with BS EN 15149-2:2010 (The British Standards Institution, 2010b). The samples were sieved into 16 size fractions (4750, 3350, 2360, 1700, 1180, 1000, 850, 600, 425, 300, 212, 150, 75, 53, 45, 38 µm sieves) unless specified otherwise. Sieving was conducted on a Retsch AS200 Control (Hann, Germany) vibratory sieve shaker in two stages. In the first stage, 8 coarse sized sieves (4750-600µm) were used, and in the second stage, 8 finer sieves (450 µm to 38 µm) were used. Each sieving stage was conducted for 15 minutes at 3 mm amplitude.

3.1.5. Digital Image Processing

Particle size distributions and imaging was conducted on a Retsch Camsizer® P4 (Hann, Germany). The Retsch Camsizer P4 measuring system is based on 3D digital imaging processing (Allen, 2003). The biomass flows along a vibratory bed feeder until it drops into a slot where it flows between a light source and two high speed cameras, where the particles are individually detected as projected areas, digitalised and processed. The two cameras perform different measurement functions; the first basic camera detects large particles, while the second zoom camera registers the small particles. The measurement range of the Camsizer is theoretically 15 µm to 90 mm, with a practical measurement of 30 µm to 30 mm. Electronic processing of the images takes place in 10,000 size classes and saved in 1,000 size classes. The outputs from the Camsizer are all standard particle distributions combined with microscopy shape factors such as Martin and Ferret Diameter, and longest chord, as defined in section 3.1.8. The measurements were further analysed in the Retsch Particle Library software in wizard mode (Retsch Gmbh, 2015). By screening for the 50th percentile of the shape cumulative distribution (Q_{50}) and mean values of particle sphericity, symmetry, aspect ratio and circularity (defined in section 3.1.8), and the 80th percentile of particle size (d_{80}), a particle list was provided for the filtered sizes (particles within the range of the set value + 0.001). From the list, a representative particle contour was selected and used to create the particle image tables in the discussion chapter (chapter 9).

3.1.6. Particle Distribution Analysis

Particle distribution analysis provides a vital element of biomass milling characterisation. The analysis is conducted in 3 parts; the first was the analysis of the fit of the Rosin-Rammler distribution equation for the sieved (by mass) and the digital imaging (by volume) particle size distributions. The second looked at size, dispersion, and the distribution shape parameters for sieved (by mass) and digital imaging (by volume) particle size distributions. The third analysed the shape parameters of the particle size distributions from the digital image analysis results. Particle size distributions are represented graphically on semi-logarithmic charts of normalised cumulative distribution against particle size (The British Standards Institution, 1998b).

3.1.6.1. Rosin-Rammler

The Rosin-Rammler distribution equation was originally developed to describe the distributions of coals fines from coal mills (Rosin et al., 1933), and it has been shown in several studies that the Rosin-Rammler distribution equation is a good fit for biomass

comminution in hammer mills (Bitra, Womac, Chevanan, et al., 2009; Gil et al., 2012). The Rosin-Rammler equation is:

$$R(d) = 100\left(1 - e^{-\left(\frac{d}{d'}\right)^n}\right) \quad \text{(eq.3.2)}$$

Where *R* is cumulative percentage mass undersize (%), *d* is particle diameter (µm), *d'* is the characteristic particle size (µm), defined as the size at which 63.2% (*1 - 1/e = 0.632*) of the particles (by weight) are smaller, and *n* is the Rosin-Rammler size distribution parameter (dimensionless). A lower value of *n* means a lower slope and thus a wider distribution and higher diversity of the particles sizes. *d'* corresponds mathematically to d_{63}, and is therefore a distribution percentile. The Rosin-Rammler parameters were found for the fuels in this paper using the Matlab® GUI Tool developed by Brezáni and Zelenak (2010) using a non-linear curve fitting technique. The Camsizer uses a linear curve fitting technique as described by DIN 66 145 (1976) between the 5th and 95th percentiles.

3.1.6.2. Distribution Analysis

The distribution of the particles can be analysed through three categories of parameter; size parameters, dispersion parameters, and distribution shape parameters. The particle size distributions of percentage retained mass against particle size were plotted on semi-logarithmic plots from to visualise the data and the percentiles were calculated in Matlab 2015a through interpolation using the piecewise cubic hermite interpolation (pchip) interpolation function (The MathWorks Inc., 2015).

3.1.6.3. Size Parameters

Geometric mean diameter by mass, d_{gw}, was calculated according to ANSI/ASAE S319.4 (2008). Mathematically, the geometric mean diameter is always greater than the particle size at 50th percentile of cumulative distribution, or median mean diameter (d_{50}). The geometric mean diameter (d_{gw}) is found by:

$$d_{gw} = log^{-1}\left[\frac{\sum_{i=1}^{n}(M_i \log \bar{d}_i)}{\sum_{i=1}^{n} M_i}\right] \quad \text{(eq. 3.3)}$$

Where M_i is the mass on ith sieve (g), $\bar{d}_i$ is the mean geometric diameter (µm) of particles on the ith sieve (d_i), or $[d_i \times d_{i+1}]^{1/2}$.

3.1.6.4. Dispersion Parameters

The geometric standard deviation of log-normal distribution by mass in ten-based logarithm (*s*, dimensionless), is (ANSI/ASAE S319.4 FEB2008 (R2012), 2008; The British Standards Institution, 2014e):

$$s = log^{-1}\left[\frac{\sum_{i=1}^{n} M_i(\log \bar{d}_i - \log d_{gw})^2}{\sum_{i=1}^{n} M_i}\right]^{1/2} \quad \text{(eq. 3.4)}$$

Mathematically *s* gives the difference between each particle size in relation to d_{gw}. The geometric standard deviation, *s*, can also be expressed as (ANSI/ASAE S319.4 FEB2008 (R2012), 2008; The British Standards Institution, 2014e):

$$s = \exp(\ln\left({}^{d_{84}}/_{d_{50}}\right) = \exp(\ln\left({}^{d_{50}}/_{d_{16}}\right) = {}^{d_{84}}/_{d_{50}} = {}^{d_{50}}/_{d_{16}} \quad \text{(eq. 3.5)}$$

Where d_{84} is the particle size at 84th percentile of cumulative distribution (µm), d_{50} is the particle size at 50th percentile of cumulative distribution or median mean diameter (µm), d_{16} is the particle size at 16th percentile of cumulative distribution (µm), This can be further split into the distribution geometric standard deviation of high region (*hs*) and distribution geometric standard deviation of low region (*ls*) (Bitra, Womac, Yang, Miu, et al., 2009; Gil & Arauzo, 2014):

$$hs = {}^{d_{84}}/_{d_{50}} \quad \text{(eq. 3.6)}$$

$$ls = {}^{d_{50}}/_{d_{16}} \quad \text{(eq. 3.7)}$$

The Mass Relative Span (*MRS*) describes the span of the distribution, with a value greater than 1.0 indicating a wide distribution (Bitra, Womac, Yang, Miu, et al., 2009; Gil et al., 2012). The higher the *MRS*, the higher the heterogeneity in particle sizes.

$$MRS = \frac{d_{90} - d_{10}}{d_{50}} \quad \text{(eq. 3.8)}$$

Where d_{90} is the particle size at 90th percentile of cumulative distribution (µm) and d_{10} is the particle size at 10th percentile of cumulative distribution or effective size (µm) (Gil & Arauzo, 2014). In soil mechanics the Uniformity Coefficient (C_u) and Coefficient of Curvature (C_c) are used in conjunction with each other to give a quantitative means for describing the shape of the grading curve. The uniformity coefficient is defined as a measure of the shape of the grading curve within the range d_{10} and d_{60} (The British Standards Institution, 2013a):

$$C_u = {}^{d_{60}}/_{d_{10}} \quad \text{(eq. 3.9)}$$

Where d_{60} is the particle size at 60th percentile of cumulative distribution (µm). As most biomass milling research has been concentrated in the agriculture sector in the US (Bitra, Womac, Yang, Miu, et al., 2009; Gil & Arauzo, 2014; Himmel et al., 1985; Mani et al., 2003), the literature follows the Unified Soil Classification System according to ASTM D2487-11 (2011). For biomass, milled samples with a uniformity coefficient of < 4.0 are considered to contain particles of approximately uniform size (Bitra, Womac, Yang, Miu, et al., 2009; Budhu, 2011; Gil & Arauzo, 2014), which is based on the gravel classification. C_u > 4 indicates good graduation of particle sizes for smooth and reasonably symmetrical curves. The Coefficient of Curvature is defined as a measure of the shape of the grading curve within the range d_{10}, d_{30} and d_{60} (The British Standards Institution, 2013a):

$$C_c = \frac{(d_{30})^2}{d_{60}\, x\, d_{10}} \quad \text{(eq. 3.10)}$$

Where d_{30} is the particle size at 30th percentile of cumulative distribution (µm). A Coefficient of Curvature between 1 and 3 represents well graded particles (Budhu, 2011), although both C_C and C_u conditions need to be met to be considered well-graded (C_u > 4 and 1 < C_c <3). This means there is a good distribution of sizes in a wide distribution, thus small grains will fill the voids generated by the larger grains and thus produce a more dense packing.

3.1.7. Distribution Shape Parameters

Skewness measures the asymmetry of a distribution and occurs when significant quantities of particles, either in coarser or in finer regions, are removed from the region of predominant size (Bitra, Womac, Yang, Miu, et al., 2009). The formula below includes the "tails" of the cumulative curve as well as the central portion. Symmetrical curves will have skewness equal to 0, those with a large proportion of fine material positively skewed, and those with a large proportion of coarse material are negatively skewed. Inclusive graphic skewness (GS_i) of particle size distribution, which includes 90% of the curve, is defined as (Folk, 1974):

$$GS_i = \frac{(d_{16} + d_{84} - 2d_{50})}{2(d_{84} - d_{16})} + \frac{(d_5 + d_{95} - 2d_{50})}{2(d_{95} - d_5)} \quad \text{(eq. 3.11)}$$

Where d_5 is the particle size at 5th percentile of cumulative distribution (µm), and d_{95} is the particle size at 95th percentile of cumulative distribution (µm). The geometric kurtosis (K_g) measures the peakedness or flatness of the distribution, relative to the log-normal (Bitra,

Womac, Yang, Miu, et al., 2009). By definition, the flatness of distribution represents a higher diversity or heterogeneity on particle size, and therefore an important relation with dispersion parameters, and is defined as (Folk, 1974):

$$K_g = \frac{(d_{95} - d_5)}{2.44\,(d_{75} - d_{25})} \qquad \text{(eq. 3.12)}$$

Where d_{25} is the particle size at 25th percentile of cumulative distribution (µm), and d_{75} is the particle size at 75th percentile of cumulative distribution (µm). A normal Gaussian distribution will have a kurtosis of 1, which is a curve with the sorting in the tails equal to the sorting in the central portion. If a sample curve is better sorted in the central part than in the tails, the curve is said to be excessively peaked, or leptokurtic; if the sample is better sorted in the tails than in the central portion, the cure is flat peaked or platykurtic. For leptokurtic curves, $K_g > 1.00$, and platykurtic curves have $K_g < 1.00$ (Folk, 1974).

3.1.8. Digital Imaging Shape Analysis

In addition to the parameters detailed in section 3.1.6, digital imaging analysis of particulate samples can be characterised through several additional shape parameters. Three different diameters are measured for each particle in the Retsch Camsizer software; shortest chord diameter (d_{c_min}), Feret diameter (d_{Fe_max}), and area diameter (d_{area}), as defined in figure 3.2.

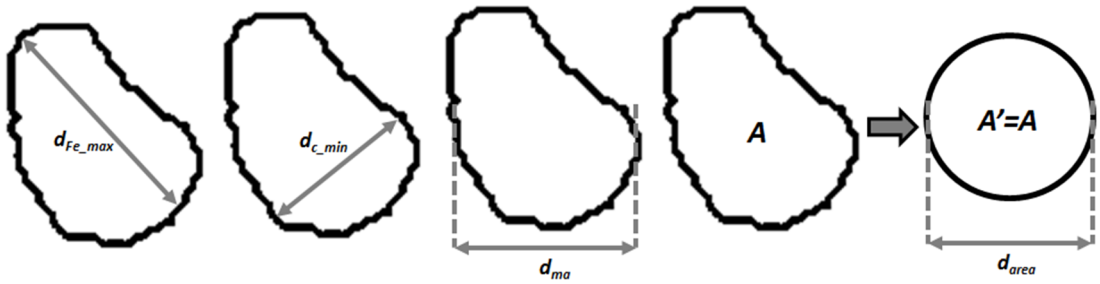


Figure 3.2: Definition of Feret Diameter (d_{Fe_max}), Shortest Chord/Sieving Diameter (d_{c_min}), Martin Diameter (d_{ma}), and Area Diameter (d_{area}) (Retsch Gmbh, 2009)

The shortest chord diameter (d_{c_min}) is the particle diameter which is the shortest chord of the particle being analysed, and can be considered as equivalent to the particle size achieved from sieving (Retsch Gmbh, 2009). The Feret diameter (d_{Fe_max}) is defined as the distance between two parallel tangents on opposite sides of the image of a randomly orientated particle, and is equivalent to the Feret diameter used in microscopy. The area diameter (d_{area}) is the particle diameter calculated from the area of particle projection (A), and is equivalent to diameter found from laser diffraction particle analysis. It is defined as:

$$d_{area} = \frac{\sqrt{4A}}{\pi} \quad \text{(eq. 3.13)}$$

The particle aspect ratio (*AR*) is the ratio of the width of a particle to its length, which in the case of the measured parameters is equivalent to the ratio of the shortest chord diameter to the maximum Feret diameter (Retsch Gmbh, 2009):

$$AR = \frac{d_{c_min}}{d_{Fe_max}} \quad \text{(eq. 3.14)}$$

In addition the sphericity, circularity, and symmetry of the particles are measured. The measured sphericity is the operational sphericity (φ) (Krumbein et al., 1963), which is expressed as:

$$\varphi = \frac{d}{a} \quad \text{(eq. 3.15)}$$

Where *d* is the nominal diameter of the particle and *a* is the maximum intercept through the particle (Fig. 2.6). Circularity (*C*) is a measure of how closely a particle resembles a sphere and is determined in accordance with BS 9276-6 (The British Standards Institution, 2008).

$$C = \sqrt{\frac{4\pi A}{p}} = \frac{d_A}{d_P} \quad \text{(eq. 3.16)}$$

Where p is the measured circumference of a particle projection (µm), x_A is the area equivalent diameter of the particle (µm), and x_P is the perimeter equivalent diameter of a particle (µm). The Camsizer software squares the circularity to give a value between 0 and 1, with an ideal circle having a value of 1 (Retsch Gmbh, 2009). The Symmetry (*Symm*) of particles gives an indicator of the level of symmetry in the particles in a gives size class, and is defined as (Retsch Gmbh, 2009):

$$Symm = \frac{1}{2}\left(1 + min\left(\frac{r_1}{r_2}\right)\right) \quad \text{(eq. 3.17)}$$

Where r_1 and r_2 are distances from the centre of area to the borders in the measuring directions (µm). For asymmetric particles *Symm* is < 1. If the centre of area is outside the particle i.e. $r_1 / r_2 < 0$, then *Symm* < 0.5. The symmetry is a is the minimum value of measured set of symmetry values from different directions, and is related to the Martin diameter (d_{ma}), which is the length of the area bisector of an irregular object in a specified measuring direction, and is also used in microscopy as a measure of particle size. It is defined as:

$$d_{ma} = r_1 + r_2 \qquad \text{(eq. 3.18)}$$

3.1.9. Moisture Re-Adsorption Test

To analyse the moisture re-adsorption of the biomass in atmosphere, 100 g ± 1 g of each sample was dried according to BS EN 14774-1:2009 (The British Standards Institution, 2009a) above and then placed on a Ohaus Pioneer balance PA4102c (Nänikon, Switzerland) for 24 hours. The weight was logged via a laptop using the Ohaus DAS (Data Acquisition Software) at 10 second intervals over a 24 hour period in an air conditioned laboratory. Temperature and humidity of the space during the re-adsorption test were measured using a Lascar Electronics UK EL-USB-1 USB temperature and humidity data logger (Salisbury, UK) set to read at 5 minute intervals.

3.1.10. Mechanical Strength of Pellets

Material properties of materials are usually obtained under quasi-static loading conditions, but there is little data available on the compressive strength of different biomass pellets. Quasi-static mechanical compression tests were used to ascertain the mechanical strength of the pellets for low strain rates. The pellets were tested in three orientations; axial, diametric and flexure, using an Instron Mechanical 5969 Testing System (High Wycombe, UK) as illustrated in figure 3.3.

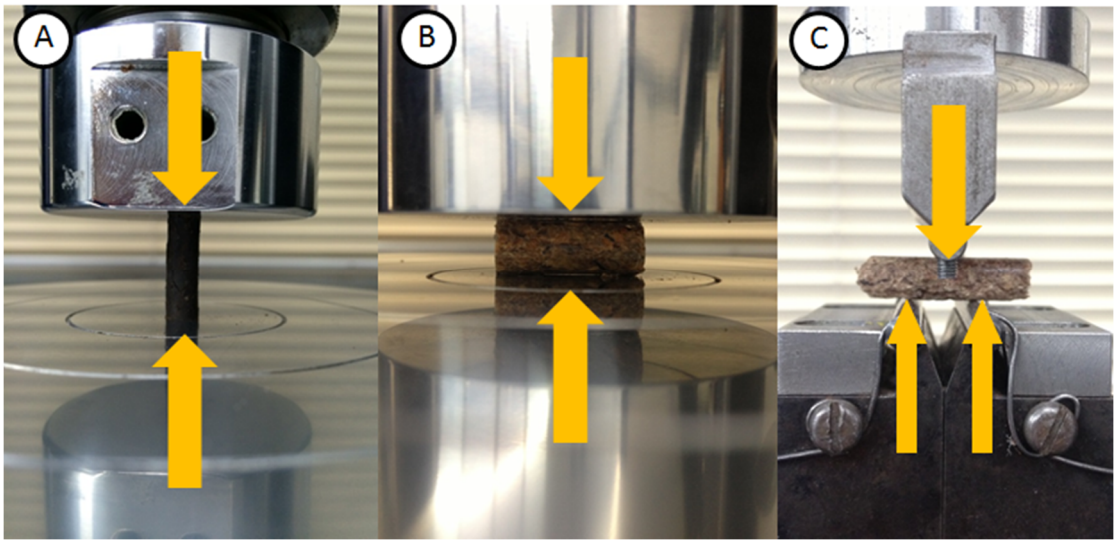


Figure 3.3: Mechanical testing of Pellets in a) Axial, b) Diametric, c) Flexure Modes

For the axial tests, the ends of each pellet were first ground square using a bench grinder. For the diametric tests, the pellets were placed on their sides and compressed laterally with two flat plates, while the flexure tests used a 3-point loading rig. 10 pellets of each sample were tested in axial, diametric and flexure orientations (30 runs in total per sample). For

wood specimens the modulus of rupture (denoted as flexure stress) reflects the maximum load-carrying capacity of a member in bending and is proportional to maximum moment borne by the specimen. The modulus of rupture is an accepted criterion of wood strength, although it is not a true stress because the formula by which it is computed is valid only to the elastic limit (Kretschmann, 2010). The modulus of rupture gives the pellet overall strength, while its modulus of elasticity measures the pellet deflection, but not its ultimate strength. For the axial tests, the compressive stress σ_a was found by using:

$$\sigma_a = \frac{F}{\pi r^2} \quad \text{(eq. 3.19)}$$

Where *F* is the applied force (kN) and *r* is the radius of the pellet (mm). For the diametric test, the compressive stress σ_d was found from:

$$\sigma_d = \frac{F}{rl} \quad \text{(eq. 3.20)}$$

Where *l* is the length of the pellet (mm), and there is an assumed contact area of 50% of the diameter. The compressive strain ε was found by:

$$\varepsilon = \frac{l - l_i}{l} = \frac{\Delta l}{l} \quad \text{(eq. 3.21)}$$

Where l_i is the compressed length (mm) of the pellet. The compressive Modulus of Elasticity or Young's Modulus E_a for the axial compression tests was found by:

$$E_a = \frac{\sigma_a}{\varepsilon} = \frac{F}{\pi r^2} . \frac{l}{\Delta l} = \frac{kl}{\pi r^2} \quad \text{(eq. 3.22)}$$

Where *k* is the gradient of the Force-displacement curve (kN/mm). The compressive Young's Modulus E_d for the diametric compression tests was found by:

$$E_d = \frac{\sigma_d}{\varepsilon} = \frac{F}{rl} . \frac{l}{\Delta l} = \frac{k}{r} \quad \text{(eq. 3.23)}$$

For the 3-point bend test, the flexure stress or Modulus of Rupture σ_f is found by:

$$\sigma_f = \frac{FL}{\pi r^3} \quad \text{(eq. 3.24)}$$

Where *L* is the span length between supposed (mm) which was set to 10.2 mm for all tests. The Flexure Young's Modulus E_{Flex} was found for the flexure tests by:

$$E_{Flex} = \frac{kL^3}{48I} \quad \text{(eq. 3.25)}$$

Where I is the second moment of area (mm^4), which for a cylinder is found by:

$$I = \frac{\pi r^4}{4} \qquad \text{(eq. 3.26)}$$

3.1.11. Split Hopkinson Pressure Bar Test

The Split Hopkinson Pressure Bar (SHPB), also known as a Kolsky bar, is a characterisation tool for the mechanical response of materials deforming at high strain rates (10^2 s^{-1} to 10^4 s^{-1}), and thus gives the dynamic stress-strain response of materials (W. W. Chen et al., 2010). Ball mills use impact forces to break down materials (Perry et al., 2008), and the SHPB induces strain-rates by hammer-blowing impact conditions which corresponds to dynamic events such as ball milling. A SPHB consists of 3 major components as shown in Figure 3.4: a loading device, bar components and a data acquisition and recording system.

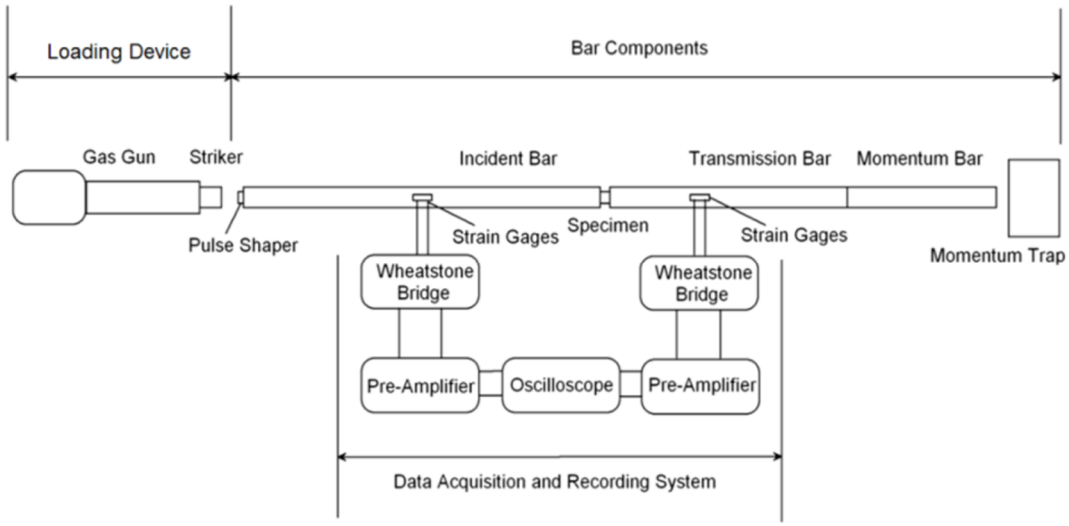


Figure 3.4: SHPB Schematic Arrangement (W. W. Chen et al., 2010)

The system used at the University of Nottingham is shown in figure 3.5. The system uses a dynamic loading method; that is a striker is launched which then impacts the incident bar. The incident and transmission bars used were acrylic bars with a Young's Modulus of 28,000 MPa, mass of 0.65 kg, diameter of 25 mm and length 0.97 m. The striker is launched via a gas gun of compressed air in a pressure storage vessel in a long gun barrel, where is accelerates until it impacts the incident bar at constant speeds. The striking velocities were measured using a light bridge and were set by setting the pressure to 0.5 bar for all tests. The sample to be tested is placed between the incident and transmission bar, and a small amount of lubricant was used to hold the sample in place during the test. Data was collected via strain gauges attached on the incident and transmission bar. One strain gauge was located on the incident bar and two were located symmetrically to each other on the

transmission bar. The signals from the strain gauges are conditioned with a quarter Wheatstone bridge with an internal dummy resistor.

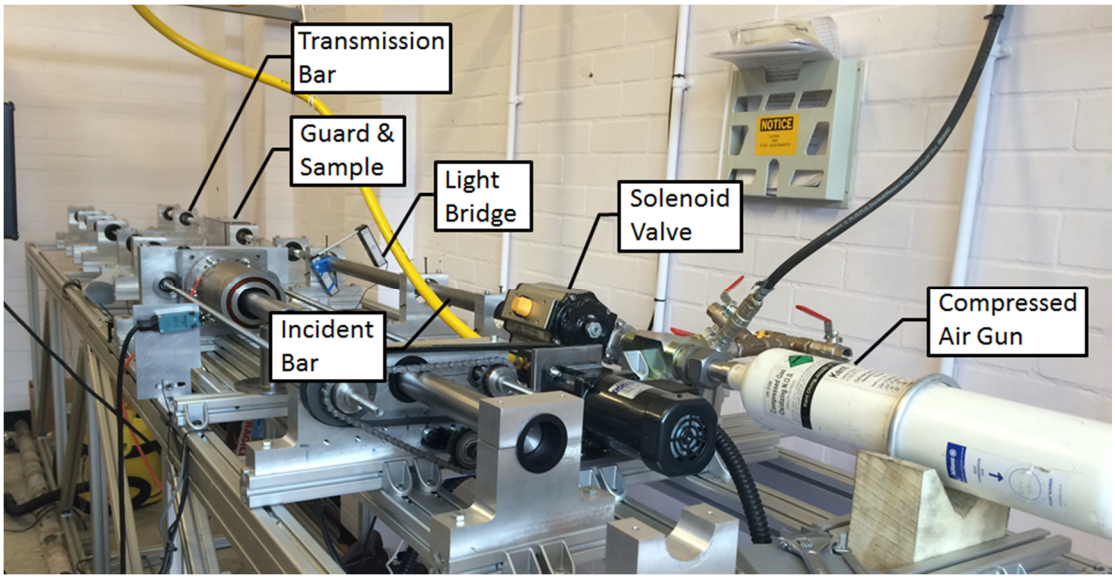


Figure 3.5: SHPB Arrangement at the University of Nottingham

The signal is amplified using a signal amplifier which is then recorded on a pc using the AD-logger data acquisition software (version 1.13) with a correction factor of 0.21 from the oscilloscope calibration. The sampling frequency of the data acquisition software was 2 MHz. The quarter Wheatstone bridge has an excitation voltage V_{ex} of 2 V, and the signal amplifier has an amplification factor (*AF*) of 100. The strain ε is calculated using:

$$\varepsilon = \frac{4V_{out}}{V_{ex}GF\ AF} \qquad \text{(eq. 3.27)}$$

Where V_{out} is the voltage measured by the strain gauge and *GF* is the gauge factor. The strain gauges used were Tokyo Sokki Kenkyujo Co. Ltd FLA-6-11-3L strain gauges (Tokyo, Japan) with a gauge factor of 2.12 ± 1%.

During the experiment a stress wave is generated by the impact of the striker on the incident bar. Figure 3.6 shows the incident and transmitted pulse for the no sample condition for the rig shown in figure 3.5 with the acrylic bar set up. Virtually all the impact energy is transferred to the transmission bar upon impact. However, when a specimen is placed between the two acrylic bars, as shown in figure 3.8, the energy transferred is significantly reduced. Figure 3.7 shows how most of the impact energy is reflected back through the incident bar rather than to the transmission bar upon impact when a pellet is placed between the two bars. When the compression wave in the incident bar propagates to the interface between the incident bar and specimen, part of the wave is reflected back and the

rest is transmitted into the specimen and is reflected back and forth within the sample due to the mismatch of the wave impedance between the sample and bars.

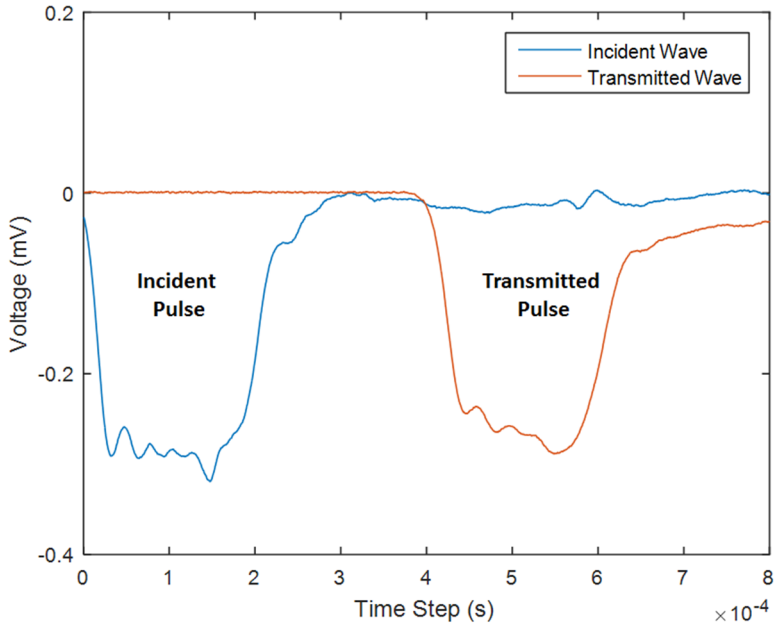


Figure 3.6: Incident and Transmitted Pulse for No Sample Condition

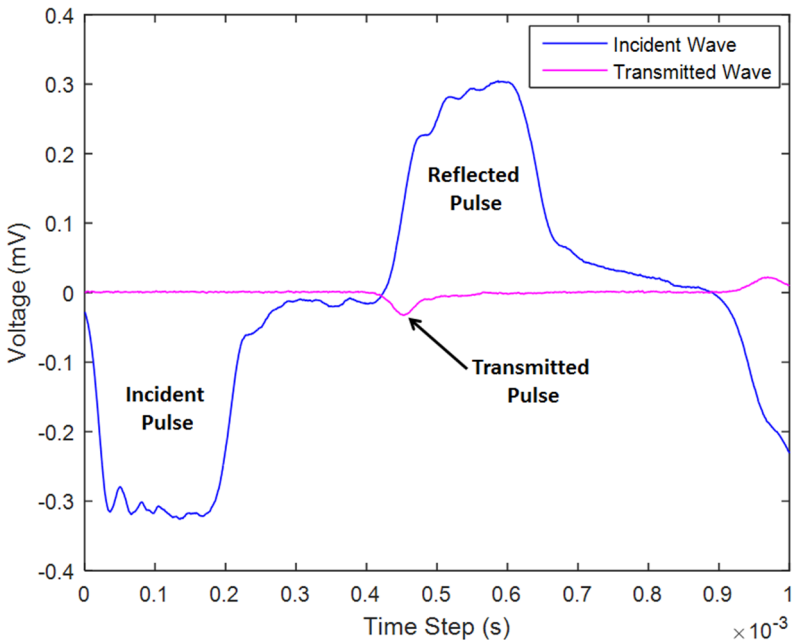


Figure 3.7: Incident, Reflected and Transmitted Pulse for Eucalyptus Pellets in Diametric Orientation

These reflections build up the stress level in the specimen and compress the specimen. Part of the unloading wave is reflected back and the rest transmits into the transition bar at the bar/specimen interface, while the specimen is unloaded. The incident and reflected pulses are measured by the strain gauge in the incident bar, and the transmitted pulse is measured

by the strain gauges on the transmission bar. When stress waves propagate in a long rod, the mechanical energy of the stress wave take the form of the strain energy though bar deformation and the kinetic energy of the bar motion.

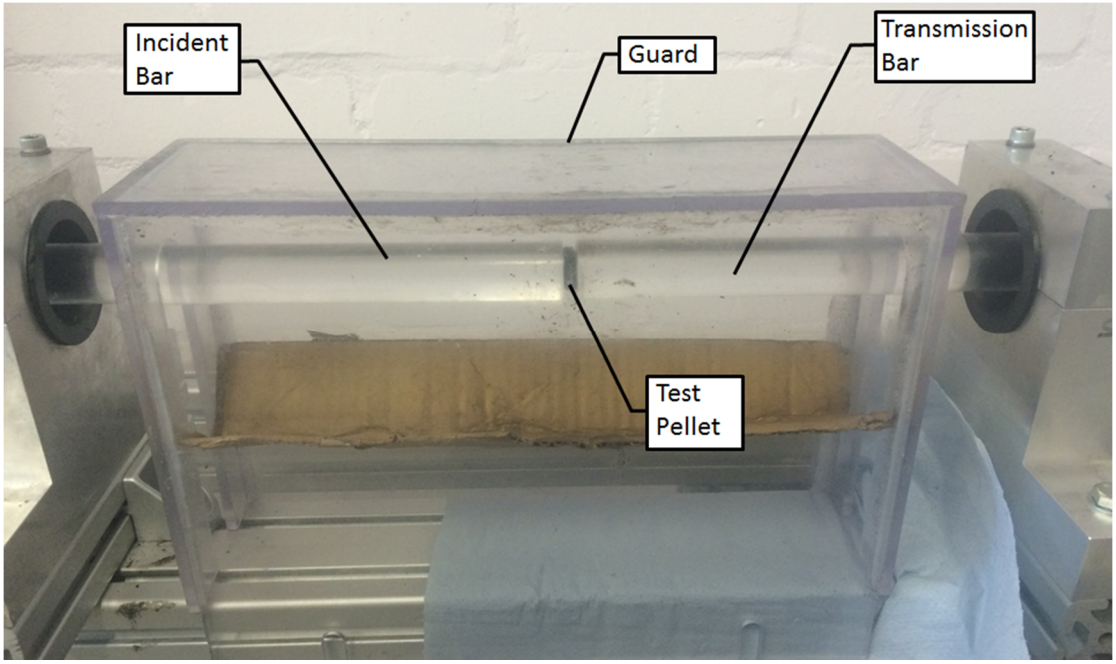


Figure 3.8: Positioning of Test Pellet in SHPB Rig

The specimen is assumed to be stress equilibrated in the SHPB experiment. The wave propagation is shown in the Lagrangian wave propagation diagram of Figure 3.9, where time t =0 corresponds to the instant of projectile impact. Several reverberations of the loading wave occur within the specimen; a transmitted pulse is sent into the output bar and a reflected pulse is sent back into the input bar (Ramesh, 2008). Typically, resistance strain gages are placed on the input and output bars for measuring; the incident pulse generated by the impacting projectile, the reflected pulse from the input bar/specimen interface and transmitted pulse through the specimen to the output bar.

Since the strains in the elastic bars are known, the bar stresses and thence the normal forces at the two specimen/bar interfaces are:

$$P_A = E_b(\varepsilon_I + \varepsilon_R)A_b$$

$$P_B = E_b(\varepsilon_T)A_b$$

Where P_A is the normal force on the incident side of the bar, P_B is the normal force on the transmitted side of the bar, strain in the incident pulse is ε_I, strain in the reflected pulse is ε_R, and the strain in the transmitted pulse is ε_T (each measured by a strain gages), E_b is the Young's modulus of the bar, and A_b is the cross sectional area of the bar.

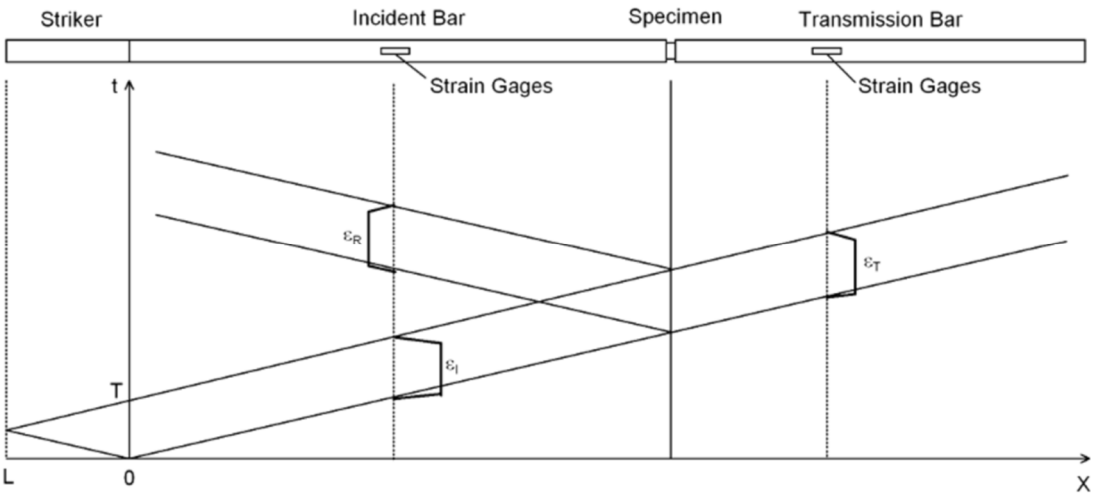


Figure 3.9: Langrangian Wave Propagation Diagram showing Stress Wave Propagation through space and time in SHPB (W. W. Chen et al., 2010)

Once an equilibrium condition has been achieved, $P_A = P_B$, and thus

$$\varepsilon_I + \varepsilon_R = \varepsilon_T$$

By assuming stress equilibrium, uniaxial stress conditions in the specimen and 1-D elastic stress wave propagation without dispersion in the bars, the nominal strain rate $\dot{e}_s$, nominal strain e_s and nominal stress s_s (all in the specimen) can be estimated. The average engineering strain rate $\dot{e_s}$ in the specimen can be found by:

$$\dot{e_s}(t) = -2\frac{C_b}{L_s}\varepsilon_R(t) \qquad \text{(eq. 3.28)}$$

Where L_s is the specimen length, and C_b is the elastic bar wave speed, which can be found from:

$$C_b = \sqrt{\frac{E_b}{\rho_b}} \qquad \text{(eq. 3.29)}$$

Where ρ_b is the density of the bar. The average engineering strain in the specimen can be found by:

$$e_s(t) = 2\frac{C_b}{L_s}\int_0^t \varepsilon_R\, dt \qquad \text{(eq. 3.30)}$$

Where t is the duration of the reflected pulse. The engineering stress in the specimen can be found by:

$$s_s(t) = \frac{A_B}{A_s}E_B\varepsilon_T(t) \qquad \text{(eq. 3.31)}$$

Where A_S is the cross sectional area of the specimen. The true strain ε_s and true strain σ_s rate in the specimen are then given by:

$$True\ Strain, \varepsilon_s(t) = -\ln[1 - e_s(t)]$$

$$True\ Strain\ Rate, \dot{\varepsilon}_s = \frac{\dot{e_s}(t)}{1 - e_s(t)}$$

Assuming plastic incompressibility, the true stress σ_s in the specimen is obtained as:

$$True\ Stress, \sigma_s(t) = s_s(t)[1 - e_s(t)]$$

From the equations for e_s and s_s, a stress-strain curve is obtained at a strain rate defined by an average taken over $\dot{e_s}$. Pellets were tested in axial and diametric orientations in the SHPB test and 10 repeats were conducted per sample. Once the data has been collected it was processed in Matlab® 2015a. The strain signal is differentiated in order to analyse the rate of change and inflection of strain rates in the experiment. Signal smoothing was conducted using the `smoothn.m` script by Garcia (Garcia, 2010), which is an automated smoothing procedure for uniformly sampled data sets based on a penalised least squared method which allows smoothing of data in one or higher dimensions by means of the discrete cosine function. The results are presented as engineering not true strain, strain rate and stress.

3.1.12. Differential Scanning Calorimetry

Heat flow analysis was conducted on a TA Instruments Q10 (New Castle, DE, USA) Differential Scanning Calorimeter (DSC). 10 mg to 15 mg of each sample with a particle size range of 75 µm to 300 µm was placed in an aluminium pan and equilibrated at -50 °C, then heated at 10 °C/min to 150 °C (first heating scan), cooled to -50 °C at 20 °C/min (cooling scan), and finally heated back to 150 °C at 20 °C/min (second heating scan) in 50 ml/min of Nitrogen (Perinović et al., 2010). As some materials exhibit a glass transition phase at atmospheric conditions, such as with freeze dried lemon juice, which shows a high tendency to cake at 25°C and 60% relative humidity (Aguilera et al., 1995), the samples were equilibrated at -50 °C. The results were analysed in the Universal Analysis Software (Version 4.5A, TA Instruments) and the glass transition temperature (T_g) was taken as the inflection point of the specific heat decrement at the glass transition on the second heating scan.

3.1.13. Thermogravimetric Analysis

Due to the samples being procured in large quantities from commercial suppliers, and supplied on a commercially sensitive basis, limited information was available on the source

and species of the material, and thus Thermogravimetric Analysis (TGA) was used to give a basis upon which to compare the thermal characterization of the samples based on their ratio of combustible to incombustible constituents. TGA was conducted in a TA Instruments Q500 auto sampler Thermogravimetric analyser (New Castle, DE, USA), using 10 mg to 15 mg of milled sample with a particle size range of 75 µm to 300 µm for a slow heating pyrolysis method and reactivity method.

3.1.13.1. Slow Heating Pyrolysis Test

The method used was based on the slow pyrolysis method developed by Lester et al. (2007) for analysing the composition of biomass. The sample was heated in a furnace at 5 °C/min in 100 ml/min of Nitrogen from atmospheric temperature to 900 °C, after which the gas was switched to air at 100 ml/min. The results were processed and analysed in Matlab® 2014a in order to establish the sample composition and peak volatiles release rate. The composition of the samples is given by moisture, dry volatile, dry fixed carbon, and dry ash contents and was found according to BS EN ISO 16993:2015 (The British Standards Institution, 2015b). The peak volatile release rate and corresponding temperature were obtained from the derivative thermogravimetric curves.

3.1.13.2. Reactivity Test

The reactivity test identifies the weight loss through either the loss of moisture, devolatilisation or combustion (or a combination of these) and the rate at which it happens (Pang, 2012). The heating protocol includes heating the sample at a constant ramp rate of 10 °C from room temperature to 900 °C in air. The derivative thermogravimetric profiles (DTA) generated from the test determine the following characteristic temperatures:

- Start-up temperature: the temperature at which the profile shows an initial weight loss of 1 wt%/min
- Burnout peal temperature: the temperature at which the reaction is at its maximum rate of weight loss
- Final burnout temperature: temperature when 99 wt% of the carbonaceous material has been combusted

3.1.14. Bomb Calorimeter

The Higher Heating Value (*HHV)* of the samples were found using an IKA C5000 Bomb Calorimeter (Staufen, Germany) in accordance with BS ISO 1928:2009 (The British Standards Institution, 2009b). Certified Benzoic Acid tablets were used as a standard, and the sample

weight was calibrated to give the same temperature rise as the standard. The test was conducted on as received samples, and thus the moisture content (*M)* found in section 3.1.1 was removed from the HHV values to give the dry HHV (HHV_d):

$$HHV_d = \frac{HHV}{1-M} \quad \text{(eq. 3.32)}$$

3.1.15. Ultimate Analysis

Ultimate analysis was carried out on by Warwick Analytical Service (Coventry, UK), a UKAS 17025 Accredited Service for CHN analysis. Carbon, Hydrogen and Nitrogen (CHN) analysis was conducted on the biomass samples on an Exeter Analytical CE440 Elemental Analyser. CHN analysis was conducted according to BS EN ISO 16948:2015 (The British Standards Institution, 2015a). Oxygen was found through the by difference method in BS EN ISO 16993:2015 (The British Standards Institution, 2015b).

3.1.16. Pellet and Particle Density

The pellet density was calculated according to the British Standard for pellets (The British Standards Institution, 2010c) and has been shown to be the most reproducible way to test pellet density (Rabier et al., 2006). This method is not suitable for particles as it's a buoyancy based test in water and the particles would float or sink in the water, and it would not be possible to measure the particle density in this way. Thus the helium pycnometer was used to calculate the particle density. 4 pellets were weighed then placed in a buoyancy determination rig on a balance readable to 0.0001 g. The pellets are submerged in deionised water and supported on a submergence apparatus. Immediately following submersion, the weight of the pellets in water is measured. The density of the pellets is determined by the following equation:

$$\rho_M = \frac{m_a}{m_a - m_i} \cdot \rho_i \quad \text{(eq. 3.33)}$$

Where ρ_M is the density of the pellet (g/cm^3), m_a is the mass of the pellet in air (g), m_i is the mass of the pellet in water (g), and ρ_i is the density of the deionised water (g/cm^3).

The particle density of the samples was determined in a Micrometrics Accupuc II 1330 gas pycnometer (Lincolnshire, UK). The gas used was helium using an equilibrate rate of 0.01psig/min, and samples weighed between 0.9 g to 2.2 g.

3.1.17. Pellet Durability

Pellet durability of the biomass pellets was evaluated in accordance with BS EN ISO 17831-1 (The British Standards Institution, 2013b) at Environmental Scientific Group test facilities in Bretby, UK. A test portion of 500 g ± 0.1 g is placed in the tumbling box device, and then tumbled at 50 RPM ± 2 RPM for 500 rotations. After this number of rotations the sample is removed and passed manually through a sieve with round screen holes of 3.15 mm diameter and suitable for manual screening in accordance with ISO 3310-2:2013 (The British Standards Institution, 2013c). After sieving the sample remaining on the sieve is weighed. The mechanical durability of pellets shall be calculated using the following equation:

$$D_U = \frac{m_A}{m_E}.100 \qquad \text{(eq. 3.34)}$$

Where D_U is the mechanical durability (%), m_E is the mass of pre-sieved pellets before the tumbling treatment (g), m_A is the mass of sieved pellets after the tumbling treatment (g). The test is performed in duplicate.

3.1.18. Abrasion Index

The Abrasion Index (*AI*) of the biomass was evaluated in accordance with BS 1016-111:1998 (The British Standards Institution, 1998a) at Environmental Scientific Group test facilities in Bretby, UK. 2 kg ± 0.1 kg of test portion is weighed and set aside. Each blade is weighed to the nearest 0.1 mg. The quadrant and blades are then placed in the mill mortar. The 2 kg test portion is placed in the mill mortar and the surface is levelled. The cover is then fitted and secured, with the automatic counter set to run for 12,000 revolutions ± 20 revolutions. After the test the blades are cleaned and dried, and then each blade is then re-weighed to the nearest 0.1 mg. The abrasiveness of the sample in milligrams of metal lost per kilogram of sample is calculated using the following equation:

$$AI = \frac{(m_1 - m_2)\text{x}10^3}{m_3} \qquad \text{(eq. 3.35)}$$

Where m_1 is the total initial mass of the four blades (g); m_2 is the total final mass of the four blades (g); m_3 is the mass of the test portion (kg).

3.2. Milling of Samples

The milling of biomass was conducted on several mills in order to analyse the impact of different milling techniques on the different biomasses. Table 3.1 summarise the tests which were conducted for each sample. Three laboratory scale mills were used for analysing the optimisation of milling techniques for biomass and the impact of moisture on milling behaviour. These mills were the Retsch PM100 Planetary Ball mill, Retsch SM300 Cutting mill, and the Lopulco flat table ring-roller LM1.6 mill. In addition, two standard grindability tests for coal were used on the samples; the Hardgrove Grindability Index and Bond Work Index Test, using standard coal grindability testing mills. For the tests where samples were not dried, the mass used to calculate the specific effective energy includes the moisture content.

Sample	Planetary Ball Mill	Cutting Mill	Bond Work Index	Ring-Roller Mill	Hardgrove Grindability Index
Olive Cake 2013	x	x	x	-	x
Olive Cake 2014	x	-	-	-	-
Eucalyptus Pellets	x	x	x	x	x
Mixed Wood Pellets	x	x	x	x	x
Olive Pellets	x	x	-	x	x
Sunflower Pellets	x	x	x	x	x
Steam Exploded Pellets	x	x	x	x	x
Bagasse	-	x	-	-	-
Miscanthus Pellets	x	x	x	x	x
Torrefied Pellets	-	-	x	-	-
White Wood Pellets	-	x	x	-	-
Microwave Pellets	x	x	x	x	-
La Loma Coal	-	-	x	x	x

Table 3.1: Matrix of Milling Experiments Conducted for Each Sample

Not all tests were conducted on all samples. This was due to either sample or equipment availability issues. The samples became available at different times during the project, with the majority of the samples being acquired in the third year of the project. Olive cake 2013 was not milled in the ring-roller mill as it caked during initial tests. Olive cake 2014 was only

tested in the planetary ball mill due limited sample availability. Olive pellets were not tested in the BWI test as they did not mill in the planetary ball milling test. The bagasse was only tested in the cutting mill as it was not suitable for comminution in the other mills. The torrefied pellets were only used in the BWI test due to limited sample availability. The white wood pellets were only tested in the cutting mill and BWI test due to project time constraints. The microwave pellets were not tested for HGI as they only became available to the project during the final year, and it was not possible to arrange for the HGI test to be performed. Finally, the La Loma coal was not tested in the planetary ball mill or cutting mill due to limited sample availability.

3.2.1. Energy Data Logging

The total milling energy was recorded using an Elcomponent SPCPro (Bishop's Stortford, UK) data logger for the planetary ball mill, cutting mill, and ring-roller mill. The parameters measured were the current, voltage, and phase angle at one second intervals. The data was processed using the Elcomponent Powerpack Pro software to give the true power data for the runs. The specific energy is analysed in three sections. The total specific energy (E_s) was calculated by integrating the Power-Time curve obtained from the data logger and then dividing by the material mass (Gravelsins et al., 2013) to give the total energy consumed during the milling process (kWh/t):

$$E_s = \int_0^t \frac{P dt}{m} \qquad \text{(eq. 3.36)}$$

Where P is the instantaneous power consumption (kW), t is time (hour), and m is mass (tonne). The total specific effective energy (E_e) was obtained by subtracting the specific idle energy from total specific energy for the run as measured by the energy logger (Bitra, Womac, Chevanan, et al., 2009; Himmel et al., 1985):

$$E_e = \int_0^t \frac{P dt}{m} - \int_0^t \frac{P_i dt}{m} \qquad \text{(eq. 3.37)}$$

Where P_i is the average idle power consumption (kW). The measured power during the tests is the true power of the mill. When powering certain alternating currents (AC) loads, the dynamic nature of alternating current causes a portion of the energy delivered to the load to be momentarily stored then returned back to the electricity grid (Brultech, 2015). As a result, the increase of electrical current makes it appear as if more power is being consumed than is in reality. In AC circuits, the product of multiplying the current by the voltage is called “apparent power”. As power companies’ only charges for the power consumed (True

Power), “apparent power” is not a practical parameter for determining energy consumption. To determine energy consumption, it is necessary to measure the portion of energy consumed by the load, and disregard the amount of energy stored and returned of the source. The ratio of the “True Power” which is the power actually consumed, to “Apparent Power” is called the “Power Factor”. To obtain the true power consumed, the current and voltage of each phase is multiplied by its power factor. Due to the limits of the energy meter, only one voltage power factor is measured for the three currents, and this voltage and its associated power factor were used to determine the true power consumption by the energy meter PowerPackPro software.

3.2.2. Regression Analysis

The majority of biomass milling studies which look at the impact of milling variables have used empirical relationships to analyse the relationship between mill settings and material type. Empirical relationships have been used to analyse hammer mills (Bitra, Womac, Chevanan, et al., 2009) and knife milling behaviour in literature (Bitra, Womac, Yang, Igathinathane, et al., 2009; Chevanan et al., 2010). Regression analysis was selected to analyse the impact of mill variables for the planetary ball mill and cutting mill in order to compare the results to previous biomass milling studies. While the results of the optimisation studies for the planetary ball mill (Chapter 6) and cutting mill (Chapter 7) are material and condition dependent, the results from the regression analysis were also used to develop the test conditions for the subsequent tests on multiple materials.

Linear regression analysis was conducted for the correlation between particle sphericity and size for the ring-roller mill. Regression analysis was conducted in the Minitab 17 software (Minitab Inc, 2013) regression assistant. The regression analysis fitted a linear model with one continuous response and one predictor. The linear model used in the software is of the form:

$$F(x) = \beta_0 + \beta_1 X_2 \qquad \text{(eq. 3.38)}$$

Terms are entered or removed from the model based on a level of significance (α) of $\alpha = 0.05$. For purposes of selecting the model terms, the predictors are standardised by subtracting the mean and dividing by the standard deviation. The final model is displayed in units of unstandardized terms. Unusual data is identified in the model as observations with large standardised residuals, and the model is edited to remove unusual readings from the analysis.

Multiple regression analysis was conducted on the planetary ball mill and hammer mill optimisation tests. Regression analysis was conducted in Minitab 17 software (Minitab Inc, 2013) multiple regression assistant. The regression analysis fitted a quadratic model with one continuous response and two to five predictors. The quadratic model used in the software is of the form:

$$F(x) = \beta_0 + \sum_i \beta_i X_i + \sum_i \beta_{ii} X_i^2 + \sum_{i<j} \beta_{ij} X_i X_j \qquad \text{(eq. 3.39)}$$

Stepwise regression analysis was used as it allows the introduction of each predictor to the model in turn and subsequently to be removed, depending on the other terms in the model. The hierarchy of the model is maintained at each step and multiple terms can be entered into the model in the same step, thus allowing the identification of important square or interaction terms, even if the associated linear term is not strongly related to the response. Terms are entered or removed from the model based on a level of significance (α) of $\alpha = 0.10$. Two forms to regression analysis are used; model fitting and optimised response analysis. For model fitting the data from the trial is inputted and a final model equation will be produced based on the experimental data which can be used to estimate the response with a high degree of certainty (coefficient of determination $R^2 > 0.9$). For optimised response analysis, the final model equation can once more be used to predict the response with a high degree of certainty, but also the optimal conditions to achieve the targeted response, be that to maximise, minimise or achieve a specific target response. Also main effect and interaction plots are provided for the selected response.

3.2.3. Planetary Ball Milling

A Retsch PM100 planetary ball mill (Hann, Germany) was used for the milling trials with a 500 ml stainless steel milling bowl and eight 30 mm diameter stainless steel balls in a batch milling process. The PM100 planetary ball mill has a 0.75 kW drive unit, and total power draw of 1.25 kW, with a single milling pot with a counter weight directly opposite, as illustrated in figure 3.10. The pot and counter weight are attached to a disk that rotates around a common central axis, while the pot simultaneously rotates around its own axis in a counter direction to the disk revolution. The high rotational speed leads to high impact energies, which results in an effective grinding performance. The biomass under comminution is crushed due to impact with the milling balls, and/or due to frictional forces that are caused by collisions (Perry et al., 2008).

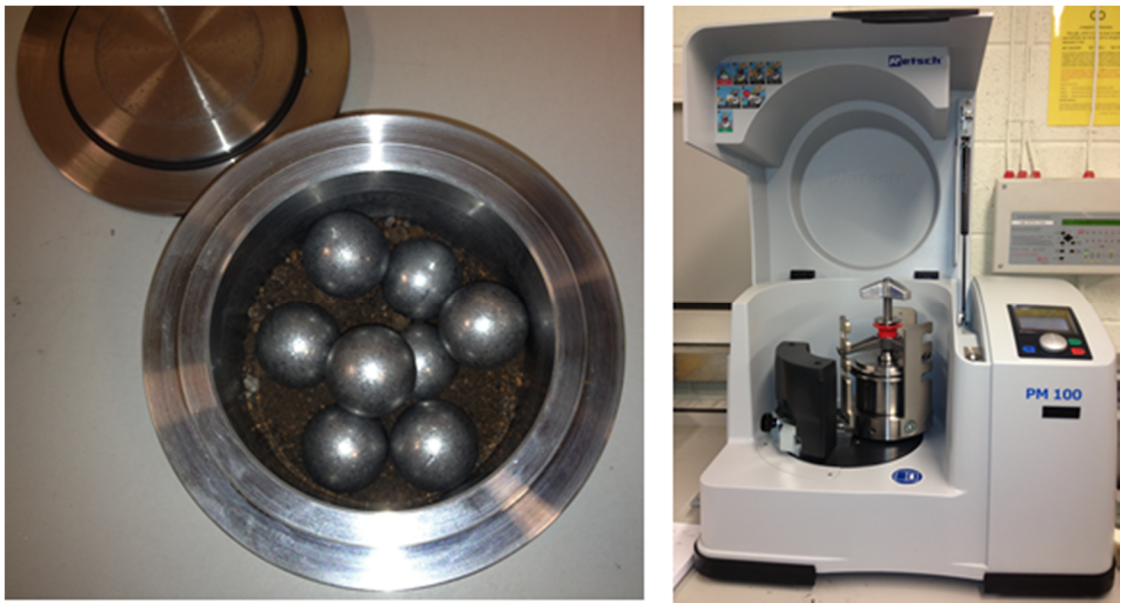


Figure 3.10: Planetary Ball Milling Pot containing Milling Balls and Olive Cake (left) and Milling Pot Secured in Retsch PM100 Planetary Ball Mill (right)

A FLIR T400 thermal imaging camera (Wilsonville, USA) was used to qualitatively investigate the impact of the heat generated during the milling process. A temperature scale of 18.5 °C to 50 °C ± 0.1 °C was used for all images, and the images were taken immediately after the milling process completed. The images show the effect of heat generation for the milling bowl, milling balls and olive cake. After milling the temperature of the milling balls were measured by attaching two type "K" thermocouples (class 1: ± 1.5 °C, ± 0.25%, -100 °C to 250 °C) connected to a YCT YC-747UD Data Logging Thermometer (Taiwan, China) to give the average biomass point temperatures post milling, as illustrated in figure 3.11.

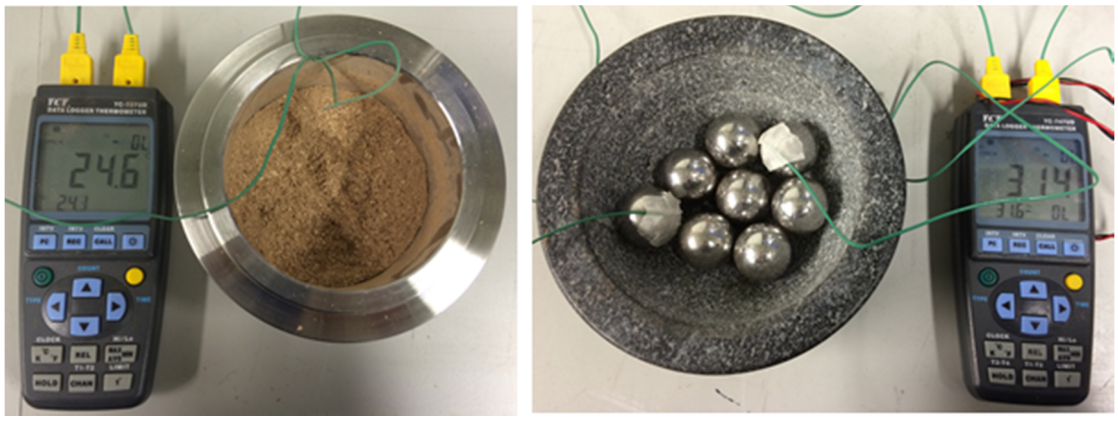


Figure 3.11: Point Temperature Measurements of Comminuted Biomass (left) and Milling Balls (right) immediately after Planetary Ball Milling Test

3.2.3.1. Optimisation

Milling behaviour of the planetary ball mill was investigated for three variables; volume, speed and input energy, for a single sample; 2013 Spanish olive cake. Three approximate filling volumes were used for the milling trials; 100 ml (70 g), 150 ml (105 g), and 200 ml (140 g). The recommended filling volume for the 500 ml bowl and 30 mm diameter stainless steel balls is between 70 ml to 220ml (Retsch Gmbh, 2012), and therefore the fill volumes were kept within these limits to avoid damage to the milling bowl and balls through under or overloading. The 100 ml and 200 ml trails were conducted for all speed and energy inputs combinations, while the 150 ml trials were conducted at 400 RPM for all energy inputs. The PM100 planetary ball mill allows for variable speed settings between 100 and 650 RPM. The speed settings used for this investigation were 200, 300, 400, 500, and 600 RPM for the 100 ml and 200 ml trials and 400 RPM for the 150 ml trials. The PM100 planetary ball mill has an energy input function which allows for a measurement of the input energy for a specified time period, or vice-versa. This total energy input into the milling bowl is defined as the difference between the energy drawn from the machine's drive unit when the milling bowl is empty and that when it is filled with the material to be ground and milling balls (Retsch Gmbh, 2012). To do this, the idling energy level is established over a 45 second period with only the milling bowl in place, and is taken as the zero point by the mill electronics for subsequent milling, similar to a balance tare. Thus during the actual milling of the material, the only energy input taken into account is that which exceeds the level of idling energy. This difference can be regarded as equal to the energy input into the milling bowl by the mill balls and the material being ground. For the purpose of comparing different combinations of parameters, the energy input can be specified instead of the milling time, as only the volume and type of material being ground need to be the same to allow a proper comparison to be made. In this case, the milling process is not ended after a specified time, but rather after the input of the pre-set energy. For the optimisation study, energy inputs of 0.1, 0.5, 1, 2, and 4 kJ were used for all speeds and volumes, and 8 kJ for 300-600 RPM trials. The specific effective energy transfer rate ($\dot{E}_i$) was obtained by taking the energy input value measured by the Retsch PM100 mill (E_I) and dividing by the sample mass, m, and time take to input the set energy, t, and is expressed as:

$$\dot{E}_i = \frac{E_I}{m.t} \qquad \text{(eq. 3.40)}$$

Immediately after milling thermal imaging and point temperature measurements were taken in accordance with section 3.2.3. The sample was sieved according to section 3.1.4 and the

resultant particle size distribution was analysed in accordance with section 3.1.6. All tests were repeated in triplicate.

3.2.3.2. Impact of Drying on Different Biomass Materials

100ml of each sample was milled 3 minutes at a milling speed of 300 RPM for two conditions; in their "As Received" state and dried as per section 3.1.1. Constant volume was selected for testing instead of constant mass, as milling has been shown to be a volumetric process (Agus et al., 1971), and keeping the mass constant favours denser fuels with smaller volumes, and thus constant mass is unsatisfactory for making direct comparisons between fuels. Immediately after milling thermal imaging and point temperature measurements were taken in accordance with section 3.2.3 and then sieved in accordance with section 3.1.4. The samples were the analysed for heat flow behaviour in a DSC (section 3.1.12) and passed through the Camsizer for digital image analysis of particle size and shape as per section 3.1.5. All tests were repeated in triplicate.

3.2.4. Cutting Milling

A Retsch SM300 cutting mill (Hann, Germany) was used to conduct the cutting milling trials. The mill is a continuous feed system, as illustrated in figure 3.12. The SM300 has a 3 kW drive with additional auxiliary flywheel mass of approximately 28.5 kg, and speed range of 700 RPM to 3000 RPM which increase in 100 RPM increments. Four screen sizes are available with the mill; 6 mm and 4 mm square hole screens, as well as 1.5 mm and 0.75 mm trapezoid screens. Cutting mills use primarily impact forces to reduce the particle size of the material (Perry et al., 2008). The rotor is 129.5 mm in diameter and is a 3 bladed parallel section rotor. The feed size is limited to sub 80 mm and can produce a final fineness of 0.25 mm to 20 mm. Material was fed into the mill via a Fritsch Laborette vibratory bed feeder to provide a controllable mass flow rate into the mill, as illustrated in figure 3.13.

3.2.4.1. Cutting Mill Optimisation Experiments

The optimal settings for milling were investigated through three controllable variables on the mill; mill speed, screen size, and feed rate. Seven speeds were selected for the optimisation study; 700, 1000, 1500, 1800, 2200, 2500, and 3000RPM. Idle runs were conducted in triplicate over 10 minute periods for these speeds. A square screen of 4 mm and a trapezoid screen of 1.5mm were selected for screen sizes.

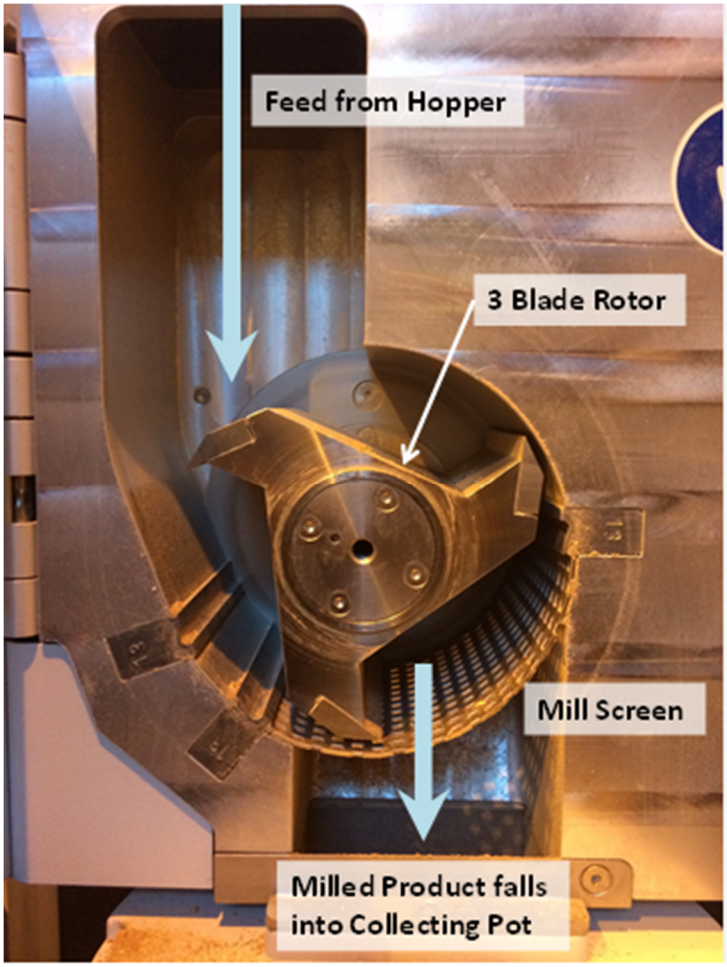


Figure 3.12: Mill Rotor and Screen of Retsch SM300 Cutting Mill



Figure 3.13: Retsch SM300 Cutting Mill with Vibrating Bed Feeder (left) and Fritsch Vibrating Bed Feeder with Biomass Pellets Being Fed into Mill Hopped (right)

The same mass of 250 g was used for all runs. Three mass flow rates were selected by varying the speed of a vibratory bed feeder. A low feed rate of approximately 0.0006 kg/s, a medium flow rate of 0.001 kg/s, and a high feed rate of 0.006 kg/s were used for the speed range and two screen sizes. Energy consumption was measured via an energy meter as per section 3.2.1 and mass of the sample milled within the specified time frame was weighed after each experiment to analyse mill choking. The particle size distribution was obtained via sieving (section 3.1.4), and digital image analysis (section 3.1.5). Multiple non-linear regression analysis was conducted for specific effective energy, mass loss and Rosin-Rammler distribution parameter *n* (section 3.2.2). All tests were repeated in triplicate.

3.2.4.2. Material Comparison & Impact of Drying Experiments

Based on the particle target size of 1 mm in coal fired power stations (Tamura et al., 2001), a screen size of 4 mm has been shown to provide the optimal product in a hammer mill (Esteban et al., 2006). The screen size used at EDF Cottam is 3.2 mm to 3.8mm for the milling of olive cake, sunflower pellets and steam exploded pellets. Thus in order to balance the three responses of energy consumption, mass loss and particle distribution, as well as matching as closely the requirements of full scale mills in the power sector, the mill operating conditions were selected to be a speed of 1500 RPM, feed rate of approximately 0.0025 kg/s ± 0.0003 kg/s, and a screen size of 4 mm. Energy consumption was measured via an energy meter as per section 3.2.1. The particle size distribution was obtained via according to section 3.1.4 and the shape characteristics were obtained via digital image processing in section 3.1.5. The first stage of the experiment was to conduct milling on all the selected samples in their “As Received” state. The second stage of the experiment involves drying the pellets in accordance with section 3.1.1 and milling them in the same conditions within the cutting mill. All tests were repeated in triplicate.

3.2.5. Ring-Roller Milling

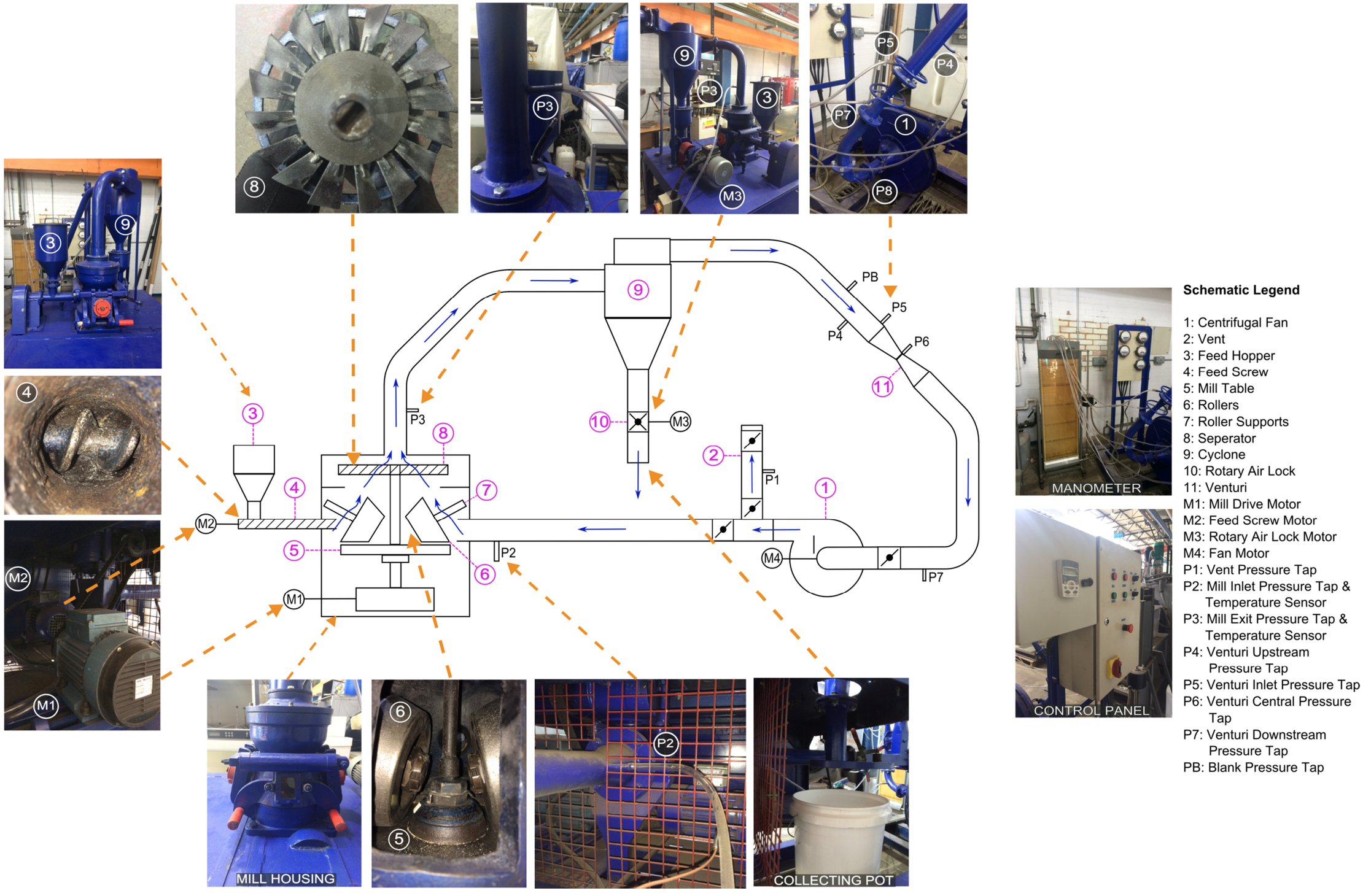
The Lopulco LM 1.6 is a laboratory scale ring-roller mill, similar to the Lopulco ring-roller mills at EDF West Burton coal fired power station (section 2.17), as shown in figure 3.14. It is a continuous through put mill and uses compression and abrasion fracture mechanisms (Perry et al., 2008) to break down materials. The mill is around 40 years old (Pang, 2012), and no documentation was available on the setup and operation of the mill. In addition, the mill required a full restoration before any testing could be conducted, which left limited time available for testing during this study. A schematic illustration of the mill is shown in figure

3.15**.** In the system the air is recirculated in a closed loop system, with air being fed to the underside of the mill and then pulled through the mill, and through the cyclone where the particles drop out and the air returns to the fan. The material to be ground is placed in a hopper (3) which feeds directly into a 1 ½" variable speed screw feeder (4). The feed flows directly into the mill which has a 160 mm variable speed rotating table (5) and two rollers (6) supported by adjustable hinged spring lever arms (7) that rest clear of the table, setting the roll gap. The material is pushed under the rollers by oncoming feed and the spinning table.



Figure 3.14: Lopulco LM 1.6 Flat Bed Ring-Roller Mill

The strength of the spring determines the grinding force available. The rollers are made of BS 1474-NS4 aluminium with a hardness of 80 Brinell. The separator (8) is connected to the mill table via a vertical shaft and thus rotates at the same speed as the mill table. This speed will partly determine the particle fineness obtained from the mill. The separator consists of 16 individually adjustable blades, which were set to 90° in this study to allow maximum passage with reasonable fineness for the biomass, as was done by Pang for biomass milling in this mill (Pang, 2012). Milled materials flow to the outer rim of the table and are lifted pneumatically by the air entering the base up through the separator. If the material is sufficiently fine it will pass through the separator while the oversize material is returned to the mill for further comminution. Dense oversized rejected material is captured by a chute at the base of the mill and released by a flap when there is a sufficient build-up of material.



Schematic Legend

1: Centrifugal Fan
2: Vent
3: Feed Hopper
4: Feed Screw
5: Mill Table
6: Rollers
7: Roller Supports
8: Seperator
9: Cyclone
10: Rotary Air Lock
11: Venturi
M1: Mill Drive Motor
M2: Feed Screw Motor
M3: Rotary Air Lock Motor
M4: Fan Motor
P1: Vent Pressure Tap
P2: Mill Inlet Pressure Tap & Temperature Sensor
P3: Mill Exit Pressure Tap & Temperature Sensor
P4: Venturi Upstream Pressure Tap
P5: Venturi Inlet Pressure Tap
P6: Venturi Central Pressure Tap
P7: Venturi Downstream Pressure Tap
PB: Blank Pressure Tap

Figure 3.15: Lopulco LM 1.6 Flat Table Ring-Roller Mill Schematic

The milled product which is classified by the separator flows pneumatically to a cyclone (9) where the material is separated from the air stream after which the air returns back to the fan. The material from the cyclone falls into a surge bin that feeds a constant speed rotary air lock (10), which maintains the pressure within the system to allow the cyclone to continuously remove material from the air stream. The energy requirements of the four motors (fan, mill bed, screw feeder and rotary air valve) were be analysed in idle condition and the set speeds for the mill bed and screw feeder were compared to the observed speeds for these components. The fan (1) operates at a mass flow rate of 85 kg/hr to 100 kg/hr and operates at below atmospheric pressures to main a negative pressure system so that dust cannot escape.

The air flow is controlled by a number of manual gate valves at the fan inlet, mill inlet, mill vent and separator exit (locations noted on figure 3.15). The air flow is monitored by a venture meter (11) positioned after the cyclone and before the fan entry. The pressure at the fan exit is relieved by a vent pip under a slight vacuum (2). Seven pressure readings are taken from the mill during operation; fan vent (P1), mill inlet (P2), mill exit (P3), venturi upstream (P4), Venturi inlet (P5), Venturi Contraction (P6), and Venturi exit (P7). All pressure tapings are noted on figure 3.15. The pressure tapings were connected via plastic pipes to a water manometer and the pressure readings were recorded on an Apple iphone 5s. The video of the pressure readings were processed in the VLC media player (version 2.2.1), using the scene video filter to output images every 10 seconds. The pressure readings were then taken from these images.

Temperature measurements are taken by type “K” thermocouples (class 1: ± 1.5 °C, ± 0.25%, -100 °C to 250 °C) connected to a YCT YC-747UD Data Logging Thermometer (Taiwan, China) in 3 locations. The thermocouples were located before the mill in pressure tap P2, in the mill chamber via two thermocouples by placing them between the removable viewing window and mill housing, and a thermocouple located in the mill exit pressure tap P3. The temperatures are logged at a 1 second interval over the test and downloaded via the Temp Monitor_S2 (version 1.0.17) software. Due to the limited time available for the study, it was decided that the investigation would be a preliminary exploratory analysis of the ring-roller mills idle operating conditions and how densified biomass and La Loma coal would behave in milling the conditions used by Pang (Pang, 2012). 1 kg of densified biomass was used in triplicate, and 600 g of La Loma coal was used in duplicated tests due to limited supplies.

3.2.6. Bond Work Index Test

The Bond Work Index (*BWI*) is determined using a dry grinding test in a standardised testing machine, the Bico Ball Mill (Bico Braun International, 2007). The mill contains 285 steel balls of total weight 20.13 kg with a drum size of 305 mm in diameter by 305 mm in length, and rotates at a constant speed of 70RPM, as shown in figure 3.16. The coal sample was crushed in a Retsch Jaw Crusher (Hann, Germany) to 3.35 mm and (prior to testing) a full cumulative size distribution was performed on the coal and olive cake to obtain the 80% passing size of the feed (F_{80}), while the average pellet diameter of 100 measured pellets was used as F_{80} for the pellets. The La Loma coal and olive cake were sampled using a riffle type splitter to provide representative sampling of the materials for the tests.

The BWI test used 700 ml of dry sample (Warren Spring Laboratory, 1962) and run for 100 revolutions and the contents were sieved to a set target equilibrium sieve size (P_1). While the normal BWI test is defined on ascertaining the energy consumption in comminuting material to pass 100 microns, the target sizes used in full scale coal mills for biomass and coal are different and based on the burner requirements.



Figure 3.16: Bico-Braun Bond Work Index Test Mill (left) and Milling Balls within (right)

The target size was set to 1mm for biomass based on pulverised fuel (PF) burner requirements for biomass (Esteban et al., 2006; Freeman et al., 2000; Tamura et al., 2001) and 90 µm for the La Loma coal based on the operating requirements for this coal in a tube and ball mill at EDF Energy plc coal fired power station in Cottam, UK, and the industry standard for a coal classifier is that 75% of coal delivered to the burner must pass a 200 mesh screen (75 µm) and <0.3%, a 50 mesh screen (300 µm) (Afolabi, 2012). The fines from the sieving were weighed and placed to one side, and new product was added to the oversized milled material to bring it back to its original weight. The new number of revolutions required was calculated from the results of the previous test to produce sieve

undersize equal to 1/3.5 of the total charge of the mill. This process was repeated until the gram per revolution (*G*) reaches a constant value for a minimum of three cycles. A full sieving analysis was performed on the last three cycles and the 80% passing size of the product (P_{80}) was determined to calculate the BWI. As noted in section 2.15, the BWI is derived from the third theory of comminution (Bond, 1952). The Bond Work Index, W_i, is calculated by using the following expression:

$$W_i = \frac{44.5}{{P_1}^{0.23} G^{0.82} \left(\frac{10}{\sqrt{P_{80}}} - \frac{10}{\sqrt{F_{80}}} \right)} \quad \text{(eq. 3.41)}$$

The work input, *W*, for the mill can be found from the general form of the BWI equation:

$$W = 10 W_i \left(\frac{1}{\sqrt{P_{80}}} - \frac{1}{\sqrt{F_{80}}} \right) \quad \text{(eq. 3.42)}$$

The non-linear regression analysis of the BWI and HGI correlations was performed on IBM SPSS Statistics 22. The pre-densified particle size distribution was obtained for the pellets using the method detailed in section 3.1.4 and the BWI values (WPP_i) and Work Input (*WPP*) were also obtained for the pre-densified pellet particle size (FPP_{80}). The test was repeated in duplicate as per the standard methodology, and the results were averaged over the two runs.

3.2.7. Hardgrove Grindability Index

The Hardgrove Grindability Index (*HGI*) test used followed BS 1016-112:1995 (The British Standards Institution, 1995) and was conducted at Environmental Scientific Group, Bretby, UK for the biomass samples, and at Alfred H Knight, Ayrshire, UK for the coal, both on a standard Hardgrove testing machine. The samples were dried in accordance with BS EN 14774-1:2009 (The British Standards Institution, 2009a), then crushed and sieved to using 1.18 mm and 600 µm size sieves. 50 g ± 0.01 g of the 1.18 mm and 600 µm size fraction was disbursed evenly into the Hardgrove machine bowl with evenly spaced balls and then secured into the apparatus, as shown in figure 3.17. The apparatus was then run for 60 ± 0.25 revolutions. The sample was then removed from the bowl and sieved in a 75 µm sieve size for 10 minutes. Mass *m* (g) is calculated based the of the test portion passing through the 75 µm sieve, using the formula:

$$m = 50 - m_f \quad \text{(eq. 3.43)}$$

where m_f is the mass, in grams, of test portion retained on the 75 µm sieve. The HGI index was found using the calibration chart in Annex A of BS 1016-112:1995 (The British Standards Institution, 1995). The process was then repeated and the mean of the two determinations, rounded to the nearest whole number, is the HGI rating for the sample.



Figure 3.17: Environmental Scientifics Group HGI Test Machine (left) and Biomass Sample Post HGI Test in Milling Pot with Balls (right)

Chapter 4 - Biomass Characterisation

In understanding the impact of comminution on a material, it is necessary to know its characteristics prior to milling. The variation of these characteristics before and after milling provides a basis upon which the impact of milling can be evaluated. To understand the fracture mechanisms involved in milling, the influence of mill type on particle size and shape must be evaluated. In addition, analysing the hydroscopic behaviour of the different biomasses after drying provides an understanding on the impact of surface and bound moisture on milling. Finally the mechanical response of biomass at low and high strain rates provides an insight into of the forces required to initiate pellet failure within mills.

4.1. Materials and Methods

This section characterises the main samples used in the milling studies prior to testing. The samples characterised are 2013 and 2014 olive cake, olive pellets, mixed wood pellets, eucalyptus pellets, steam exploded pellets, miscanthus pellets, sunflower pellets, microwave pellets, torrefied pellets, white wood pellets, and La Loma coal. Biomass pellets are composed of comminuted material as described in section 2.8. No data was available on the densification processes used to produce the pellets used in this study.

The methods used within this section include pellet diameter and length measurements (section 3.1.3), pellet disintegration test (section 3.1.2), particle size distributions by sieving (section 3.1.4) and digital image analysis (section 3.1.5), with particle size distribution analysis (section 3.1.6). Moisture content (section 3.1.1) and reabsorption (section 3.1.9) of the samples were analysed, along with thermal characteristics (section 3.1.13), higher heating value (section 3.1.14), ultimate analysis (section 3.1.15) pellet and particle density (section 3.1.16), pellet durability (section 3.1.17), and abrasion index (section 3.1.18). In addition the mechanical strength of the pellets in low strain rates (section 3.1.10) and high strain rates (section 3.1.11) were investigated.

4.2. Biomass Pellet Dimensions

Biomass pellet specifications are detailed in BS EN ISO 17225-2 for woody pellets (The British Standards Institution, 2014c) and BS EN ISO 17225-6 for non-woody biomass (The British Standards Institution, 2014d). Woody pellets should have a diameter of either 6 mm ± 1 mm or 8 mm ± 1mm with a length between 3.15 mm and 40 mm. Non-woody biomasses should have a diameter between 6 mm to 25 mm ± 1 mm and a length of 3.15 mm to 40 mm. The

thermally treated biomasses used in this study are from wood based products, and therefore are assumed to fall into the BS EN ISO 17225-2 specifications. Figure 4.1 shows a box and whisker plot of the diameters for the densified biomass samples used in this study as measured per BS EN ISO 17829 (The British Standards Institution, 2014f). These diameters are of pellets which have been delivered from source via BF2RA members, and thus are representative of samples prior to comminution, not of the pellets immediately after manufacture.

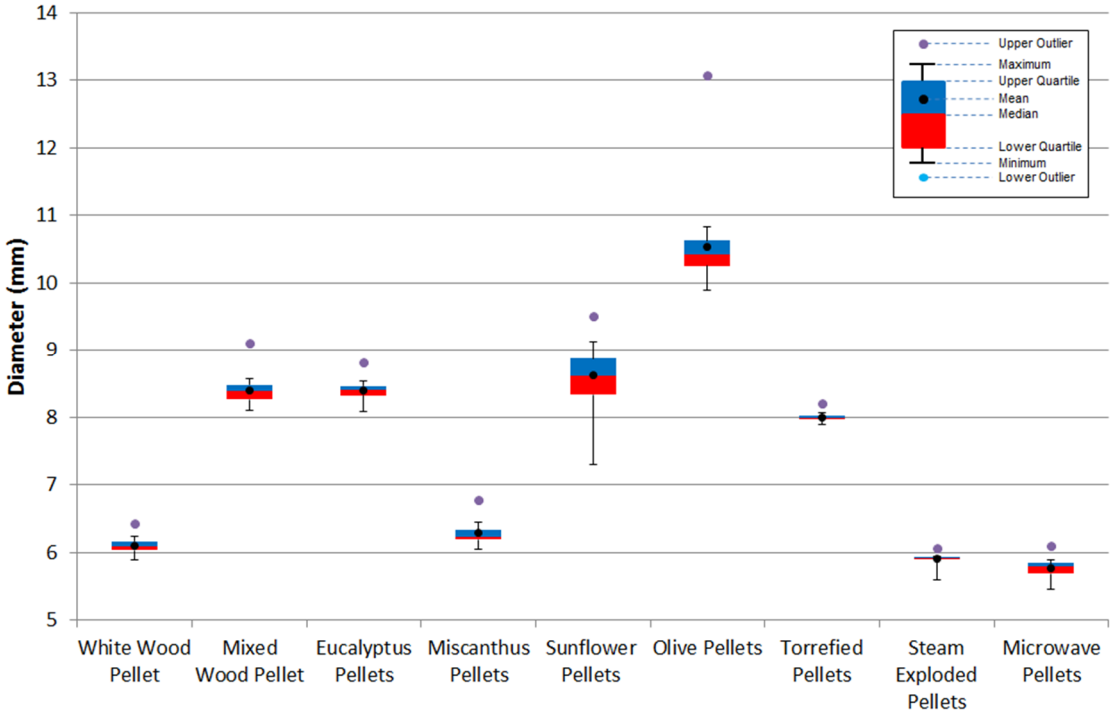


Figure 4.1: Range of Pellet Diameters of Biomass Pellets

No data is available on the dimensions of the pellets immediately after manufacture; apart from that they conform to the required standards. For the woody pellets, the white wood, steam exploded, and microwave pellets were all 6 mm in diameter; and the mixed wood, eucalyptus and torrefied pellets were all 8 mm in diameter. For the non-woody biomasses, miscanthus was 6mm, sunflower pellets were 8 mm and the olive pellets were 10mm in diameter. While all pellets conformed to the standards (The British Standards Institution, 2014c, 2014d), the tolerance ranges varied greatly amongst the samples. Apart from sunflower and olive pellets, most samples showed small interquartile ranges for the diameter. While several samples showed outliers above the maximum whisker, none showed minimum outliers, which would be expected from any pelleting process as pellet die wear would lead to increased pellet sizes. A study by Obernberger and Thek (2004) of densified biomass fuels showed similar physical characteristics for a wide range of European biomass pellets, with pellet diameters falling into 6, 8 or 10 mm categories.

Figure 4.2 shows the range of aspect ratios for the pellets. According to ÖNORM M 7135 (ÖNORM, 2000), the aspect ratio of biomass pellets should be below 5 to avoid comminution system blockages. While Obernberger and Thek (2004) observed that their pellets fell below this guidance, it can be seen that white wood, steam exploded , miscanthus and microwave pellets all exceed this value. These are all 6 mm pellets, and also have mean aspect ratios above 3, while the 8 and 10 mm pellets show mean aspect ratios of 1.5 to 2.5. This indicates that pellets with smaller diameters are likely to have higher aspect ratios, and if blocking in conveying systems is observed; then pellet specifications should include the requirement of limiting pellet aspect ratios according to below 5.

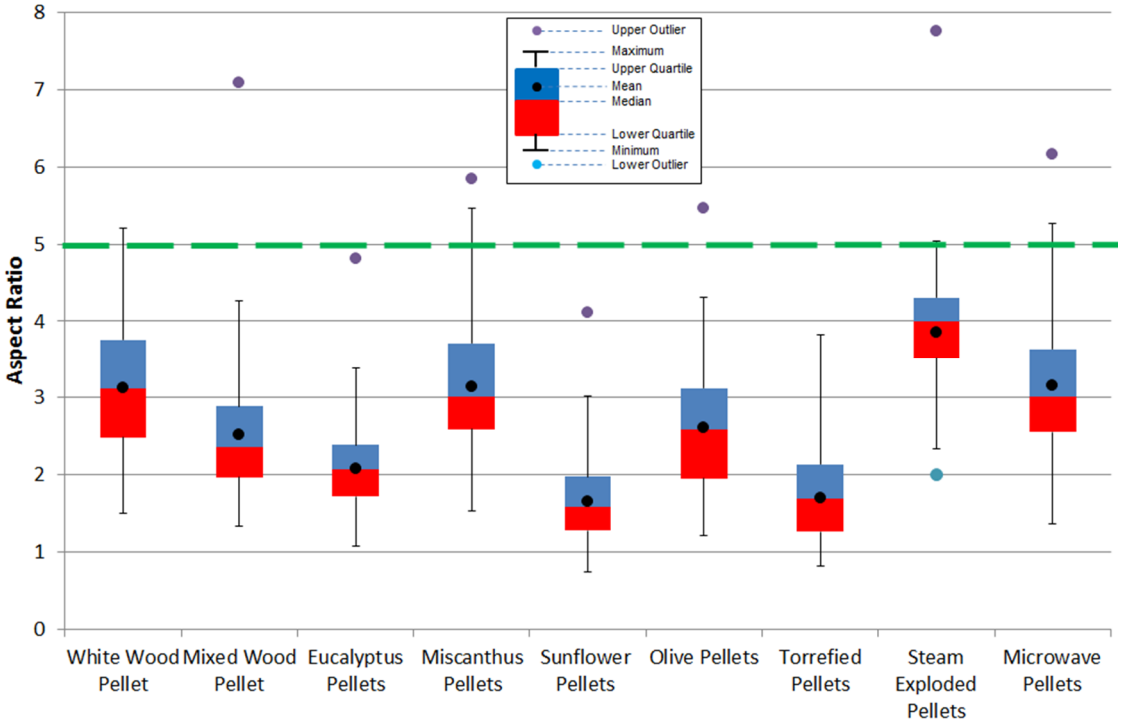


Figure 4.2: Range of Aspect Ratios for Biomass Pellets (Aspect Ratio Tolerance Line of 5 Indicated)

4.3. Particle Size Distributions of Pre-milled Samples

To obtain a physical composition of the pellets prior to milling, the pellets were disintegrated according to BS EN 16126:2012 (The British Standards Institution, 2012), as described in section 3.1.2. Part of this test is to obtain the cumulative distribution of particle size via sieving. The curves obtained are generally of a sigmoid function to which the Rosin-Rammler distribution equation (eq.3.2) can be fitted. In addition the geometric mean diameter (eq. 3.3) and associated dispersion and shape distribution parameters (section 3.1.6) can be obtained. This was also undertaken for the powdered samples; La Loma coal and olive cake. These distributions can be seen in Figure 4.3. Two pellet samples could not

be disintegrated using the standard test; olive pellets and microwave pellets. Both samples proved to be hydrophobic and retained their original pellet shape and composition. Olive cake also showed hydrophobic behaviour, indicating that the material rather than the pellet is hydrophobic. Microwave pellets were the only thermally treated pellet which showed hydrophobic behaviour. This suggests that the microwave torrefaction process has changed the material from hydrophilic to hydrophobic. Unfortunately no data on the pre-densified particle size distributions was available for these samples.

The standard method for disintegrating pellets is based on BS EN 16126:2012 (The British Standards Institution, 2012), but several methods for pellet disintegration have been analysed in literature. Jensen et al. (2011) analysed several different methods of disintegrating biofuel pellets found that mechanical methods of disintegrating pellets resulted in finer particle sizes than the standard disintegration method. No details are provided in BS EN 16126 for hydrophobic pellets. Using a hammer mill would potentially be a way of disintegrating the pellet, but if the pellet did not break up easily there would be a risk that the pellet would just break into chunks and not give the true pre-densified particle size distribution. Alternatives would be to add disintegrants into the pellets, as is done in the pharmaceutical industry, to allow them to break up with water; however this would change the composition of the pellet and add in additional contaminants to the combustion system. Another alternative would be to use a chemical to dissolve the binding agents within the pellets, although the chemical or solvent used would depend on the binding agent within the pellet. If the hydrophobic nature of the pellets was due to cross-linking bonds within the structure, then it is likely that the pellet would not disintegrated back to the pre-densified particles. In this case, it would be necessary for customers to require information on the pre-treatment particle size distribution as part of their specification requirements.

La Loma coal was reduced in size prior to sieving to 3.35 mm in accordance with the requirements of the BWI test (section 3.2.6). Olive cake showed a distinct profile compared to the other biomasses, as unlike the other samples it is a composite of three distinct sections; olive pulp (0-850 µm), olive pips (850-3350 µm) and olive pellets/self-formed lumps (3350 µm+). Spanish olive cake from the same source was provided over two seasons (2013 and 2014) and the profiles are very similar apart from 2014 having a higher concentration of the largest size fraction (3350 µm+). The disintegrated pellets showed sigmoid function curves. The results have been banded by biomass group; blue for wood, green for herbaceous, purple for fruit, red for treated biomass, and black for coal. For the

disintegrated pellets there are no trends in the particle size distributions by group which implies that there was no common milling method for the virgin biomass prior to densification. The particle size distribution for of the wood pellets is described by BS EN ISO 17225-2 (The British Standards Institution, 2014c) and ISO 17830 (The British Standards Institution, 2015c), with the ranges being ≥ 98% (< 3.15 mm), ≥ 90% (< 2 mm), and ≥ 50% (< 1 mm) for chemically untreated wood residues (class I2), and ≥ 97% (< 3.15 mm), ≥ 85% (< 2 mm), and ≥ 40% (< 1 mm) for by-products from wood processing industries (class I3). There are no particle size distribution requirements for non-woody biomass pellets in BS EN ISO 17225-6 (The British Standards Institution, 2014d). The particle size required for biomass combustion has been noted by Ryckmans et al. (2006), but there is little consensus in literature on what particle size distribution should be required for biomass combustion (Ayhan Demirbas, 2005; Jensen et al., 2011). In addition, while the impact of matching the size and shape to the Stokes number requirements for the classifier and burners has not been analysed in comminution studies, it has been noted for combustion and mill classifier studies (Afolabi, 2012; Larsen, 2012). For this study, all the biomass pellets conform to the particle size requirements of BS EN ISO 17225-2 apart from the sunflower pellets, which exceed the requirements for both class I2 and I3 materials.

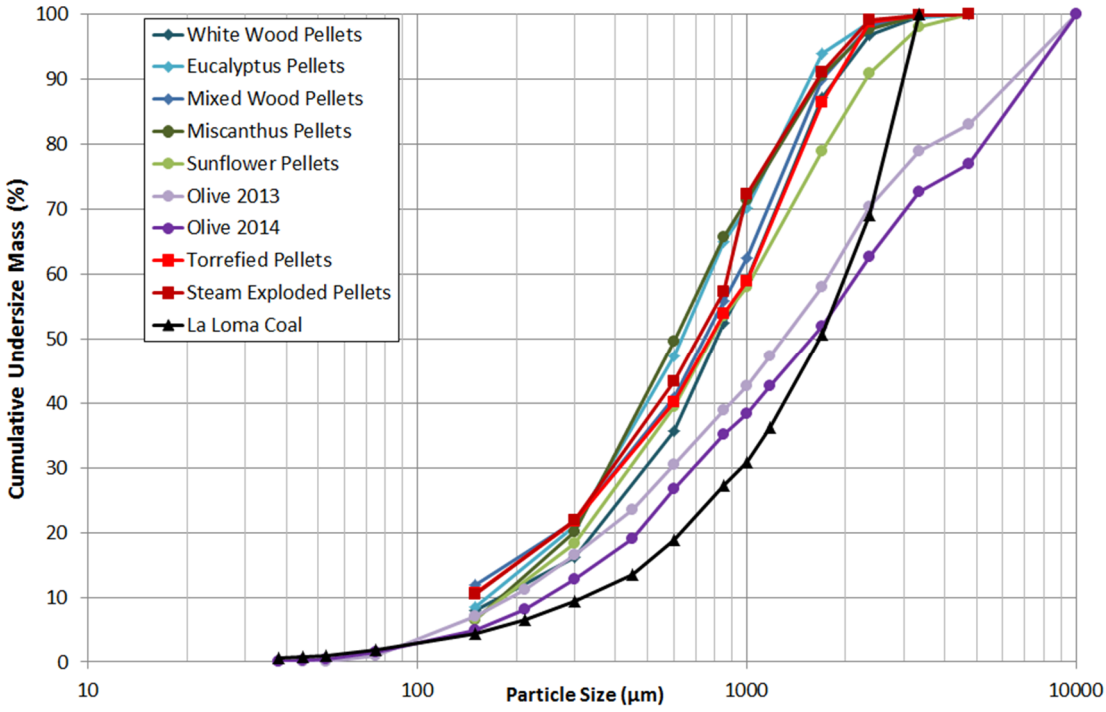


Figure 4.3: Cumulative Distribution of Particle Size for Disintegrated Pellets, La Loma coal and Olive Cake by Sieving

4.4. Sieved and Camsizer Pre-Milled Particle Size Distributions

The following section describes the analysis of the pre-milled particle size distributions in terms of the Rosin-Rammler parameters, size parameters, dispersion parameters and distribution shape parameters from sieving and digital image analysis in the Camsizer. This is the typical particle size analysis which is used in milling studies (Bitra, Womac, Chevanan, et al., 2009; Bitra, Womac, Yang, Miu, et al., 2009; Gil & Arauzo, 2014; Gil et al., 2012). The aim is to provide a starting point for the material particle size comparison prior to milling so that the impact of milling on particle size can be determined. Sieving calculates the particle size distribution on a mass fraction basis, while digital image analysis uses a volume fraction basis. Both methods are related by the specific density of the material (The British Standards Institution, 1998b). Previous studies comparing sieving and the Camsizer results have shown a good correlation for biomass (Trubetskaya et al., 2014). Figure 4.4 shows the fit between cumulative distributions obtained by sieving and for the shortest chord diameter (d_{c_min}) via the Camsizer for disintegrated sunflower pellets and La Loma coal.

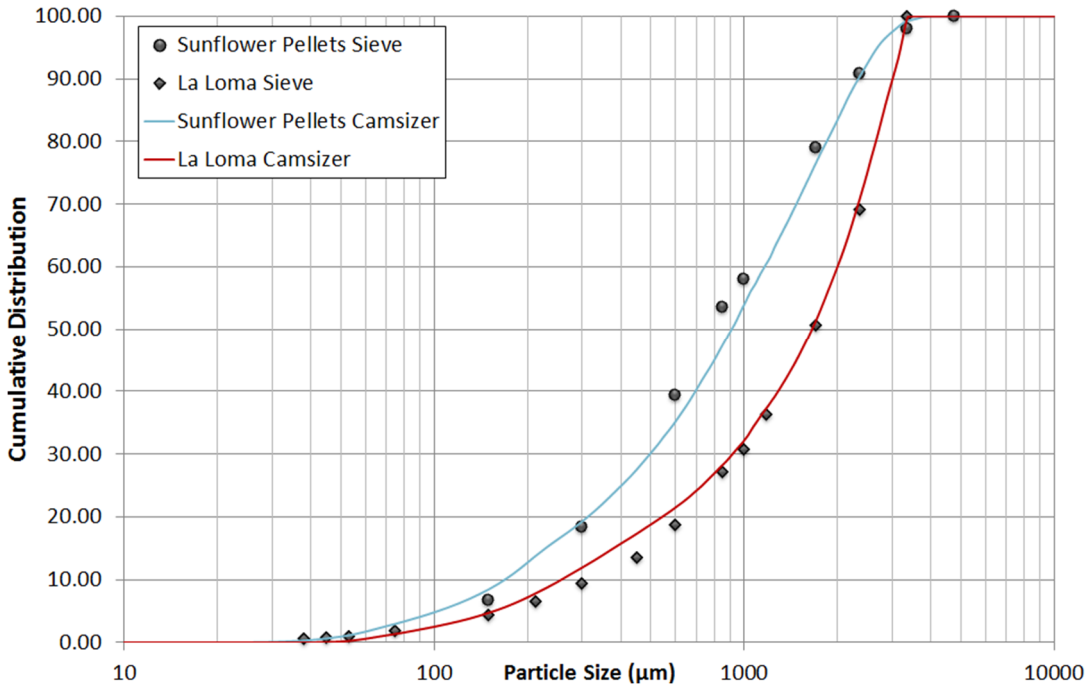


Figure 4.4: Comparison of Camsizer and Sieving Cumulative Distributions of Particle Size for La Loma Coal and Disintegrated Sunflower Pellets

Table 4.1 shows the sieved Rosin-Rammler results, and interpolated data for the size parameters, dispersion parameters, and distribution shape parameters. Table 4.2 shows the same data for the same samples via the Camsizer digital image analysis. Table 4.3 shows the percentage difference between the sieved and Camsizer results. A positive difference indicates that the sieve size was greater than that attained in the Camsizer, while a negative

difference indicates the reverse. Overall the particle sizes are quite similar between the sieve and Camsizer results, but the dispersion and shape factors show greater variation. For the Rosin-Rammler analysis, there is little difference in the fit (R^2 variance below 1%). For the characteristic particle size, *d'*, there is little difference in the size for most samples, but eucalyptus pellets show a significant difference (8.3%), with a sieve size of 833 µm and Camsizer size of 767 µm, and olive cake 2014 shows a larger Camsizer size of 2778 µm, compared to 2353 µm from sieving. These variances are due to the Camsizer recording 300 points between 10 µm and 6000 µm, while the sieving is limited to 8 - 16 sieve sizes.

Sample	Rosin-Rammler			Size Parameters (µm) – Cubic Interpolation			Dispersion Parameters					Distribution Shape Parameters	
	d' (µm)	n	R^2	d_{10}	d_{gw}/d_{50}	d_{80}	hs	ls	MRS	C_u	C_c	GS_i	K_g
White Wood Pellets	1051	1.42	0.999	188	**808**	1458	1.96	2.73	2.01	5.43	1.38	0.26	**0.94**
Eucalyptus Pellets	833	1.40	0.999	172	**631**	1215	2.07	2.59	2.10	4.43	1.23	0.31	0.88
Mixed Wood Pellets	966	1.29	0.998	124	744	1373	1.99	3.53	2.12	7.57	1.57	0.22	**0.86**
Miscanthus Pellets	832	1.38	0.992	197	604	1251	2.3	2.33	2.43	3.79	1.08	0.44	1.02
Sunflower Pellets	1115	1.18	0.995	198	774	1744	2.49	2.87	2.70	5.37	1.00	0.45	0.94
Olive Cake 2013	1953	0.93	0.997	194	1303	3660	3.75	4.49	4.11	9.22	1.00	0.58	1.03
Olive Cake 2014	2353	0.93	0.994	246	1589	5406	3.91	4.21	4.40	8.85	0.88	0.60	0.89
Torrefied Pellets	1016	1.27	0.999	140	766	1500	2.11	3.47	2.17	7.33	1.28	0.25	0.77
Steam Exploded Pellets	889	1.35	0.998	143	724	1196	1.86	3.25	2.06	6.16	1.32	0.19	**1.04**
La Loma Coal	1954	1.46	0.992	322	**1676**	2723	1.7	3.21	**1.62**	6.33	1.43	**0.01**	0.70

Table 4.1: Shape, Dispersion, and Distribution Shape Parameters of the Cumulative Size Distributions Disintegrated & Powdered Biomass & Coal by Sieving

While the Camsizer outputted measured particle sizes, the sieve data was interpolated between measured points to provide the required percentile particle size. However there are issues with both methods relating to the material. Some of the samples agglomerated during the digital image analysis due to the fineness of the samples (e.g. steam exploded pellets and La Loma coal), or due to static (sunflower). The application of filters reduced the agglomeration issues, but some samples showed a variance of around hundred microns from the sieved data, as seen with the eucalyptus and olive cake 2014 *d'* values. The largest

percentage difference in particle size is for the effective size, d_{10}, where eucalyptus was 51.8% larger in the sieve (172 µm) than in the Camsizer (101µm). The mean geometric diameter, d_{gw}, showed less variance, with sunflower showing a variance of 16.1%, and overall the 80th percentile particle size, d_{80}, showed the least variance, apart for steam exploded pellets (21. 4%) and olive cake 2013 (15.4%).

Sample	Rosin-Rammler			Size Parameters (µm) - Camsizer Output			Dispersion Parameters					Distribution Shape Parameters	
	d' (µm)	n	R^2	d_{10}	d_{gw}/d_{50}	d_{80}	hs	ls	MRS	C_u	C_c	GS_i	K_g
White Wood Pellets	1001	1.20	0.999	155	731	1514	2.32	3.31	2.62	5.97	1.16	0.49	**1.61**
Eucalyptus Pellets	767	1.10	0.998	101	564	1213	2.41	3.84	2.73	7.28	1.08	0.40	0.95
Mixed Wood Pellets	952	1.18	1.000	141	687	1457	2.39	3.27	2.67	6.21	1.19	0.42	**1.05**
Miscanthus Pellets	840	1.16	0.995	130	581	1213	2.59	3.3	2.96	5.87	0.98	0.48	1.02
Sunflower Pellets	1200	1.16	0.999	169	909	1841	2.22	3.74	2.38	6.87	1.25	0.31	0.85
Olive Cake 2013	1914	0.87	0.991	169	1190	3136	3.37	5.06	5.16	9.91	0.92	0.60	1.40
Olive Cake 2014	2778	0.91	0.998	234	1798	5170	3.62	4.59	4.06	10.2	1.23	0.55	0.95
Torrefied Pellets	1028	1.21	0.991	184	762	1592	2.3	3.34	2.51	5.34	0.86	0.40	0.91
Steam Exploded Pellets	895	1.04	0.996	104	666	1483	2.44	4.27	2.65	8.57	1.01	0.36	**0.78**
La Loma Coal	2043	1.13	0.991	257	1652	2653	1.69	4.06	1.66	7.76	1.63	**-0.02**	0.71

Table 4.2: Shape, Dispersion, and Distribution Shape Parameters of the Cumulative Size Distributions Disintegrated & Powdered Biomass & Coal by Digital Image Analysis (Camsizer)

The compounding of the differences is highlighted in table 4.3 for the dispersion and shape parameters. Steam exploded pellets showed the greatest variation in results for the distribution geometric standard deviation of high region (*hs*) and low region (*ls*), which is to be expected as it showed one of the largest variances in d_{10} and d_{80}. The difference in a Mean Relative Span (*MRS*) and Rosin-Rammler distribution parameter (*n*) are almost identical and are greatest for eucalyptus and steam exploded pellets. The difference in the Coefficient of Uniformity C_u is greatest once more for the eucalyptus pellets, but both the Camsizer and sieve data show C_u values above 4, which indicates a good range of particle sizes and good graduation to the distributions. There were more contrasting differences in the distribution shape parameters. Some biomasses showed large variances, such as white

wood (63.1%), mixed wood (62.1%) and steam exploded pellets (60.3%), with their sieved data showing much lower graphical skewness (GS_i), indicating a more symmetrical distribution for the sieved results. Other samples showed much lower variance, for instance olive cake had a 4.5% variation. The largest difference was seen for La Loma coal at 200%. However this is due to the GS_i being almost zero, hence the large variance in the results relative to each other. The kurtosis of the distributions (k_g) also showed a wide variation in results. White wood showed the largest variance ay 51.9%, and it's curve went from being platykurtic (k_g < 1.00) for sieving to leptokurtic curves (k_g > 1.00) for the Camsizer, as did the mixed wood pellets, while the steam exploded pellets showed the opposite behaviour.

Sample	Rosin-Rammler			Size Parameters (µm)			Dispersion Parameters					Distribution Shape Parameters	
	d' (µm)	n	R^2	d_{10}	d_{gw}/d_{50}	d_{80}	hs	ls	MRS	C_u	C_c	GS_i	K_g
White Wood Pellets	4.9	16.9	0.1	19.2	9.9	-3.7	-16.8	-19.1	-26.2	-9.6	17.5	**-63.1**	**-51.9**
Eucalyptus Pellets	**8.3**	**24.1**	0.2	**51.8**	11.2	0.2	-15.3	-38.9	**-26.2**	**-48.7**	12.9	-25.9	-7.4
Mixed Wood Pellets	1.4	9.3	-0.2	-12.6	7.9	-5.9	-18.0	7.5	-23.0	19.6	27.2	**-62.1**	-19.9
Miscanthus Pellets	-1.0	16.9	-0.3	40.8	3.9	3.1	-11.8	-34.6	-19.8	-43.1	9.6	-8.6	0.2
Sunflower Pellets	-7.4	1.9	-0.4	15.7	**-16.1**	-5.4	11.3	-26.4	13.0	-24.5	-21.7	35.6	9.7
Olive Cake 2013	2.0	5.9	0.6	13.9	9.0	**15.4**	10.6	-12.0	-22.6	-7.2	8.0	-4.5	**-30.6**
Olive Cake 2014	**-16.6**	2.4	-0.4	4.9	-12.4	4.5	7.7	-8.5	8.1	-14.0	-33.6	8.6	-6.0
Torrefied Pellets	-1.1	4.3	0.8	-27.0	0.6	-6.0	-8.5	3.7	-14.6	31.4	39.7	-45.7	-16.5
Steam Exploded Pellets	-0.7	**25.6**	0.2	31.6	8.3	**-21.4**	**-26.9**	**-27.1**	**-25.1**	-32.7	26.9	**-60.3**	**28.5**
La Loma Coal	-4.5	25.7	0.1	22.5	1.4	2.6	1.0	-23.5	-2.3	-20.4	-13.3	**200**	-1.4

Table 4.3: Percentage Difference between Sieved and Camsizer Rosin-Rammler, Size, Shape and Distribution Shape Parameters

The variance in the sieving and Camsizer results for particle size distributions show that the different methods can produce different results with contradicting interpretations; however the variance is material dependent. In the following sections and in the milling trials, the particle size data from sieving is used due to the late availability of the Camsizer in the project and the use of sieving in several standard coal grindability tests, such as the Bond Work Index test (Warren Spring Laboratory, 1962) and Hardgrove Grindability Test (The

British Standards Institution, 1995). The particle shape data is obtained for the same samples from the Camsizer digital image analysis, and the particle size distributions were checked for close correspondence with the sieving results for all tests.

4.5. Comparison of Pre-Milled Particle Size Distributions

As a starting point for comparing comminuted materials, it is necessary to understand the variance in the physical composition of the samples being analysed prior to comminution. Table 4.1 (sieved data) is used for the analysis of difference in material particle size distributions of the disintegrated and powdered samples. Wood samples show a mean geometric diameter (d_{gw}) range of 631 µm for eucalyptus to 808 µm for white wood. Sunflower and miscanthus show similar d_{gw} to wood (774 µm and 604 µm, respectively). Treated biomasses had similar d_{gw} to wood, indicating that the treatment has a small impact on initial particle size, however it should be noted that the disintegration of the pellets resulted in fragmented pellets as well as individual particles. Not all of material in the thermally treated pellets was treated, as large untreated white wood particles were seen to be present within the disintegrated sample for the torrefied and steam exploded pellets. For the powdered samples, olive cake has a much larger mean particle size (1303 µm for 2013 and 1589 µm for 2014). This is also influenced by the tri-modal composition of the olive cake. La Loma coal had a large initial particle size (d_{gw} 1676 µm) compared to the biomass. There was a good fit with the Rosin-Rammler distribution equation for all wood and treated wood samples.

The dispersion parameters give an interesting insight into the grading of the samples. All samples showed a Mean Relative Span (*MRS*) above 1, indicating a wide distribution, which is also reflected in the low Rosin-Rammler distribution parameter (*n*) values. However the range varied significantly across the samples. La Loma coal's MRS was 1.62, while all other samples apart from olive cake were between 2 and 3. For *hs* and *ls,* wood, treated wood, coal and herbaceous samples had slightly higher *ls* than *hs.* Apart from miscanthus, the biomass and coal samples can be considered to have good graduation in particle size (Coefficient of Uniformity $C_u > 4$) and are well graded particles, as the Coefficient of Curvature (C_c) is between 1 and 3.

All wood samples, sunflower, torrefied and La Loma are platykurtic curves ($k_g < 1.00$) indicating that the distributions are better sorted in the tails than central portion, hence excessively peaked. However olive cake, miscanthus and steam exploded pellets show

leptokurtic curves (k_g > 1.00), which means that the samples are better sorted in the central portion than in the tails, giving a flatter distribution. All the samples show a positive graphical skewness (GS_i), which indicates the samples are composed of a large proportion of fine material. La Loma coal shows an almost symmetrical distribution, with a skewness of 0.01.

4.6. Cumulative Shape Distributions of Pre-Milled Samples

Comminution studies usually focus on the particle size distributions of the milled product, (Bitra, Womac, Yang, Igathinathane, et al., 2009; Bitra, Womac, Yang, Miu, et al., 2009; Gil & Arauzo, 2014; Gil et al., 2012, 2015) but rarely look at the impact on the particle shape factors. Using the Camsizer digital image analysis, the particle shape distributions prior to milling were obtained for the disintegrated and powdered samples. The results have been banded by biomass group; blue for wood, green for herbaceous, purple for fruit, red for treated biomass, and black for coal. While the data for the shape characteristics is based on the information collected for the shortest chord diameter (d_{c_min}), the cumulative distributions are not related to the size of the particles they were measured for, rather the percentage volume of the sample tested.

The mean sphericity, circularity, aspect ratio and symmetry are shown in table 4.4, and the cumulative distribution for particle sphericity is shown in figure 4.5. No correlation was observed between the shape factors and pre-milled particle sizes. As none of the samples were manufactured by the same pellet manufacturer and were all produced in different locations around the world, the comminution and densification process used will have been different for each pellet. Thus this lack of relationship between shape and size is to be expected. The trends in particle sphericity can be seen across all shape factors. Surprisingly olive cake has the highest sphericity (both years have very similar profiles despite variation in particle size distributions shown in figure 4.3) followed by La Loma coal, which one would expect to have the most spherical shape.

This is due to the structure of olive cake being different to that of the other biomasses. As noted in section 2.6, the olive pulp is mainly made of cellulose and hemicellulose, with the lignin concentrated in the pip section of the fruit (Kailis et al., 2007). Woody and herbaceous biomass have a longitudinal structure which is dictated by the lignin structure, with fracture occurring parallel to the lines of lignin, resulting in the needle like structures commonly observed for milling these materials. This lack of lignin structure in the olive pulp results in

the spherical structures observed in the digital imaging. The woods and herbaceous materials show similar profiles with the white wood pellets showing lowest sphericity.

Sample	Mean Sphericity	Mean Circularity	Mean Aspect Ratio	Mean Symmetry
White Wood Pellets	0.406	0.473	0.516	0.765
Eucalyptus Pellets	0.432	0.545	0.544	0.745
Mixed Wood Pellets	0.376	0.492	0.484	0.781
Miscanthus Pellets	0.353	0.508	0.455	0.796
Sunflower Pellets	0.375	0.567	0.481	0.797
Olive Cake 2013	0.584	0.757	0.692	0.863
Olive Cake 2014	0.609	0.767	0.709	0.872
Torrefied Pellets	0.494	0.683	0.612	0.836
Steam exploded	0.458	0.620	0.577	0.816
La Loma Coal	0.532	0.710	0.645	0.836

Table 4.4: Mean Sphericity, Circularity, Aspect Ratio, and Symmetry for Disintegrated and Powdered Samples

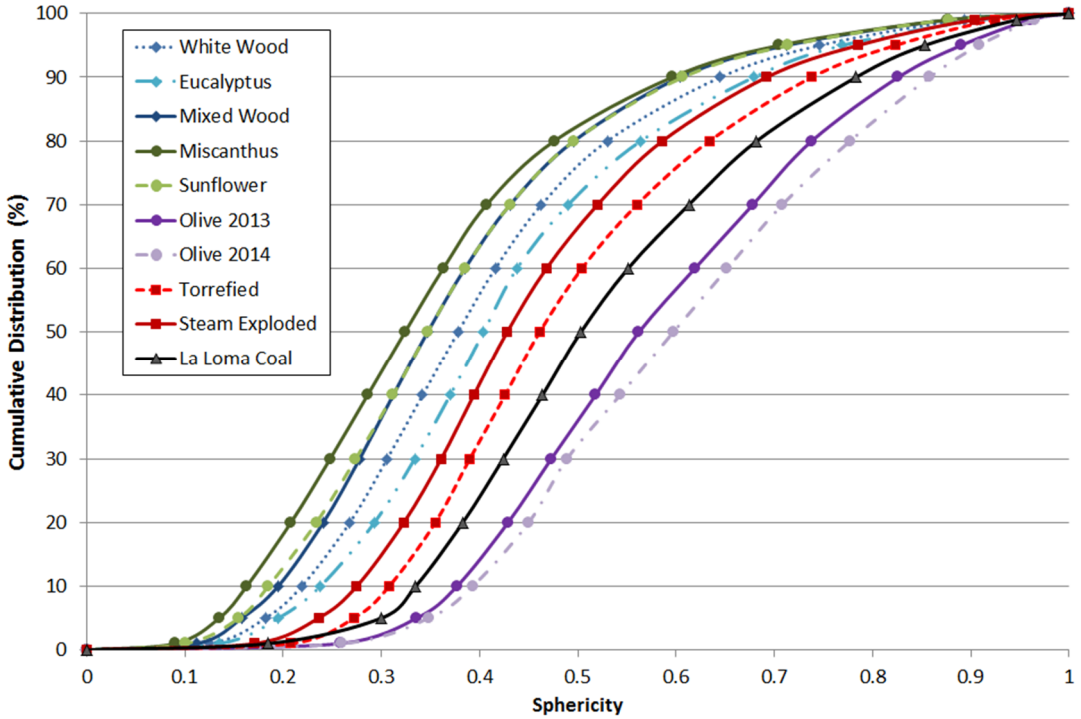


Figure 4.5: Cumulative Distribution of Particle Sphericity

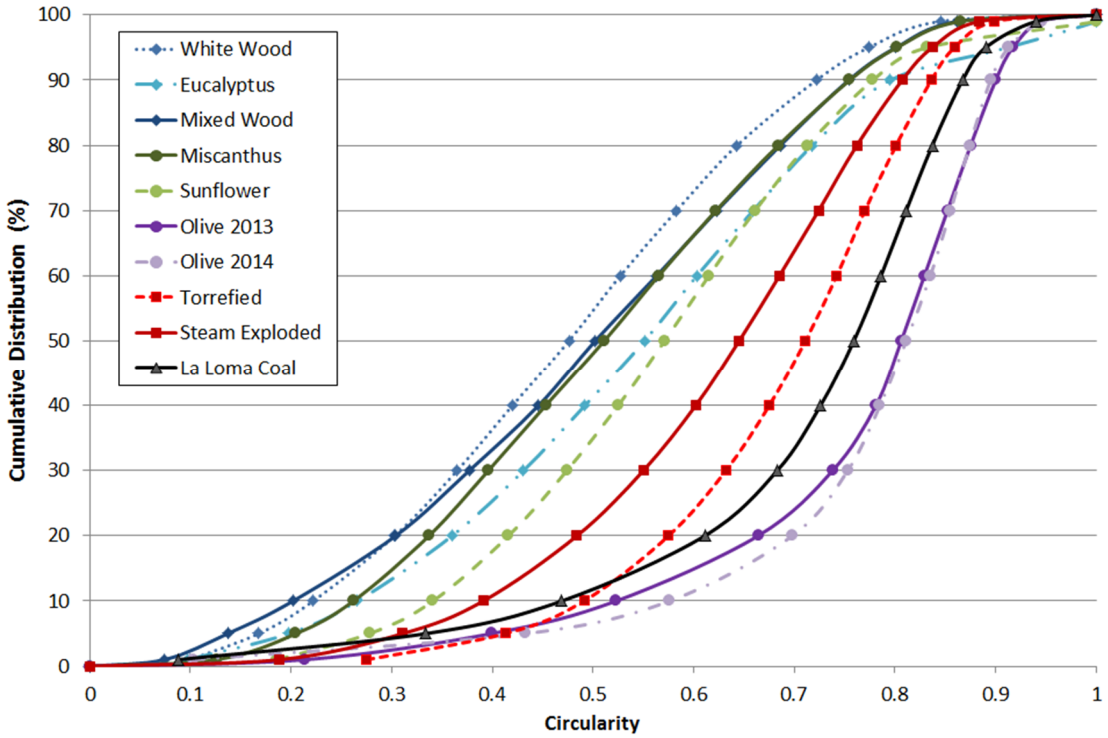


Figure 4.6: Cumulative Distribution of Particle Circularity

Torrefied and steam exploded pellets show a definite improvement on the wood pellets in terms of sphericity, and this improvement in shape factors through torrefaction has also been noted by Phanphanich et al. (2011). Torrefied pellets showed slightly more spherical particles than the steam exploded pellets. Particle circularity gives an indication of the roundness of a particle (Wadell, 1934), and combined with the sphericity of the particle can give an indication of the shape and surface contours of a particle. As with sphericity, olive cake has the most circular of all the particles (Fig. 4.6). This was followed by La Loma coal, thermally treated pellets, and the woods and herbaceous materials. This indicates that the structure of the herbaceous and wood materials is such that their particles will form with low roundness. In wood, cracks will generally grow along the wood fibres, irrespective of both the original notch orientation and the mode of fracture (Jernkvist, 2001), which leads to the needle like shapes.

The aspect ratio of the particles shows the same trends as the other shape factors (Fig. 4.7). This indicates that olive cake has the most square and non-needle like shaped particles. Herbaceous samples show the lowest aspect ratios, which would be expected as miscanthus which is a straw material with needle like particles. These results correlate with the results of Guo et al. (2012), who showed through microscopy that ground pine, beanstalk, rice straw and reed particles have needle like shapes and variable aspect ratios, and by Gil et al. (2014).

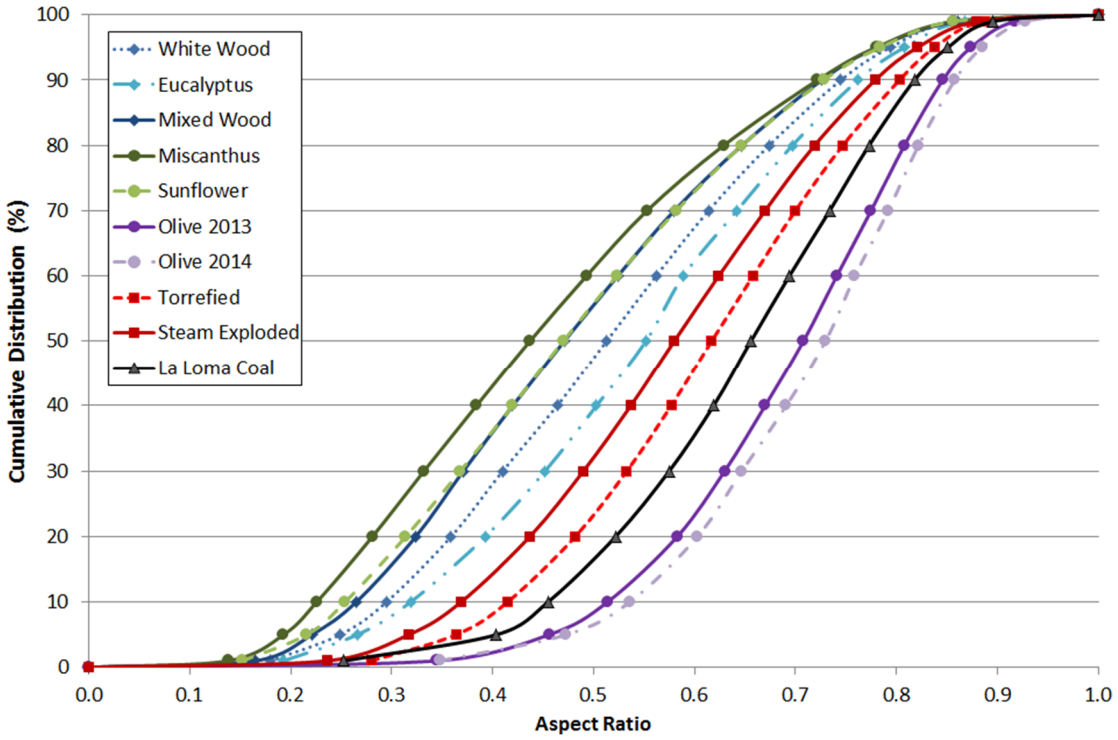


Figure 4.7: Cumulative Distribution of Particle Aspect Ratio

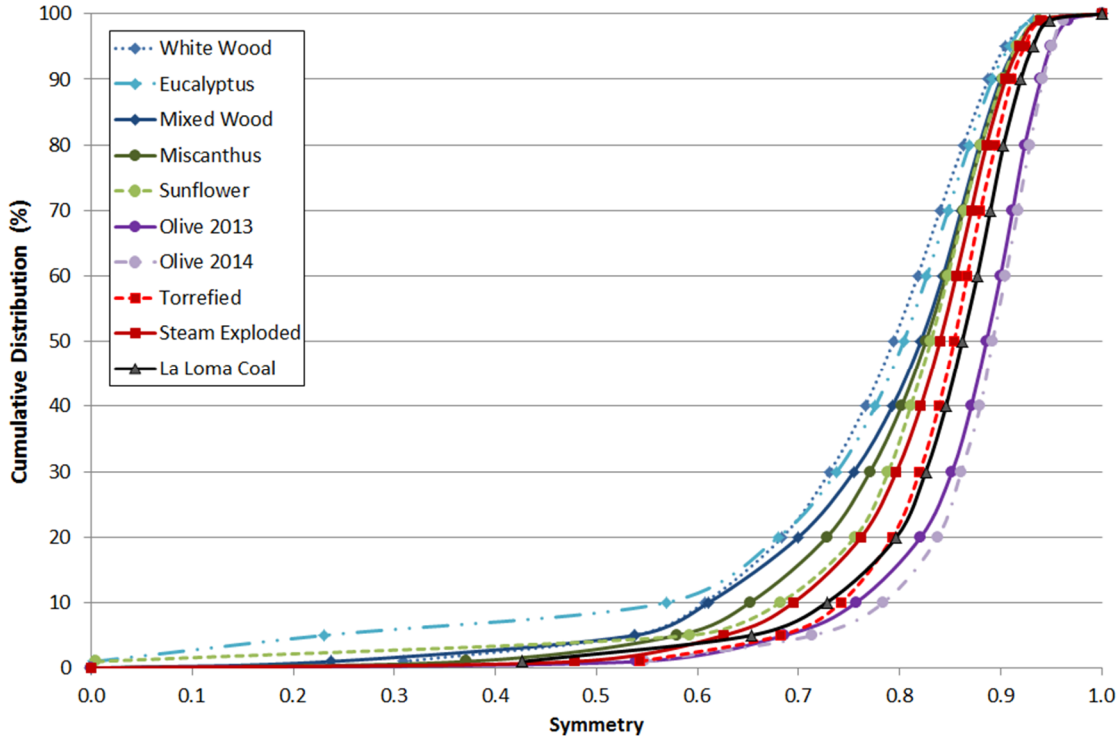


Figure 4.8: Cumulative Distribution of Particle Symmetry

The cumulative distribution for particle symmetry is shown in figure 4.8. Once more olive cake has the highest symmetry of all the samples followed by La Loma coal. Compared to the other shape factors, the symmetry of the samples was more closely matched. There is little difference in the symmetry of herbaceous and wood samples, and torrefied and steam

exploded pellets show an improvement in symmetry compared to pine pellets, but the eucalyptus and sunflower are very similar to the thermally treated pellets.

This section has shown how biomass pellet particles have similar particle size distributions but a large variance in particle shape. From a mill particle size selection perspective, knowledge of the pre-milled particle size and shape can help inform the likely required particle size for classification.

4.7. Moisture Content and Moisture Re-adsorption

Table 4.5 shows the moisture content for the various biomass samples tested under British Standard conditions (The British Standards Institution, 2009a) when supplied to the project. Also shown are the results from the moisture reabsorption tests, and the impact of storing the samples in zip locked bags on moisture reabsorption. The moisture content of the as received pellets varied widely for each of the samples.

Sample	Moisture content (%)	Moisture Reabsorption after 24 hours after Drying	Moisture Content of Dried Samples after for 6 days of sealed storage
White Wood Pellets	8.5	1.9	0.29
Eucalyptus Pellets	10.5	4.6	0.17
Miscanthus Pellets	7.6	4.5	0.16
Mixed Wood Pellets	9.4	4.3	0.24
Olive Cake 2013	17.9	2.1	0.27
Olive Cake 2014	12.4	1.6	0.09
Olive Pellets	11.2	1.3	0.29
Microwave Pellets	4.7	1.7	0.21
Shredded Bagasse	33.3	2.7	0.16
Torrefied Pellets	6.4	2.1	0.26
Sunflower Pellets	11.8	4.1	0.14
Steam Exploded Pellets	7.2	2.0	0.23

Table 4.5: Moisture Content and Moisture Reabsorption for Exposed Biomass and Biomass Stored in Sealed Bags

The thermally treated pellets showed the lowest moisture contents, with Microwave pellets having the lowest at 4.7%. The thermal treatment has been shown to reduce the equilibrium

moisture content (EMC) for given biomass (Acharjee et al., 2011). Miscanthus showed the lowest moisture content (7.6%) for non-treated pellets and olive pellets showed the highest (11.2%). The seasonal variability of olive cake was seen in the moisture content of the 2013 and 2014 samples, with 2013 samples having 5% more moisture. The shredded Bagasse showed the highest as received moisture content of 33.3% but the moisture content varied significantly throughout the sample.

Figure 4.9 shows the moisture reabsorption for the biomass samples over 24 hours. Most samples reabsorb around 1.5-4% moisture after 24 hours, but the white wood pellets, olive cake and pellets and thermally treated pellets show much lower reabsorption levels. The samples which were stored in sealed bags immediately after drying showed a low level of moisture increase after 6 days, with moisture uptake limited to 0.09-0.29%.

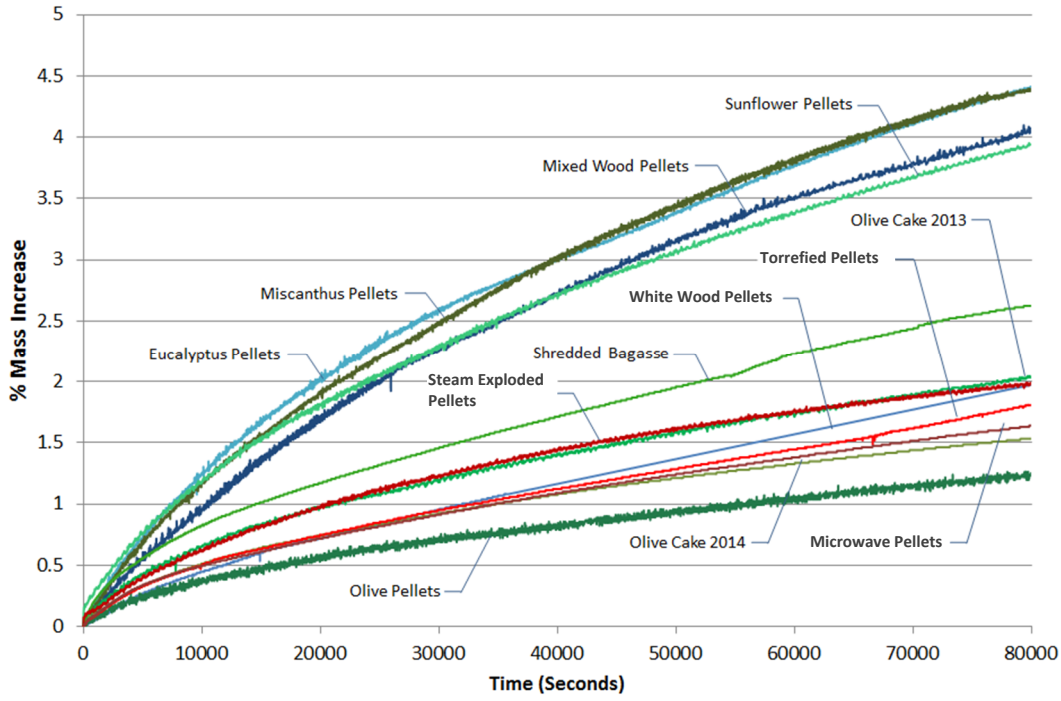


Figure 4.9: Moisture Reabsorption over 24 hours for Various Biomass

The storing of biomass samples in sealed bags has also been used in other studies to control the moisture content of biomass prior to milling (Mani et al., 2004; Miao et al., 2011). It is expected that physical and/or chemical interactions that occur during harvest, handling, transportation, and storage of biomass will induce changes on the sorption properties of its components.

The addition and removal of water changes the composition and size of the material and can cause phase change transitions (dissolution, sugar crystallisation etc.) (Tsami et al., 1990).

The moisture content of samples is known to be influenced by the changing relative humidity of the surroundings, and the moisture sorption isotherm describes the relationship between the equilibrium relative humidity (ERH) and the EMC of a specific bioenergy crop at a given temperature (Bell et al., 2000).

This is illustrated in Figure 4.10; eucalyptus pellets were oven dried then the moisture reabsorption was measured over a 6 day period in conjunction with measurements in temperature and relative humidity. Once a stable EMC was reached (approximately 6%), the EMC cycled with the ERH and temperature of the space, as illustrated in the top part of figure 4.10. The EMC was lower than the as received moisture content. Chen and Danao (2015) also found that higher sucrose contents in bioenergy crops resulted in increased changes of EMC per ERH at the same temperature.

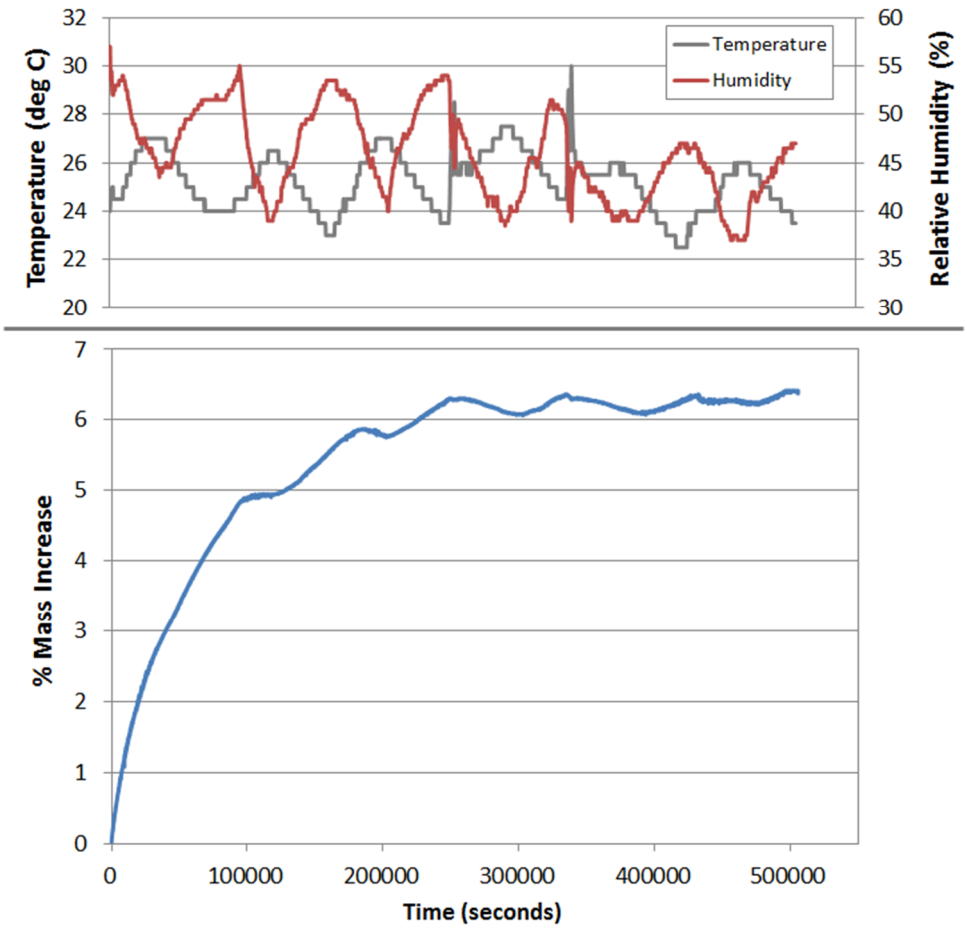


Figure 4.10: Trend of Moisture Reabsorption for Varying Temperature and Relative Humidity for Eucalyptus Pellets over 6 Day Period

4.8. Pellet Durability

Figure 4.11 shows the pellet durability results for the pellets from the standard pellet durability test (The British Standards Institution, 2013b). Steam exploded pellets showed the highest durability, which would be expected as they were thermally treated. The olive and eucalyptus pellets showed the highest non treated durability, followed by miscanthus, wood and sunflower pellets. BS EN ISO 17225-2:2014 (The British Standards Institution, 2014c) has a lower limit of 96.5% pellet durability for wood pellets (class A3) and BS EN ISO 17225-6:2014 (The British Standards Institution, 2014d) has a lower limit of 97.5% specifically for miscanthus pellets and the same for all other generic herbaceous and fruit biomass pellets. Based on this, the mixed wood and sunflower pellets do not meet the requirements of the standards for mechanical durability. Biomass durability has been shown to be impacted by material composition, pre-conditioning process and densification equipment (Kaliyan et al., 2009), in particular process temperature, material moisture content and particle size (Carone et al., 2011; Fasina, 2008; Mani, Tabil, et al., 2006).

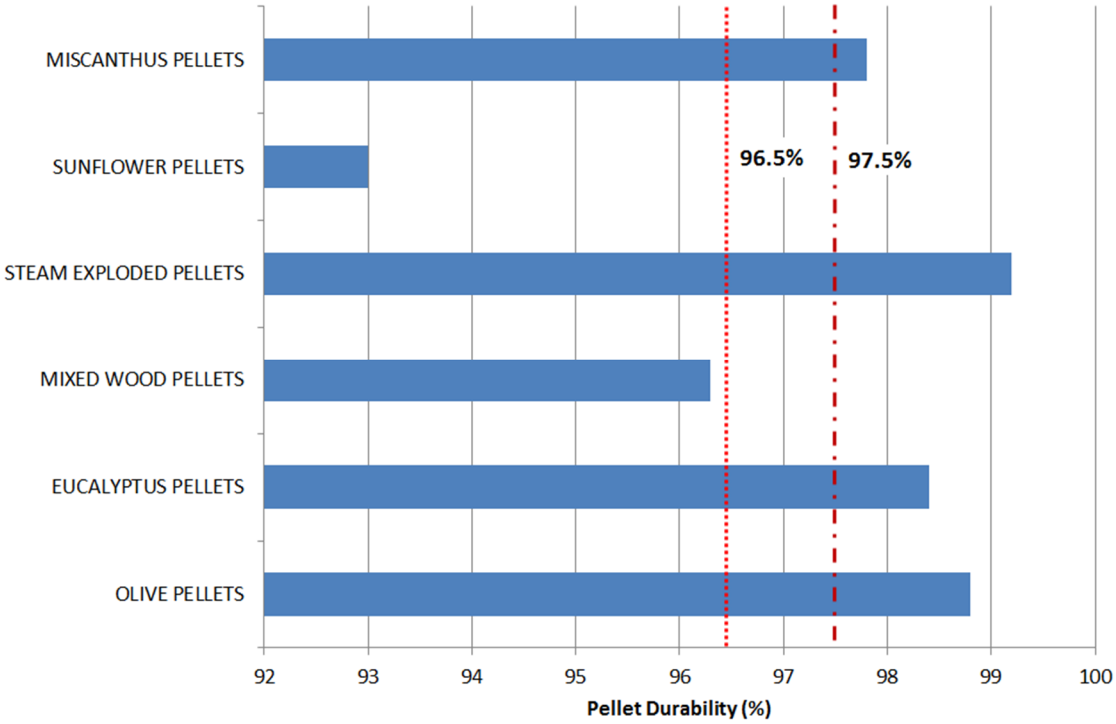


Figure 4.11: Pellet Durability of Samples Tested in Accordance with BS EN ISO 17831-1 (The British Standards Institution, 2013b)

Little is known about the densification process used to manufacture the pellets used in this study beyond the pre-densified particle size distribution. Smaller particle size have been found to improve pellet durability for olive tree pruning residue pellets (1 mm and below) (Carone et al., 2011). The recommended particle size for good pellet quality is 0.6 mm

0.8 mm (Turner, 1995), with Franke and Ray (2006) recommending a particle size of 0.5 mm to 0.7mm for more durable pellets. Particles greater than 1 mm will act as predetermined breaking points in pellets but the increased cost of production of fine pellets results in pellets with the composition seen in this study (Fig. 4.3), with average particle sizes in excess of 1 mm.

4.9. Quasi Static Mechanical Strength of Pellets

The quasi-static mechanical strength was found in three modes; axial, diametric, and flexure (section 3.1.10) for raw and dried pellets. The mean values of compressive stress and Young's Modulus for all samples can be found in Appendix A. Figure 4.12 shows a sample bar and whisker plot for the compressive stress of raw and dried steam exploded pellets. The bar and whisker plots of the compressive stress for all other tested samples can be found in Appendix A, with a summary for all shown in figure 4.13. The tests were done over a range of lengths to ensure the aspect ratio of the pellets was within the maximum and minimum range of those in figure 4.2 in order to give a realistic spread of results across the range of pellets encountered during milling and conveyance.

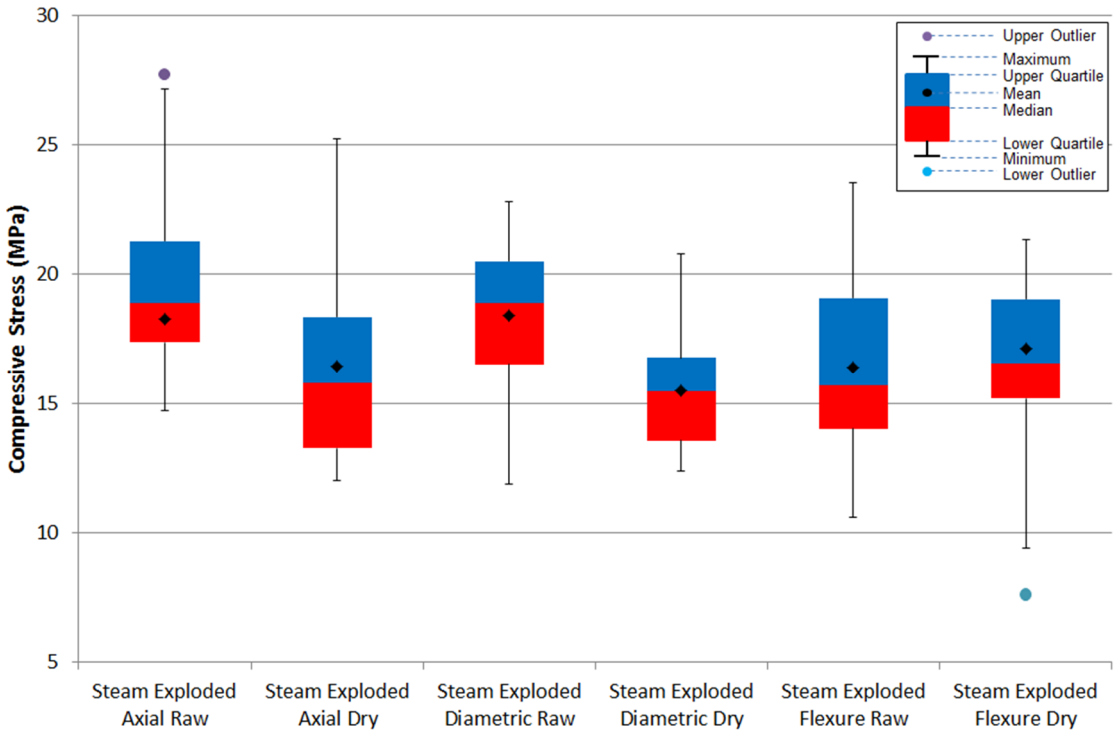


Figure 4.12: Quasi-static Compressive Axial, Diametric, and Flexure Stress for Raw and Dry Steam Exploded Pellets

As figure 4.12 shows, there is a large amount of variability in the compressive strength across all tests, and no correlation was found between pellet length and stress or Young's Modulus for the pellets, indicating that the determining factor in pellet mechanical strength is the material composition and manufacturing process used to create the pellets. A point for further study would be an investigation into the impact of densification type on the mechanical strength of biomass pellets.

The compressive stress results for tested pellets are shown in figure 4.13. Overall the diametric test showed the highest compressive stress, followed by axial then flexure or Modulus of Rupture. Thus pellet strength is greatest when a uniformly distributed load is applied and weakest when a point load is applied. During storage the load will be a uniformly distributed one, indicating that high strength in the diametric orientation will ensure durability in the pellets, while in milling the load is a point one, with a low flexure strength allowing the pellet to break up more easily. A balance between these two strengths will ensure a pellet which is durable but will easily break down in a mill. Across the spectrum of tested pellets there is a wide range of variability in the mean compressive strength. No real trends can be observed across biomass groups or by moisture content.

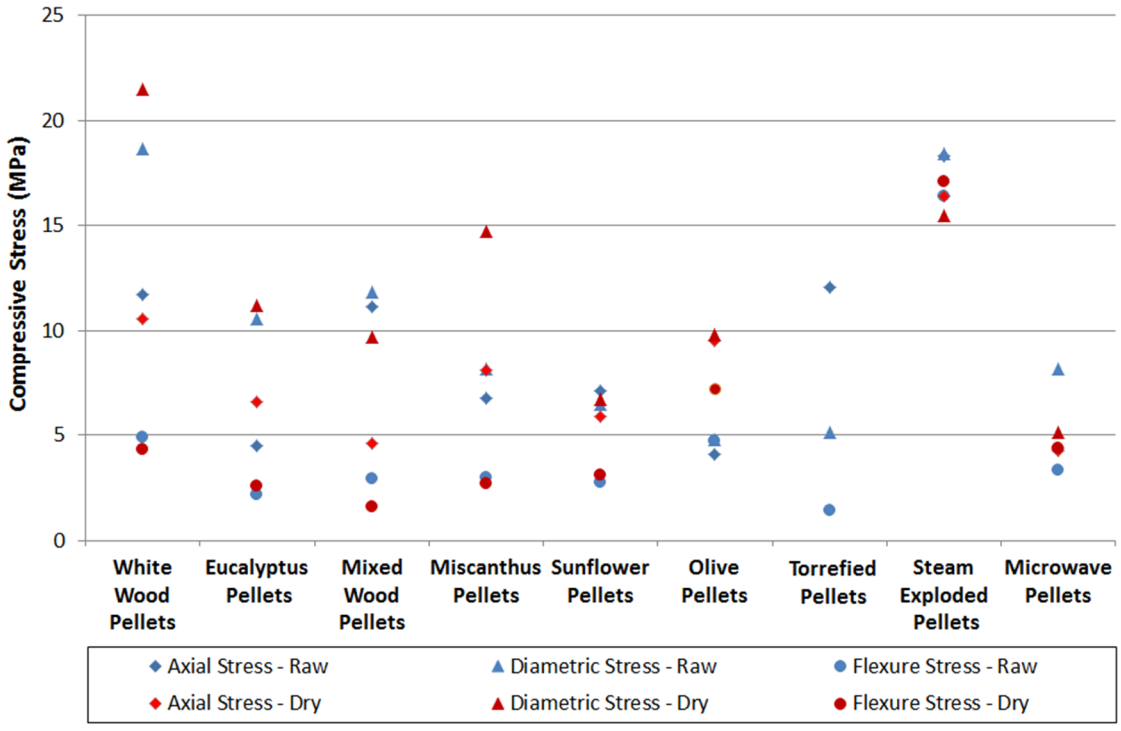


Figure 4.13: Quasi-Static Mean Compressive Axial, Diametric, and Flexure Stress for Raw and Dry Biomass Pellets

Given the pellets were of low moisture (< 12%) prior to drying, the drying process is not expected to yield any significant increase in pellet mechanical strength. Steam exploded pellets showed the highest compressive stress and sunflower pellets showed the lowest. This result relates back to the durability test results in figure 4.11, where steam exploded pellets showed the highest durability and sunflower pellets the lowest. For steam exploded, mixed wood and sunflower pellets a linear correlation was observed between durability and compressive axial and diametric stress, but the other samples showed no correlation. No correlation was observed between compressive flexure stress and durability. Thus future studies are required to investigate the relationship between pellet durability and axial and diametric strength. Two main failure modes were observed in axial and diametric testing. The first is shear, as shown in figure 4.14a and 4.14c for sunflower pellets, which were also observed for steam exploded, torrefied and microwave pellets. The second is delamination, which is shown for mixed wood pellets in figure 4.14b and 4.14d, which was also observed for olive, white wood, eucalyptus and miscanthus pellets.

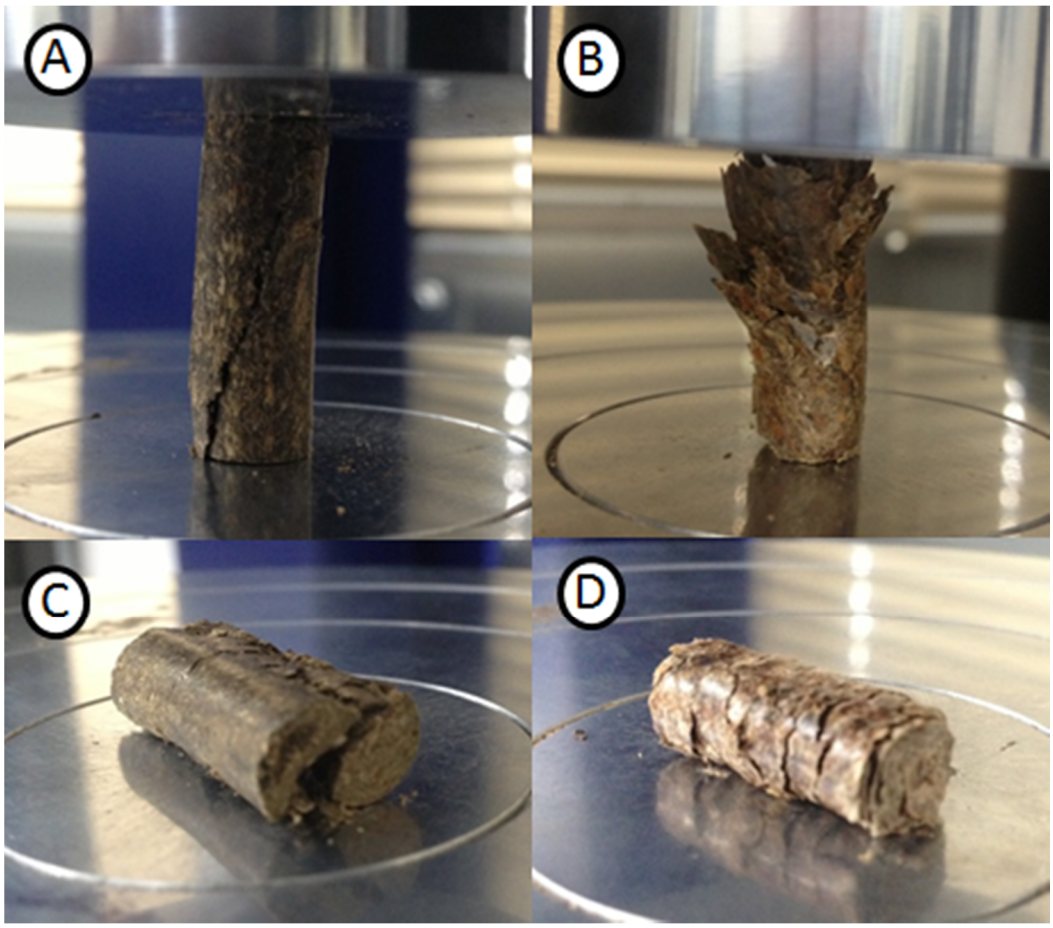


Figure 4.14: a) Axial Failure by Shear (Sunflower Pellets) b) Axial Failure by Delamination (Mixed Wood Pellets), c) Diametric Failure by Shear (Sunflower Pellets), d) Diametric Failure by Delamination (Mixed Wood Pellets)

Several pellets, such as miscanthus, showed a combination of failure modes, especially in diametric tests where a delamination would result in a shear failure across the cross section of the pellet. Figure 4.15 shows a typical bar and whisker plot for the compressive Young's Modulus of raw and dried steam exploded pellets. The bar and whisker plots of the compressive Young's Modulus for all other tested samples can be found in Appendix A. Even though the compressive stress values provided similar mean values in all tests, the resultant Young's Modulus are very different. Diametric showed the highest values, followed by axial and the flexure with the lowest. The compressive stress results in figure 4.12 showed a wide spread of results, however the Young's Modulus shows much tighter bands. This indicates that the test over a wide range of pellet lengths provides consistent and repeatable data on the compressive Young's Modulus of pellets. The overall results of mean Young's Modulus for all pellets tested in figure 4.16 is more distinctive than for the compressive stress in figure 4.13. As shown for the steam exploded pellets, the diametric test showed the highest values, followed by axial and then flexure.

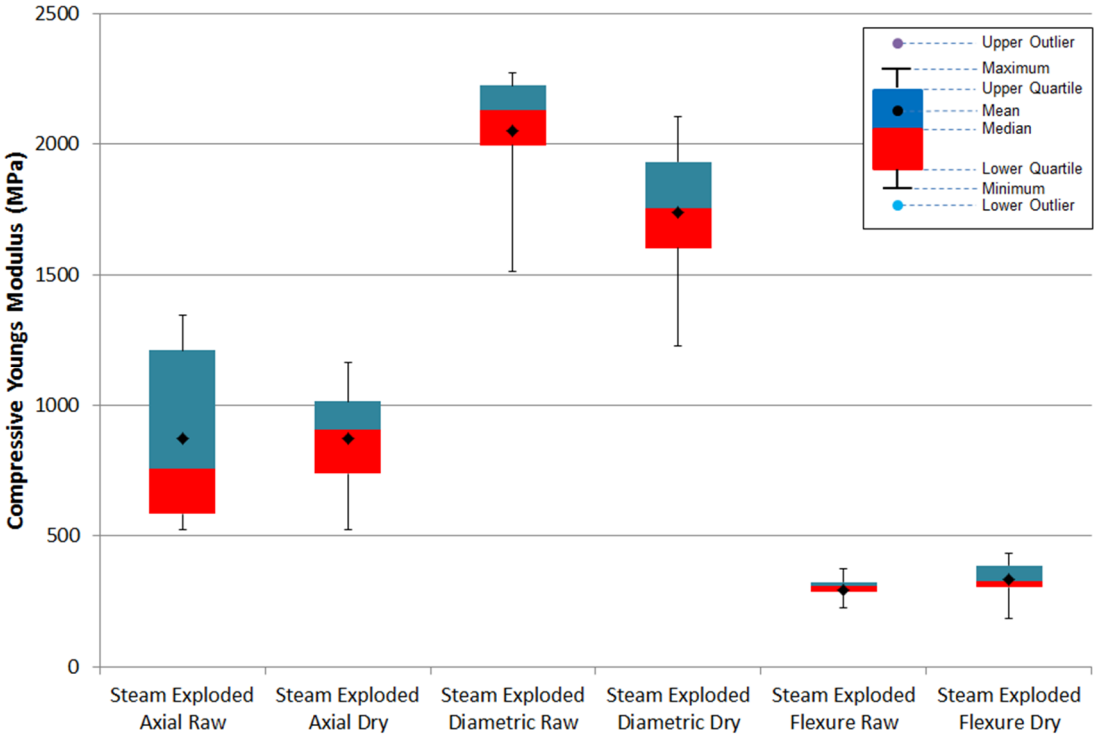


Figure 4.15: Quasi-Static Compressive Axial, Diametric, and Flexure Young's Modulus for Raw and Dry Steam Exploded Pellets

In comparison to wood beams, biomass pellets have much lower values of Young's Modulus (Kretschmann, 2010), which is to be expected as biomass pellets are heterogeneous particulate composites with no inherent structural components unlike timber (Bodig et al.,

1993). The strength of biomass pellets is crucial in ensuring durability, while allowing easy comminution and the breaking up of the pellets back into its constituent particles.

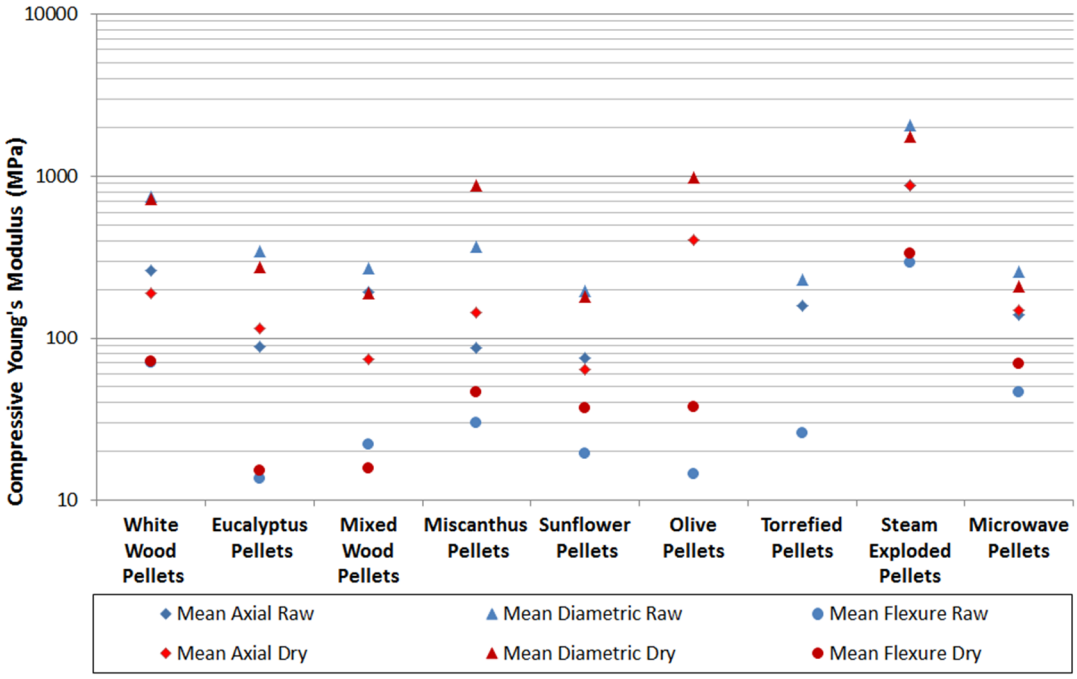


Figure 4.16: Quasi-Static Mean Compressive Axial, Diametric, and Flexure Young's Modulus for Raw and Dry Biomass Pellets

4.10. Split Hopkinson Pressure Bar Data

While the quasi-static mechanical tests can give the response of biomass pellets under storage loading conditions, the actual strain rates experienced during milling are significantly higher. The Hopkinson Bar test has been used to analyse the forces within mill in previous studies (Fandrich et al., 1998). In the study, the Split Hopkinson Pressure Bar (*SHPB*) test was used to analyse the dynamic mechanical response of the pellets at high strain rates (section 3.1.11). The testing of soft materials on SHPB is notoriously difficult (W. Chen et al., 1999; Song et al., 2004), and for this reason, viscoelastic materials are often used for the pressure bars (Butt et al., 2014). Figure 4.17 shows the stages of the test recorded on a slow motion video (iphone 5s 120 frames per second) for a mixed wood pellet in the diametric orientation. The top image (1) shows the pellet suspended between the incident and transmission bars at the start of the test. The incident bar is hit by the striker and compresses the specimen into the transmission bar (2). Both bars and the specimen travel horizontally until the transmission bar hits the stop and reverses direction and collides with the incident bar (3). The energy transfer causes the transmission bar to accelerate away from the bar, resulting in the specimen material being released in an explosion like manner.

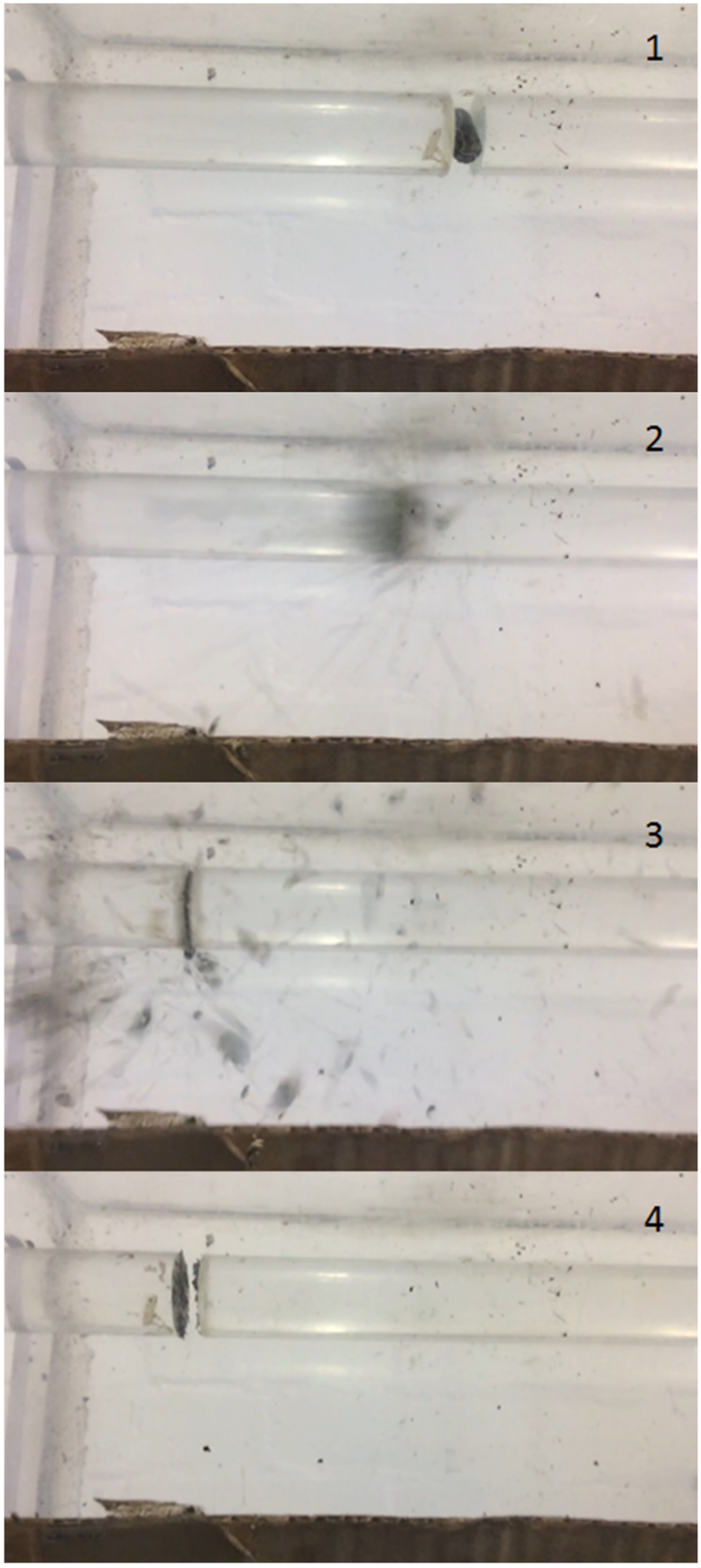


Figure 4.17: Slow Motion Video Stills of SHPB Test on Mixed Wood Pellet in Diametric Orientation

The final image (4) shows the end of the test, where the pellet has completely disintegrated and a small amount of pellet is deposited on the contact faces of the bars.

Table 4.6 shows the summary of the results of SHPB tests for the biomass pellets. The diametric orientation showed higher Young's Modulus and maximum compressive stress than in the axial orientation, which was also generally observed for the quasi-static mechanical tests in section 4.9. Unlike the results of Pierre et al. (2013) for spruce wood, the samples did not compress but disintegrated upon impact, which is the desired effect for biomass pellets. However this means that obtaining an accurate measurement of the pellet Young's Modulus is difficult, as a constant strain rate condition was not achieved during the test. Also due to the heterogeneous nature of the pellets, the data obtained is only valid for the samples tested. The maximum compressive stress did however occur within the area of constant strain rate, and can be taken as a measure of the strength of the materials.

Sample	Diametric Young's Modulus (MPa)	Average Diametric Strain Rate (s^{-1})	Max Diametric Compressive Stress (MPa)	Axial Young's Modulus (MPa)	Average Axial Strain Rate (s^{-1})	Max Axial Compressive Stress (MPa)
Eucalyptus	129	1257	11	15	1301	5
Mixed Wood	124	1130	11	40	1400	7
Miscanthus	205	679	12	28	719	7
Sunflower	113	1274	12	21	1283	8
Steam Exploded	707	1040	19	140	830	15
Microwave	57	1820	10	22	1329	3

Table 4.6: Mean Diametric and Axial Young's Modulus, Maximum Stress and Strain Rates

Steam exploded pellets showed the highest Young's modulus and maximum compressive stress in axial and diametric orientations and are thus the strongest of all the pellets. The other pellets had similar maximum compressive strengths in the diametric orientation (10 MPa to 12 MPa) but more of a spread in the axial orientation. This is partly due to the difficulty in squaring off the pellets as they easily disintegrate or chip, and ensuring a good contact area across the diameter of the pellet was difficult in the axial orientation. Interestingly the other thermally treated pellet tested, Microwave, showed the lowest Young's modulus in the diametric orientation.

Figure 4.18 and 4.19 compares the quasi-static and dynamic mechanical responses of the pellets. The maximum compressive stress observed in both tests is quite similar (Fig. 4.18). For all samples apart from the quasi-static sunflower pellets, the diametric maximum

compressive stress is greater than the axial. Thus the pellets are stronger when a uniformly distributed load is applied across its length rather than across its diameter. The same trends are observed in both tests, with steam exploded pellets being the strongest of all the pellets and microwave the weakest. The other pellets show similar results to each other, showing that for non-treated pellets, the strength of the pellets will be similar irrespective of material type. In general, the dynamic mechanical tests showed higher maximum compressive stresses, which has also been observed for other cellulosic materials tested in a SHPB (Palamidi, 2010). In contrast to the maximum compressive stress results (Fig. 4.18), the Young's Modulus results showed the opposite trend, with the quasi-static tests showing higher Young's Modulus results (Fig. 4.19).

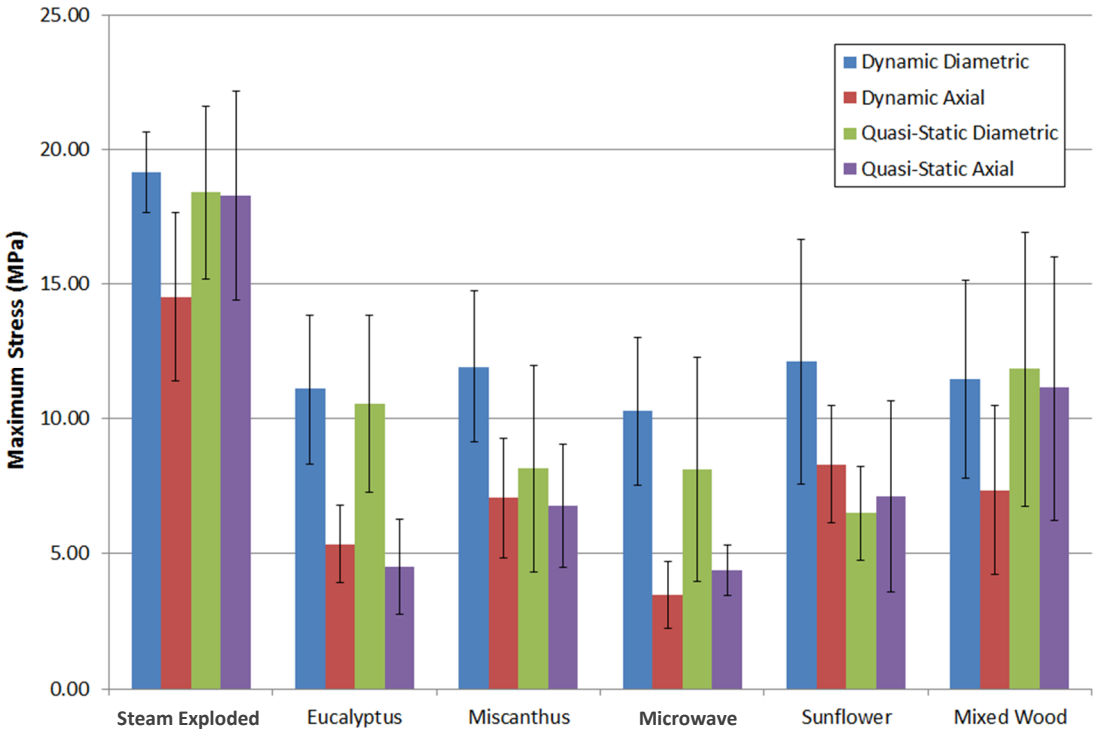


Figure 4.18: Axial and Diametric Maximum Compressive Stress in Quasi-Static and Dynamic Mechanical Tests

While the trend of higher Young's Modulus is observed in the diametric orientation compared to the axial orientation, there is a significant difference in the modulus' obtained between the tests, with the dynamic results being significantly lower than those of the quasi-static tests. This is most likely due to two issues. The main issue is that the Young's Modulus is recorded in the non-linear strain rate region in the dynamic test, whereas the strain rate is constant throughout the quasi-static test. This is a limitation of the dynamic test for soft materials with no structural integrity such as biomass pellets, as they cannot withstand the impact long enough for failure to occur within the constant strain rate region.

The second reason is due to the impedance mismatch with the bars and specimen. Conventional pressure bars have an impedance mismatch with soft materials due to the significant difference in longitude wave speed and density between the bars and the specimen (Song et al., 2004). This causes most of the wave to be reflected back into the incident bar at the specimen bar interface. The stress wave which is transmitted through the sample is of very low amplitude, thus the signal to noise ratio can be of the same magnitude, making it impossible to record measurements. Further study is required into alternative bars with impedances closer to that of the biomass pellets to increase the signals and increase the accuracy of the readings.

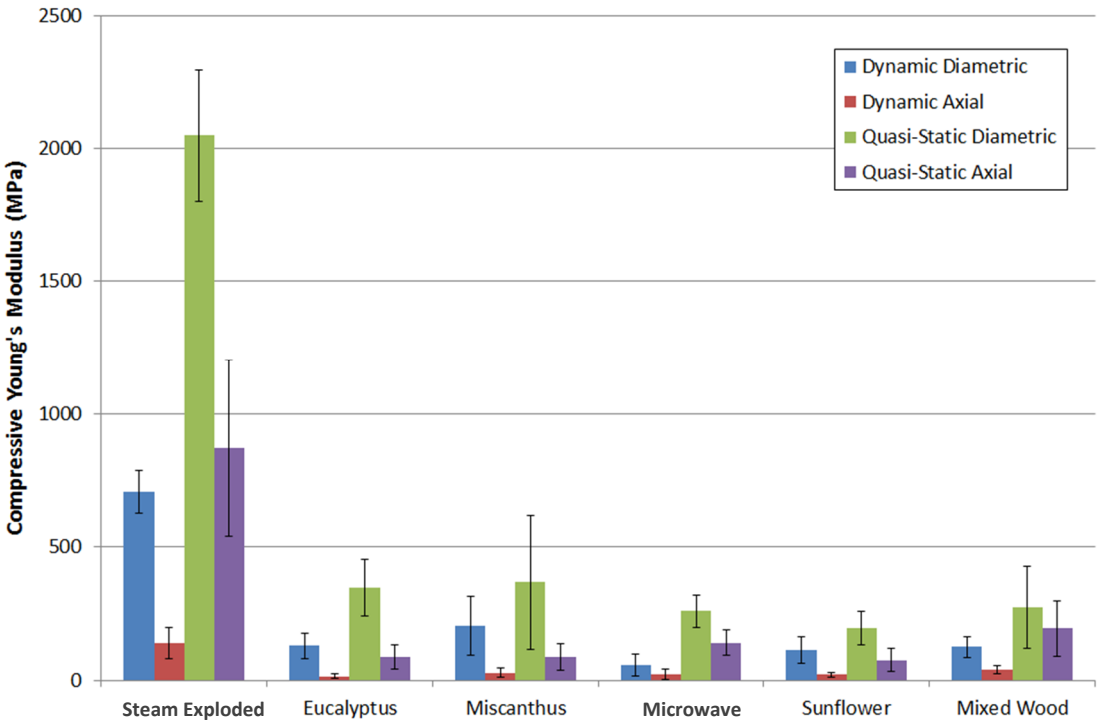


Figure 4.19: Axial and Diametric Young's Modulus in Quasi-Static and Dynamic Mechanical Tests

4.11. Abrasion Index

The standard Abrasion Index (AI) test for coal (The British Standards Institution, 1998a) was tested on a limited number of biomass samples. Most woody and herbaceous samples caused the testing equipment to catch fire and it was not possible to perform the test. This was partly due to the test is based on mass (2 kg of sample) rather than volume, which resulted in an over loading of the equipment with material due to the low density of the biomass samples. However three of the samples were tested successfully, the results of which are shown in Figure 4.20. A selection of Australian coals were found to have abrasion indexes of 7 mg/kg to 45 mg/kg for air dried coals, with significantly higher values for as

received samples (Scott, 1995), and moisture has been shown to be the main influencer in the abrasiveness of coal (Tlotleng, 2011). Air dried olive cake and pellets produced similar results (10 mg/kg to 11 mg/kg), and steam exploded pellets showed very low AI values (1.1 mg/kg) compared to air dried La Loma coal and other coals. Wells et al. (2004) showed that only minerals that are harder than steel will significantly contribute to the abrasiveness of coals, and angular particles are more abrasive than round particles. No published results on the use of the standard or a modified AI test for biomass have been found in the literature, and given the limited success of the test during this project; it is proposed that a new test for biomass abrasion is required.

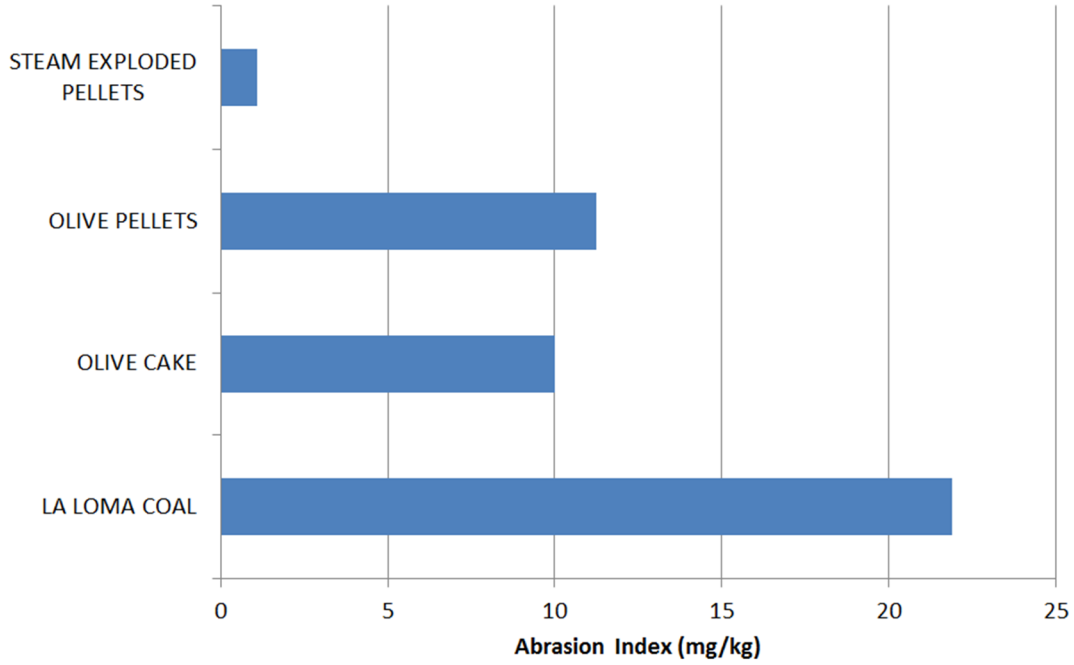


Figure 4.20: Abrasion Index for Biomass & Coal

4.12. Thermal Characterisation

The reactivity TGA results (table 4.7) indicate that all samples have similar moisture release temperatures and rates (36-48 °C, 0.55-1.46 %wt./min), but vary in volatile and burnout behaviour. Herbaceous materials have the lowest volatile release temperatures and rates, with final burnout temperatures similar to that of the wood samples. Olive cake had the highest volatile release temperatures but lowest volatile release rate of all samples. Olive also had a significantly higher final burnout temperature compared to the other samples at over 560 °C. There were similar results for all wood samples, with volatile release temperatures around 320 °C, and eucalyptus showing the has highest volatile release rate at 17.7 %wt/min. Torrefied pellets showed a slightly lower volatile temperature but higher

release rate than steam exploded pellets, with both exhibiting final burnout temperatures similar to woods and herbaceous materials.

Sample	Moisture Release		Volatile Release		Burnout Stage		Final Burnout (°C)
	1st Peak (°C)	Rate (wt/min)	2nd Peak (°C)	Rate (wt/min)	3rd Peak (°C)	Rate (wt/min)	
Bagasse	42	1.2	313	17.5	380	2.4	486
White wood	43	1.0	323	17.4	442	5.3	474
Eucalyptus	36	1.2	321	17.7	451	2.8	496
Mixed Wood	42	1.1	320	13.1	439	3.1	496
Miscanthus	42	1.5	274	8.6	410	5.8	481
Sunflower	43	0.8	283	10.2	433	6.4	490
Olive Cake 2013	38	0.9	444	4.9	532	1.0	569
Olive Cake 2014	48	0.8	436	4.6	528	0.3	563
Stramproy	36	0.9	305	11.4	405	6.3	490
Steam exploded	39	0.6	315	9.1	392	6.4	486

Table 4.7: Reactivity Analysis of Pre-Milled Biomass & Coal

The slow pyrolysis test gives the thermal composition of the materials (table 4.8). Bagasse has the lowest dry fixed carbon content and one of the highest ash contents. Wood samples exhibited a fixed carbon content of around 11-13%, and herbaceous and olive samples had around 18% fixed carbon. While torrefied pellets showed a significant increase in fixed carbon content compared to the wood samples (23.8%), steam exploded pellets showed a lower increase in fixed carbon (18.0%), which suggests that the steam explosion process shows a lower increase in fixed carbon than torrefaction. La Loma coal has the highest fixed carbon at 51.3%. The wood samples have the lowest ash content, while the torrefied materials show around double the ash content of the wood samples. The wood samples also had the highest volatile contents of all the samples.

The calorific value (*H*) of the samples is crucial in determining the amount of sample required for combustion. The lower the value of *H*, the more material will be required to achieve the same thermal output from the boiler. Bagasse and miscanthus have lowest calorific value at 18.67 MJk/g (table 4.9).

Sample	Moisture (%)	Dry Fixed Carbon (%)	Dry Ash (%)	Dry Volatiles (%)
Bagasse	5.3	8.1	13.0	79.0
White wood	5.0	12.3	1.9	85.9
Eucalyptus	4.9	11.3	1.9	86.8
Mixed Wood	5.4	13.8	2.5	83.7
Miscanthus	7.3	18.8	8.1	73.2
Sunflower	4.7	18.5	4.3	77.2
Olive Cake 2013	6.3	18.1	11.5	70.4
Olive Cake 2014	5.6	18.6	9.1	72.4
Stramproy	4.5	23.8	4.7	71.5
Steam exploded	3.1	18.0	4.8	77.2
La Loma Coal	5.4	51.3	13.7	35.1

Table 4.8: Slow Pyrolysis Results for Pre-Milled Biomass and Coal

Sample	HHV_d (MJ/kg)	Particle Density (g/cm^3)	Pellet Density (g/cm^3)	Ultimate Analysis (as received)			
				Carbon (%)	Hydrogen (%)	Nitrogen (%)	Oxygen (%)
Bagasse	18.67	-	-	-	-	-	-
White wood	20.35	-	1.29	-	-	-	-
Eucalyptus	20.35	1.46	1.20	46.2	5.7	0.13	47.9
Mixed Wood	20.65	1.45	1.20	47.0	5.9	0.02	47.2
Miscanthus	18.67	1.48	1.19	43.0	5.7	0.30	51.0
Sunflower	20.76	1.42	1.14	45.9	5.6	0.90	47.6
Olive Cake 2013	20.26	1.42	-	44.4	5.4	1.55	48.7
Torrefied	21.86	1.46	1.21	52.0	5.3	0.44	42.3
Steam exploded pellets	20.40	1.47	1.36	48.3	5.5	0.23	46.0
Microwave	21.26	-	1.11	46.2	5.7	0.13	47.9
La Loma Coal	29.67	-	-	68.6	4.6	1.42	25.4

Table 4.9: Dry Higher Heating Value, Particle and Pellet Density and Ultimate Analysis for Pre-milled Biomass and Coal

The wood, sunflower, olive and surprisingly steam exploded pellet samples have similar *H* values between 20 MJ/kg and 21 MJ/kg. Only microwave and torrefied pellets show an improvement on the untreated samples with *H* values over 21 MJ/kg. La Loma has the highest calorific value at 29.67 MJ/k g. Elemental data is provided for the samples where available (table 4.9). Only La Loma and torrefied pellets showed significantly higher carbon

content compared to the other samples. Steam exploded pellets only shows a marginal improvement in carbon compared to the other samples. The pellet density was similar for most of the samples (table 4.9). Steam exploded pellets showed the highest at 1.36 g/cm^3. Microwave had the lowest at 1.11 g/cm^3, but it was difficult to measure as some of the pellets sunk while others floated during the test.

4.13. Conclusions

Biomass pellet particles have similar particle size distributions but a large variance in particle shape and knowledge of the pre-milled particle size and shape can help inform the likely required particle size for classification and help select target particle sizes for grindability tests

The use of quasi static and the novel use dynamic mechanical response test found that biomass pellets are strongest in the diametric orientation and weakest in a flexure or point load test. Biomass pellets showed slightly higher strength in dynamic tests. A balance between high diametric and low flexure strength will allow for pellets to be durable during storage, but break up easily within a mill. Further research is required to explore the relationship between pellet durability and mechanical strength.

The standard coal abrasion index test does not work for biomass as it caused the apparatus to catch fire. With the increase use of biomass in pulverised fuel combustion systems and there being no standard tests for biomass abrasion, a new test is required to quantify the abrasiveness of biomass

Chapter 5 - Application of Standard Coal Grindability Tests on Biomass

There are 2 main standard grindability tests for coal; the Hardgrove Grindability Index (HGI) for vertical spindle mills (ASTM D409 / D409M-12, 2012; The British Standards Institution, 1995), and the Bond Work Index (BWI) for tube and ball mills (Bond, 1952; Scott, 1995). Currently no standard grindability tests currently exist for biomass. Grindability studies of biomass have focused on using non-standard mills for HGI tests (Bridgeman et al., 2010; Ibrahim et al., 2013; Ohliger et al., 2013) or developing modified version of the BWI test such as the Hybrid Work Index in a planetary ball mill (Van Essendelft et al., 2013). Other milling theories have successfully been applied to hammer mills (Temmerman et al., 2013) for wood chips and wood pellet comminution. However there is no record in literature of the testing of biomass in a standard BWI test mill, and only limited studies on non-densified biomass have been conducted in a standard HGI test mill (Shang et al., 2012).

Given that the HGI and BWI tests are the standard grindability tests for coal mills used in the power generation sector, it is prudent to start this study with knowledge of the milling behaviours of the selected biomasses and coals in the standard coal grindability tests. This chapter will address the gap in knowledge of the applicability of standard coal grindability tests for densified biomasses. The chapter will also look at the grindability of a non-densified biomass (olive cake) and coal. The chapter will assess the suitability of the standard coal grindability tests for predicting biomass grindability, and if the tests can be provide to provide additional insight into mill behaviour beyond the traditional mill indices. This chapter has been published as a journal article in the journal Fuel (O. Williams et al., 2015).

5.1. Materials and Methods

This chapter investigates the applicability of the Hardgrove Grindability Index (HGI) and Bond Work Index (BWI) test on 2013 olive cake, mixed wood pellets, eucalyptus pellets, steam exploded pellets, miscanthus pellets, sunflower pellets, microwave pellets, torrefied pellets, white wood pellets, and La Loma coal. The two main milling methods tested in this section are the HGI Test (section 3.2.7) and the BWI Test (section 3.2.6). Additional methods used include pellet diameter and length measurements (section 3.1.3), pellet disintegration test (section 3.1.2), particle size distributions by sieving (section 3.1.4) with particle size distribution analysis (section 3.1.6), moisture content (section 3.1.1), thermal characteristics from the slow pyrolysis method (section 3.1.13.1), and higher heating value (section 3.1.14).

The chapter also reviews the appropriateness of each method as a test of biomass grindability.

5.2. HGI Test

Table 5.1 surmises the HGI and BWI results. Microwave, white wood, miscanthus and torrefied pellets were not tested in the HGI test due to limited quantities of material being available and limited access to the test equipment. On average, coals used in UK power stations have a HGI around 40-60 (Scott, 1995); the La Loma coal tested falls within this range with a HGI of 46. The biomasses tested performed very poorly (HGI of 14 to 22), indicating a high resistance to grinding.

Sample	HGI	F_{80} (µm)	P_{80} (µm)	G (g/rev)	RF	W_i (KWh/t)	W (kWh/t)	HHV_d (MJ/kg)	W/ HHV_d (%)
White Wood Pellets	-	6100	825	0.180	790	169	37	20.27	0.66
Eucalyptus Pellets	22	8390	757	0.340	411	87	22	19.81	0.40
Mixed Wood Pellets	18	8400	786	0.053	2141	413	102	20.41	1.80
Miscanthus Pellets	-	6290	811	0.057	2168	426	96	18.57	1.86
Sunflower Pellets	20	8620	764	0.059	1699	366	93	20.24	1.66
Olive Cake	14	3712	590	0.202	390	136	34	19.32	0.63
Torrefied Pellets	-	8000	758	2.655	60	16	4	21.77	0.07
Steam exploded pellets	29	5910	355	0.283	556	64	26	20.05	0.46
Microwave Pellets	-	5970	881	2.000	62	25	5.1	22.13	0.08
La Loma Coal	46	2709	77	0.664	242	23	22	30.00	0.26

Table 5.1:Summary of HGI and BWI Data for all Samples; Hardgrove Grindability Index HGI, 80% Passing Feed Size F_{80}, 80% Passing Product Size P_{80} , Grindability per Revolution G, Final Revolution Count RF, Bond Work Index W_i, Work Input W, Dry Higher Heating Value HHV_d, Work Input- Dry Higher Heating Value Ratio W/HHV_d

Even the steam exploded pellets showed only a nominal improvement (HGI of 29) in comparison to non-treated biomasses. The majority of samples showed the same result in the repeat test, or varied by ± 1 HGI value.

5.3. BWI Test Overall Results

In addition to the main HGI and BWI indices, table 5.1 also details the values obtained for the BWI values W_i and W calculations (equations 3.41 and 3.42 in section 3.2.6). Table 5.2 also lists the Higher Heating Values (HHV_d) and what percentage the mill work input *W* represents of the HHV_d. The HHV_d are for the milled BWI sample, and the results are very similar to those found for the pre-milled samples in section 4.12. Thus the milling process is not affecting the HHV_d values of the samples. The biomasses all had the same equilibrium sieve size of 1000 µm, while coal was set to 90 µm in order to achieve a particle size close to the 70% passing at 75 µm criterion. Miscanthus pellets had the highest Bond Work Index W_i at 426 ± 29.5 kWh/t, which had high variability due to mill choking, with mixed wood pellets (413 ±3.7 kWh/t) and sunflower pellets (366 ± 0.5 kWh/t) showing similar results. Surprisingly, eucalyptus pellets showed a much lower W_i at 87 ± 8.7 kWh/t, which was close to that of the steam exploded pellets (64 ± 0.8 kWh/t). The lowest W_i for the biomasses was for the torrefied pellets (16 ± 1.1 kWh/t), followed by microwave pellets (25 ± 0.5 kWh/t) with the La Loma coal having a similar W_i at 23 ± 0.1 kWh/t with a target size of 90 µm. La Loma coal has the highest calorific value (30 MJ/kg), with torrefied and microwave pellets having higher HHV_d than steam exploded pellets, which was on a par with the other wood pellets. The heating values for the samples found in this study corresponded to similar samples tested in literature (14-21 MJ/kg for biomass (A Demirbas, 2004; Obernberger et al., 2004) and 26-33 MJ/kg for coal (Scott, 1995)). The work input represents a low percentage of the heating value of the samples, with values ranging from 0.07% for the torrefied pellets, up to 1.86% for miscanthus pellets. Although the percentage the work input represented of its HHV_d for biomasses which choked was below 2%, it is still an order of magnitude greater than that of those biomass samples which did not choke. In the entire life cycle energy balance of the material, energy loss potential of this scale would represent a significant loss in net energy produced for sale to a power generator.

The work input (*W)* and the grindability per revolution (*G)* showed a similar order of results. Wood pellets had the highest *W* and lowest *G* at 102.3 kWh/t and 0.053 g/rev, followed closely by miscanthus and sunflower pellets (95.9 kWh/t, 0.057 g/rev and 93.1 kWh/t, 0.059 g/rev respectively). This reversal of order between these samples is due to the difference in

feed size (F_{80}) used in the calculations; miscanthus pellets are approximately 6mm in diameter, while wood and sunflower pellets diameter was approximately 8mm. Miscanthus also had a higher product size (P_{80}) value than wood and sunflower pellets, which means the difference between F_{80} and P_{80} is lower for miscanthus than for wood and sunflower pellets.

The results from the BWI tests show a wide spread of BWI values amongst the biomass samples. As expected the wood, miscanthus and sunflower pellets had W_i values an order of magnitude greater than that of the coal, and the olive cake was five times greater than coal. However the eucalyptus, which is an untreated biomass, performed almost as well as steam exploded pellets. The torrefied and microwave pellets had a significantly lower BWI than steam exploded pellets, indicating that the torrefaction processes used result in a more grindable pellet in a tube and ball mill compared to the steam exploded thermal treatment.

5.4. BWI Mill Behaviour

Figures 5.1 to 5.3 show the mass per size fraction and revolution count for each run of each sample. For wood, miscanthus and sunflower pellets the trend is very similar. The mass size fraction below the target size of 1 mm stabilises quickly to a constant mass, especially for the mixed wood pellets (a). Even though the revolution count increases from 260 to 2104, the mass produced below 1 mm remains around 100 g after the second run. Therefore the increase in revolutions is not producing any more fines, which indicates that the forces within the mill are not sufficient to break down the material. This is indicative of mill choking, which is a known issue with biomass in full scale tube-ball mills, where increasing the revolutions appears to have no impact on the amount of fines produced. The decrease in the 3.35mm+ size fraction indicates that the mixed wood pellets are breaking down into smaller sizes, so the forces are sufficient to break down the pellets. However the increase in the 1-1.7 mm size for mixed wood (a), miscanthus (b), and sunflower (c) shows that the mill is struggling to break down the pellets beyond their pre-densified particle size, FPP_{80}, (1446 µm for wood, 1311 µm for miscanthus, and 1757 µm for sunflower pellets).

Therefore the breakage mechanisms within a tube and ball mill are not suitable for the comminution of ductile materials. This test highlights that fundamentally mills that use impact, compression and attrition will struggle to breakdown ductile materials such as biomass to sizes required for pulverised fuel systems.

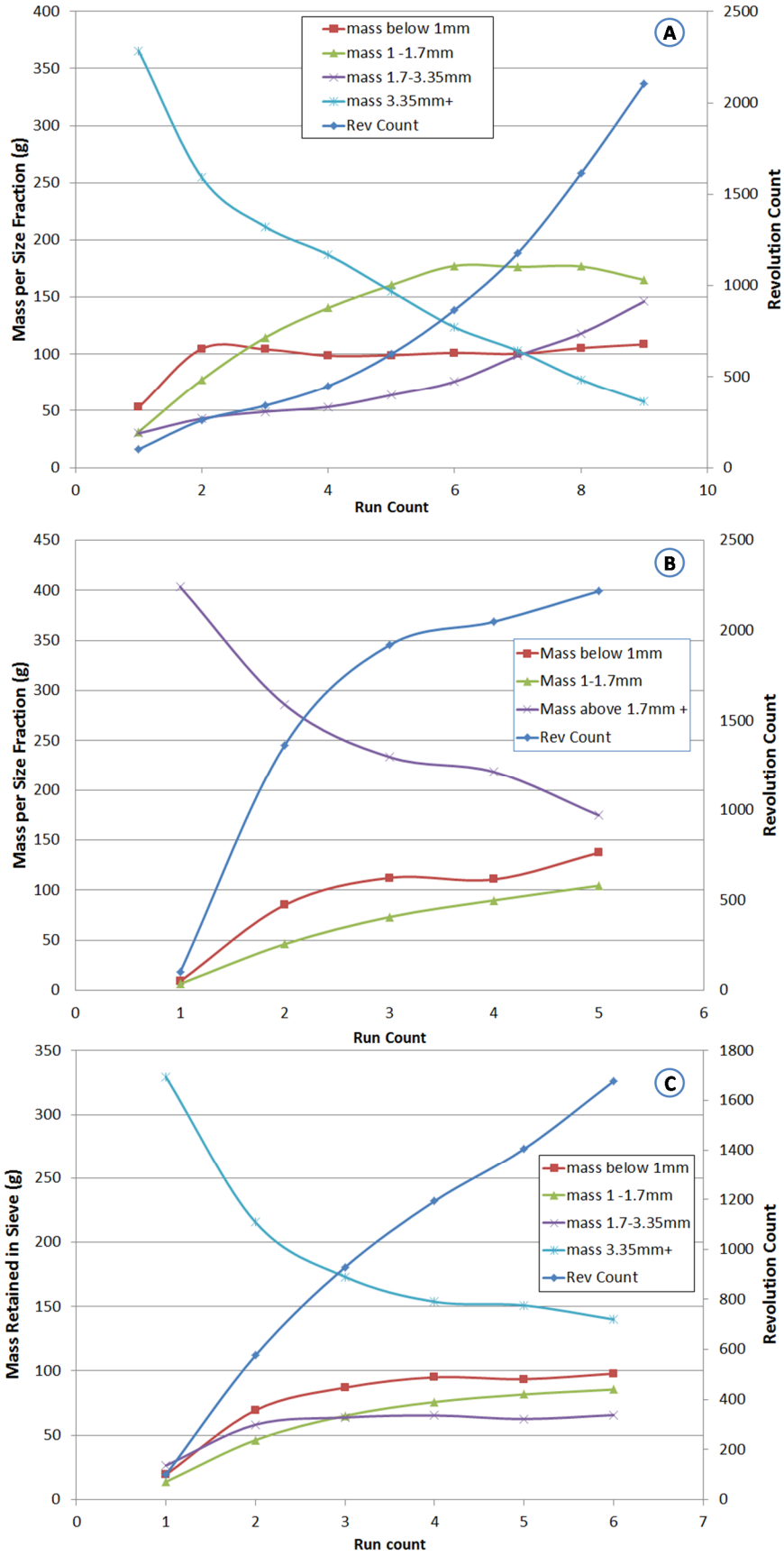


Figure 5.1: Mass per Size Fraction & Revolution Count against Run Count for BWI Test: a) Wood Pellets, b) Miscanthus Pellets, and c) Sunflower Pellets

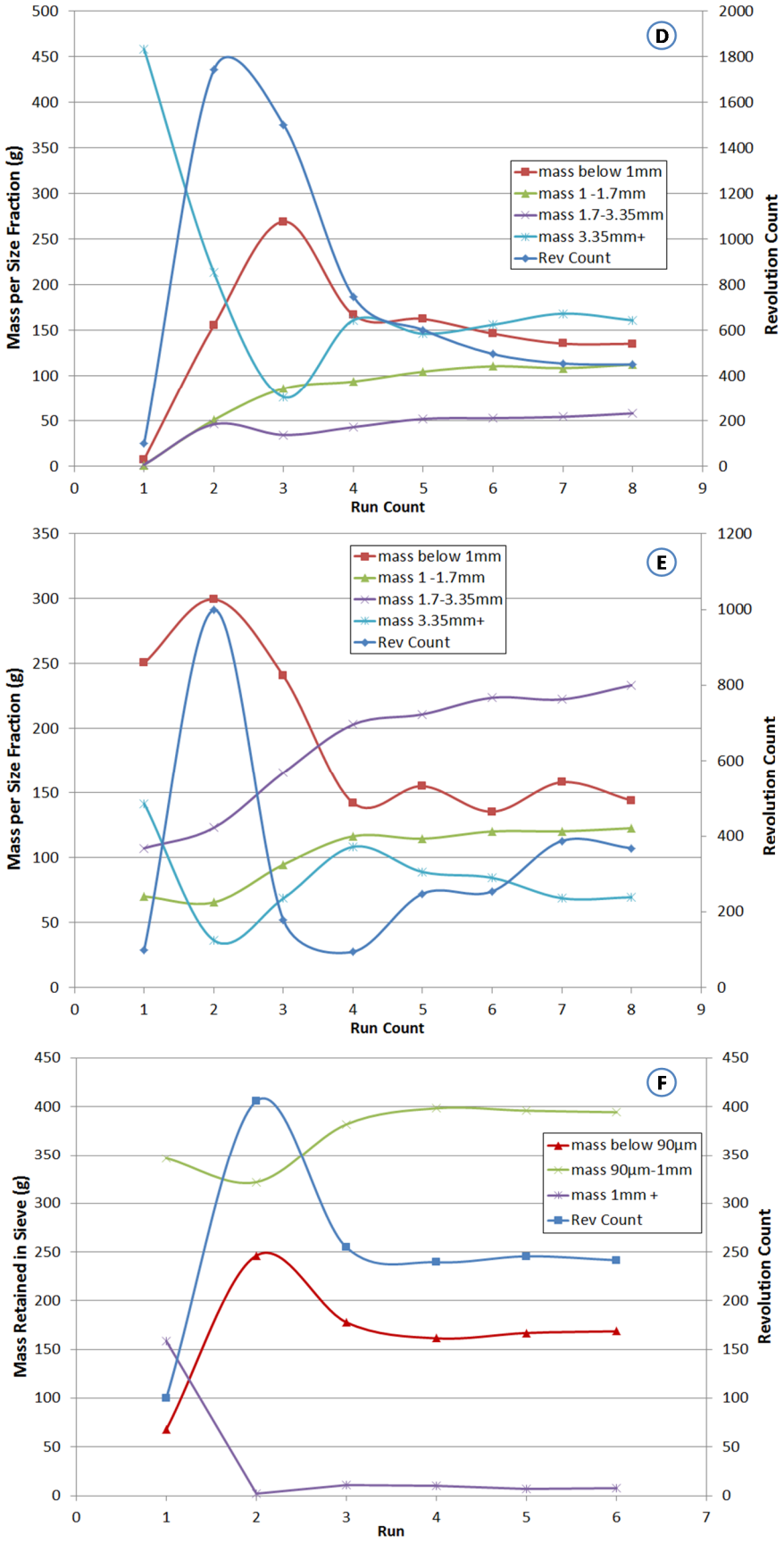


Figure 5.2: Mass per Size Fraction & Revolution Count against Run Count for BWI Test: d) Eucalyptus Pellets, e) Olive Cake, and f) La Loma Coal

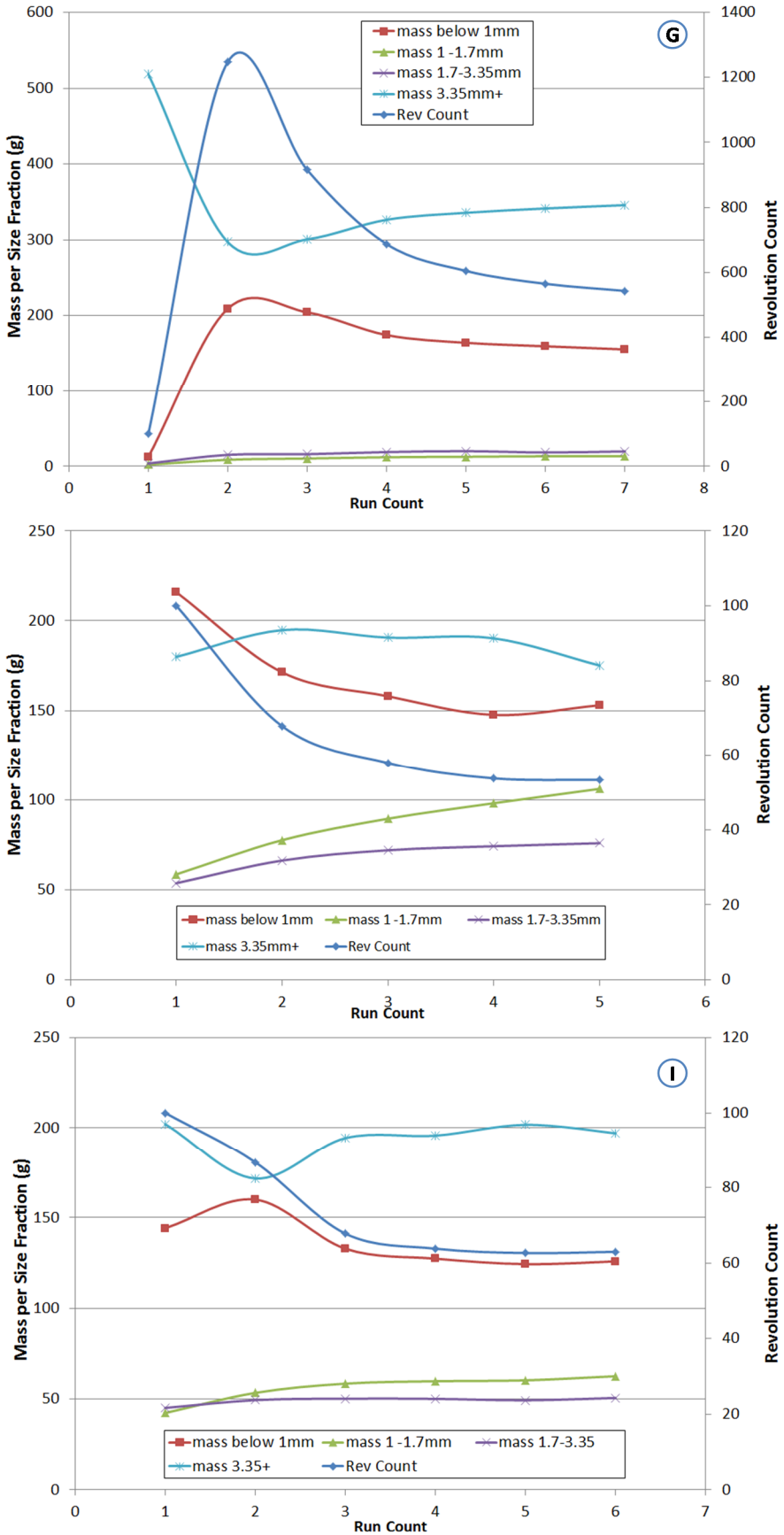


Figure 5.3: Mass per Size Fraction & Revolution Count against Run Count for BWI Test: g) Steam Exploded Pellets, h) Torrefied Pellets and, i) Microwave Pellets

Eucalyptus pellets (d) shows a different behaviour to the other untreated biomasses (Fig. 5.2). It has a FPP_{80} of 1279 µm, which although smaller than the other samples, is still above the target equilibrium size of 1 mm. The pattern of mass per size fraction and revolution count for eucalyptus indicates that the forces within the mill are sufficient to break down the material beyond its pre-densified particle size, and as the FPP_{80} is close to P_1, less energy is required to comminute compared to sunflower pellets (c) whose FPP_{80} is far from P_1. The percentage of mass produced below 1 mm follows the same pattern as the revolution count, and thus it can be deduced that the revolution count has a direct impact on the amount of fines produced, and that mill choking is not experienced in the same manner as for the other untreated biomasses.

As noted in section 6.2, olive cake is made of 3 sections: olive pulp (0-850 µm), olive pips (850-3350 µm) and olive pellets/self-formed lumps (3350 µm+), and 43% of the feed sample fell into the sub 1mm category. The graph for olive cake (e) in Figure 5.2 does not show a linear or smooth trend compared to the other samples due its heterogeneous nature despite splitting the sample to try to reduce this issue. Two distinct patterns emerged; while the revolution count does impact the amount of fines produced, the mass percentage in the 1 mm to 1.7 mm size range continually increases as the run count increases. This shows that the forces in the mill are sufficient to break down a portion of the olive cake, but not all of it, which could lead to mill choking in a full scale mill over time.

The La Loma coal (f) showed adequate grindability in the mill for its much finer target size of 90 µm. The target for La Loma coal in a tube and ball mill at EDF Energy plc coal fired power station in Cottam, UK, is 70% passing at 75 µm, and from this study the 70% passing from the 90 µm equilibrium size was 68 µm, showing a close approximation to the full scale targets. Figure 5.2 (f) shows that the mill behaviour for La Loma was similar to that of the olive cake (e), eucalyptus (d) and steam exploded pellets (g) in figure 5.3.

The thermally treated biomasses showed very different milling behaviours to the untreated biomasses as well as each other (Fig. 5.3). Steam exploded pellets (g) showed a vast improvement on milling performance compared to the untreated pellets and olive cake, but the results were comparable to the eucalyptus pellets (d). Steam exploded pellets had one of the lowest FPP_{80} at 1286 µm, but also had the finest P_{80} at 355 µm. As with olive cake (e), eucalyptus pellets (d) and La Loma (f), the first 100 revolutions led to a high second run revolution count, which quickly reduced as the runs proceeded and the material started to break down. For steam exploded pellets (g) there is virtually no sample in the 1-3.35 mm size

range, indicating that the pellets either remain intact or break up into fines during the milling process. The torrefied (h) and microwave (i) pellets showed similar behaviours within the mill (Fig. 5.3). The torrefied pellets had the highest FPP_{80} of 1537 µm but interestingly a P_{80} of 758 µm, which was comparable to the untreated biomasses. Figures 5.1 to 5.3 shows that the forces within the mill are sufficient to easily break down torrefied and microwave pellets, but some remain in the 1-3.35 mm range unlike the steam exploded pellets.

5.5. Bond Index Test Particle Size Distributions

Once the BWI test stabilised to a constant grindability rate, 3 runs were conducted at this rate and the product of these runs was combined and sieved to obtain its particle size distribution and subsequently its P_{80} value for the BWI calculations (Warren Spring Laboratory, 1962). Figure 5.4 shows the combined cumulative distributions for the product of last 3 runs of the BWI test for the biomass samples.

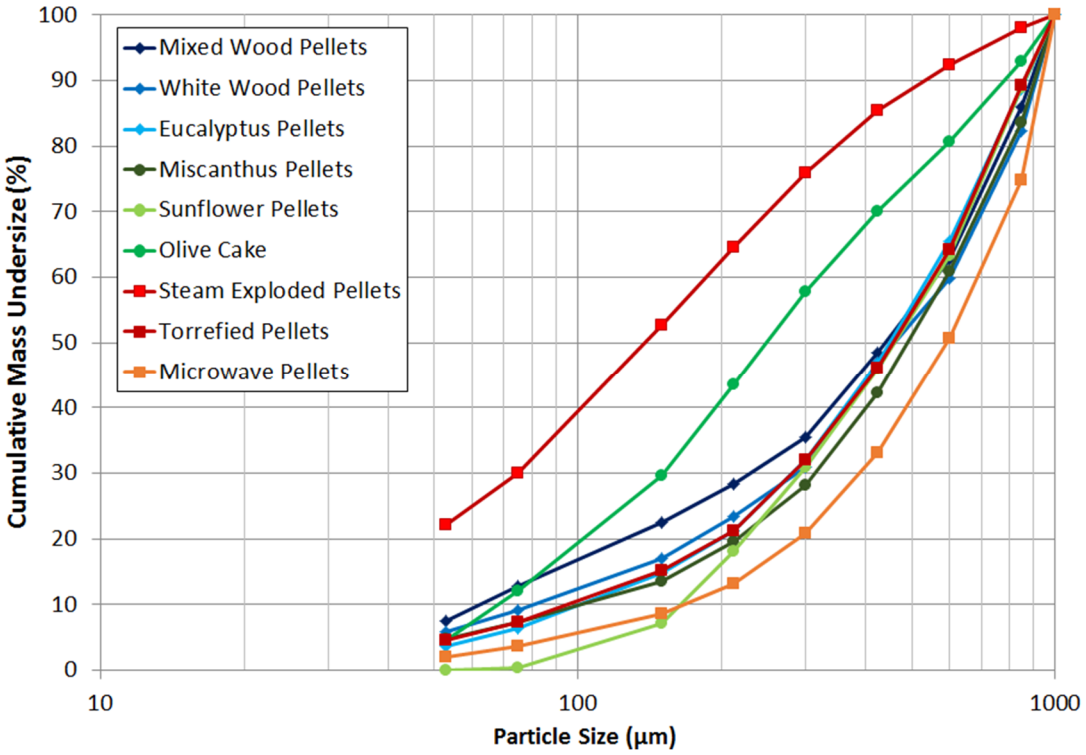


Figure 5.4: Cumulative Distributions for the Final 3 runs for Biomass Sample

Apart from olive cake and the steam exploded pellets, the particle size distributions of the biomass samples were very similar, which is reflected in the P_{80} values for the samples in table 5.1 of around 750-880 µm. Olive cake had a finer distribution due to the inclusion of 43% of the feed being fines below 1mm, while steam exploded pellets produced the finest cumulative distribution of all the biomass samples, which is reflected in its P_{80} value of

355 µm and in Figure 5.3 (g) which shows that the pellets break down into fines rather than larger particles. Microwave pellets produced the coarsest distribution. Table 5.2 shows the Rosin-Rammler data and mean geometric diameter data for the samples. There is a good fit for the samples with the Rosin-Rammler distributions (R^2 > 0.995), but quite a spread in the Rosin-Rammler distribution parameter *n*, varying between 0.97 for the steam exploded pellets up to 1.96 for the microwave pellets. Lower *n* represents a wider distribution, and thus a higher diversity of particle sizes. This is also reflected in the higher geometrical standard deviations (*s*) with steam exploded and olive cake having highest values (2.89 and 2.60 respectively).

Sample	P_{80} (µm)	d' (µm)	n	R^2	d_{gw} (µm)	s
White wood Pellets	825	568	1.5	0.990	466	1.9
Eucalyptus Pellets	757	541	1.6	0.997	410	1.8
Mixed Wood Pellets	786	530	1.3	0.989	412	1.9
Miscanthus Pellets	811	582	1.6	0.994	451	1.7
Sunflower Pellets	764	557	1.8	0.997	409	1.7
Olive Cake	590	360	1.2	0.997	276	2.6
Torrefied Pellets	758	544	1.6	0.996	420	1.7
Steam exploded Pellets	355	210	1.0	0.999	141	2.9
Microwave Pellets	881	668	2.0	0.990	593	1.4
La Loma Coal	77	59	2.8	0.983	50	1.6

Table 5.2: Rosin-Rammler and Geometric Mean Diameter Analysis of Cumulative Distributions of Product from Final 3 Runs; 80% Passing Product Size P_{80} , Rosin-Rammler Characteristic Particle Size d', Rosin-Rammler Size Distribution Parameter n, Rosin-Rammler Coefficient of Determination R^2, Geometric Mean Diameter d_{gw}, Geometric Standard Deviation s

This indicates that the product output is very dependent on material type, but for most untreated biomasses the output will be similar in product size and distribution, regardless of the W_i values obtained. As expected from other biomass milling studies (Bitra, Womac, Chevanan, et al., 2009; Gil et al., 2012) and mathematically, the geometric mean diameter from the ball milling is smaller than the Rosin-Rammler size parameter for all samples.

5.6. Impact of Pre-densified Pellet Particle Size on Bond Work Index

Table 5.3 shows the impact of changing the feed size from pellet diameter (F_{80}) to the 80% passing size for the pre-densified pellet particle size (FPP_{80}) on the BWI (WPP_i) and Work Input

(*WPP*) values. By using FPP_{80}, the WPP_i value of BWI is significantly higher than the W_i value for pellet diameter, as the FPP_{80} creates a lower denominator in the BWI equation (eq. 3.41 in section 3.2.6). This implies that less energy is required to break the pellets back down to their pre-densified particle size than is involved in breaking the particles into smaller particles. The implication is that for biomass pellets there are two stages of milling occurring. The first is the breaking down of the pellets into smaller parts or back to the pre-densified particle sizes, and the cohesive forces involved in holding together the pellets are weak and easy to overcome in the mills. The second stage of milling is the breaking down of the pre-densified particles into smaller particles. This suggests that to reduce energy consumption and potential for mill choking, the pellets should be formed of particles close to the required target size. This would reduce the milling to solely the pellet comminution phase and minimise mill choking by eliminating the particle comminution stage.

	Wood Pellets	Miscanthus Pellets	Sunflower Pellets	White Wood Pellets	Eucalyptus Pellets	Steam exploded Pellets	Torrefied Pellets	Olive Cake	La Loma Coal
FPP_{80} (µm)	1446	1311	1757	1458	1279	1286	1537	3712	2709
WPP_i (KWh/t)	1086	1271	756	430	263	102	38	136	23
WPP (KWh/t)	102	95	93	37	22	26	4	33	22

Table 5.3: Pellet Particle Size FPP_{80}, and Revised Bond Work Index WPP_i, Work Input WPP for Pellet Particle Size FPP_{80}

5.7. Thermal Composition of the Samples

Table 5.4 shows the thermal characterisation of the samples on a dry basis across all the BWI runs. There is no appreciable difference in the composition of the samples during the test based on the standard deviations shown for each value. The highest fixed carbon for the biomasses was for torrefied pellets at 23.9%, followed by olive cake (18.4%) and the steam exploded pellets at 17.3%. Both treated biomasses had higher fixed carbon than the other untreated woody biomasses. The percentage component values for the samples in this study corresponded to similar samples tested in literature (A Demirbas, 2004).

The values obtained from the BWI milled samples were virtually the same as those obtained for the pre-milled samples in section 4.12. Thus, as with the higher heating values, milling has no significant impact on the thermal composition of the biomass or coal samples.

Eucalyptus, torrefied, wood and steam exploded pellets showed a similar peak volatile release rate (0.8-1.1 %/°C) and peak volatile release temperature (327-338 °C).

Sample	Moisture (%)	Fixed Carbon (%)	Ash (%)	Dry Volatiles (%)	Peak Vol. Release Temperature (°C)	Peak Vol. Release Rate (%/°C)
Eucalyptus Pellets	8.2 (0.1)	11.6 (1.8)	3.2 (0.4)	85.2 (2.0)	338 (0.5)	1.1 (0.03)
Mixed Wood Pellets	8.4 (0.3)	13.3 (1.9)	4.1 (0.4)	82.6 (1.9)	337 (0.6)	0.8 (0.02)
Miscanthus Pellets	7.9 (0.3)	15.9 (1.3)	12.6 (1.8)	71.6 (1.0)	285 (1.0)	0.6 (0.03)
Sunflower Pellets	9.1 (0.2)	15.7 (0.6)	5.8 (0.9)	78.5 (0.5)	310 (0.5)	0.8 (0.04)
Olive Cake	7.5 (1.3)	18.4 (1.3)	10.3 (0.7)	71.4 (1.7)	288 (1.9)	0.5 (0.02)
Torrefied Pellets	6.6 (0.2)	23.9 (1.3)	3.7 (0.1)	72.4 (1.2)	327 (0.2)	1.0 (0.02)
Steam exploded Pellets	5.7 (0.3)	17.3 (1.5)	4.3 (0.6)	78.5 (1.1)	330 (0.5)	1.0 (0.03)
La Loma Coal	7.1 (1.2)	53.8 (0.9)	5.9 (1.0)	40.3 (1.1)	419 (0.5)	0.3 (0.01)

Table 5.4: Thermal Composition Data for the Samples from TGA on wt.% of Dry Fuel (Standard Deviation Across all Runs are shown in Brackets)

Olive cake and miscanthus pellets showed a much lower peak volatile release rate (0.5 and 0.6 %/°C respectively) and peak volatile release temperature (288 and 285 °C respectively), which is an important consideration in coal mills, which can introduce preheat air between 200 °C to 300 °C. La Loma showed the highest peak volatile release temperature (420 °C), but lowest peak volatile release rate (0.3 %/°C).

5.8. Suitability of HGI test for Biomass

The HGI test is the most commonly used grindability test for biomass, although usually in modified form. Ohliger et al. (2013) found very high HGI values for torrefied beech wood, but the crushing ratio (the average particle size before milling divided by the average particle size after milling) for the same samples were lower than that of lignite, indicating that the high HGI values can be misleading when analysed by themselves. A HGI equivalent using a Retsch PM100 planetary ball mill was developed by Bridgeman et al. (2010), and has been used by Ibrahim et al. (2013) to find HGI values as high as 86.4 for torrefied willow. These

figures have been compared to coals tested as per international HGI testing standards (ASTM D409 / D409M-12, 2012; The British Standards Institution, 1995) by Li et al. (2014), and superficially appear to show a vast improvement in grindability, with the potential to be better than some coals. However the HGI figures reported by Bridgeman and Ibrahim are not from the same method (and apparatus) and caution is required when comparing HGI values that are not derived from a Hardgrove machine. Hardgrove testing machines use compression breakage modes similar to those in a vertical spindle mill, whereas planetary ball mills use high impact breakage modes (Perry et al., 2008). The HGI test was developed for coal fired power plants, and the target 75 µm size is based on what is required for combustion in pulverised fuel coal burners (Afolabi, 2012; Freeman et al., 2000). However biomass has a target particle size closer to 1000µm for pulverised fuel burners. For a 150 kW pilot burner, the optimal burn conditions for wood feed stocks was 95% of particles (by weight) were smaller than 1000 µm with a moisture content lower than 15% (Esteban et al., 2006), and Tamura et al. (2014) showed that unblended pulverised wood smaller than 1 mm shows volatile release and char burnout behaviour similar to that of high volatile sub-bituminous coal when 75% by weight is smaller than 75 µm. As noted in section 2.11, the Stokes number is dependent not only on the sphericity of the particle but also its Reynolds number, it's possible for large biomass particles to have similar aerodynamic properties to that of a much smaller coal particle provided it has a sufficiently low sphericity (Mandø et al., 2010). Therefore a grindability test which aims to analyse the grindability of biomass to 75 µm is inappropriate, as the target size for optimal combustion of biomass and the setting for the classifier output from full scale mills is an order of magnitude of higher than this. In addition, the critical particle size for compressed fracture should be ascertained for biomasses to be milled in coal mills, as below this size the biomass will behave as a ductile material and mills which use compression and impact forces will not be able to further reduce the particle size. Coal has a critical particle size of 5 µm, while polystyrene's is 4.48 mm (Kendall, 1978), but the critical crack length of biomasses used in PF combustion is unknown.

5.9. Comparison of HGI and BWI Methods

Table 5.5 compares the BWI and HGI tests. The HGI test is very constricted in its setup compared to the BWI test. The feed sample is already within the target size range (600 µm to 1180 µm) and the mass size is small in comparison to the BWI test. Even with the modified HGI test the volume is still limited to a small unrepresentative volume (50 cm^3)

(Agus et al., 1971; Bridgeman et al., 2010; Ibrahim et al., 2013; Ohliger et al., 2013; Sengupta, 2002). The BWI test has the advantage of being based on a larger volume (700 ml) and with a variable target size, so the impact of target particle size on the grindability of materials can be investigated.

	BWI	**HGI**
Mill Comparison	Tube & Ball mill	Babcock & Wilcox mill (ring-ball)
Target Particle Size	Any size below 3.35mm	75µm
Particle Size Range	<3.35mm (powder) or pellet size	1.18mm-600µm
Mass constriction	Volume – 700ml	Mass – 50g
Output	kWh/ton	HGI Index
Suitable materials	Brittle materials	Good quality coals

Table 5.5: Comparison of HGI & BWI Test Conditions

The output of the BWI test is also in a more useable form of energy consumption per ton (kWh/t), which allows the method to be compared to other forms of milling such as hammer mills (Temmerman et al., 2013) or planetary ball mills (Van Essendelft et al., 2013) which already have modified work indices based on the theories of comminution. Therefore, it can be concluded that HGI is a poor method of testing the grindability of biomass in vertical spindle mills and a new standard grindability test is required to test the grindability of biomasses. A larger, more representative, volume of material and a target particle size close to that required for the PF burners and mill classifiers is important. It is also important that the grindability test identifies the failure mechanism in use and subsequent impact on particle characteristics.

5.10. HGI and BWI Correlations for Biomass

Figure 5.5 shows BWI plotted against HGI for the biomass and coal samples. In addition to the experimental data, the Bond and McIntyre and Plitt correlations are plotted for the sample HGI data. The wood and sunflower pellets show no relation to the other points due to the mill choking experienced during the BWI test. While none of the experimental results are close to the Bond correlation, the La Loma coal does lie near the McIntyre and Plitt correlation. This is to be expected as this correlation was based on similar materials with a W_i above 8.5 kWh/ton (McIntyre et al., 1980). While the olive cake, eucalyptus and steam exploded pellets do not sit close to the Bond or McIntyre and Plitt correlations, they do show a similar trend of decreasing BWI with increasing HGI. Using non-linear regression analysis, the biomass best fit line was determined by Gauss-Newton method is defined as:

$$W_i = \frac{2017}{HGI^{1.02}} \quad \text{(eq. 5.1)}$$

However it should be noted that this correlation is based on a very limited number of samples and is only applicable for the test equipment and experimental conditions used to obtain the W_i and HGI values.

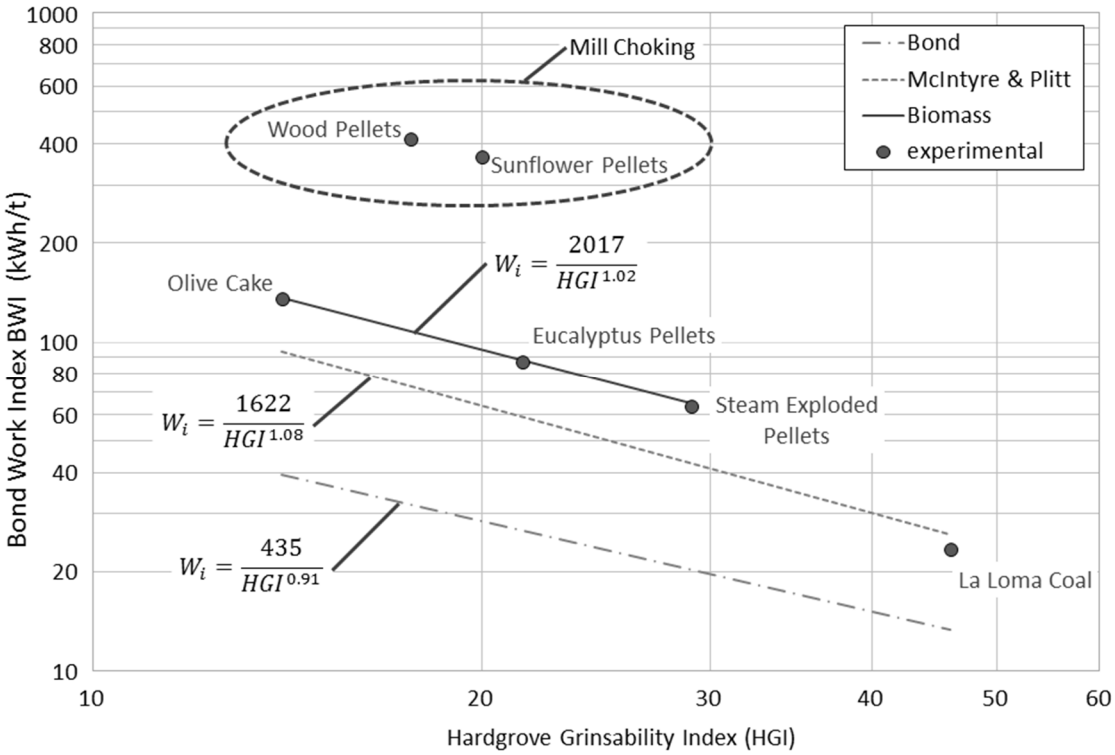


Figure 5.5: Bond Work Index (BWI) versus Hardgrove Grindability Index (HGI)

5.11. Conclusions

HGI is a poor indicator of the grindability of biomass in a vertical spindle mill, and can give misleading results when analysed alone. Grindability tests which aim to analyse the grindability of biomass to 75 µm are inappropriate, as the target size for optimal combustion of biomass and the setting for the classifier output from full scale mills is an order of magnitude of higher than this. The BWI test can be used to analyse the mill behaviour of biomass in a tube and ball mill. Wood, miscanthus and sunflower pellets exhibited mill choking during the BWI test, as the amount of fines produced did not increase with an increasing revolution count. Thus the BWI can be used to see if biomass samples are likely to encounter mill choking prior to full scale mill trials. The BWI results show that there are two stages of milling occurring in biomass pellets. The first is the breaking down of the pellets into smaller parts or back to the pre-densified particle sizes, where the cohesive forces involved in holding together the pellets are weak and easy to overcome in the mills. The

second stage of milling is the breaking down of the pre-densified particles into smaller particles. However, the forces involved in this second stage are much greater than the initial pellet breakage stage. Therefore, to optimise milling in a coal mills, biomass pellets should be composed of particles close to the required size so that only the pellet comminution stage occurs.

Whilst it has been shown that the BWI test is a useful test for analysing and predicting the mill behaviour of biomass in a tube and ball mill, the HGI test is not suitable for predicting the grindability of biomass in vertical spindle mills. A new standardised grindability test is therefore required to test the grindability of biomasses in these types of mills.

Chapter 6 - Planetary Ball Mill

In biomass applications, planetary ball mills are mainly used to reduce the crystallinity of biomass in the biological conversion of cellulosic biomass into fuels and chemicals (Blair, 2014). Planetary ball milling optimisation studies have focused on the impact of dry ball milling on cellulose structure, morphology and properties (Avolio et al., 2012), and have also been used to investigate the increase in surface area of biochars through process optimisation (Peterson et al., 2012).

Planetary ball mills have been used to assess the grindability of biomass through modified HGI tests (Bridgeman et al., 2010; Ohliger et al., 2013), which have been used to analyse the improvement in grindability through the torrefaction of biomass materials (Ibrahim et al., 2013). Planetary ball mills have also been used to develop hybrid work indexes for torrefied materials (Van Essendelft et al., 2013). However neither the milling of densified materials within a planetary ball mill nor the optimisation of a planetary ball mill for biomass particle size reduction has been examined in the literature. This chapter will investigate the impact of changing mill variables on the comminution of biomass in a planetary ball mill, and the optimising these variables for analysing the impact of drying on milling behaviour.

6.1. Materials and Methods

Olive cake 2013 was used for the optimisation study as it was being co-combusted with coal at EDF Cottam at the time of the study. Olive cake 2013 was also used for the heat generation and caking study within planetary ball mills. For the material comparison study, 2013 and 2014 olive cake, olive pellets, mixed wood pellets, eucalyptus pellets, steam exploded pellets, miscanthus pellets, sunflower pellets, and microwave pellets were used. The planetary ball mill optimisation study followed the method outlined in section 3.2.3.1. Data analysis used multiple non-linear regression analysis to analyse model fit and model optimisation as described in section 3.2.2. The material comparison and impact of drying study was conducted as per section 3.2.3.2. DSC was conducted as per section 3.1.12.

6.2. Planetary Ball Mill Optimisation Study

The planetary ball milling study analysed the impact of changing mill settings on the milling behaviour of olive cake 2013. Olive cake is a composite material composed of three distinct sections: 0-850 µm pulp section, 850-3350 µm pip section, and 3350 µm+ pellet or self-formed lumps section, as illustrated in figure 6.1. The particle size distribution was obtained

by sieving a portion of the as received product (split using a riffle box) in 16 size fractions according to section 3.1.4. The olive cake was known block screw augers and other parts of the milling and conveying system at EDF Cottam, as it forms a solid cake during the process which is difficult to remove. Thus one of the aims of the study was to try to replicate the caking phenomenon on a laboratory scale and understand the conditions under which caking occurred. From a power generation perspective, the caking of materials is undesirable as it causes blockages and increased motor loads in the conveying and comminution system.

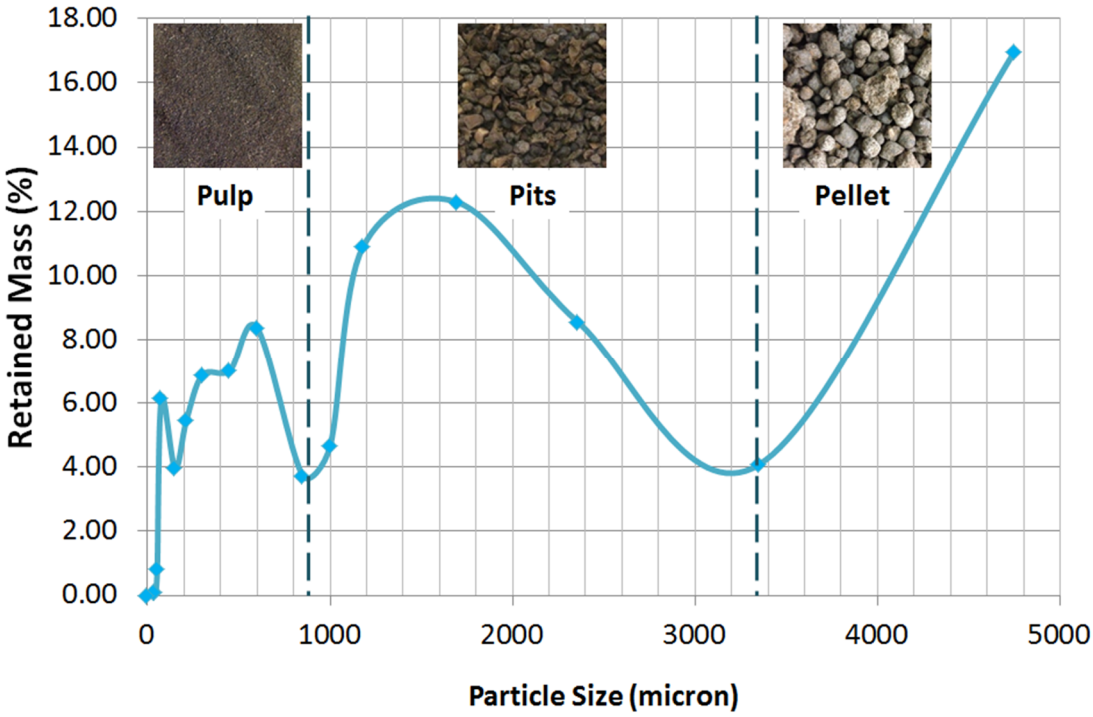


Figure 6.1: Tri-modal Structure of as Received Olive Cake 2013 Obtained by Sieving

Three main mill variables were analysed during the study, as described in detail in section 3.2.3.1.; these being speed, volume and energy input. The milling time and particle size distribution were obtained for the settings in table 6.1. All speeds and energy settings were tested for 100 and 200 ml. For 150 ml, the energy inputs were measured for one speed (400RPM). The mass of the sample at 100 ml was 70 g, 150 ml was 105 g, and at 200 ml was 140 g. All tests were conducted in triplicate, resulting in 192 runs in total.

Energy Input (kJ)	0.1	0.5	1	2	4	8
Speed (RPM)	200	300	400	500	600	
Volume (ml)	100	150	200			

Table 6.1: Mill Settings used for Mill Optimisation Tests in Planetary Ball Mill

6.2.1. Milling Specific Effective Energy Consumption Rate Optimisation

The specific effective energy consumption rate ($\dot{E}_i$) is a measure of how quickly the specified energy input (table 6.1) was consumed during the experiment for the set volume and speed. Multiple nonlinear regression analysis was used to analyse impact of different speeds, volumes and energy inputs on $\dot{E}_i$, and the data used in the regression analysis can be found in Appendix B. In order to eliminate unusual data points, the 192 measured points were reduced by the model to 114 points, which is a large enough sample size to provide a precise estimate of the strength of the relationship with no issues with normality. Most of the points removed were at low energy inputs, where the mill only ran for short periods and resulted in similar data points across all speeds and volumes. The model had a 98.9% fit for the model with a *p-value* below 0.001, thus the relationship obtained is statistically significant and almost completely explained by the model. The final model equation obtained for the specific effective energy consumption rate ($\dot{E}_i$) is:

$$\dot{E}_i = 0.057 + 0.006353x_1 - 0.01114x_2 - 0.0066x_3 + 0.000002x_1^2 + 0.000059x_2^2 - 0.01375x_3^2 - 0.000036x_1x_2 \quad \text{(eq. 6.1)}$$

Where x_1 is speed (RPM), x_2 is volume (ml) and x_3 is energy input (kJ). From the stepwise regression, speed was the greatest contributor to the model, with around a 60% increase in the fit of the model compared to 45% for volume and 5% for energy input. Thus the order of impact on energy consumption is Speed > Volume > Energy input for a planetary ball mill. Burgio et al. (1991) demonstrated that speed is the dominant element in collision theory in ball mills, which is reflected by the results of this regression model. The model showed a strong interaction between all the variables, as noted in figure 6.2.

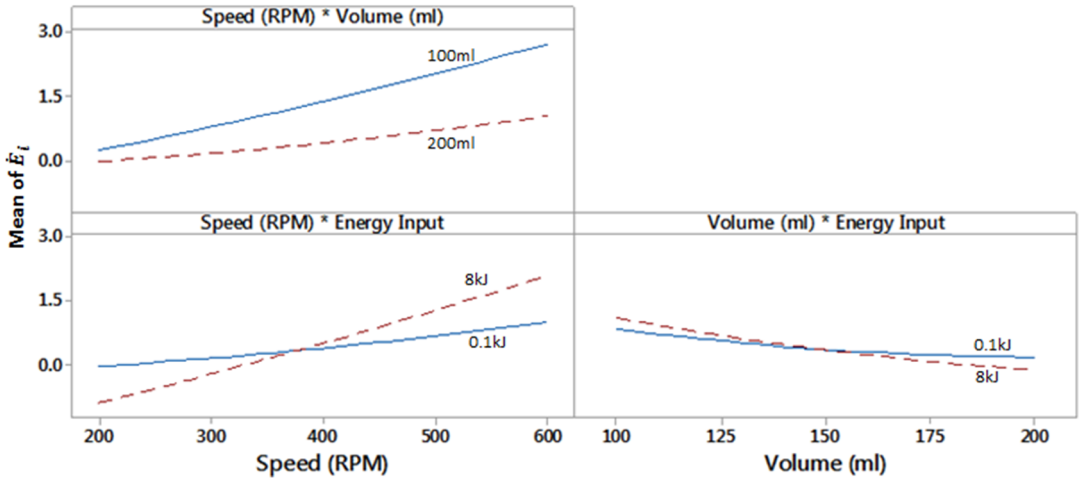


Figure 6.2: Interaction Plots of the Variables in the Specific Effective Energy Consumption Rate Regression Analysis for the Planetary Ball Mill

The strongest interaction in the model was between speed and volume, which are also the largest individual contributors. There was a reduction in specific effective energy consumption rates with increasing volume (Fig. 6.2), and this is due to there being less space for balls to move within the milling bowl with larger volumes, resulting in lower momentums and impact forces, thus taking longer for the mill to use the set energy input. The next strongest interaction is between speed and energy input; low speeds and energy inputs will result in higher energy consumption rates, but at speeds over 375 PRM high speeds and high energy inputs will result in higher energy consumption rates. This is due to the time it takes for the energy consumption rate to stabilise within the mill. Figure 6.3 shows $\dot{E}_i$ against time for the 5 speeds for 100 ml of sample.

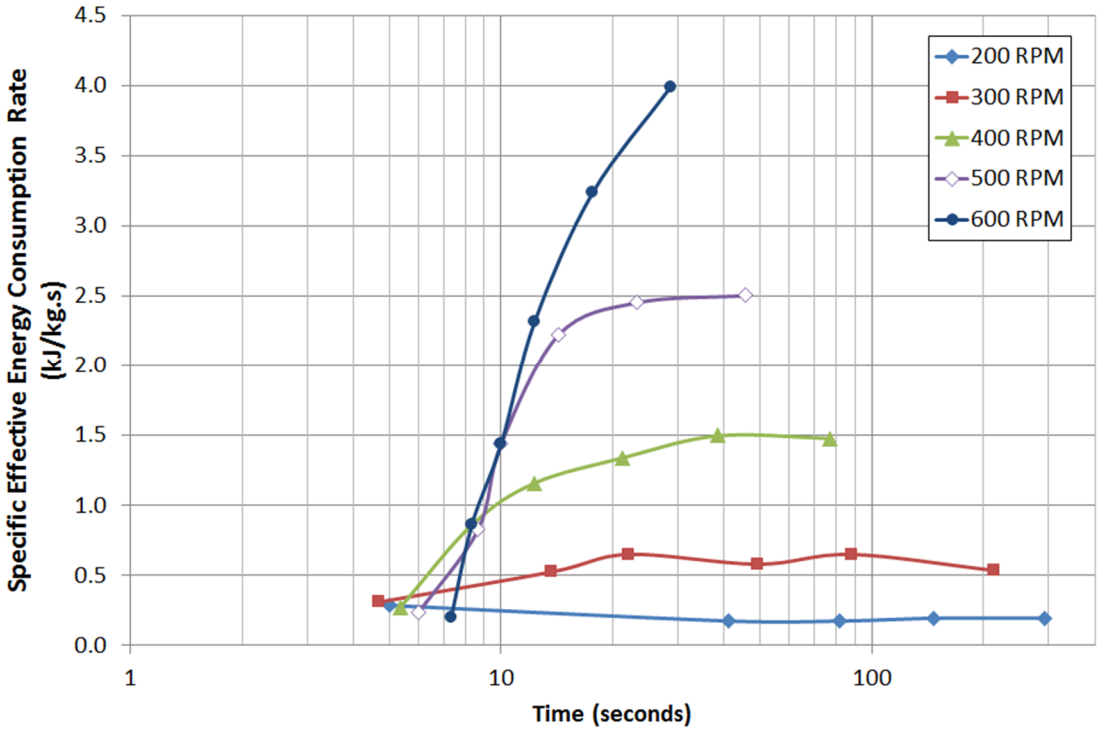


Figure 6.3: Specific Effective Energy Consumption Rate against Time for 100ml of Sample

For low energy inputs, the time taken to input the energy is similar for all speeds. However as the energy input increases, $\dot{E}_i$ can be seen to stabilise for each speed after 30 to 40 seconds of running. For 200 RPM the energy consumption rate reduces to a lower level as the energy input increases, which is reflected in figure 6.2. The weakest interaction in the model is between volume and energy input. During the tests the caking effect was noted in higher speed and volume runs and thus following the optimisation study, the impact of speed and time on heat generation within the mill was investigated, which is discussed in section 6.3.

6.2.2. Optimisation of Rosin-Rammler Size Parameter

The Rosin-Rammler size parameter, *d'*, is the characteristic particle size of the distribution, and equivalent to 63.2% of particles undersize (section 3.1.6). A multiple non-linear regression analysis was conducted on *d'* of the sieved product from the planetary ball milling optimisation experiments to analyse how the characteristic particle size changed with varying mill conditions. The data used in the regression analysis can be found in table in Appendix B. The 192 measured points were reduced by the model to 143 points in order to eliminate unusual data points, which is a large enough sample size to provide a precise estimate of the strength of the relationship with no issues with normality. The model had an 89.4% fit for the model with a *p-value* below 0.001, thus the relationship obtained is statistically significant and almost completely explained by the model. The 10.7% unexplained portion of the model is likely to be related to the heterogeneous nature of the material. The final model equation obtained for Rosin-Rammler size parameter, *d'*, for olive cake is:

$$d' = 1111.4 - 0.5433x_1 + 2.436x_2 - 318.3x_3 + 17.31x_3^2 + 0.2553x_1x_3 \qquad \text{(eq. 6.2)}$$

Where x_1 is speed (RPM), x_2 is volume (ml) and x_3 is energy input (kJ). From the stepwise regression used to create the model, energy input is by far and away the largest contributor to the model, with a 65% increase in fit with its addition to the model. Volume is the next significant factor, with speed only making a small impact on the model. This suggests that the reduction in particle size is mainly due to the duration of milling time, and thus while a constant energy consumption rate will be reached after 30 to 40 seconds (Fig. 6.3), for olive cake, the continued application of force will result in a finer particle size. To minimise the particle size, the regression model suggests a low speed (200 RPM), low volume (100 ml) and large energy input (8 kJ). Only one interaction was found in the model, which was between speed and energy input, as shown in figure 6.4.

The interaction shows that at low energy inputs there is a small reduction in *d'* as speed increases, and this is likely to be due to the very short running times experienced at low energy inputs (Fig. 6.3). At higher energy inputs the opposite trend can be seen. This is due to two factors. Firstly there is a significant difference in the mill durations for an 8 kJ input at 300 RPM (213 seconds) compared to 600 RPM (29 seconds). As the energy consumption rate takes 30 to 40 seconds to stabilise (Fig. 6.3), an energy input of 8 kJ is not enough to reach

the stable energy consumption rate for high speeds, and thus the mill does not operate for long enough to comminute the material to a fine particle size.

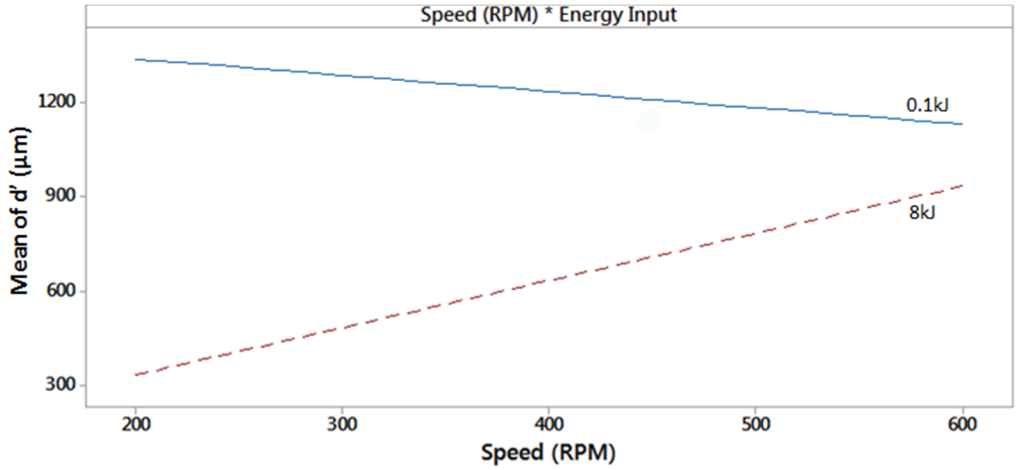


Figure 6.4: Interaction between Speed and Energy Input for Rosin-Rammler Size Parameter Regression Analysis

The second factor is that at higher speeds, caking is observed, and thus the material agglomerates and forms a large solid mass within the mill, as shown in figure 6.5 (a). At low speeds and high energy inputs, i.e. long milling durations, the olive cake started to dust as it was milled to a finer and finer particle size, also illustrated in figure 6.5 (b).



Figure 6.5: Caking of Olive Cake within the Planetary Ball Mill at 600 RPM, 200 ml and 8 kJ mill settings (a) and dusting at 200 RPM, 200 ml and 8 kJ mill settings (b)

6.3. Heat Generation and Caking within a Planetary Ball Mill

During the optimisation study, it was noted that in addition to the caking phenomenon, some conditions generated high amounts of heat during the milling process. In order to investigate these phenomena, two tests were conducted. The first test analysed the impact

of time on heat generation for a set speed and volume. The mill was operated at 200 RPM for 100 ml of olive cake for 10, 20, 30, 40, and 50 minutes. Immediately after milling thermal images were taken of the milling bowl, milling balls and comminuted sample to see how much heat had been generated during the milling process. The second test investigated the impact of speed on heat generation for a set time and volume. The mill was operated for 60 seconds for 100 ml of olive cake at 100, 200, 300, 400, 500, and 600 RPM. As with the time test, immediately after milling thermal images (section 3.5) were taken of the milling bowl, milling balls and comminuted sample.

From the thermal imaging results (Fig. 6.6 and 6.7), increasing speed will have a greater impact on heat generation within the mill than increasing time. Even after 50 minutes of operation, the heat generated within the mill at 200 RPM is similar to that of operating the mill for 60 seconds at 500 RPM. Given that speed is the greatest influencer on the energy consumption rates (section 6.2.1), the thermal imaging results show that a large portion of this imparted energy is transferred into heat. Venkataraman and Narayanan (1998) showed that the contact area during collisions in a ball mill will be relatively small, but result in high average stresses in the contact areas. As contact times are short, there is little time for heat dissipation and stress relaxation, leading to high stress gradients in the particles caught between the colliding bodies, with high energy densities in the contact areas. These factors result in localised and transient hotspots, as emphasised by the higher speed thermal images in figure 6.7, when the energy densities will be at their greatest. As caking was observed also at higher speeds, it can be inferred that caking is related to the heat generation within the olive during the milling process.

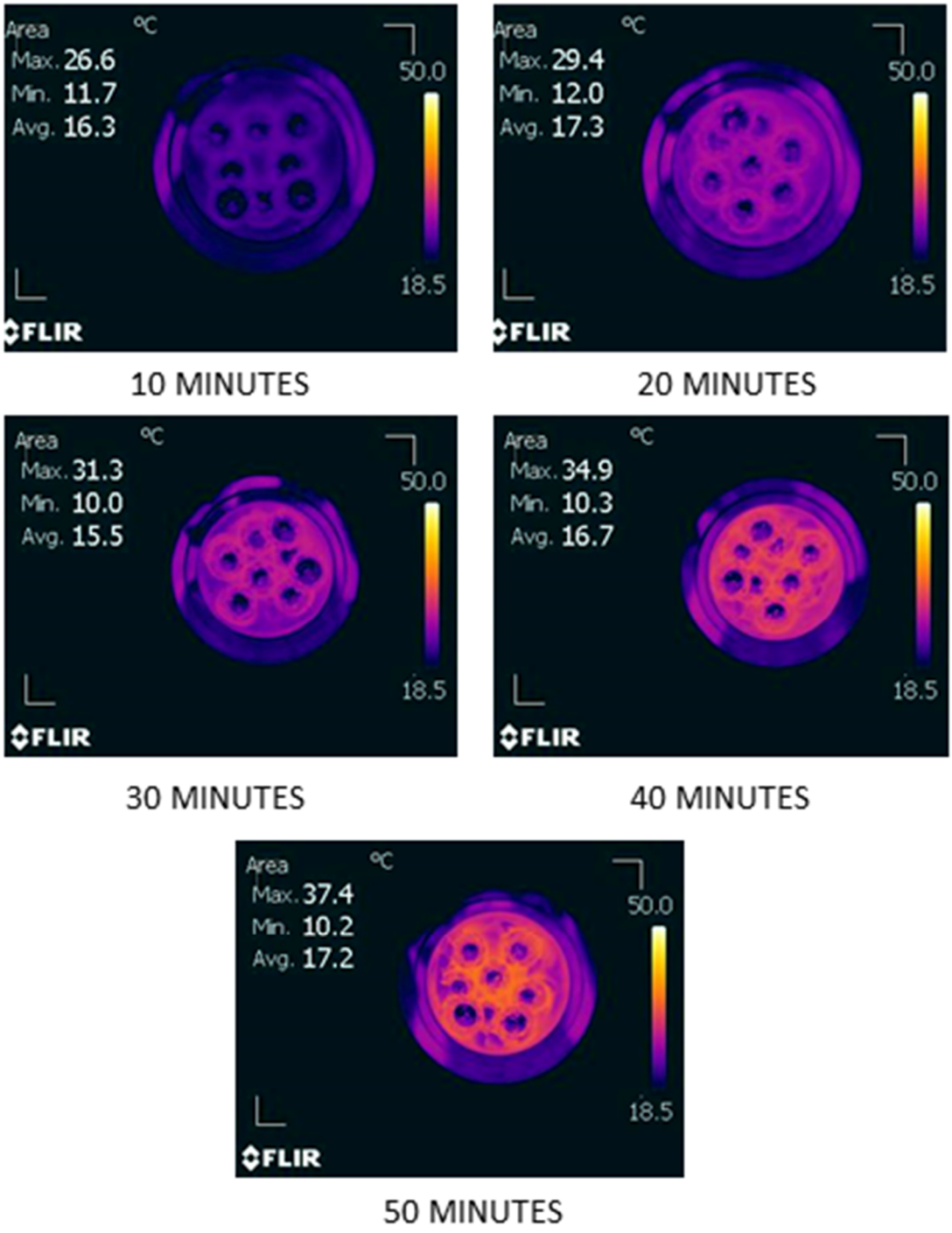


Figure 6.6: Thermal Imaging of Heat Generation in Olive Cake Milled in a Planetary Ball Milling at 200 RPM for 10-50 Minutes

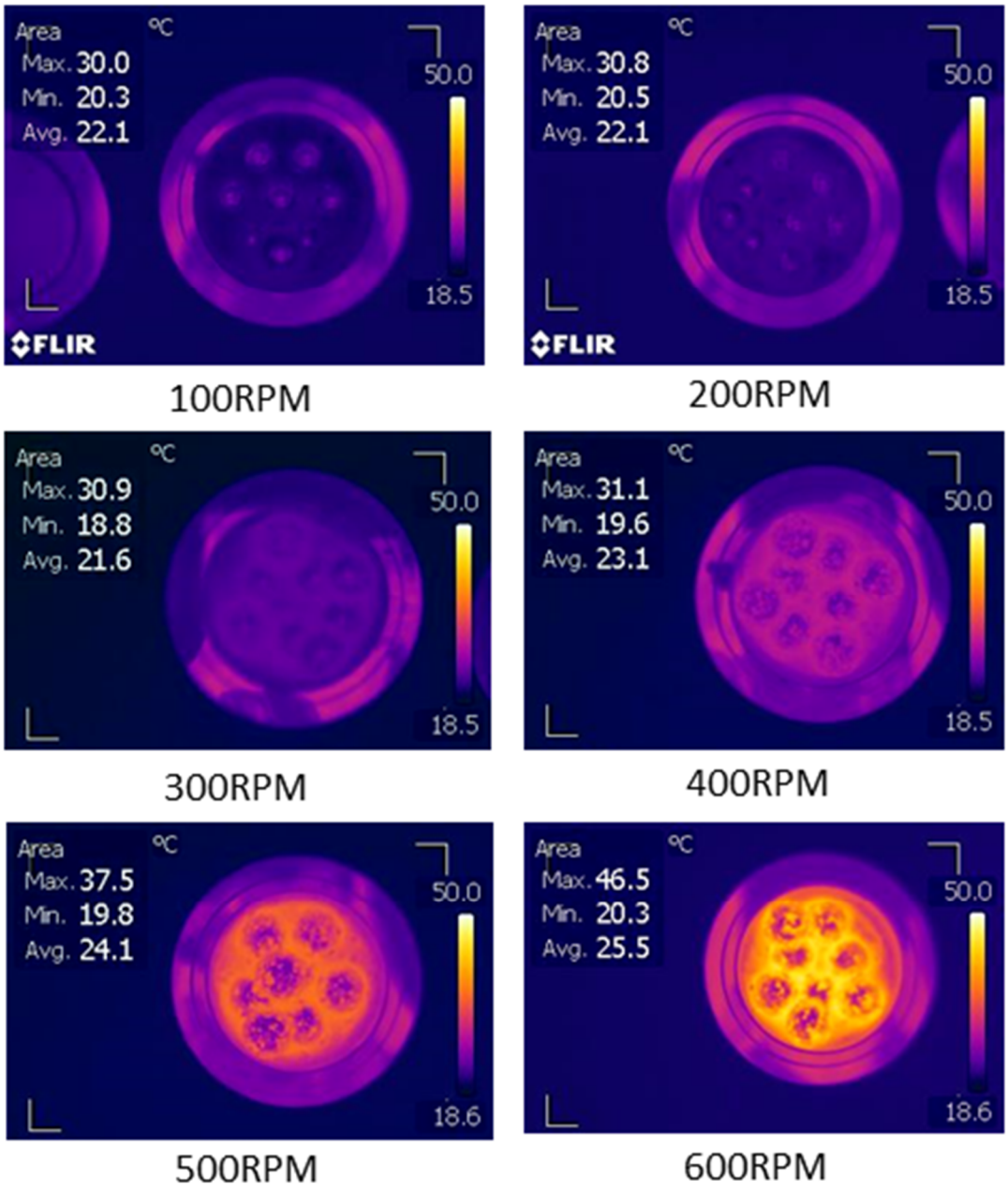


Figure 6.7: Thermal Imaging of Heat Generation in Olive Cake Milled in a Planetary Ball Milling for 60 Seconds at 100-600 RPM

To investigate this heat generation and caking phenomenon further, the specific energy consumption and loose mass available after milling were measured for a 60 second run for 100 and 200 ml of olive cake at speeds between 200 and 600 RPM (Fig. 6.8). The specific energy increases in a power relationship with speed, and there is greater energy consumption for 100 ml volume of olive cake compared to 200 ml. The relationship was similar for both volumes, and further work should involve investigating this relationship for varying times and materials. The loose mass available drops off dramatically after 300 RPM for 100 ml, and there is a drop off in loose mass at 200 RPM for 200 ml, indicating that

caking is happening at lower speeds for higher volumes of olive cake. Once speeds exceed 400 PRM, less than 10% loose mass is available after milling for both volumes.

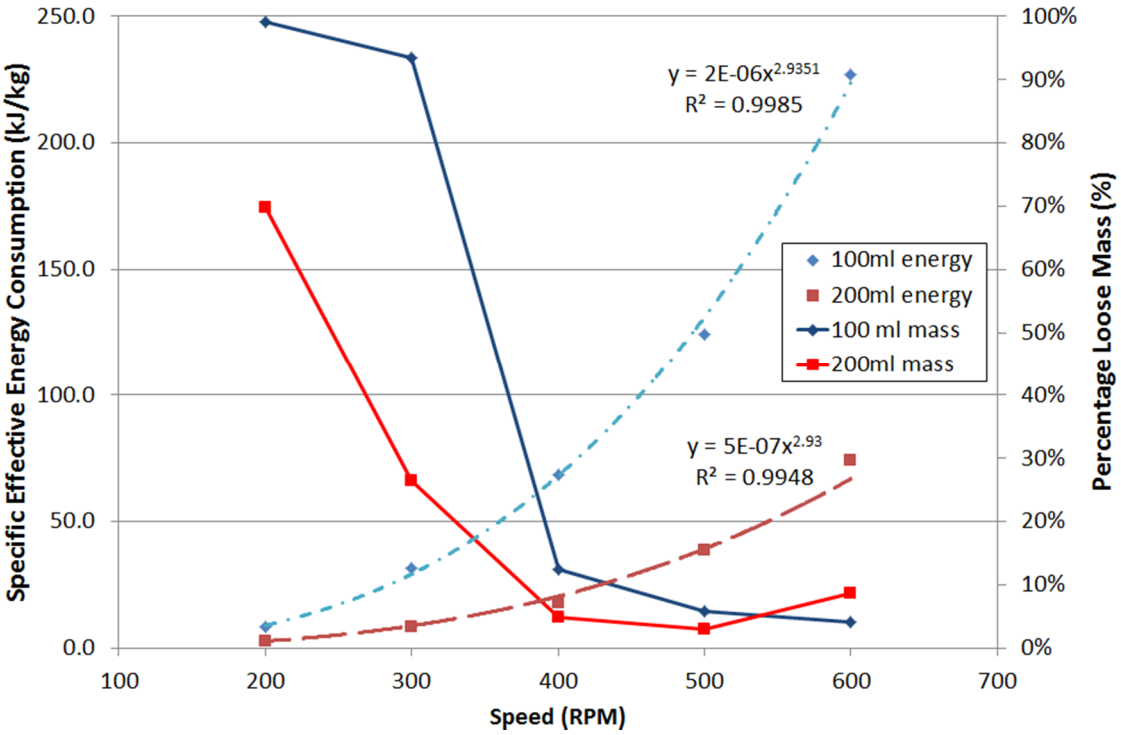


Figure 6.8: Impact of Varying Speed and Volume on Specific Effective Energy Consumption and Percentage Loose Mass of Olive Cake Milled in a Planetary Ball Mill for 60 Seconds

Olive cake is the only fruit based biomass analysed in this project. As a waste product of olive oil production, it is available in large quantities for combustion. Compared to the other biomass materials used in this project, it has a fundamentally different composition. As detailed in section 2.6, olive cake is made of two components (Kailis et al., 2007), a stone where the lignin is concentrated (850-3350 µm in figure 6.1) and the outer pulp or flesh where the hemicellulose and cellulose is concentrated (0-850 µm in figure 6.1). In comparison, wood is a low density, cellular polymeric composite of hemicellulose, cellulose, and lignin (Dinwoodie, 2000). In order to investigate if any specific section of the olive showed a greater propensity to caking, the olive cake was split into its constituent components (pulp (0-850 µm), pip (850-350 µm) and lumps (3350 µm+)), and the tendency to cake in individual (pulp/pip) or combined sections (un-sieved samples or lumps) was investigated. The four sets of olive cake (un-sieved, pulp, pip, and lumps) were milled at 300 RPM, for 100 ml for 3 minutes to ascertain the impact on energy consumption, particle size, heat generation and caking for each section. In order to investigate the impact moisture played in the tendency to cake, the same test was conducted for the four sets after drying as

per section 3.1.1. All tests were conducted in triplicate. The moisture content of the un-sieved portion was 17.9 ± 0.04%, 17.1 ± 0.07 % for the pulp section, 14.9 ± 1.31% for the pip section, and 16.6 ± 0.06% for the lumps section. Prior to drying the makeup of the un-sieved material was 42.6% pulp, 40.5% pip and 17.0% lump, and after drying was 46.1% pulp, 39.4% pip, and 14.6% lumps.

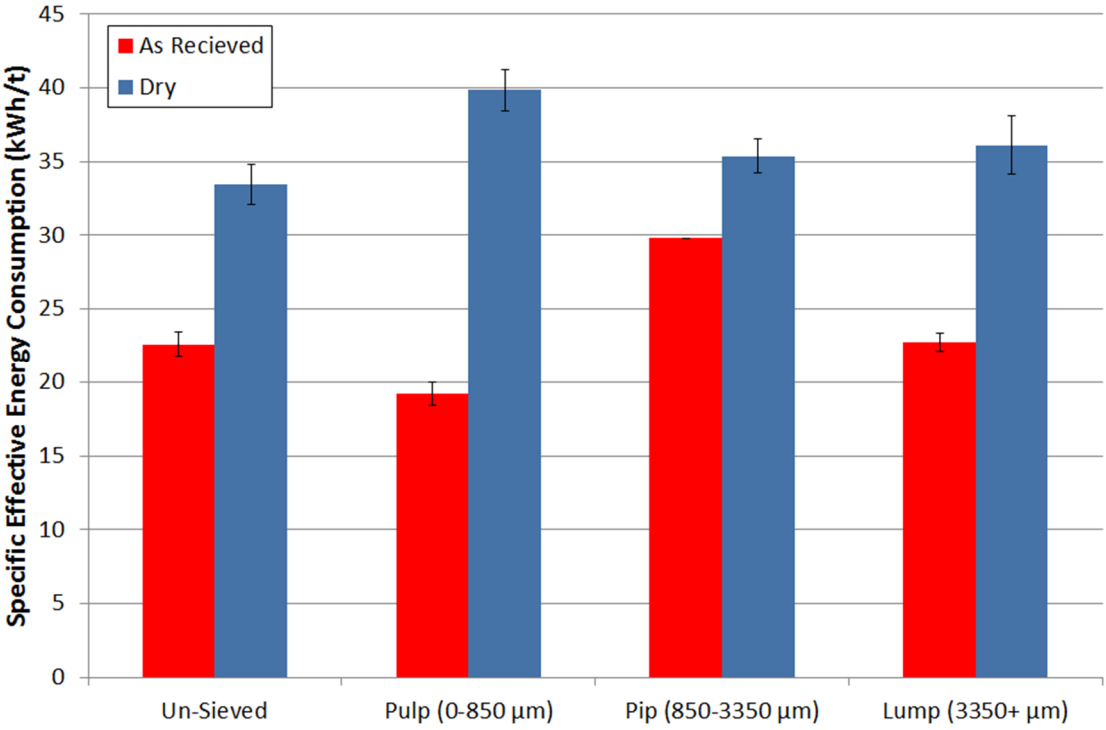


Figure 6.9: Specific Effective Energy Consumption for As Received and Dried Olive Cake in Un-sieved, Pulp, Pip, and Lump Sections

The specific effective energy consumption, E_e, of the caking tests is shown in figure 6.9. There was a variation in the E_e for the different sections in the as received (non-dried state) and dried tests. For the as received tests, the lowest E_e was in the pulp section and the highest was for the pip section. The lump and un-sieved sections has similar E_e, and lay in between the pulp and pip results, which was expected as they are a mix of the pulp and pip sections. When the pulp was dried, it had the highest E_e of all the sections, over double its as received value. The dried un-sieved portion had the lowest energy consumption, but its error bars were within the values of E_e for the dried pip and lump sections. The change in E_e in the pulp section is due to its moisture and residual oil content. Most of the moisture in an olive is bound within the pulp section, and the pulp is main source of oil in an olive (Kailis et al., 2007).

A planetary ball mill is a pot filled with balls connected to a rotating disk, both of which rotate around a common central axis (section 2.20). This rotation results in the high impact energies of the milling balls within the pot. The material under comminution is trapped between the colliding balls and makes the collision less elastic, which results in slower ball motion and a reduction of energy dissipation (Burmeister et al., 2013). During comminution, low volumes of olive cake have resulted in larger energy consumption than high volumes, and high speeds also result in higher energy consumption than low speeds (section 6.2.1). This is because at high speeds and low volumes there is more space for the balls to move within the pot, and higher speeds result in higher momentums and impact energies. This results in greater forces acting upon on the mill pot, disk and consequently the motor drive of the mill. In order to maintain the set speed of the mill, the motor must draw more current, as motor current is proportional to the torque on the motor, resulting in the increased energy consumption of the mill under load.

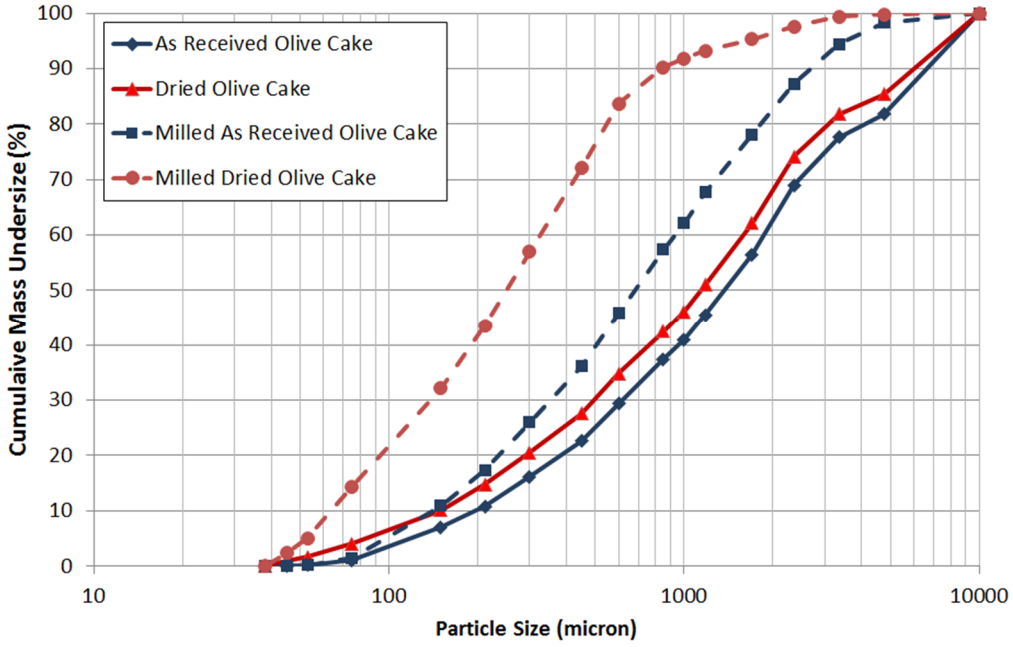


Figure 6.10: Cumulative Particle Size Distribution for Pre-Milled and Milled As Received and Dried Olive Cake

The moisture in the olive cake acts as an plasticiser of the material and energy absorber during the collision with the milling balls, reducing the coefficient of restitution (ratio of the exit speed of a ball after contact to the incoming speed of the ball prior to contact with a material (ASTM F1887-14, 2014)) between the milling ball and olive cake. This reduces the exit speed of the ball and consequently the momentum and impact energy of the ball. As a result the forces experienced within the mill are reduced, resulting in lower energy

consumption for set milling conditions compared to dried materials. When the moisture is no longer present to absorb the impact energy, there is a larger coefficient of restitution. Thus higher exit velocities are achieved from the collision, and greater ball momentum is achieved and the forces acting upon the mill pot are increased, resulting in higher energy consumption for dried materials.

In addition to energy consumption, the tendency to cake affects the particle size distribution of the olive cake. Figure 6.10 shows the pre-milled and milled as received and dried olive cake particle size distributions. There is a large difference in the milled particle size distributions despite the similarity in the pre-milled distributions. The dried olive cake produces a much finer particle size than the as received olive cake, with the 80th percentile particle size, Q_{80}, being over three times as great for the as received sample (1835 µm) compared to the dried (553 µm). No caking was observed for the dried sample, but as figure 6.12 illustrates, the heat generation in the dried sample was significantly higher.

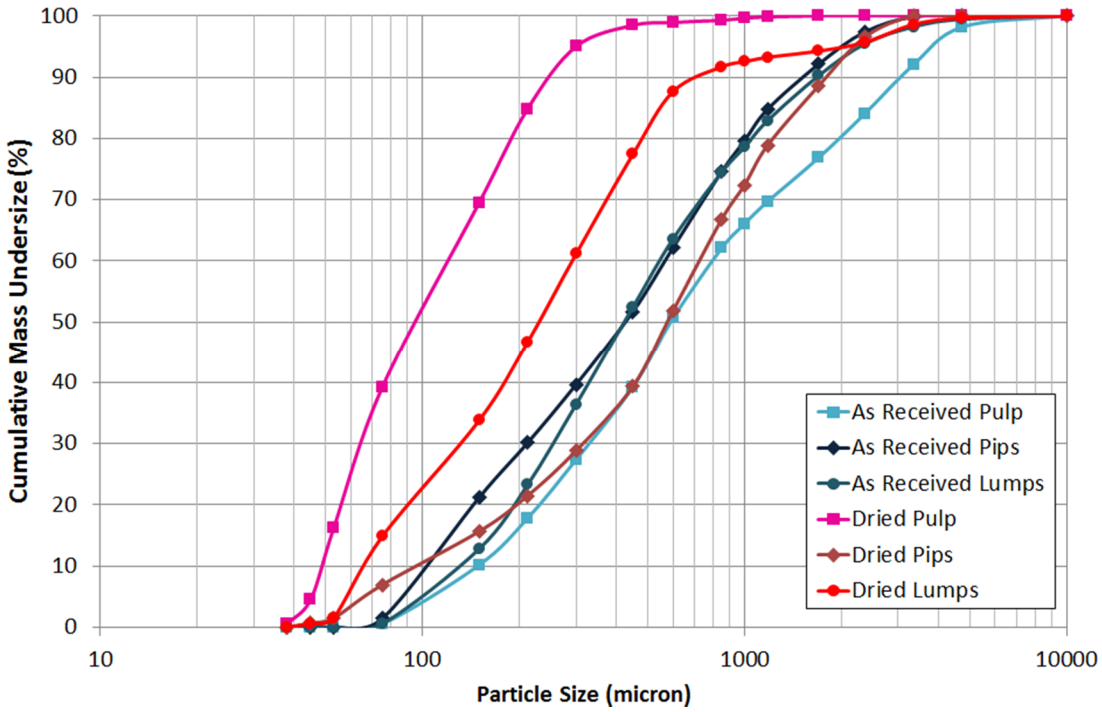
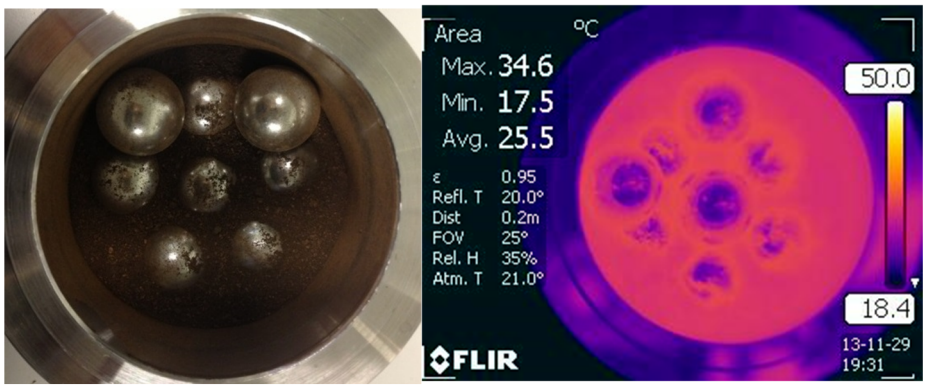


Figure 6.11: Cumulative Particle Size Distribution for Milled as Received and Dried Olive Cake Pulp (0-850 µm), Pips (850-350 µm), and Lumps (3350+ µm)

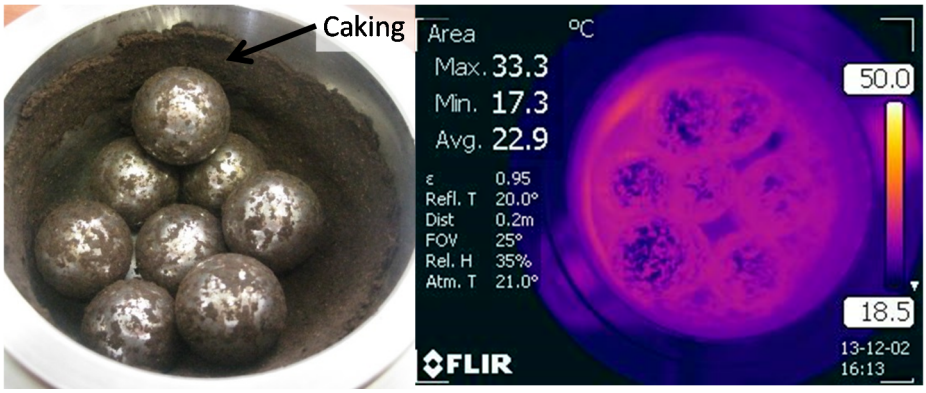
When the particle size distributions of the three sections are analysed (Fig. 6.11), it can be seen that the pulp section shows the most dramatic change in behaviour through drying. It's as received Q_{80} was 1990 µm, but drying reduces Q_{80} dramatically by an order of magnitude to 193 µm. After milling, 37.9% of the as received pulp section was above 850 µm, indicating that extreme caking had occurred, which is evident in figure 6.12.



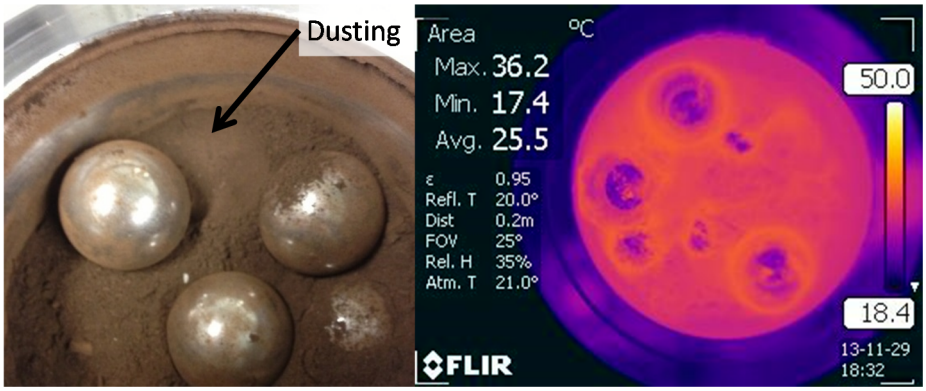
As Received Un-sieved



Dried Un-sieved

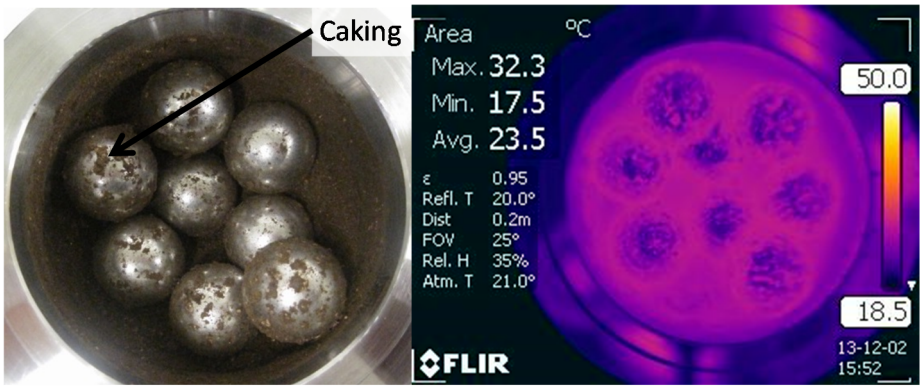


As Received Pulp (0-850 µm)

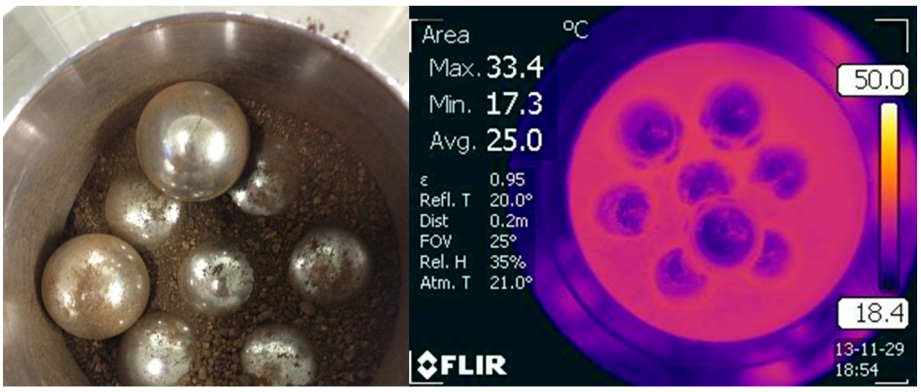


Dried Pulp (0-850 µm)

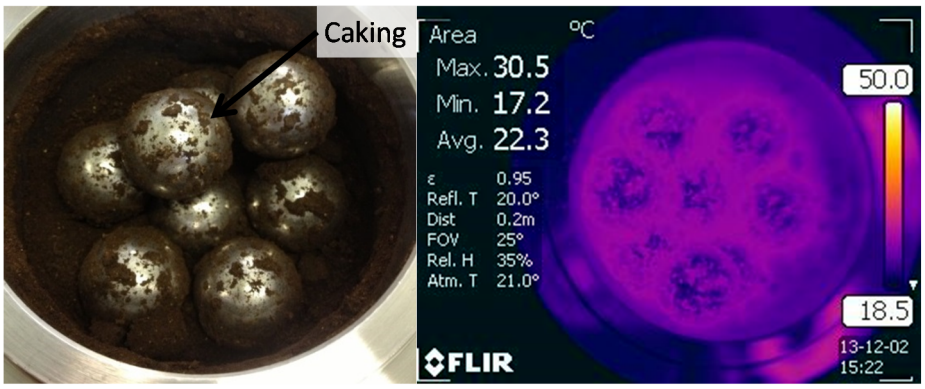
Figure 6.12: Caking and Heat Generation for Milled As Received and Dried Olive Cake in Un-sieved and Pulp Sections



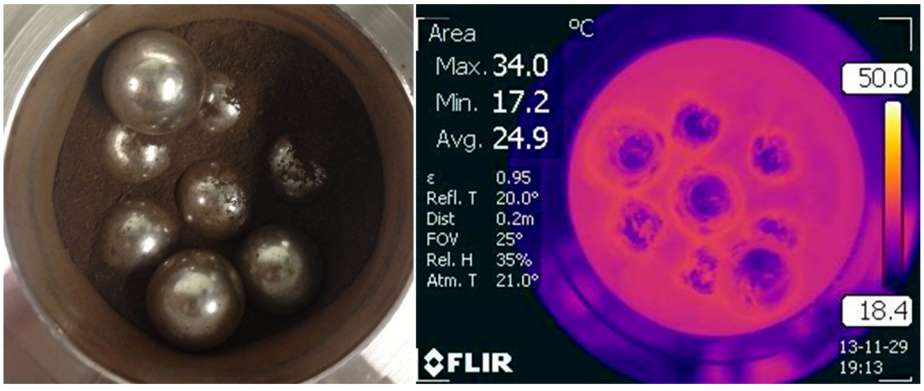
As Received Pip (850-3350 µm)



Dried Pip (850-3350 µm)



As Received Lumps (3350 µm+)



Dried Lumps (3350 µm+)

Figure 6.13: Caking and Heat Generation for Milled As Received and Dried Olive Cake in Pip and Lump Sections

However when dried, the caking disappeared and the milled pulp section had the finest particle size distribution (Fig. 6.11) and the highest heat generation (Fig. 6.12) of all the sections. In fact a burning smell was observed for the dried pulp section after milling. The pip section showed a different trend to the pulp section, as the particle size distribution was coarser after drying (as received Q_{80} 1013 µm, dried Q_{80} 1240 µm). Caking was observed for the as received sample, but as with the other sections, drying eliminated the caking effect (Fig. 6.12). Higher heat generation was also noted in the dried state, which suggests that pips become harder with drying and thus harder to mill, resulting in the coarser particle size distribution. The lump section showed the same trend as the pulp and un-sieved sections, with much finer particle size distributions after milling (as received Q_{80} 1059 µm, dried Q_{80} 488 µm). Thus along with heat generation, moisture can be seen to be a key factor in the caking of olive in a planetary ball mill.

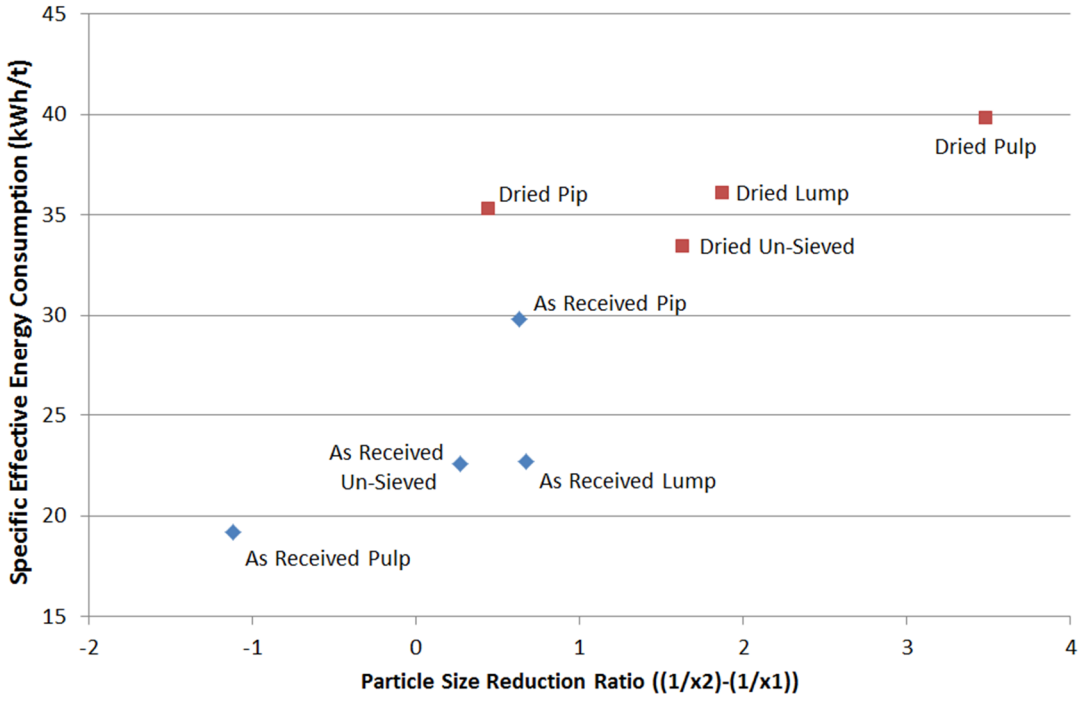


Figure 6.14: Specific Effective Energy Consumption against Particle Size Reduction Ratio for Milled and Dried Olive Cake

By using Von Rittinger's theory (section 2.12), the combined impact of specific energy consumption and particle size reduction can be analysed for as received and dried olive cake sections (Fig. 6.13). The un-sieved and lump sections show similar results to each other in the as received and dried tests, which is to be expected due to the similarity of the samples. The pip section shows an increase in energy consumption, but decrease in particle size through drying, illustrating the hardening of the pips through drying. However the clearest

impact of caking is on the pulp section. There is a negative particle size reduction in the as received state as particle size increases after milling due to the caking effect. When the pulp section is dried and the caking effect is removed, the pulp section has the highest energy consumption and largest reduction in particle size of all the samples. This illustrates that the caking issue is most prevalent in the pulp section of the olive cake.

A comparison of the Von Rittinger's constant in table 6.2 further illustrates the impact of caking on the pulp section in particular. It can be seen that there is little change in the constant for the pips, indicating that there is little change in the milling behaviour of the pips through drying. However there is a dramatic change for the pulp section through drying, indicating a completely different milling behaviour in the two states, which has been previously shown to be related to the caking effect. The un-sieved and sieved portions show an increase in constant through drying, indicating that the pulp section is influencing the behaviour of the olive cake.

	Un-Sieved	Pulp (0-850 µm)	Pip (850-3350 µm)	Lump (3350+ µm)
As Received	6.1	-21.5	18.8	16.0
Dried	54.4	138.6	15.5	62.4

Table 6.2: Von Rittinger's Constant for As Received and Dried Milled Olive Cake Sections

The reason for the tendency to cake in the pulp section of the biomass is related to the sugar and moisture content of the pulp. The pulp section contains a high level of sugars, with the main soluble sugars in olive flesh being glucose, fructose, sucrose, and mannitol (Kailis et al., 2007). The level of soluble sugars in raw olive flesh ranges from 0.5 % w/w to over 5 % w/w depending on olive variety and growing conditions, with glucose predominating. Soluble sugars decrease as the olive fruit develops and oil synthesis begins, with soluble sugars in green-ripe olives being twice the level of black-ripe olives, and their levels are inversely related to the oil content, and concentrations are also dependent on the moisture content of the olive flesh. Spanish green-ripe olives have around 4% fermentable substrates (sugars), while untreated black-ripe olives have a fermentable substrate level of typically 2-2.5%.

Stickiness and caking is a commonly experienced in the food and pharmaceutical industries (Palzer, 2011), and the influence of sticky behaviour of amorphous food products is well recognised due to its influence on the process and handling abilities and qualities of powders (Boonyai et al., 2004). The stickiness and caking of food products has been shown to be related to the glass transition temperature, T_g, of the material, which is related to its

moisture content (Gabbott, 2008). Moisture has been shown to reduce the glass transition temperature of food products to atmospheric temperatures and humidity (Aguilera et al., 1995), and the rate of crystallisation of amorphous sucrose has been shown to be dependent on relative humidity. The pure glass transition temperature of glucose is around 30 °C (Gabbott, 2008), and the crystallisation of sugars is used to produce chews and candy dough. It has also been shown in several studies that the crystallisation of amorphous sugars is related to the rate of browning, stickiness and caking (Roos et al., 1991), as the rate of crystallisation above glass transition temperature is related to viscosity, which decreases rapidly above the glass transition temperature, and the composition of the amorphous mix. Thus the key to a materials propensity to cake is related to whether or not the sugar and moisture content of the material is such that a glass transition step occurs within the environmental conditions experienced within the planetary ball mill.

The most common way of investigating the glass transition temperatures of materials is through differential scanning calorimetry (DSC). The four olive sections were tested in a DSC in as received and dried conditions as per section 3.1.12, and figure 6.15 shows the results for the two heating scans in the DSC. The first heating scan shows the impact of moisture on the heat flow in the sample. There is a large endothermic dip (negative direction) at around 60 °C for all the as received samples, which is related to moisture release, after which it rises exothermically (positive direction) and levels out around 120 °C.

There is an additional exothermic-endothermic shift between 80 and 100 °C which is indicative of a glass transition step occurring within the olive cake. Below this temperature the material is immobile and rigid, but above which it becomes fluid or rubbery. This shift is particularly strong in the pulp section of the material, and decreases in intensity for the un-sieved and lump sections, and is weakest in the pip section. When relating the DSC results back to the milling tests, it is proposed that during the ball-olive collisions high levels of localised heat is generated within the olive cake which results in the pulp section reaching the conditions where a glass transition step occurs, and induces caking within the olive cake (Gabbott, 2008; Kingsly et al., 2011). Given that caking was most prevalent and extreme for the pulp section, and there is a visible glass step transition occurring within this section of the olive cake, it can be surmised that the olive pulp has caked due to a glass step transition related to its sugar and moisture contents. This glass transition is brought about by the high localised heat generated within the mill from ball-material collisions (Venkataraman et al., 1998) which results in higher heat generation at high speed (Fig. 6.7). Thus as mill speed

increases, the heat generated within the olive cake due to the olive-ball collisions will increase, resulting in the increasing severity of caking seen in figures 6.5 and 6.12.

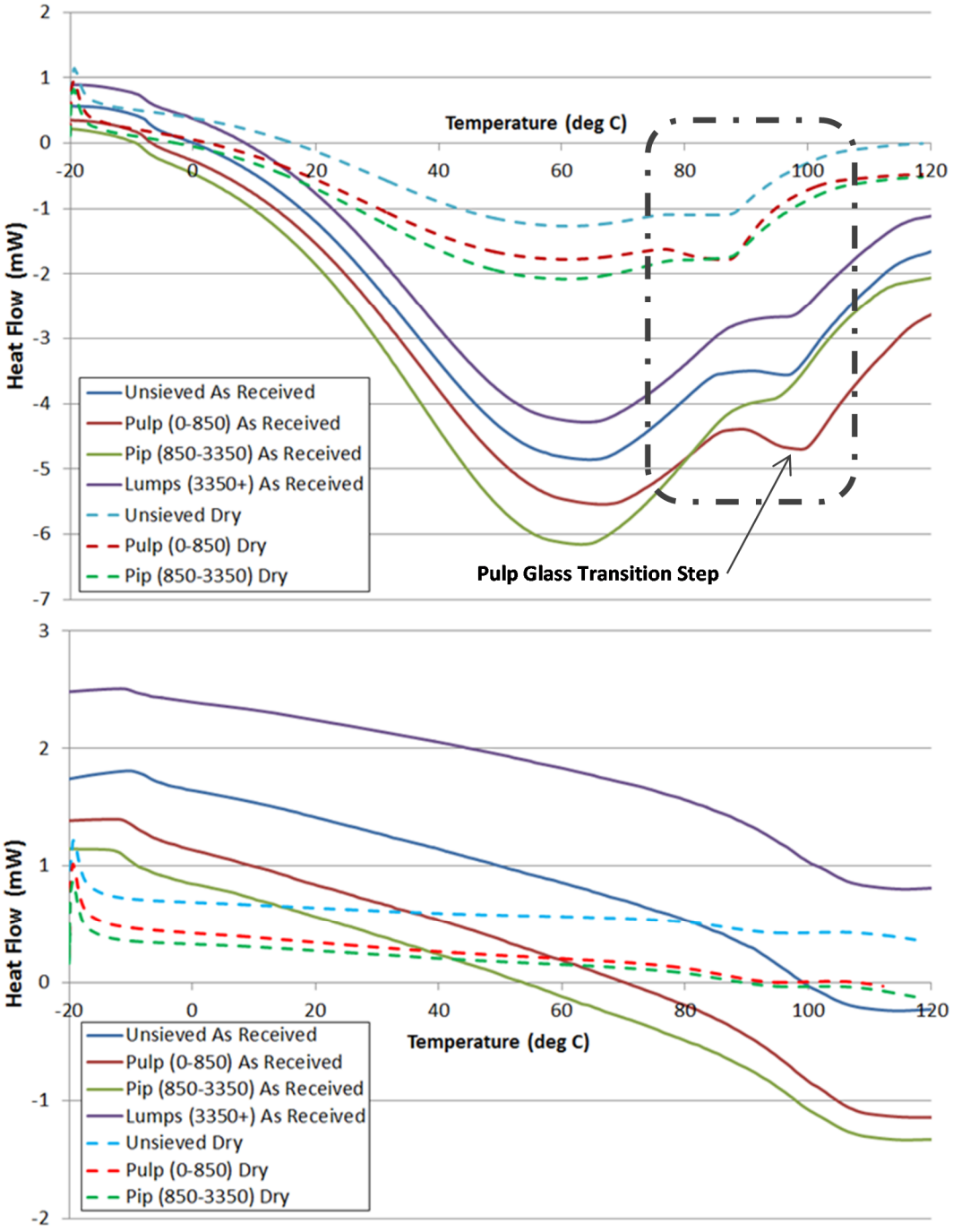


Figure 6.15: First (top) and Second (bottom) Heating Scan in DSC for As Received and Dried Olive Cake

The dried samples show much shallower heat flows than the as received samples due to the absence of moisture. The only moisture being released is that which has been absorbed from the atmosphere, and as demonstrated in section 4.7, the reabsorption moisture levels are very low. On the second heating scan, the as received pulp and pip sections show

negative endothermic heat flows, while all other samples appear mainly within the positive heat flow region. The dried materials have become almost stable in heat flow on the second heating scan. Thus by removing the moisture from the olive cake, the conditions for the glass step transition are not being achieved within the mill and caking does not occur in the dried samples. However, it must be noted that higher levels of heat were generated for the dried samples, and resulted in dusting of the olive cake, which increases the potential risk of mill fires. Thus from a power generation perspective, the optimal solution would be to remove all olive cake below the required combustion particle size, which is typically 1mm (Esteban et al., 2006; Tamura et al., 2001) and thus would include the pulp section, prior to comminution and send these fines directly to the burner.

6.4. Impact of Drying on Milling Behaviour of Different Biomass Materials

Based on the results of the specific energy consumption rate (section 6.2.1) and particle size (section 6.2.2) optimisation experiments, a set of conditions upon which to test the milling behaviour of a range of biomasses commonly used in the power generation sector were selected. The selected settings for the planetary ball mill were a speed of 300 RPM, a volume of 100ml, and mill duration of 3 minutes. These settings were selected as the particle size optimisation study results suggested that lower speeds, lower volumes and longer milling durations would provide finer particle size distributions. The mill duration needed to be above 30-40 seconds to ensure the constant energy consumption condition was achieved (Fig. 6.3). Figure 6.8 showed mass drop off at over 400 RPM for olive cake, and as the propensity to caking for the other materials was not known prior to the tests, it was decided that the speed should be 300 RPM in order to avoid caking. Too low a speed would result in a low energy consumption rate and a coarse particle size distribution, but high speeds would result in the complete pulverisation of the material and increase the risk of mill fires due to the excessive heat generation observed in dried olive cake (section 6.3). As moisture has been shown to be factor in caking of olive cake (section 6.3), the impact of drying the other materials was analysed. The temperature of the biomass and mill balls after milling was measured via thermal imaging and point temperature measurement. Heat flow properties of the milled samples were also measured. The dried samples were dried as per section 3.1.1 and then stored in sealed bags until use. The samples were milled within 5 days of drying. Moisture uptake in sealed bags for the samples is noted in section 4.7. Moisture uptake for samples stored in this way did not exceed 0.3% after 6 days for any of the samples, and hence can be considered dry at the point of milling.

6.4.1. Energy Consumption and Particle Size

Figure 6.16 shows the Specific Effective Energy consumption (E_e) results for the as received and dried samples in the planetary ball mill. The highest E_e was for woody and sunflower pellets. The lowest E_e was for olive cake, olive pellets, and steam exploded pellets. As was observed in figure 6.9, drying increased the specific energy consumption for all materials apart. Olive pellets saw the largest increase in energy consumption (60%), followed by olive cake 2013 (39%) and eucalyptus pellets (35%). Microwave pellets showed a slight increase in energy consumption (0.9%), but also had the lowest moisture content of all the pellets at 4.7% (table 4.5 in section 4.7). The effectiveness of milling on disintegrating the densified biomass pellets back to their constituent particles varied greatly amongst the samples. While eucalyptus, steam exploded, mixed wood and microwave pellets disintegrated completely during milling, miscanthus, sunflower and olive pellets did not disintegrate completely. Based on the pellet disintegration test results (section 4.3), the miscanthus pre-milled 99th percentile particle size was 3049 µm, and 95th percentile particle size of 2326µm. After milling in a planetary ball mill, 45.6% of the miscanthus sample was above 2360 µm in the as received state, and 59.4% for the dried state. Thus a significant portion of the miscanthus pellets remained in densified form after comminution in a planetary ball mill.

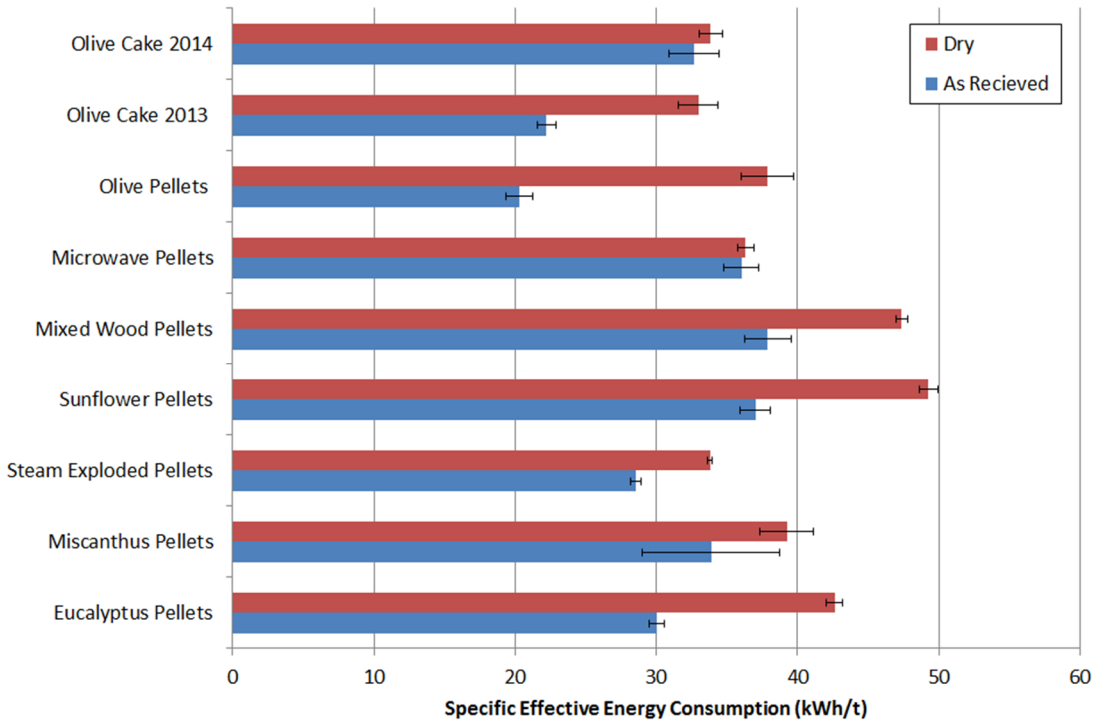


Figure 6.16: Specific Effective Energy Consumption for Densified Biomasses and Olive Cake in As Received and Dried States in a Planetary Ball Mill

For sunflower, the pre-milled 99th percentile particle size was 2929 µm. 8.5% of the as received sunflower pellets and 22.1% of the dried miscanthus pellets were above 3350 µm after comminution. Above 3350 µm the olive cake consisted of self-formed lumps or pellets. For olive 2013, after milling 5.6% as received olive cake was above 3350 µm and 0.6% for the dried. For olive 2014, 27.2% of the as received and 19.7% of the dried comminuted samples was above 3350 µm. The worst example of non-comminuted material was for the olive pellets, where 63.9% of the as received and 64% of the dried olive pellets was above 3350µm after milling. High impact forces could not easily disintegrate these pellets, and in a full scale mill this could lead to increased throughput times and potential mill blockages. In order to compare the comminuted parts of the sample with the pre-milled particle sizes, the milled particle sizes listed in table 6.3 are below the 99th percentile pre-milled particle size for olive 2013, olive pellets, sunflower and miscanthus pellets.

Table 6.3 summarises the particle size distribution size, dispersion and distribution shape parameters, along with the Rosin-Rammler results for the particle size distributions. In general, the Rosin-Rammler particle size, *d',* and geometric mean diameter, d_{gw}, reduced with drying. Also there was an increase in the Rosin-Rammler distribution parameter and decrease in mean relative span for the dried samples. The distribution geometric standard deviation of high and low regions (*hs* and *ls*) generally became equal for the dried samples, with a reduction in the higher region and increase in the lower region values. This indicates a more balanced distribution for dry comminution, which is reflected in the geometric kurtosis (K_g) of the distributions. Generally it is closer to 1 after drying, apart from olive cake 2013 which sees its as received symmetrical curve (K_g of 1) increase dramatically when dried to 1.71. This is due to the large change in particle size seen through drying (*d'* 925 µm for as received, 357 µm for dried). All the samples show well graduated samples throughout (Uniformity Coefficient above 4), and the Inclusive graphic skewness (GS_i) was not significantly affected by drying.

Figure 6.17 uses the Von Rittinger's theory (section 2.12) to analyse the impact of drying on the energy consumption and particle size reduction. While for most samples drying increase the particle size reduction ratio, for some there is very little change. Miscanthus shows virtually no change in particle size between its disintegrated size of 1310 µm (table 4.1 in section 4.3) to its comminuted size of 1181 µm as received and 1237 µm dried. However it is clear that very little if any comminution of the particles has occurred.

Sample	Rosin-Rammler			Size Parameters (µm) - Camsizer Output			Dispersion Parameters					Distribution Shape Parameters	
	d' (µm)	n	R^2	d_{10}	d_{gw}/d_{50}	d_{80}	hs	ls	MRS	C_u	C_c	GS_i	K_g
Eucalyptus Pellets AR	493	1.27	1.000	78	366	705	2.15	3.04	2.54	6.14	1.25	0.37	1.08
Eucalyptus Pellets Dry	389	1.36	1.000	71	298	552	2.06	2.85	2.22	5.34	1.22	0.34	1.09
Mixed Wood Pellets AR	628	1.15	0.999	69	466	975	2.29	4.40	2.48	9.39	1.43	0.34	0.91
Mixed Wood Pellets Dry	486	1.34	0.999	82	361	708	2.17	2.89	2.38	5.88	1.18	0.36	0.96
Miscanthus Pellets AR	898	1.32	0.999	193	591	**1181**	2.22	2.30	2.33	4.07	0.98	0.42	1.00
Miscanthus Pellets Dry	841	1.38	0.999	187	604	**1237**	2.28	2.37	2.41	4.37	0.97	0.42	0.99
Olive Cake 2013 AR	**925**	1.09	0.998	138	627	1553	2.82	3.31	3.23	6.66	0.84	0.52	**1.00**
Olive Cake 2013 Dry	**357**	1.21	0.997	64	250	521	2.38	3.14	2.97	5.34	0.88	0.53	**1.71**
Olive Cake 2014 AR	1226	1.00	0.999	155	798	2141	3.04	3.48	3.48	7.95	0.88	0.54	0.96
Olive Cake 2014 Dry	333	1.09	0.999	51	228	505	2.55	3.38	3.10	6.37	0.95	0.52	1.39
Olive Pellets AR	631	0.88	1.000	68	356	1191	4.13	3.77	5.44	8.49	0.84	0.70	1.38
Olive Pellets Dry	590	0.81	0.993	58	312	1219	4.88	4.20	6.36	9.06	0.72	0.73	1.23
Sunflower Pellets AR	822	1.24	0.999	143	592	1220	2.34	2.96	2.72	5.54	1.05	0.45	1.14
Sunflower Pellets Dry	397	1.59	1.000	79	315	529	1.83	2.50	1.91	4.96	1.36	0.26	1.07
Steam exploded Pellets AR	310	1.14	0.998	45	221	466	2.38	3.62	2.77	6.95	1.02	0.44	1.10
Steam exploded Pellets Dry	218	1.29	0.999	42	168	318	2.05	3.25	2.14	5.33	0.84	0.31	0.86
Microwave Pellets AR	185	1.13	0.999	37	133	285	2.37	3.18	2.53	5.05	0.67	0.45	0.93
Microwave Pellets Dry	165	1.13	0.999	32	117	254	2.41	2.87	2.60	5.25	0.71	0.43	0.94

Table 6.3: Shape, Dispersion and Distribution Shape Parameters of the Cumulative Particle Size Distributions for As Received (blue) and Dried (red) Biomass Milled in the Planetary Ball Mill. Sunflower Particle Sizes are for Sub 4750 µm, Olive Cake 2013 and Pellets sub 3350 µm, and Miscanthus sub 2360 µm. Notable Results are in Bold

This is further exemplified in figure 6.18, which shows there is virtually no change in the as received or dried milled miscanthus particle size distributions compared to the pre-milled distribution after comminuting in a planetary ball mill.

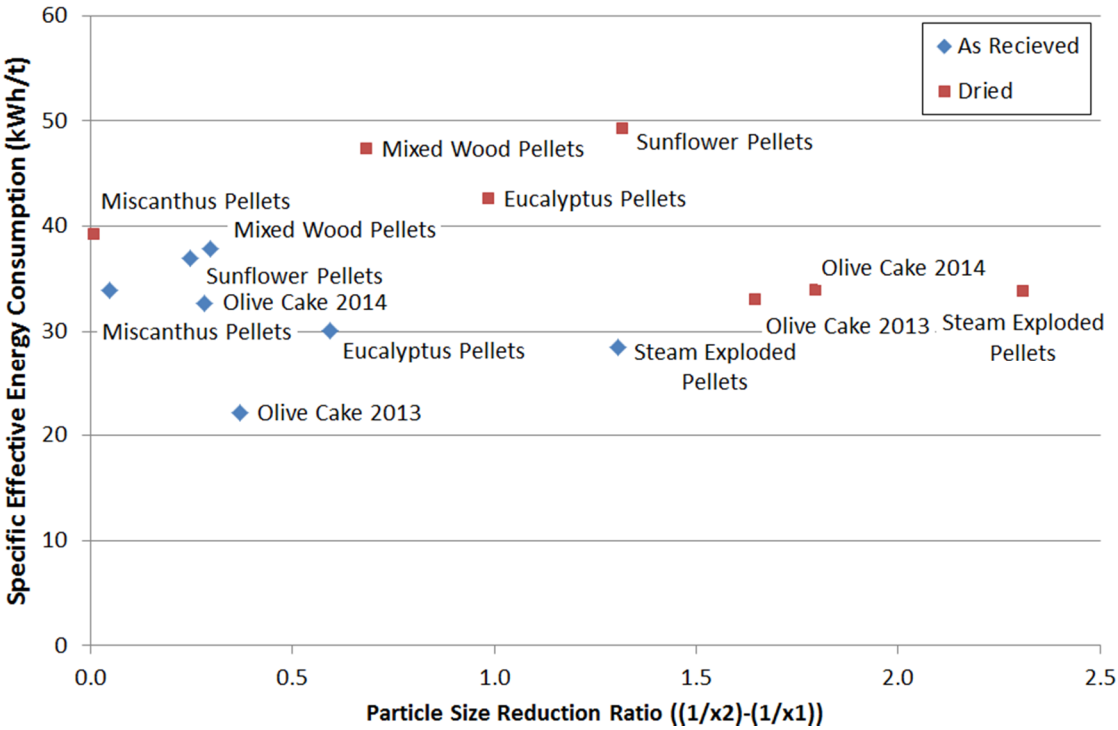


Figure 6.17: Specific Effective Energy Consumption against Particle Size Reduction for As Received and Dried Densified Biomasses and Olive Cake in a Planetary Ball Mill

This indicates that despite the high impact forces within the mill, the miscanthus particles have reached their critical particle size for compressed fracture, and below this size the biomass is behaving as a ductile material (Kendall, 1978). In comparison, steam exploded pellets see a 17% increase in energy consumption by drying, but also significantly increase in the particle size reduction. By comparing the impact of drying on the Von Rittinger's constants for the milled samples (table 6.4), it can be seen how a range of milling behaviours are observed for the tested samples. eucalyptus, steam exploded, mixed wood pellets and olive cake 2013 see at least a doubling in constant value.

	Eucalyptus Pellets	**Miscanthus Pellets**	**Steam Exploded Pellets**	**Sunflower Dry**	**Mixed Wood Pellets**	**Olive Cake 2013**	**Olive Cake 2014**
As Received	17.9	1.6	37.3	9.1	11.3	8.2	9.8
Dried	42.1	0.4	78.1	64.9	32.4	54.3	60.8

Table 6.4: Von Rittinger's Constant for As Received and Dried Milled Densified Biomass and Olive Cake

Given that there was not a doubling in energy consumption for these samples (Fig. 6.16) there has been a significant improvement in the particle size reduction through drying for

these samples. Miscanthus sees very little change in the constant, and has a very low constant value due to the negligible change in particle size (Fig. 6.18).

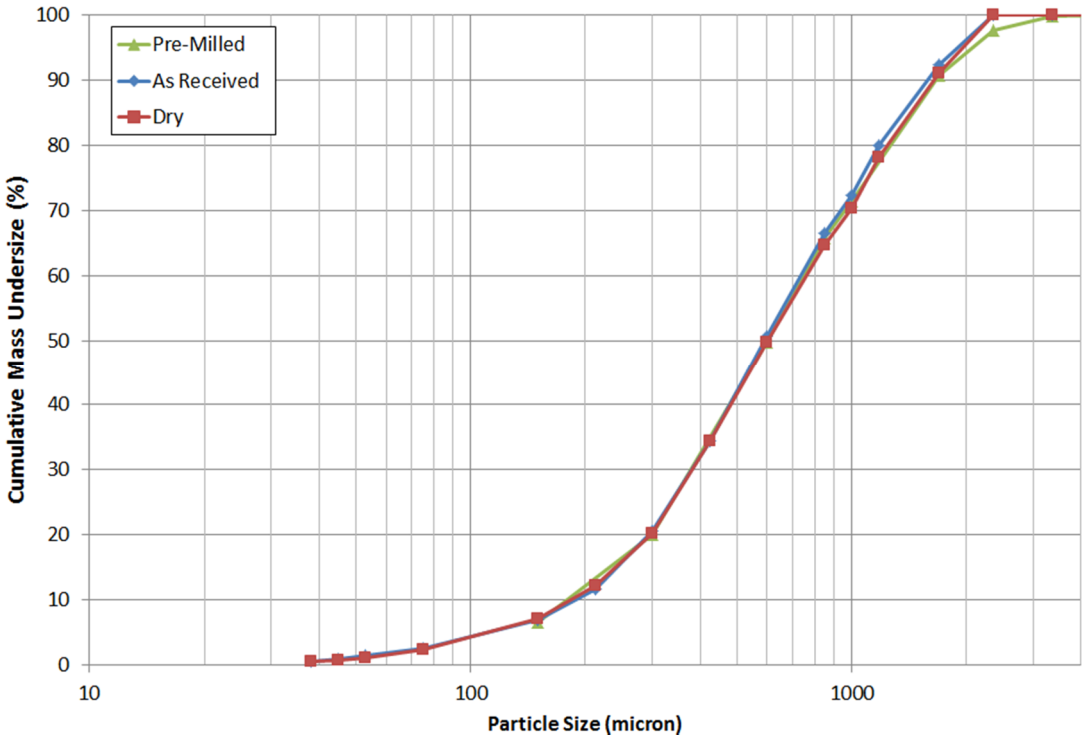


Figure 6.18: Cumulative Particle Size Distributions for Disintegrated, Planetary Ball Mill Comminuted Miscanthus in As Received and Dried States

6.4.2. Particle Shape

For most samples, milling in the as received or dried state has little impact on shape factors compared to the material type. As with the pre-milled samples in figures 4.5 to 4.8 in section 4.3, figures 6.19 and 6.20 show that olive cake had the most spherical, circular, symmetrical and square (aspect ratio) particles, followed by the thermally treated samples (microwave and steam exploded), sunflower, eucalyptus, miscanthus, and the mixed wood pellets showing the lowest values in all shape parameters. The mean shape factors detailed in table 6.5 illustrate that there has been little change in the values compared to the mean values for the pre-milled samples (table 4.4 in section 4.6). The only sample which saw a significant change in shape parameter values was dried olive cake 2013. By drying olive cake 2013, not only was a much finer particle size distribution obtained, but there was a reduction in the shape parameter values as well. In the as received tests, olive cake 2013 showed the most spherical particles, but in the dried tests olive cake 2014 showed the most spherical particles. The same trends can be seen for circularity and aspect ratio, with all samples having similar values of circularity in dry tests. For symmetry, the same trends are also

observed, but olive cake 2013 and olive pellets are as symmetrical as eucalyptus in the dried state. This is likely to be related to the finer particle size distributions obtained in the dried state. However, overall there was no significant change in the particle shape factors compared to their pre-milled values in spite of the significant variation in pre-milled and milled particle size distributions.

Sample	Average Sphericity	Average Circularity	Average Symmetry	Average Aspect Ratio
Eucalyptus Pellets AR	0.428	0.504	0.742	0.539
Eucalyptus Pellets Dry	0.387	0.545	0.788	0.495
Mixed Wood Pellets AR	0.409	0.439	0.743	0.519
Mixed Wood Pellets Dry	0.371	0.501	0.766	0.476
Miscanthus Pellets AR	0.356	0.461	0.747	0.461
Miscanthus Pellets Dry	0.374	0.475	0.734	0.474
Olive Cake 2013 AR	**0.592**	**0.741**	**0.853**	**0.698**
Olive Cake 2013 Dry	**0.541**	**0.640**	**0.795**	**0.654**
Olive Cake 2014 AR	0.580	0.759	0.860	0.687
Olive Cake 2014 Dry	0.541	0.712	0.836	0.655
Olive Pellets AR	0.533	0.721	0.784	0.651
Olive Pellets Dry	0.547	0.653	0.800	0.660
Sunflower Pellets AR	0.412	0.499	0.742	0.521
Sunflower Pellets Dry	0.433	0.525	0.731	0.542
Steam exploded Pellets AR	0.484	0.518	0.760	0.602
Steam exploded Pellets Dry	0.487	0.560	0.757	0.602
Microwave Pellets AR	0.480	0.577	0.769	0.597
Microwave Pellets Dry	0.488	0.547	0.754	0.604

Table 6.5: Impact of Drying on Average Particle Sphericity, Circularity, Symmetry and Aspect Ratio for Biomass Milled in Planetary Ball Mill (As Received in Blue, Dried in Red). Notably Results in Bold

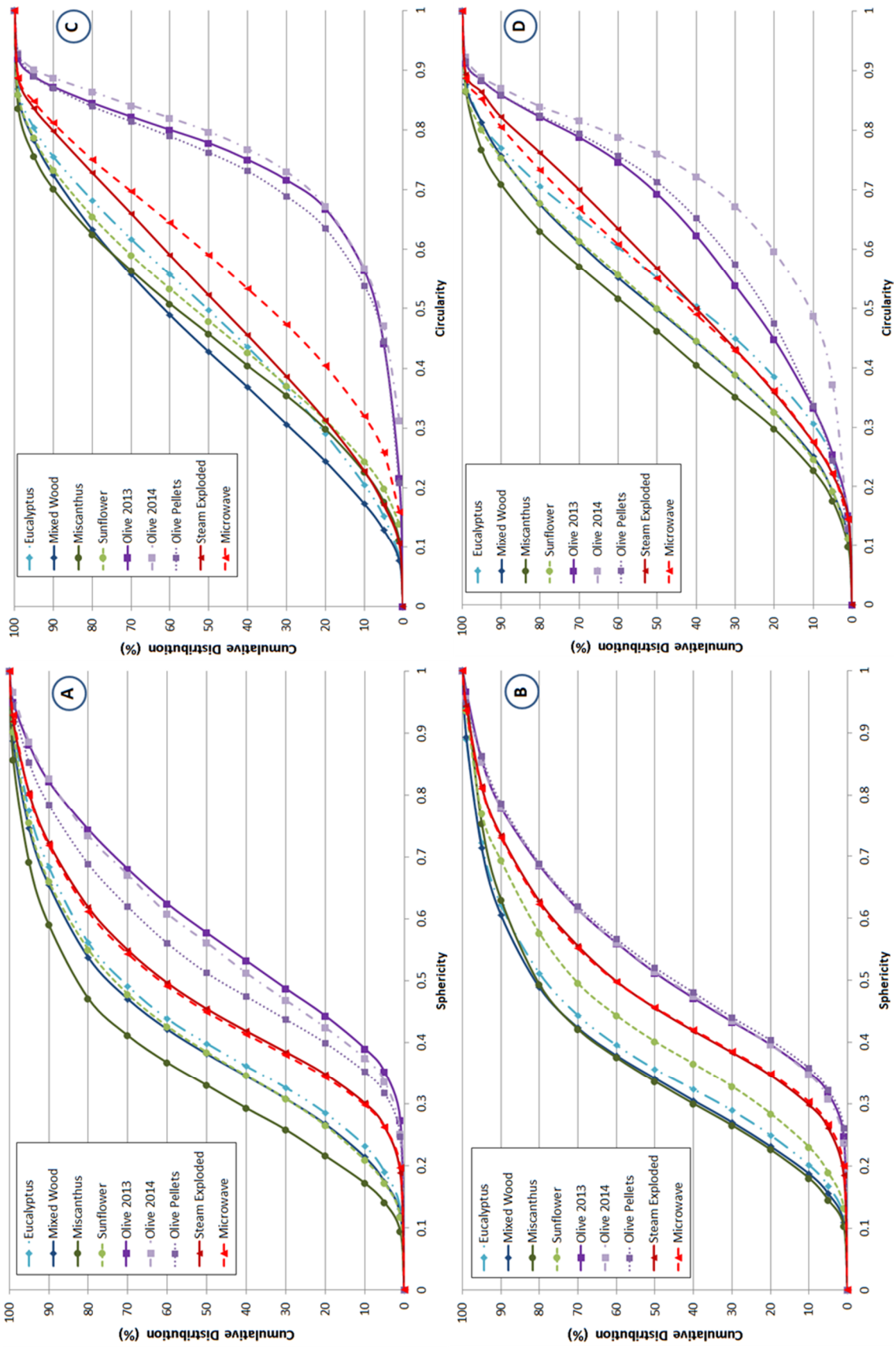


Figure 6.19: Planetary Ball Mill Comminuted Biomass Particle as Received (a) and Dried (b) Sphericity and Circularity (c and d) Cumulative Particle Shape Distributions

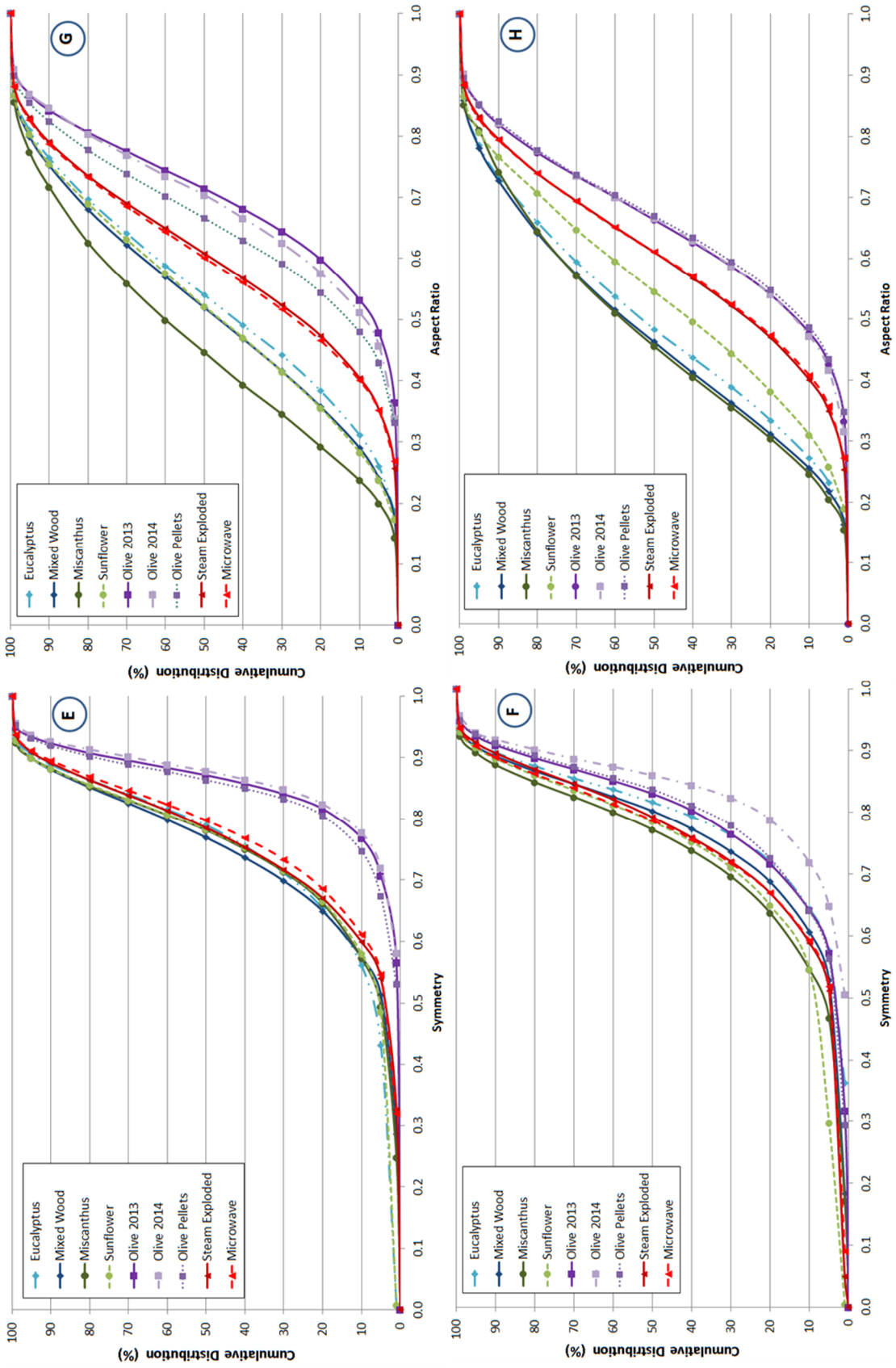


Figure 6.20: Planetary Ball Mill Comminuted Biomass Particle as Received (e) and Dried (f) Symmetry and Aspect Ratio (g and h) Cumulative Particle Shape Distributions

6.4.3. Heat Transfer with Materials

The olive cake optimisation trials (section 6.2) showed that heat generation and caking was influenced by the moisture content of the material and milling conditions experienced within the mill. To analyse these phenomena for a wide range of biomass samples, the heat generated during the milling process was analysed via thermal imaging and point temperature measurements of the biomass ball and biomass material immediately after comminution.

The heat flow behaviour of the materials was analysed via DSC of the milled as received samples. The heat generation within the mills after comminution in as received and dried states is shown in figures 6.21 and 6.22. There is a high amount of heat transfer within the materials, and as with the olive cake tests (Fig. 6.12) the dried milling condition results in higher heat generation than for the as received samples. The highest heat transfer was seen in the dried steam exploded pellets, which was also noted in the point measurement temperature (Fig. 6.23). The lowest heat generation was for as received olive cake 2013. Only miscanthus showed little difference in the heat generation in the thermal images (Fig. 6.22 and measured temperatures between as received and dried states (Fig. 6.23). As noted in section 6.4.1, a negligible particle size reduction was observed for miscanthus pellets (Fig. 6.18). The pellet partially reduced back to its constituent particles and did not reduce further in particle size beyond the pre-milled particle sizes.

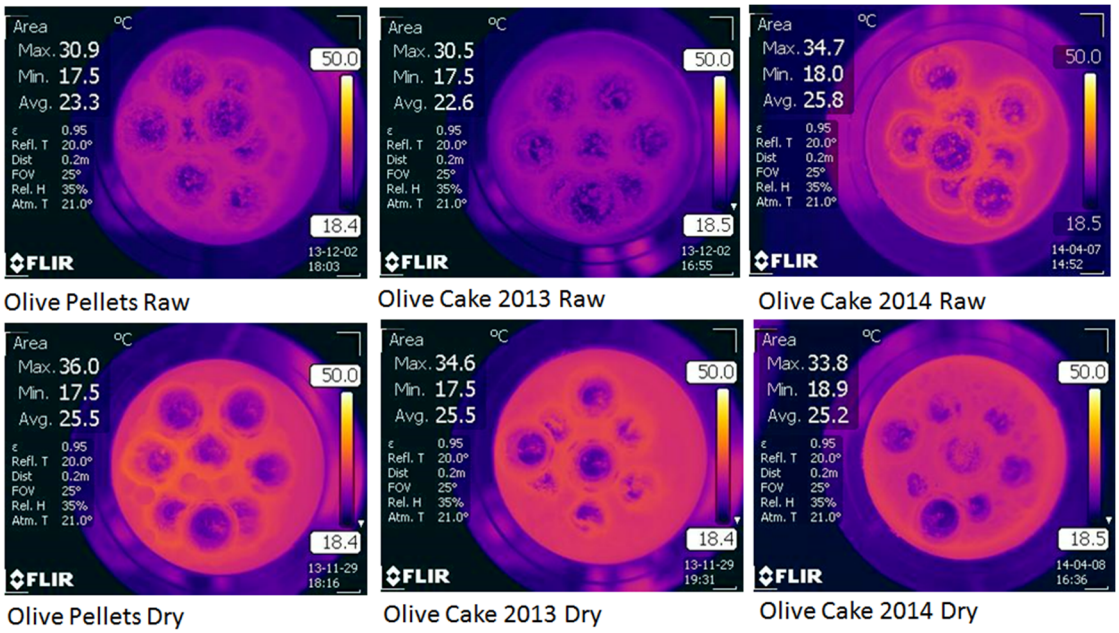


Figure 6.21: Thermal Imaging of Heat Generation in As Received (above) and Dried (below) Olive Pellets, Olive Cake 2013 and 2014 (left to right) Milled in a Planetary Ball Mill

The point measurements of the biomass and milling balls after milling (Fig. 6.23) support the thermal imaging results in figures 6.21 and 6.22. The milling balls attain a higher temperature (usually around 2 °C higher) than the comminuted biomass during the experiment.

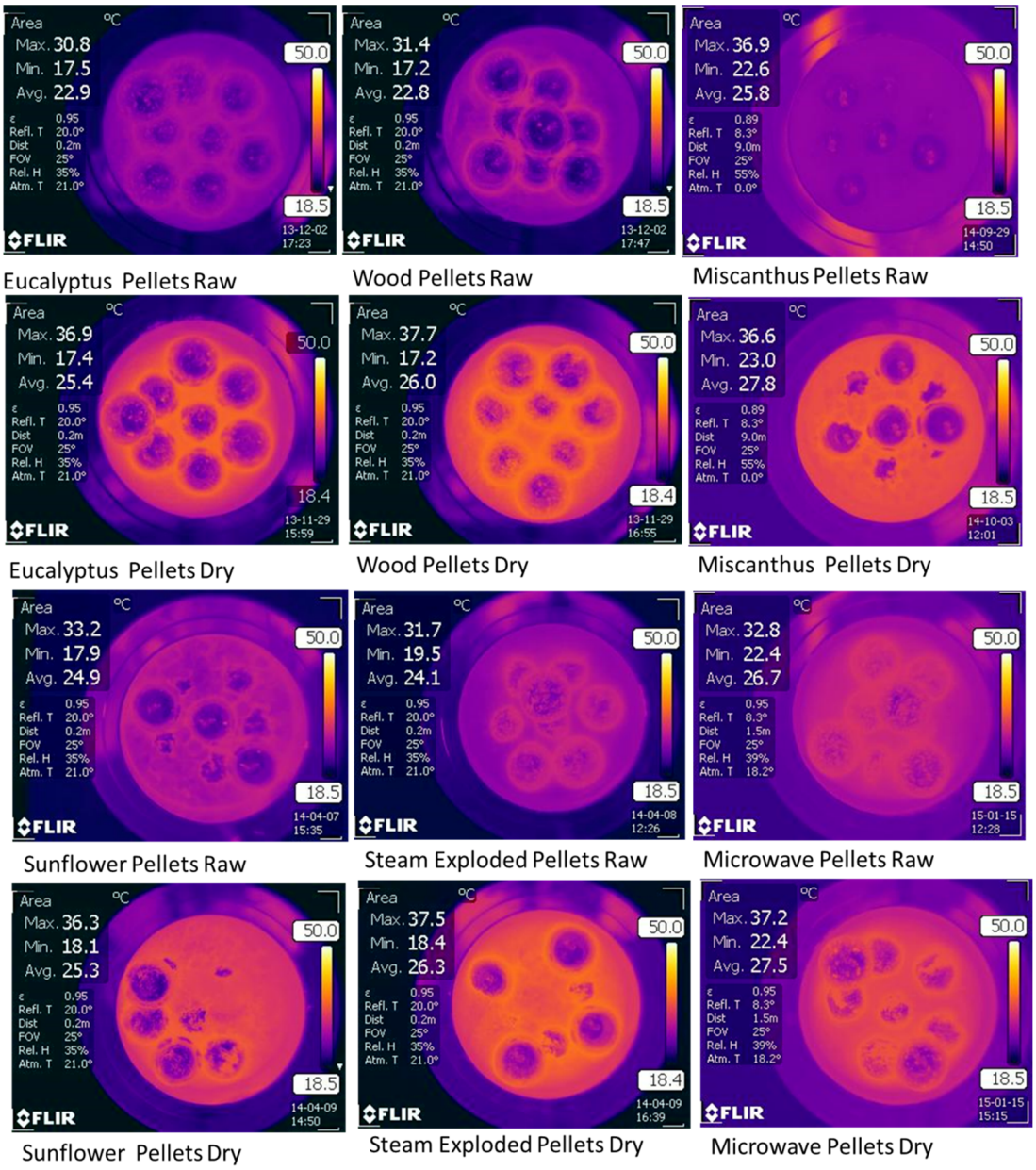


Figure 6.22: Thermal Imaging of Heat Generation in As Received (Above) and Dried (Below) Eucalyptus, Mixed Wood, and Miscanthus Pellets (Top 2 Rows left to right) and Sunflower, Steam Exploded and Microwave Pellets (Bottom 2 Rows left to right) Milled in a Planetary Ball Mill

These results supported by the thermal imaging results in figure 6.21. Overall, the point temperature measurements show that there is more consistent milling ball and comminuted

temperatures in the dried condition. The milled ball temperatures are between 30-32 °C (apart from steam exploded which saw higher levels of heat generation) and biomass temperatures of 28-30 °C. There is greater variability in the temperatures observed for the as received samples, with milling ball temperatures between 25-31 °C and comminuted biomass temperatures of 24-28 °C. This illustrates the impact moisture content has on the heat generated within the mills, as it acts as an inhibitor to milling and plasticises the biomass, reducing the energy consumption rates and heat generated within the mill, as described in section 6.3.

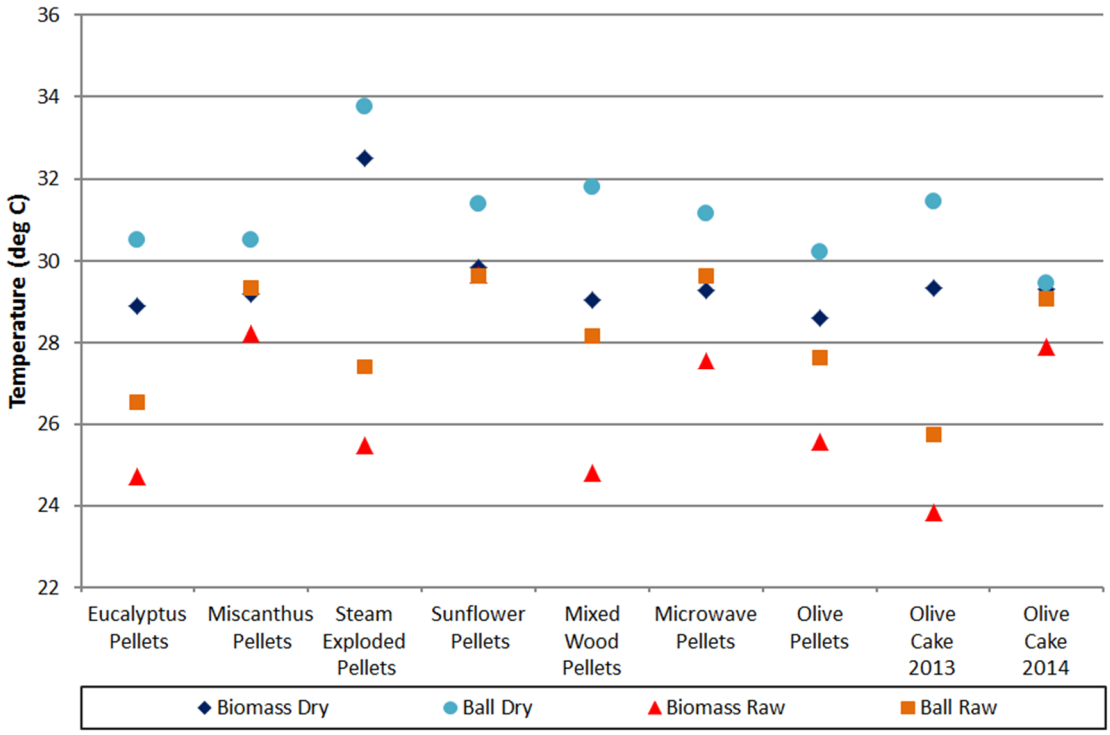


Figure 6.23: Biomass and Ball Temperatures for Biomass Milled in a Planetary Ball Mill

Caking was only observed for olive cake 2013 during the tests, which indicates that different thermal heat flow behaviours are in effect for the other materials. To investigate the heat flow behaviour of the samples, the comminuted as received samples were tested in a DSC as per section 3.1.12. Figure 6.24 shows the first heating scan of the DSC test on the comminuted biomass samples in as received state. It is clear that only olive cake 2013 shows the glass transition step around 80-100 °C (exothermic-endothermic shift). The other biomass samples are not fruit biomasses but composite structures of hemicellulose, cellulose and lignin, unlike olive cake which has the lignin concentrated in the pip and hemicellulose and cellulose concentrated in the pulp. For these materials no glass transition step was observed as no caking occurred during the milling process. From an industrial perspective, if caking issues occur in the conveying and comminution system, DSC can be

used to analyse the heat flow behaviour of a material and see if a glass transition step is present. Drying of the samples has been shown to alleviate the caking issue, but results in higher heat generation and finer particle size distributions, which could lead to mill fires or explosions.

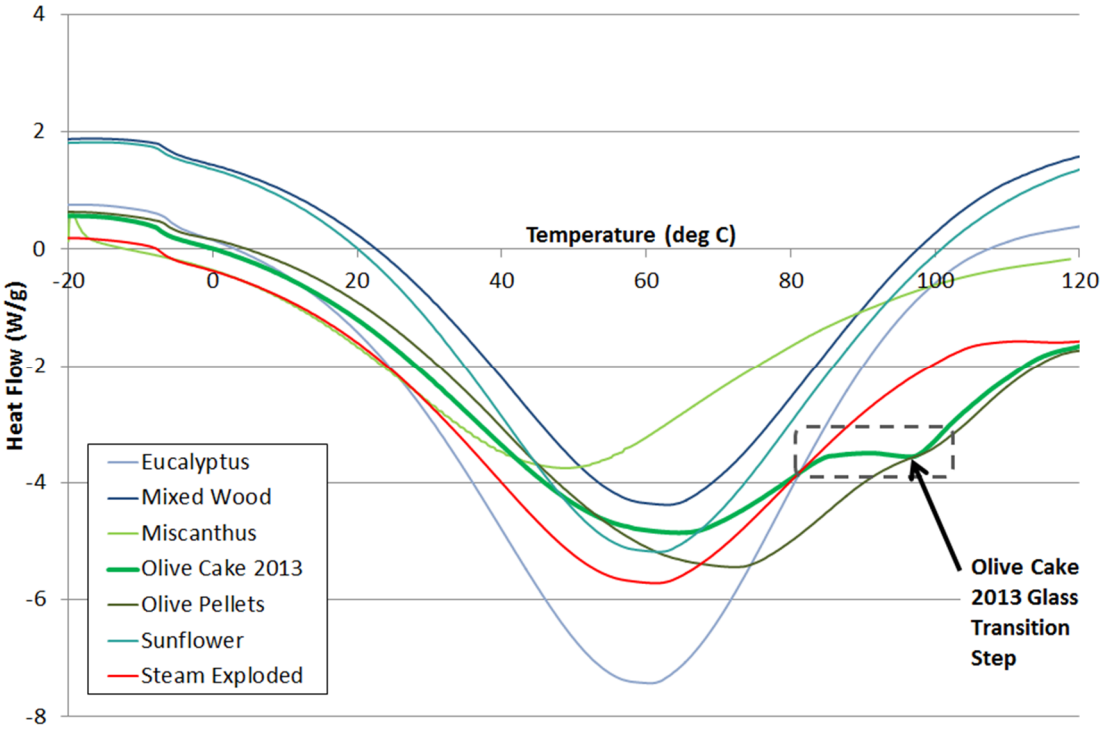


Figure 6.24: First Heating Scan in DSC for As Received Biomass Samples

6.5. Conclusions

The multiple non-linear regression analysis showed that the specific effective energy consumption rate in a planetary ball mill is primarily influenced by mill speed, followed by mill volume and energy input, while the comminuted particle sizes obtained are primarily influenced by milling duration. Thus a continuous application of force will result in finer particles size distributions in a planetary ball mill. As noted in previous biomass milling studies in hammer mills, moisture was shown to act as an inhibitor to milling and plasticiser of biomass, increasing its ductility and resulting in lower energy consumption rates and heat generation in a planetary ball mill.

The main novelty of the chapter was in the analysis of the olive caking phenomenon. Not only was the phenomenon replicated in the mill, the study analysed how it was impacted by different mill settings. The study showed for the first time that the olive caking phenomenon is associated with the pulp section of the material. The sugar and moisture content of the

pulp section are such that, when combined with the heat generation within the mill, a glass transition step occurred which results in the caking of the olive.

The study proved that by removing the moisture from the olive cake that the caking phenomenon could be eliminated and the glass transition step did not occur.

The industrial implication of this result is that olive cake fines below 1 mm should be sieved out and sent directly to the burner and not comminuted. This will remove the pulp section of the olive, and thus reduce the risk of caking in comminution equipment and eliminate unnecessary milling of material already at the desired particle size. In addition, if caking issues occur in the conveying and comminution system for any biomass, heat flow analysis can be used to analyse the heat flow behaviour of a material and see if a glass transition step is present.

Chapter 7 - Cutting Mill

Historically Biomass comminution research has primarily focused on the milling behaviour of woody and herbaceous biomass in hammer or cutting mills. Extensive studies have been conducted on non-processed or chipped biomass, but as noted by Temmerman et al. (2013) there is little research on the milling of densified biomass products in any mills.

In previous studies into biomass hammer milling optimisation, the following outcomes have been noted. Biomass milling energy consumption is influenced by the material variables; the material moisture content, initial particle size and the material composition itself (Temmerman et al., 2013). Specific energy consumption has a negative correlation with screen size in hammer mills (Adapa et al., 2011), thus energy consumption will decrease with increasing screen size (Zhang et al., 2012). A strong correlation has been found between hammer mill speed and specific effective energy consumption (Bitra et al., 2008; Bitra, Womac, Chevanan, et al., 2009). There is a simple linear relationship between energy consumption and the ratio of initial to final screen sizes (Ghorbani et al., 2010). In knife mills, screen size and feed rate have been found to be the main influencer on particle size (Bitra, Womac, Yang, Igathinathane, et al., 2009), but in hammer mills, the particle size is influenced by the screen and angular velocity of the hammers, with higher angular velocity resulting in a lower dispersion. However screen size and moisture content are the main variables in the hammer mill (Gil et al., 2013). Based on the wood particle target size of 1mm in coal fired power stations (Tamura et al., 2001), a screen size of 4mm provided the optimal product in a hammer mill (Esteban et al., 2006).

Thermal pre-treatments have been showed to have a positive effect on the grindability of biomass in hammer and cutting mills. Specific energy and mean particle size reduce with increasing torrefaction temperature (Phanphanich et al., 2011). Steam explosion pre-treatments result in reduced mean geometric diameters and bulk densities (Adapa et al., 2010), and microwaving results in a reduction of mean particle size (Satpathy et al., 2014).

However, few papers look at the impact of hammer or cutting mills on mill choking and the impact on particle shape. This chapter will focus on outlining the optimal conditions for milling biomass in a cutting mill based on either minimising specific effective energy consumption, minimising the percentage mass loss during milling, or maximising the Rosin-Rammler distribution parameter. Based on these studies and the settings used in full scale mills, the impact of drying biomass on energy consumption, and the variation in particle size

and shape for the same mill settings will be investigated for a range of densified biomass materials. The aim is to explore the variance in mill settings on biomass milling behaviour, then investigate how material type and drying impacts the milling behaviour for set conditions.

7.1. Materials and Methods

As received white wood pellets were used for the cutting mill optimisation study. This material was selected for the optimisation study based on availability from BF2RA in suitable quantities at the time the study was conducted and due to it being a woody biomass which is well suited to cutting mills (section 2.18). For the material comparison study, shredded bagasse straw, 2013 olive cake, olive pellets, mixed wood pellets, eucalyptus pellets, steam exploded pellets, miscanthus pellets, sunflower pellets, microwave pellets, and white wood pellets were used.

For the study investigating the impact of drying, all samples apart from microwave and white wood pellets were tested. The cutting mill optimisation study followed the method outlined in section 3.2.4.1. Data analysis used multiple non-linear regression analysis to analyse model fit and model optimisation as described in section 3.2.2. The material comparison and impact of drying study was conducted as per section 3.2.4.2.

7.2. Cutting Mill Optimisation Study

The initial stage of the optimisation study was to investigate the idle run behaviour of the cutting mill at different speeds. The energy consumption was measured over a 10 minute period (in triplicate) and the average instantaneous idle energy consumption was obtained for a range of mill rotor speeds. Figure 7.1 shows that there is a strong linear relationship between the instantaneous energy consumed and mill speed, with a fit of 98.9%. The trend line does not go through the origin, which implies that there is a base load in the mill energy consumption which is not related to rotor speed but does not vary with increasing mill speed. The average of the idle instantaneous energy consumption was used as a base line for the subsequent cutting mill experiments.

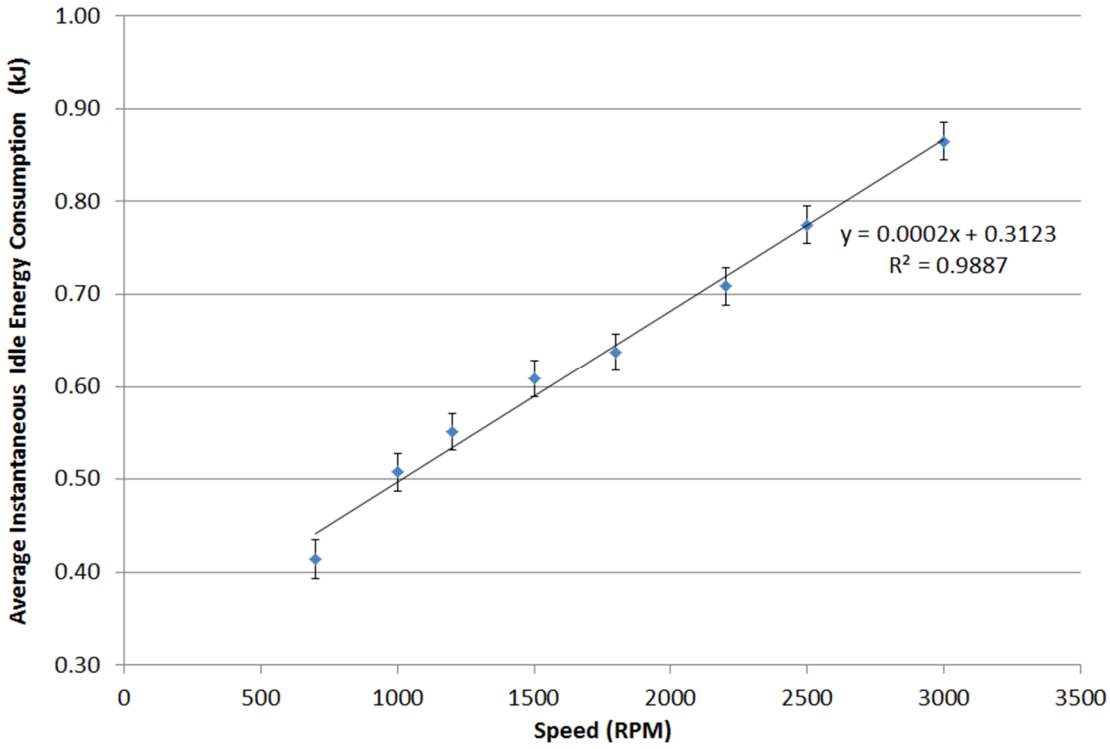


Figure 7.1: Cutting Mill Idle Average Energy Consumption versus Mill Speed

7.2.1. Specific Effective Energy Optimisation

The specific effective energy consumption (E_e) is indicative of the resistance to milling for a given sample. The aim of the optimisation analysis is to find a model equation for the system, and based on this find the optimal conditions to minimise energy consumption. Specific effective energy consumption was measured for seven speeds (700, 1000, 1500, 1800, 2200, 2500 and 3000 RPM), for three feed rates (approximately 0.0006, 0.001 and 0.006 kg/s), and for two screen sizes (4 mm and 1.5 mm), the results of which are shown in Appendix B.

These results were inputted into a multiple non-linear regression model set to minimise the specific effective energy. The analysis was repeated several times to remove unusual data points from the study, as unusual data points can strongly influence the results. This reduced the total number of points used from 78 points to 55, which is a sufficient number of data points to obtain a precise estimate of the strength of the relationship. From this analysis, the equation of the model to minimise energy consumption is:

$$E_e = 4.21 + 0.01792x_1 - 61620x_2 - 5.06x_3 + 16279172{x_2}^2 - 2.74x_1x_2 \qquad \text{(eq. 7.1)}$$

Where x_1 is speed (RPM), x_2 is feed rate (kg/s), and x_3 is screen size (mm). The analysis showed that the relationship between the specific effective energy and the three variables is

significantly high, as the *p-value* was less than 0.001 (a relationship is statically significant if *p-value*< 0.1) with a fit of 92.5. The 7.5% remainder which is not explained by the model is likely to be related to the material itself, as pellets are heterogeneous materials of variable moisture contents, and as in previous studies (Temmerman et al., 2013).

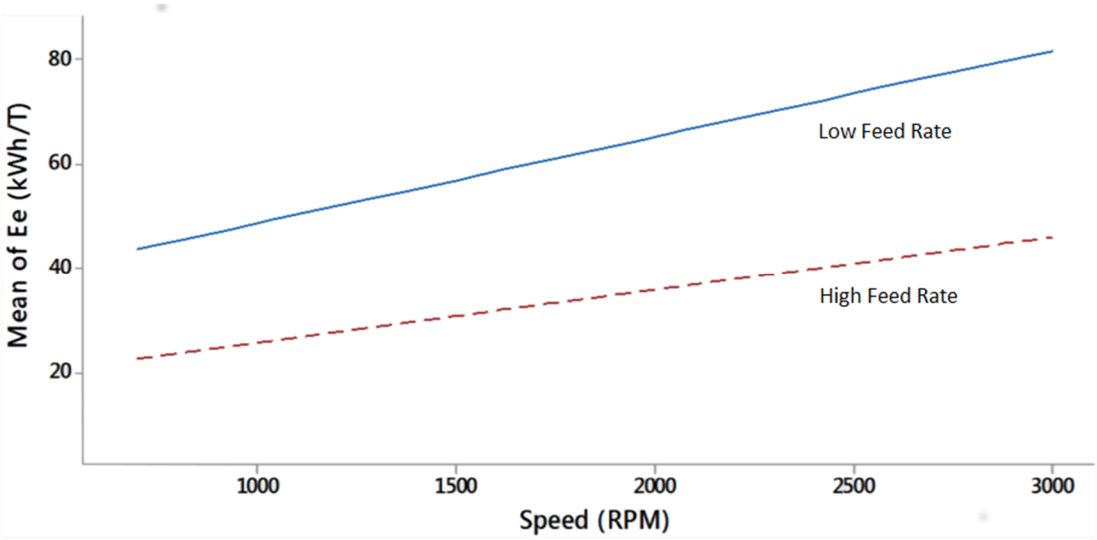


Figure 7.2: Interaction plots for Speed and Feed Rate for the Cutting Mill Optimisation Experiments

Figure 7.2 shows the interaction plots between speed and feed rate and its impact on mean specific effective energy consumption. No interaction was observed between speed and screen size, or screen size and feed rate. Higher feed rates result in lower specific effective energy consumption, as the mill is running for less time. The linear relationship between energy and speed which was seen in the idle condition in figure 7.1 is also noted here for the load condition. The energy consumption during the load condition is made of two components. There is the rotor speed, which consumes more energy as speed increases. The second is the resistance on the rotor from the milling action which is dictated by the screen and feed rate. In order to maintain the specified speed, more energy is required to overcome the resistance to milling from the material being comminuted. Figure 7.2 shows that the speed setting makes up a significant portion of this energy consumption, and this energy consumption shifts linearly upwards as the feed rate decreases.

Based on the results of the regression analysis, the optimal conditions to minimise energy consumption are a speed of 700 RPM, feed rate of 0.00195 kg/s, and a screen size of 4 mm screen. The predicted specific effective energy consumption is 4.5 KWh/t. The fit of the model against the measured values of specific effective energy consumption can be seen in figure 7.3. Two predicted zones are shown; one being the range of specific effective energy

for varying feed rates and speeds for the 4 mm screen, and the second is for the 1.5 mm screen. As expected, the 1.5 mm zone provides greater specific effective energy consumption than the 4mm screen, but there is significant overlap between the two screen sizes.

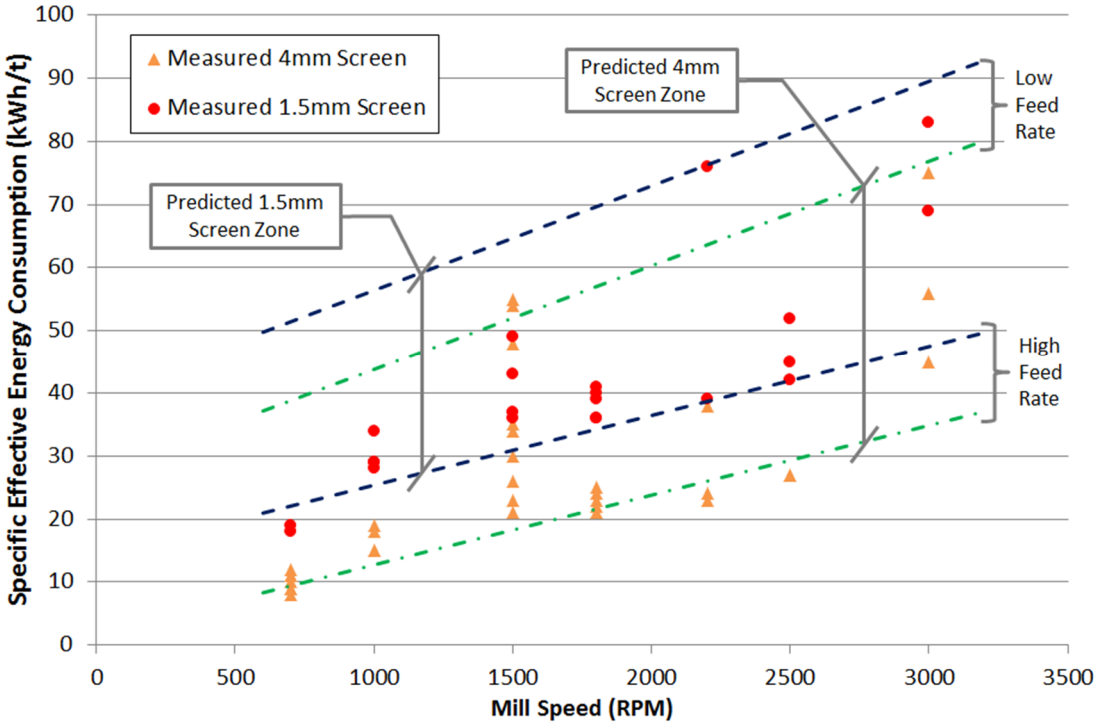


Figure 7.3: Predicted and Measured Specific Energy Consumption for the Cutting Mill

The implication from this analysis is that to minimise energy consumption the mill should be run at low speeds, high feed rates and with larger screen sizes. This is the first time this relationship has been identified for densified biomass in a cutting milling. The result is supported by the work of Bitra et al. (2009), who used a single variable non-linear regression analysis and Pearson correlation between hammer mill variables and found that same trends were observed for non-densified biomass. That is to minimise energy consumption in a hammer or cutting mill, the speed should be set as low as possible with a high feed rate and a screen size of 3-4 mm. While the model equation will vary by material type, the trend for mill settings for optimal energy consumption for hammer and cutting mills seems to be the same. Thus more research is required to see how the relationship varies for different types of non-densified and densified biomasses, and if these relationships can be correlated to full scale hammer mills. This would allow for biomass milling behaviour models in hammer and cutting mills to be developed which would help power generators understand and optimise the milling behaviour of a new sample prior to full scale milling trials. However energy consumption is just one parameter which needs to be considered in the optimisation of

biomass milling in hammer and cutting mills. High feed rates can lead to feed overload in the mill, thus the impact of mill choking needs to be considered when selecting to optimal general conditions for the cutting mill.

7.2.2. Optimisation of Mass Holdup

Mass output from a mill is an important milling parameter for controlling power generation production. However the impact of mill settings on mass output has not been analysed as part of previous biomass milling optimisation studies for hammer, knife or cutting mills. A reduction in mass output from a mill is indicative of mill choking. An increase in percentage mass holdup from milling (ratio of mass output to mass input) implies that the mill has not been able to empty, as the material is building up within the mill. The aim of this optimisation is to explore which variables impact mass output and find the optimal conditions to minimise the percentage mass holdup during.

The results are from the same tests as the specific effective energy consumption in section 7.2.1, and the results for mass holdup are shown in Appendix B. These results were inputted into a multiple non-linear regression model set to minimise percentage of mass holdup. Once more, unusual data points were removed from the analysis, reducing the number of points from 78 to 60. This is a sufficient number of points to give a very precise estimation of the strength of the relationship. From this analysis, the equation of the model to minimise mass holdup is:

$$\%\, Mass\ Holdup = -11.042 + 0.005663x_1 + 10086x_2 + 3.249x_3 + 1.252x_1x_2 - 0.001699x_1x_3 - 2789x_2x_3 \quad \text{(eq. 7.2)}$$

Where x_1 is speed (RPM), x_2 is feed rate (kg/s), and x_3 is screen size (mm). The analysis showed that the relationship between the mass holdup and the three variables is very strong, as the *p*-value was less than 0.001 with a fit of 99.3%. Figure 7.4 shows the interaction plots for the analysis. Unlike the specific effective energy consumption analysis, there is a strong interaction between all the variables. The strongest interaction can be seen with feed rate and screen size. For the 4mm screen there is little impact on the percentage mass holdup with increasing feed rate, but for the 1.5mm screen, there is a significant increase in mass holdup with increasing feed rate.

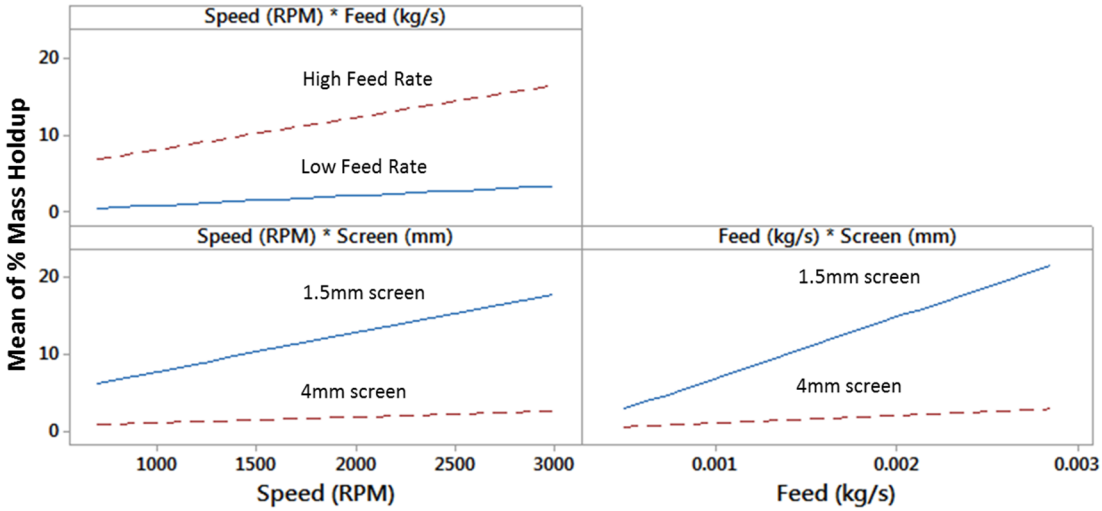


Figure 7.4: Interaction Plots of the Variables in the Mass Holdup Regression Analysis for the Cutting Mill

Figure 7.5 shows the particle size distribution for the 2200 RPM runs and the pre-milled disintegrated pellet. The 80th percentiles for the 4 mm screen are very close to that of the pre-milled runs, and shows a coarser profile below this, which implies the larger particles are only being milled to a coarse size, not fines. The 1.5 mm screen shows a much finer profile with an increased number of fines compared to the 4 mm screen. However, for the 1.5 mm screen, the percentage of mass holdup is higher, indicating that the mill is struggling to reduce the particle size to a smaller size. Thus if the screen size is smaller than the particle size of the pellet, the potential for mill choking will increase as the feed rate increases.

The interactions between speed-feed rate and speed-screen size showed similar trends to the feed rate-screen size interaction. In general, higher speeds with higher feed rates and small screen sizes will exasperate mill choking, but the main interaction is due to too much material entering the mill for screen size smaller than the pre-densified size. In order to minimise mill choking, the recommended mill operating conditions are a speed of 3000 RPM, feed rate of 0.000507 kg/s, and a screen size of 4 mm screen, which is predicted to give a mass holdup of 4.4×10^{-16}% (approximately zero mass holdup). The measured percentage mass holdup and predicted bands for varying speeds and feed rates for 4 mm and 1.5 mm screens can be seen in figure 7.6. As with figure 7.3, the 1.5 mm screen results in higher percentage mass holdup than the 4mm screen. Distinct bands between the screen sizes are visible for all speeds and feed rates with only slight overlapping at low feed rates and speeds below 1300 RPM. This clear difference is also visible in the interaction plot for speed and screen size in figure 7.4.

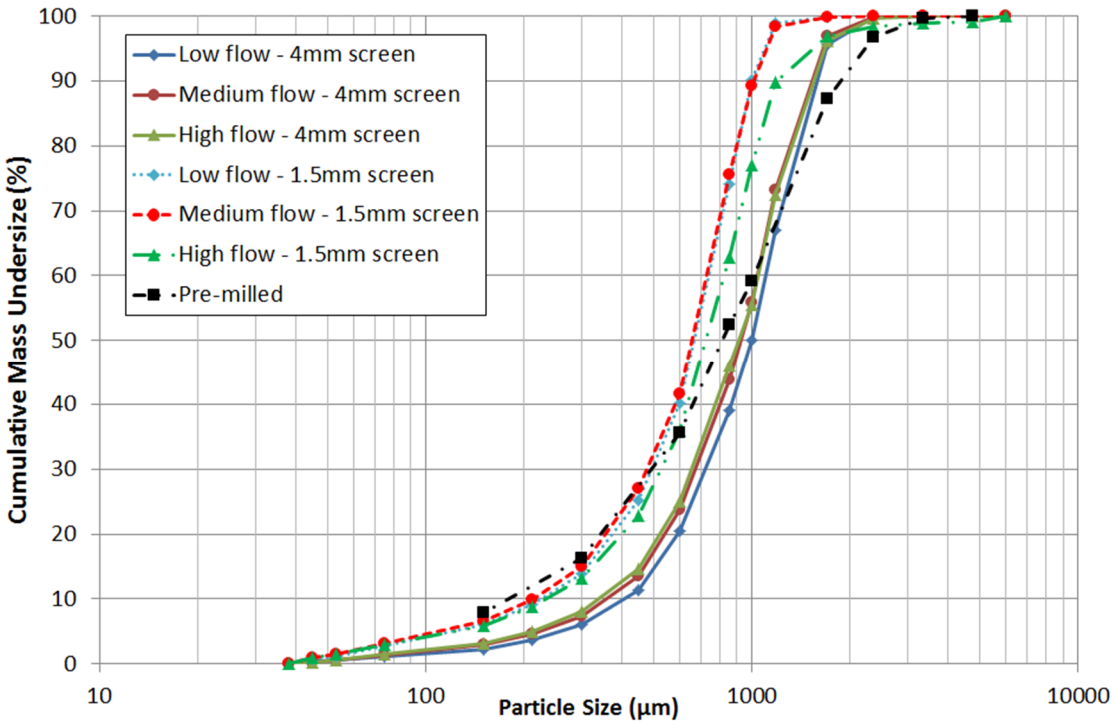


Figure 7.5: Pre-milled and Milled Particle Size Distribution at a Speed of 2200 RPM for low (0.006 kg/s), Medium (0.01 kg/s) and High (0.06 kg/s) Feed Rates and 1.5 mm and 4 mm Screens

The 4 mm screen results in low mass holdup for all speeds and feed rates. The 1.5 mm screen results in a wide range of mass holdup based on the mill conditions. Low feed rates results in mass holdup slightly higher than that seen at high feed rates for the 1.5 mm screen (circa 5% mass holdup). At high feed rates there is a significant increase in percentage mass holdup, with mass holdup over 15-20% for the highest feed rates. This indicates that the impact of mill choking become more extreme and unpredictable at higher speeds and feed rates.

This study provides a useful complement of data to the specific effective energy optimisation study. While low speeds and high feed rates result in optimal energy consumption, the opposite is true for mass holdup. Thus while minimising energy consumption is an important part of milling optimisation, maintaining a high level of mass throughput is essential for maintaining the thermal output. Thus a balance between energy consumption and mass holdup needs to be found for a biomass comminuted in a hammer or cutting mill. Future milling optimisation investigations into specific effective energy consumption should also take into account the impact on mass holdup as part of the study. The final part of the optimisation analysis is to look at the impact of mill operating conditions on the particle distributions produced by the cutting mill.

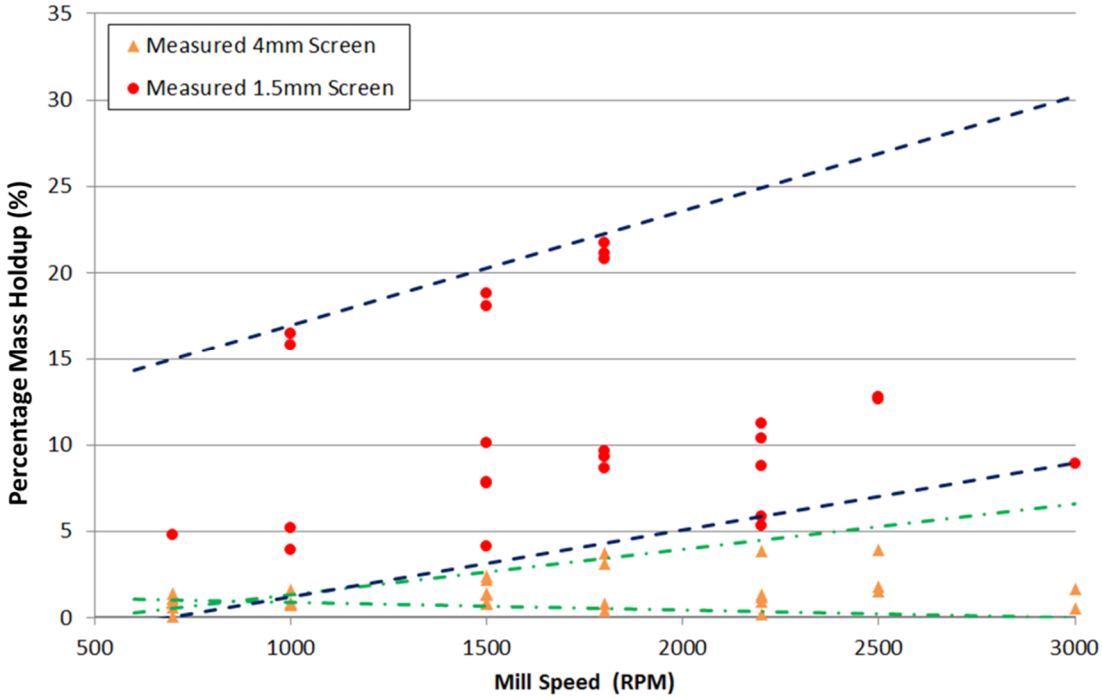


Figure 7.6: Predicted & Measured Percentage Mass Holdup

7.2.3. Optimisation of Rosin-Rammler Distribution Parameter

The final milling optimisation analysis is the investigation into the optimal conditions to maximise Rosin-Rammler distribution parameter (*n*). The distribution parameter is an indicator of the width of the particle size distribution, and a lower value of *n* is an indicator of a wider span (Bitra, Womac, Chevanan, et al., 2009; O. Williams et al., 2015). Thus the aim of the optimisation is to find the conditions where narrower spans are produced. Using the milled product from the previous sections, the samples were sieved to obtain a cumulative particle size distribution. The results of the Rosin-Rammler analysis of these cumulative distributions are shown in Appendix B.

These results were inputted into a multiple non-linear regression model set to maximise the Rosin-Rammler distribution parameter. Only 26 data points were available for this analysis, thus only an indicative strength of the relationship can be estimated from this analysis. From this analysis, the equation of the model to maximise the distribution parameter, *n*, is:

$$n = 2.6556 + 0.000032x_1 - 127.5x_2 - 0.0496x_3 - 0.00000007{x_1}^2 + 0.000023x_1x_3 \quad \text{(eq.7.3)}$$

Where x_1 is speed (RPM), x_2 is feed rate (kg/s), and x_3 is screen size (mm). The analysis showed that the relationship between the distribution parameter *n* and the three variables was high, as the *p*-value was less than 0.001 and fit of 91.3%.

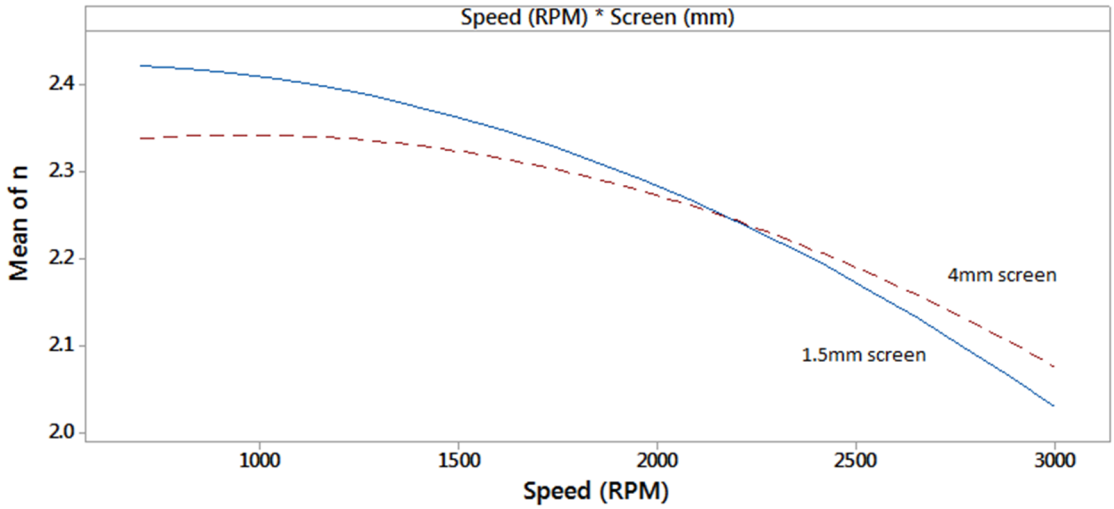


Figure 7.7: Interaction Plots of the Variables in the Distribution Parameter Regression Analysis for the Cutting Mill

Figure 7.7 shows the interaction plots between speed–screen size and its impact on distribution parameter. No interaction was observed between feed rate-speed or feed rate-screen in this analysis. The interaction between screen size and speed overlaps around 2200 RPM, indicating a change in behaviour in the mill. At low speeds the 1.5 mm screen results in higher n values, while at higher speeds the 4 mm screen provides the higher n values. This is related to the mass holdup which is occurring for the 1.5 mm screen at higher feed rates and speeds, resulting in a wider distribution as the mill struggles to empty once it is overloaded.

In order to maximise the distribution parameter the recommended mill operating conditions are a speed of 700 RPM, feed rate of 0.000505 kg/s, and a screen size of 1.5 mm, which is predicted to result in a distribution parameter of 2.532. The measured distribution parameters are plotted with predicted distribution parameter bands by screen size in figure 7.8. This also shows the cross-over of distribution by increasing speed for the screen sizes as indicated in figure 7.7. As with figure 7.7, there is little variation in *n* for varying screen size, in spite of the increasing energy consumption and mill choking at higher feed rates and speeds for the 1.5 mm screen. The scatter in the measured in the results is likely to be related to the heterogeneous nature of the pellet. Each pellet will have a slightly different particle size composition which will result in variations in the product when milled.

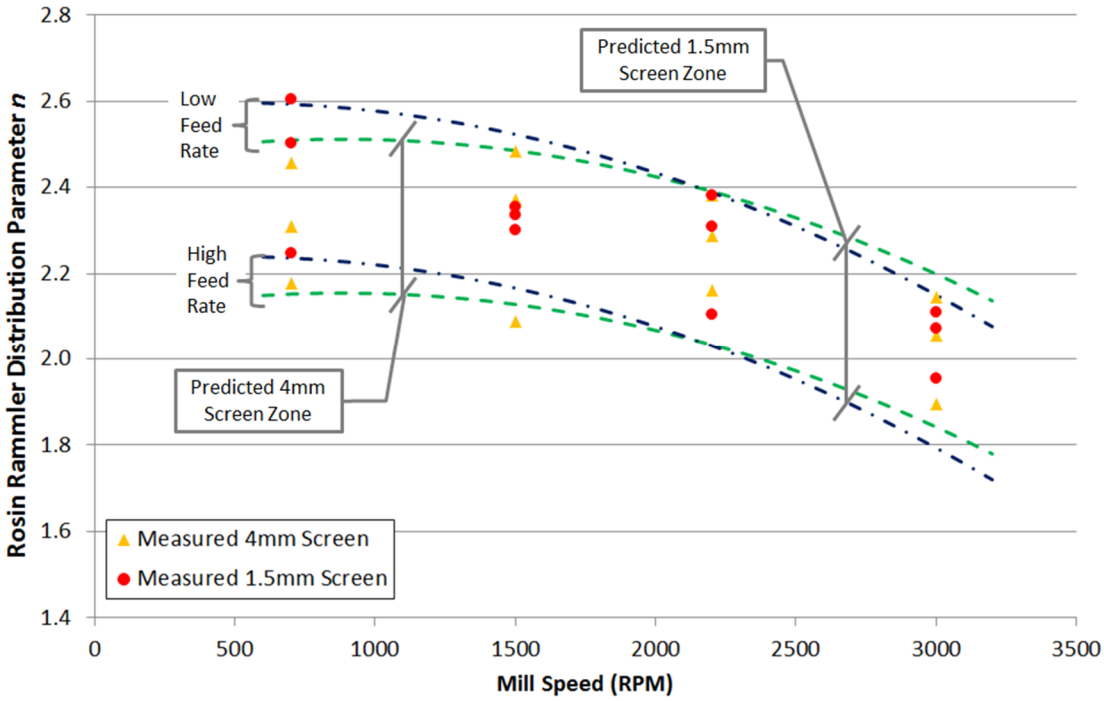


Figure 7.8: Predicted & Measured Rosin-Rammler Distribution Parameter

Bitra el al (2009) also found that the mill speed, screen size and feed rate had a significant impact on the Rosin-Rammler distribution parameter for switch grass comminution in a knife mil. Using a Pearson correlation, a moderate interaction was found for screen size and a weak interaction for feed rate and speed. However in a hammer mill, Bitra et al. (2009) found this correlation varied by material type. A moderate negative correlation was found for wheat straw, but switch grass and corn stover showed a weak positive correlation. Bitra el al studies (2009; 2009; 2009) were for non-densified biomasses, and as the feed had previously been comminuted through a 25.4 mm screen in a knife mill, the feed size was significantly greater than the screen sizes used. Thus comminution would be achieved for all screen sizes. However in this study, the use of densified materials means that the pre-milled particle size distribution meant that the 4 mm screen size resulted in little change in the particle size distributions through milling, as previously discussed and illustrated in figure 7.5. Thus the relationship between the Rosin-Rammler distribution parameter is different for densified biomasses compared to non-densified biomasses.

7.3. Optimal Conditions for Impact of Drying Tests

The optimisation study of mill operating conditions in a cutting mill has shown that the optimal conditions vary depending upon on the objective response from the mill. The study has shown how multiple variables interact and impact certain responses more than others, and show similar trends and observations to previous studies. For specific effective energy

consumption, the main interaction is between the feed rate and speed, with speed being the main influencer on energy consumption. This is the first time this relationship has been identified for densified biomass in a cutting milling, but is supported by similar studies for non-densified biomass (Bitra, Womac, Chevanan, et al., 2009). Thus to minimise energy consumption in a hammer or cutting mill, the speed should be set as low as possible with a high feed rate and a screen size of 3-4 mm.

The impact of mill variables on the mass output of a cutting mill for densified biomasses has not previously been studied in literature. The mass holdup during milling was due to an interaction between all the variables in different combinations, but feed rate and screen size was the main influencer. When the screen size is close to the pre-densified particle size distribution, the material will pass easily through the screen once it has broken down from pellet form. However when the screen size is smaller, the mill needs to perform two stages of milling; breaking down the pellet and then reducing the particle size. This leads to mill choking as the mill struggles to empty as the time the material spends in the milling chamber increases, and this is significantly compounded as the feed rate increases. While low speeds and high feed rates result in optimal energy consumption, the opposite is true for mass holdup. Thus while minimising energy consumption is an important part of milling optimisation, maintaining a high level of mass throughput is essential for maintaining the thermal output of a pulverised fuel burner. Thus a balance between energy consumption and mass holdup needs to be found for a biomass comminuted in a hammer or cutting mill.

Finally the Rosin-Rammler distribution parameter, *n*, is influenced by an interaction of speed and screen, but the main variable is the material itself and its pre-densified composition. In terms of mill variables, screen size and speed have been identified as key variables in determining product particle size in previous studies (Gil et al., 2013). However the relationship between the Rosin-Rammler distribution parameter is different for densified biomasses compared to non-densified biomasses due to the influence of the pellet particle size distribution on the resultant product, especially for the 4 mm screen size.

7.4. Impact of Drying on Material Comminution in a Cutting Mill

Material composition and moisture content have been shown to be key variables in biomass milling (Carone et al., 2011; Gil et al., 2013; Kobayashi et al., 2007; Miao et al., 2011; Temmerman et al., 2013). In full scale coal mills, coal is dried during the milling process to remove moisture and increase its brittleness. Coal mills operate on an inlet temperature of

350 °C and a controlled exit temperature of 70 °C (Scott, 1995). However dedicated biomass hammer mills are generally agricultural mills (Roskamp Champion, 2000) which do not include a drying section like coal mills. Thus for co-milling or dedicated biomass milling in coal mills, and for milling in biomass hammer mills, the impact of using as received biomass and dried biomass needs to be ascertained to understand the comminution performance of biomass in different situations. This study is in two parts; the first is a short study of the impact of drying shredded bagasse on energy consumption for varying speeds and screen sizes, and the second is for the impact of drying on the comminution performance for a wide range of biomasses commonly used in the power sector for fixed mill operating conditions.

7.5. Impact of Drying on Milling Behaviour of Shredded Bagasse

Shredded Bagasse was milled in the cutting mill at 3 different speeds (700, 1500 and 3000 RPM) and 3 different screen sizes (6 mm, 4 mm and 1.5 mm) for an approximate feed rate of 0.00064-0.00095 kg/s. The Bagasse was milled in two conditions: at it's as received moisture content (33.25 ± 9.9%), and dried. The moisture content of the as received sample varied greatly throughout the as received sample. However this is indicative of how the sample would be received in a full scale situation. The moisture reabsorption of Bagasse was 2.7% over a 24 hour period (section 4.7), and the dried samples used within this study were milled within 8 hours of drying to minimise moisture reabsorption.

Figure 7.9 shows how the specific effective energy consumption varies by screen size and moisture content. For the wet samples (as received), the energy consumption is significantly higher for all speeds and screen sizes. On average, drying the sample reduces the specific effective energy consumption by 79%. In addition, the variation in the result was significantly reduced by drying. The error bars shown in figure 7.9 vary widely for the wet samples, which is due to the inconsistent moisture content in the samples. However once the sample was dried the error bars reduce significantly, and the remaining error is likely to be related to the heterogeneous particle size of the sample. The study has shown that moisture is a significant variable in the milling effectiveness of biomass, which has been noted in previous studies (Carone et al., 2011; Gil et al., 2013; Miao et al., 2011; Temmerman et al., 2013).

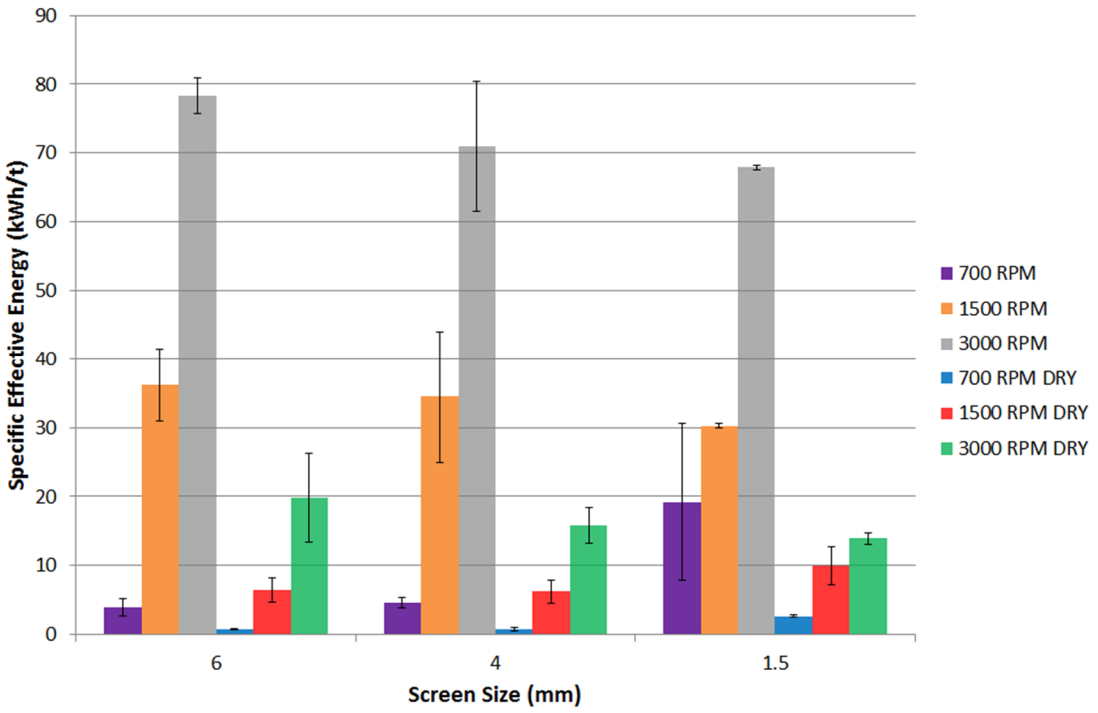


Figure 7.9: Specific Effective Energy Consumption against Screen Size for Bagasse

As with the optimisation study in section 7.2.1, increasing speed will result in an increase in energy consumption, and this trend is observed through all the screen sizes and for both the wet and dry tests. However decreasing screen size doesn't result in increasing energy consumption, particularly for the wet samples for the 1500 and 3000 RPM samples, and this is most likely the result of the variation in moisture content and the heterogeneous particle size of the sample. For 700 RPM, there is a clear increase in energy consumption as the screen size decreases, and this negative correlation between energy and screen size has been noted in previous studies (Adapa et al., 2011; Ghorbani et al., 2010; Zhang et al., 2012). For the dried samples, 700 and 1500 RPM show this negative correlation with screen size, but for 3000 RPM, the 6 mm screen size shows the highest average energy consumption. However the error bars for the analysis indicate that the correlation could be correct for 6mm, but anomalous readings have led to a higher average values.

The moisture released from the bagasse during milling can be in one of two forms; water droplets or steam. Given that the latent heat of evaporation of water is 2257 kJ/kg, it is possible to tell what form the water was released in via the energy difference in milling between the wet and dried samples. The moisture content of the bagasse was 33.25% on average, and each run used approximately 100 g of sample. Thus the mass of the moisture in the wet bagasse was approximately 33.25 g. Table 7.1 shows that the evaporation energy is approximately 75 kJ, but the energy difference between the wet and dried bagasse milling

energies is significantly lower. Thus the water released is in the form of water droplets not steam as not enough energy is being supplied to evaporate the water from the samples.

Speed (RPM)	Screen (mm)	Energy Difference (kWh/t)	Energy Difference (kJ/Kg)	Total Mass (Kg)	Evaporation Energy (kJ)	Energy Difference (kJ)
700	**6**	10.5	37.7	0.100	75.3	3.8
700	**4**	11.3	40.8	0.101	75.6	4.1
700	**1.5**	32.2	115.8	0.100	75.3	11.6
1500	**6**	61.1	219.7	0.100	75.1	22.0
1500	**4**	57.4	206.4	0.101	75.8	20.9
1500	**1.5**	41.6	149.6	0.100	75.3	15.0
3000	**6**	90.6	326.1	0.105	78.9	34.3
3000	**4**	92.7	333.6	0.100	75.4	33.5
3000	**1.5**	76.2	274.1	0.101	76.0	27.8

Table 7.1: Comparison of Evaporation Energy for Wet Bagasse and the Difference in Milling Energies of Wet and Dried Bagasse

This study has shown that milling samples in a variable moisture condition can led to significantly higher energy consumption than for dried samples, and that water is released in the form of water droplets not steam. Also the variability in moisture can be a greater influencer on energy consumption than the operational settings.

7.6. Selected Cutting Milling Conditions

Based on the particle target size for biomass of 1mm in coal fired power stations (Tamura et al., 2001), a screen size of 4 mm has been shown to provide the optimal product in a hammer mill (Esteban et al., 2006). The screen size used at EDF Cottam is 3.2-3.8 mm for the milling of olive cake, sunflower pellets and steam exploded pellets. Thus in order to balance the three responses of energy consumption, mass holdup and particle distribution, the mill operating conditions were selected to be a speed of 1500 RPM, feed rate of approximately 0.0025 ±0.0003 kg/s, and a screen size of 4 mm.

7.7. Impact of Drying on Biomasses Comminution in a Cutting Mill

Olive cake, miscanthus, sunflower, steam exploded, olive, eucalyptus and mixed wood pellets were tested at their as received moisture content and dried in the cutting mill for the set conditions. Microwave pellets were also tested at their as received moisture content but not dried due to their late inclusion in the project. The dried samples were dried as per section 3.1.1 and then stored in sealed bags until use. The samples were milled within 5 days

of drying (section 4.7). Moisture uptake for samples stored in this way did not exceed 0.3% after 6 days for any of the samples, and hence can be considered dry at the point of milling. Low levels of mass holdup was observed for all samples in the as received and dried moisture conditions. For the as received moisture condition, the percentage mass loss was between 1.2% (eucalyptus pellets) to 2.2% (sunflower pellets), and for dried was between 0.9% (miscanthus pellets) to 2.6% (olive cake).

7.7.1. Energy Consumption

Figure 7.10 shows the Specific Effective Energy (E_e) results for the as received and dried samples. The highest E_e was for woody and miscanthus pellets. The lowest E_e was for microwave, sunflower, steam exploded pellets and olive cake. Drying reduced energy consumption for all the samples. Moisture acts as a plasticiser in the pellets, making them more ductile and thus difficult to break by shear failure (Pierre et al., 2013). There was a significant reduction in E_e for mixed wood pellets (38%) and eucalyptus pellets (34%). Steam exploded pellets showed a much lower reduction (2%), and thermal treatments are known to improve the hydrophobic tendencies of biomass (Repellin et al., 2010; Jaya Shankar Tumuluru et al., 2011), reducing the influence of moisture on the mechanical properties of the pellets.

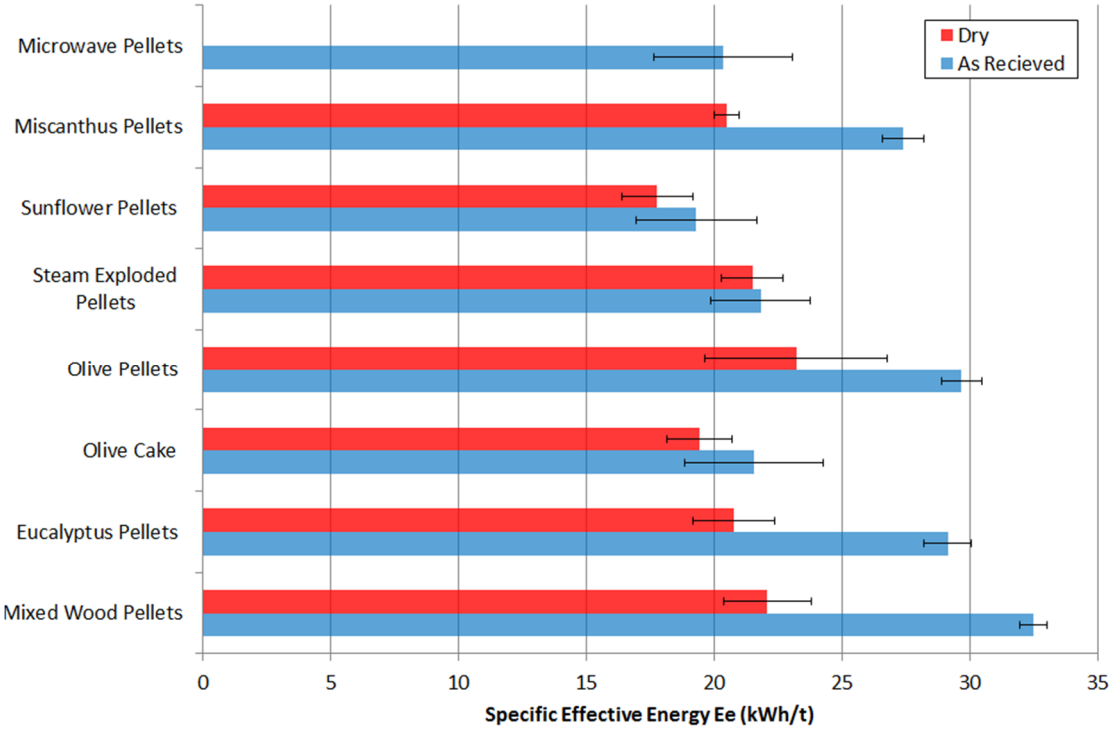


Figure 7.10: Specific Effective Energy Consumption for As Received and Dried Samples for the Cutting Mill

The results show that despite some samples such as olive pellets and sunflower pellets having similar moisture contents of around 11%, the impact of drying resulted in significantly different reductions in energy consumption (8% for sunflower and 24% for olive pellets). Thus it is likely that the impact of drying will vary by material type for the same reduction in moisture content due to pellet composition variances.

Cutting mill specific energy consumption represented a small percentage of the Higher Heating Value (HHV_d) of the tested samples (table 4.9 in section 4.12), with sunflower consuming the least (0.3%) to mixed wood consuming the highest (0.6%). The drying method used (section 3.1.1) is not realistic of what would be used in industry. In coal mills, dry hot air is used to dry the coal within the mill, and for high moisture coals, recycled heat from the flue gas is used (Scott, 1995). Biomass drying can consume as much as 70% of the energy used in pellet production (Murray, 2010), but this is related to drying virgin wood from moisture contents of around 50% down to 10% (H. Li et al., 2012). A typical tube-ball coal mill generally requires 7-30 kWh/Mg of milling energy depending on the material type, with an additional 5-10 kWh/Mg for the fan (Mujumdar et al., 2014). The heating is typically 1.3 kg/kg for brown coals and 2.0 kg/kg for anthracite. For coals with moisture levels of 10-14% air at 300-400 °C should be used, for 15-20% a temperature of 700-1000 °C are required and coals with moisture contents above 25% should be partially dried in the chute prior to the mill with hot combustion gases. Coal mills converted to run biomass operate at lower temperatures (Obernberger et al., 2010b), thus the drying requirements will be similar to that of coal within a coal mill.

As noted in section 7.5, the water can be released in two forms during the milling process. Assuming that the latent heat of evaporation for water is 2257 kJ/kg, table 7.2 shows how the evaporation energy for the moisture contained in the raw biomasses is much lower than the energy difference between raw and dried pellets. Thus as with the bagasse milling, the water released during milling is in the form of water droplets not steam.

Section 4.8 reported the durability of several of the pellets used in this study, and showed that sunflower pellets had lowest durability. Figure 7.11 shows the relationship between energy consumption and pellet durability. A trend can be seen between pellet durability and energy consumption for non-treated biomass in cutting mill, but more samples are required to test this trend. Sunflower had the lowest durability and energy consumption of the non-treated samples, thus the pellets broke up easily in the mill, hence the lower energy consumption. Mixed wood pellets and steam exploded did not fit the trend. This is likely to

be related to the mixed wood pellets struggling to reduce in size, hence the higher energy, while the steam exploded pellets showed little resistance and easily broke down for the 4mm screen.

Sample	Energy Difference (kWh/t)	Energy Difference (kJ/Kg)	Total mass (Kg)	Moisture content (%)	Evaporation Energy (kJ)	Energy Difference (kJ)
Mixed Wood Pellets	10.4	37.4	0.25	9.4	53.3	9.3
Eucalyptus Pellets	8.4	30.1	0.25	10.5	59.1	7.5
Olive Cake	2.1	7.6	0.25	15.9	89.9	1.9
Olive Pellets	6.5	23.2	0.25	11.2	63.0	5.8
Steam Exploded Pellets	0.3	1.2	0.25	7.2	40.5	0.3
Sunflower Pellets	1.5	5.5	0.25	11.8	66.5	1.4
Miscanthus Pellets	6.9	24.8	0.25	7.6	43.0	6.2

Table 7.2: Comparison of Evaporation Energy for Wet Biomass and the Difference in Milling Energies of Wet and Dried Biomass

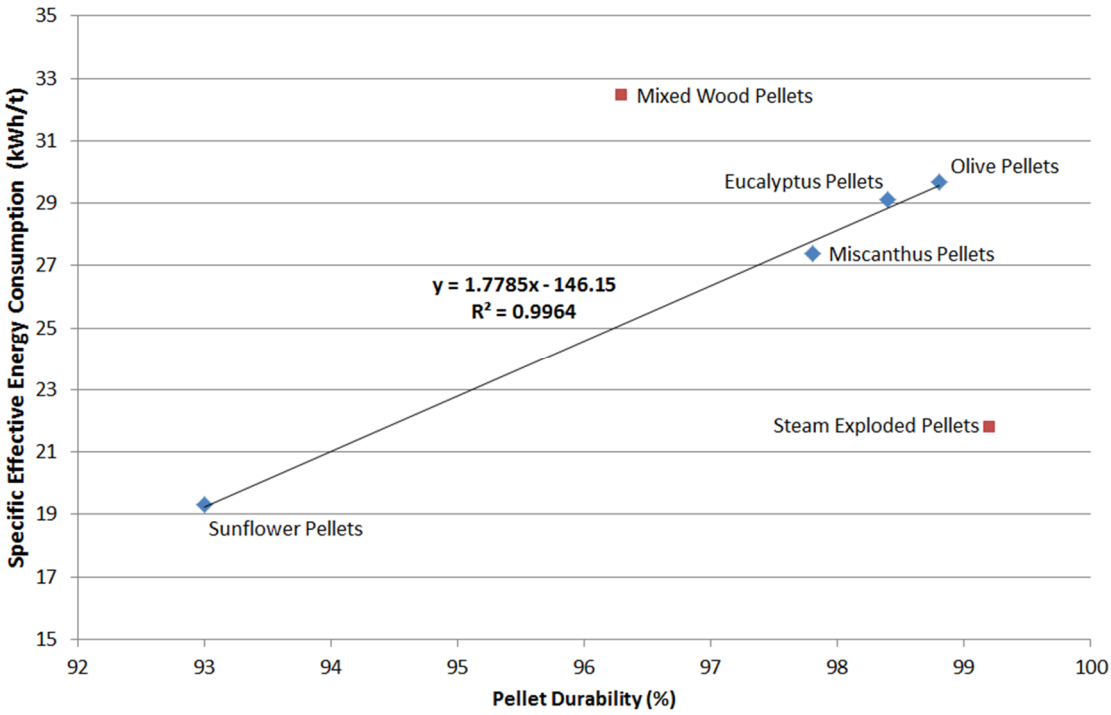


Figure 7.11: As Received Cutting Mill Specific Effective Energy Consumption against Pellet Durability

7.7.2. Particle Size

In a cutting mill, the screen size will play a determining role in dictating the particle size, as seen in section 7.2.3. The use of the 4mm screen has seen varying impacts on the particle size of the tested materials, and is closely linked to the composition of the pellets. The Von Rittinger relationship has been found to be the best match of the milling theories for hammer mills (Temmerman et al., 2013). Using this theory, figure 7.12 relates energy consumption to the change in particle size through milling in relation to the pre-densified particle sizes detailed in section 4.3.

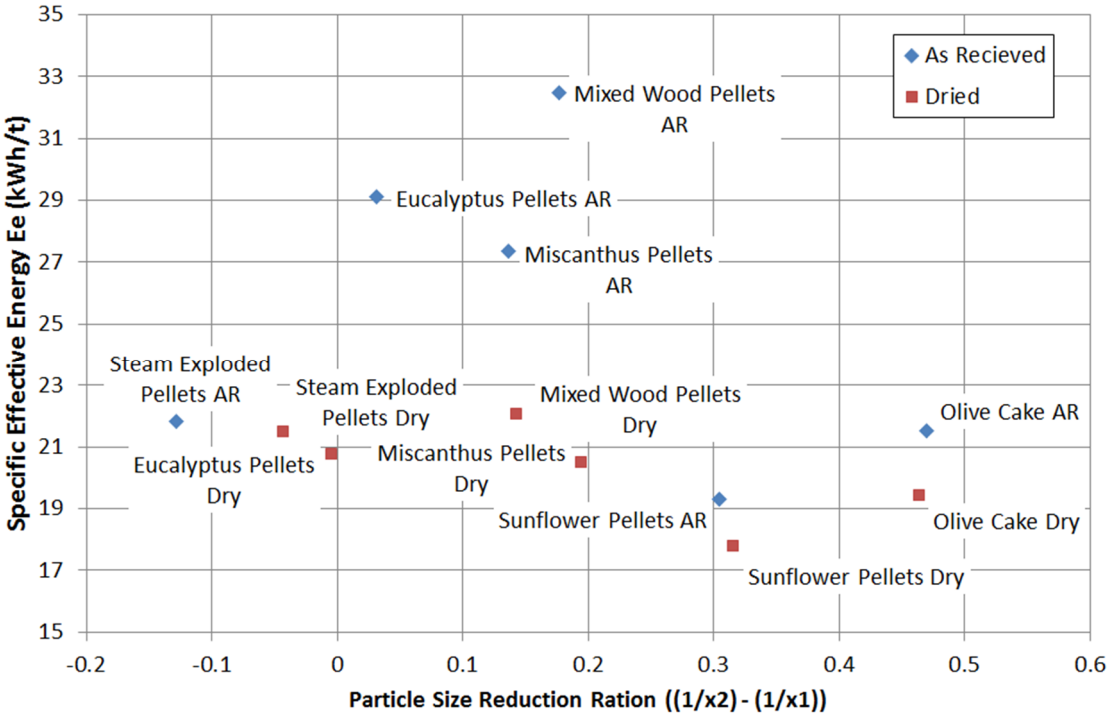


Figure 7.12: Specific Effective Energy Consumption E_e against Particle Size Reduction Ratio for the Cutting Mill

Several of the samples show no change from disintegrated particle size. Both steam exploded and the dry eucalyptus pellets show negative size change, indicating that pellets breaking into pre-densified particle size or pellet fragments slightly larger in size than pre-densified particle. For eucalyptus, mixed wood and miscanthus pellets, drying significantly reduces energy consumption but does not significantly change the product particle size. This implies that the pellets are just breaking down into pre-densified size. The energy is related to overcoming the pellet bonds, and moisture increases the strength of these bonds. Thus drying can be seen to have a beneficial impact as there is a significant reduction in energy for a similar particle size reduction. These specific energy values are on the lower end of report values for non-densified biomass in cutting and hammer mills, as summarised by

Temmerman et al. (2013). While there has been little change in particle size through milling (Fig. 7.12), there is energy associated with breaking up the pellets, and this milling energy is low compared to milling non-densified biomasses.

Olive cake shows largest change in diameter by milling, but 43% of the sample was already below 1 mm, thus a large portion of the sample was not milled, resulting in lower energy consumption. This is reflected in figure 7.13, which shows no real change in the particle size distribution below 1 mm for olive cake. These fines should be sieved and removed prior to milling as this represents wasted milling capacity. Miscanthus pellets particle distributions for milled samples is very similar to the disintegrated distribution (Fig. 7.14), thus no real milling of particles happening. To minimise energy consumption in a cutting mill, pellets should be composed of particles of the required size and milled with a screen size so that only pellet disintegration is required, and the pellets should be dried in order to weaken the pellet bonds and reduce energy consumption even further.

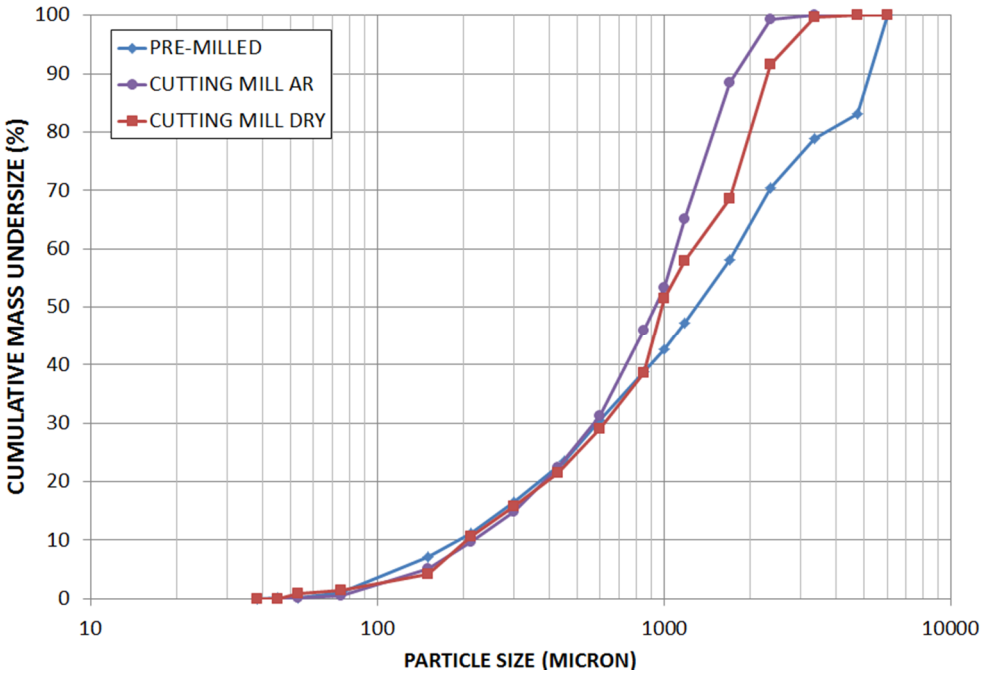


Figure 7.13: Cumulative Particle Size Distributions for Disintegrated, Cutting Mill Comminuted As Received and Dried Olive Cake

Table 7.3 lists the Rosin-Rammler, size parameters, dispersion parameters, and distribution shape parameters for the tested samples. Most comminuted samples have a geometric mean diameter (d_{gw}) in range of 600-700 µm. The as received olive cake has the highest d_{gw} at 878 µm, and olive pellets 1004 µm. Olive pellets were hydrophobic and didn't break up in the pellet disintegration test, so it is likely that pellets broke into fragments rather than

individual particles. Dried olive pellets also showed largest reduction in d_{gw} compared to as received milling. Moisture and any olive oil remaining in the pellets is acting as binder and holding the pellet together, but when dried, the fragments are smaller as pellet bonds are weaker. Dried miscanthus pellets had the smallest d_{gw} at 533 µm. Drying the samples showed little change for mixed wood, eucalyptus and sunflower pellets despite a significant reduction in energy consumption, but did show a decrease in d_{gw} for miscanthus and steam exploded pellets.

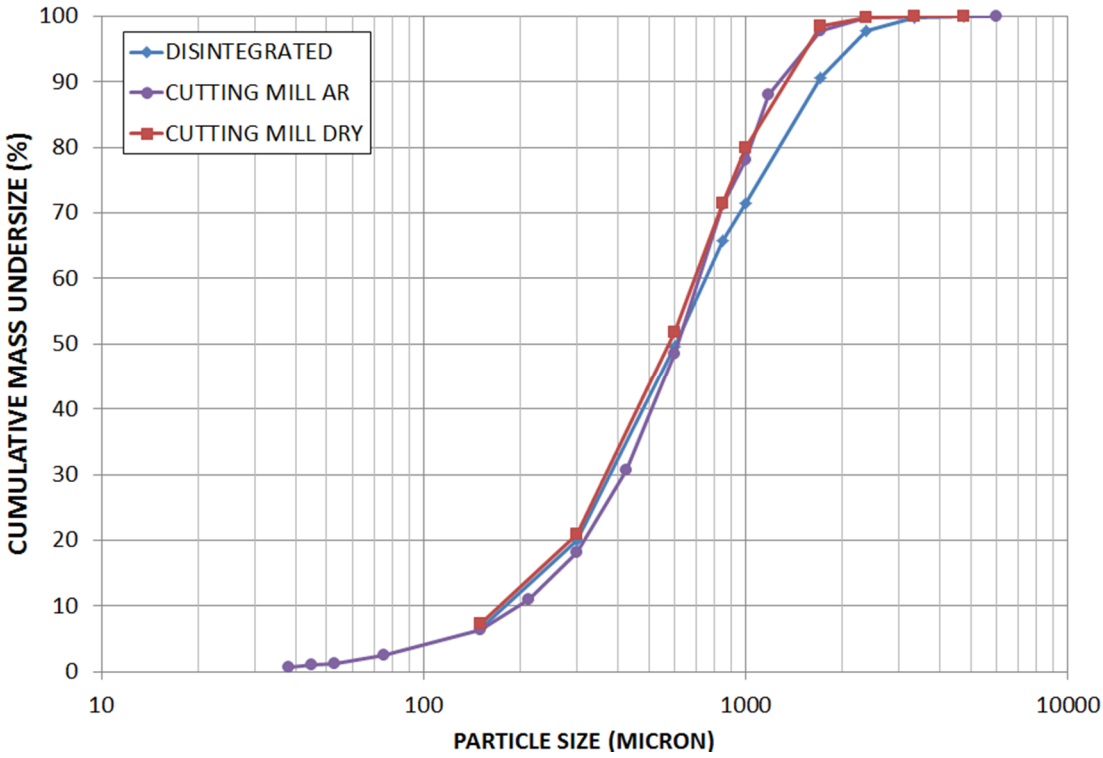


Figure 7.14: Cumulative Particle Size Distributions for Disintegrated, Cutting Mill Comminuted As Received and Dried Miscanthus

The Rosin-Rammler distribution parameter, *n*, increased for mixed wood, eucalyptus and steam exploded pellets by drying, indicating a narrowing of the span. However it reduced for miscanthus and sunflower pellets, olive cake and pellets, indicating a wider span through drying.

The Inclusive graphic skewness (GS_i) increased across the board by drying, which is to be expected as d_{gw} reduced, resulting in more positively fine skewed distributions. Eucalyptus and wood pellets showed an increase in distribution geometric standard deviation of high region (*hs*), but a reduction in distribution geometric standard deviation of low region (*ls*). However this resulted in similar *hs* and *ls* values after drying. This is reflected in the geometric kurtosis (K_g) value which is almost 1 for dried eucalyptus pellets, and is 1 for dried

mixed wood pellets, resulting in a normal Gaussian distribution. Miscanthus and sunflower pellets saw increased *hs* and *ls* through drying, which again was reflected in the K_g values, which were increased to almost 1 for sunflower pellets, while miscanthus pellets go from a platykurtic curve ($K_g < 1$) in the as received state to a leptokurtic curve ($K_g > 1$) in the dried state.

Sample	Rosin-Rammler			Size Parameters (µm)			Dispersion Parameters					Distribution Shape Parameters	
	d' (µm)	n	R^2	d_{10}	d_{gw}/d_{50}	d_{80}	hs	ls	MRS	C_u	C_c	GS_i	K_g
Eucalyptus Pellets AR	862	1.57	0.999	199	696	1171	**1.81**	**2.53**	1.78	4.15	1.24	0.20	0.89
Eucalyptus Pellets Dry	919	1.78	0.990	286	696	1222	**1.92**	**2.05**	1.84	**2.93**	**0.94**	0.37	**1.02**
Mixed Wood Pellets AR	813	1.45	0.999	166	659	1105	**1.81**	**2.71**	1.78	4.70	1.35	0.17	0.88
Mixed Wood Pellets Dry	878	1.91	0.993	289	686	1148	**1.82**	**1.99**	1.67	**2.78**	**0.99**	0.32	**1.00**
Miscanthus Pellets AR	780	1.46	1.000	164	615	1069	1.87	2.58	1.92	4.48	1.32	0.24	**0.95**
Miscanthus Pellets Dry	706	1.37	0.999	137	**533**	1006	2.09	2.78	2.26	4.72	1.18	0.35	**1.06**
Olive Cake 2013 AR	1037	1.66	0.999	269	**878**	1345	**1.69**	**2.52**	1.68	**3.75**	1.05	0.16	0.98
Olive Cake 2013 Dry	835	1.08	0.995	106	627	1356	**2.36**	**4.13**	2.52	**8.01**	**0.95**	0.35	0.78
Olive Pellets AR	1226	1.46	0.989	255	**1004**	1517	1.61	2.41	1.53	4.51	1.61	0.05	0.96
Olive Pellets Dry	897	1.08	0.995	111	720	1372	2.06	4.53	2.18	8.26	1.11	0.22	0.76
Sunflower Pellets AR	848	1.57	0.999	199	690	1145	1.78	2.48	1.70	4.12	1.22	0.17	0.87
Sunflower Pellets Dry	832	1.48	0.999	179	674	1130	1.80	2.64	1.80	4.49	1.26	0.20	**0.94**
Steam exploded Pellets AR	944	1.30	0.995	176	718	1412	2.16	3.15	2.30	5.19	0.97	0.34	0.87
Steam exploded Pellets Dry	862	1.38	0.995	178	664	1261	2.09	2.89	2.16	4.67	0.95	0.33	0.88
Microwave Pellets AR	822	1.70	0.999	215	667	1091	1.77	2.34	1.70	3.64	1.18	0.22	0.96

Table 7.3: Shape, Dispersion and Distribution Shape Parameters of the Cumulative Particle Size Distributions for As Received and Dried Biomass Milled in the Cutting Mil. Notable results in Bold

Olive cake and pellets show a significant increase in *hs* and *ls* through drying, and *ls* is twice the value *hs* after drying (*hs* 2.36, *ls* 4.13 for dried olive cake). Their reduction in K_g shows the curves have become even more platykurtic through drying, as opposed to gaining a more Gaussian distribution seen in the wood and herbaceous samples. Steam exploded pellets showed little impact on distribution shape despite change in d_{gw}. *hs* and *ls* changed slightly, while K_g remained virtually unchanged by drying.

Mixed wood and eucalyptus pellets went from being well graduated and graded to poorly graduated and graded through drying, as the Uniformity Coefficient (C_u) dropped below 4 and the Coefficient of Curvature (C_c) dropped below 1. Sunflower, steam exploded, and miscanthus pellets remained well graduated and graded through drying ($C_u > 4$ and $1 < C_c < 3$). Olive cake and pellet showed doubling in C_u (4 to 8), and C_c dropped to slightly below 1 for olive cake.

7.8. Particle Shape

For most samples, milling in the as received or dried state has little impact on shape factors compared to the material type. Figure 7.14 shows that the orders of shape factors were the same as the disintegrated pellets (Fig. 4.5-4.8 in section 4.6). Table 7.4 shows that miscanthus pellets have the lowest mean shape factor values, followed by mixed wood, sunflower, eucalyptus, microwave, and steam exploded pellets, with olive cake and pellets having the highest mean shape factors. This shows that material type and pre-densified shape determine the milled shape factors in a cutting mill. Only olive cake and pellets showed a significant change in circularity and symmetry by drying, and were the only samples which showed a significant reduction in particle size through milling and drying. Little impact was seen on olive cake and pellet sphericity and aspect ratio in spite of significant change in size through drying. Compared to the pre-milled particles, milling caused a reduction in the sphericity and circularity, but an increase in symmetry and aspect ratio.

Little change was observed in shape factors of wood, eucalyptus, sunflower and miscanthus particles through drying. In comparison to the pre-milled shape factors, eucalyptus showed virtually no change. Mixed wood showed an increase in aspect ratio and sphericity, and drying improved circularity. Miscanthus showed slight increase in sphericity, circularity and symmetry compared to pre-milled particles, but reduction in aspect ratio.

Sample	Average Sphericity	Average Circularity	Average Symmetry	Average Aspect Ratio
Eucalyptus Pellets AR	0.441	0.543	0.772	0.553
Eucalyptus Pellets Dry	0.449	0.550	0.735	0.560
Mixed Wood Pellets AR	0.413	0.494	0.765	0.526
Mixed Wood Pellets Dry	0.405	0.539	0.765	0.515
Miscanthus Pellets AR	0.384	0.486	0.754	0.492
Miscanthus Pellets Dry	0.396	0.482	0.739	0.502
Olive Cake 2013 AR	0.560	0.742	0.851	0.673
Olive Cake 2013 Dry	0.565	0.719	0.834	0.676
Olive Pellets AR	0.551	0.724	0.844	0.665
Olive Pellets Dry	0.546	0.700	0.800	0.659
Sunflower Pellets AR	0.426	0.525	0.771	0.539
Sunflower Pellets Dry	0.432	0.575	0.794	0.545
Steam exploded Pellets AR	0.498	0.648	0.821	0.615
Steam exploded Pellets Dry	0.487	0.662	0.821	0.605
Microwave Pellets AR	0.445	0.629	0.813	0.561

Table 7.4: Impact of Drying on Average Particle Sphericity, Circularity, Symmetry and Aspect Ratio for Biomass Milled in Cutting Mill

Sunflower showed increase in sphericity and aspect ratio, but no real change in symmetry and circularity from the pre-milled particles. Steam exploded showed no real change in shape factors through milling, indicating milling just broke up pellets to pre-densified particle size and did not mill the actual particles. However it must be noted that the distributions showed that, apart from olive cake, the pellets are being milled back to pre-densified particle size, with no comminution on the particles themselves; hence little change in shape factors. However, even olive cake did not show a significant change in shape factor, as it remained the highest in all shape factors after milling.

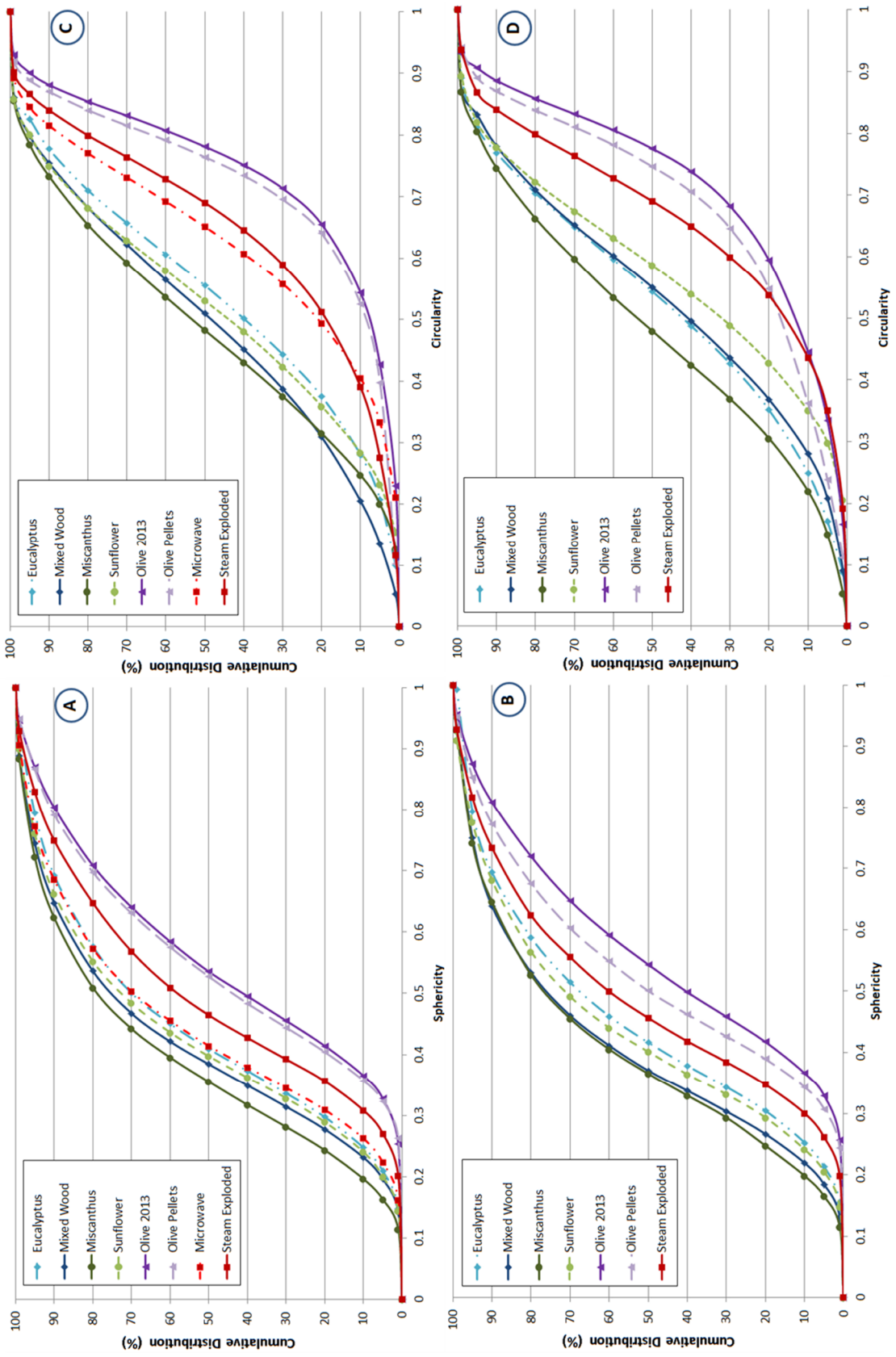


Figure 7.15: Cutting Mill Comminuted Biomass Particle as Received (a) and Dried (b) Sphericity, and As Received (c) and Dried (d) Circularity

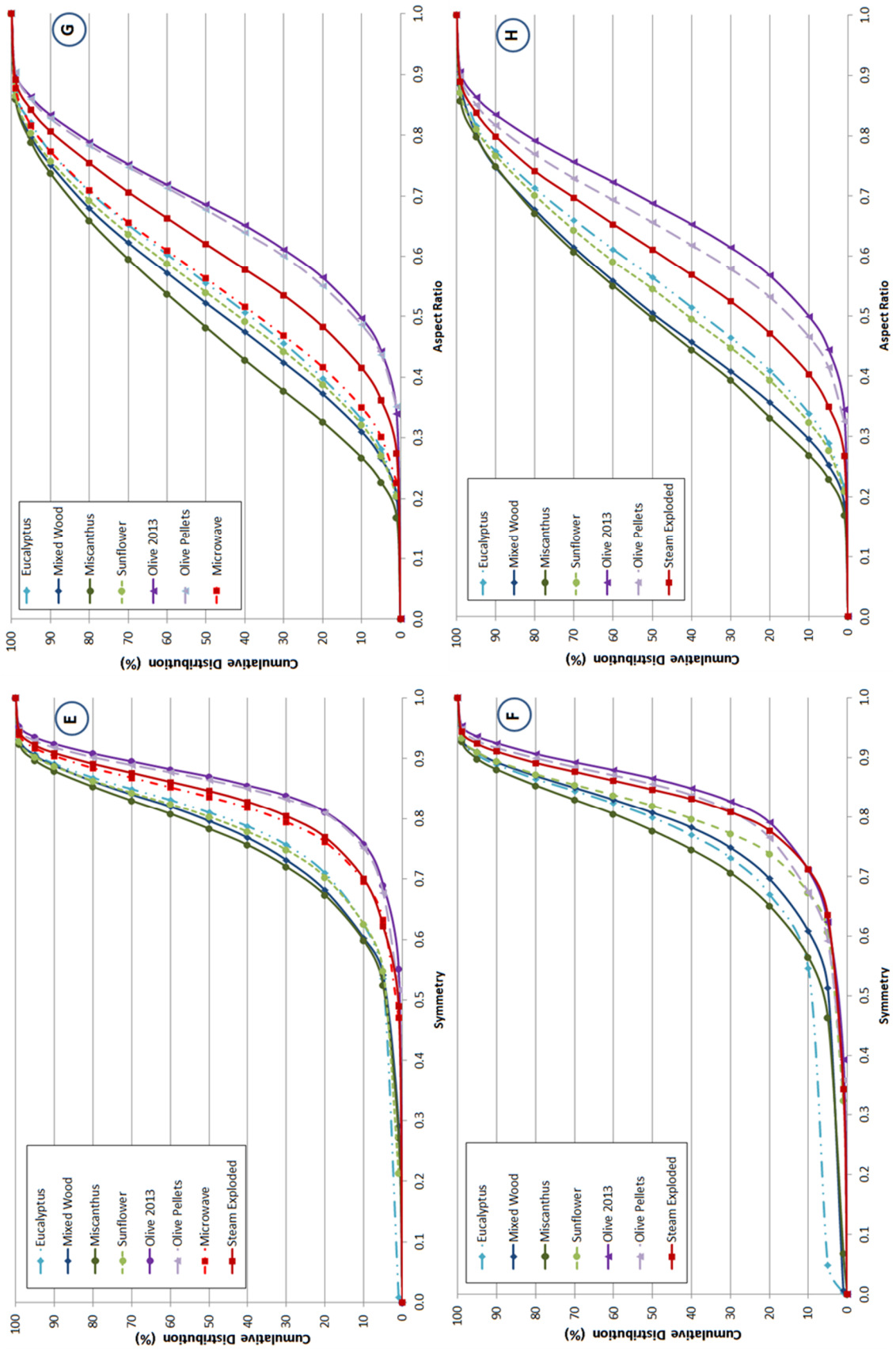


Figure 7.16: Cutting Mill Comminuted Biomass Particle as Received (e) and Dried (f) Symmetry, and As Received (g) and Dried (h) Aspect Ratio

7.9. Conclusions

The optimisation study of mill operating conditions in a cutting mill has shown that the optimal milling conditions vary depending upon on the objective response from the mill. For specific effective energy consumption, the main interaction is between the feed rate and speed, with speed having the most impact on energy consumption. This is the first time this relationship has been identified for densified biomass in a cutting milling, and is supported by previous studies of biomass milling in hammer mills. The impact of mill variables on the mass holdup of a cutting mill for densified biomasses has not previously been studied in literature. Mass holdup is due to interactions between all the mill variables, but feed rate and screen size had the most impact. While minimising energy consumption is an important part of milling optimisation, maintaining a high level of mass throughput is essential for maintaining the thermal output of a pulverised fuel burner, thus a balance between the two needs to be found.

The Rosin-Rammler distribution parameter was influenced by an interaction of speed and screen size, but the main variable was the material itself and its pre-densified composition. The relationship between the Rosin-Rammler distribution parameter is different for densified biomasses compared to non-densified biomasses due to the influence of the pellet particle size distribution on the resultant product. Further research is required to analyse the specific effective energy, mass holdup and Rosin-Rammler distribution parameter relationships for different types of non-densified and densified biomasses, and if these relationships can be correlated to full scale hammer mills. This would allow for biomass milling behaviour models in hammer and cutting mills to be developed which would help power generators understand and optimise the milling behaviour of a new sample prior to full scale milling trials.

The bagasse milling study showed that the variability in moisture can have the greatest impact energy consumption and significant energy savings are possible through drying. For biomass pellets, drying reduced energy consumption but did not significantly change the product particle size for a 4 mm screen. Thus drying biomass pellets can be seen to have a beneficial impact as there is a significant reduction in energy for a similar particle size reduction. For most samples, milling had little impact on shape factors as comminution was related to breaking down the pellets. However, olive cake saw a significant reduction in particle size, but did not see a significant change in shape factors. Thus that material type and pre-densified shape determine the milled shape factors in a cutting mill.

Chapter 8 - Ring and Roller Mill

There are limited accounts of biomass milling trials in coal mills in literature. Literature generally focuses on the standard coal grindability tests such as the Hardgrove Grindability Index (Shang et al., 2012) or Bond Work Index test (O. Williams et al., 2015). There have been limited studies into the use of vertical spindle mills for biomass milling. Zulfiquar et al. (2006) looked into co-milling of biomass with coal in a pilot scale vertical spindle mill and found biomass could be co-milled up to 5%. Tamura (2014) analysed waste cedar wood chip, pinus bark and wood pellet in co-firing experiments and simulations. They milled woody biomass in a ball mill, vertical roller mill and a vibration mill, and used an industrial scale ring-roller mill to test wood chip and pellet grindability compared to coal. For a target size of particles below 1mm it was found that a ring-roller mill is suitable for woody biomass comminution. Livingston et al. (1998) use a mini-ring-ball mill with static classification to analyse the comminution of biomass and coal and found a relationship between the new surface area created and the energy consumption per unit new surface area. The Lopulco ring-roller mill featured in this chapter was previously used by Pang (2012) to comminute biomass as part of sample preparation for combustion trials. This chapter aims to look at the milling performance of a range of densified biomass materials within a laboratory scale vertical spindle mill with aerodynamic classification system. This chapter will analyse the mill idle settings and milling characteristics for a range of densified biomasses to provide a basis for future testing and simulations.

8.1. Materials and Methods

The biomass samples tested in this study were mixed wood, eucalyptus, miscanthus, sunflower, steam exploded, and microwave pellets. In addition Columbian La Loma coal was tested to provide a basis of comparison for the densified biomass products. Olive cake was not included in the trial as it formed a cake within the mill during initial tests and was known to cake and block the full scale Lopulco ring-roller mill at EDF West Burton. The samples were tested as per the method detailed in section 3.2.5. The settings used in the test are based around those used by Pang for biomass milling (Pang, 2012) due to the limited time available for testing after the refurbishment and subsequent set up of the mill. The material tests measured mill energy consumption, mass output, pressure and temperatures for each sample in triplicate. The milled product was then sieved to obtain their particle size distributions (section 3.1.4), and digital image analysis was used to analyse particle shape characteristics (section 3.1.5).

8.2. Idle Conditions

The energy consumption of the ring-roller mill is composed of four components: a fan, rotary air lock, mill bed and a screw feeder. Each component has a separately controlled motor linked to the control panel. While the fan and rotary air valve have fixed speed control, the mill bed and feeder have variable speed control. During the initial setup of the mill, it was noted that the settings on the control panel did not correspond to the observed speeds of the feeder and mill bed. Due to limited documentation being available for the mill, there was no data on what these settings corresponded to. Thus the first step was to analyse the relationship between the set and observed mill bed and feeder speeds. The screw feeder settings on the control panel were between 50 and 400 Hz and could be increased incrementally to any value between these two limits. The observed speed of the feeder (in RPM) was noted for 50, 60, 100, 150, 200 and 250 Hz and plotted to give figure 8.1. There is a linear relationship between the observed speed and set Hertz value, with a high coefficient of determination (99.6%) between the two. Pang (Pang, 2012) used a control setting of 100 Hz setting for his milling trials in the same mill, which equates to an observed feeder speed of 71 RPM.

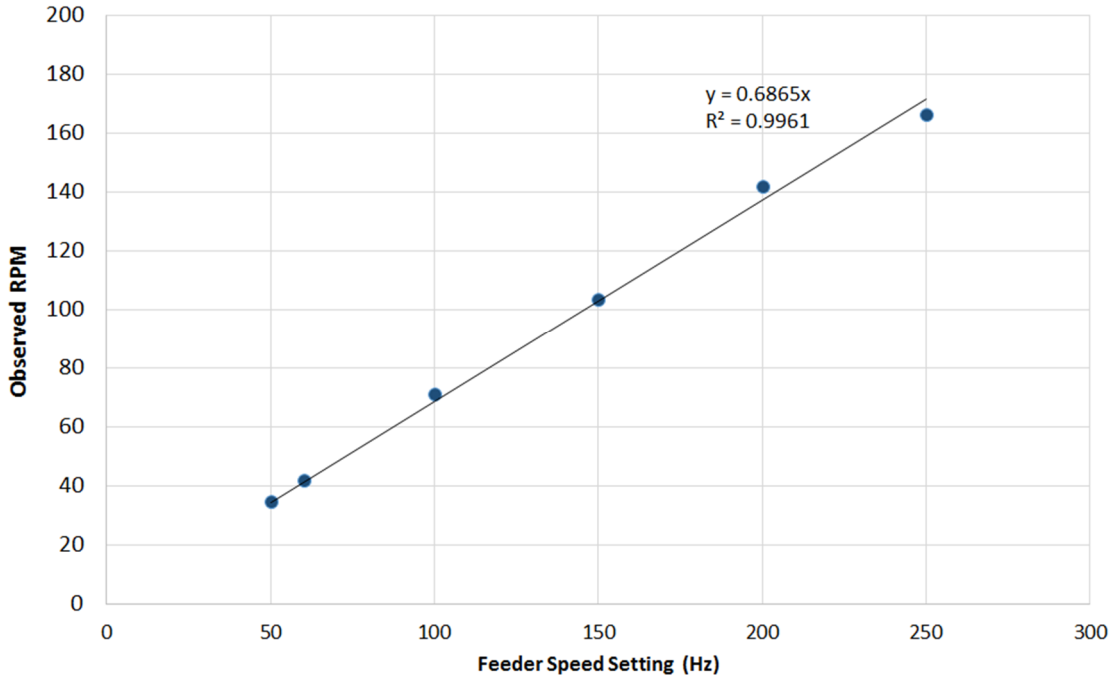


Figure 8.1: Observed Speed (RPM) against Speed Setting (Hz) for Screw Feeder

For the mill bed, the same observation test was conducted in order to obtain information on the actual mill bed speeds. As noted in section 3.2.5, the separator is connected to the mill bed, and thus the mill bed speed is also the separator speed. As the separator is the

classifying system for the mill, and as the output particle size is dependent on its settings, knowledge of the mill bed speed is crucial in determining the conditions under which the milled particles can pass the aerodynamic barrier of the separator classifying system. The mill bed speed was observed for set speeds of 300, 500, 800, 1000, 1300, 1400 and 1500 RPM and plotted to give figure 8.2. As with the screw feeder, there is a linear relationship between the observed speed and set control speed, with a high coefficient of determination (99.9%) between the two speeds. Pang (Pang, 2012) used a 800 RPM setting for his milling trials in the same mill, which equates to an observed mil bed speed of 160 RPM.

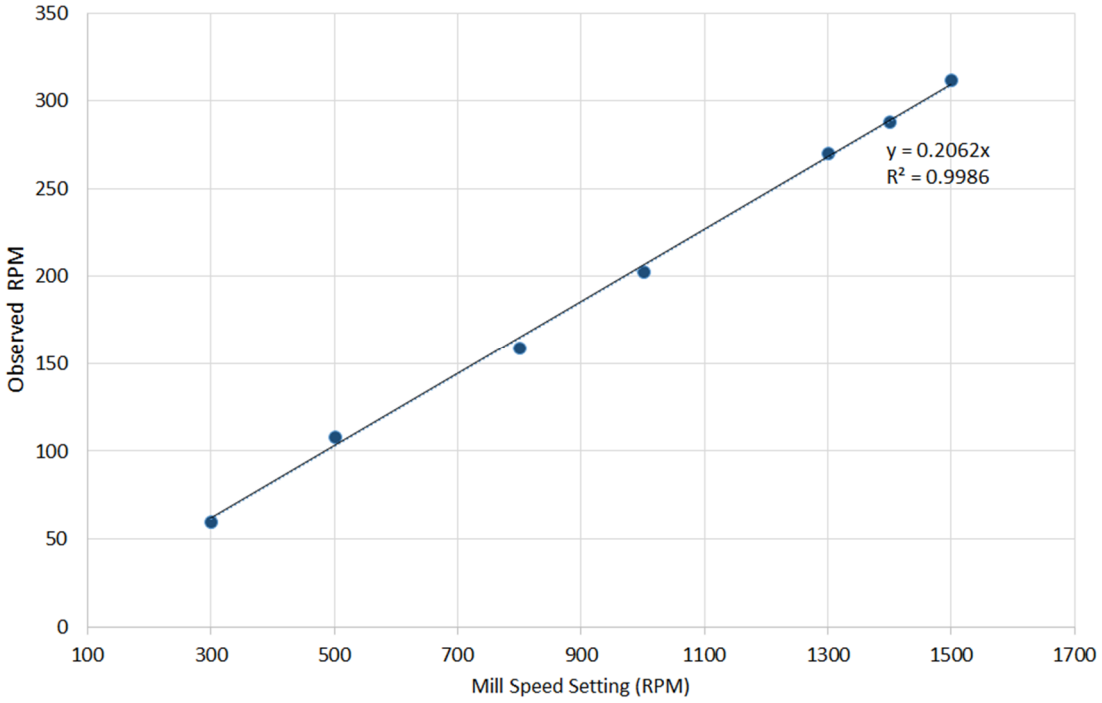


Figure 8.2: Observed Speed against Speed Setting for the Mill Bed

Based on the mill bed and screw feeder speed studies, the chosen settings for the mill bed were 100 Hz for the screw feeder (71 RPM observed speed) and 1000 RPM for the mill bed (200 RPM observed speed). In order to obtain the idle conditions for the mill for the set operating conditions, the energy consumption and mill pressures were observed for an idle run. Figure 8.3 shows composition of energy consumption for an idle run of the mill. The energy consumption is built up by four stages; firstly the fan, followed by the rotary air valve (100 Hz setting), then the mill bed (1000 RPM setting) and finally the screw feeder. The average instantaneous power consumption for all components was 1.48 kW, which is the baseline idle power consumption, used for the specific effective energy calculations in section 8.3. Fan power is the largest individual consumer of energy. It shows large a spike at start up (Fig. 8.3) as it over comes inertia and then settles to constant power draw of around

1.2 kW. The mill bed is the next largest single consumer of power at 0.24 kW, followed closed by the rotary air valve at 0.15 kW. The screw feed consumes the lowest amount of power at 0.087 kW and is also the only single phase draw.

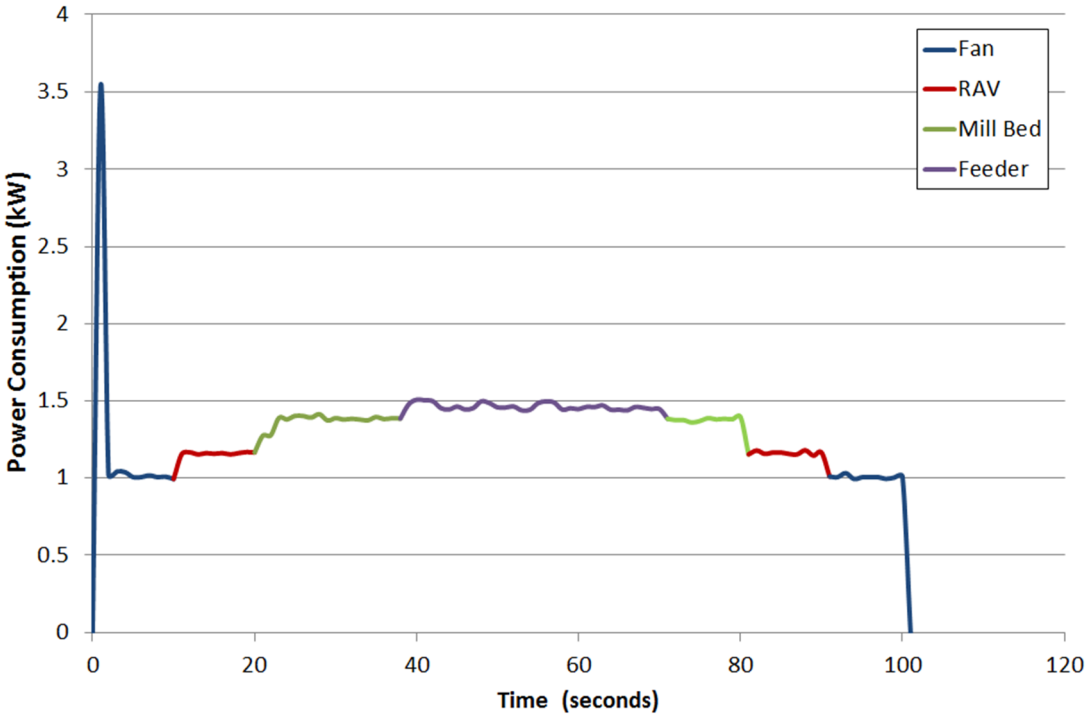


Figure 8.3: Fan, Rotary Air Valve, Mill Bed and Screw Feeder Idle Energy Consumption Profile

Due to the configuration of the system, it was not possible to measure the power consumption of the individual components. However the total energy consumption can be measured through the energy logger, the configuration of which is detailed in section 3.2.1. Figure 8.4 shows the idle pressures for the 7 pressure tappings on the mill, the locations of which are noted on the schematic of the mill in figure 3.14 in section 3.2.5. Once the mill is in operation, in idle condition there is little variance in the pressure despite the addition of the rotary air valve, mill bed and feeder, as per (Fig. 8.3). The readings in table 8.1 show the average idle pressure readings.

Prior to the mill, pressure tapings P1 and P2 show negative pressures. Immediately after the mill the pressure becomes positive (P3). The pressure increases after the cyclone (P4 and P5) with the highest pressure being seen in the venturi contraction (P6), and second highest pressure being observed after the venturi (P7). The pressure readings in table 8.1 are used as the base line pressures for the load tests in section 8.3.

Pressure Tapping	**P1**	**P2**	**P3**	**P4**	**P5**	**P6**	**P7**
Pressure (Pa)	-463	-366	844	1772	1776	4364	2702

Table 8.1: Average Idle Pressure Readings for Ring-Roller Mill: Vent Pressure Tap (P1), Mill Inlet Pressure Tap (P2), Mill Outlet Pressure Tap (P3), Venturi Upstream Pressure Tap (P4), Venturi Inlet Pressure Tap (P5), Venturi Central Pressure Tap (P6), Venturi Downstream Pressure Tap (P7)

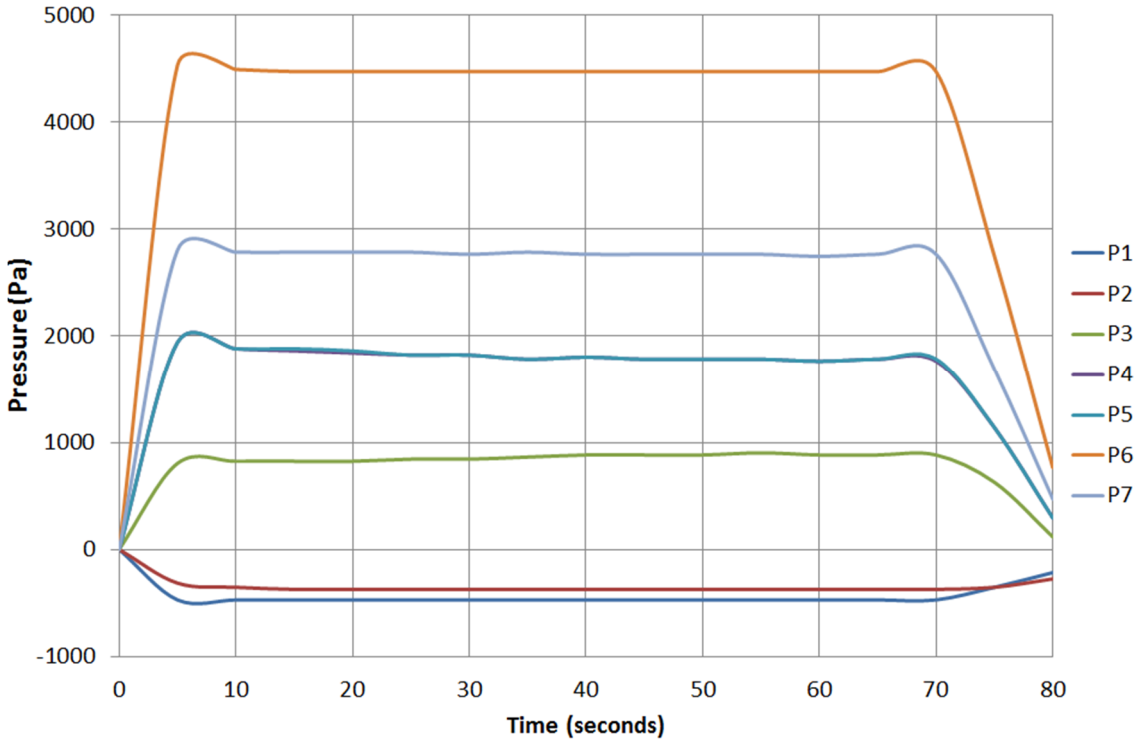


Figure 8.4: Idle Pressures for Ring-Roller Mill: Vent Pressure Tap (P1), Mill Inlet Pressure Tap (P2), Mill Outlet Pressure Tap (P3), Venturi Upstream Pressure Tap (P4), Venturi Inlet Pressure Tap (P5), Venturi Central Pressure Tap (P6), Venturi Downstream Pressure Tap (P7)

8.3. Material Runs

After the idle setting energy consumption and pressure readings were obtained, milling trials on 7 samples were conducted. 1kg of material was milled each time for each of the densified biomasses in triplicate runs, apart from La Loma coal, for which only 600g was milled for two runs due to limited material supply.

The specific effective energy consumption of the mill for each material is shown in figure 8.5. Mixed wood showed the highest specific effective energy consumption (E_e) of all the materials at 24.9 kWh/t. This was followed by steam exploded (17.1 kWh/t) and eucalyptus (16.4 kWh/t), then miscanthus 12.8 kWh/t) and microwave (12.1 kWh/t) and sunflower

pellets showing the lowest E_e for the densified biomasses at 7.9 kWh/t. As expected, La Loma coal had the lowest E_e of all the samples at 4.8 kWh/t. Interestingly, as with the cutting mill in section 7.7.1, a correlation was observed between specific effective energy consumption and pellet durability, which is shown in figure 8.6.

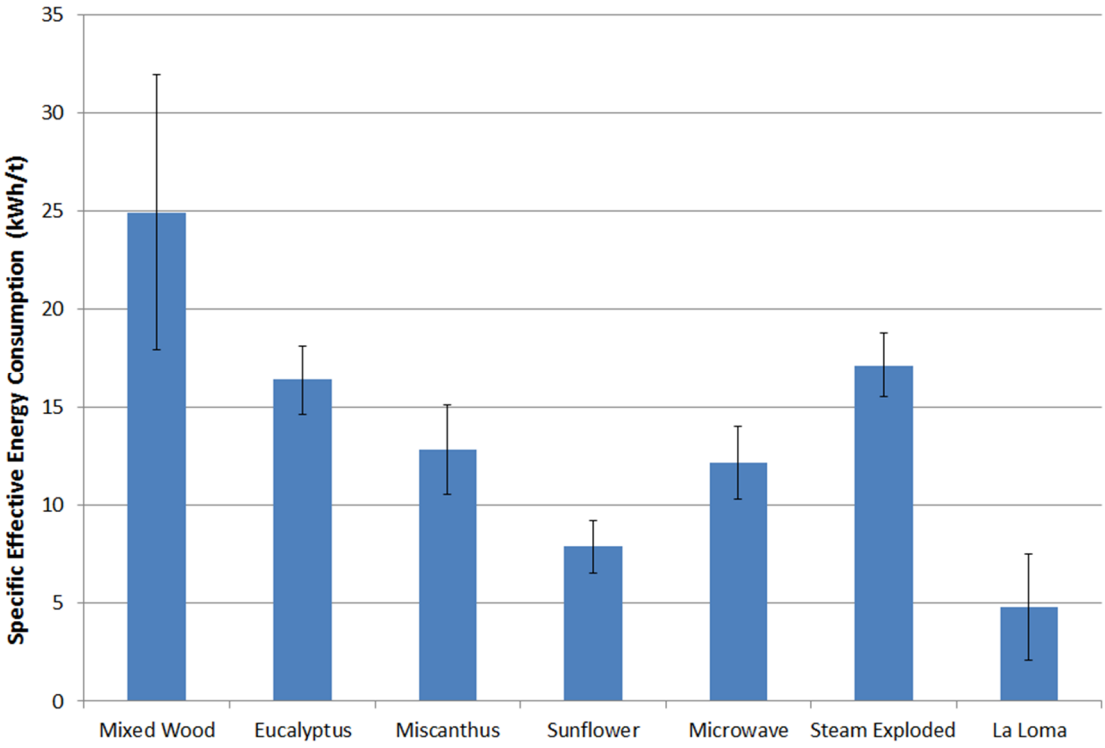


Figure 8.5: Specific Effective Energy Consumption for Densified Biomass & La Loma Coal in the Ring-Roller Mill

As with the cutting mill, the mixed wood was an anomaly in the results. This is interesting given the two different classification systems being used. The cutting mill uses a screen to roughly classify the material while the ring-roller mill uses a separator. The separator is an aerodynamic barrier which selects particles based on buoyancy effects and the Stokes number (section 2.11). The separator was set up for biomass particles with the blades set to allow as much material through as possible. The speed selected for the mill bed and separator was selected arbitrarily as no data on the optimal performance of the separator in terms of blade angle or speed was available. In addition, the mixed wood pellets were shown to choke in the Bond Work Index test (section 5.4), which uses the same classification system as the cutting mill. Given the anomalous results for all three mills for mixed wood pellets, there seems to be something related to the composition of the pellets which is not allowing the milled mixed wood particles to easily pass through the classification systems in any of the mills, resulting in the increased energy consumption.

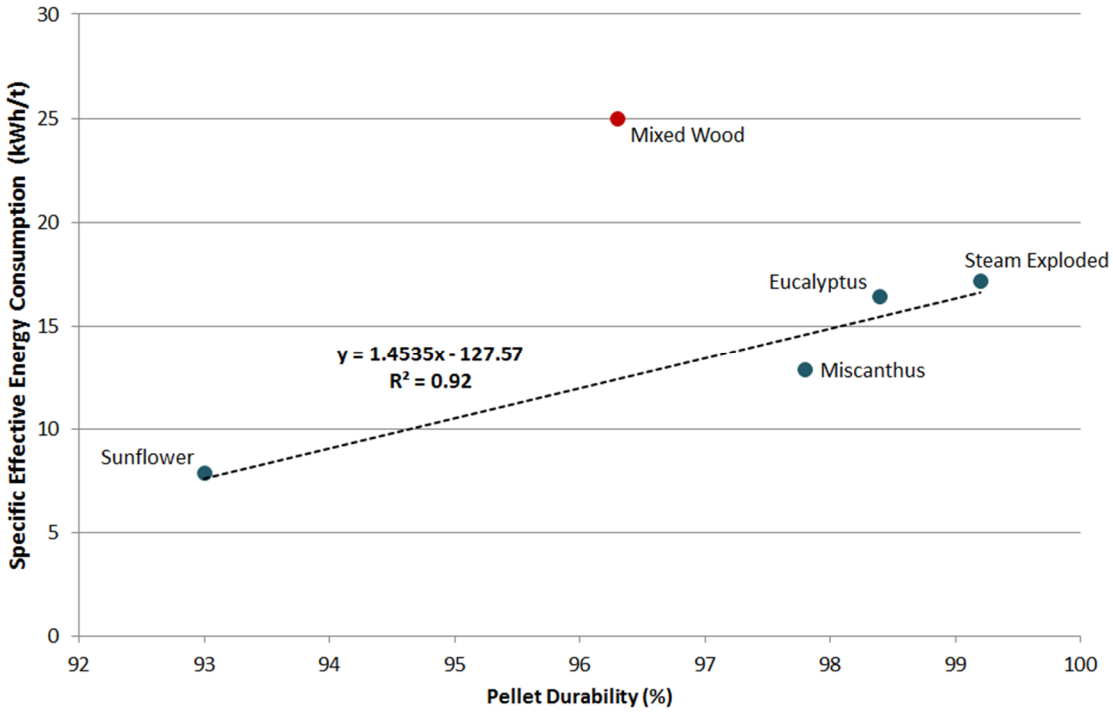


Figure 8.6: Ring-Roller Mill Specific Effective Energy Consumption against Pellet Durability for Biomass Pellets

8.4. Mill Pressures, Temperatures and Mass Output

Figures 8.7 shows the inlet and outlet differential pressures (P2 and P3, respectively), and inlet, chamber and outlet temperatures for the mill during the microwave pellets trails. The differential pressure is the measured pressure during the mill under load minus the idle pressures noted in table 8.1. The microwave pellets showed one of the lowest specific effective energy consumptions for the biomass pellets (12.1 kWh/t). The inlet pressure (P2) rises slightly above 50 Pa during the feeding portion of the run (30 seconds to 167 seconds) and then drops slightly below 50 Pa.

The outlet mill pressure (P3) builds up rapidly as material is fed into the mill and stabilises just over 250 Pa during the period that material is being fed into the mill. Once material stops being fed into the mill at 167 seconds, there is a sudden drop in outlet pressure to a level similar to that of the inlet pressure (approximately 50 Pa). This indicates the material evacuates the mill rapidly during the milling process. This is illustrated in figure 8.8, which shows the mass output from the mill and the associated output mass flow rate (differentiated from the mass output).

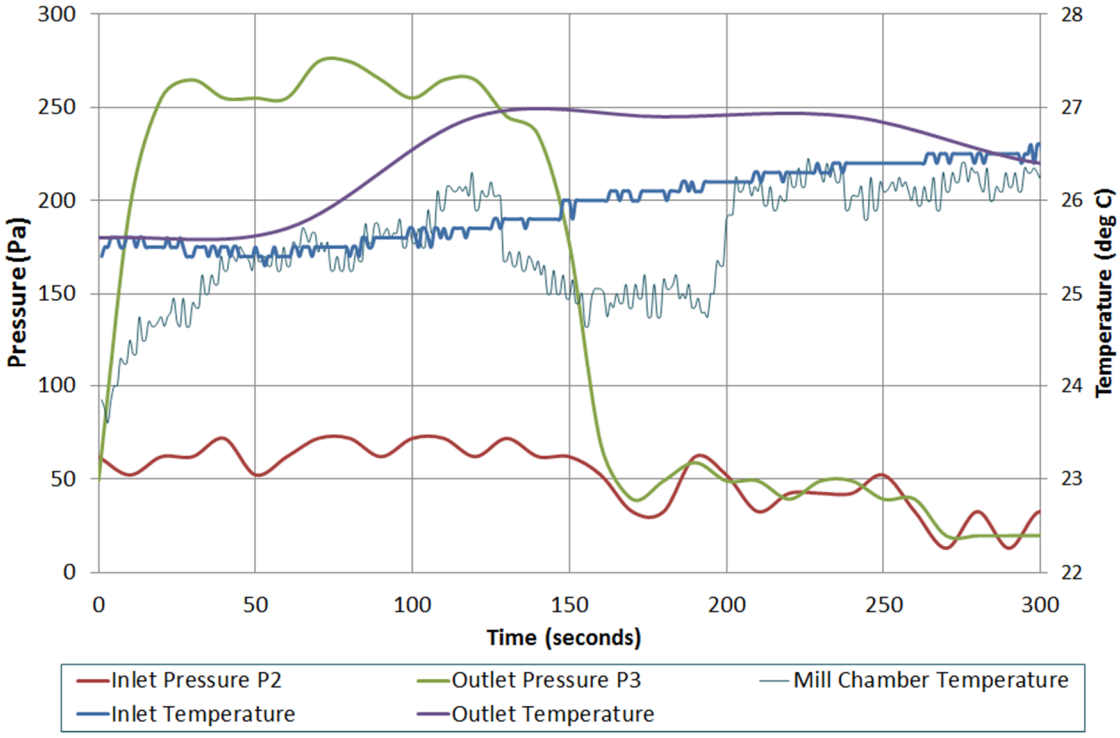


Figure 8.7: Microwave Mill Inlet, Chamber, and Outlet Temperatures and Inlet (P2) and Outlet (P3) Differential Pressures

The figure shows a smooth linear increase in mass output during the feed period of the run (0-137 seconds), after which the curve levels out rapidly to a stable level. This rapid decrease in mass output is demonstrated by the associated mass flow rate, which is relatively constant during the run but drops off rapidly to around zero with 20 seconds of the feed finishing. This large mass throughput is highlighted by the fact that 93% of the mass comminuted by the end of the feed period. There is a gradual increase in the inlet temperatures and a cycling of the output temperature. The only significant change in temperatures is seen in the mill chamber temperatures, which increases as material is fed into the mill and then drops. However the temperatures return to those of the inlet temperatures within 30 seconds of the feed stopping, indicating that the system is stabilising in temperatures and pressures rapidly after the load on the mill is removed.

In contrast, the mixed wood pellets show a very different behaviour to the microwave pellets (Fig. 8.9). The inlet pressures show a sharp increase to over 100 Pa as material starts to be fed into the mill. For 250 seconds into the run, the inlet pressure (P2) cycles in intensity, indicating the mill is struggling to push air through due to the amount of material in the mill.

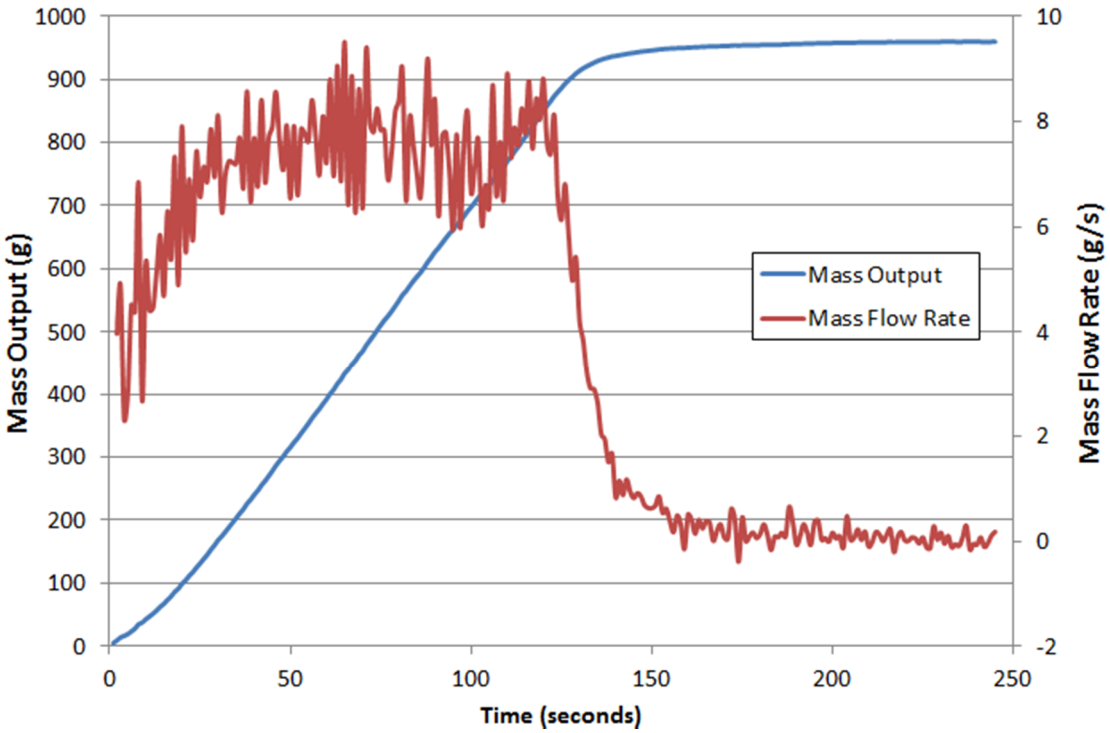


Figure 8.8: Microwave Mass Output from the Ring-Roller Mill and Associated Output Mass Flow Rate

While the similar feed rates for the mixed wood pellets (7.0 g/s) and microwave pellets (7.3 g/s) show that similar operating conditions were exhibited for both materials, the mill uses more energy for the mixed wood pellets (Fig. 8.5). The mill is choking with the mixed wood pellets and cannot easily evacuate the material from the mill. This is highlighted in the outlet pressure (P3), as it has the highest differential outlet pressure for any material at over 350 Pa during the feed period. As with the inlet pressure, it is not until around 100 seconds after the feed has stopped (250 seconds into the run at 200 Pa) that the pressures start to stabilise again. While the mill chamber temperature was below or close to the inlet temperatures for the microwave pellets, the mill chamber temperatures were significantly higher for the entire duration of the milling process for the mixed wood pellets. The mill outlet temperatures also cycled more dramatically than they did for the microwave pellets. Thus mill choking is resulting in increased temperatures and pressures within the mill, in addition to increased energy consumption and milling comminution times.

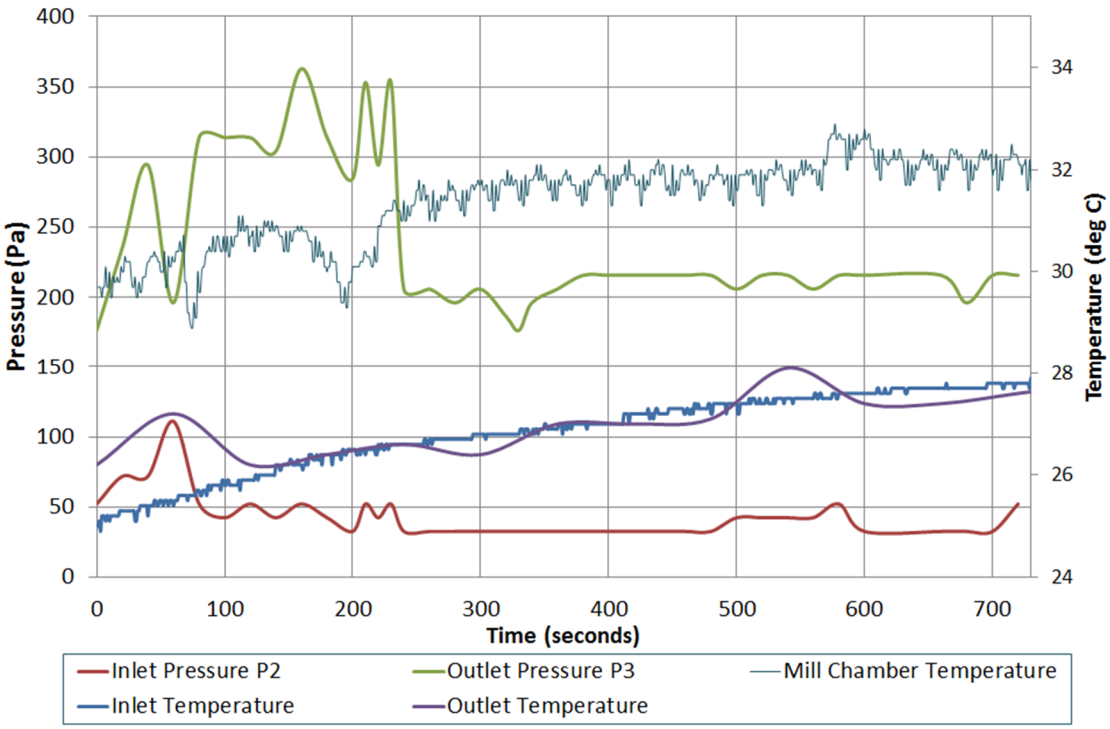


Figure 8.9: Mixed Wood Mill Inlet, Chamber, and Outlet Temperatures and Inlet (P2) and Outlet (P3) Differential Pressures

This mill choking of the mixed wood pellets is shown clearly in the mass output and output mass flow rate (Fig. 8.10). Unlike the microwave pellets, during the feed period (0 -143 seconds) the mass flow rate is less constant and cycles more, indicating that the mill builds up material and then releases it in bursts. The interesting part is once the feed stops; it takes over 7 minutes for the mass flow rate to stabilise around zero, nearly 3 times longer than for any other sample. For microwave pellets, the feed rate is virtually identical to the output rate (7.3 g/s and 7.4 g/s respectively), indicating a very short milling duration, and the material is being comminuted to the correct size and shape and can pass the aerodynamic barrier almost instantly. The mixed wood pellets exhibited a very different behaviour. While the feed rate is similar to microwave pellets (7 g/s) the mass output rate is 4.1 g/s, a 41% reduction in mass flow rate. At the end of the feed process only 61% of the material fed into the mill had been evacuated, and it over 7 minutes to output the remaining 34% of the material (taking into account the 4.9% material loss during the process).

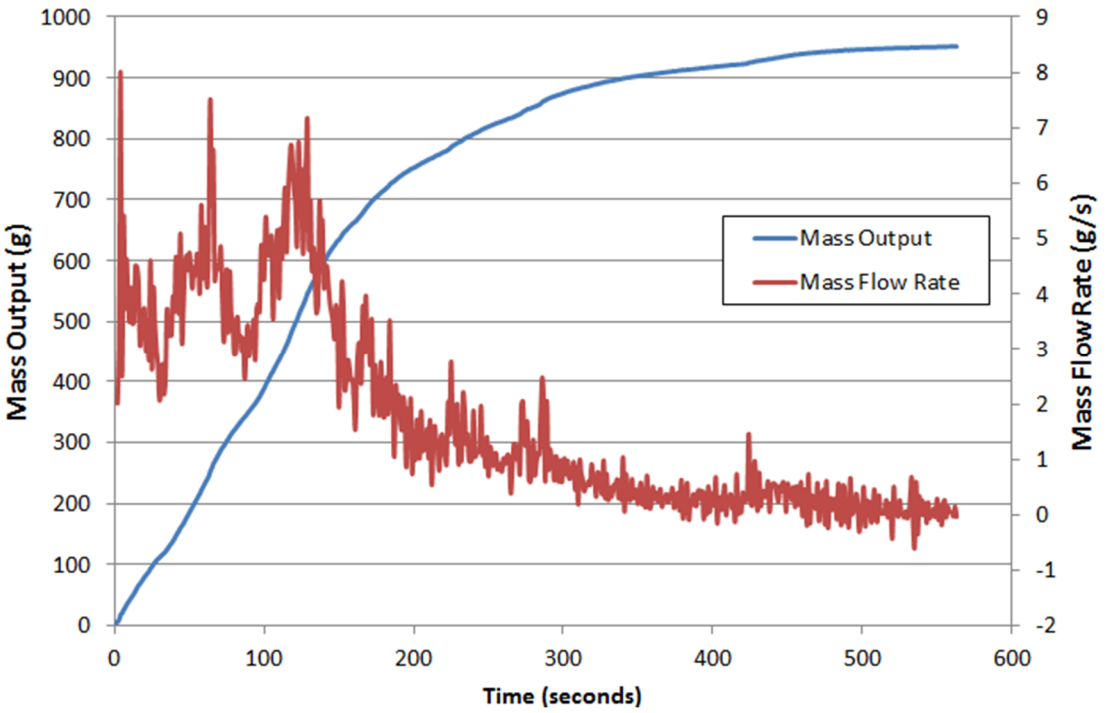


Figure 8.10: Mixed Wood Mass Output from the Ring-Roller Mill and Associated Output Mass Flow Rate

The mill inlet and outlet pressure and temperature curves for the other samples are provided in Appendix C. Table 8.2 summarises the milling behaviour data for all the samples. Most samples see a slight drop in mill output rate compared to the feed rate, apart from the mixed wood pellets. La Loma has the highest feed rate (10 g/s), which is to be expected as it was a powdered sample. For the biomass samples, most samples had similar feed rates (7-7.7 g/s) apart from steam exploded pellets which have a higher feed rate (8.5 g/s). Steam exploded pellets have one of the highest pellet densities (1.36 g/cm^3) and smaller pellet diameters at approximately 6 mm (sections 4.2 and 4.12). Sunflower pellets had the second highest mass output at the end of the feed time (89%). Most samples showed similar levels of mass loss, but sunflower pellets showed a much higher loss at 8%. The electrostatic nature of the sunflower particles was noted during the Camsizer testing, where static agglomeration was often present. It's proposed that the higher mass loss is due to a layer of particles coating the inside of the ducts and mill system due to a static charging of the particles. Once this layer has formed the remainder of the sunflower particles could pass uninhibited through the mill. Most samples showed similar mass stabilisation times apart from mixed wood pellets, and La Loma coal, which had a very short stabilisation time of 60 seconds.

Sample	% Mass Output at End of Feed	% Mass Loss	Feed Rate (g/s)	Mass Output Rate (g/s)	Mass Stabilisation Time Post Feed (s)
Mixed Wood	61	4.9	7.0	4.1	421
Eucalyptus	75	2.4	7.0	6.2	153
Miscanthus	61	2.3	7.7	6.1	160
Sunflower	89	8.0	7.2	7.6	141
Microwave	93	4.1	7.3	7.4	137
Steam exploded	79	6.6	8.5	7.3	117
La Loma	74	6.4	10.0	9.4	60

Table 8.2: Percentage Mass Output at End of Feed, Percentage Mass Loss, Feed Rate, Mass Output Rate, and Mass Stabilisation Time Post Feed for Densified Biomass and La Loma Coal Comminuted in the Ring-Roller Mill

8.5. Von Rittinger and HGI Relationships

The Von Rittinger relationship (section 2.12) is used to analyse the relationship between specific effective energy consumption and the particle size reduction through comminution for the ring-roller mill (Fig. 8.11). The non-treated densified biomasses show small particle size reduction ratios for varying energy consumptions. Sunflower pellets had a similar particle size reduction ratio to mixed wood pellets, but used almost a fifth of the energy consumption to achieve the same result. Steam exploded pellets showed a much larger particle size reduction for similar energy consumption to eucalyptus, while La Lom lad the lowest energy consumption and the greatest particle size reduction, highlighting how the mill is best suited to brittle materials.

From the Von Rittinger relationship, a constant can be obtained relating the energy consumption and particle size reduction for a given material. From the Bond Work Index tests (section 5.10) a relationship was obtained for biomasses which did not choke between the Bond Work Index (BWI) test and the Hardgrove Grindability Index (HGI) test. The HGI test was designed to test the grindability of coal in vertical spindle mills such as the Lopulco ring-roller mill used in this study (section 2.17). Figure 8.12 shows the Von Rittinger constant for the Ring-Roller mill tests plotted against the Hardgrove Grindability Index results for the biomass and La Loma coal. It can be seen that a correlation exists between the two values, but more testing is required to validate this result. As with the BWI-HGI correlation, La Loma is not on the correlation line. The result is only valid for the materials tested and conditions used, and more research is required into this relationship.

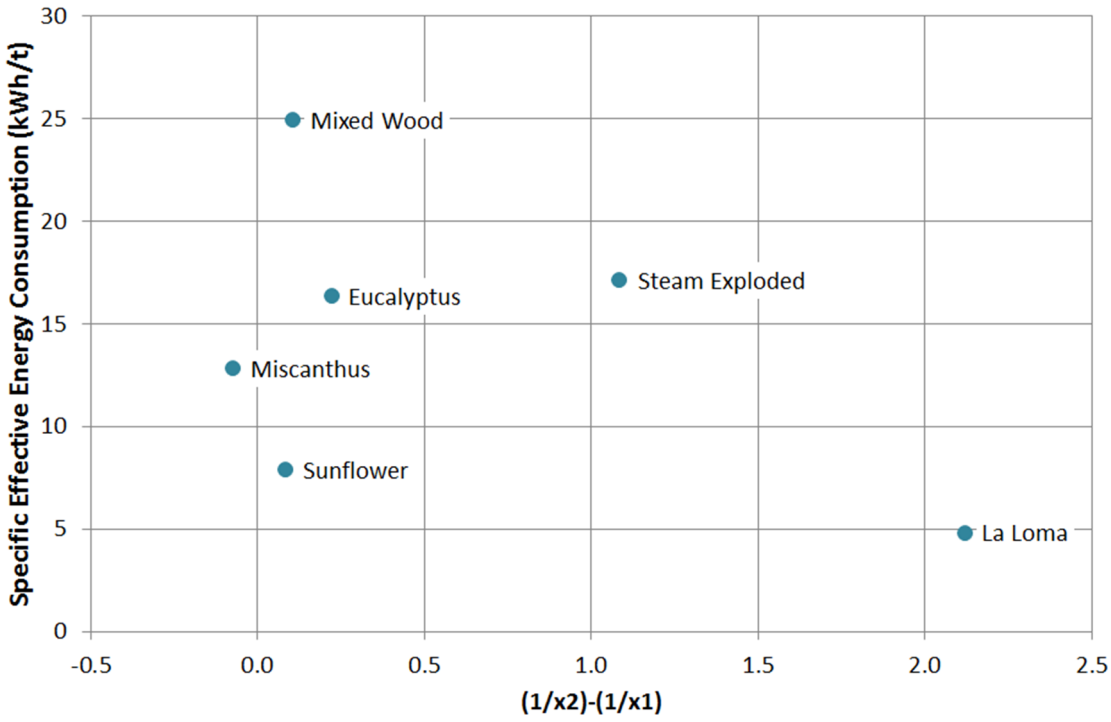


Figure 8.11: Specific Effective Energy Consumption E_e versus Difference in Feed and Product Particle Size for the Ring-Roller Mill

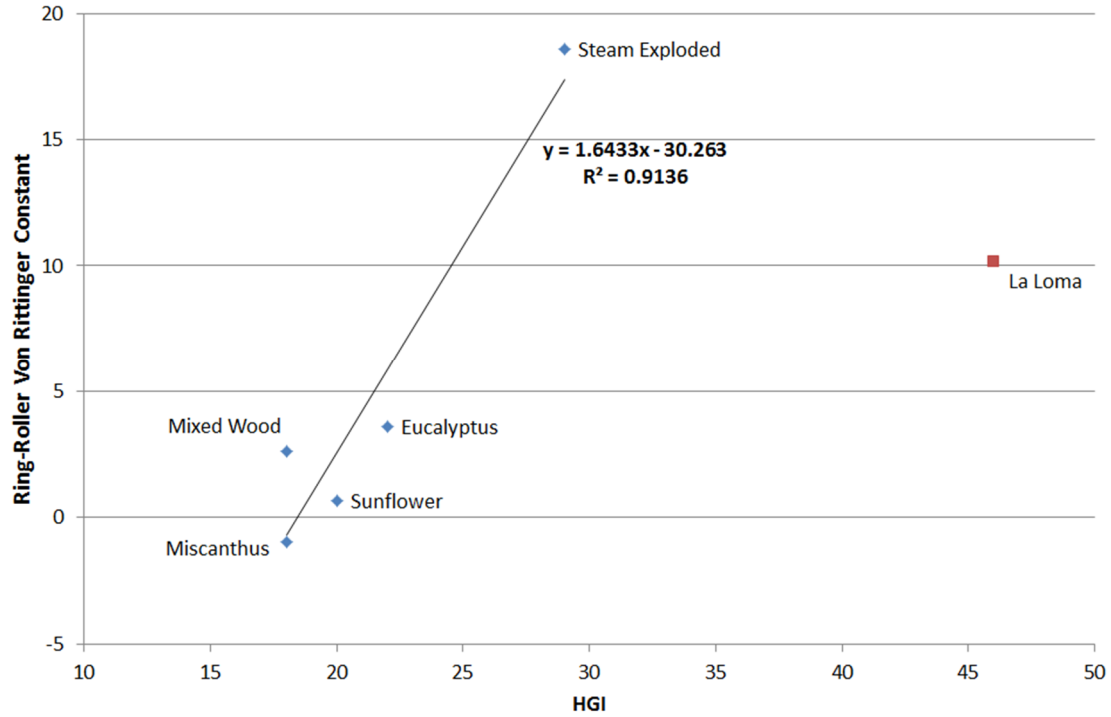


Figure 8.12: Ring Roller Mill Von Rittinger's Constant against HGI Values for Biomass and La Loma Coal

8.6. Particle Size and Shape Characteristics

The aerodynamic barrier which classifies the comminuted particles in the ring-roller mill uses the Stokes number to select which particles can pass. The Stokes number is related to the physical properties of a particle, namely its particle density, diameter and shape factors (section 2.11). It's possible for large biomass particles to have similar aerodynamic properties to that of a much smaller coal particle provided it has a sufficiently low sphericity (Mandø et al., 2010). Thus particle shape is a crucial parameter in the selection of particles which can travel through the classifier. This study has shown that most of the samples passed through the classifier relatively easily. However mixed wood pellets did not. The setup of the separator was for biomass, with the blades being set to allow as large a particle through as possible. This resulted in an 80th percentile particle size, d_{80}, value of 402 µm for coal. The target for La Loma coal at EDF Cottam is for 70% to pass 75 µm, the industry standard for a mill classifier is that 75% of coal delivered to the burner must pass a 200 mesh screen (75 µm) and < 0.3%, a 50 mesh screen (300 µm) (Afolabi, 2012). Mill classifiers are setup to obtain particles which will have as close to complete combustion as possible in the burners. Thus the setup of the classifier for biomass co-combustion with coal should be such that it meets the Stokes number criteria to provide the industry requirements for coal. The d_{80} for the comminuted biomasses at the current setting varies greatly amongst the biomasses (table 8.3), and thus the d_{80} which would be required for industry settings is material dependent, and a blanket size requirement for all biomasses would not be appropriate.

Sample	Rosin-Rammler			Size Parameters (µm)			Dispersion Parameters					Distribution Shape Parameters	
	d' (µm)	n	R^2	d_{10}	d_{gw}/d_{50}	d_{80}	hs	ls	MRS	C_u	C_c	GS_i	K_g
Miscanthus	1035	1.64	0.998	236	797	1377	1.82	2.34	1.71	4.90	1.05	0.19	0.81
Sunflower	1089	1.09	0.999	211	822	1523	2.00	2.59	2.06	5.59	1.00	0.30	0.93
Steam exploded	394	1.61	0.999	85	329	521	1.71	2.75	1.68	4.71	1.20	0.14	0.94
Mixed Wood	814	1.36	0.998	123	631	1201	1.99	3.08	2.00	6.44	1.54	0.22	0.78
Eucalyptus	721	1.63	0.999	170	583	958	1.81	2.38	1.83	4.22	1.28	0.24	1.11
Microwave	417	1.76	0.999	109	350	538	1.65	2.42	1.56	3.84	1.16	0.14	0.97
La Loma	281	1.29	0.999	42	226	402	1.94	3.56	2.01	7.03	1.30	0.21	0.87

Table 8.3: Shape, Dispersion and Distribution Shape Parameters of the Cumulative Particle Size Distributions for Biomass and Coal Milled in the Ring-Roller Mill

The choking of the mixed wood pellets provides a greater insight into the behaviour of the classifier. Its pre-densified particle size distribution was coarser than that obtained from the mill (pre-milled d_{80} 1373 µm, milled d_{80} 1201 µm). For miscanthus, there was little change from the miscanthus pre-milled particle size distributions (pre-milled d_{80} 1251 µm, milled d_{80} 1377 µm). Thus the mixed wood pre-milled particle size distribution was too coarse to pass through the separator based on its pre-densified physical characteristics, and extra comminution was required to allow it to pass. Thus the choking exhibited with the mixed wood pellets is related to its particle size reduction and material characteristics. The material is not breaking down easily in the mill, and this is indicative of the material reaching its critical particle size for comminution through compression, the length of which is material dependent, and particles below this size are ductile in compression (Kendall, 1978).

This will result in the mixed wood pellets taking longer to break down as comminution through compression is not easily achieved, causing a build-up of material within the mill which results in increased energy consumption, and mill pressure and temperatures. The planetary ball milling tests showed that the mixed wood pellets disintegrated easily under high impact loads (section 6.4.1), unlike sunflower pellets, and while the mixed wood pellets are more durable than sunflower pellets (Fig. 8.6), they are not as durable as the other biomass pellets tested, none of which choked in the mill. The variance in d_{80} of the milled samples (table 8.3) shows that it is not just particle size which is important in passing the aerodynamic barrier of the separator. Figure 8.13 shows the cumulative distributions of particle sphericity, circularity, symmetry and aspect ratio for the milled materials, the average values of which can be found in table 8.4.

Sample	Average Sphericity	Average Circularity	Average Symmetry	Average Aspect Ratio
Eucalyptus	0.414	0.504	0.751	0.524
Miscanthus	0.375	0.457	0.735	0.480
Sunflower	0.413	0.500	0.763	0.525
Steam exploded	0.477	0.609	0.795	0.594
La Loma	0.543	0.617	0.758	0.650
Mixed Wood	0.429	0.490	0.696	0.540
Microwave	0.435	0.577	0.786	0.551

Table 8.4: Impact of Drying on Average Particle Sphericity, Circularity, Symmetry and Aspect Ratio for Biomass Milled in Ring-Roller Mill

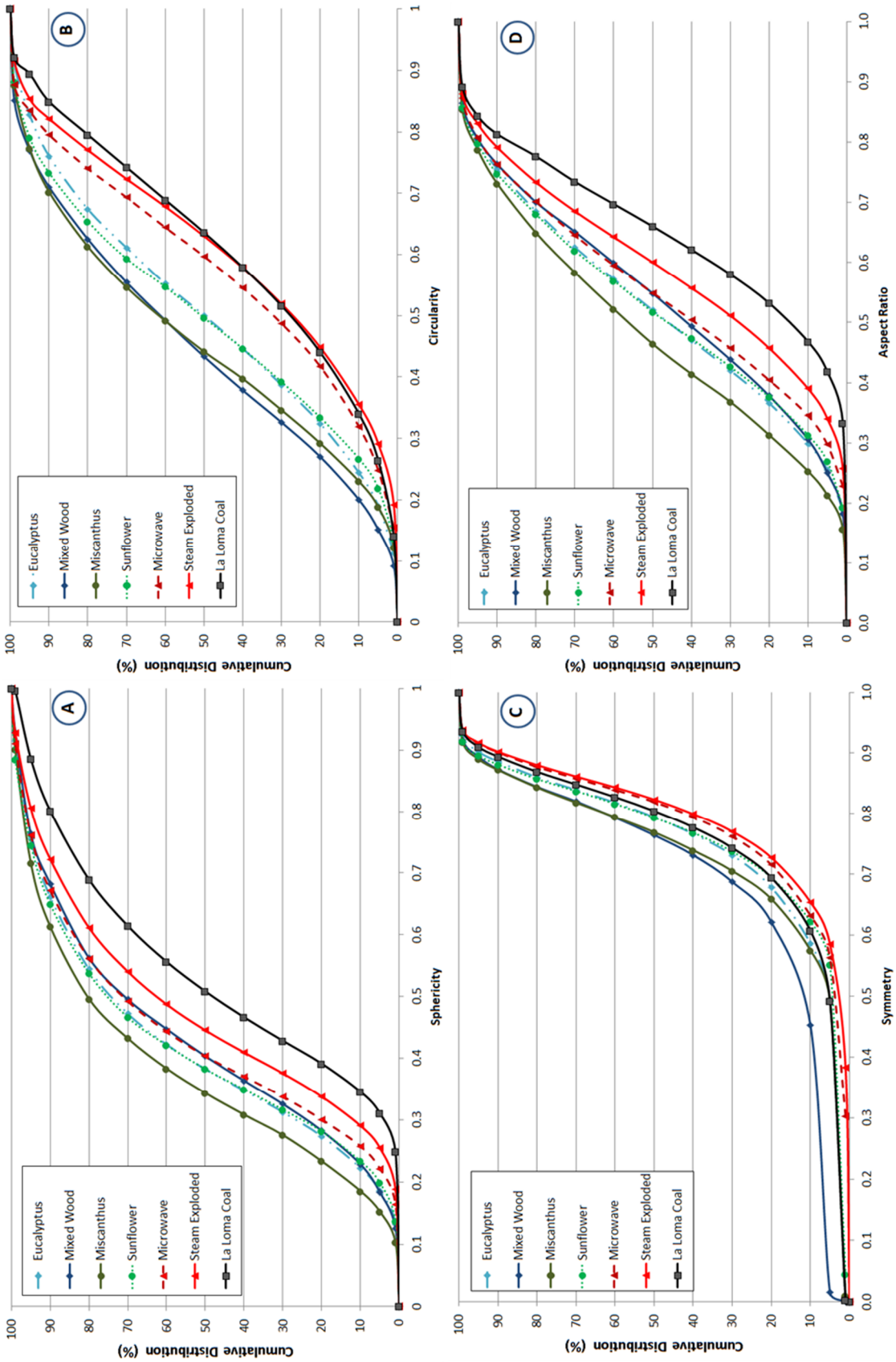


Figure 8.13: Ring-Roller Mill Comminuted Biomass and Coal Cumulative Particle Shape Distributions for Sphericity (a), Circularity (b), Symmetry (c), and Aspect Ratio (d)

In line with the results from the other milling trials in this thesis, La Loma coal has the highest particle shape factors, followed by the thermally treated pellets (steam exploded and microwave), with the herbaceous and wood pellets showing the lowest values. All the samples have seen an increase in sphericity as a result of comminution in the ring-roller mill, apart from eucalyptus which showed a slight decrease. La Loma coal saw the smallest increase in sphericity, but has the greatest reduction in particle size. Notably it was the mixed wood pellets which showed the greatest change in sphericity, with a 14% increase in average sphericity for a relatively small reduction in particle size.

Figure 8.14 shows the statistically significant relationship (p-value of 0.035) between particle size and sphericity for the milled products, which was obtained through linear regression analysis (section 3.2.2). No similar trend was observed for the particle size and sphericity of the pre-milled samples. From the regression analysis, a strong negative correlation (linear correlation coefficient, *r*, of -0.79) was obtained between comminuted particle size and shape. The correlation showed that as smaller particles are more spherical than larger particles. This fits with the theory of Stokes numbers and classifiers, in that as the Stokes number is dependent not only on the sphericity of the particle but also its Reynolds number, it's possible for large biomass particles to have similar aerodynamic properties to that of a much smaller coal particle provided it has a sufficiently low sphericity (Mandø et al., 2010).

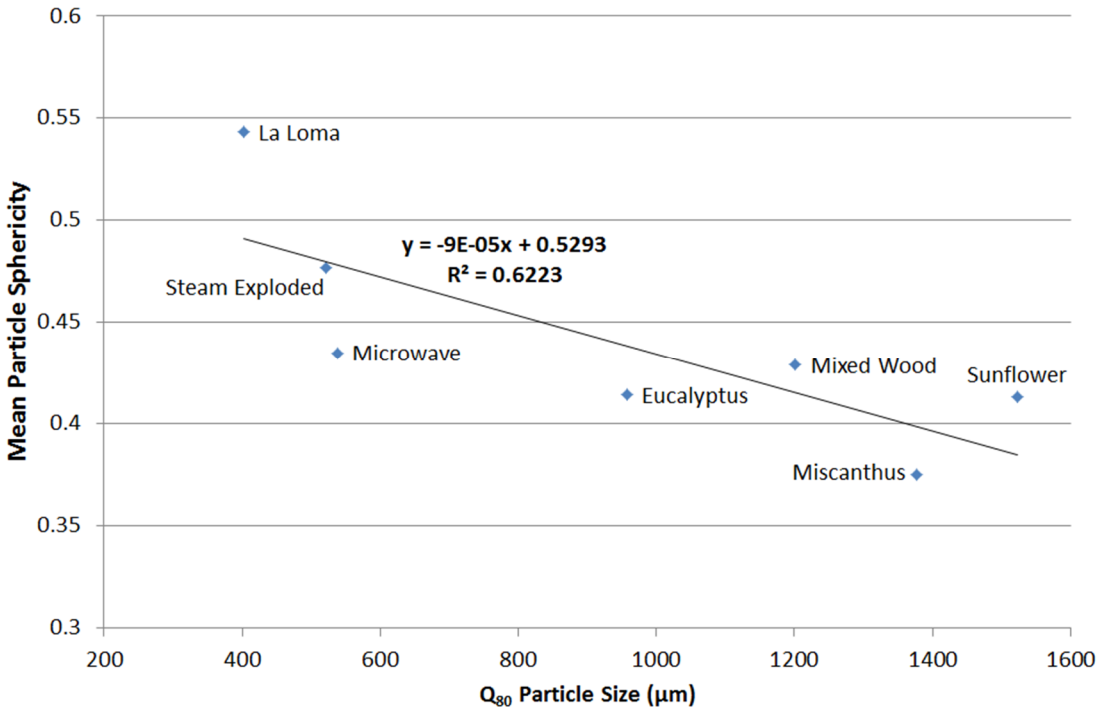


Figure 8.14: Relationship between Particle Sphericity and Particle Shape of Milled Biomass and Coal

The variation in the fit (62%) of the line in figure 8.14 is related to the particle density variations of the materials and the limited results available. Thus the fundamental link between particle size and shape has been proven to be in effect in the working of the separator system. In order to reduce comminution effort and avoid mill choking, densified biomass pellets should to be composed of a particle size distribution which can pass the aerodynamic barrier, but this particle size distribution is material dependent. In addition, the critical particle size for comminution through compression needs to be obtained for the material to be ground to minimise the risk of mill choking.

8.7. Conclusions

This was the first study into the milling behaviour of densified biomass in a laboratory scale ring-roller mill with dynamic classification. It was found that as particle size decreases, the particle sphericity required to pass the aerodynamic barrier increases, which fits with the Stokes theory for mill classifiers. The significance of this result is that for biomass co-combustion with coal, biomass mill classifiers should be set to the Stokes requirements for coal rather than a blanket particle size for all biomasses. In addition, grindability tests should be set to the classifier requirement rather than just a blanket target size. As with the cutting mill study, a correlation was obtained between the specific effective energy consumption and biomass pellet durability. Mixed wood pellets choke in a ring-roller mill due to their ductile behaviour which makes it difficult to adjust the particle size and shape to allow them to pass the aerodynamic barrier.

There are several improvements which could easily be made to the ring-roller mill to improve the experimental data. Apart from the pressure readings, all existing measurements could be synchronised into one computerised logging system. Individual energy meters could be fitted to each motor, with voltage, power factor and current readings for all three phases to provide more accurate real time information. Currently a water manometer was used with a camera to obtain the pressure readings, and this could be modified to provide a digital output to a central logging system. The duct work could be modified to allow for re-circulation and full fresh air settings as per full scale Lopulco ring-roller mill at EDF West Burton. In the full scale mills, the separator operates from its own motor, and splitting the drive for the separator and mill bed would allow the separator to be independent of mill bed.

Chapter 9 - Practical Implications of the Study for Industry and Academia

This chapter draws on the results of chapters 4 to 8 to provide a comprehensive overview of the practical implications of this study for industry and academia, with future work being identified from the results. The purpose of this chapter is to answer the original aim of the study outlined in the introduction, which was to analyse and characterise the milling behaviour of a wide range of biomasses in several different types of mills. There are no studies available in literature which compares the comminution properties of densified biomass from all major biomass groups in coal and biomass mills. There are limited studies available which compare the milling behaviour of different biomasses in different mills. These studies are generally limited to one biomass group such as woods in several coal mills (Tamura et al., 2014), woods in a range of hammer mills (Paulrud et al., 2002), or herbaceous biomasses in a range of cutting mills (Miao et al., 2011).

This chapter looks at six of the densified biomasses tested (mixed wood, eucalyptus, miscanthus, sunflower, steam exploded and microwave pellets) and olive cake. This chapter classifies milling behaviour through the common milling indices of milling energy and particles size, as well as drawing out common relationships for the materials between mills. The novel parameter of particle shape is used to analyse the classification relationships of mills, and an illustrative particle shape guide is provided for each biomass to provide a practical guide for industrialists of the expected particle size and shape prior to and after comminution for different mills.

9.1. Energy Consumption, Pellet Durability and Von Rittinger Relationships

The specific effective energy consumption of a mill is one of the main parameters, along with particle size, which characterise milling behaviour. All milling theories are based on the relationship between these two parameters (section 2.12). Figure 9.1 shows energy consumption for the BWI mill, planetary ball mill, cutting mill, and ring-roller mill by biomass type. All these values have been taken from chapters 5 to 8. Apart from the BWI mill, most mills show similar specific effective energy consumption for a given biomass. The energy consumption of the BWI mill shows how mill choking results in increased energy consumption and how the critical particle size for comminution through compression needs to be known to avoid mill choking. The choking is related to the equilibrium sieve size

selected for the BWI test, which was 1 mm. The cutting mill had a screen size of 4 mm, and the ring-roller mill was set to allow the biomass particles pass easily through the classifier leading to coarser particle sizes than the BWI test.

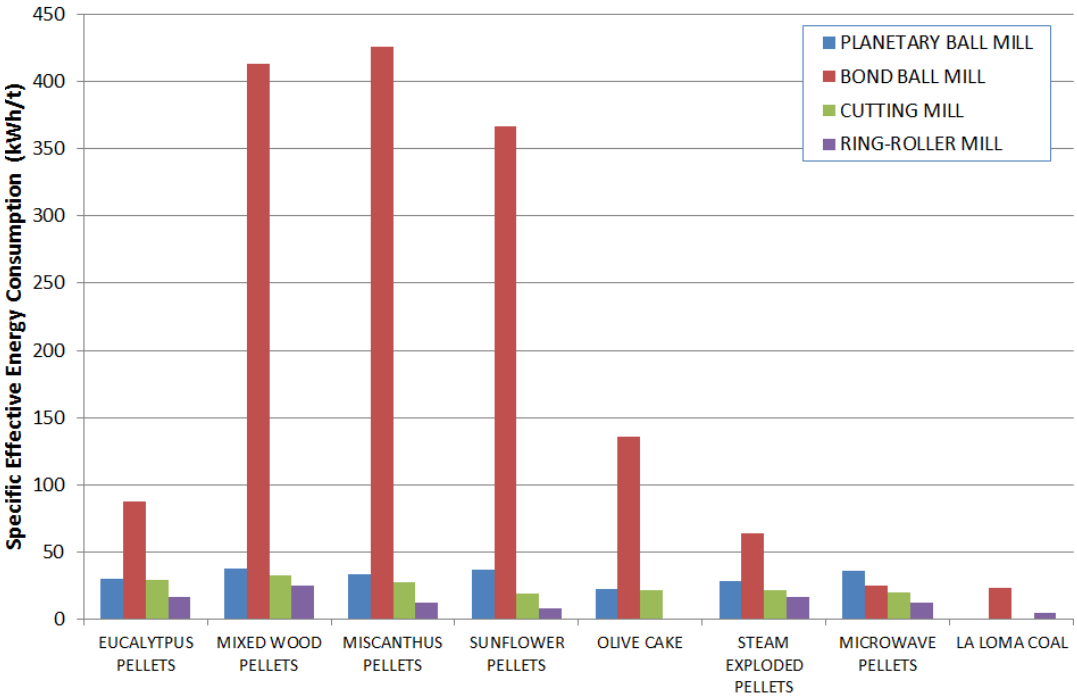


Figure 9.1: Specific Effective Energy Consumption for Different Mills by Biomass and Coal Type

Table 9.1 summarises the energy consumption, percentage energy consumption represents of the pre-mill higher heating value (table 4.9 in section 4.12), Rosin-Rammler analysis, and the Von Rittinger constant for the biomasses, grouped by woods, herbaceous, fruit, thermally treated and coal. In general, the ring-roller mill shows the lowest specific effective energy consumption for each biomass type, but had the greatest spread in particle size distributions due to the use of the classifier to select the particles rather than a sieve size (BWI mill) or screen (cutting mill). The largest energy consumption was observed for the BWI test. The planetary ball mill and cutting mill show similar energy consumptions to each other for eucalyptus, mixed wood, miscanthus, olive cake and steam exploded. However it is important to note that the target particle size varied by mill. As previously noted, the screen size for the cutting mill was 4 mm, and the equilibrium sieve size for the BWI test was 1 mm. The ring-roller mill classifier was set for maximum passage with reasonable fineness and the planetary ball mill did not have a screen or classification system.

Sample/Mill	Specific Effective Energy E_E (kWh/t)	E_e / HHV_d (%)	Rosin-Rammler			VR Constant
			d' (µm)	n	R^2	
Eucalyptus Pellets (HHV_d 20,348 J/g)						
Pre-Milled	-	-	833	1.40	1.000	-
Planetary Ball Mill	30.0	0.53	493	1.27	1.000	17.9
Bond Ball Mill	87.3	1.54	541	1.62	0.997	-
Cutting Mill	29.1	0.52	901	1.69	1.000	0.9
Ring-Roller Mill	16.4	0.29	721	1.63	1.000	3.6
Mixed Wood Pellets (HHV_d 20,652 J/g)						
Pre-Milled	-	-	966	1.29	0.998	-
Planetary Ball Mill	37.9	0.66	628	1.15	0.999	11.3
Bond Ball Mill	413.0	7.20	530	1.28	0.989	-
Cutting Mill	32.5	0.57	847	1.72	0.999	5.7
Ring-Roller Mill	24.9	0.43	814	1.36	0.998	2.6
Miscanthus Pellets (HHV_d 18,669 J/g)						
Pre-Milled	-	-	832	1.38	0.992	-
Planetary Ball Mill	33.9	0.65	898	1.32	0.999	1.6
Bond Ball Mill	425.9	8.21	582	1.64	0.994	-
Cutting Mill	27.4	0.53	1038	1.47	0.999	3.7
Ring-Roller Mill	12.8	0.25	1035	1.64	0.998	-0.9
Sunflower Pellets (HHV_d 20,755 J/g)						
Pre-Milled	-	-	1115	1.18	0.995	-
Planetary Ball Mill	37.0	0.64	822	1.24	0.999	9.1
Bond Ball Mill	366.3	6.35	557	1.82	0.997	-
Cutting Mill	19.3	0.33	763	1.70	1.000	5.9
Ring-Roller Mill	7.9	0.14	1089	1.09	0.999	0.7
Olive Cake (HHV_d 20,264 J/g)						
Pre-Milled	-	-	1953	0.93	0.997	-
Planetary Ball Mill	22.2	0.39	925	1.09	0.998	8.2
Bond Ball Mill	136.2	2.42	360	1.22	0.997	-
Cutting Mill	21.5	0.38	1122	1.55	0.999	10.1
Steam exploded Pellets (HHV_d 20,397 J/g)						
Pre-Milled	-	-	889	1.35	0.998	-
Planetary Ball Mill	28.5	0.50	310	1.14	0.998	37.3
Bond Ball Mill	63.9	1.13	201	0.97	0.999	-
Cutting Mill	21.8	0.38	1038	1.75	1.000	-2.8
Ring-Roller Mill	17.1	0.30	394	1.61	0.999	18.6
Microwave Pellets (HHV_d 21,261 J/g)						
Planetary Ball Mill	36.0	0.61	185	1.13	0.999	-
Bond Ball Mill	24.8	0.42	668	1.96	0.992	-
Cutting Mill	20.4	0.34	859	1.80	1.000	-
Ring-Roller Mill	12.1	0.20	417	1.76	1.000	-
La Loma Coal (HHV_d 29,665 J/g)						
Pre-Milled	-	-	1954	1.46	0.992	-
Bond Ball Mill	23.4	0.28	59	2.81	0.983	-
Ring-Roller Mill	4.8	0.06	281	1.29	0.999	10.2

Table 9.1: Pre-milled and Milled Specific Effective Energy Consumption E_E, Ratio of E_E to Dry Higher Heating Value (HHV_d), Rosin-Rammler Analysis and Von Rittinger (VR) Constants

For a true comparison of different mills specific effective energy consumption, the target particle size would need to be the same. In addition, this target particle size should also not be a blanket target size for all biomass, but a target size based on the classifier requirements for that specific biomass. This would allow for all physical properties to be taken into account, as they would be in the classifier of a full scale mill. As the ring-roller mill results showed in chapter 8, the target size for different biomasses varies greatly when a classifier is used to select the particles. Traditional lab scale milling tests only provide information on the grindability of a material to a target size. The do not look at whether or not those particles will pass an aerodynamic barrier based on their combined physical characteristics, which for the ring-roller mill led to significantly different particle sizes for biomass pellets.

The specific effective energy consumption generally represented a small amount of the dry higher heating value (HHV_d) of the materials. The planetary ball mill saw the lowest percentage for olive cake (0.39%) and highest for mixed wood (0.66%), sunflower showed the lowest (0.33%) percentage and mixed wood the highest (0.57%) for the cutting mill, and La Loma showed the lowest (0.06%) and mixed wood the highest (0.43%) for the ring-roller mill. Mixed wood showed the highest energy consumption in three out of the four mills, and was second highest for the BWI mill (7.20%), thus mixed wood pellets will show poor milling performance in all the mills and this reduces the energy available for combustion from this material. The BWI test showed significantly higher percentages for the materials which chocked, with miscanthus (8.21%), mixed wood (7.20%) and sunflower (6.35%) showing a percentage of HHV_d an order of magnitude higher than La Loma (0.28%) and microwave pellets (0.42%). This highlights the impact mill choking has not just on mill performance but on how thermal output is compromised by non-optimal milling conditions.

Figure 9.2 shows the specific effective energy consumption and pellet durability relationships for the mills. The BWI mill results were not included as the choking of several samples meant there was not enough data to analyse the relationship. The planetary ball mill did not show a relationship between durability and specific effective energy consumption due to the fact that no screening was used to provide a target particle. Also, some of the materials didn't completely disintegrate within the mill despite the mills high impact forces. The cutting mill and ring-roller mill do show a similar linear relationship with a strong fit ($R^2 > 0.9$), and interestingly the mixed wood was an outlier for both mills. However only limited data is available for these correlations and more results are required to validate the correlations. The outliers are denoted by red points on figure 9.2. The test should be

expanded to include more samples and look into the impact of target size on the results. In addition, pilot and full scale data should be compared to see if the same trends also exist for larger scale mills. The significance of this trend is that it's possible to estimate the energy consumption of a mill for a given target particle size purely on pellet durability.

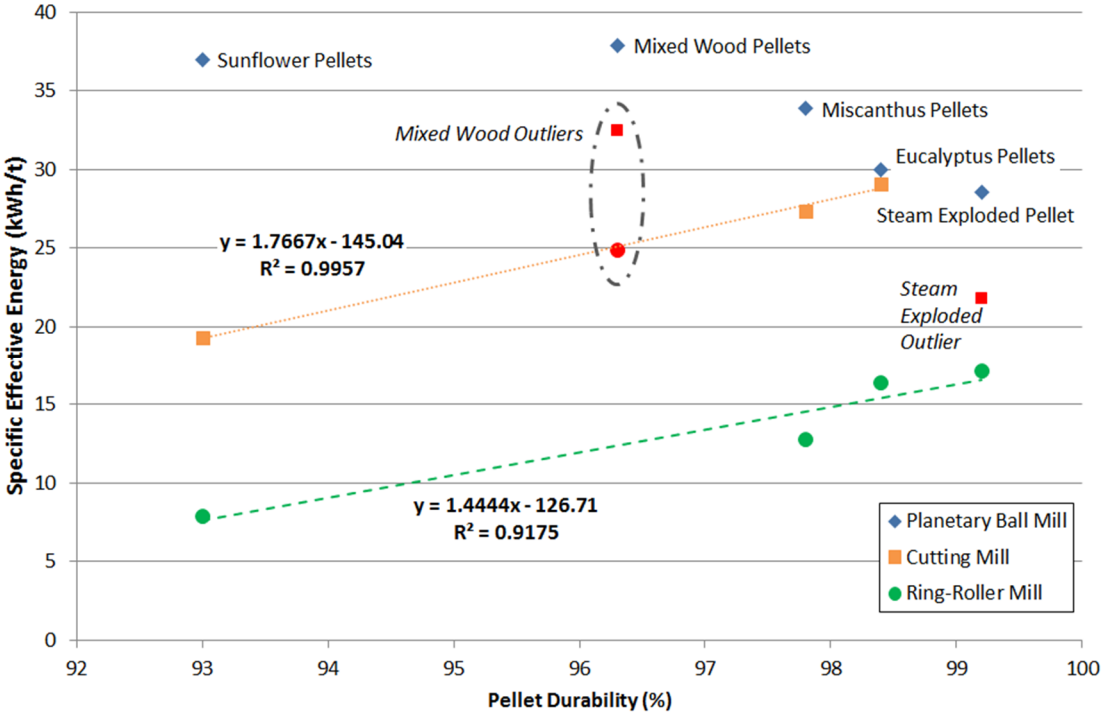


Figure 9.2: Relationship between Specific Effective Energy Consumption and Pellet Durability for a Planetary Ball Mill, Cutting Mill, and Ring-Roller Mill for Different Densified Biomasses. Biomass Samples have same Pellet Durability for Each Mill Type.

Table 9.1 also provides the Rosin-Rammler analysis of the particle size distributions of the pre-milled and milled biomass. The results show that when a screen or sieve is used to classify the material, as done for the BWI and cutting mill, the obtained Rosin-Rammler particle sizes are quite similar for non-treated biomasses. However when no screen is used or a classification system is used, a range of particle size distributions are obtained. Thus it is not possible to compare the Von Rittinger constants obtained for different mills on a like for like basis as they depend on the target particle size of a mill.

However figure 9.3 shows that there is a correlation between the Von Rittinger constant and Rosin-Rammler particle size for eucalyptus and steam exploded pellets. Steam exploded saw the highest Von Rittinger constant for the planetary ball mill, followed by the ring-roller mill, and the lowest for the cutting mill. The same patter was observed for the eucalyptus pellets. There is a strong fit for both materials and very similar relationships were obtained. However for sunflower, miscanthus, and mixed wood pellets, no relationship was obtained.

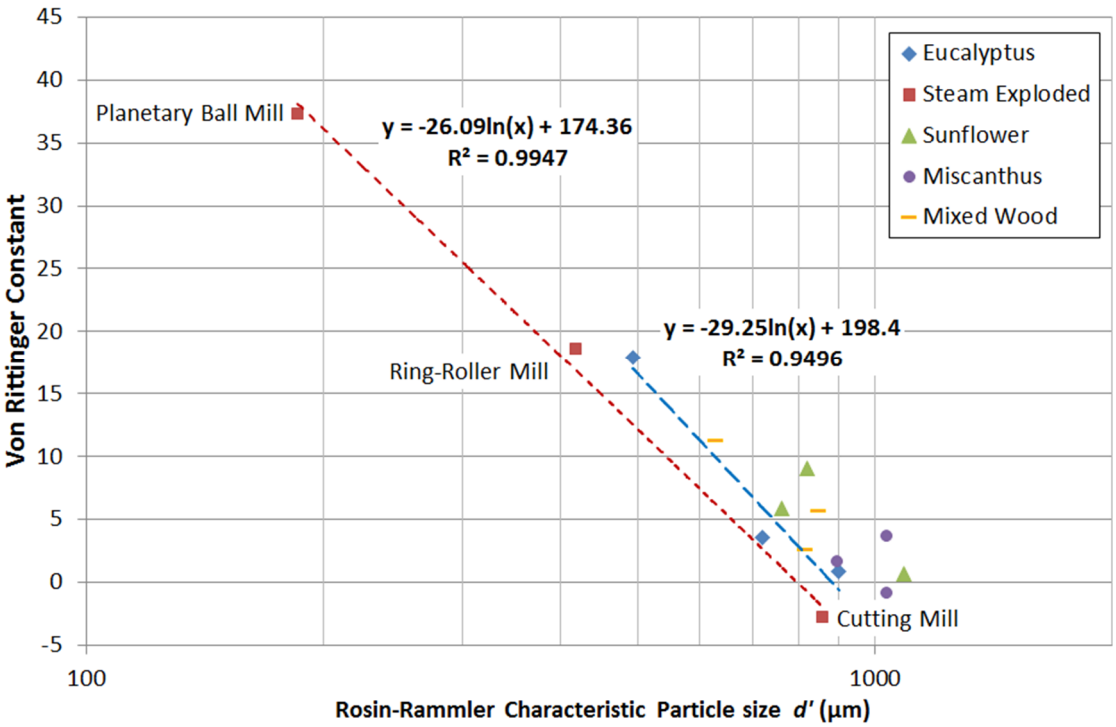


Figure 9.3: Von Rittinger Constant against Rosin-Rammler Characteristic Particle Size for Biomass Milled in Different Mills

Steam exploded and eucalyptus pellets were the only samples which did not choke in at least one of the mills. Steam exploded and eucalyptus pellets saw a significant decrease in particle size in all the mills, and thus milling was not only related to the breaking down of the pellet, but also the comminution of the particles. More research is required into these relationships, especially for the other pellets tested in this study, to ascertain if a similar relationship exists if the pellets do not choke in mills.

9.2. Von Rittinger Constant and Particle Size Relationships

As with the specific effective energy consumption and pellet durability relationship in figure 9.2, several correlations are common to the mills. Bond proposed a relationship between BWI and HGI results (Bond, 1961), which was confirmed by McIntyre and Plitt, who proposed a different relationship for materials with a BWI value above 8.5 kWh/t (McIntyre et al., 1980). Section 5.10 showed that a correlation exists between densified biomass which did not choke in the BWI test and HGI (O. Williams et al., 2015). As noted in section 8.5, a relationship was also noted between the Von Rittinger constant and HGI value for the ring-roller mill. This relationship is also present for the planetary ball mill and more weakly for the cutting mill (Fig. 9.4).

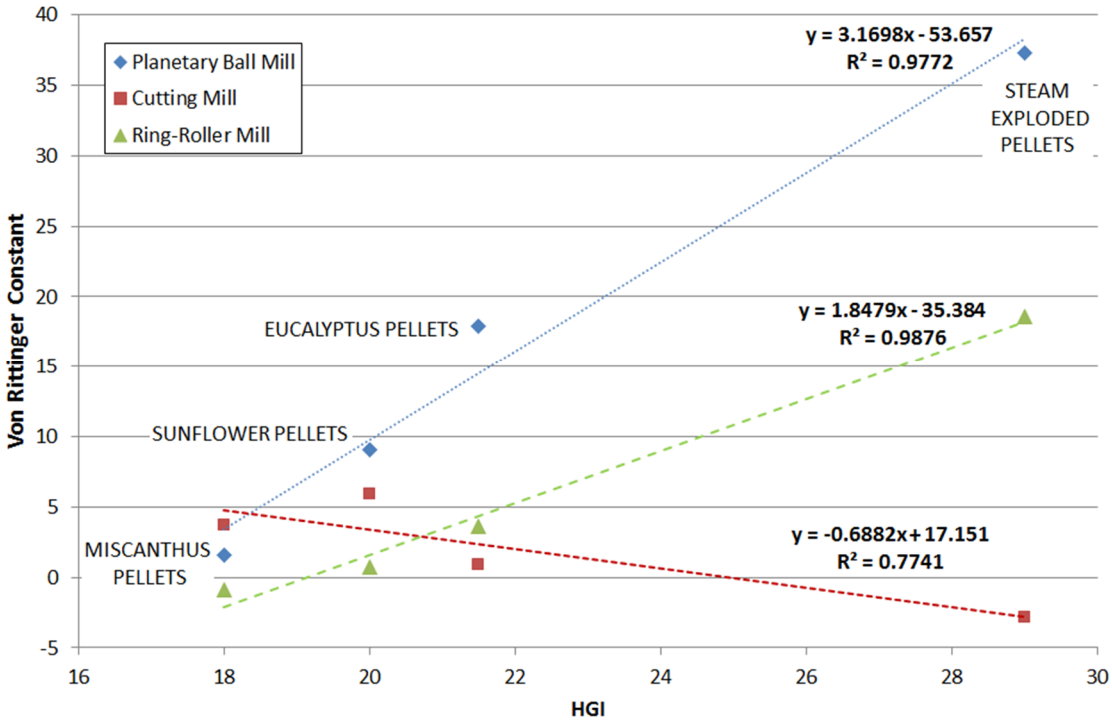


Figure 9.4: Von Rittinger & HGI Relationships for a Planetary Ball Mill, Cutting Mill, and Ring-Roller Mill for Different Densified Biomass

The planetary ball mill and ring-roller mill show linear relationships, with the Von Rittinger constant increasing with increasing particle size reduction for the mill (table 9.1). The cutting mill sees an inverse relationship, and given the relatively similar energy consumptions and low particle size reduction (table 9.1) this relationship is not representative of this mill given very little comminution actually occurs. A finer screen than the 4mm one used would result in actual comminution, as seen in section 7.2.3, rather than the disintegration of the pellets back to their pre-milled sizes. But this relationship requires further testing to be validated for finer screen sizes.

9.3. Mechanical Response and Milling Energy Relationships

Mechanical response testing provides an insight into the mechanical strength of materials under high and low strain rates. Section 4.9 surmises the low strain rate tests and section 4.10 surmises the high strain test results for the biomass pellets used in this study. Previous studies by Laskowski et al. (1997, 1998, 1999) found that there was a relationship between the characteristic compression curve of quasi-static mechanical response tests and the grinding energy requirement for legume seeds. No studies have been conducted on the dynamic mechanical response of biomass pellets using the Split Hopkinson Pressure Bar (SHPB), and thus the relationship between pellet strength in quasi static and dynamic modes

and milling energy consumption has not previously been investigated. The BWI results were not included in the analysis as the milling choking of several samples led to large scatter in the data and steam exploded pellets were not included as they had significantly higher strength than the other pellets and fell as an outlier in all correlations.

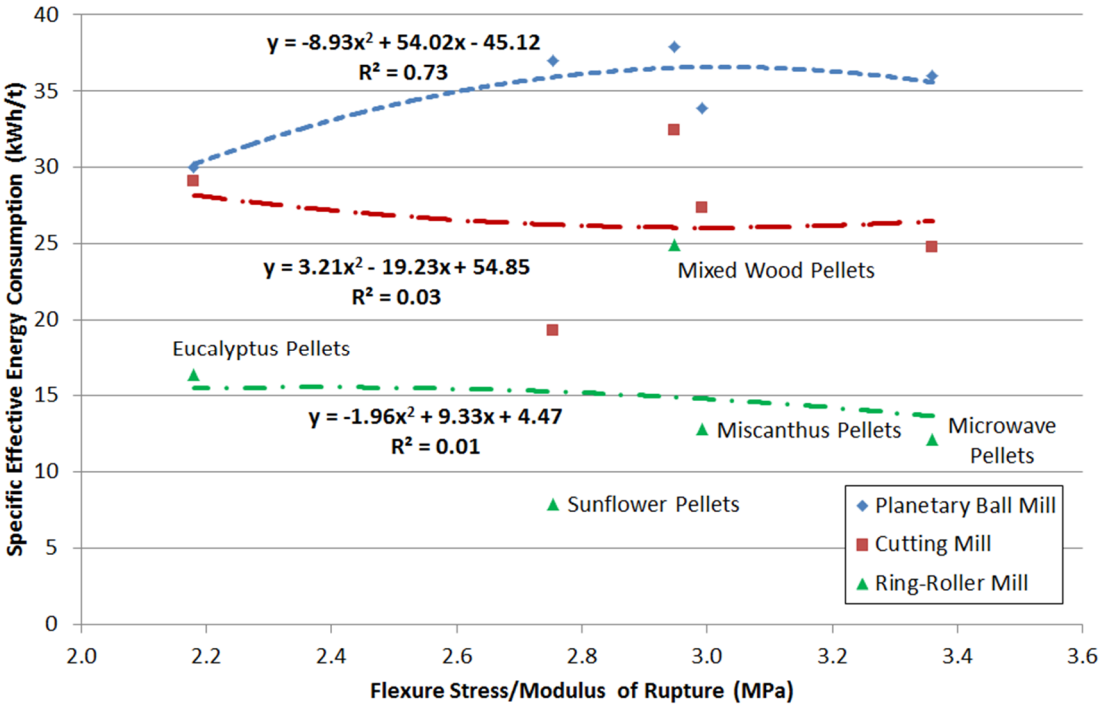


Figure 9.5: Specific Effective Energy Consumption against Flexure Stress for Planetary Ball Mill, Cutting Mill and Ring-Roller Mill.

The maximum flexure stress or Modulus of Rupture can be considered to be a measure of the ultimate strength of a biomass pellet. Figure 9.5 shows the quasi static strength against specific effective energy consumption E_e. No correlation was found for the cutting and ring-roller mills. A good fit was obtained for a polynomial relationship for planetary ball mill (73%), which indicates that E_e increases with increasing strength. The measurements obtained in the quasi-static and dynamic mechanical response tests are related to the strength of the biomass pellet and not the particles which compose it. Fracture will occur along the lines of least resistance, which will be the bonds between the particles. Biomass pellets have no structural integrity beyond weak adhesive bonds unlike virgin wood or coal. The first stage of milling is the breaking down of the pellets by overcoming the weak bonds which hold the pellet together. The second and more energy demanding stage of milling is the reduction of the composite particles. Due to the variance in the material composition and structure of the wide range of biomasses analysed, along with their unknown critical particle size for comminution through compression, the effort to achieve this particle size

and shape change varies immensely. It was not possible to apportion the energy consumption associated for each stage of milling to the results of the tests conducted. Thus the particle size distribution of the pellet plays a crucial role in determining how much milling is required to obtain the required particle size and shape. To apportion the pellet grinding energy, milling tests are required to find the point of zero particle size reduction ratios for a mill, and then reduce the target particle size to see how increasing particle size reduction ratio impacts mill energy consumption for different materials and mills.

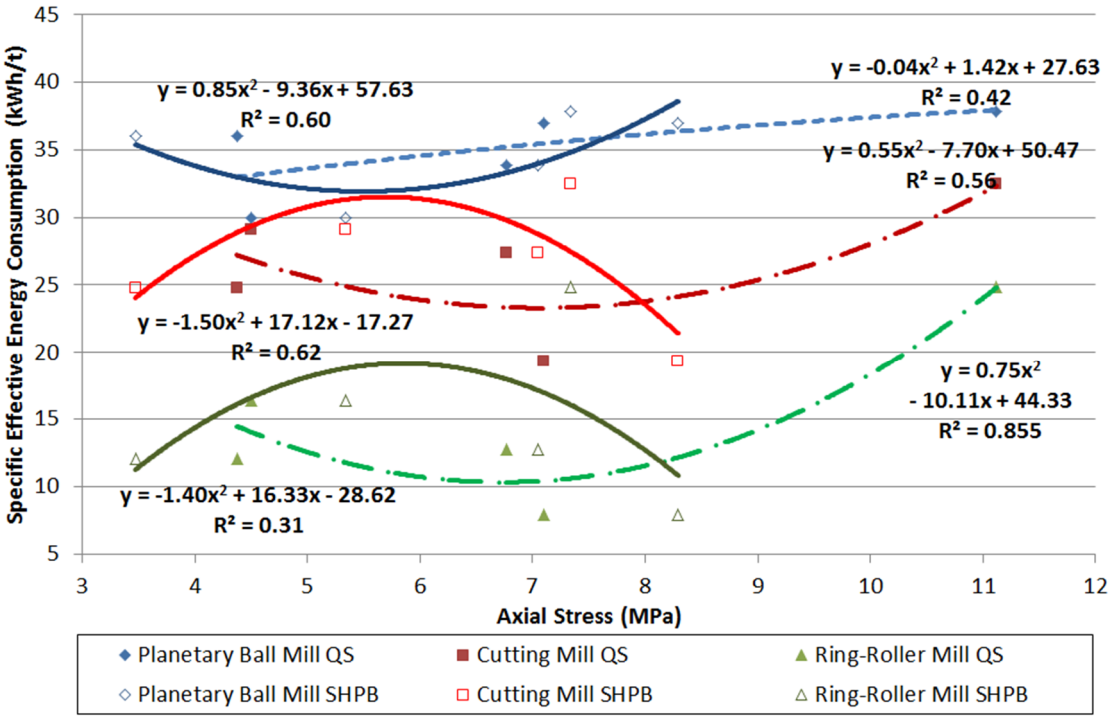


Figure 9.6: Specific Effective Energy Consumption against Maximum Axial Stress for Planetary Ball Mill, Cutting Mill and Ring-Roller Mill.

Figure 9.6 shows E_e against maximum compressive axial stress for the quasi-static and dynamic modes. A large variance was found in the fit of polynomial relationships. The quasi-static tests saw a general trend of increasing E_e for increasing axial strength for all mills. This was also noted for the planetary ball mill in the SHPB test but the other mills saw a peak E_e around 6 MPa and dropped off for higher axial stress. Apart from mixed wood pellets, the maximum axial stress was similar for the quasi-static and dynamic tests. As with the flexure tests, it is not possible to apportion energy to pellet breakdown and thus further work is required to understand the energy required to break down a pellet in a mill.

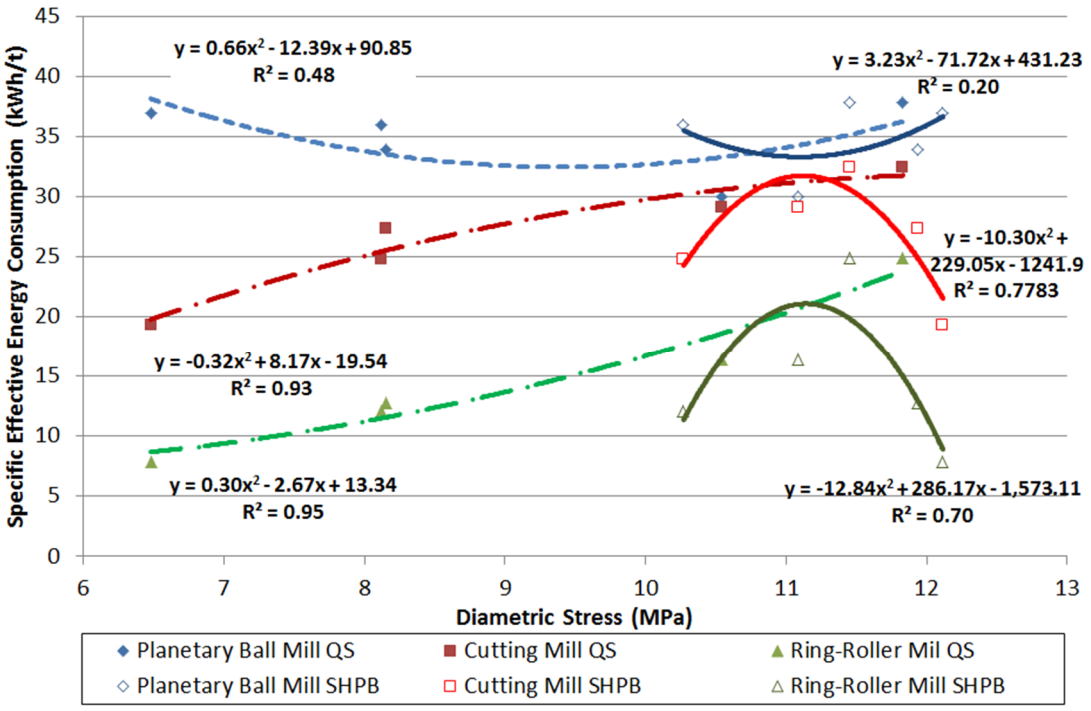


Figure 9.7: Specific Effective Energy Consumption against Maximum Diametric Stress for Planetary Ball Mill, Cutting Mill and Ring-Roller Mill.

Figure 9.7 shows that there is a larger spread in diametric strength for the biomass pellets in the quasi-static tests compared to the dynamic tests, and the dynamic results are all in the higher end of the quasi-static results. As with the axial tests a general trend of increasing E_e for increasing axial strength was seen for all mills in the quasi-static tests. The dynamic tests showed the same trends as the axial in the dynamic tests. More data is required to validate these relationships.

9.4. Particle Size and Particle Shape Relationships

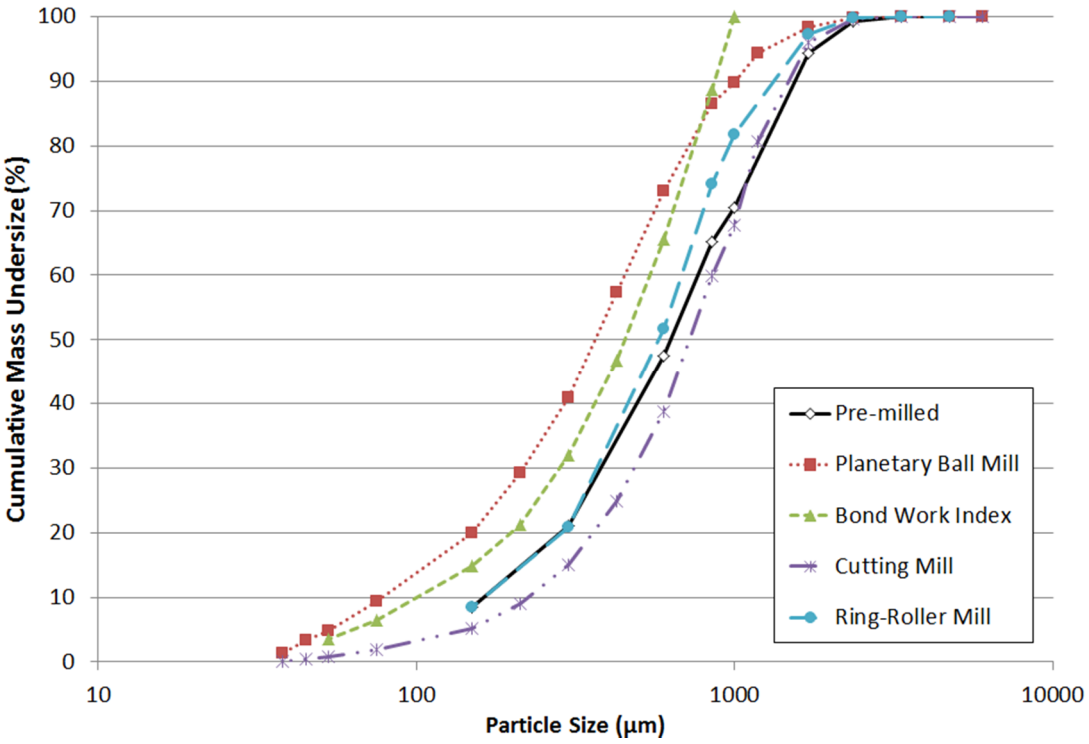
In general milling studies provide an analysis of the grindability of a material to a set size. The tests do not take into account the impact of particle shape and density on the selection of a particle in an aerodynamic barrier (classifier) commonly used on full scale coal mills. Chapters 4 to 8 have shown that the pre-milled particle shape of biomass and coal is inherent in informing the particle shape after milling, even if there is an order of magnitude change in the particle sizes obtained. This section analyses the impact of mill type on particle size and shape by biomass group and ascertain what trends can be observed from the results. The following figures for each of the main biomasses show the particle size distributions obtained the pre-milled (where available) and milled biomasses, with a particle size and shape table for that biomass beneath. The shape table gives the indicative particle

images for the 80th percentile particle size (d_{80}), 50th percentile (Q_{50}) sphericity, symmetry, aspect ratio and circularity, along with the mean shape factor values. This provides an illustrative guide to the typical particles obtained for that biomass type prior to and after milling in different mills. The images were obtained from the Camsizer digital image analysis results and using the Retsch particle library software (version 1.4.1) to obtain sample particle outlines of the characteristic size and shape values.

9.4.1. Woody Biomass

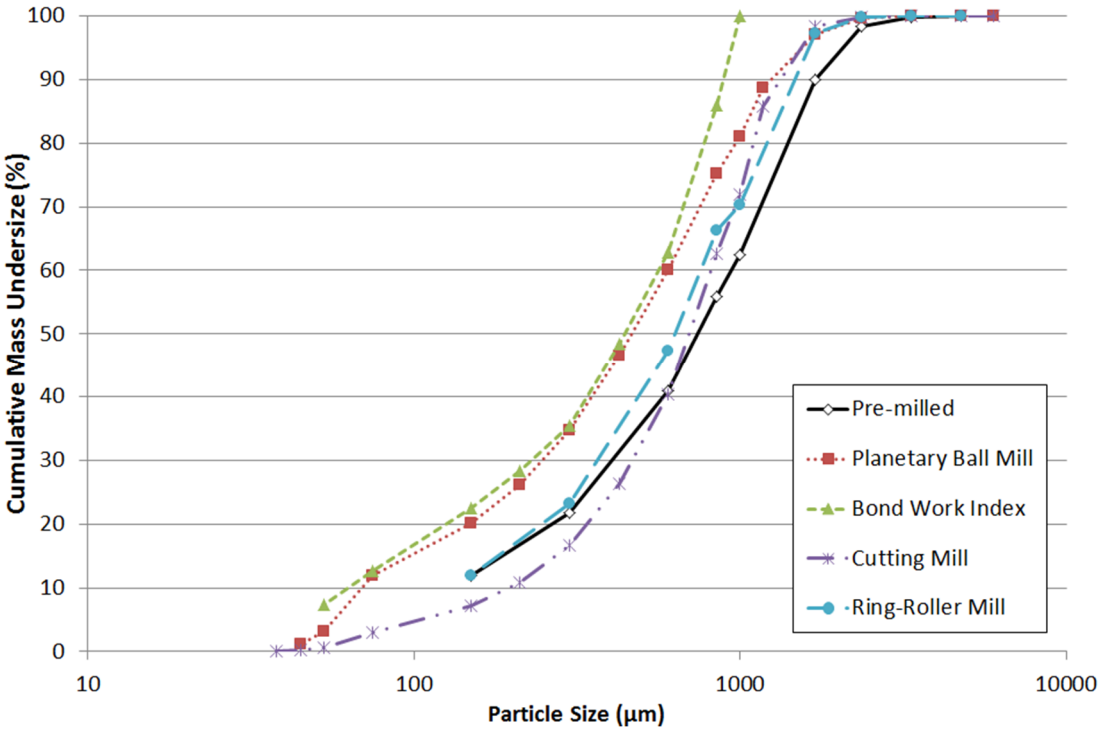
Figures 9.8 and 9.9 show the particle size distributions and particle size and shape images for eucalyptus and mixed wood, respectively. There is a similar impact on particle size for both woods, with eucalyptus producing a finer particle size distribution than the mixed wood for lower energy consumptions (Fig. 9.1). For eucalyptus pellets, the planetary ball mill produced the finest distribution followed by the BWI, while the opposite trend was observed for mixed wood pellets. The cutting and ring-roller mills show little impact on the pre-milled particle sizes. This is related to the selected screen size for the cutting mill, which was 4mm, and resulted in the pellets just breaking down to their pre-milled size and passing through the screen. The pre-milled particle shape factors were higher for eucalyptus particles than the mixed wood particles. Eucalyptus particles see little change in their sphericity through milling despite a significant change in particle size in the planetary ball mill and BWI mill. Mixed wood particles increase in sphericity in all the mills, especially for the ring-roller mill, for a smaller change in particle size compared to the eucalyptus pellets.

When the energy consumption is also taken into account (Fig. 9.1), eucalyptus pellets show a greater change in particle size for lower levels of energy consumption compared to the mixed wood pellets, which choked in 3 of the mills. Thus eucalyptus particles reduce easily in size with little change in shape for less milling effort than the mixed wood particles. This suggests that for eucalyptus particles, it is easier for them to reduce in size than change shape, while the opposite is true for mixed wood particles, resulting in higher mill energies and mill choking. Thus biomasses from the same group can have very different milling behaviours. Given that eucalyptus is a hard wood and mixed wood is composed primarily of pine, a soft wood, further studies are required to see if this milling behaviour can be further broken down into a soft and hard wood classification. This is likely to be linked to the critical particle size for comminution through compression of the material, with hard woods potentially having smaller critical particle sizes than soft woods. The other particle shape parameters followed the same patterns as particle sphericity for the wood samples.



Characteristic	Pre-milled	Planetary Ball Mill	Bond Work Index	Cutting Mill	Ring-Roller Mill
Particle Size d_{80}	1215 µm	705 µm	751 µm	1171 µm	958 µm
Sphericity Q_{50}	0.404	0.398	0.409	0.409	0.382
Mean Sphericity	**0.432**	**0.428**	**0.440**	**0.441**	**0.414**
Symmetry Q_{50}	0.804	0.789	0.764	0.810	0.794
Mean Symmetry	**0.745**	**0.742**	**0.702**	**0.772**	**0.751**
Aspect Ratio Q_{50}	0.552	0.540	0.554	0.555	0.520
Mean Aspect Ratio	**0.544**	**0.539**	**0.548**	**0.553**	**0.524**
Circularity Q_{50}	0.551	0.506	0.466	0.555	0.500
Mean Circularity	**0.545**	**0.504**	**0.487**	**0.543**	**0.504**

Figure 9.8: Pre-milled and Milled Eucalyptus Particle Size Distributions (top) and Particle Size (based on d_{c_min}) and Shape Images (bottom)



Characteristic	Pre-milled	Planetary Ball Mill	Bond Work Index	Cutting Mill	Ring-Roller Mill
Particle Size d_{80}	1373 µm	975 µm	787 µm	1105 µm	1201 µm
Sphericity Q_{50}	0.347	0.381	0.387	0.384	0.403
Mean Sphericity	**0.376**	**0.409**	**0.414**	**0.413**	**0.429**
Symmetry Q_{50}	0.821	0.769	0.766	0.796	0.764
Mean Symmetry	**0.781**	**0.743**	**0.736**	**0.765**	**0.696**
Aspect Ratio Q_{50}	0.471	0.519	0.527	0.522	0.548
Mean Aspect Ratio	**0.484**	**0.519**	**0.524**	**0.526**	**0.540**
Circularity Q_{50}	0.502	0.427	0.465	0.509	0.433
Mean Circularity	**0.492**	**0.439**	**0.422**	**0.494**	**0.490**

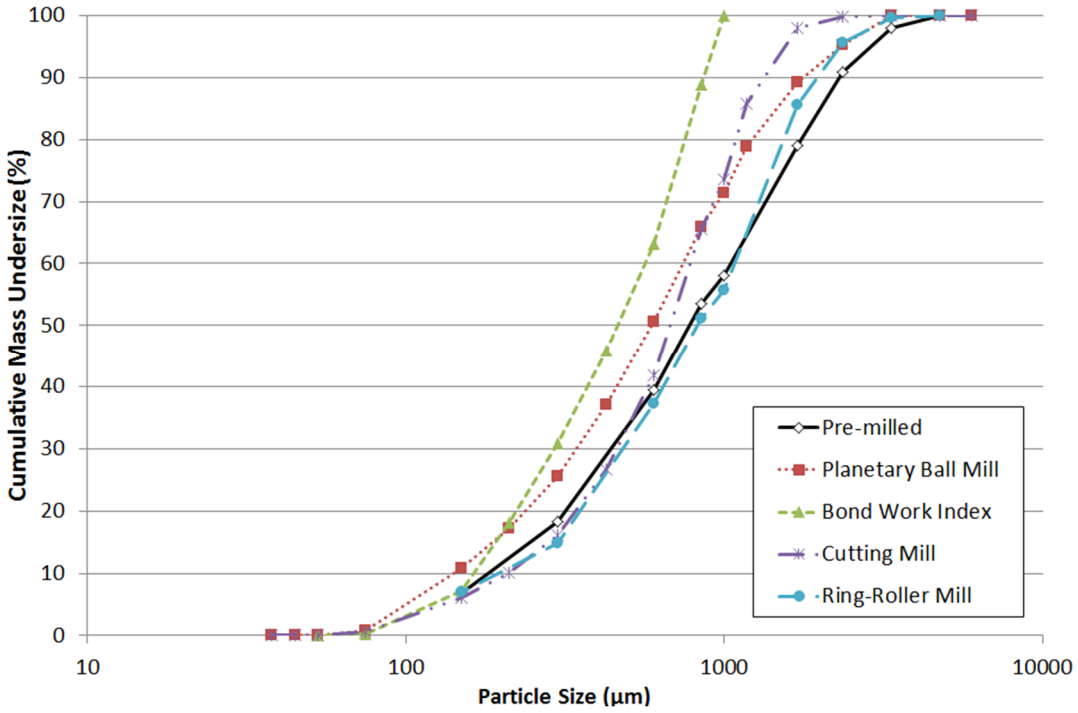
Figure 9.9: Pre-milled and Milled Mixed Wood Particle Size Distributions (top) and Particle Size (based on d_{c_min}) and Shape Images (bottom)

Eucalyptus particles show little change across the board, while mixed wood particles show decreasing symmetry and circularity, with increasing aspect ratio, which is to be expected with increasing sphericity.

9.4.2. Herbaceous Biomass

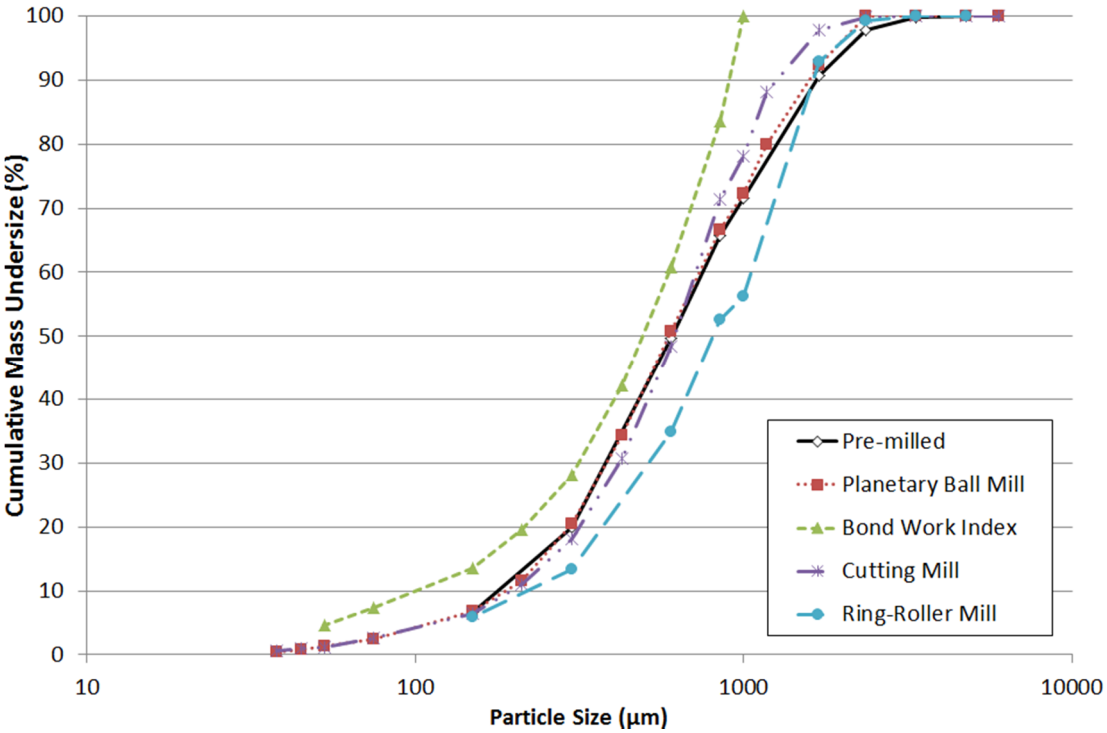
Figures 9.10 and 9.11 illustrate that the BWI test provided the finest particle size distributions for sunflower and miscanthus pellets. In the ring-roller and cutting mill, there was no change in the particle size below 800 µm, indicating that the fines are passing through the classification system without further comminution and only the coarser particles are being comminuted. Miscanthus has a coarser particle size distribution than its pre-milled profile in the ring-roller mill. This is likely to be related to the fines sticking to and lining the inside of the duct work while the coarser fraction passes through the mill uninhibited, as well as the heterogeneous nature of the material meaning a coarser particle size distribution could be present in the milled sample than those used for the disintegration test. The only real difference in d_{80} is seen in the BWI test, and both the sunflower and miscanthus pellets choked in this test. This indicates that the critical size for comminution had been reached in this mill but not the other mills. It is notable that in the ring-roller mill test, where both samples did not choke, sunflower had the lowest energy consumption of all the densified biomasses (table 9.1). The BWI test showed the biggest increase in sphericity as well as a reduction in particle size for sunflower pellets.

The high energy consumption for the BWI test indicates that a significant effort was required to achieve a change in particle size and shape. While a similar particle size was obtained for sunflower and the other non-treated biomasses in the BWI test, the ring-roller mill showed a wide range of particle sizes for the same classifier settings, with sunflower having the coarsest particle size of all the biomasses (table 9.1). Thus the result from the BWI test could be misleading on the potential of a biomass to choke in the ball mill. The test is assessing a materials' grindability to a set target size, but this target size was not based on classifier requirements. For a more informed result, the material dependent particle size for classification should be estimated and then used as the target particle size for the BWI test. For the other shape factors, sunflower and miscanthus particles saw a decrease in symmetry and circularity, and increase in aspect ratio with milling, which is the same trend as seen for the mixed wood pellets.



Characteristic	Pre-milled	Planetary Ball Mill	Bond Work Index	Cutting Mill	Ring-Roller Mill
Particle Size d_{80}	1744 µm	1220 µm	757 µm	1145 µm	1523 µm
Sphericity Q_{50}	0.347	0.384	0.418	0.397	0.382
Mean Sphericity	**0.375**	**0.412**	**0.452**	**0.426**	**0.413**
Symmetry Q_{50}	0.831	0.782	0.745	0.803	0.793
Mean Symmetry	**0.797**	**0.742**	**0.670**	**0.771**	**0.763**
Aspect Ratio Q_{50}	0.470	0.521	0.567	0.540	0.517
Mean Aspect Ratio	**0.481**	**0.521**	**0.559**	**0.539**	**0.525**
Circularity Q_{50}	0.571	0.479	0.452	0.530	0.496
Mean Circularity	**0.567**	**0.499**	**0.495**	**0.525**	**0.500**

Figure 9.10: Pre-milled and Milled Sunflower Particle Size Distributions (top) and Particle Size (based on d_{c_min}) and Shape Images (bottom)



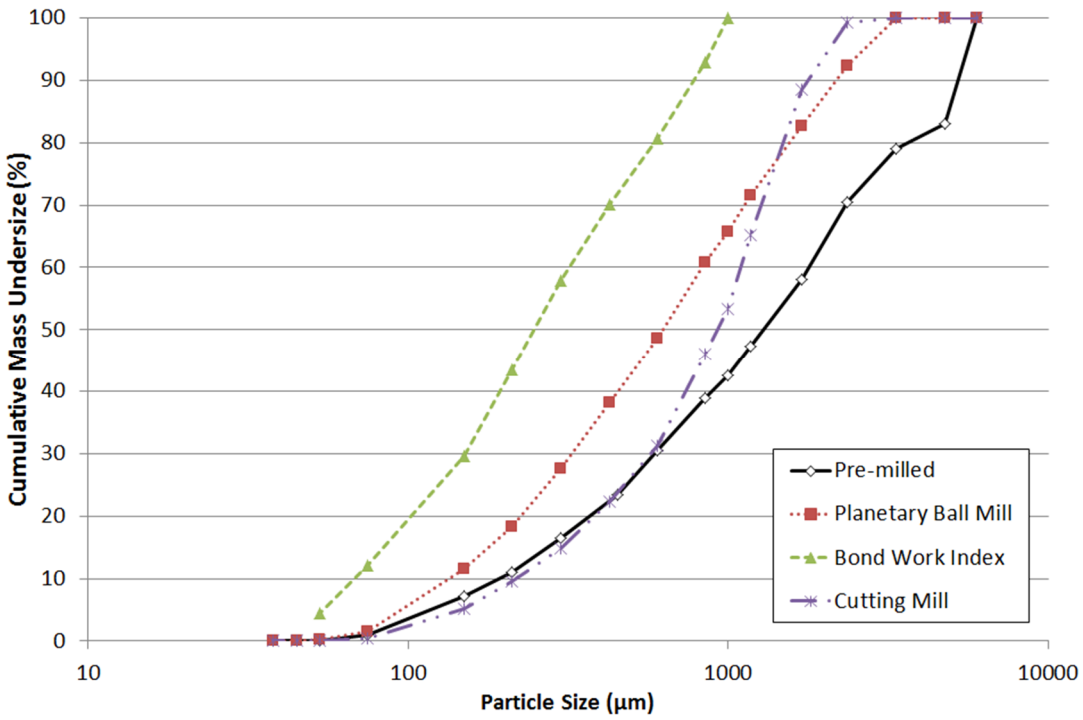
Characteristic	Pre-milled	Planetary Ball Mill	Bond Work Index	Cutting Mill	Ring-Roller Mill
Particle Size d_{80}	 1251 µm	 1181 µm	 813 µm	 1069 µm	 1377 µm
Sphericity Q_{50}	 0.324	 0.330	 0.339	 0.355	 0.343
Mean Sphericity	**0.353**	**0.356**	**0.366**	**0.384**	**0.375**
Symmetry Q_{50}	 0.826	 0.781	 0.757	 0.783	 0.769
Mean Symmetry	**0.795**	**0.747**	**0.728**	**0.754**	**0.735**
Aspect Ratio Q_{50}	 0.437	 0.446	 0.460	 0.482	 0.464
Mean Aspect Ratio	**0.455**	**0.461**	**0.470**	**0.492**	**0.480**
Circularity Q_{50}	 0.511	 0.457	 0.413	 0.482	 0.441
Mean Circularity	**0.508**	**0.461**	**0.431**	**0.486**	**0.457**

Figure 9.11: Pre-milled and Milled Miscanthus Particle Size Distributions (top) and Particle Size (based on d_{c_min}) and Shape Images (bottom)

9.4.3. Fruit Biomass

Olive cake was the only fruit biomass tested in this study, and showed a very different milled product, with a very large pre-milled particle size and the most spherical of all the samples tested (Fig. 9.12). Olive cake produced the finest non-treated biomass particle size distribution in the BWI, but much coarser product in the planetary ball mill and cutting mill. It was the only biomass which experienced caking, which was so severe in the ring-roller mill that it wasn't included in the tests. The planetary ball mill milled product size was impacted by the caking of the pulp section. Drying the biomass resulted in a significantly finer particle size (section 6.4.1) with a d_{80} of 521 µm. The olive cake was the only non-treated biomass to show a significantly different milling output in all the mills. In the cutting mill, the fines were not impacted by milling, and given the caking issues experienced in the planetary ball mill; the fines below the required target particle size should be removed prior to milling and sent straight to the burner so that comminution is only performed on material which needs to be comminuted. This would also remove the pulp section, which shows the greatest tendency to cake, and the potential for caking would be significantly reduced. Olive cake produced the most spherical particles of all the materials tested, including the coal. This increases its suitability for co-combustion with coal as the particle shape is similar to coal, giving it similar flow properties. However this does raise an issue about the classifier settings for olive cake. From the milling tests conducted, olive cake does not mill to as fine a particle size as steam exploded or microwave pellets in a planetary ball mill (Fig. 9.13 and 9.14) or as fine as steam exploded in a BWI mill.

Based on the classifier settings for coal, there could be the potential for the olive cake to choke if it cannot easily reduce to the required particle size based on its high sphericity. The olive cake only saw a change in sphericity in the BWI mill. The change in particle size was almost an order of magnitude in this mill but also resulted in an 11% decrease in sphericity. This was also true for the symmetry, aspect ratio and circularity, which also saw little change apart from in the BWI mill.



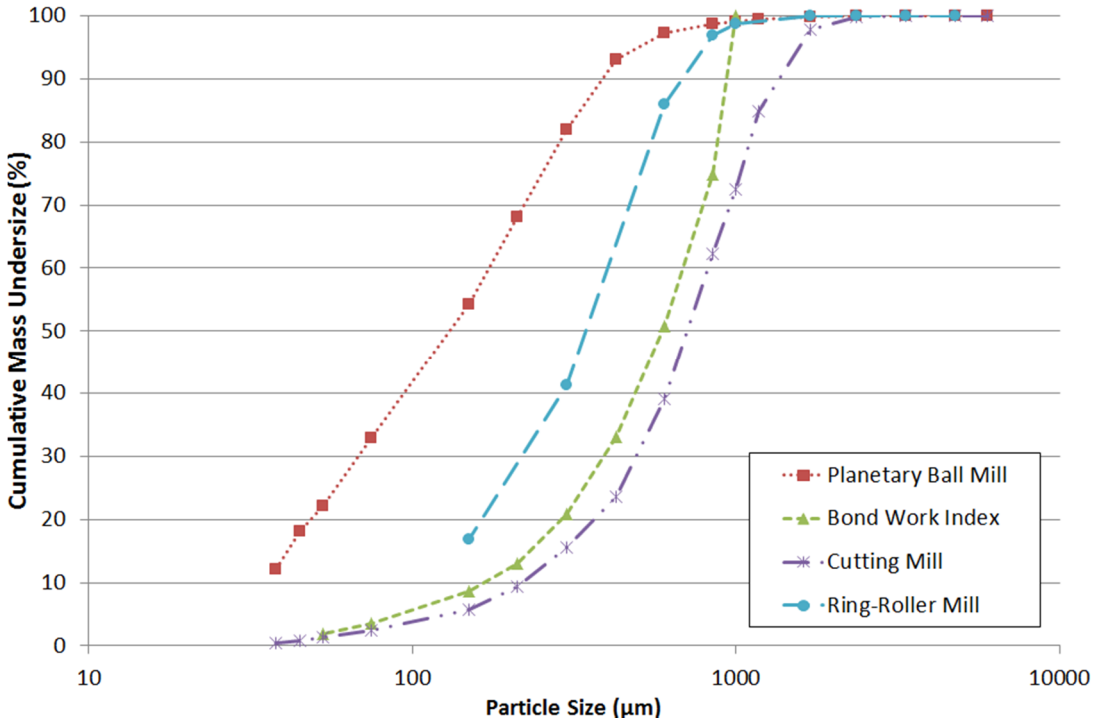
Characteristic	Pre-milled	Planetary Ball Mill	Bond Work Index	Cutting Mill
Particle Size d_{80}	 3660 µm	 1553 µm	 589 µm	 1461 µm
Sphericity Q_{50}	 0.562	 0.577	 0.490	 0.535
Mean Sphericity	**0.584**	**0.592**	**0.520**	**0.560**
Symmetry Q_{50}	 0.886	 0.871	 0.833	 0.870
Mean Symmetry	**0.863**	**0.853**	**0.802**	**0.851**
Aspect Ratio Q_{50}	 0.708	 0.714	 0.645	 0.685
Mean Aspect Ratio	**0.692**	**0.698**	**0.637**	**0.673**
Circularity Q_{50}	 0.806	 0.778	 0.682	 0.781
Mean Circularity	**0.757**	**0.741**	**0.625**	**0.742**

Figure 9.12: Pre-milled and Milled Olive Cake Particle Size Distributions (top) and Particle Size and (based on d_{c_min}) Shape Images (bottom)

9.4.4. Thermally Treated Biomass

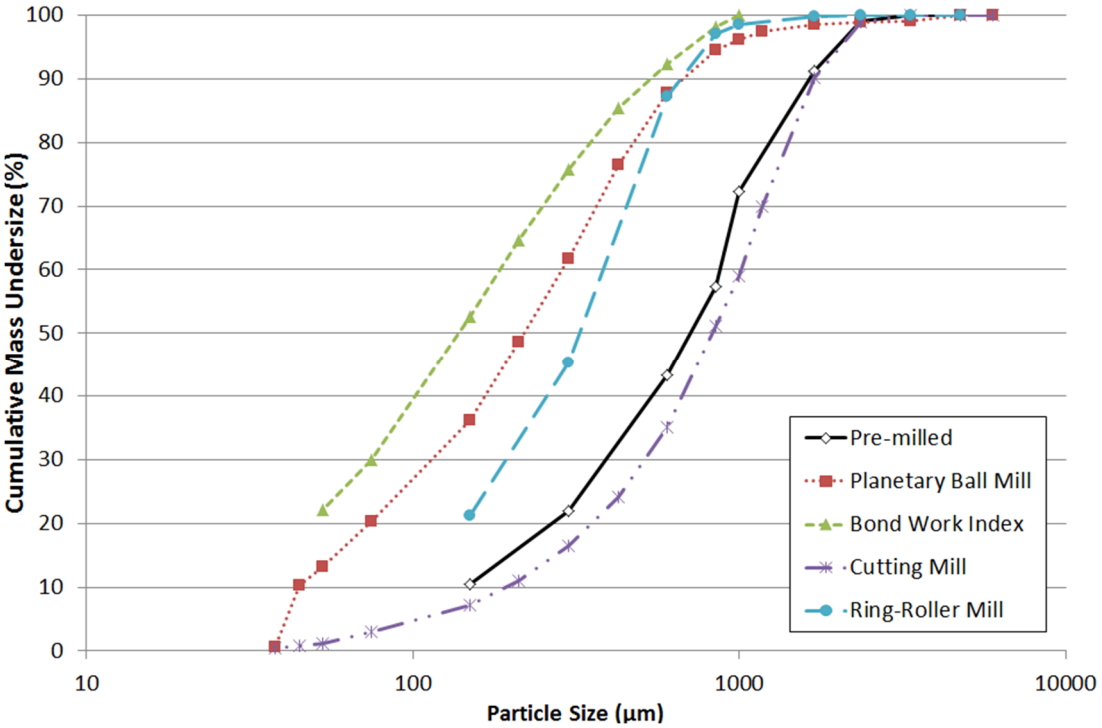
Two thermally treated biomasses; steam exploded treated white wood, and microwave thermally treated white wood pellets, were tested extensively in this study. The microwave pellets did not disintegrate in the pellet disintegration tests, and thus it was not possible to assess the impact of milling on the pre-densified particle size distribution. The thermally treated biomasses show very different particle size distributions and particle shape images (Fig. 9.13 and 9.14) compared to the woody pellets in section 9.3.1. The particle size distributions for the thermally treated woods show a significant reduction in particle size for different mills compared to the woody biomasses which saw little change, highlighting that thermal treatment does significantly improve the grindability of woody biomasses. Microwave pellets finest distribution was in the planetary ball mill, followed by the ring-roller mill, while the BWI and cutting mill show similar distributions to the woody biomasses. Microwave pellets had one of the lowest energy consumptions in the BWI mill. The d_{80} particle size for microwave in the BWI test (888 µm) was significantly above that obtained in the planetary ball mill (285 µm), while steam exploded obtained a finer d_{80} in the BWI test (346 µm) than in the planetary ball mill (466 µm). Steam exploded pellets' energy consumption was nearly 3 times that of the microwave pellets in the BWI mill, but similar to microwave pellets in the other mills when the milled product was coarser than that obtained in the planetary ball mill.

Microwave and steam exploded have noticeably increased shape factor values compared to the woody biomasses, indicating that thermal pre-treatment not only improves its grindability and ability to produce finer particle size distributions, but also the shape profile of the particles. The d_{80} for the ring-roller mill was almost identical for both steam exploded and microwave (521 µm for steam exploded and 538 µm for microwave), which was only slightly coarser than that obtained for La Loma (402 µm). When the sphericity of these particles is also compared, steam exploded had a sphericity of 0.477, microwave 0.435, and La Loma a sphericity of 0.543. The BWI test used the particle size specifications for coal of 70% passing 75 µm (Afolabi, 2012) and 1 mm for biomass (Esteban et al., 2006; Tamura et al., 2001). This gave La Loma a d_{80} of 78 µm and sphericity of 0.536. However the BWI test uses a sieve to classify the particles and not an aerodynamic barrier. Thus the particle selected is based purely on its size rather than a combination of its physical properties as would be in a full scale tube-ball mill with classifier.



Characteristic	Planetary Ball Mill	Bond Work Index	Cutting Mill	Ring-Roller Mill
Particle Size d_{80}	 285 µm	 888 µm	 1091 µm	 538 µm
Sphericity Q_{50}	 0.464	 0.385	 0.414	 0.403
Mean Sphericity	**0.480**	**0.414**	**0.445**	**0.435**
Symmetry Q_{50}	 0.763	 0.827	 0.836	 0.819
Mean Symmetry	**0.769**	**0.805**	**0.813**	**0.786**
Aspect Ratio Q_{50}	 0.621	 0.524	 0.563	 0.549
Mean Aspect Ratio	**0.597**	**0.528**	**0.561**	**0.551**
Circularity Q_{50}	 0.520	 0.605	 0.651	 0.597
Mean Circularity	**0.577**	**0.590**	**0.629**	**0.577**

Figure 9.13: Pre-milled and Milled Microwave Particle Size Distributions (top) and Particle Size (based on d_{c_min}) and Shape Images (bottom)



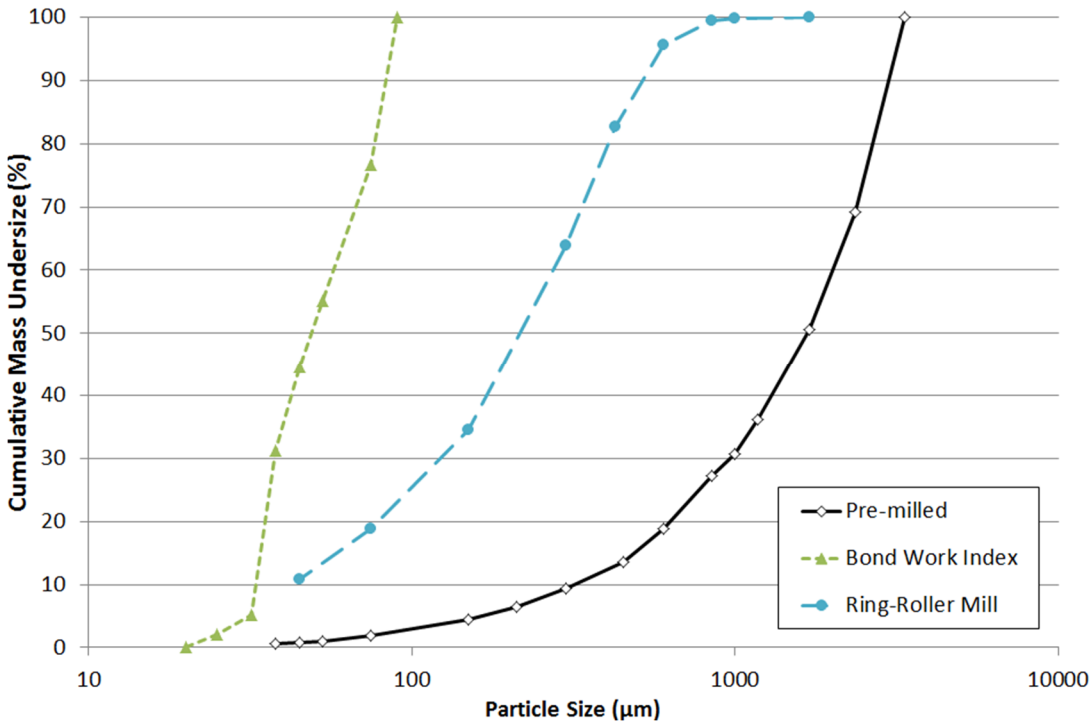
Characteristic	Pre-milled	Planetary Ball Mill	Bond Work Index	Cutting Mill	Ring-Roller Mill
Particle Size d_{80}	1196 µm	466 µm	346 µm	1412 µm	521 µm
Sphericity Q_{50}	0.428	0.454	0.455	0.464	0.445
Mean Sphericity	**0.458**	**0.484**	**0.484**	**0.498**	**0.477**
Symmetry Q_{50}	0.840	0.785	0.770	0.846	0.823
Mean Symmetry	**0.816**	**0.760**	**0.749**	**0.821**	**0.795**
Aspect Ratio Q_{50}	0.580	0.608	0.608	0.620	0.600
Mean Aspect Ratio	**0.577**	**0.602**	**0.601**	**0.615**	**0.594**
Circularity Q_{50}	0.645	0.522	0.506	0.690	0.630
Mean Circularity	**0.620**	**0.518**	**0.511**	**0.648**	**0.609**

Figure 9.14: Pre-milled and Milled Steam exploded Particle Size Distributions (top) and Particle Size (based on d_{c_min}) and Shape Images (bottom)

The ring-roller classifier was set up for biomass, and this resulted in a much coarser coal particle size than would be set for a full scale coal mill. But based on this setting the microwave and steam exploded particles were not that dissimilar to the La Loma milled particles. If the ring-roller classifier was set to the coal conditions used in the BWI test and industry standard (70% passing 75 µm), as would be required for co-combustion of biomass and coal (Mandø et al., 2010), a much smaller particle size would be required for the biomasses. Given that the shape factors of biomasses and coal are inherent properties which do no change significantly compared to particle size during milling, a model is required which can predict the required particle size for a classifier based on the physical characteristics of the pre-milled particles. This would provide a material specific target particle size for the BWI test. In addition, the planetary ball mill can be used to provide information on whether or not the biomass is likely to choke in trying to achieve the target particle size for classification.

9.4.5. Coal

La Loma was the only coal tested in this study and was only tested in the coal mills. It had the lowest energy consumption and smallest particle size in the ring-roller mill, and achieved similar energy consumption to microwave for a much finer particle target size in the BWI test (Fig. 9.15). The La Loma coal provides a bench mark against which the settings for biomass can be ascertained. This is particular true of the classifier on the ring-roller mill. The model proposed for selecting target particle sizes based on coal classifier settings should be validated against full scale sampling from the Lopulco mill at EDF West Burton or similar. By matching the output from the lab scale rig to the full scale output, the requirements of biomasses can be predicted for full scale applications. There is little change in the shape factors despite a massive change in particle size for the La Loma coal. This shows how the pre-milled shape factors are inherent for coal as well as biomass, and if a particle size change can be easily achieved, then this will be the route of least resistance in a mill over a particle shape change. More testing is required across the range of coals commonly used in pulverised fuel combustion to see if this is behaviour common to all coals and is related to the critical particle size of materials.



Characteristic	Planetary Ball Mill	Bond Work Index	Ring-Roller Mill
Particle Size d_{80}	 2723 µm	 78 µm	 402 µm
Sphericity Q_{50}	 0.503	 0.506	 0.403
Mean Sphericity	**0.532**	**0.536**	**0.543**
Symmetry Q_{50}	 0.862	 0.796	 0.804
Mean Symmetry	**0.836**	**0.771**	**0.758**
Aspect Ratio Q_{50}	 0.656	 0.657	 0.660
Mean Aspect Ratio	**0.645**	**0.651**	**0.650**
Circularity Q_{50}	 0.579	 0.628	 0.636
Mean Circularity	**0.710**	**0.605**	**0.617**

Figure 9.15: Pre-milled and Milled La Loma Coal Particle Size Distributions (top) and Particle Size (based on d_{c_min}) and Shape Images (bottom)

9.5. Particle Size-Shape Correlation

As the Stokes number is dependent on particle sphericity and its Reynolds number (section 2.11), it is possible for a large biomass particles to have similar aerodynamic properties to a much smaller coal particle provided they have sufficiently low sphericity for a similar density (Mandø et al., 2010). Thus an inverse relationship exists between the particle size and shape, which should be evident in the product from a mill. Figure 9.16 shows the relationship between particle shape and size for the four main mills tested in this study. No correlation was observed for the planetary ball mill. The cutting mill showed a linear relationship, with increasing particle size resulting in increasing sphericity, which doesn't fit with the classifier theory. As a screen was used in the cutting mill rather than an aerodynamic classifier, there is a risk that a screen is not producing the correct physical properties for optimal combustion.

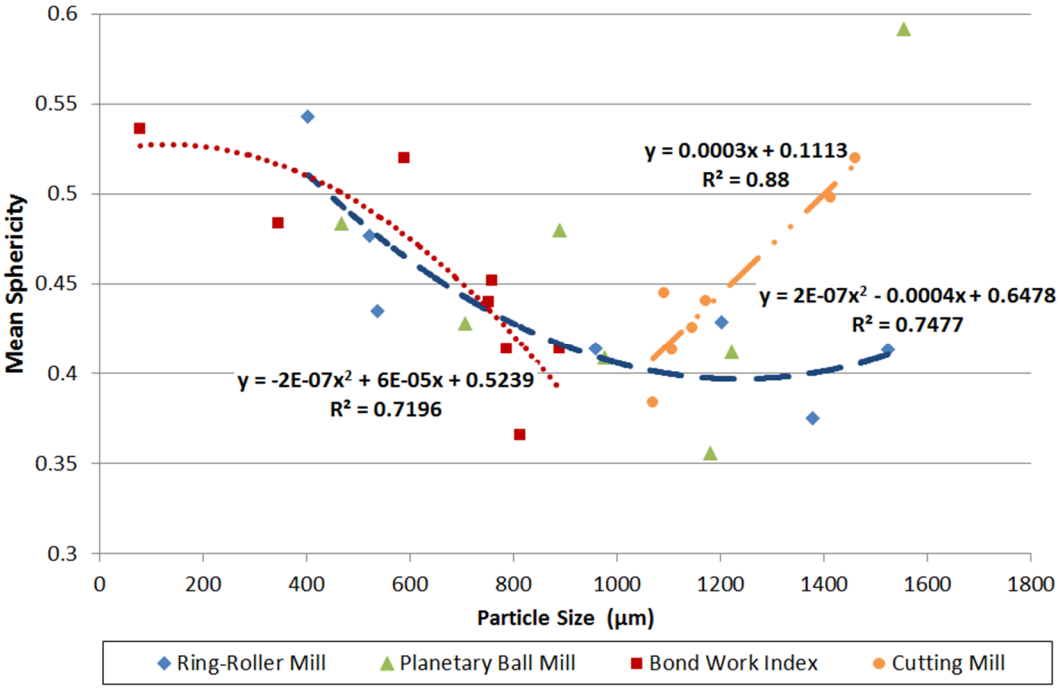


Figure 9.16: Mean Sphericity and Particle Size (d_{80}) for Different Biomasses and Coals Comminuted in Different Mills

Full scale hammer mills also used screens to classify the particles (Roskamp Champion, 2000) and a comparison of the product from a full scale mill is required to see if this trend also true for full scale mills. Studies have shown that a 4 mm screen on a full scale mill produces the correct particle sizes for biomass combustion (Esteban et al., 2006) and chapter 7 showed that a 4 mm screen will result in little change in the pre-densified particle size distribution. The implication of this is that if the cutting mill particle size-shape trend is present in full

scale hammer mills, it will be necessary for power generators to ensure the biomass pellets are composed of particles which are of the correct size, density and shape for optimal combustion, as hammer mills do not classify particles in accordance with the Stokes conditions. Both the BWI and ring-roller mills showed increasing sphericity with decreasing particle size, which fits the classifier theory. The ring-roller mill shows that when aerodynamic classification is used, the particle sizes obtained are much more varied for relatively similar sphericity. Given the wide spread in particle sphericity which can be seen in the particle shape outlines in figures 9.8-9.15, a blanket target size for comminution tests is not appropriate, and the particle shape and density need to be taken into account on a material by material basis. More data is required from lab, pilot and full scale mills with actual classification systems. While the ring-roller mill uses a dynamic classifier, other pilot mills in literature have static classifiers, such as the MBEL 0.34 E10 ring-ball mill (Livingston et al., 1998). By comparing and matching the output of these mills to the output from similar full scale mills, predictor models of material specific target sizes can be developed and validated, which will be invaluable in the optimisation and operation of full scale mills with classification.

9.6. Use of the Planetary Ball Mill for Critical Particle Size Determination

The planetary ball mill was the only mill which did not use a screen, sieve or classification system to control the product particle size. However the planetary ball mill provided similar particle size distributions to the BWI test. Thus there is potential for the planetary ball mill to be used as a preliminary stage of the BWI test to give a quick estimate of what the likely particle size distributions will be for a densified biomass. More importantly, the test gives an indication of whether or not the distribution will easily mill below the required target particle size. The biomasses which did not choke in the BWI and milled with relatively low energy consumptions all had finer particle size distributions in the planetary ball milling test than was obtained in the BWI test. For example, eucalyptus has a planetary ball mill d_{80} of 705 µm and BWI d_{80} of 751 µm, and microwave has a planetary ball mill d_{80} of 285 µm and BWI d_{80} of 888 µm. Mixed wood however choked in several of the mills. Its planetary ball mill d_{80} was 975 µm, but struggled to reduce to a BWI d_{80} of 787 µm. Sunflower pellets had a planetary ball mill d_{80} of 1220µm, but choked in the BWI when obtaining a much finer d_{80} of 787 µm. Miscanthus pellets which also choked in the BWI test, and had a planetary ball mill d_{80} of 1181 µm and BWI d_{80} of 813 µm. Steam exploded showed significantly higher energy consumption compared to the other thermally treated biomasses in the BWI test, and had a

planetary ball mill d_{80} of 466 µm and BWI d_{80} of 366 µm. This indicates that the critical particle size for comminution through compression (Kendall, 1978) is being reached in the planetary ball mill as the samples are reducing to this size without classification under high impact forces. If the d_{80} of a material milled in the planetary ball mill is close to or greater than the target particle size of the mill, then it is likely that the mill will choke or result in higher energy consumption. Further work is required to obtain the true critical particle size for a wide range of biomasses commonly used in the power generation section. This data is crucial in understanding the choking phenomena in mills and the practical limits of comminuting biomass in mills which use compression forces. The data is also crucial for milling simulations models, and can help to develop applicable models which will provide crucial optimisation and operation data for power generators or for researchers investigating the comminution of biomass in industry or academia.

9.7. Conclusions

The studies presented in this thesis have shown that mill choking can have a massive energy penalty on a fuel, which would result in a loss of potential power generation for a power generator. Biomass milling tests in literature are grindability tests and do not take into account the impact of particle density on shape on the correct size for classification. Thus current grindability tests can potentially give false information on the suitability of a material for comminution in mills with aerodynamic classification. Classification requirements should inform the target particle size of grindability tests rather than selecting a blanket target size for all materials.

Pellet durability has been shown to be related to mill energy consumption for a given target particle size for a given mill, and Von Rittinger's constant has been showed to be correlated to HGI data and the Rosin-Rammler characteristic particle size. By exploring these correlations further, guidance can be given on the likely grindability and energy consumption for a given target size in a given mill. The critical particle size for comminution through compression is key to understanding milling behaviour in different mills. By knowing a materials critical particle size and the target size of the specific biomass based on the classifier settings for a mill, it will be possible to tell:

i. Whether or not a biomass pellet will break down easily within the mill
ii. If the biomass particles which compose the pellet will need extra comminution to reach its required particle size for combustion

iii. If the biomass particles will struggle to reduce in size if comminution is required due to their critical particle size being larger than the target particle size for combustion

In terms of particle size and shape, milling had little impact on particle shape even when an order of magnitude difference was seen in the particle size. Thus particle shape is inherent to a pellet and is determined by the pre-densified comminution processes. Milling had little impact on herbaceous pellets compositional particles in terms of size or shape. Woody biomass saw more impact, but different behaviours were observed between soft and hard woods, with hard woods potentially being more amenable to milling in coal mills. Olive cake had the most spherical of all the materials and thermal pre-treatments of woody biomass not only sees a significant improvement in grindability in all mills, but also a significant improvement in shape factors.

Chapter 10 - Conclusions

10.1. Biomass Characterisation

Knowledge of the pre-milled particle size and shape can help inform the likely required particle size for classification and target particle sizes for grindability tests. A balance between high diametric and low flexure strength will allow for pellets to be durable during storage, but break up easily within a mill. With the increased use of biomass in pulverised fuel combustion systems and there being no standard tests for biomass abrasion, a new test is required to quantify the abrasiveness of biomass

10.2. Applicability of Standard Coal Grindability Tests for Biomass

HGI is a poor indicator of the grindability of biomass, and can give misleading results when analysed alone. Grindability tests which aim to analyse the grindability of biomass to 75 µm are inappropriate, and should be based on classifier requirements. The BWI can be used replicate mill choking and to analyse the choking potential of biomass pellets prior to full scale mill trials. To optimise milling in a coal mills, biomass pellets should be composed of particles close to the required size so that only the pellet comminution stage occurs.

10.3. Olive Caking

The olive caking phenomenon was replicated in a planetary ball mill, and it was shown for the first time that it is associated with the pulp section. The study proved that by removing the moisture from the olive cake that the caking phenomenon could be eliminated as the glass transition step did not occur. The industrial implication of this result is that olive cake fines below 1mm should be sieved out and sent directly to the burner and not comminuted. In addition, if caking issues occur in the conveying and comminution system for any biomass, heat flow analysis can be used to analyse its glass phase transition behaviour.

10.4. Mill Optimisation

The optimisation study of mill operating conditions in a planetary ball mill and cutting mill showed that the optimal conditions vary depending upon on the objective response from the mill. While minimising energy consumption is an important part of milling optimisation, maintaining a high level of mass throughput is essential for maintaining the thermal output of a pulverised fuel burner. The bagasse cutting mill study showed that the variability in moisture can have a greater impact on energy consumption than the operational settings.

Drying biomass pellets results in a significant reduction in energy for a similar particle size reduction.

10.5. Ring-Roller Mill

No previous studies exist for testing densified biomasses in laboratory scale ring-roller mills in literature. For biomass co-combustion with coal, mill classifiers should be set to the Stokes requirements. In addition, grindability tests should be set to the classifier requirements rather than just a blanket target size.

10.6. Overall Results

In summary, the studies detailed in this thesis have shown that mill choking can have a massive energy penalty on a fuel, which would result in a loss of potential power generation for a power generator. Biomass milling tests in literature are grindability tests and do not take into account the impact of particle density or shape on the correct size for classification. Thus current grindability tests can potentially give false information on the suitability of a material for comminution in mills with aerodynamic classification. Classification requirements should inform the target particle size of grindability tests rather than selecting a blanket target size for all materials.

The particle size distribution of the pellet plays a crucial role in determining how much milling is required to obtain the required particle size and shape. The critical particle size for comminution through compression is key to understanding milling behaviour in different mills. By knowing a materials critical particle size and the target size of the specific biomass based on the classifier settings for a mill, it will be possible to tell:

i. Whether or not a biomass pellet will break down easily within the mill
ii. If the biomass particles which compose the pellet will need extra comminution to reach its required particle size for combustion
iii. If the biomass particles will struggle to reduce in size if comminution is required due to their critical particle size being larger than the target particle size for combustion

Particle shape is inherent to biomass and coal particles and is determined by the pre-densified comminution processes.

10.7. Directions for Future Research

The results of this thesis have already led to a subsequent Engineering Doctorate with BF2RA which is developing numerical models of biomass comminution based on the results reported in this thesis. In addition, the samples used in this study will be used in an additional Engineering Doctorate with BF2RA which is investigating the use of biomass co-firing to improve the burn-out of unreactive coals. However there are several additional future avenues of future work with of high value to academia and industry.

One of the main areas of research in biomass comminution and conveying should be the development of a new standard test to quantify the abrasiveness of biomass in pneumatic conveying systems. In addition, a new standard HGI test is required for biomass which incorporates larger volumes and targets sizes based on classifier requirements. The future biomass grindability standard should be based around a similar methodology to the Bond Work Index Test, and include the following features:

- The test should establish the critical particle size for comminution of the biomass and use a target particle size based on that classifier requirements for that specific biomass
- The test mill should be scaled so that the ratio between and individual pellet and milling surfaces is in proportional to that of a full scale mill.
- The test should be volume based test
- The test will be based on one of the three theories of comminution (Von Rittinger, Kick or Bond), and relate specific energy consumption to particle size reduction
- An output in kWh/t so the results can be compared to other milling tests such as the BWI test

Further investigations are required into the relationship between pellet mechanical strength, comminution energy, and pellet durability. Milling tests are required to find the point of zero particle size reduction ratios for a given mill and pellet, which will give the comminution energy to reduce the particle down. Once this has been ascertained, the target particle size should be incrementally reduced to analyse how increasing particle size reduction ratio impacts mill energy consumption for different materials and mills, which can then be related to the particle comminution for that biomass.

Given that the shape factors of biomasses and coal are inherent properties which do no change significantly compared to particle size during milling, a model is required which can predict the required particle size for a classifier based on the physical characteristics of the

pre-milled particles. This would provide a material specific target particle size for standard grindability tests such as BWI and HGI.

The HGI-BWI correlation needs to be confirmed for more varieties of biomass pellets. The impact of changing equilibrium size on the BWI test needs to be analysed in order to ascertain if there is a drop off in the value once target size is greater than the critical particle size for comminution through compression. In order to do this, a major study into the critical particle size of comminution through compression for biomass is required which covers all types of biomasses, and these values should be compared to the particle size distributions of disintegrated pellets. In addition, the planetary ball mill results should be compared to the critical particle size to see if it can be used to give an indicative critical particle size for comminution.

Further research is required to see how the specific effective energy, mass loss and Rosin-Rammler distribution parameter relationships vary for different types of non-densified and densified biomasses in cutting mills, and if these relationships can be correlated to full scale hammer mills. This would allow for biomass milling behaviour models in hammer and cutting mills to be developed which would help power generators understand and optimise the milling behaviour of a new sample prior to full scale milling trials.

Due to time constraints, only limited testing was conducted on the ring-roller mill. The study has proved to be very successful and has provided several avenues of future work. These include:

- Optimisation study of mill settings for industry standard classifier settings, analysing the impact of feeder and mill bed speed, and separator blade angle, and use multiple non-linear regression analysis to optimise the. The results should be used to validate milling energy consumption and particle size prediction models
- Experiments to analyse how a non-treated biomass, a treated wood and a coal behave at the industry settings, which would provide insight into mill behaviour for 3 diverse materials (ductile, semi ductile and brittle)
- Energy consumption and particle size correlations should be conducted on the experimental and simulation results with data from a full scale Lopulco ring-roller mill at EDF West Burton and the pilot scale ring-ball mill at Doosan (Livingston et al., 1998)

References

Acharjee, T. C., Coronella, C. J., & Vasquez, V. R. (2011). Effect of thermal pretreatment on equilibrium moisture content of lignocellulosic biomass. *Bioresource Technology*, *102*(7), 4849–4854.

Adams, T. N., Raymond, D. R., & Schmid, C. (1988). Optimisation of a swirl burner for pulverised wood fuels. *Tappi Journal*, *71*(5).

Adapa, P., Tabil, L. G., & Schoenau, G. (2010). Physical and frictional properties of non-treated and steam exploded barley, canola oat and wheat straw grinds. *Powder Technology*, *201*(3), 230–241.

Adapa, P., Tabil, L. G., & Schoenau, G. (2011). Grinding performance and physical properties of non-treated and steam exploded barley, canola, oat and wheat straw. *Biomass and Bioenergy*, *35*(1), 549–561.

Afolabi, J. L. (2012). *The performance of a static coal classifier and its controlling parameters*. University of Leicester.

Aguilera, J. M., Valle, J. M., & Karel, M. (1995). Caking phenomena in amorphous food powders. *Trends in Food Science & Technology*, *6*(5), 149–155.

Agus, F., & Waters, P. L. (1971). Determination of the grindability of coals, shales and other minerals by a modified Hardgrove-machine method. *Fuel*, *50*(4), 405–431.

Ahmadi, R., & Shahsavari, S. (2009). Procedure for determination of ball Bond work index in the commercial operations. *Minerals Engineering*, *22*(1), 104–106.

Allen, T. (2003). *Powder Sampling and Particle Size Determination*. Elsevier.

ANSI/ASAE S319.4 FEB2008 (R2012). (2008). Method of Determining and Expressing Fineness of Feed Materials by Sieving. ASABE.

Argus Media Ltd. (2012). Fire halts biomass operations at Dong's Avedore plant. Retrieved from https://www.argusmedia.com/pages/NewsBody.aspx?id=810108&menu=yes

Arias, B., Pevida, C., Fermoso, J., Plaza, M. G., Rubiera, F., & Pis, J. J. (2008). Influence of torrefaction on the grindability and reactivity of woody biomass. *Fuel Processing Technology*, *89*(2), 169–175.

Ashby, M. F., & Jones, D. R. H. (1998). *Engineering materials 2: an introduction to their properties and applications.* (Second Ed.). Butterworth-Heinemann.

ASTM D2487-11. (2011). Standard Practice for Classification of Soils for Engineering Purposes (Unified Soil Classification System). ASTM.

ASTM D409 / D409M-12. (2012). Standard Test Method for Grindability of Coal by the Hardgrove-Machine Method. ASTM.

ASTM F1887-14. (2014). Standard Test Method for Measuring the Coefficient of Restitution (COR) of Baseballs and Softballs. ASTM.

Austin, L. G., Klimpel, R. R., & Luckie, P. T. (1984). *Process Engineering of Size Reduction: Ball Milling*. Society of Mining Engineers of the American Institute of Mining, Metallurgical and Petroleum Engineers.

Avolio, R., Bonadies, I., Capitani, D., Errico, M. E., Gentile, G., & Avella, M. (2012). A multitechnique approach to assess the effect of ball milling on cellulose. *Carbohydrate Polymers*, *87*(1), 265–273.

Axelsson, L., Franzén, M., Ostwald, M., Berndes, G., Lakshmi, G., & Ravindranath, N. H.

(2012). Perspective: Jatropha cultivation in southern India: Assessing farmers' experiences. *Biofuels, Bioproducts and Biorefining*, *6*(3), 246–256.

Barranco, R., Colechin, M., Cloke, M., Gibb, W. H., & Lester, E. (2006). The effects of pf grind quality on coal burnout in a 1 MW combustion test facility. *Fuel*, *85*(7), 1111–1116.

Basu, A. (2016). THERMAL COAL-Prices tumble as industrial demand weakens; oil prices weigh. Retrieved from http://www.hellenicshippingnews.com/thermal-coal-prices-tumble-as-industrial-demand-weakens-oil-prices-weigh/

BBC. (2012). Tilbury power station blazes as wood pellets catch fire. Retrieved from http://www.bbc.co.uk/news/uk-england-essex-17177035

BBC. (2014). Ironbridge Power Station fire tackled. Retrieved from http://www.bbc.co.uk/news/uk-england-shropshire-26029524

Bell, L. N., & Labuza, T. P. (2000). *Moisture Sorption: Practical Aspects of Isotherm Measurement and Use*. American Association of Cereal Chemists.

Bergander, A., & Salmen, L. (2002). Cell wall properties and their effects on the mechanical properties of fibers. *Journal of Materials Science*, *37*(1), 151–156.

Bico Braun International. (2007). Ball Mill Operating Manual.

Biswas, A. K., Umeki, K., Yang, W., & Blasiak, W. (2011). Change of pyrolysis characteristics and structure of woody biomass due to steam explosion pretreatment. *Fuel Processing Technology*, *92*(10), 1849–1854.

Biswas, A. K., Yang, W., & Blasiak, W. (2011). Steam pretreatment of Salix to upgrade biomass fuel for wood pellet production. *Fuel Processing Technology*, *92*(9), 1711–1717.

Bitra, V., Womac, A. R., Chevanan, N., Petre, I. M., Igathinathane, C., Sokhansanj, S., … Miu, P. I. (2009). Direct mechanical energy measures of hammer mill comminution of switchgrass, wheat straw, and corn stover and analysis of their particle size distributions. *Powder Technology*, *193*(1), 32–45.

Bitra, V., Womac, A. R., Chevanan, N., & Sokhansanj, S. (2008). Presentation Paper Number 083785: Comminution Properties of Biomass in Hammer Mill and its Particle Size Characterization. In *2008 Providence, Rhode Island, June 29–July 2, 2008*. American Society of Agricultural and Biological Engineers.

Bitra, V., Womac, A. R., Yang, Y. T., Igathinathane, C., Miu, P. I., Chevanan, N., & Sokhansanj, S. (2009). Knife mill operating factors effect on switchgrass particle size distributions. *Bioresource Technology*, *100*(21), 5176–5188.

Bitra, V., Womac, A. R., Yang, Y. T., Miu, P. I., Igathinathane, C., & Sokhansanj, S. (2009). Mathematical model parameters for describing the particle size spectra of knife-milled corn stover. *Biosystems Engineering*, *104*(3), 369–383.

Blair, R. G. (2014). Chapter 10: Mechanical and Combined Chemical and Mechanical Treatment of Biomass. In F. Zhen, R. L. Smith Jr., & Q. Xinhua (Eds.), *Biofuels and Biorefineries Volume 4 - Production of Biofuels and Chemicals with Ultrasound* (pp. 257–273). Springer Netherlands.

Bochat, A., Wesolowski, L., & Zastempowski, M. (2015). A Comparative Study of New and Traditional Designs of a Hammer Mill. *Transactions of ASABE*, *58*(3), 585–596.

Bodig, J., & Jayne, B. A. (1993). Failure. In *Mechanics of Wood and Wood Composites* (Reprint Ed, pp. 280–335). Melbourne, Florida: Krieger Publishing Company.

Bond, F. C. (1952). The Third Theory of Comminution. *Transactions AIME (Mining)*, *193*, 484–494.

Bond, F. C. (1961). Crushing and Grinding Calculations. Allis-Chalmers Manufacturiing Company.

Boonyai, P., Bhandari, B., & Howes, T. (2004). Stickiness measurement techniques for food powders: a review. *Powder Technology*, *145*(1), 34–46.

BP plc. (2014). BP Statistical Review of World Energy June 2014. London: BP.

Brezáni, I., & Zelenak, F. (2010). Improving the effectivity of work with Rosin-Rammler diagram by using MATLAB ® GUI tool. *Acta Montanistica Slovaca*, *15*(2), 152–157.

Bridgeman, T. G., Jones, J. M., Williams, A., & Waldron, D. J. (2010). An investigation of the grindability of two torrefied energy crops. *Fuel*, *89*(12), 3911–3918.

Brultech. (2015). Difference between True Power and Volt-Amp (VA). Retrieved from https://www.brultech.com/home/files/Difference Between Power and VA.pdf

Budhu, M. (2011). *Soil mechanics and foundations* (3rd ed.). John Wiley & Sons, Inc.

Burgio, N., Iasonna, A., Magini, M., Martelli, S., & Padella, F. (1991). Mechanical Alloying of the Fe-Zr System . Correlation between Input Energy and End Products . *Il Nuovo Cimento*, *13*(4), 459–476.

Burmeister, C. F., & Kwade, A. (2013). Process engineering with planetary ball mills. *Chemical Society Reviews*, *42*(18), 7660–7.

Butt, H. S. U., & Xue, P. (2014). Determination of the wave propagation coefficient of viscoelastic SHPB: Significance for characterization of cellular materials. *International Journal of Impact Engineering*, *74*, 83–91.

Carone, M. T., Pantaleo, A., & Pellerano, A. (2011). Influence of process parameters and biomass characteristics on the durability of pellets from the pruning residues of Olea europaea L. *Biomass and Bioenergy*, *35*(1), 402–410.

Chee, F. Y. (2015). EU approves UK state aid for RWE biomass-fired power plant. Retrieved from http://uk.reuters.com/article/uk-eu-energy-uk-biomass-idUKKBN0TK44P20151201

Chen, Q., Rao, A., & Samuelsen, S. (2014). H 2 coproduction in IGCC with CCS via coal and biomass mixture using advanced technologies. *Applied Energy*, *118*, 258–270.

Chen, S., & Danao, M. C. (2015). Modeling the equilibrium moisture content (EMC) of Miscanthus sinensis, miscane, energy cane, and energy sorghum. *Fuel*, *147*, 18–26.

Chen, W. W., & Song, B. (2010). *Split Hopkinson (Kolsky) Bar: Design, Testing and Applications* (Vol. 1). Springer Science & Business Media.

Chen, W., Zhang, B., & Forrestal, M. J. (1999). A split Hopkinson bar technique for low-impedance materials. *Experimental Mechanics*, *39*(2), 81–85.

Chevanan, N., Womac, A. R., Bitra, V., Igathinathane, C., Yang, Y. T., Petre, I. M., & Sokhansanj, S. (2010). Bulk Density and Compaction Behaviour of Knife Mill Chopped Switchgrass, Wheat Straw, and Corn Stover. *Bioresource Technology*, *101*(1), 207–214.

Chiaramonti, D., Rizzo, A. M., Prussi, M., Tedeschi, S., Zimbardi, F., Braccio, G., … Pardelli, P. T. (2011). 2nd generation lignocellulosic bioethanol: is torrefaction a possible approach to biomass pretreatment? *Biomass Conversion and Biorefinery*, *1*(1), 9–15.

Chiueh, P. Te, Lee, K. C., Syu, F. S., & Lo, S. L. (2012). Implications of biomass pretreatment to cost and carbon emissions: Case study of rice straw and Pennisetum in Taiwan. *Bioresource Technology*, *108*, 285–294.

Christiansen, E. B. P. E. S. (1948). Effect of particle shape on free-settling rates of isometric particles. *Chemical Engineering Progress*, *44*(2), 157–172.

ClickGreen. (2012). Huge explosion rips through Europe's first biomass power plant. Retrieved from http://www.clickgreen.org.uk/news/international-news/123720-huge-explosion-rips-through-europe%5Cs-first-biomass-power-plant.html

Climate Change Act. Chapter 27 (2008). United Kingdom.

Committee on Climate Change. (2011). The Renewable Energy Review. London: CCC.

Cremers, M. F. G. (2009). *IEA Bioenergy Task 32: Deliverable 4: Technical status of biomass co-firing*. Arnhem.

Csőke, B., Faitli, J., Mucsi, G., Antal, G., & Bartók, F. (2009). Comminution of forest biomass by modified beater wheel mill in a power plant. *12th European Symposium on Comminution and Classification. Finland*, *113*, 1–9.

Demirbas, A. (2004). Combustion characteristics of different biomass fuels. *Progress in Energy and Combustion Science*, *30*(2), 219–230.

Demirbas, A. (2005). Potential applications of renewable energy sources, biomass combustion problems in boiler power systems and combustion related environmental issues. *Progress in Energy and Combustion Science*, *31*(2), 171–192.

Deniz, V. (2004). Relationships between Bond's grindability (G bg) and breakage parameters of grinding kinetic on limestone. *Powder Technology*, *139*(3), 208–213.

Department of Energy & Climate Change. (2007). *Electricity Generating Plant Closures*. London.

Department of Energy & Climate Change. (2013). UK Renewable Energy Roadmap Update 2013. Retrieved from http://www.decc.gov.uk/en/content/cms/meeting_energy/renewable_ener/re_roadmap/re_roadmap.aspx

Department of Energy & Climate Change. (2015a). 2010 to 2015 government policy: UK energy security. Retrieved from https://www.gov.uk/government/publications/2010-to-2015-government-policy-uk-energy-security/2010-to-2015-government-policy-uk-energy-security

Department of Energy & Climate Change. (2015b). DUKES 2015 Chapter 6: Renewable Sources of Energy. Retrieved from https://www.gov.uk/government/statistics/renewable-sources-of-energy-chapter-6-digest-of-united-kingdom-energy-statistics-dukes.

Department of Energy & Climate Change. (2015c). Government response to consultation on changes to grandfathering policy with respect to future biomass co-firing and conversion projects in the Renewables Obligation. Retrieved from https://www.gov.uk/government/uploads/system/uploads/attachment_data/file/447327/Biomass_RO_Govt_Response.pdf.

Department of Energy & Climate Change. (2015d). Press release: Changes to renewables subsidies. Retrieved from https://www.gov.uk/government/news/changes-to-renewables-subsidies

Department of Energy & Climate Change. (2015e). Statutory Security of Supply Report. London: Retrieved from https://www.gov.uk/government/publications/statutory-security-of-supply-report-2015.

DIN 66 145. (1976). RRSB-Netz. DIN.

Dinwoodie, J. M. (2000). *Timber: Its Nature and Behaviour*. E & FN Spon; with the support of the Centre for Timber Technology and Construction at BRE.

Directorate-General for Energy. (1990). *Coal Breakage Characteristics in Various Forms of*

Comminution Equipment. Commission of the European Communities.

Disavino, S. (2016). Natural gas likely overtook coal as top U.S. power source in 2015. Retrieved from http://www.reuters.com/article/us-usa-natgas-coal-idUSKCN0UY2LT

EDF Energy plc. (1981a). Pulverised Fuel System - Cottam Coal Fired Power Station. Internal EDF Manual.

EDF Energy plc. (1981b). Pulverised Fuel System - West Burton Coal Fired Power Station. Internal EDF Manual.

Edwards, G. R., Evans, T. M., Robertson, S. D., & Summers, C. W. (1980). Assessment of the standard method of test for the grindability of coal by the Hardgrove machine. *Fuel*, *59*(12), 826–830.

Esteban, L. S., & Carrasco, J. E. (2006). Evaluation of different strategies for pulverization of forest biomasses. *Powder Technology*, *166*(3), 139–151.

European Commission. (2007). Commission Decision 2007/589/EC of 18 July 2007 establishing guidelines for the monitoring and reporting of greenhouse gas emissions pursuant to Directive 2003/87/EC of the European Parliament and the Council. Official Journal of the European Union.

European Parliament and Council. (2001). Directive 2001/80/EC of the European Parliament and of the Council of 23 October 2001 on the limitation of emissions of certain pollutants into the air from large combustion plants. Brussels, Belgium, European Union: Official Journal of the European Union.

European Parliament and Council. (2009). Directive 2009/29/EC of the European Parliament and of the council of 23 april 2009 ammending Directive 2003/87/EC so as to improve and extend the greenhouse gas emission allowance trading scheme of the Community. Official Journal of the European Union.

Evans, S. (2016). Levy Control Framework: The unanswered questions. Retrieved from http://www.carbonbrief.org/levy-control-framework-unanswered-questions

Fandrich, R. ., Clout, J. M. ., & Bourgeois, F. . (1998). The CSIRO Hopkinson Bar Facility for large diameter particle breakage. *Minerals Engineering*, *11*(9), 861–869.

Fasina, O. O. (2008). Physical properties of peanut hull pellets. *Bioresource Technology*, *99*(5), 1259–1266.

Fernandez, A. G., Fernandez Diaz, M. J., & Adams, M. R. (1997). Physical and chemical characteristics of olive fruit. In *Table Olives - Production and Processing* (pp. 67–102). Chapman & Hall.

Folk, R. L. (1974). *Petrology of the sedimentary rocks*. Hemphill Publishing Company.

Franke, M., & Rey, A. (2006). Pelleting quality. *World Grain*, *24*(5), 78–79.

Freeman, M. C., O'Dowd, W. J., Brown, T. D., Jr, R. A. H., James, R. A., Plasynski, S. I., … Battista Jr., J. J. (2000). Pilot-scale air toxics R&D assessment of creosote-treated and PCP-treated wood cofiring for pulverized coal utility boiler applications. *Biomass and Bioenergy*, *19*(6), 447–456.

Fuerstenau, M. C., & Han, K. N. (2003). Chapter 4: Size Separation. In *Principles of Mineral Processing* (pp. 119–172). Society for Mining, Metallurgy and Exploration, Inc. (SME).

Gabbott, P. (2008). *Principles and Applications of Thermal Analysis*. John Wiley & Sons.

Garcia, D. (2010). Robust smoothing of gridded data in one and higher dimensions with missing values. *Computational Statistics and Data Analysis*, *54*(4), 1167–1178.

Gent, M., Menendez, M., Toraño, J., & Torno, S. (2012). A correlation between Vickers Hardness indentation values and the Bond Work Index for the grinding of brittle minerals. *Powder Technology*, *224*, 217–222.

Gera, D., Mathur, M. P., Freeman, M. C., & Robinson, A. (2002). Effect of large aspect ratio of biomass particles on carbon burnout in a utility boiler. *Energy and Fuels*, *16*(6), 1523–1532.

Ghorbani, Z., Masoumi, a. a., & Hemmat, a. (2010). Specific energy consumption for reducing the size of alfalfa chops using a hammer mill. *Biosystems Engineering*, *105*(1), 34–40.

Gibson, J. (1979). Coal: An Introduction to its formation and Properties. In G. J. Pitt & G. R. Millward (Eds.), *Coal & Modern Coal Processing: An Introduction* (1st Ed., pp. 1–25). London: Academic Press.

Gil, M., & Arauzo, I. (2014). Hammer mill operating and biomass physical conditions effects on particle size distribution of solid pulverized biofuels. *Fuel Processing Technology*, *127*, 80–87.

Gil, M., Arauzo, I., & Teruel, E. (2013). Influence of Input Biomass Conditions and Operational Parameters on Comminution of Short-Rotation Forestry Poplar and Corn Stover Using Neural Networks. *Energy & Fuels*, *27*(5), 2649–2659.

Gil, M., Arauzo, I., Teruel, E., & Bartolomé, C. (2012). Milling and handling Cynara Cardunculus L. for use as solid biofuel: Experimental tests. *Biomass and Bioenergy*, *41*, 145–156.

Gil, M., Luciano, E., & Arauzo, I. (2015). Population balance model for biomass milling. *Powder Technology*, *276*, 34–44.

Gil, M., Oulego, P., Casal, M. D., Pevida, C., Pis, J. J., & Rubiera, F. (2010). Mechanical durability and combustion characteristics of pellets from biomass blends. *Bioresource Technology*, *101*(22), 8859–8867.

Gil, M., Teruel, E., & Arauzo, I. (2014). Analysis of standard sieving method for milled biomass through image processing. Effects of particle shape and size for poplar and corn stover. *Fuel*, *116*, 328–340.

Gilbert, P., Ryu, C., Sharifi, V. N., & Swithenbank, J. (2009). Effect of Process Parameters on Pelletisation of Herbaceous Crops. *Fuel*, *88*(8), 1491–1497.

Graham, S., Eastwick, C., & Snape, C. (2012). EFFECTS OF STORAGE METHODS ON THE PROPERTIES OF BIOMASS FUELS. In *20th European Biomass Conference and Exhibition* (pp. 1–3). Milan.

Gravelsins, R. J., & Trass, O. (2013). Analysis of grinding of pelletized wood waste with the Szego Mill. *Powder Technology*, *245*, 189–198.

Guo, Q., Chen, X., & Liu, H. (2012). Experimental research on shape and size distribution of biomass particle. *Fuel*, *94*, 551–555.

Himmel, H., Tucker, M., Baker, J., Rivard, C., Oh, K., & Grohmann, K. (1985). Comminution of Biomass: Hammer and Knife Mills. *Biotechnology & Bioengineering Symposium*, *15*, 39–58.

Hoque, M., Sokhansanj, S., Naimi, L., Bi, X., & Lim, J. (2007). Review and analysis of performance and productivity of size reduction equipment for fibrous materials. In *American Society of Agricultural and Biological Engineers Annual International Meeting Paper (No. 076164)*.

Ibrahim, R. H. H., Darvell, L. I., Jones, J. M., & Williams, A. (2013). Physicochemical characterisation of torrefied biomass. *Journal of Analytical and Applied Pyrolysis*, *103*, 21–30.

Ipek, H., Ucbas, Y., & Hosten, C. (2005). The bond work index of mixtures of ceramic raw materials. *Minerals Engineering*, *18*(9), 981–983.

Jankovic, A., Dundar, H., & Mehta, R. (2010). Relationships between comminution energy and product size for a magnetite ore. *The Journal of the South African Institute of Mining & Metallurgy*, *110*(3), 141–146.

Jeffries, T. W. (1993). Chapter 8 . Biodegradation of lignin and hemicelluloses. In C. Ratledge (Ed.), *Biochemistry of Microbial Degradation* (pp. 233–277). Netherlands: Kluwer Academic Publishers.

Jensen, P. D., Temmerman, M., & Westborg, S. (2011). Internal particle size distribution of biofuel pellets. *Fuel*, *90*(3), 980–986.

Jernkvist, L. O. (2001). Fracture of wood under mixed mode loading I . Derivation of fracture criteria. *Engineering Fracture Mechanics*, *68*(5), 549–563.

Jones, C. S., & Mayfield, S. P. (2012). Algae biofuels: versatility for the future of bioenergy. *Current Opinion in Biotechnology*, *23*(3), 346–351.

Jones, R. B., McCourt, C. B., Morley, C., & King, K. (1985). Maceral and rank influences on the morphology of coal char. *Fuel*, *64*(10), 1460–1467.

Kailis, S., & Harris, D. J. (2007). *Producing Table Olives* (first). Australia: Landlinks Press.

Kaliyan, N., & Vance Morey, R. (2009). Factors affecting strength and durability of densified biomass products. *Biomass and Bioenergy*, *33*(3), 337–359.

Kendall, K. (1978). The impossibility of comminuting small particles by compression. *Nature*, *272*(20), 710–711.

Kick, F. (1885). *Das Gesetz der proportionalen Widerstände und seine Anwendungen*. Leipzig: Arthur Felix.

Kingsly, a. R. P., & Ileleji, K. E. (2011). Glass transition behavior of corn distillers dried grains with solubles (DDGS). *Journal of Cereal Science*, *54*(3), 332–338.

Kirk, T. K., & Cullen, D. A. N. (1998). *Environmentally Friendly Technologies for the Pulp and Paper Industry- Chapter 9 - Enzymology and Molecular Genetics of Wood Degradation by White-Rot Fungi*. (R. A. Young & M. Akhtar, Eds.)*Young*. John Wiley & Sons, Inc.

Klimpel, R. R. (1987). Fine Coal Grinding. In B. K. Mishra & R. R. Klimpel (Eds.), *Fine Coal Processing* (pp. 19–58). Noyes Publications.

Kobayashi, J., Itaya, Y., Tsukada, S., Mizuno, K., Ueda, M., Morikawa, H., … Mori, S. (2007). Drying technology for woody biomass for fine grinding by vibration mills. *Asia-Pacific Journal of Chemical Engineering*, *2*(2), 83–89.

Kretschmann, D. E. (2010). Chapter 5 - Mechanical Properties of Wood. In *Wood Handbook - Wood as an engineering material* (pp. 1–46).

Krumbein, W. C., & Sloss, L. L. (1963). Properties of Sedimentary Rocks. In J. Gilluly & A. O. Woodford (Eds.), *Stratigraphy and Sedimentation* (2nd ed., pp. 106–113). W. H. Freeman and Company.

Lanigan, B. A. (2010). *Microwave processing of lignocellulosic biomass for production of fuels*. University of York.

Larsen, K. J. (2012). *Pulverised Biomass and Coal Co-Firing Simulation Using Computational Fluid Dynamics*. The University of Leeds.

Laskowski, J., & Lysiak, G. (1997). Relationships between resistance characteristics of barley kernels and energy consumption during grinding on hammer mill. *International Agrophysics*,

11, 265–272.

Laskowski, J., & Lysiak, G. (1999). Use of compression behaviour of legume seeds in view of impact grinding prediction. *Powder Technology*, *105*(1), 83–88.

Laskowski, J., Lysiak, G., & Melcion, J. P. (1998). Cereal grains' resistance analysis in the aspect of energy utilisation in the process of disintegration. *International Agrophysics*, *12*, 205–208.

Lester, E., Gong, M., & Thompson, A. (2007). A method for source apportionment in biomass/coal blends using thermogravimetric analysis. *Journal of Analytical and Applied Pyrolysis*, *80*(1), 111–117.

Lester, E., & Kingman, S. (2004). The effect of microwave pre-heating on five different coals. *Fuel*, *83*(14), 1941–1947.

Li, H., Chen, Q., Zhang, X., Finney, K. N., Sharifi, V. N., & Swithenbank, J. (2012). Evaluation of a Biomass Drying Process Using Waste Heat From Process Industries: a Case Study. *Applied Thermal Engineering*, *35*, 71–80.

Li, J., Zhang, X., Pawlak-Kruczek, H., Yang, W., Kruczek, P., & Blasiak, W. (2014). Process simulation of co-firing torrefied biomass in a 220MWe coal-fired power plant. *Energy Conversion and Management*, *84*, 503–511.

Livingston, W. R., Horne, P. A., McGhee, B. F., Gibson, J. R., & Chakraborty, R. K. (1998). The Characteristics of Coal Blends -Milling Behaviour & Ash Fusion Temperatures.

Lodge, T. (2015). Carbon tax was misjudged and made coal uneconomic. Retrieved from http://www.telegraph.co.uk/finance/newsbysector/energy/11631729/Carbon-tax-was-misjudged-and-made-coal-uneconomic.html

Loo, V., & Koppejan, S. J. (2008). Chapter 7 - Co-combustion. In *The handbook of biomass combustion and co-firing* (pp. 203–248).

Luque, R., Menéndez, J. A., Arenillas, A., & Cot, J. (2012). Microwave-assisted pyrolysis of biomass feedstocks: the way forward? *Energy & Environmental Science*, *5*(2), 5481.

Mafakheri, F., & Nasiri, F. (2014). Modeling of biomass-to-energy supply chain operations: Applications, challenges and research directions. *Energy Policy*, *67*, 116–126.

Man, Y. T. (2002). Why is the Bond Ball Mill Grindability Test done the way it is done? *The European Journal of Mineral Processing and Environmental Protection*, *2*(1), 34–39.

Mandø, M., Rosendahl, L., Yin, C., & Sørensen, H. (2010). Pulverized straw combustion in a low-NOx multifuel burner: Modeling the transition from coal to straw. *Fuel*, *89*(10), 3051–3062.

Mani, S., Sokhansanj, S., Bi, X., & Turhollow, A. (2006). Economics of producing fuel pellets from biomass. *Applied Engineering in Agriculture*, *22*(3), 421–426.

Mani, S., Tabil, L. G., & Sokhansanj, S. (2003). An overview of compaction of biomass grinds. *Powder Handling & Processing*, *15*(3), 160–168.

Mani, S., Tabil, L. G., & Sokhansanj, S. (2004). Grinding Performance and Physical Properties of Wheat and Barley Straws, Corn Stover, and Switchgrass. *Biomass and Bioenergy*, *27*(4), 339–352.

Mani, S., Tabil, L. G., & Sokhansanj, S. (2006). Specific energy requirement for compacting corn stover. *Bioresource Technology*, *97*(12), 1420–1426.

Mathews, J. P., Hatcher, P. G., & Scaroni, A. W. (1997). Particle size dependence of coal volatile matter: is there a non-maceral-related effect? *Fuel*, *76*(4), 359–362.

McIntyre, A., & Plitt, L. R. (1980). The interrelationship between Bond and Hardgrove grindabilities. *CIM BULLETIN*, *73*(818), 149–155.

Mcken, A., & Williams, S. (2005). An Overview of the Small-scale Tests Available to Characterize Ore Grindability for Design Purposes. *SGS Minerals Technical Bulleting*, *2005*(06), 8.

McKendry, P. (2002). Energy production from biomass (Part 1): Overview of biomass. *Bioresource Technology*, *83*(1), 37–46.

Miao, Z., Grift, T. E., Hansen, a. C., & Ting, K. C. (2011). Energy requirement for comminution of biomass in relation to particle physical properties. *Industrial Crops and Products*, *33*(2), 504–513.

Minitab Inc. (2013). Minitab Assistant White Paper - Multiple Regression. *Minitab 17 Lecture Notes*.

Mohan, D., Pittman, C. U., & Steele, P. H. (2006). Pyrolysis of wood/biomass for bio-oil: a critical review. *Energy & Fuels*, *20*(3), 848–889.

Mroczek, K. (2009). Analysis of Coal Mill Operation at Co-milling of Wood Biomass. *Chemical and Process Engineering*, *30*(1), 83–98.

Mujumdar, A. S., Jangam, S. V., & Pikon, J. (2014). 51.3.8 Mill-Type Dryers. In A. S. Mujumdar (Ed.), *Handbook of Industrial Drying* (pp. 1011–1012). CRC Press.

Murray, G. (2010). *Lillooet Biomass Energy Corporation Business Plan for a Wood Pellet Plant*.

Neslen, A. (2015). Carbon floor price hike will trigger UK coal slowdown, say analysts. Retrieved from http://www.theguardian.com/environment/2015/apr/02/carbon-floor-price-hike-will-trigger-uk-coal-slowdown-say-analysts

Nikolopoulos, N., Violidakis, I., Karampinis, E., Agraniotis, M., Bergins, C., Grammelis, P., & Kakaras, E. (2015). Report on comparison among current industrial scale lignite drying technologies (A critical review of current technologies). *Fuel*, *155*, 86–114.

Obernberger, I., & Thek, G. (2004). Physical characterisation and chemical composition of densified biomass fuels with regard to their combustion behaviour. *Biomass and Bioenergy*, *27*(6), 653–669.

Obernberger, I., & Thek, G. (2010a). Pellet Production and Logistics. In *The Pellet Handbook* (First, pp. 85–129). Earthscan Ltd.

Obernberger, I., & Thek, G. (2010b). Wood Pellet Combustion Technologies. In I. Obernberger & G. Thek (Eds.), *The Pellet Handbook* (pp. 229–231). Earthscan Ltd.

Ofgem. (2015). Climate Change Levy (CCL) exemption. Retrieved from https://www.ofgem.gov.uk/environmental-programmes/climate-change-levy-ccl-exemption

Ohliger, A., Förster, M., & Kneer, R. (2013). Torrefaction of beechwood: A parametric study including heat of reaction and grindability. *Fuel*, *104*, 607–613.

ÖNORM, M. (2000). 7135: Compressed Wood or Compressed Bark in Natural State, Pellets and Briquettes, Requirements and Test Specifications. Österreichisches Normungsinstitut, Vienna, Austria.

Palamidi, E. (2010). *Hopkinson Bar testing of cellular Materials*. University of Manchester.

Palzer, S. (2011). Agglomeration of pharmaceutical, detergent, chemical and food powders — Similarities and differences of materials and processes. *Powder Technology*, *206*(1-2), 2–17.

Pang, C. H. (2012). *The Characterisation of Biomass and Biomass/Coal Blends*. University of Nottingham.

Paolotti, L., Martino, G., Marchini, A., Pascolini, R., & Boggia, A. (2015). Economic and environmental evaluation of transporting imported pellet: A case study. *Biomass and Bioenergy*, *83*, 340–353.

Park, S. H., Chung, S. W., Lee, S. K., Choi, H. K., & Lee, S. H. (2015). Thermo-economic evaluation of 300 MW class integrated gasification combined cycle with ash free coal (AFC) process. *Applied Thermal Engineering*, *89*, 843–852.

Paulrud, S., Mattsson, J. E., & Nilsson, C. (2002). Particle and handling characteristics of wood fuel powder: Effects of different mills. *Fuel Processing Technology*, *76*(1), 23–39.

Pérez, J., Muñoz-Dorado, J., de la Rubia, T., & Martínez, J. (2002). Biodegradation and biological treatments of cellulose, hemicellulose and lignin: an overview. *International Microbiology*, *5*(2), 53–63.

Perinović, S., Andričić, B., & Erceg, M. (2010). Thermal properties of poly (l-lactide)/olive stone flour composites. *Thermochimica Acta*, *510*(1), 97–102.

Perry, R. H., & Green, D. W. (2008). Section 21: Solid-Solid Operations and Processing. In *Perry Chemical Engineers' Handbook* (8th Editio, pp. 21:47–21:49). McGraw-Hill.

Peterson, S. C., Jackson, M. a., Kim, S., & Palmquist, D. E. (2012). Increasing biochar surface area: Optimization of ball milling parameters. *Powder Technology*, *228*, 115–120.

Phanphanich, M., & Mani, S. (2011). Impact of torrefaction on the grindability and fuel characteristics of forest biomass. *Bioresource Technology*, *102*(2), 1246–1253.

Pierre, F., Almeida, G., Huber, F., Jacquin, P., & Perré, P. (2013). An original impact device for biomass characterisation: Results obtained for spruce and poplar at different moisture contents. *Wood Science and Technology*, *47*(3), 537–555.

Prins, M. J., Ptasinski, K. J., & Janssen, F. J. J. G. (2006). Torrefaction of wood. I. Weight loss kinetics. *Journal of Analytical and Applied Pyrolysis*, *77*(1), 28–34.

Rabier, F., Temmerman, M., Böhm, T., Hartmann, H., Daugbjerg Jensen, P., Rathbauer, J., … Fernández, M. (2006). Particle density determination of pellets and briquettes. *Biomass and Bioenergy*, *30*(11), 954–963.

Ramesh, K. T. (2008). Part D 33. High Strain Rate and Impact Experiments. In W. N. Sharpe, Jr. (Ed.), *Springer Handbook of Experimental Solid Mechanics* (pp. 1–31). Springer.

Repellin, V., Govin, A., Rolland, M., & Guyonnet, R. (2010). Energy requirement for fine grinding of torrefied wood. *Biomass and Bioenergy*, *34*(7), 923–930.

Retsch Gmbh. (2009). CAMSIZER® Characteristics. Retrieved from http://www.horiba.com/fileadmin/uploads/Scientific/Documents/PSA/Manuals/CAMSIZER_Characteristics_Nov2009.pdf.

Retsch Gmbh. (2012). Operating Instructions Ball Mills. Retrieved from http://www.retsch.com/products/miling/ball-mills/planetary-ball-mill-pm-100/information-downloads/.

Retsch Gmbh. (2015). Installation & Operation Manual - PARTICLE LIBRARY: WIZARD MODE. Hann, Germany: Retsch Gmbh.

Rimmer, S. M., Yoksoulian, L. E., & Hower, J. C. (2009). Anatomy of an intruded coal, I: Effect of contact metamorphism on whole-coal geochemistry, Springfield (No. 5) (Pennsylvanian) coal, Illinois Basin. *International Journal of Coal Geology*, *79*(3), 74–82.

Robinson, J., Kingman, S., Baranco, R., Snape, C. E., & Al-Sayegh, H. (2010). Microwave

pyrolysis of wood pellets. *Industrial and Engineering Chemistry Research*, *49*(2), 459–463.

Roos, Y. H., & Karel, M. (1991). Plasticizing Effect of Water on Thermal Behavior and Crystallization of Amorphous Food Models. *Journal of Food Science*, *56*(1), 38–43.

Rosin, P., & Rammler, E. (1933). The Laws Governing the Fineness of Powdered Coal. *The Institute of Fuel*, *7*(31), 29–36.

Roskamp Champion. (2000). Advantages and Disadvantages of Particle Size Reduction Techniques. Waterloo, IA, USA: Roskamp Champion.

Rotawave Ltd. (2010). *THE CASE FOR ENERGY DENSIFICATION OF BIOMASS & THE ADVANTAGE OF THE ROTAWAVE TIES SYSTEM - Executive Summary*.

Rubiera, F., Arenillas, A., Fuente, E., Miles, N. J., & Pis, J. J. (1999). Effect of the grinding behaviour of coal blends on coal utilisation for combustion. *Powder Technology*, *105*(1), 351–356.

Ryckmans, Y., Allard, P., Liegeois, B., & Mewissen, D. (2006). Conversion of a pulverized coal power plant to 100% wood pellets in Belgium. In *Proceedings of the 2nd Conference on pellets, 30 May-1 June 2006, Jönköping, Sweden* (pp. 59–61). Jönköping, Sweden, Sweden.

Samuelsson, R., Thyrel, M., Sjöström, M., & Lestander, T. a. (2009). Effect of biomaterial characteristics on pelletizing properties and biofuel pellet quality. *Fuel Processing Technology*, *90*(9), 1129–1134.

Satpathy, S. K., Tabil, L. G., Meda, V., Naik, S. N., & Prasad, R. (2014). Torrefaction of wheat and barley straw after microwave heating. *Fuel*, *124*, 269–278.

Scott, D. H. (1995). *Coal Pulverisers - Performance and Safety*. *Fuel and Energy Abstracts* (Vol. 36). London: IEA Coal Research.

Sengupta, A. N. (2002). An assessment of grindability index of coal. *Fuel Processing Technology*, *76*(1), 1–10.

Shang, L., Ahrenfeldt, J., Holm, J. K., Sanadi, A. R., Barsberg, S., Thomsen, T., … Henriksen, U. B. (2012). Changes of chemical and mechanical behavior of torrefied wheat straw. *Biomass and Bioenergy*, *40*, 63–70.

Sierra, R., Smith, A., Granda, C., & Holtzapple, M. T. (2008). Producing Fuels and Chemicals from Lignocellulosic Biomass. *Chemical Engineering Progress*, *104*(8), S10–S14.

Sjostrom, E. (1993). *Wood Chemistry - Fundamentals and Applications*. *Cellulose* (Second). London: Academic Press Limited.

Song, B., & Chen, W. (2004). Dynamic Stress Equilibration in Split Hopkinson Pressure Bar Tests on Soft Materials. *Experimental Mechanics*, *44*(3), 300–312.

Stelte, W., Holm, J. K., Sanadi, A. R., Barsberg, S., Ahrenfeldt, J., & Henriksen, U. B. (2011). A study of bonding and failure mechanisms in fuel pellets from different biomass resources. *Biomass and Bioenergy*, *35*(2), 910–918.

Sun, Y., & Cheng, J. (2002). Hydrolysis of lignocellulosic materials for ethanol production: a review. *Bioresource Technology*, *83*(1), 1–11.

Sütçü, V. D. N., & Umucu, Y. (2003). The Effect of Circulating Load and Test Sieve Size on The Bond Work Index Based on Natural Amorphous Silica. In *18th International Mining Congress and Exhibition of Turkey-IMCET 2003* (pp. 517–522).

Swaan, J. (2012). Torrefaction Technology Session - Horizon BioEnergy Overview. In *5th International BioEnergy Conference and Exhibition* (p. 12). Prince George, British Columbia.

Tamura, M., & Van de Kamp, W. (2001). Characteristics of alternative fuel for blend with

pulverised coal. In *6th conference on energy for a clean environment* (pp. 585–89). Lisbon.

Tamura, M., Watanabe, S., Kotake, N., & Hasegawa, M. (2014). Grinding and combustion characteristics of woody biomass for co-firing with coal in pulverised coal boilers. *Fuel*, *134*, 544–553.

Temmerman, M., Jensen, P. D., & Hébert, J. (2013). Von Rittinger theory adapted to wood chip and pellet milling, in a laboratory scale hammermill. *Biomass and Bioenergy*, *56*, 70–81.

Temmerman, M., Rabier, F., Jensen, P. D., Hartmann, H., & Bohm, T. (2006). Comparative Study of Durability Test Methods for Pellets and Briquettes. *Biomass and Bioenergy*, *30*(11), 964–972.

The British Standards Institution. (1995). BS 1016-112: 1995 Methods for Analysis and testing of coal and coke — Part 112: Determination of Hardgrove grindability index of hard coal. BSI.

The British Standards Institution. (1998a). BS 1016-111:1998, ISO 12900:1998 - Methods for analysis and testing of coal and coke - Part 111: Determination of abrasion index of coal. BSI.

The British Standards Institution. (1998b). BS ISO 9276-1:1998 -- Representation of results of particle size analysis - Part 1: Graphical Representation. BSI.

The British Standards Institution. (2008). BS ISO 9276-6:2008 - Representation of results of particle size analysis. Descriptive and quantitative representation of particle shape and morphology. BSI.

The British Standards Institution. (2009a). BS EN 14774-1:2009 - Solid biofuels. Determination of moisture content. Oven dry method. Total moisture. Reference method. BSI.

The British Standards Institution. (2009b). BS ISO 1928:2009 Solid mineral fuels — Determination of gross calorific value by the bomb calorimetric method and calculation of net calorific value. BSI.

The British Standards Institution. (2010a). BS EN 14961-1:2010 Solid biofuels — Fuel specifications and classes - Part 1: General requirements. *Management*. United Kingdom: BSI.

The British Standards Institution. (2010b). BS EN 15149-2:2010: Solid biofuels. Determination of particle size distribution. Vibrating screen method using sieve apertures of 3,15 mm and below. BSI.

The British Standards Institution. (2010c). DD CEN/TS 15405:2010 - Solid recovered fuels - Determination of Density of Pellets and Briquettes. BSI.

The British Standards Institution. (2012). BS EN 16126:2012 — Solid biofuels. Determination of particle size distribution of disintegrated pellets. BSI.

The British Standards Institution. (2013a). BS EN ISO 16888-2:2004+A1:2013 Geotechnical investigation and testing — Identification and classification of soil — Part 2: Principles for a classification. BSI.

The British Standards Institution. (2013b). BS EN ISO 17831-1 - Solid biofuels — Determination of mechanical durability of pellets and briquettes — Part 1: Pellets. BSI.

The British Standards Institution. (2013c). BS ISO 3310-2:2013 Test sieves — Technical requirements and testing Part 2 : Test sieves of perforated metal plate. BSI.

The British Standards Institution. (2014a). BS EN ISO 16559:2014 Solid recovered fuels — Terminology , definitions and descriptions. BSI.

The British Standards Institution. (2014b). BS EN ISO 17225-1:2014 Solid biofuels. Fuel

specifications and classes. General requirements. BSI.

The British Standards Institution. (2014c). BS EN ISO 17225-2:2014 - Solid biofuels — Fuel specifications and classes Part 2 : Graded wood pellets. BSI.

The British Standards Institution. (2014d). BS EN ISO 17225-6:2014 - Solid biofuels — Fuel specifications and classes Part 6 : Graded non-woody pellets. BSI.

The British Standards Institution. (2014e). BS ISO 9276-2:2014 Representation of results of particle size analysis Part 2 : Calculation of average particle sizes / diameters and moments from particle size. BSI.

The British Standards Institution. (2014f). Draft BS EN ISO 17829 Solid Biofuels - Determination of length and diameter of pellets. BSI.

The British Standards Institution. (2015a). BS EN ISO 16948:2015 - Solid Biofuels - Determination of total content of sulfur and chlorine. BSI.

The British Standards Institution. (2015b). BS EN ISO 16993:2015 - Solid biofuels — Conversion of analytical results from one basis to another. BSI.

The British Standards Institution. (2015c). Draft BS ENISO 17830 Solid Biofuels - Determination of particle size distribution of material within pellets. BSI.

The MathWorks Inc. (2015). pchip.

Theerarattananoon, K., Xu, F., Wilson, J., Ballard, R., Mckinney, L., Staggenborg, S., … Wang, D. (2011). Physical properties of pellets made from sorghum stalk, corn stover, wheat straw, and big bluestem. *Industrial Crops and Products*, *33*(2), 325–332.

Tlotleng, M. T. (2011). *Coal characteristics that lead to abrasion during grinding*. University of the Witwatersrand.

Toneva, P., Wirth, K. E., & Peukert, W. (2011). Grinding in an air classifier mill - Part II: Characterisation of the two-phase flow. *Powder Technology*, *211*(1), 28–37.

Trubetskaya, A., Beckmann, G., Jensen, P. A., Jensen, A. D., & Glarborg, P. (2014). A way of a single biomass particle shape characterization in a CFD model. In *22nd European Biomass Conference and Exhibition* (p. 9).

Tsami, E., Marinos-Kouris, D., & Maroulis, Z. B. (1990). Water Sorption Isotherms of Raisins, Currants, Figs, Prunes and Apricots. *Journal of Food Science*, *55*(6), 1594–1597.

Tumuluru, J. S., Sokhansanj, S., Hess, J. R., Wright, C. T., & Boardman, R. D. (2011). REVIEW: A review on biomass torrefaction process and product properties for energy applications. *Industrial Biotechnology*, *7*(5), 384–401.

Tumuluru, J. S., Tabil, L. G., Song, Y., Iroba, K. L., & Meda, V. (2014). Grinding energy and physical properties of chopped and hammer-milled barley, wheat, oat, and canola straws. *Biomass and Bioenergy*, *60*, 58–67.

Turner, R. (1995). Bottomline in feed processing: achieving optimum pellet quality. *Feed Management*, *46*, 30–33.

Unsworth, J. F., Barratt, D. J., & Roberts, P. T. (1991). Coal Quality and Combustion Performance - An International Performance. *Coal Science and Technology*, *19*, 1–609.

US EIA. (2013). *International Energy Outlook 2013 - DOE/EIA-0484(2013)*. *Outlook 2013*. Washington, D.C.

Uslu, A., Faaij, A., & Bergman, P. C. A. (2008). Pre-treatment technologies, and their effect on international bioenergy supply chain logistics. Techno-economic evaluation of torrefaction, fast pyrolysis and pelletisation. *Energy*, *33*(8), 1206–1223.

Van Der Lans, R. P., Glarborg, P., Dam-Johansen, K., Knudsen, P., Hesselmann, G., & Peter, H. (1998). Influence of coal quality on combustion performance. *Fuel*, *77*(12), 1317–1328.

van der Put, T. a. C. M. (2007). A new fracture mechanics theory for orthotropic materials like wood. *Engineering Fracture Mechanics*, *74*(5), 771–781.

Van Essendelft, D. T., Zhou, X., & Kang, B. S.-J. (2013). Grindability Determination of Torrefied Biomass Materials using the Hybrid Work Index. *Fuel*, *105*, 103–111.

Vassilev, S. V., Baxter, D., Andersen, L. K., Vassileva, C. G., & Morgan, T. J. (2012). An overview of the organic and inorganic phase composition of biomass. *Fuel*, *94*, 1–33.

Vassilev, S. V., Vassileva, C. G., & Vassilev, V. S. (2015). Advantages and disadvantages of composition and properties of biomass in comparison with coal: An overview. *Fuel*, *158*, 330–350.

Venkataraman, K. S., & Narayanan, K. S. (1998). Energetics of collision between grinding media in ball mills and mechanochemical effects. *Powder Technology*, *96*(3), 190–201.

von Rittinger, P. R. (1867). *Lehrbuch der Aufbereitungskunde*. Berlin: Ernst and Korn.

Wadell, H. (1932). Volume, Shape, and Roundness of Rock Particles. *The Journal of Geology*, *40*(5), 443–451.

Wadell, H. (1934). The Coefficient of resistance as a function of Reynolds number for solids of various shapes. *Journal of the Franklin Institute*, *217*(4), 459–490.

Wadell, H. (1935). Volume, Shape and Roundness of Quartz Particles. *The Journal of Geology*, *43*(3), 250–280.

Walker, W. H., Lewis, W. K., McAdams, W. H., & Gilliland, E. R. (1937). *Principles of Chemical Engineering*. McGraw-Hill.

Ward, C. R., & Burdon, R. G. (1987). Process Development and Selection for Fine Coal Treatment. In S. K. Mishra & R. R. Klimpel (Eds.), *Fine Coal Processing* (pp. 59–77). Noyes Publications.

Warren Spring Laboratory. (1962). Grindability test procedure and ball-mill size selection (Mineral processing information notes No.3). Warren Spring Laboratory.

Wells, J. J., Wigley, F., Foster, D. J., Gibb, W. H., & Williamson, J. C. (2004). The relationship between excluded mineral matter and the abrasion index of a coal. *Fuel*, *83*(3), 359–364.

Williams, D. (2012). Vattenfall's CHP plant in Copenhagen suffers fire damage. Retrieved from http://www.cospp.com/articles/2012/12/vattenfalls-chp-plant-in-copenhagen-suffers-fire-damage.html

Williams, O., Eastwick, C., Kingman, S., Giddings, D., Lormor, S., & Lester, E. (2015). Investigation into the applicability of Bond Work Index (BWI) and Hardgrove Grindability Index (HGI) tests for several biomasses compared to Colombian La Loma coal. *Fuel*, *158*, 379–387.

Xie, H. Y., & Zhang, D. W. (2001). Stokes shape factor and its application in the measurement of sphericity of non-spherical particles. *Powder Technology*, *114*(1), 102–105.

Yin, C., Rosendahl, L., Kær, S. K., & Condra, T. J. (2004). Use of numerical modeling in design for co-firing biomass in wall-fired burners. *Chemical Engineering Science*, *59*(16), 3281–3292.

Yu, D., Xu, M., Sui, J., Liu, X., Yu, Y., & Cao, Q. (2005). Effect of coal particle size on the proximate composition and combustion properties. *Thermochimica Acta*, *439*(1), 103–109.

Zavala, J. M. R. (2012). *Particle Shape Quantities and Measurement Techniques – A Review*.

Zhang, M., Song, X., Deines, T. W., Pei, Z. J., & Wang, D. (2012). Biofuel manufacturing from

woody biomass: Effects of sieve size used in biomass size reduction. *Journal of Biomedicine and Biotechnology*.

Zhu, Q. (2012). *Update on lignite firing*. IEA Clean Coal Centre.

Zilkha Biomass Energy. (2011). *Zilkha Black TM Pellet Safety Information and Test Reports*.

Zulfiquar, M. H., Wall, T. F., & Moghtaderi, B. (2006). *Co-Milling of Coal and Biomass in a Pilot-Scale Vertical Spindle Mill*. *QCAT Technology Transfer Centre*.

Zuo, W., Zhao, Y., He, Y., Shi, F., & Duan, C. (2012). Relationship between coal size reduction and energy input in Hardgrove mill. *International Journal of Mining Science and Technology*, *22*(1), 121–124.

Appendix A – Quasi-Static Mechanical Response Data

Table A.1 – Table of Mean Quasi-Static Compressive Stress for Biomass Pellets

Sample	Mean Axial Raw (MPa)	Mean Axial Dry (MPa)	Mean Diametric Raw (MPa)	Mean Diametric Dry (MPa)	Mean Flexure Raw (MPa)	Mean Flexure Dry (MPa)
White wood Pellets	11.7	10.6	18.7	21.5	4.9	4.3
Eucalyptus Pellets	4.5	6.6	10.5	11.2	2.2	2.6
Mixed Wood Pellets	11.1	4.6	11.8	9.7	3.0	1.6
Miscanthus Pellets	6.8	8.1	8.2	14.7	3.0	2.7
Sunflower Pellets	7.1	5.9	6.5	6.7	2.8	3.1
Olive Pellets	4.1	9.5	4.8	9.8	4.7	7.2
Torrefied Pellets	12.1	-	5.1	-	1.4	-
Steam exploded Pellets	18.3	16.4	18.4	15.5	16.4	17.1
Microwave Pellets	4.4	4.3	8.1	5.2	3.4	4.4

Table A.2 – Table of Mean Quasi-Static Compressive Young's Modulus for Biomass Pellets

Sample	Mean Axial Raw (MPa)	Mean Axial Dry (MPa)	Mean Diametric Raw (MPa)	Mean Diametric Dry (MPa)	Mean Flexure Raw (MPa)	Mean Flexure Dry (MPa)
White wood Pellets	264	192	753	720	70	72
Eucalyptus Pellets	88	116	347	278	14	15
Mixed Wood Pellets	193	74	273	191	22	16
Miscanthus Pellets	87	144	367	877	30	47
Sunflower Pellets	75	63	197	181	19	37
Olive Pellets	-	406	-	985	14	37
Torrefied Pellets	159	-	229	-	26	-
Steam exploded Pellets	871	874	2049	1741	295	333
Microwave Pellets	140	149	258	208	47	69

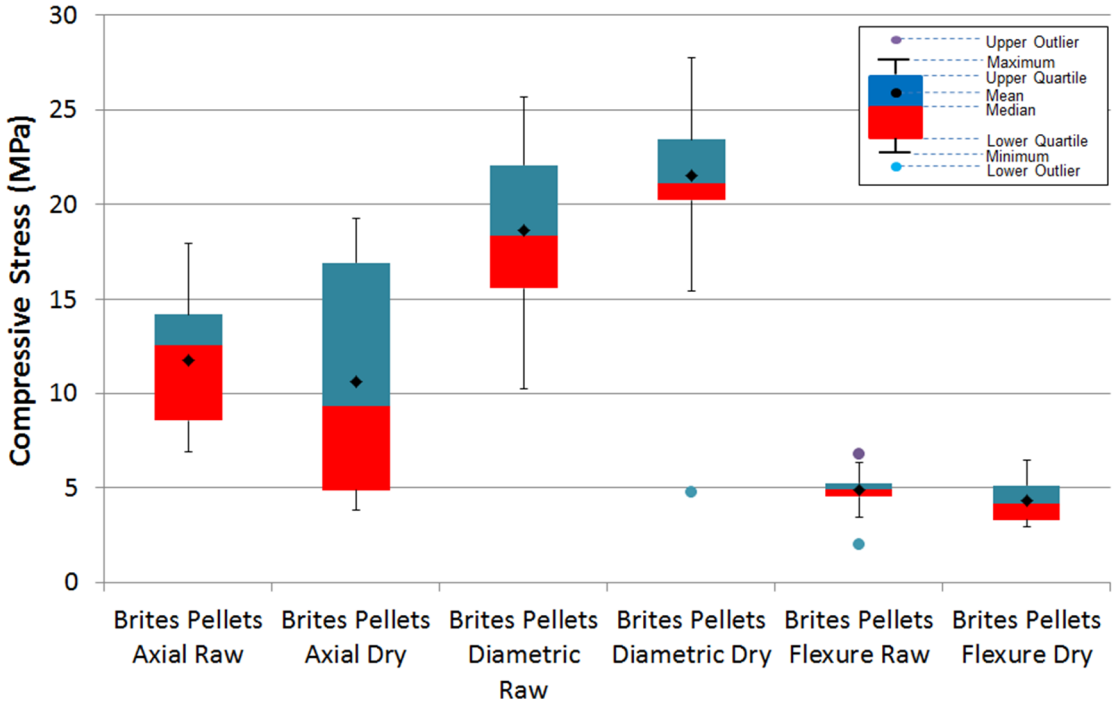


Figure A.1 – Quasi-Static Compressive Stress for Raw and Dry White wood Pellets in Axial, Diametric and Flexure Orientations

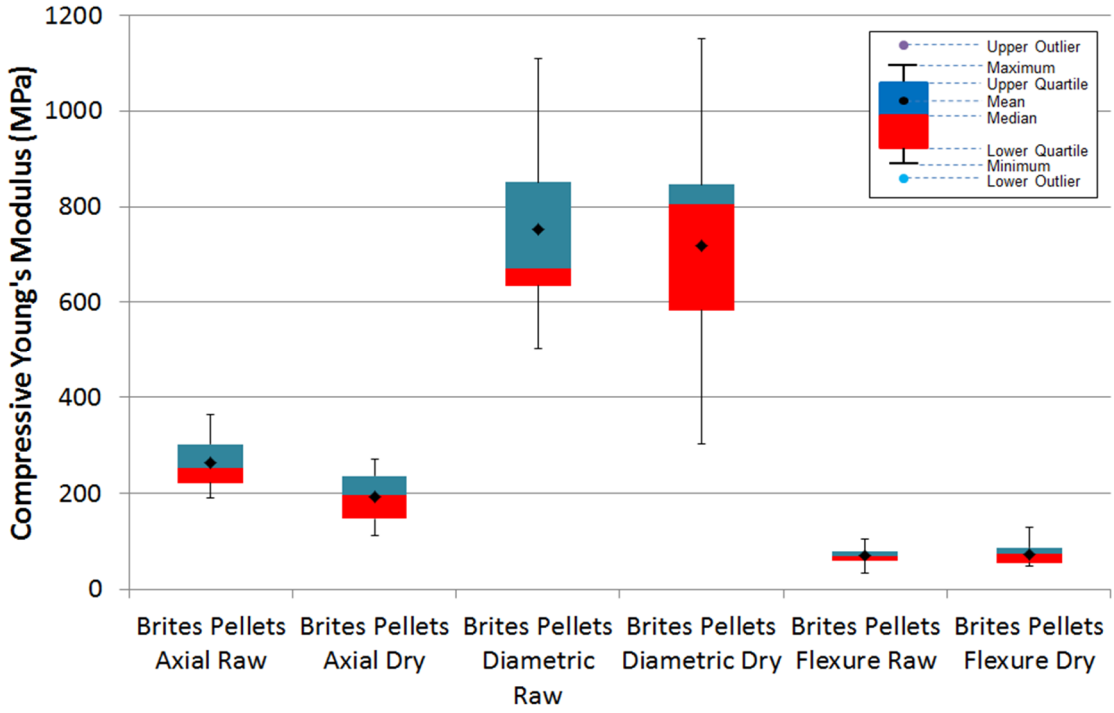


Figure A.2 – Quasi-Static Compressive Young's Modulus for Raw and Dry White wood Pellets in Axial, Diametric and Flexure Orientations

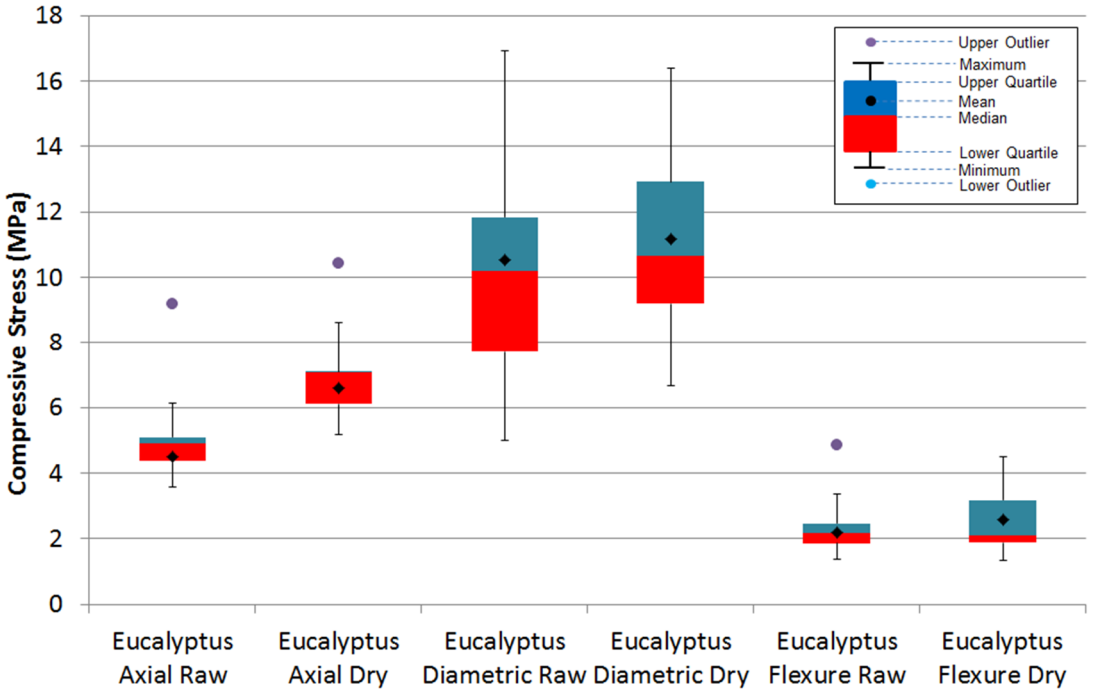


Figure A.3 – Quasi-Static Compressive Stress for Raw and Dry Eucalyptus Pellets in Axial, Diametric and Flexure Orientations

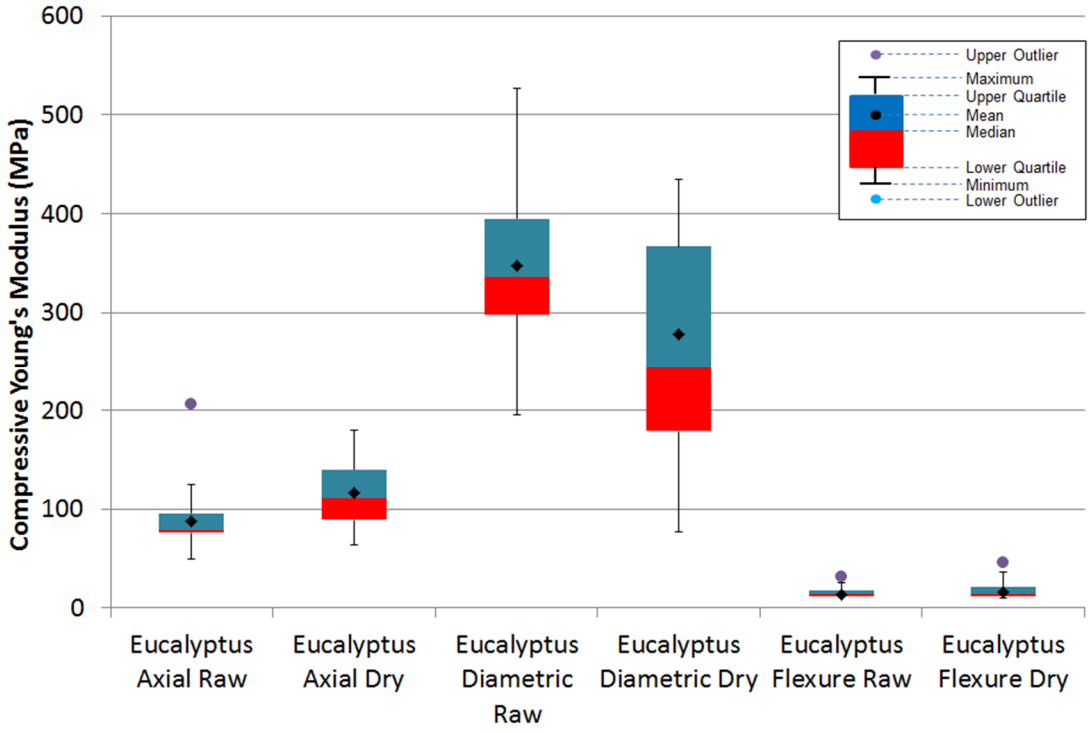


Figure A.4 – Quasi-Static Compressive Young's Modulus for Raw and Dry Eucalypts Pellets in Axial, Diametric and Flexure Orientations

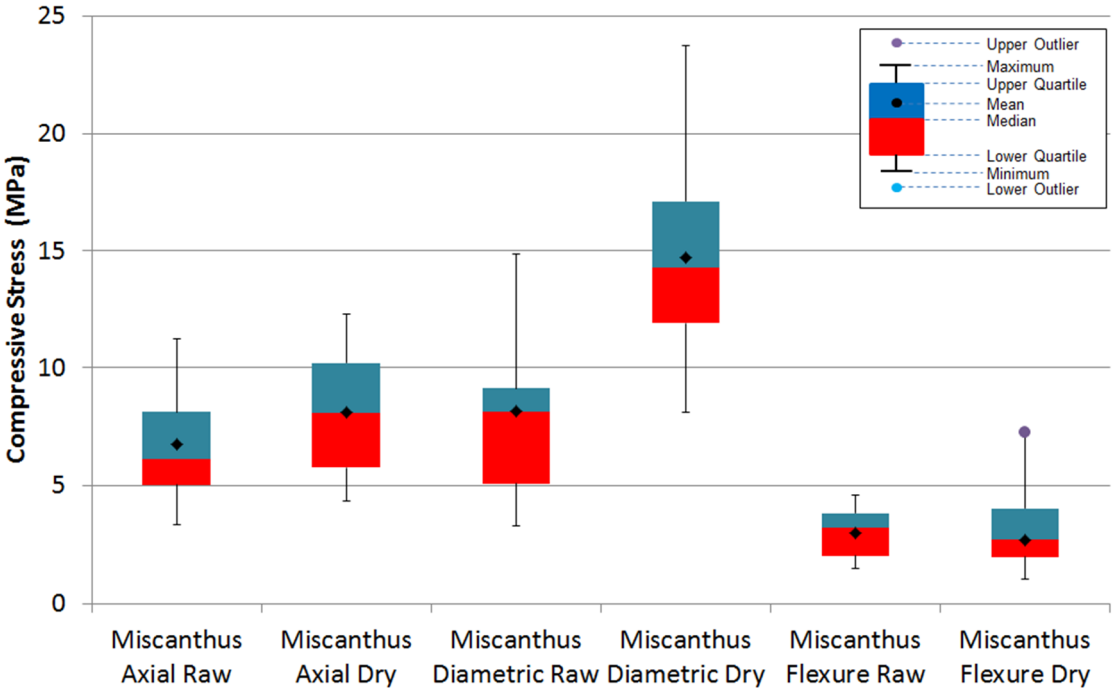


Figure A.5 – Quasi-Static Compressive Stress for Raw and Dry Miscanthus Pellets in Axial, Diametric and Flexure Orientations

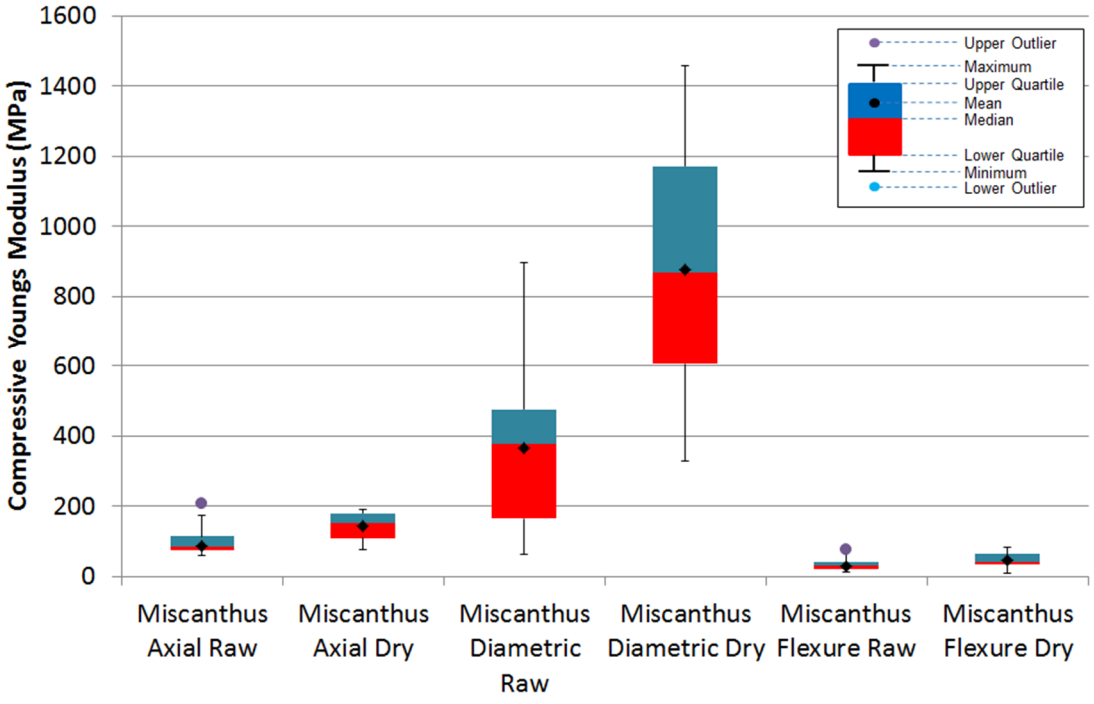


Figure A.6 – Quasi-Static Compressive Young's Modulus for Raw and Dry Miscanthus Pellets in Axial, Diametric and Flexure Orientations

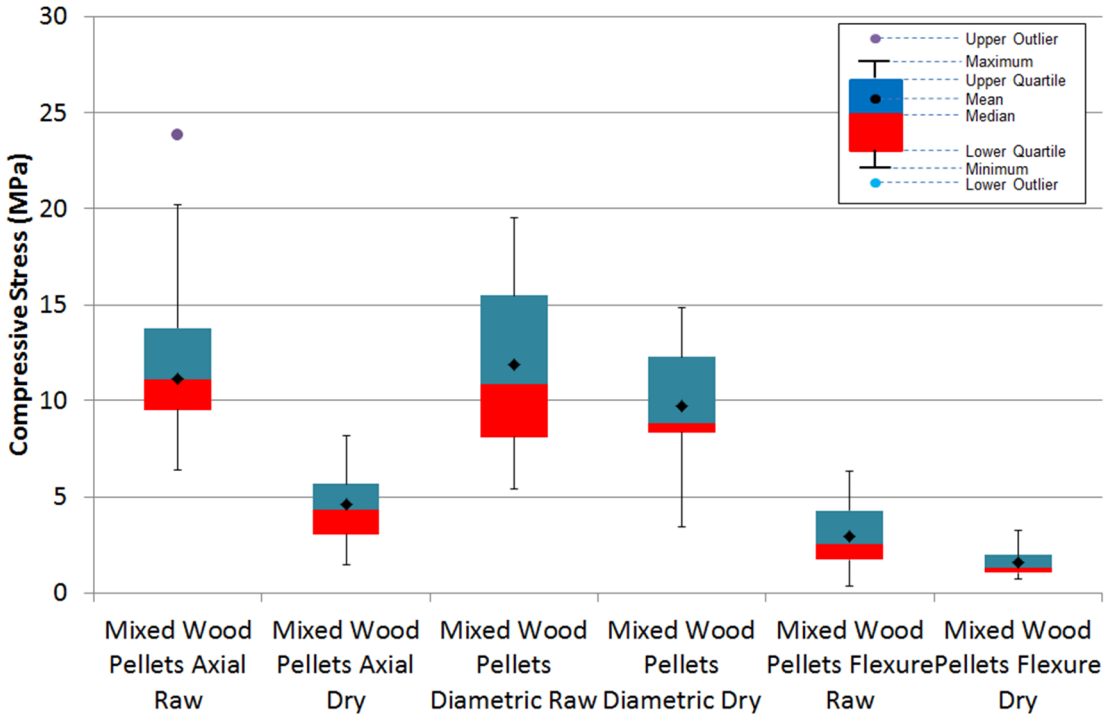


Figure A.7 – Quasi-Static Compressive Stress for Raw and Dry Mixed Wood Pellets in Axial, Diametric and Flexure Orientations

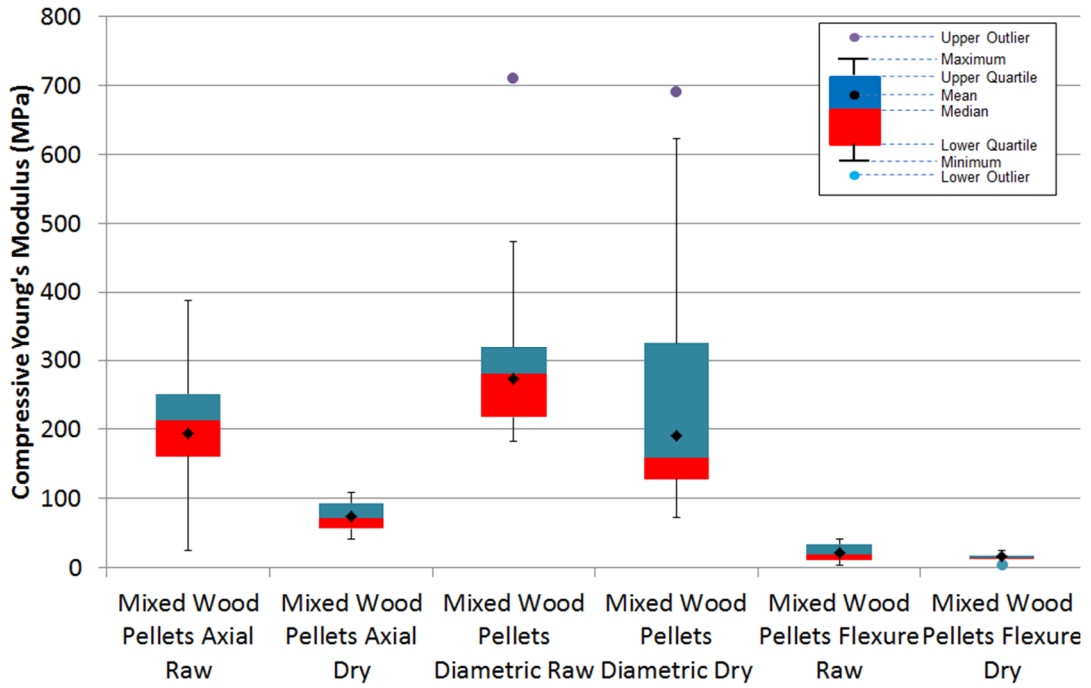


Figure A.8 – Quasi-Static Compressive Young's Modulus for Raw and Dry Mixed Wood Pellets in Axial, Diametric and Flexure Orientations

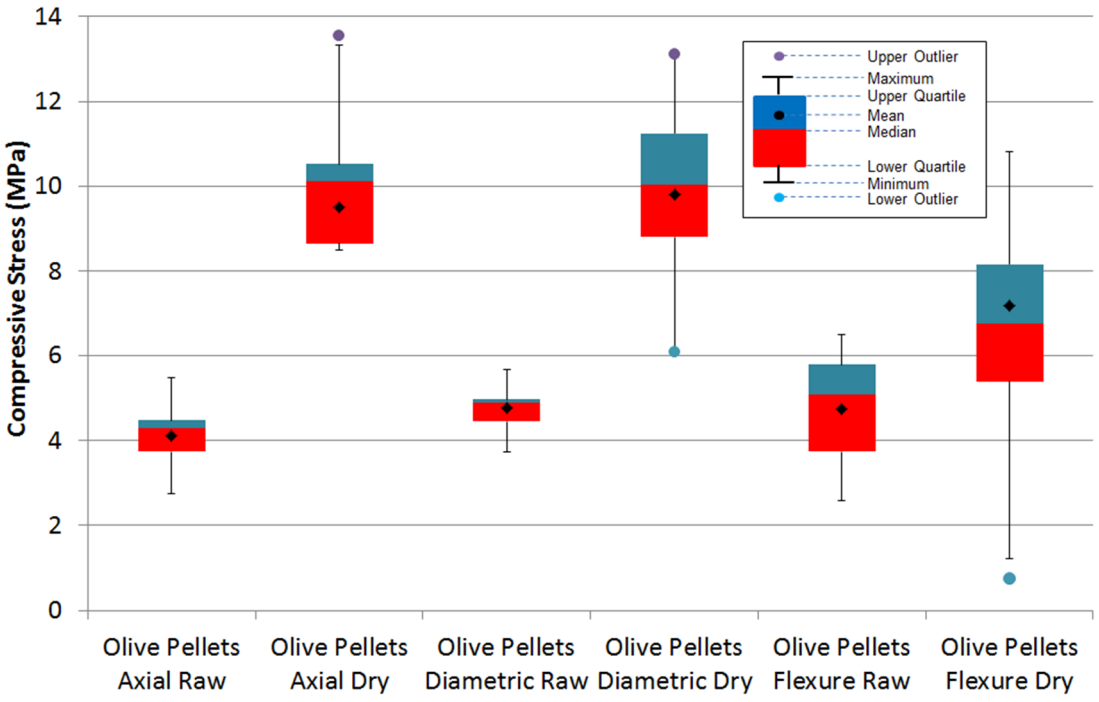


Figure A.9 – Quasi-Static Compressive Stress for Raw and Dry Olive Pellets in Axial, Diametric and Flexure Orientations

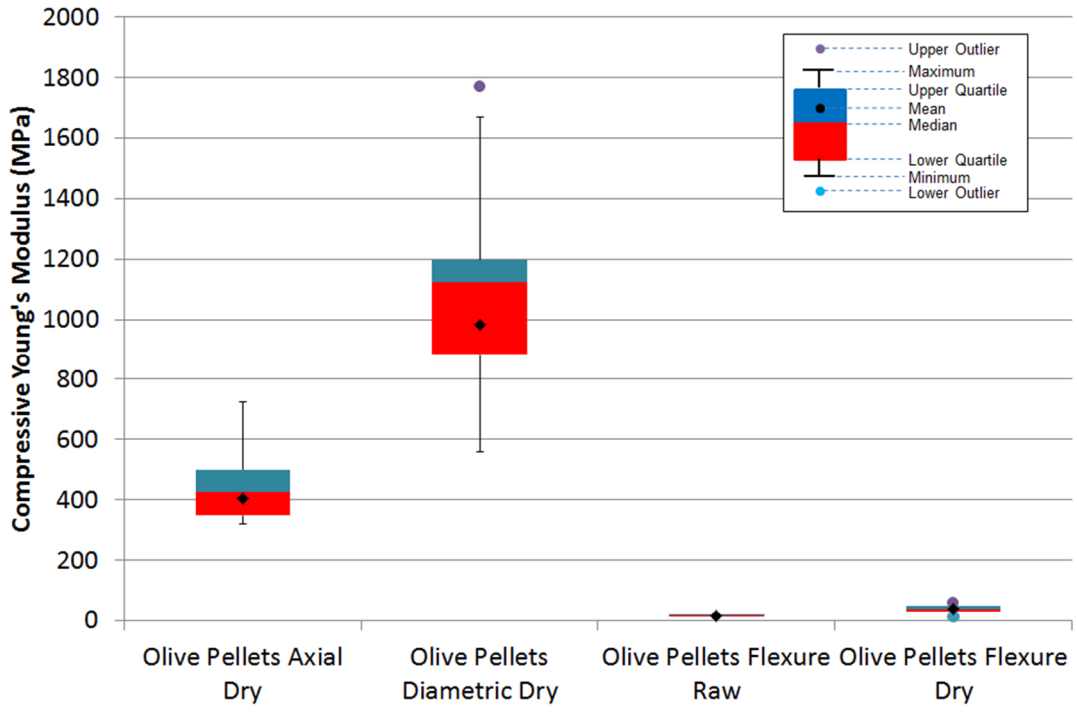


Figure A.10 – Quasi-Static Compressive Young's Modulus for Raw and Dry Olive Pellets in Axial, Diametric and Flexure Orientations

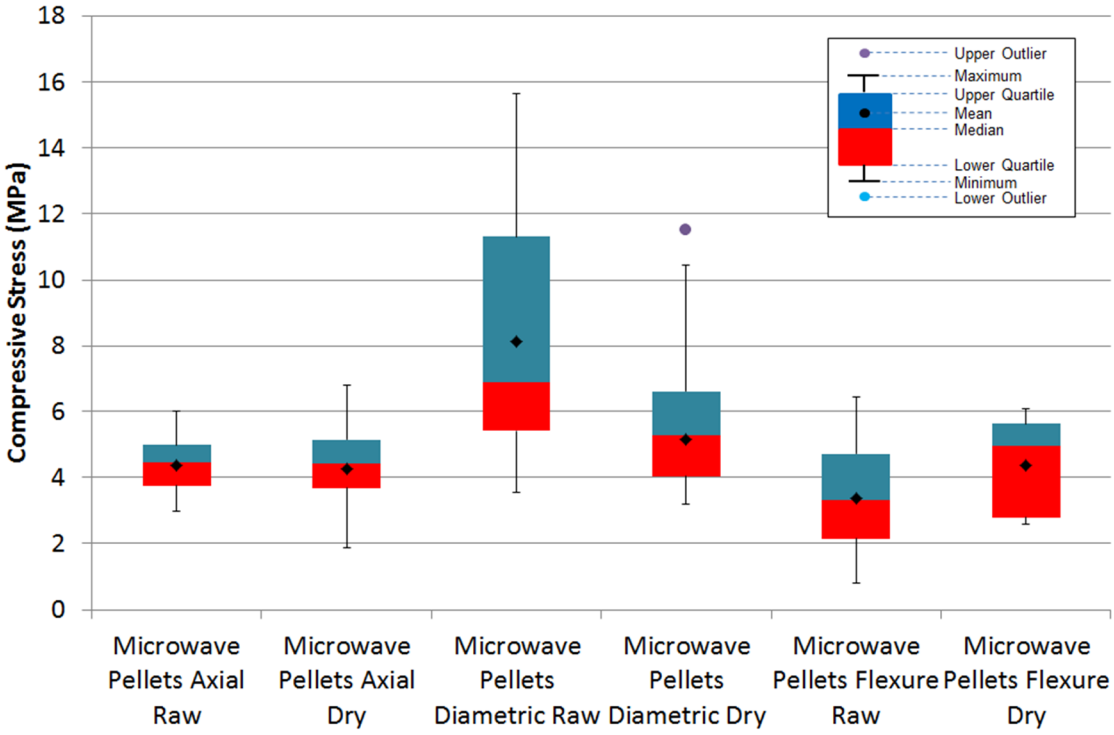


Figure A.11 – Quasi-Static Compressive Stress for Raw and Dry Microwave Pellets in Axial, Diametric and Flexure Orientations

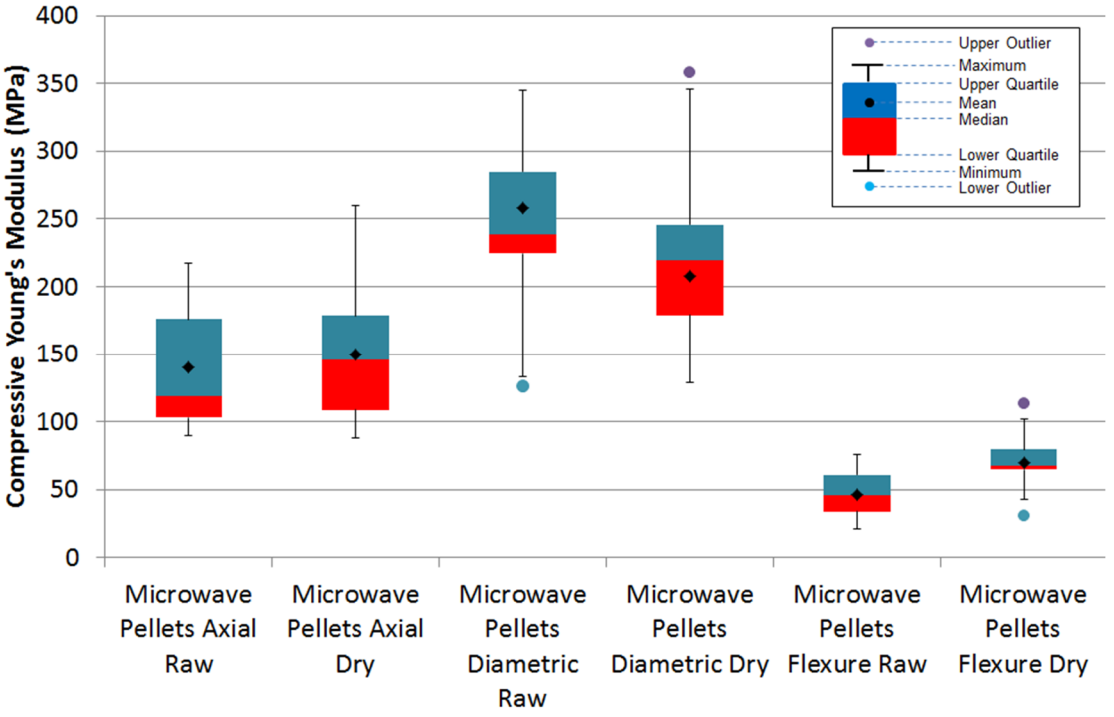


Figure A.12 – Quasi-Static Compressive Young's Modulus for Raw and Dry Microwave Pellets in Axial, Diametric and Flexure Orientations

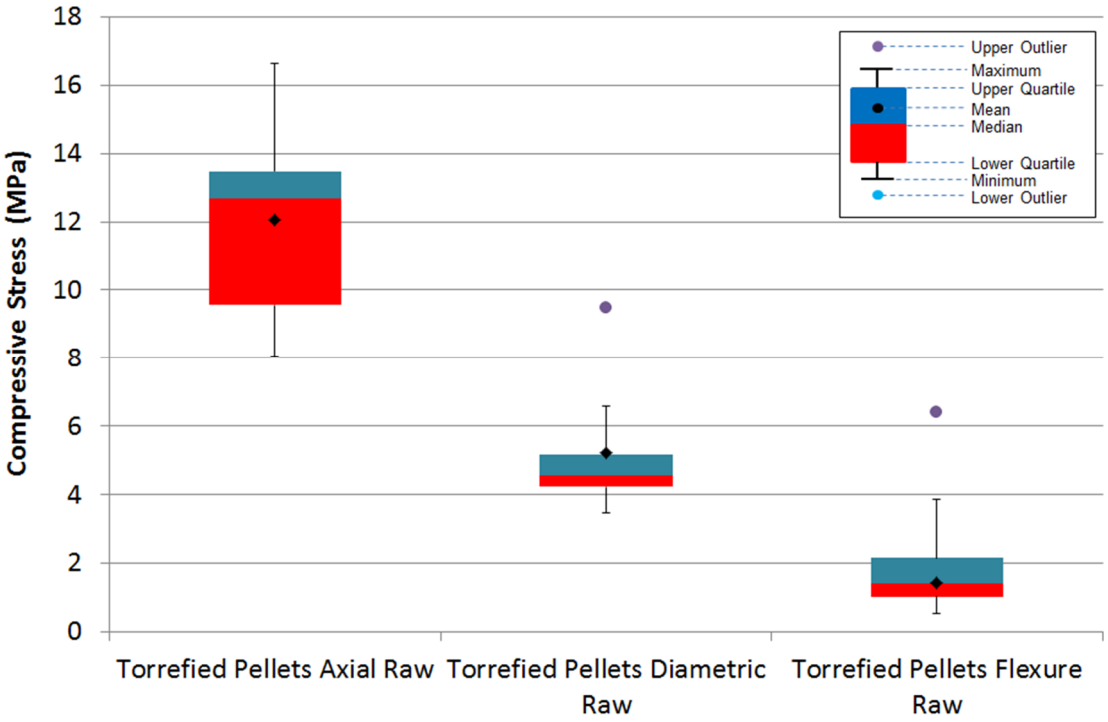


Figure A.13 – Quasi-Static Compressive Stress for Raw Torrefied Pellets in Axial, Diametric and Flexure Orientations

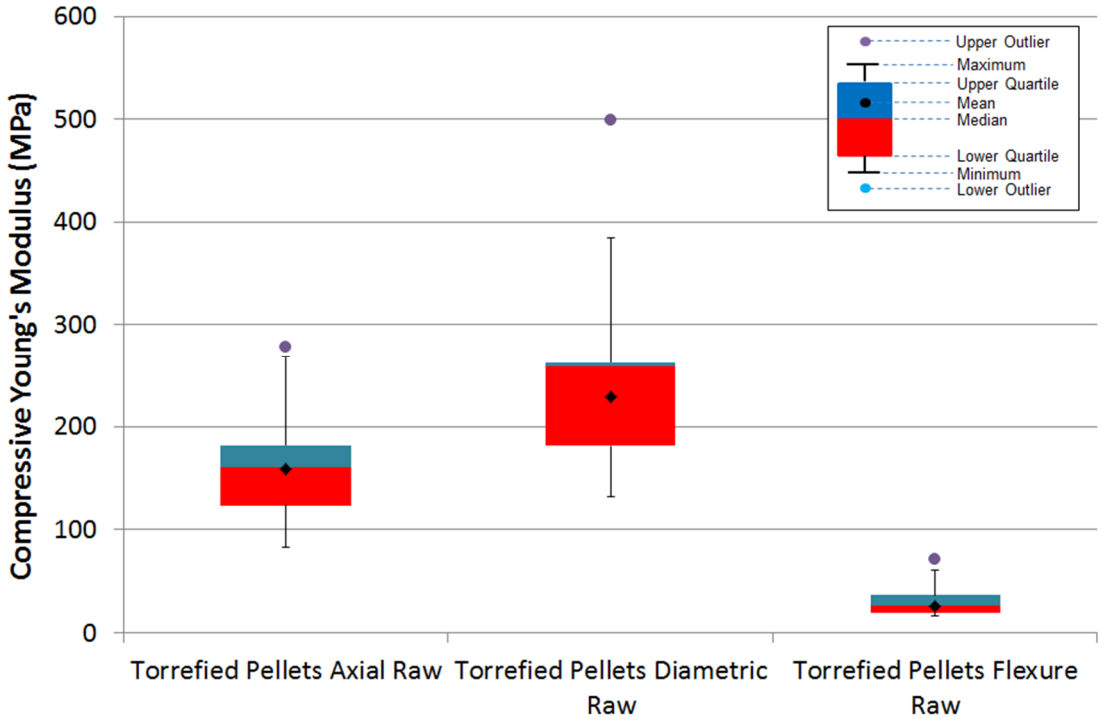


Figure A.14 – Quasi-Static Compressive Young's Modulus for Raw Torrefied Pellets in Axial, Diametric and Flexure Orientations

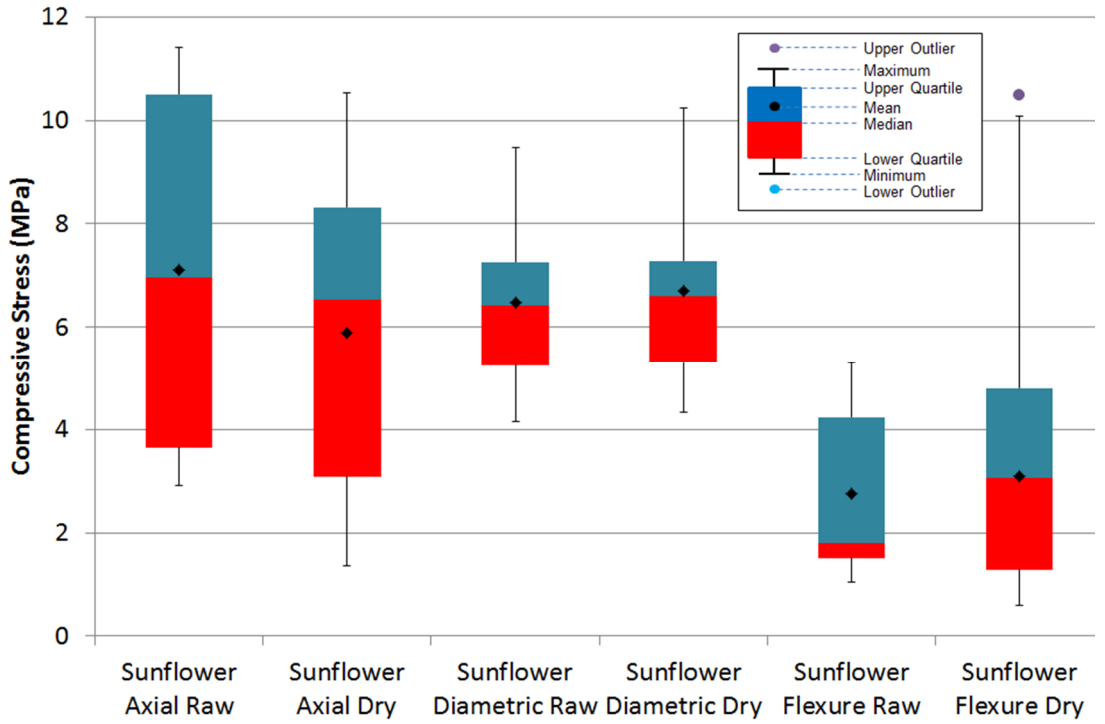


Figure A.15 – Quasi-Static Compressive Stress for Raw and Dry Sunflower Pellets in Axial, Diametric and Flexure Orientations

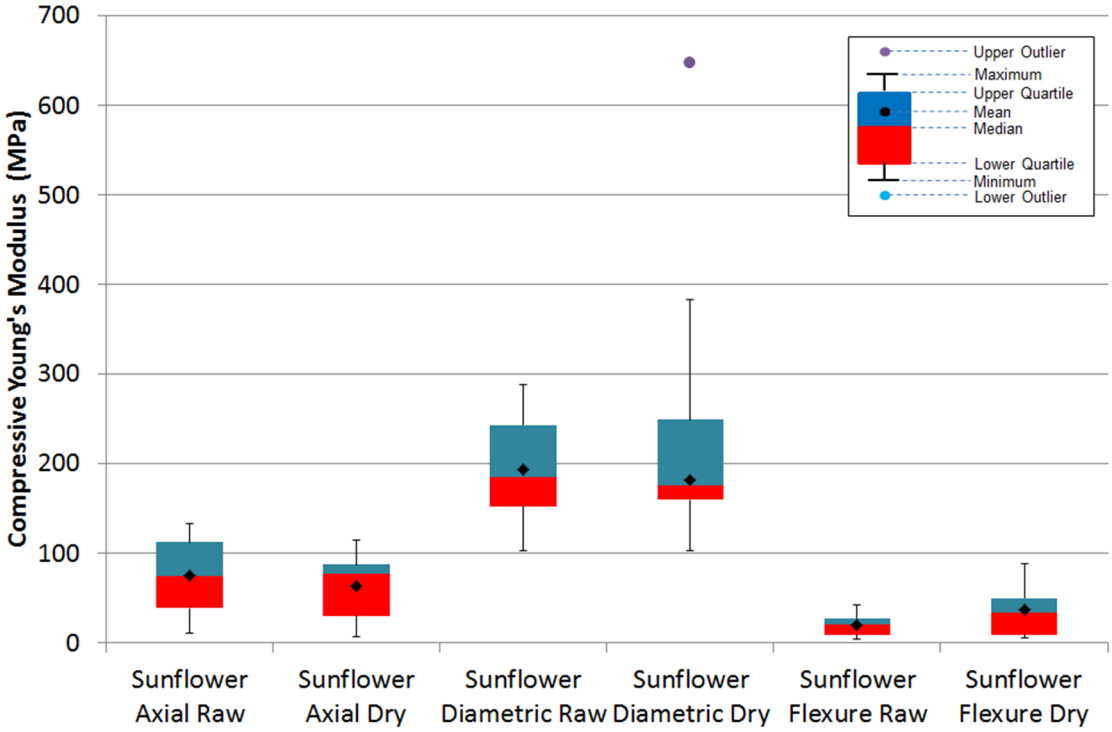


Figure A.16 – Quasi-Static Compressive Young's Modulus for Raw and Dry Sunflower Pellets in Axial, Diametric and Flexure Orientations

Appendix B – Mill Optimisation Regression Data

Table B.1 – Data Used in Planetary Ball Milling Regression Models

Speed (RPM)	Volume (ml)	Energy Input (kJ)	Specific Energy Consumption Rate (kJ/kg.s)	Rosin-Rammler Data			
				d' (µm)	n	R^2	Q_{80} (µm)
200	100	0.1	0.29	1765	0.97	0.999	2878
200	100	0.1	0.29	2614	0.96	0.999	4289
200	100	0.1	0.29	1634	0.98	0.999	2658
200	100	0.5	0.19	1361	1.12	1	2082
200	100	0.5	0.16	1089	1.07	0.999	1702
200	100	0.5	0.17	1152	1.06	0.999	1803
200	100	1	0.18	1064	1.07	0.999	1660
200	100	1	0.16	920	1.07	0.999	1435
200	100	1	0.18	1024	1.07	0.999	1598
200	100	2	0.19	747	1.04	0.998	1179
200	100	2	0.20	776	1.06	0.998	1217
200	100	2	0.19	816	1.11	0.999	1254
200	100	4	0.20	587	0.99	0.996	951
200	100	4	0.20	553	1.00	0.996	889
200	100	4	0.19	522	1.00	0.996	839
300	100	0.1	0.36	1781	1.06	1	2787
300	100	0.1	0.29	1854	0.99	0.999	3004
300	100	0.1	0.29	1414	1.00	0.999	2272
300	100	0.5	0.55	1398	1.21	1	2069
300	100	0.5	0.48	1070	1.09	0.999	1654
300	100	0.5	0.55	1091	1.05	0.999	1717
300	100	1	0.65	881	1.09	0.999	1365
300	100	1	0.68	708	1.13	0.999	1079
300	100	1	0.62	999	1.15	1	1513
300	100	2	0.62	720	1.09	0.999	1113
300	100	2	0.57	726	1.11	0.999	1114
300	100	2	0.55	657	1.08	0.998	1023
300	100	4	0.68	578	1.03	0.997	917
300	100	4	0.64	544	1.04	0.997	859
300	100	4	0.63	510	1.05	0.997	801
300	100	8	0.57	380	1.08	0.995	591
300	100	8	0.52	381	1.17	0.996	572
300	100	8	0.52	369	1.10	0.997	568
400	100	0.1	0.29	1252	1.07	1	1955
400	100	0.1	0.24	1521	1.10	1	2344

Speed (RPM)	Volume (ml)	Energy Input (kJ)	Specific Energy Consumption Rate (kJ/kg.s)	d' (µm)	n	R^2	Q_{80} (µm)
400	100	0.1	0.29	1391	1.13	1	2117
400	100	0.5	0.89	1197	1.11	1	1840
400	100	0.5	0.89	1116	1.04	0.999	1766
400	100	0.5	0.79	964	1.06	0.999	1513
400	100	1	1.19	1031	1.15	1	1560
400	100	1	1.19	929	1.19	1	1386
400	100	1	1.10	928	1.11	0.999	1426
400	100	2	1.30	671	1.12	0.999	1027
400	100	2	1.36	666	1.10	0.999	1027
400	100	2	1.36	620	1.07	0.998	968
400	100	4	1.63	505	1.03	0.997	802
400	100	4	1.43	586	1.09	0.998	906
400	100	4	1.43	552	1.09	0.998	856
400	100	8	1.47	413	1.07	0.998	645
400	100	8	1.47	422	1.05	0.997	664
400	100	8	1.50	395	1.09	0.997	611
500	100	0.1	0.24	1331	1.20	1	1980
500	100	0.1	0.24	1330	1.11	1	2044
500	100	0.1	0.24	1158	1.03	0.999	1843
500	100	0.5	0.89	1445	1.09	1	2235
500	100	0.5	0.79	839	1.07	0.999	1309
500	100	0.5	0.79	1030	0.99	0.999	1665
500	100	1	1.43	1062	1.10	1	1640
500	100	1	1.30	1293	1.12	1	1977
500	100	1	1.59	1059	1.01	0.999	1694
500	100	2	1.91	731	1.02	0.999	1163
500	100	2	2.04	674	1.04	0.999	1068
500	100	2	2.04	779	1.01	0.999	1247
500	100	4	2.60	649	1.00	0.998	1042
500	100	4	2.38	746	1.11	0.999	1146
500	100	4	2.38	687	1.14	1	1044
500	100	8	2.54	742	1.07	0.999	1158
500	100	8	2.54	554	1.10	0.999	854
500	100	8	2.43	678	1.07	0.999	1059
600	100	0.1	0.24	1277	1.16	1	1926
600	100	0.1	0.16	1063	1.16	1	1602
600	100	0.1	0.20	905	1.08	0.999	1409
600	100	0.5	0.79	819	1.08	0.999	1273

Speed (RPM)	Volume (ml)	Energy Input (kJ)	Specific Energy Consumption Rate (kJ/kg.s)	d' (µm)	n	R^2	Q_{80} (µm)
600	100	0.5	0.89	699	1.07	0.999	1089
600	100	0.5	0.89	955	1.17	1	1437
600	100	1	1.30	793	1.12	0.999	1214
600	100	1	1.43	878	1.10	0.999	1351
600	100	1	1.59	785	1.11	0.999	1205
600	100	2	2.38	673	1.06	0.999	1057
600	100	2	2.38	689	1.06	0.999	1082
600	100	2	2.20	804	1.11	0.999	1234
600	100	4	3.18	988	1.12	1	1512
600	100	4	3.36	755	1.16	1	1168
600	100	4	3.18	800	1.14	1	1212
600	100	8	3.94	709	1.13	0.999	1081
600	100	8	3.94	753	1.15	0.999	1139
600	100	8	4.08	551	1.12	0.999	842
400	150	0.1	0.24	1487	1.09	1	2298
400	150	0.1	0.16	1281	1.06	0.999	2010
400	150	0.1	0.19	1222	1.03	0.999	1942
400	150	0.5	0.60	1517	1.10	1	2337
400	150	0.5	0.53	1303	1.11	1	2003
400	150	0.5	0.60	1167	1.11	1	1794
400	150	1	0.73	1062	1.10	1	1638
400	150	1	0.79	968	1.08	0.999	1506
400	150	1	0.73	1035	1.15	1	1564
400	150	2	0.87	829	1.08	0.999	1285
400	150	2	0.73	812	1.09	0.999	1257
400	150	2	0.73	808	1.09	1	1248
400	150	4	0.76	629	1.03	0.999	997
400	150	4	0.73	607	1.01	0.998	971
400	150	4	0.71	598	1.03	0.999	949
400	150	8	0.65	706	1.09	0.999	1094
400	150	8	0.63	667	1.09	0.999	1035
400	150	8	0.61	805	1.09	1	1248
200	200	0.1	0.18	2907	0.92	0.998	4876
200	200	0.1	0.05	1814	0.96	0.999	2976
200	200	0.1	0.03	1584	0.92	0.999	2657
200	200	0.5	0.03	1428	1.04	0.999	2254
200	200	0.5	0.09	1349	1.03	0.999	2142
200	200	0.5	0.09	1579	1.13	1	2402

Speed (RPM)	Volume (ml)	Energy Input (kJ)	Specific Energy Consumption Rate (kJ/kg.s)	d' (µm)	n	R^2	Q_{80} (µm)
200	200	1	0.03	1083	1.04	0.999	1714
200	200	1	0.04	1114	1.14	1	1691
200	200	1	0.03	997	1.06	0.999	1560
200	200	2	0.04	1007	1.10	0.999	1550
200	200	2	0.04	996	1.04	0.998	1572
200	200	2	0.03	1031	1.04	0.998	1633
200	200	4	0.03	825	1.01	0.998	1322
200	200	4	0.02	837	1.06	0.998	1310
200	200	4	-	745	0.97	0.997	1217
300	200	0.1	0.14	2178	0.93	0.999	3642
300	200	0.1	0.12	1302	0.93	0.998	2173
300	200	0.1	0.09	1434	0.97	0.999	2340
300	200	0.5	0.17	1413	1.14	0.999	2143
300	200	0.5	0.17	1392	1.16	0.999	2095
300	200	0.5	0.14	1226	1.17	1	1843
300	200	1	0.20	1110	1.17	1	1666
300	200	1	0.16	1240	1.26	1	1812
300	200	1	0.15	1371	1.32	0.999	1968
300	200	2	0.14	827	1.21	1	1227
300	200	2	0.08	646	1.12	0.999	986
300	200	2	0.06	564	1.17	0.999	847
300	200	4	0.16	576	1.17	0.999	864
300	200	4	0.14	668	1.14	0.999	1016
300	200	4	0.12	644	1.10	0.999	991
300	200	8	0.14	506	1.22	0.999	749
300	200	8	0.12	573	1.16	0.999	865
300	200	8	0.12	688	1.13	0.999	1050
400	200	0.1	0.14	1704	1.03	1	2700
400	200	0.1	0.14	1625	1.00	0.999	2615
400	200	0.1	0.14	2007	1.08	1	3118
400	200	0.5	0.33	1324	1.14	0.999	2010
400	200	0.5	0.30	1276	1.08	0.999	1979
400	200	0.5	0.33	1455	1.18	0.999	2175
400	200	1	0.38	1109	1.15	1	1676
400	200	1	0.38	1187	1.14	0.999	1800
400	200	1	0.38	1050	1.12	0.999	1609
400	200	2	0.38	892	1.10	0.999	1374
400	200	2	0.36	929	1.13	0.999	1414

Speed (RPM)	Volume (ml)	Energy Input (kJ)	Specific Energy Consumption Rate (kJ/kg.s)	d' (µm)	n	R^2	Q_{80} (µm)
400	200	2	0.35	883	1.11	0.999	1357
400	200	4	0.34	847	1.17	1	1273
400	200	4	0.30	868	1.14	1	1318
400	200	4	0.28	1009	1.13	0.999	1539
400	200	8	0.31	845	1.12	0.999	1293
400	200	8	0.28	1240	1.07	1	1936
400	200	8	0.27	1262	1.20	0.999	1873
500	200	0.1	0.12	1647	1.11	1	2526
500	200	0.1	0.12	1388	1.09	1	2146
500	200	0.1	0.12	1572	1.14	0.999	2387
500	200	0.5	0.40	1147	1.10	0.999	1769
500	200	0.5	0.45	1164	1.08	0.999	1806
500	200	0.5	0.40	1368	1.14	0.999	2079
500	200	1	0.71	929	1.08	0.999	1442
500	200	1	0.60	1292	1.20	1	1922
500	200	1	0.60	952	1.07	0.999	1488
500	200	2	0.84	1255	1.19	0.999	1871
500	200	2	0.89	1109	1.13	0.999	1690
500	200	2	-	1035	1.11	0.999	1591
500	200	4	0.87	716	1.06	0.999	1121
500	200	4	0.79	940	1.08	0.999	1464
500	200	4	0.87	776	1.02	0.999	1237
500	200	8	0.79	848	1.08	0.999	1320
500	200	8	0.67	1136	1.14	0.999	1724
500	200	8	0.77	864	1.15	0.999	1310
600	200	0.1	0.10	1125	1.09	0.999	1745
600	200	0.1	0.09	1215	1.04	0.999	1916
600	200	0.1	0.09	1443	1.13	0.999	2202
600	200	0.5	0.45	1234	1.09	0.999	1911
600	200	0.5	0.40	1097	1.03	0.999	1738
600	200	0.5	0.36	1325	1.12	1	2028
600	200	1	0.65	1270	1.11	0.999	1950
600	200	1	0.71	1164	1.06	0.999	1821
600	200	1	0.65	1089	1.08	0.999	1692
600	200	2	0.95	1104	1.08	0.999	1716
600	200	2	0.95	935	1.05	0.999	1468
600	200	2	0.95	1078	1.10	0.999	1665
600	200	4	1.14	1356	1.18	0.999	2032

Speed (RPM)	Volume (ml)	Energy Input (kJ)	Specific Energy Consumption Rate (kJ/kg.s)	d' (µm)	n	R^2	Q_{80} (µm)
600	200	4	1.10	1127	1.16	1	1697
600	200	4	1.19	1005	1.12	0.999	1539
600	200	8	1.39	1150	1.14	0.999	1747
600	200	8	1.22	1285	1.16	0.999	1939
600	200	8	1.12	1160	1.16	1	1749

Table B.2 – Specific Effective Energy Consumption (E_e) and % Mass Holdup for varying Mill Speed, Feed Rates, and Screen Sizes for the Cutting Mill (Unusual Data Points Removed)

Speed (RPM)	Feed (kg/s)	Screen (mm)	Ee (kWh/T)	% Mass Holdup
700	0.0006	4	-	0.9
700	0.0013	4	9	0.09
700	0.0012	4	8	0.92
700	0.0005	1.5	19	-
700	0.0013	1.5	-	4.8
700	0.0029	4	12	1.18
700	0.0025	1.5	18	-
700	0.0021	4	10	-
700	0.0017	4	9	1.46
700	0.0019	4	11	0.62
700	0.0019	4	11	0.95
700	0.0013	4	-	0.97
1000	0.0011	4	19	0.81
1000	0.0012	4	18	0.73
1000	0.0026	4	15	1.6
1000	0.0025	4	15	0.9
1000	0.0011	1.5	34	3.92
1000	0.0012	1.5	28	5.23
1000	0.0028	1.5	29	16.52
1000	0.0027	1.5	29	15.86
1500	0.0005	4	54	-
1500	0.0005	4	-	0.85
1500	0.0005	4	55	0.82
1500	0.0005	4	48	1.35
1500	0.0014	4	30	-
1500	0.0010	4	35	0.88
1500	0.0006	1.5	-	4.13
1500	0.0014	1.5	-	10.11
1500	0.0012	4	34	1.37
1500	0.0009	4	26	1.41
1500	0.0027	4	23	2.24
1500	0.0025	4	21	2.45
1500	0.0011	1.5	49	7.78
1500	0.0012	1.5	43	7.86
1500	0.0027	1.5	37	18.8
1500	0.0026	1.5	36	18.06

Speed (RPM)	Feed (kg/s)	Screen (mm)	Ee (kWh/T)	% Mass Holdup
1800	0.0013	4	21	0.8
1800	0.0011	4	-	0.44
1800	0.0028	4	23	3.75
1800	0.0027	4	22	3.13
1800	0.0011	1.5	-	9.35
1800	0.0012	1.5	36	8.69
1800	0.0026	1.5	39	20.84
1800	0.0027	1.5	36	21.71
1800	0.0012	4	24	-
1800	0.0026	4	25	2.88
1800	0.0013	1.5	41	9.66
1800	0.0026	1.5	40	21.17
2200	0.0005	4	-	0.21
2200	0.0006	4	-	0.93
2200	0.0026	4	23	-
2200	0.0013	4	38	1.35
2200	0.0007	1.5	-	5.36
2200	0.0007	1.5	76	5.86
2200	0.0011	15	-	8.8
2200	0.0012	1.5	-	10.37
2200	0.0012	4	-	1.24
2200	0.0026	4	24	3.87
2200	0.0012	1.5	-	11.26
2200	0.0026	1.5	39	-
2500	0.0013	4	27	1.83
2500	0.0027	4	27	-
2500	0.0012	1.5	45	12.63
2500	0.0027	1.5	42	-
2500	0.0013	4	-	1.53
2500	0.0026	4	-	3.92
2500	0.0012	1.5	-	12.75
2500	0.0026	1.5	52	-
3000	0.0006	4	75	0.59
3000	0.0011	4	56	1.72
3000	0.0028	4	45	5.18
3000	0.0006	1.5	83	8.93
3000	0.0009	1.5	69	-

Table B.3 – Rosin-Rammler Characteristic Diameter (d'), Rosin-Rammler Distribution Parameter (n), and Rosin-Rammler Equation Coefficient of Determination (R^2) for varying Mill Speed, Feed Rates, and Screen Sizes for the Cutting Mill

Speed (RPM)	Feed Rate (kg/s)	Screen (mm)	d' (mm)	n	R^2
700	0.0006	4	1.27	2.46	0.999
700	0.0013	4	1.17	2.31	1.000
700	0.0012	4	1.17	2.31	1.000
700	0.0005	1.5	0.82	2.61	0.999
700	0.0012	1.5	0.86	2.50	0.998
700	0.0028	4	1.34	2.18	1.000
700	0.0025	1.5	1.00	2.25	0.999
1500	0.0005	4	1.22	2.48	0.997
1500	0.0014	4	1.16	2.37	0.997
1500	0.0010	4	1.16	2.37	0.997
1500	0.0006	1.5	0.73	2.36	0.998
1500	0.0010	1.5	0.75	2.30	0.999
1500	0.0014	1.5	0.75	2.34	0.999
1500	0.0025	4	1.13	2.09	0.998
2200	0.0005	4	1.13	2.38	1.000
2200	0.0013	4	1.06	2.29	1.000
2200	0.0007	1.5	1.13	2.38	1.000
2200	0.0012	1.5	0.77	2.31	0.999
2200	0.0024	4	1.06	2.16	0.999
2200	0.0026	1.5	0.83	2.11	0.999
3000	0.0006	4	1.09	2.15	0.998
3000	0.0011	4	1.06	2.06	0.998
3000	0.0028	4	0.98	1.89	0.998
3000	0.0006	1.5	0.72	2.11	0.997
3000	0.0009	1.5	0.69	2.07	0.997
3000	0.0023	1.5	0.64	1.96	0.997

Appendix C – Ring-Roller Mill Pressure & Temperature Data

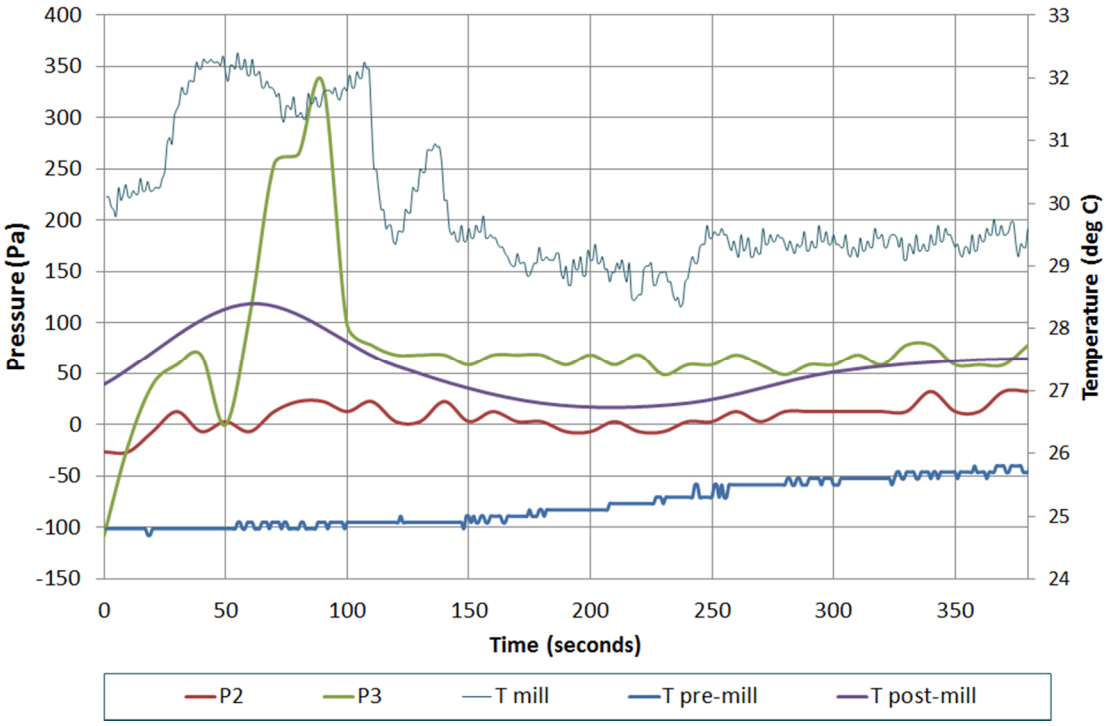


Figure C.1 – La Loma Mill Inlet, Chamber, and Outlet Temperatures and Inlet (P2) and Outlet (P3) Differential Pressures

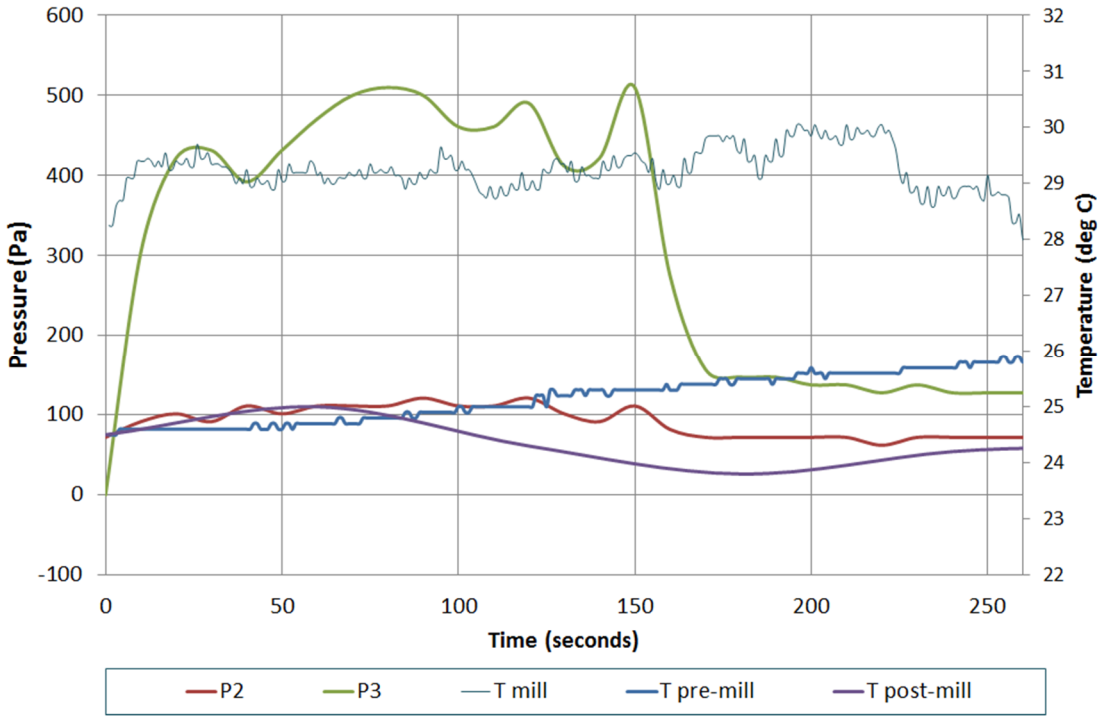


Figure C.2 – Sunflower Mill Inlet, Chamber, and Outlet Temperatures and Inlet (P2) and Outlet (P3) Differential Pressures

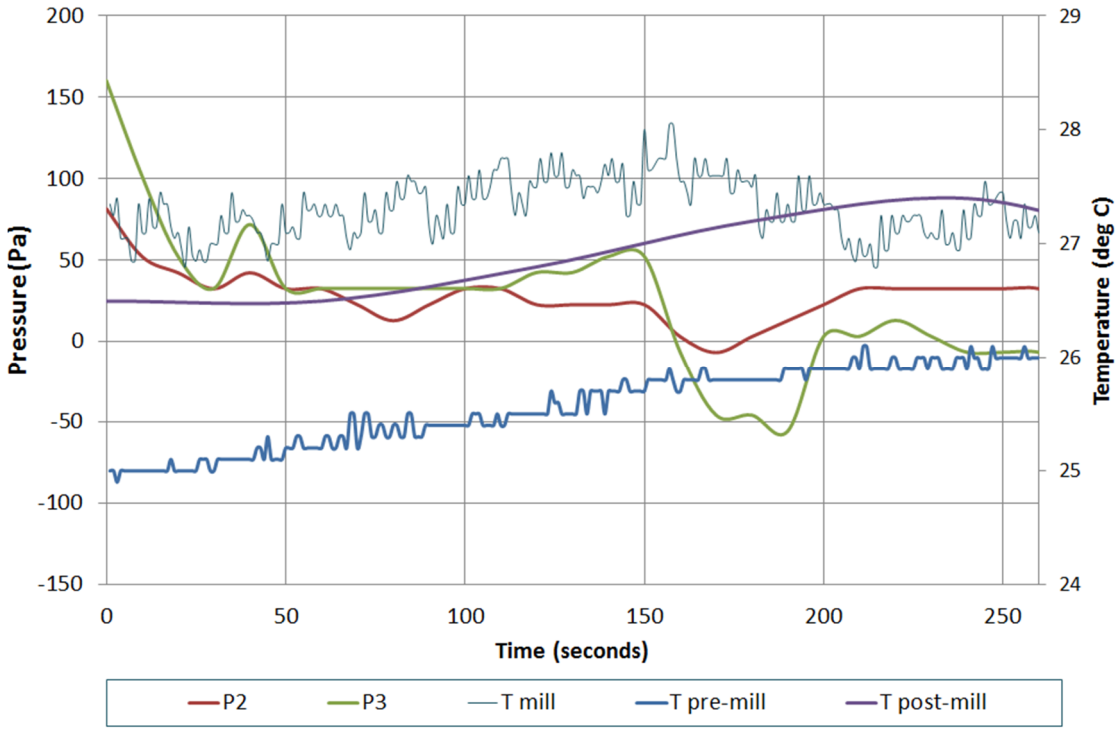


Figure C.3 – Steam exploded Mill Inlet, Chamber, and Outlet Temperatures and Inlet (P2) and Outlet (P3) Differential Pressures

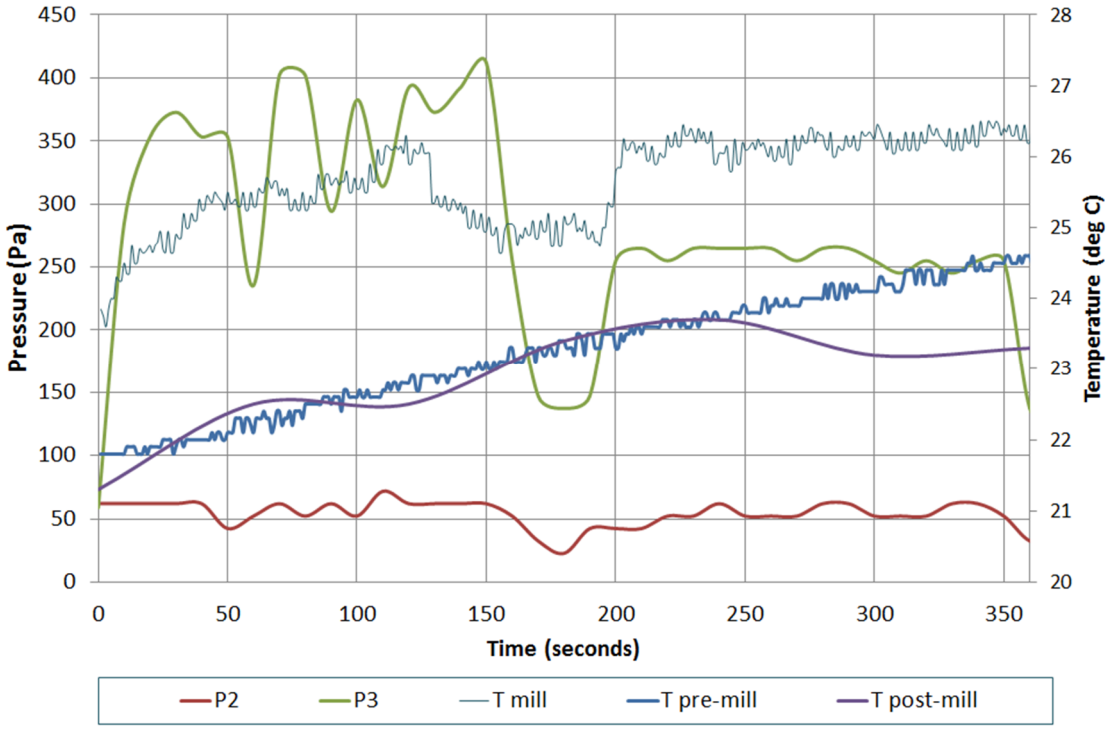


Figure C.4 – Miscanthus Mill Inlet, Chamber, and Outlet Temperatures and Inlet (P2) and Outlet (P3) Differential Pressures

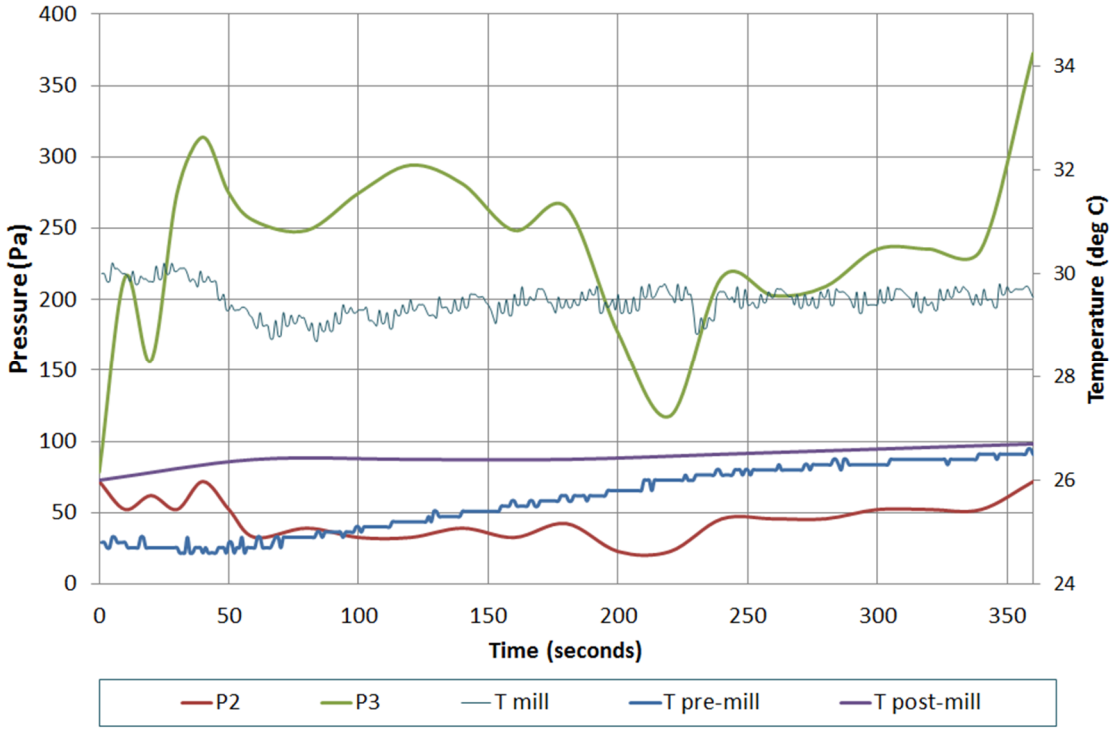


Figure C.5 – Eucalyptus Mill Inlet, Chamber, and Outlet Temperatures and Inlet (P2) and Outlet (P3) Differential Pressures